IMPERIAL

The Role of Lubricant Viscosity in Optimising Electric Vehicle Transmission Efficiency and Reliability

PhD Thesis

Duncan Alexander John MacLaren

Tribology Group
Department of Mechanical Engineering
Imperial College London

February 2025

71149 words

Abstract

Electric Vehicles (EVs) are now the most promising solution for sustainable road transport. The rapid growth of this emerging technology means there is presently considerable scope to optimise drivetrain efficiency and reliability. EV transmissions must transmit high torques at low speeds, while also operating efficiently at very high speeds, and lubricant viscosity is crucial in balancing these competing requirements.

Efficiency depends on both load-dependent (including traction) and load-independent (primarily oil churning) losses. A test rig is developed to measure churning losses in-situ in a popular EV drive-unit, and the influence of speed, oil volume and oil viscosity are examined. The relationship between churning loss and fluid viscosity in the range $4 - 200$ cSt is found to be nonmonotonic, and relatively weak compared to the influence of speed and oil fill. Measurements of total drive unit efficiency using a dynamometer are also presented.

Elastohydrodynamic traction and film thickness, which influence both efficiency and reliability, are measured simultaneously at entrainment speeds up to 20 m/s using a new optical tribometer developed during this study. Measurements are obtained for 10 fluids representing 4 API groups, and compared to existing thermal EHD film thickness predictions. A novel approach to film thickness measurement using colorimetric interferometry is also proposed, using a context-aware colour matching procedure which addresses the fringe-order ambiguity problem.

A selection of candidate transmission lubricants including a water-based formulation, are compared using a ball-on-disc contrarotation scuffing method, and a triple-disc micropitting rig. The formulated fluids are found to induce much more rapid micropitting than their unadditivised base oils, which instead rapidly fail by scuffing. In both tests with the water-based fluid, mild wear outcompetes scuffing and micropitting.

These data elucidate the influence of lubricant formulation on these hard-to-model phenomena, contributing to future holistic optimisation of EV fluid formulation and transmission architecture for efficiency and reliability.

Acknowledgements

It's not about the destination, it's about the journey.

I would like to thank Eliane, Chiara, David, Roland, Tom, Sarah and Marie-Louise, who walked the journey with me. For his support, companionship and excellent driving, I owe a lot to Joseph Shore, thanks Joe.

For their generosity and patience towards two Brits in a strange country, heartfelt thanks are extended to James Brown, Lily Xiurong Chen, Amy Ross, Tom Sikora, Sheresa Nelson, Tim Caudill, Josh Cooley, Kevin Figgatt, Amol Sawant, Jonathan Cales, and Christie Mckenzie. The support of Valvoline Inc., and in particular Fran Lockwood, Ning Ren, Anant Kolekar and Roger England, without whom this project would not have been possible, is gratefully acknowledged.

The immense kindness and support of Tom Welham, Clive Hamer, John Hutchinson, Matt Smeeth, Joanne Medhurst and Ben Wainwright from PCS Instruments, and Marc Ingram of Ingram Tribology, have been instrumental both technically and personally, I couldn't have done it without them. I owe a huge debt of gratitude to Chrissy, Kate, Naomi, Andi and Soraia, who at various times picked me up and kept me going.

It has been a joy to work with Parker LaMascus and Robert Carpick, whose enthusiasm for and partnership in work of which I am really proud has kept the spark alive. I have had the privilege of deeply interesting technical discussions with Suhaib Ardah, Benjamin Collard, Ammad Yousuf, Haochen Yao, and Jason (Jie Zhang), whose intellectual acuity I hugely admire. Many thanks are due also to my inspiring colleagues in the Tribology group at Imperial, particularly Luli, Jack, Yap, Pawel R, Pawel O, Rachel, Tristan, Janet and Catherine.

To Tom Reddyhoff, Janet Wong, Marc Masen and Daniele Dini, who invested in me even though they didn't have to, I am deeply grateful.

Finally I would like to thank my supervisor Amir Kadiric and my second supervisor Hugh Spikes, whose wisdom and generosity have enabled this work, and who have consistently encouraged me to broaden my horizons.

Statement of Originality

I confirm that the work presented in this thesis is my own and original, and that all other contributions and relevant previous works discussed herein are referenced as appropriate.

Alexander MacLaren

Copyright Statement

The copyright of this thesis rests with the author. Unless otherwise indicated, its contents are licensed under a Creative Commons Attribution-NonCommercial-ShareAlike 4.0 International Licence (CC BY NC-SA).

Under this licence, you may copy and redistribute the material in any medium or format. You may also create and distribute modified versions of the work. This is on the condition that; you credit the author, do not use it for commercial purposes and share any derivative works under the same licence.

When reusing or sharing this work, ensure you make the licence terms clear to others by naming the licence and linking to the licence text. Where a work has been adapted, you should indicate that the work has been changed and describe those changes.

Please seek permission from the copyright holder for uses of this work that are not included in this licence or permitted under UK Copyright Law.

Contents

List of Figures **10**

List of Tables **20**

Nomenclature **22**

Abbreviations **25**

1 Introduction **27**

2 Literature Review **32**

2.1 Electric Vehicle Transmissions 32

2.2 Efficiency - Gearbox Losses 34

2.3 Gearbox Efficiency Measurement 35

2.4 Load-independent Losses: Churning and Windage 37

2.4.1 Lubricant Dynamic Viscosity 38

2.4.2 Speeds 39

2.4.3 Lubrication Type: Grease, Dip, or Jet 39

2.4.4 Gear Geometry and Meshing 40

2.4.5 Immersion Depth 41

2.4.6 Rotational Direction and Swell Effects 42

2.4.7 Casing, Clearances and Orientation 42

2.4.8 Cavitation and Aeration 44

2.4.9 Ambient Pressure Inside Gearbox 45

2.5 Load-dependent Losses 46

2.5.1 Traction Prediction 48

2.5.2 Inlet Heating 49

2.5.3 Flash Heating 50

2.5.4 Film Thickness Measurement 52

2.6 Bearing Losses 53

2.7 Scuffing 55

2.8 Micropitting 58

2.9 Fluid Formulation . . . 62
2.10 Conclusions from Literature Review . . . 65
2.11 Project Goals . . . 67
3 Materials **69**
3.1 Fluids . . . 69
3.1.1 Viscosity and Density Measurement . . . 69
3.1.2 Refractive Index Measurement . . . 70
3.1.3 Pressure-Viscosity Coefficient Measurement . . . 70
3.1.4 Physical Parameters of Fluids . . . 71
3.1.5 Water-based fluid composition . . . 74
3.2 Contacting Solids . . . 74
3.3 Coatings . . . 75
4 Churning Loss Measurements **77**
4.1 Development of Gearbox Churning Loss Rig . . . 77
4.1.1 Gearbox . . . 78
4.1.2 Speeds . . . 81
4.1.3 Mesh Forces . . . 83
4.1.4 Gear Tooth Surface Roughness . . . 87
4.1.5 Contact Conditions . . . 87
4.1.6 Test Rig . . . 89
4.1.7 Power Electronics . . . 90
4.1.8 Control Electronics and User Interface . . . 92
4.1.9 Oil Fill Level . . . 97
4.1.10 Temperature Control . . . 99
4.1.11 Inertia Rundown . . . 100
4.1.12 Inertia Measurement . . . 101
4.1.13 Torque Measurement . . . 106
4.1.14 Overspeeding . . . 108
4.2 Results and Discussion . . . 110
4.2.1 Speed and Immersion Depth . . . 110
4.2.2 Oil Viscosity . . . 120

4.2.3 Steady-state vs Transient Conditions . . . 124
4.3 Summary . . . 127
5 Drive Unit Efficiency Measurements 129
5.1 T-Axle EV Dyno Rig Overview . . . 129
5.2 Drive Loss: No-Load . . . 131
5.3 Drive Efficiency . . . 134
5.4 New European Drive Cycle Test . . . 139
6 High-speed EHL Traction & Film Thickness 143
6.1 Methods . . . 144
6.1.1 Test Setup . . . 144
6.1.2 Contact Conditions . . . 144
6.1.3 Film Thickness Measurement . . . 145
6.1.4 Traction Measurement . . . 147
6.1.5 Test Procedure . . . 150
6.2 Results . . . 151
6.2.1 Measurements of Traction and Film Thickness . . . 151
6.2.2 Comparison to Film Thickness Predictions . . . 153
6.2.3 Interferometric Images of the Contact . . . 155
6.2.4 Mean Shear Stress and Shear Strain Rate . . . 156
6.2.5 Changes in Traction and Film Thickness with Sliding Direction . . . 157
6.2.6 Shear Stress Response to Viscosity and Fluid Composition . . . 160
6.3 Discussion . . . 162
6.3.1 Difference in Traction with Sliding Direction . . . 169
6.3.2 Viscoelasticity . . . 172
6.3.3 Measurement Limitations . . . 174
6.4 Conclusions . . . 175
7 Surface Damage 177
7.1 Micropitting . . . 178
7.1.1 Micropitting Test Method . . . 180
7.1.2 Effect of Fluid Formulation . . . 185
7.1.3 Effect of Roller Batch . . . 193

7.1.4 Counterface Profile Evolution . . . 197
7.2 Scuffing . . . 200
7.2.1 Scuffing Test Method . . . 200
7.2.2 Scuffing Performance of Transmission Fluids . . . 210
8 SLIM **219**
8.1 Introduction to SLIM . . . 220
8.2 The Spacer Layer Imaging Method . . . 221
8.3 Limitations of the SLIM Technique . . . 224
8.3.1 Intensity shift . . . 225
8.3.2 Fringe Order Ambiguity . . . 226
8.3.3 Test Procedure and Equipment Condition . . . 228
8.3.4 Averaging Area . . . 228
8.4 Analysis Techniques to Overcome Limitations . . . 229
8.4.1 Context-Aware Colour Matching . . . 229
8.4.2 Calibration Curve Fitting . . . 234
8.4.3 Circle Finding . . . 240
8.4.4 Refractive Index Correction . . . 242
8.5 Summary . . . 245
9 Discussion **247**
9.1 Load-independent losses . . . 247
9.2 EHL Traction and Film Thickness at High Speeds . . . 249
9.3 Surface Damage . . . 250
9.4 Influence of viscosity on load-dependent and load-independent losses . . . 255
10 Conclusions **258**
10.1 Future Work . . . 261
References **265**
Appendix A Gearbox Tooth Flank Surfaces **289**
Appendix B Gear Mesh and Bearing Reaction Force Calculation **293**
Appendix C Minimum EHL Film Thickness in Helical Gear Pairs **296**
Appendix D Referred Inertia of Bearing Rolling Elements **298**

Appendix E Contact Cycles in Ball and Roller Bearings **300**

Appendix F Aluminium Stator Core **301**

Appendix G Spin in Ball-on-Disc Contact **303**

Appendix H MTM and ETM Traction Measurements **305**

Appendix I High-Speed EHD Measurements **314**

I.1 Traction Measurements 314

I.2 Film Thickness Measurements 317

I.3 Traction and Film Thickness 3D Plots 321

Appendix J Words **325**

List of Figures

1.1 Global EV stock between 2013 and 2023 27
1.2 Map of the areas of work addressed by this thesis in the context of the principal challenges faced by EV transmission development from a tribological perspective 30

2.1 Electric vehicle powertrain architectures 33
2.2 Principal sources of load-dependent and load-independent losses in high-speed gearing 35
2.3 Factors affecting churning losses in geared transmissions 38
2.4 Quiescent and disturbed oil profiles assumed by Changenet and Velex, adapted from ref. [41] 41
2.5 Effect of rotation direction on churning torque and steady-state oil surface profile (reproduced from ref. [62] with permission from Taylor & Francis) . . 43
2.6 Schematic and interferogram of EHL contact 47
2.7 Film thickness measurement of an EHL point contact showing 3D map and longitudinal and transverse sections 47
2.8 Schematic and thermal network showing temperature rises in an EHL contact 51
2.9 Schematic showing working principle of EHL film thickness measurement by optical interferometry 52
2.10 Scuffed test gear and microscope image of scuffed tooth face 55
2.11 Micropitting of helical gear tooth surfaces (reproduced from ref. [178] with permission of SAGE publishing) 58

4.1 Drive unit showing inverter casing, gearbox casing and motor casing 78
4.2 Gearbox from front drive unit of Tesla Model S P90D 79
4.3 Photographs of bearings supporting 3 shafts in gearbox 80
4.4 Trochoid internal gear pump for spray lubrication and cooling of drive unit . 80
4.5 Polymeric 20-tooth helical pinion driving trochoid gear pump 81
4.6 Illustration of oil flow path inside gearbox 82

4.7 Estimate of wheel drive torque required to cruise at speeds between 0 and 155 mph for Tesla Model S P90D 83
4.8 Schematic representation of helical gears showing bearing arrangement, handedness and gear mesh forces 84
4.9 Photographs of stylus profilometer measurement of tooth flank surface roughness for gears on intermediary shaft 87
4.10 Photograph of churning loss measurement rig 90
4.11 Transmission assembly connecting motor to gearbox via clutch 91
4.12 Open differential and immobiliser nut added to allow drive from a single sun gear 91
4.13 Churning rig power electronics schematic 93
4.14 Churning rig power electronics enclosure 94
4.15 Churning rig control electronics 95
4.16 Shielded casing containing load cell amplifiers for reaction torque sensor . . . 96
4.17 Churning rig GUI application 97
4.18 Photograph of oil level manometer in churning rig 98
4.19 Photograph of two halves of gearbox casing showing thermocouple placement 100
4.20 Best-fit polynomials of order 1-6 used to fit speed transient, and resulting torque predictions 102
4.21 Photographs showing trifilar suspension inertia measurement jig 103
4.22 Oscillatory system used to model trifilar suspension inertia measurement . . 103
4.23 Angled beam load cells comprising the reaction torque sensor that enables torque measurement 106
4.24 Torque calibration beam with 4×100 g weights 107
4.25 Torque applied to calibration beam vs value of $P_1 + P_2 - P_3 - P_4$, showing excellent linearity 107
4.26 Correlation between torque value reported by VFD, and torque measured by reaction torque sensor 108
4.27 Speed transients and corresponding torques at several nominal immersion depths with DEX-VI ATF at ambient temperature for solely the differential and LS wheel gear, spray lubrication system removed 111

4.28 Difference between measured forward- and reverse-rotation decelerating torques with only the LS wheel gear present 112
4.29 Decelerating torques measured with LS wheel gear, intermediate shaft, and lubrication system (unpowered) present in the gearbox 113
4.30 Excess torques measured with lubrication system (unpowered) present in the gearbox with and without intermediary shaft 114
4.31 Speed transients and excess torque with the oil pump powered and the LS wheel gear present 115
4.32 Decelerating torque for the LS wheel gear and intermediate shaft, with and without the oil pump pinion installed 116
4.33 Difference in excess torque between pump powered and pump unpowered cases, with and without the intermediary shaft 116
4.34 Difference between excess torques with and without HS shaft (pump powered) 117
4.35 Decelerating torque and excess torque for fully assembled configuration . . . 118
4.36 Churning power, and as a fraction of estimated tractive power vs speed for drive unit 118
4.37 Relationship between churning torque and viscosity at 4 speeds with 2 l fill volume 121
4.38 Relationship between churning torque and viscosity at 2 immersion depths and 2 speeds 121
4.39 Temperatures measured at 7 points in the gearbox before, during and after speed transients for three oil volumes and two fluids 123
4.40 Torque and speed vs time during steady-state test with no oil in the gearbox, and stable torques and temperatures with and without oil, compared to measurements from inertia rundown (23 cSt ATF at 80°C) 125
4.41 Comparison of steady-state motor torque measurement to inertia rundown measurements with and without oil (5.4 cSt ATF at 65°C) 126

5.1 UUT, dynos and power electronics of EV T-axle rig 130
5.2 No-load loss test results - speed and torque vs. time during sampling intervals 132
5.3 No-load loss test results - dyno torque vs speed 133

5.4 Drive unit efficiency maps for driving and regenerative braking with Dexron-VI ATF (US) . . . 135
5.5 Efficiency maps - driving and regen combined, for Dexron-VI ATF (US)and SAE 75W-140 gear oil . . . 137
5.6 Efficiency maps for two oils showing $-200 \leq T_{out} \leq 200$ Nm portion of Fig. 5.5. 137
5.7 Oil sump temperature measured during efficiency tests . . . 138
5.8 Motor stator temperature measured during efficiency tests . . . 138
5.9 Voltage and Current measurements throughout test reported by battery simulator and Tesla drive unit . . . 139
5.10 Torque, speed, efficiency, and temperatures measured during New European Drive Cycle, performed by Tesla Model S rear drive unit in T-axle EV dyno rig. 141

6.1 EHD-HS test setup . . . 144
6.2 Schematic of film thickness measurement by ultra-thin-film interferometry . . 146
6.3 Schematic of ball drive mechanism . . . 147
6.4 Summary of ball and disc speeds under four cases used for traction measurement 149
6.5 Traction curves measured for PAO4 at three temperatures for selected entrainment speeds in forward sliding, disc faster . . . 151
6.6 EHD central film thickness vs entrainment speed measured for PAO4 at three temperatures for selected SRRs in forward sliding . . . 151
6.7 Traction and Film Thickness vs Entrainment Speed U_e and Slide-Roll Ratio SRR measured simultaneously for three temperatures with PAO4 . . . 152
6.8 Traction curves for various speeds at 20°C and 100°C, for five fluid types spanning Groups I - IV, steel ball on glass disc, 50 N load, 0.73 GPa max. Hertz pressure . . . 152
6.9 Percentage overestimation, compared to measurement in positive sliding direction, of central film thickness h_c from the Chittenden model at $20°$C and $100°$C for three SRRs . . . 154
6.10 Percentage difference between central film thickness h_c predicted by Gupta model, and measurement in positive sliding direction, for $20°$C and $100°$C . . 154
6.11 Interferometric images of ball-on-disc contact with steel-on-glass, PAO5 at 20°C, 50 N load (0.73 GPa), at four nominal entrainment speeds and 40% SRR 156

6.12 Mean shear stress $\bar{\tau}$ vs shear strain $\dot{\gamma}$ for PAO5 with a steel ball on glass disc and sapphire disc at 20°C and 50 N load 157
6.13 Difference between traction coefficient in forward and reverse sliding directions for Group I and Group IV fluids of similar ν_{100}, vs SRR for selected entrainment speeds 158
6.14 Percentage difference between central film thickness h_c in forward and reverse sliding directions for Group I and Group IV fluids of similar ν_{100}, vs entrainment speed for selected SRRs 159
6.15 Mean shear stress $\bar{\tau}$ vs shear strain rate $\dot{\gamma}$ for base fluids in Group I and Group IV at three temperatures, steel ball on glass disc at 50 N load for selected speeds 160
6.16 Mean shear stress $\bar{\tau}$ vs shear strain rate $\dot{\gamma}$ for higher-viscosity Mineral Oil at 20°C and 60°C, steel ball on glass disc at 50 N load for selected speeds . . . 161
6.17 Traction vs U_e and SRR and mean shear stress $\bar{\tau}$ vs shear strain rate $\dot{\gamma}$ of the traction fluid Santotrac 50 for SRR$\leq$20%, steel-on-glass 161
6.18 Two mean temperature predictions, one based on Eq. (6.13) assuming all of the heat is taken by the faster surface, and one based on Eyring rheology (Eq. (6.20)), for steel ball on glass disc 165
6.19 Two mean temperature predictions, one based on Eq. (6.13) assuming all of the heat is taken by the faster surface, and one based on Eyring rheology (Eq. (6.20)), for steel ball on sapphire disc 166
6.20 Nahme-Griffith number Na vs shear strain rate for the data from Fig. 6.12 . 167
6.21 Traction curves from Fig. 6.8b, highlighting four distinct traction regimes as defined by Habchi *et al.* [233] 168
6.22 Mean shear stress $\bar{\tau}$ vs shear strain $\dot{\gamma}$ for PAO5 (Group IV) with a steel ball on glass disc and sapphire disc at 20°C and 50 N load 171
6.23 Eq. (6.26) fitted to $\bar{\tau}$ vs $\dot{\gamma}$ for $\mathrm{SRR} < 5\%$ at four entrainment speeds, for PAO5 with glass disc, and values of shear modulus G_e compared to the reciprocal of the solid elastic compliance term $E'h_c/2a$ 173

7.1 Configuration of 3 rings and roller in MPR rig 180
7.2 MPR rig showing configuration of driveshafts and loading system 181

7.3 Roller configuration during stylus profilometry, enabling roughness measurement on cylindrical face of chamfered barrel 183
7.4 Roller configuration under optical microscope, enabling visual inspection of cylindrical face of chamfered barrel 183
7.5 Comparison of radius loss in micropitting tests on 5 fluids showing optical microscope images of roller surfaces after final step (11 million contact cycles) 186
7.6 Optical microscope images showing evolution of roller surface with number of contact cycles throughout tests using 5 fluids (with AISI 52100 steel, batch B) 187
7.6 (continued) 188
7.6 (continued) 189
7.7 Selected roughness parameters averaged over 4 measurements on each of the three rings vs number of roller contact cycles accrued 190
7.8 Significant foaming of water-based fluid after a test step 191
7.9 Microscope images stitched together while the roller was rotated about its axis, traversing 60° circumferentially, showing 5 complete 'ridges' 192
7.10 Friction, LVDT displacement, centreline average acceleration and peak-to-peak acceleration for six MPR micropitting tests shown in Fig. 7.6 193
7.11 Change in roller profile measured using stylus profilometry averaged over 4 positions on the roller taken in the same locations after every test step . . . 194
7.12 Radius loss comparison between roller batches J and N manufactured to the same specifications, run consecutively in the same MPR under the same test conditions 195
7.13 Comparison of optical microscope images showing evolution of roller surface with number of contact cycles accumulated during otherwise identical tests with rollers from batches J and N manufactured to the same specifications . 196
7.14 Axial profile of ring surface at end of test, highlighting the 1 mm span with minimum total absolute slope, corresponding to the worn region 198
7.15 RMS roughness R_q and reduced peak height R_{pk} averaged over 4 measurements on each of the three rings, plotted vs number of roller contact cycles accrued for batch J and N roller tests 198
7.16 Schematic of ball and disc orientation in MTM and ETM pot 201

7.17 Comparison of MTM and ETM setups showing ball, disc and lubricant . . . 202
7.18 Friction coefficient and sliding speed recorded during 7 repeats of the same suffing test running-in procedure 204
7.19 MTM disc profiles from white-light interferometer before and after running-in 206
7.20 MTM ball profiles from white-light interferometer before and after running-in 207
7.21 Ball and disc surfaces after advanced scuffing for PAO5, 45 N load, 200 mm/s entrainment speed, 3000 mm/s sliding speed, and 5 minute step time 208
7.22 Ball and disc surfaces at end of ETM scuffing test with PAO5, 75 N load . . 208
7.23 Schematic of modified contrarotation scuffing test following that of Peng [175] 210
7.24 Friction coefficient and sliding speed recorded during 6 repeats of the same scuffing procedure after running-in 211
7.25 Friction coefficient and sliding speed during scuffing tests conducted at 75 N and 300 N for two candidate transmission fluids and a blend of PAO5 and ZDDP212
7.26 Scuffing performance of four candidate transmission fluids and two base stocks 215
7.26 (continued) 216
7.27 Selected mapper images taken during scuffing tests 217
7.27 (continued) 218

8.1 SLIM setup used to capture interferometric image of contact 222
8.2 Example images of the interferogram produced by SLIM 223
8.3 2D and 3D plots showing colour channel intensities vs film thickness for films in the range 80-740 nm, experimental data from an EHD2 224
8.4 ETM-SLIM image and film thickness calculation adversely affected by intensity shift, for a rough ZDDP tribofilm 226
8.5 Pixels from an EHD-SLIM image compared to calibration line showing reduction in peak saturation and three separate regions of fringe order ambiguity, undermining the film thickness calculation 227
8.6 Example of colour matching to the calibration curve for nearest and second-nearest branch, used for proposed context-aware colour matching method . . 230
8.7 Expanding spiral sequence of pixels traversed during order correction, showing pixels used for traverse-tangential and traverse-normal derivatives 232

8.8 Example film thickness calculation for 9 EHD-SLIM images showing success of context-aware colour matching algorithm in removing regions of fringe order ambiguity . . . 233
8.9 Four possible film thickness maps created by context-aware colour matching assuming 1st, 2nd, 3rd, and 4th-nearest-colour film thicknesses respectively for the central region . . . 234
8.10 3D plots showing calibration curve and pixel colours in RGB space before and after calibration curve fitting . . . 236
8.11 Film thickness calculation for an MTM-SLIM image of a ZDDP tribofilm with severe intensity shift with and without calibration curve refitting . . . 238
8.12 2D plot showing original calibration curve colour channels compared to fit and pixels in SLIM image shown at assigned film thicknesses before and after calibration curve refitting . . . 238
8.13 SLIM images from MTM, ETM and EHD, showing crosshairs and successfully fitted circle or ellipse (white lines) . . . 240
8.14 Graphical representation of the proposed circle finding technique . . . 241
8.15 Refractive index vs pressure at three temperatures for mineral oil and PAO5 . 244

A.1 Microscope images of both driving and braking surfaces of the high-speed motor shaft pinion gear from the drive unit in Chapter 4 . . . 289
A.2 Microscope images of driving surface of the tooth shown in Fig. A.1c of the motor shaft pinion gear . . . 290
A.3 Microscope images of driving and braking surfaces of the low-speed stage pinion gear on the intermediate shaft of the drive unit in Chapter 4 . . . 291
A.4 Microscope images of driving and braking surfaces of the high-speed stage wheel gear from the drive unit in Chapter 4 . . . 291
A.5 Identically-positioned microscope images of the same location on the driving surface of a tooth on the high-speed stage wheel gear, using two illumination angles . . . 292

F.1 Pattern used to assemble 24 plates comprising aluminium stator core, using only 4 distinct parts . . . 301

F.2 Four plate designs used to build aluminium replacement stator core 302
F.3 Aluminium stator as designed (render) and as built (photograph) 302

G.1 Spin-to-Roll ratio vs Slide-to-Roll Ratio in co-rotation for a selection of ball inclination angles under contact conditions representative of the MTM . . . 304
G.2 Spin-to-Roll ratio as a function of slide-to-roll ratio with 0° inclination angle, for a selection of disc track radii representative of the EHD and EHD-HS . . 304

H.1 Traction measurements from MTM305 spanning entrainment speeds between 40 mm/s and 4 m/s and SRRs between 0 and 400%, at selected loads between 10 and 75 N using the Synthetic ATF at 60°C 306
H.2 Traction surfaces from Fig. H.1 superimposed 307
H.3 Traction measurements from MTM202 spanning entrainment speeds between 50 mm/s and 3.6 m/s and SRRs between 0 and 500%, at selected loads between 10 and 75 N using the Synthetic ATF at 60°C 308
H.4 Comparison between traction measurements from MTM202 and MTM305 as a fraction of the measurement by MTM202 309
H.5 Traction measurements from ETM102 spanning entrainment speeds between 50 mm/s and 3.6 m/s and SRRs between 0 and 500%, at selected loads between 20 and 150 N using the Synthetic ATF at 60°C 310
H.6 Comparison between traction measurements by ETM102 and MTM202 as a fraction of the MTM202 measurement 311
H.7 Traction measurements from MTM365 spanning entrainment speeds between 40 mm/s and 4 m/s and SRRs between 0 and 300% for an ATF and a traction fluid at 40°C 312
H.8 MTM traction matrices for an experimental EV bearing grease using the traction test method developed here to establish the effects of contact load and grease temperature on traction 313

I.1 EHD-HS traction measurements for Heavy Mineral Oil 314
I.2 EHD-HS traction measurements for HVI 60 Group I 314
I.3 EHD-HS traction measurements for CHN 100R Group II 315
I.4 EHD-HS traction measurements for Yubase 4 Group III 315

I.5 EHD-HS traction measurements for PAO4 Group IV 315
I.6 EHD-HS traction measurements for PAO5 Group IV 315
I.7 EHD-HS traction measurements for PAO5 Group IV (repeat) 316
I.8 EHD-HS traction measurements for PAO5 Group IV on sapphire disc 316
I.9 EHD-HS traction measurements for Santotrac 50 at 20 N 316
I.10 EHD-HS traction measurements for Low-viscosity (2.4 cSt) ATF 316
I.11 EHD-HS traction measurements for High-viscosity (23 cSt) ATF 317
I.12 EHD-HS traction measurements for model EV fluid 317
I.13 EHD-HS film thickness measurements for Heavy Mineral Oil 317
I.14 EHD-HS film thickness measurements for HVI 60 Group I 318
I.15 EHD-HS film thickness measurements for CHN 100R Group II 318
I.16 EHD-HS film thickness measurements for Yubase 4 Group III 318
I.17 EHD-HS film thickness measurements for PAO4 Group IV 318
I.18 EHD-HS film thickness measurements for PAO5 Group IV 319
I.19 EHD-HS film thickness measurements for PAO5 Group IV (repeat) 319
I.20 EHD-HS film thickness measurements for PAO5 Group IV on sapphire disc . 319
I.21 EHD-HS film thickness measurements for Santotrac 50 at 20N 319
I.22 EHD-HS film thickness measurements for Low-viscosity (2.4 cSt) ATF 320
I.23 EHD-HS film thickness measurements for High-viscosity (23 cSt) ATF 320
I.24 EHD-HS film thickness measurements for model EV fluid 320
I.25 EHD-HS traction and film thickness 3D plots for Heavy Mineral Oil 321
I.26 EHD-HS traction and film thickness 3D plots for HVI 60 Group I 321
I.27 EHD-HS traction and film thickness 3D plots for CHN 100R Group II 322
I.28 EHD-HS traction and film thickness 3D plots for Yubase 4 Group III 322
I.29 EHD-HS traction and film thickness 3D plots for PAO4 322
I.30 EHD-HS traction and film thickness 3D plots for PAO5 323
I.31 EHD-HS traction and film thickness 3D plots for PAO5 on sapphire disc . . . 323
I.32 EHD-HS traction and film thickness 3D plots for Santotrac 50 323
I.33 EHD-HS traction and film thickness 3D plots for Low-viscosity ATF 324
I.34 EHD-HS traction and film thickness 3D plots for High-viscosity ATF 324
I.35 EHD-HS traction and film thickness 3D plots for model EV fluid 324

List of Tables

3.1 Measured kinematic viscosities and fitted pressure-viscosity coefficients of lubricants used during this study 72
3.2 Regression parameters fitted from measurements of viscosity, density and refractive index for lubricants tested, as per Eqs. (3.1), (3.3) and (3.4). . . . 73
3.3 Composition of water-based fluid used in scuffing and micropitting tests in Chapter 7 74
3.4 Mechanical and thermal properties assumed for steels, glass and sapphire surfaces 75

4.1 Rolling bearings used in gearbox to support the three shafts shown in Fig. 4.8 79
4.2 Approximate geometrical parameters extracted from gear measurements. . . 85
4.3 Axial spacings in mm between centrepoints of bearings and gear meshes shown in Fig. 4.8. 86
4.4 Pitch-point mesh forces from force equilibrium applied to Fig. 4.8 86
4.5 Bearing reaction forces from force equilibrium applied to Fig. 4.8 86
4.6 Sample mean and standard deviation of roughness parameters CLA (R_a), RMS (R_q), skewness (R_{sk}) and kurtosis (R_{ku}) measured on intermediary shaft gears 88
4.7 Material and lubricant parameters for calculation of EHL film thickness in gears 88
4.8 Gear mesh parameters and contact conditions assuming $T_{\mathrm{motor}} = 330$ Nm, $v_{\mathrm{car}} = 60$ mph, where stage 1 is the high-speed stage and stage 2 is the low-speed stage. 89
4.9 Physical properties of the trifilar suspension setup including inertia of measurement jig itself 104
4.10 Inertia of gearbox components measured by trifilar suspension, and those referred about the low speed wheel shaft for comparison 105

5.1 Available instrumentation and motor specification data for T-Axle Dyno Rig . 131

6.1 Contact conditions using Glass and Sapphire discs under 50 N load 145

7.1 Micropitting test procedure of Wainwright [193] 182
7.2 Test conditions used for comparison of fluid formulations in Fig. 7.6 185
7.3 Test conditions used for batch J and N rollers 194

8.1 Contact conditions used to create images in Fig. 8.8 234
8.2 Regression parameters obtained by fit to MTM-SLIM calibration 237
8.3 Contact conditions used to create the film in Fig. 8.11 239

Nomenclature

a	[m]	Hertz contact half-width $a = \left(\frac{3wR}{2E'}\right)^{\frac{1}{3}}$
b	[m]	Gear facewidth
B	[K]	Exponential parameter in VFT viscosity model
B_ζ	[-]	Spin-to-roll ratio
Bi	[-]	Biot number
c_p	[J/kgK]	Specific heat capacity
C_D	[-]	Coefficient of drag
C_T	[-]	Thermal EHL film thickness correction factor
d_a	[m]	Addendum (tip) circle diameter
d_f	[m]	Dedendum (root) circle diameter
D	[-]	Deborah number
E_1, E_2	[Pa]	Ball (1) and Disc (2) elastic modulus
E'	[Pa]	Reduced contact modulus $E' = 2\left(\frac{1-\nu_1^2}{E_1} + \frac{1-\nu_2^2}{E_2}\right)^{-1}$
F^+, F^-	[N]	Traction force in forward $(+)$ and reverse (-) sliding
F_0^+, F_0^-	[N]	Traction force under zero-sliding for $U_e = U_1$ $(+)$ and $U_e = U_2$ (-)
Fo	[-]	Fourier number
G	[-]	Gear ratio
G_e	[Pa]	Equivalent shear modulus considering contact elasticity
G_p	[Pa]	Fluid shear modulus in contact
h	[m]	Immersion depth
h_{conv}	[W/m^{2}K]	Coefficient of convective heat transfer
h_c	[m]	EHL central film thickness
h_m	[m]	EHL minimum film thickness
L_c	[m]	Characteristic length of thermal mass
L_T	[-]	Gupta thermal loading parameter
Mo	[-]	Mouromtseff Number
m_n	[m]	Normal module
n	[-]	Refractive index
Na	[-]	Nahme-Griffith Number

$\overline{p}$	[Pa]	Mean Hertz Pressure $\overline{p} = \frac{2}{3}P_0$
p_x	[m]	Gear axial pitch
P_0	[Pa]	Maximum Hertz Pressure $P_0 = \left(\frac{3wE'^2}{2\pi^3 R^2}\right)^{\frac{1}{3}}$
P_o, P_i	[W]	Output (o) and input (i) power
P_{loss}	[W]	Power loss (friction, drag, churning)
r_w	[m]	Vehicle wheel radius
R	[m]	Ball radius
R_a	[m]	CLA roughness
R_{pk}	[m]	Reduced peak height
R_q	[m]	RMS roughness
SRR	[%]	Slide-Roll Ratio $\mathrm{SRR} = \frac{U_s}{U_e}$
t_d	[s]	Characteristic timescale for heat diffusion
t_r	[s]	Period of specimen rotation
T	[K]	Temperature
T_0	[K]	Temperature offset parameter in VFT viscosity model
T_{excess}, $T_{\text{no oil}}$	[Nm]	Excess torque, No-oil torque
T_o, T_i	[Nm]	Output (o) and input (i) torque
U_1, U_2	[m/s]	Ball (1) and Disc (2) surface velocity
U_e	[m/s]	Entrainment speed $U_e = \frac{1}{2}(U_1 + U_2)$
U_s	[m/s]	Sliding speed $U_s = U_2 - U_1$
w	[N]	Normal contact load
x	[-]	Addendum modification coefficient
z	[-]	Number of gear teeth
α_p	[Pa^{-1}]	Pressure-viscosity coefficient (film-thickness-derived)
α_n	[rad]	Normal pressure angle
α_{tw}	[rad]	Tangential working pressure angle
β	[rad]	Helix angle
β^*	[m]	Autocorrelation length
$\dot{\gamma}$	[s^{-1}]	Nominal shear strain rate $\dot{\gamma} = \frac{U_s}{h_c}$
$\overline{\Delta T_E}$	[K]	Mean total film temperature rise assuming Eyring rheology
$\overline{\Delta T_{\text{inlet}}}$	[K]	Mean film temperature rise due to inlet shear heating

$\overline{\Delta T_{\mathrm{oil}}}$	[K]	Mean temperature rise in oil film
$\overline{\Delta T_s}$	[K]	Mean 'flash' temperature rise at surfaces
$\Delta_{\parallel}$, $\Delta_{\perp}$	[-]	Backward-difference 2nd derivative of film thickness parallel ($\parallel$) and perpendicular ($\perp$) to traverse direction
ε_{α}, ε_{β}, ε_{γ}	[-]	Transverse (α), axial (β) and total (γ) contact ratio
ζ	[rad/s]	Spin
η	[Pa.s]	Bulk fluid dynamic viscosity at atmospheric pressure
η_0	[Pa.s]	Scaling parameter in VFT model
η_m	[%]	Mechanical efficiency
$\bar{\eta}_p$	[Pa.s]	Mean piezoviscous viscosity in contact
$\bar{\eta}_{p0}$	[Pa.s]	Mean isothermal equivalent piezoviscous viscosity in contact
κ	[W/mK]	Thermal conductivity
Λ	[-]	Lambda ratio
μ	[-]	Traction coefficient
μ_+, μ_-	[-]	Traction in forward (+) and reverse (-) sliding
μ_r	[-]	Coefficient of rolling resistance
ν	[cSt]	Kinematic viscosity
ρ	[kg/m^3]	Density
$\bar{\tau}$	[Pa]	Mean shear stress $\bar{\tau} = \frac{\mu w}{\pi a^2}$
τ_e	[Pa]	Eyring stress
χ	[m^2/s]	Thermal diffusivity $\chi = \frac{\kappa}{\rho c}$
ω_o, ω_i	[rad/s]	Output (o) and input (i) angular velocity

Abbreviations

ACB	Angular Contact Bearing
ADC	Analog to Digital Converter
AISI 52100	A bearing steel, also 100Cr6
API	American Petroleum Institute
ATF	Automatic Transmission Fluid
AWD	All-Wheel Drive
CCD	Charge-Coupled Device, a camera technology
CFD	Computational Fluid Dynamics
CLA	Centre-Line Average
CRB	Cylindrical Roller Bearing
CVT	Continuously Variable Transmission
DCI	Differential Colorimetric Interferometry
DEX-VI	Dexron 6, a transmission oil specification by General Motors
DGBB	Deep Groove Ball Bearing
DLC	Diamond-Like Coating
EDF	Electric Drive Fluid
EDU	Electric Drive Unit
EP	Extreme Pressure (additive)
EHD/EHL	Elastohydrodynamic (Lubrication)
EHD2	An optical tribometer by PCS Instruments
EHD-HS	EHD High Speed, an optical tribometer
ETM	Extreme Traction Machine, a ball-on-disc tribometer
EV	Electric Vehicle
FZG	Forschungsstelle für Zahnräder und Getriebebau, a gear research institution
GUI	Graphical User Interface
HS	High-Speed
HSV	Hue-Saturation-Value
ICE	Internal Combustion Engine
ICP	Inductively Coupled Plasma

I^2C	Inter-Integrated Circuit, a 2-wire digital communications protocol
KV40, KV100	Kinematic Viscosity at 40°C, 100°C
LS	Low-Speed
LVDT	Linear Variable Differential Transformer, used as a displacement transducer
MFC	Microsoft Foundation Classes
MoDTC	Molybdenum Dithiocarbamate
MPR	Micropitting Rig, a triple-disc fatigue tester
MTF	Manual Transmission Fluid
MTM	Mini-Traction Machine, a ball-on disc tribometer
NEDC	New European Drive Cycle
OEM	Original Equipment Manufacturer
PAO	Poly-Alpha-Olefin
PCB	Printed Circuit Board
PCD	Pitch-Circle Diameter
PCS	PCS Instruments, a tribology test equipment company (formerly Primelia Consulting Services, Primelia is an anagram of Imperial)
PI, PID	Proportional Integral (Derivative) control
PIO	Programmable IO, integrated programmable logic on the RP2040 chip
RCBO	Residual Current Breaker with Overcurrent protection
RGB	Red-Green-Blue
RMS	Root-Mean-Square
ROII	Relative Optical Interference Intensity
SKF	SKF, a major bearing manufacturer (originally Svenska Kullagerfabriken)
SLIM	Spacer Layer Imaging Method
SPI	Serial Peripheral Interface, a 4-wire digital communications protocol
SRR	Slide Roll Ratio
UUT	Unit Under Test
VFT	Vogel-Fulcher-Tammann (viscosity-temperature relationship)
VFD	Variable Frequency Drive
ZDDP	Zinc Dialkyldithiophosphate
3φ	Three-phase

Chapter 1

Introduction

The decarbonisation of transportation is one of the major technical challenges in reaching net zero greenhouse gas emissions. Transportation accounted for around 20% of global CO_2 emissions in 2022 [1], over 70% of which were from road transport, and the transport sector was projected by the Intergovernmental Panel on Climate Change in 2023 to be one of the slowest to decarbonise [2]. Electrification of the global fleet of road vehicles is now the most promising solution [3, 4], and the number of electric vehicles is growing rapidly (Fig. 1.1), with the International Energy Agency [5] predicting that one in every two cars sold globally in 2035 will be electric.

Roadblocks to widespread adoption of electric vehicles (EVs) include affordability and consumer range anxiety [6], considered by Ajanovic in 2015 to be the primary impediments to market uptake of EVs. Although energy storage remains the central issue, recent reductions in battery manufacturing cost and improvements in energy density have led to a shift in focus away from range anxiety towards the scalability of charging infrastructure and concerns surrounding the sustainability of manufacturing and life-cycle emissions [7, 8]. The 2020

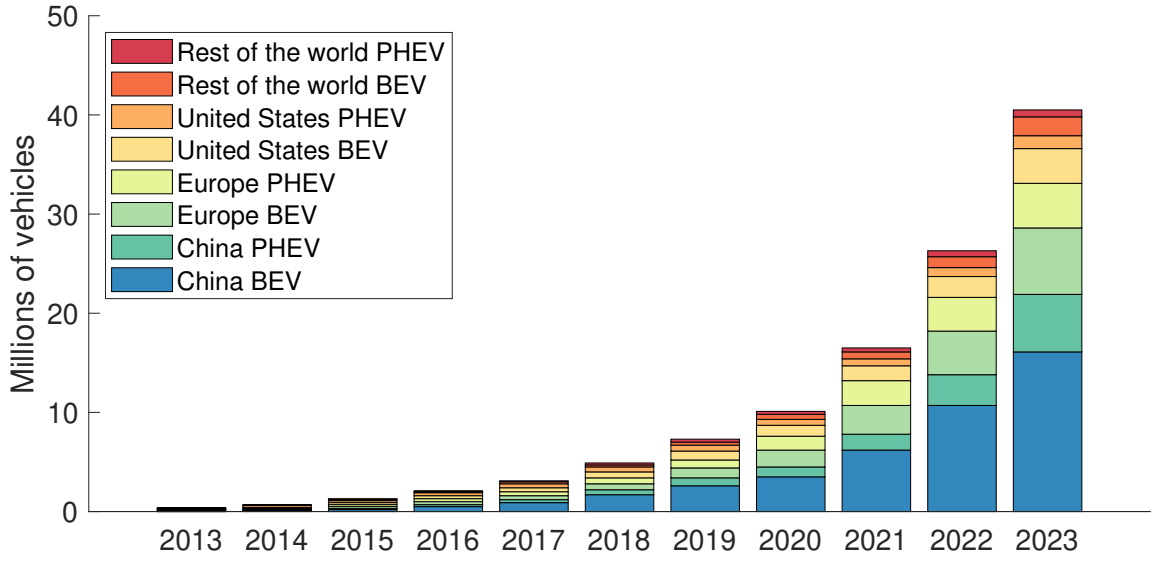


Figure 1.1: Global EV stock between 2013 and 2023, from IEA Global EV Outlook 2024 [5], including Battery Electric Vehicles (BEVs) and Plug-in Hybrid Electric Vehicles (PHEVs).

review of Muratori *et al.* [7] explores several opportunities presented by EVs, including vehicle-grid integration, automation, and the contribution of emerging (electric) urban micro-mobility solutions to behavioural changes which reduce dependence on cars in cities. Ambitious targets for reducing power density and cost of the electrical machine and power electronics also continue to drive innovation in semiconductor and cooling technologies [9].

Comparatively little research attention however has been paid towards the optimisation of a key component of the powertrain: the gearbox. Holmberg and Erdemir suggest [10] that transmission losses account for approximately 6% of total powertrain loss in a vehicle with an internal combustion engine (ICE), while for EVs, transmission losses are over 20% of powertrain losses [10]. Gearbox efficiency in EVs is therefore significant not just because of the potential energy savings, but also because of the implications for optimising the electric drive system as a whole, particularly given the strong thermal coupling due to the proximity to the motor and power electronics in many designs [11]. Motor speeds in EVs greatly exceed engine speeds in ICE vehicle transmissions, and EV motor speeds are projected to continue to rise as power density is increased [12].

EV transmissions are subject to a unique set of challenges despite their apparent simplicity by comparison to their ICE counterparts (multi-speed manual transmissions (MTs), automatic transmissions (ATs), dual clutch transmissions (DCTs), continuously variable transmissions (CVTs) and automated manual transmissions (AMTs)). They must operate at high power over an extremely wide speed range, which presents two immediate difficulties. At high speeds, battery capacity constraints demand high efficiency, which is limited both by kinematic losses such as oil churning, and by elastohydrodynamic traction in gears and bearings - this necessitates reasonably low oil viscosity. At low speeds, the contacts are often heavily loaded, leading to aggressive boundary-lubricated conditions, a potentially life-limiting situation avoided by specifying high oil viscosity (and leveraging various additives including EP, antiwear and friction modifiers). The obvious viscosity tradeoff required to optimise for these two conflicting requirements is especially challenging because the effect of viscosity on both churning and surface damage is not easy to estimate, particularly for the complex torque and speed histories EV transmissions experience during everyday driving [13]. The strong influence of additive chemistry on surface damage further complicates this optimisation, particularly given the commercial sensitivity of the chemical compositions of transmission fluid additive

packages. EV transmission fluids represent a new paradigm in lubricant formulation [14], and are still under active development.

Oil churning is a thermally coupled multiphase turbulent flow phenomenon with a strong dependence on multidimensional parameters such as casing geometry and lubrication scheme. The range of validity of existing churning loss models does not presently extend to the relevant speeds. Surface damage under boundary lubrication is a complex time-dependent multiphase micromechanical, thermal, tribochemical problem spanning several orders of magnitude in both length- and timescales. The influence of parameters such as fluid rheology, additive chemistry and the microstructure of steels on the mechanisms underlying empirically identifiable damage modes such as scuffing and micropitting are the subject of continuing academic debate.

The optimisation of lubricant properties considering the tribological requirements of both efficiency and reliability in an EV gearbox therefore requires a body of empirical data that captures the effects of several complex phenomena, to which this thesis aims to contribute. A schematic overview of the relationships between these phenomena, and the direction taken by this thesis, is given in Fig. 1.2. Lubricant viscosity (a strong function of temperature, pressure, shear strain rate and both base oil and additive chemistries) in particular plays a central role in mediating many of the relevant energy loss and surface damage phenomena, because energy lost by both viscous drag and contact friction, and also the nature and rate of progression of surface damage, are coupled by the viscosity-temperature relationship. This project therefore aims to explore the influence of transmission fluid viscosity on efficiency and reliability in EV transmissions.

A review of previous work elucidating the relevant tribological phenomena is presented in Chapter 2, after which the overarching goals of the project are determined and research tasks are formulated. The physical properties of the materials (both lubricants and test specimens) used in the following chapters are detailed all together in Chapter 3 for easy reference. In Chapter 4, the development of a test rig to perform a systematic study of churning losses in the drive unit of a popular EV is presented, along with the results of this study, focusing on the influence of speed, oil fill volume, and oil viscosity. A systematic efficiency test with a similar drive unit from the same EV, spanning its full power capability, is presented in Chapter 5, along with measurements conducted during a simulated NEDC drive cycle. In

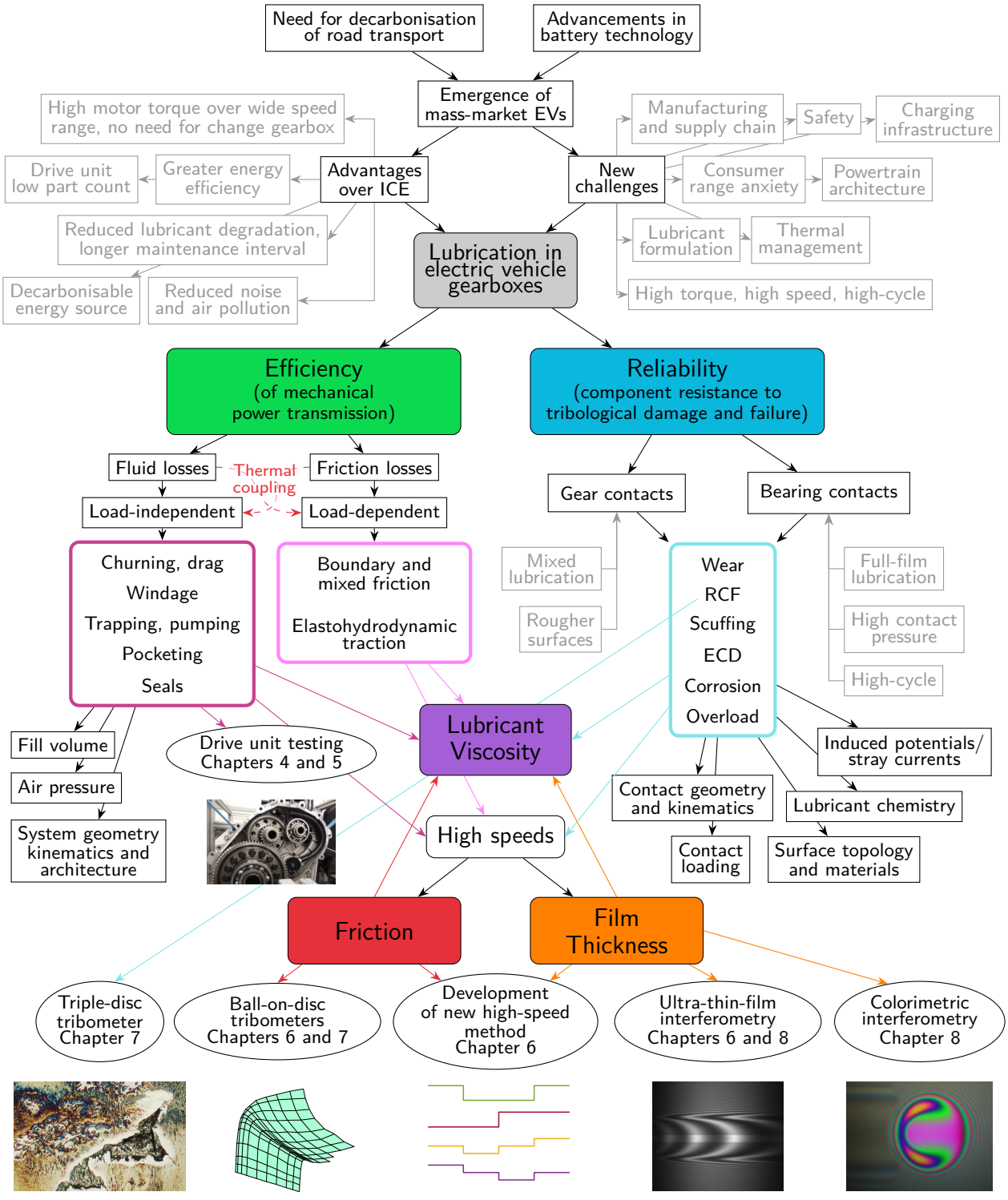


Figure 1.2: Schematic showing some of the principal challenges faced by EV transmission development from a tribological perspective, how they interconnect, and how the areas of work addressed by this thesis fit together. Methods employed, developed or created during this work are enclosed by ellipses. This is not an exhaustive list, neither is every issue included within the scope of this work, rather it is intended as an overview. Note that several key underlying phenomena have significant temperature-dependence, and that the system is strongly thermally coupled by energy lost to heat via friction, which both controls and is controlled by temperature, because of the effect of temperature on lubricant viscosity.

Chapter 6, a new optical tribometer is modified to enable simultaneous measurement of elastohydrodynamic traction and film thickness (pertinent to load-dependent losses in EV gearboxes) at entrainment speeds up to 20 m/s, and measurements are conducted for 10 oils, illustrating the effect of viscosity and base fluid chemistry at high speeds. Chapter 7 contains two studies which investigate the influence of fluid formulation for fluids of comparable viscosities on gear failure modes likely to occur in EV transmissions at the extremes of the design parameter space: scuffing and micropitting. It was discovered during this study that the Spacer Layer Imaging Method, a powerful technique for EHD film thickness measurement using colorimetric interferometry with extensive additive development industry penetration, has several key flaws which are usually hidden from the user. Chapter 8 illustrates these flaws and their implications, and provides a series of analytical techniques with which to interrogate and correct for them, in so doing considerably extending the reliability and useful range of the measurement. A discussion of the mutual implications of the outcomes of these separate studies for the design of future EV transmissions is given in Chapter 9, and conclusions are presented in Chapter 10.

Chapter 2

Literature Review

This chapter provides a review and discussion of previous work relevant to efficiency and durability in EV transmissions. These are both directly influenced by a wide range of tribological phenomena, each in their own right a mature field of study, so this literature review casts its net quite widely. Those topics which are of direct relevance to the work presented in this thesis, namely gear churning loss, thermal elastohydrodynamic lubrication, scuffing and micropitting, are reviewed in the most detail. The chapter is concluded by the development of a set of goals for this work.

2.1 Electric Vehicle Transmissions

An 'electric' vehicle is considered in this work to be one whose tractive power is (or is sometimes) supplied entirely by one or more electric motors. This definition encompasses several distinct powertrain categories, including battery (or 'pure') electric vehicles, hydrogen fuel cell electric vehicles, and also several 'hybrid' powertrains including plug-in, self-charging and range-extender hybrids (wheels driven by an electric motor powered either by a battery or by a small ICE via a generator), and 'true' hybrids (wheels driven either by an electric motor or by an ICE) when the engine is not operating, see Fig. 2.1. Almost all of these designs presently have a geared transmission connecting the motor(s) to the wheels, and despite their distinct architectures and design requirements (the hybrid, dual-motor eCVT transmission of a Toyota Prius differs fundamentally from the drive unit of the battery-electric Tesla Model 3 for example), they share a common design envelope in terms of output speeds, output power capacity, and operating environment.

Gearbox architecture strongly influences efficiency. This work focuses on gearboxes to which the power is supplied exclusively by a single electric motor (as in BEVs, REXs, HFCEVs and some PHEVs). By far the most prevalent configuration in 2024, both on the market and of those considered in literature, is a single-speed, two stage helical gear reducer with a total speed reduction ratio between 6 and 10 [15–19]. Two-speed transmissions such as that of the

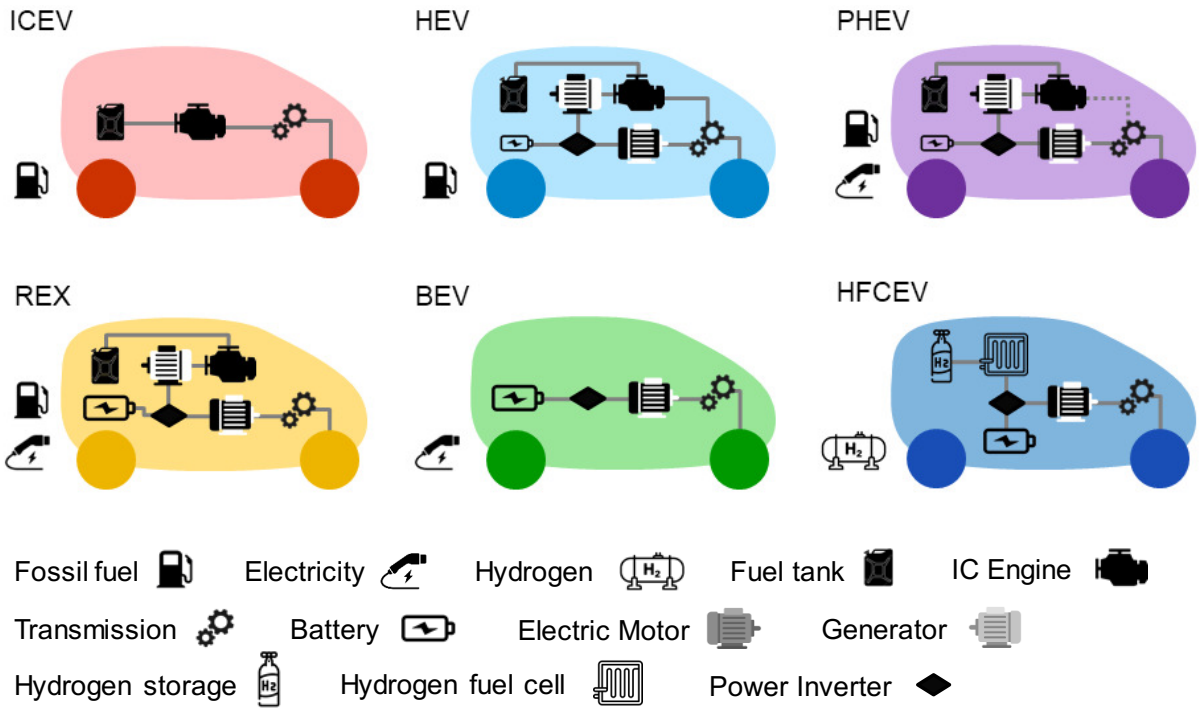


Figure 2.1: Various electric vehicle architectures compared to an Internal Combustion Engine powered Vehicle (ICEV), including Hybrid Electric Vehicle (HEV), Plug-in Hybrid Electric Vehicle (PHEV), battery electric vehicle with Range EXtender (REX), Battery Electric Vehicle (BEV), and Hydrogen Fuel Cell Electric Vehicle (HFCEV) as discussed by Ajanovic [6].

Porsche Taycan have been produced, and have the advantage that they can simultaneously optimise for torque and efficiency requirements [20]. Several studies [21–23] have suggested 2-speed transmissions may eventually be widely adopted, albeit without consideration of the cost, weight and reliability tradeoffs. Multi-ratio transmissions promise still more efficient motor operation in principle [24, 25], but the greater losses associated with the larger number of components, particularly wet clutch packs, may decrease drive cycle efficiency overall [26]. Electrified truck axles however may require multi-ratio transmissions with 3 or 4 speeds to meet gradeability requirements [27], and may employ split-transmission architectures enabling multiple motors to run at different speeds, improving driveability during upshift and downshift. A pericyclic reducer has also been proposed for truck e-axles [28]. Epicyclic architectures in high-end EVs such as the Lucid Air [29] have claimed to improve efficiency compared to their helical counterparts.

Ensuring the reliability of EV transmissions over their lifetimes also poses considerable challenge. Very few detailed studies of component damage and failure in electric vehicle gearboxes are presently in the public domain, perhaps due to the commercial sensitivity of

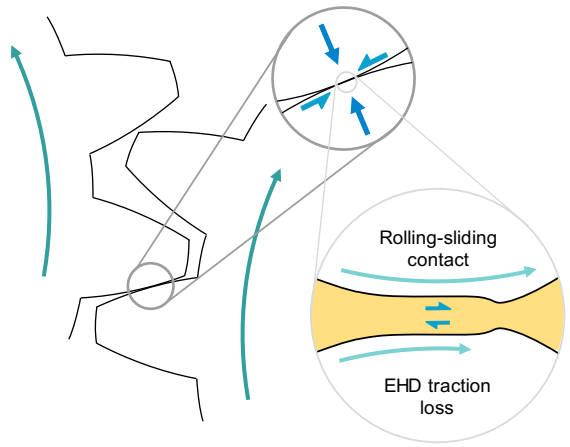
such information at a time of rapid market evolution. Severe damage to the low-speed pinion gear in a two-stage helical reducer, amounting to tooth breakage by brittle fracture possibly preceded by surface-initiated tooth-bending fatigue, is reported by Feng *et al.* [15]. Tokozakura *et al.* from the Toyota company [30] noted the unsuitability of ATF formulations for EV transmission architectures not containing wet clutches, and demonstrated consequent pitting of the sun gear in a durability test of a planetary transmission. Anecdotal reports have observed an increase in transmission noise termed 'milling' soon after 10,000 miles in Tesla Model S 2013 drive units, and also in an early electric model of the Toyota RAV4 [31, 32], containing a very similar drive unit manufactured by Tesla. The transmission noise appears to be accompanied by damage to one or more bearings on the high-speed rotor shaft, with electrical damage to the bearing raceways a possible cause.

Possible damage modes for a single-speed helical EV gearbox include bending fatigue, surface fatigue (pitting, micropitting), wear (abrasive, adhesive, corrosive, fretting), scuffing, electrically induced damage (fluting, electropitting) and overload damage (Brinelling, ridging and gross plastic yield) [33]. All of these except overload inherently depend on the tribological conditions within the gearbox, specifically the lubrication condition of contacts between pairs of meshing gear teeth, bearing raceways and rolling elements, shafts and seals, and other sliding interfaces. These same contacts are the ones which contribute to frictional power losses, and so gearbox tribology lies at the nexus of efficiency and reliability. EV transmission lubricants must therefore be designed to simultaneously optimise both efficiency and reliability, imposing a series of conflicting requirements which necessitate key tradeoffs such as lubricant viscosity [30, 34, 35], additive chemistry (particularly sulphur content due to the copper compatibility requirement) [36] and 'cooling performance' [37] (strongly influenced by a number of parameters including thermal conductivity, specific heat capacity and dynamic viscosity).

2.2 Efficiency - Gearbox Losses

Mechanical transmission efficiency is limited by energy losses due to viscous dissipation in the oil and air surrounding the rotating components, and friction in rolling and sliding contacts. Losses may be divided into load-dependent losses, varying with both transmitted torque

(a) Load-dependent losses



(b) Load-independent losses

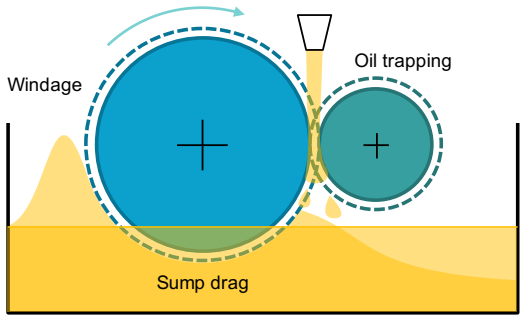


Figure 2.2: Principal sources of load-dependent (a) and load-independent (b) losses in high-speed gearing (equivalent loss modes also exist for bearings).

and rotational speed, and load-independent losses, which vary with speed only for given lubricant, transmission architecture and environmental conditions. The aggregate of the load-independent losses is sometimes termed 'spin loss', a term avoided in this work to prevent confusion with 'spin', the situation in which the pair of surfaces in non-conformal contact have unequal rate of gyration. The principal loss mechanisms for gears are illustrated in Fig. 2.2. Equivalent mechanisms also apply to bearings (although the division between load-dependent and load-independent mechanisms is less clear, traction losses due to cage friction may classify as load-independent for example). Other sources of loss include grease-lubricated bearing losses, and seal friction.

2.3 Gearbox Efficiency Measurement

Measuring gearbox mechanical efficiency η_m requires the measurement of output power P_o and input power P_i. Power loss is the difference between these, and efficiency is their ratio.

$$\eta_m = \frac{P_o}{P_i} \tag{2.1}$$

$$P_{\text{loss}} = P_i - P_o \tag{2.2}$$

When load-dependent losses are considered, the dual dependence on torque and speed requires a matrix of points in the torque-speed space to be measured, from which an iso-efficiency

map can be constructed, as given by Vanhooydonck *et al.* [38] for electric motors, and for gearboxes by Dereyne *et al.* [39]. This is conventionally presented as an efficiency contour plot superimposed on an efficiency colourmap in the torque-speed plane.

Considering only load-independent losses however, it is possible to measure the losses under the condition of zero output torque ($P_o = 0$), by measuring only P_i. The original iteration of Changenet and Velex's test rig [40, 41] simply measured the electrical power demand of their drive motor at steady speed, and subtracted the power required to spin the gears in the absence of lubricant. Several other studies [42–48] measured the drive torque required to sustain a given steady-state speed. An alternative method involves spinning the gearbox to a high speed, decoupling the driver, and measuring speed during the resulting speed transient. The rate of change of speed, at each speed, may be converted to a decelerating torque by Newton's 2nd law if the rotating inertia of the components is known, a technique commonly known as *inertia rundown*. This technique has been successfully used in several previous studies concerning spur gears [49], hypoids [50, 51], and worms [52].

For both of these methods, the torque measured can only be balanced by internal forces in the gearbox, hence $P_i = P_{\text{loss}}$. In this case, efficiency is not measurable, nor would it be well-defined, as $P_o = 0$ so $\eta_m = 0$. If the losses obtained by these methods are to be considered purely load-independent, the assumption must be made that when $P_o = 0$, load-dependent losses fall to zero, which may not be the case if the weight of the components is supported by the bearings, or if the bearings take preload forces. These intrinsic losses, though load-dependent at the component level, may be considered independent of gearbox loading, but in this case the relevant component-level loss models must be updated to reflect this recategorisation, before comparisons to experimental data may be made. In addition, given that P_{loss} is nonzero, and the power losses from each bearing, gear and seal are not simultaneously resolvable, the distribution of load-independent loss throughout the gearbox components is unknown, and each component is loaded due to the transmission of some unknown fraction of P_{loss}. Measurement of so-called load-independent losses must either attempt to estimate and subtract these intrinsic traction losses, or assume they are negligible. The steady-state case where $P_i = P_{\text{loss}}$ is different from the inertia rundown case in this regard, because, unless they are neglected, the internal power flows, and their resultant load-independent losses, are different. In the inertia rundown case, even the direction of the power

flows within the gearbox is not necessarily known - an output stage with high inertia may in fact power an input stage with low inertia, and indeed in regions of oil flow regime transition, the power flow may change direction during the transient, but this behaviour is only possible to predict if power loss distribution between components is known *a priori*. In systems with significant backlash this could even impact the flow in the meshing region, which could impact trapping losses at transition speeds. However, if it is the case that the value of P_{loss} under the condition of interest (for example under significant lubricant immersion) is much greater than the intrinsic losses (for example those measured with no lubricant immersion), then any errors incurred in the measurement of truly load-independent losses such as oil churning, due to the effect of small variations in load-dependent losses at the component level, are relatively small.

2.4 Load-independent Losses: Churning and Windage

Churning losses occur by viscous dissipation in the fluid in the gearbox, and at high speeds may become the dominant power loss. A drag torque is imparted on the gears due to both viscous shear and fluid impulse, as the lubricant is displaced by the teeth and the sides of the gear. The term 'windage' is used to describe losses due to interactions with the gaseous phase, while 'churning' implies interaction with oil, and often is used to refer to drag due to both fluid phases. Windage losses are commonly divided into pumping (outwith the mesh, where the gear teeth act like the vanes on an axial-radial mixed-flow impeller, axially aspiring and radially expelling fluid) and pocketing (in the mesh, where gear teeth displace gas from the dedendum of the mating gear). The terms drag loss and trapping loss are commonly used for the respective, broadly equivalent phenomena for oil churning.

The problem of characterising churning loss is complicated by the large number of factors on which this multi-phase, free-surface phenomenon depends. The most significant parameters considered in literature to date are illustrated in Fig. 2.3, and discussed in turn in the following sections.

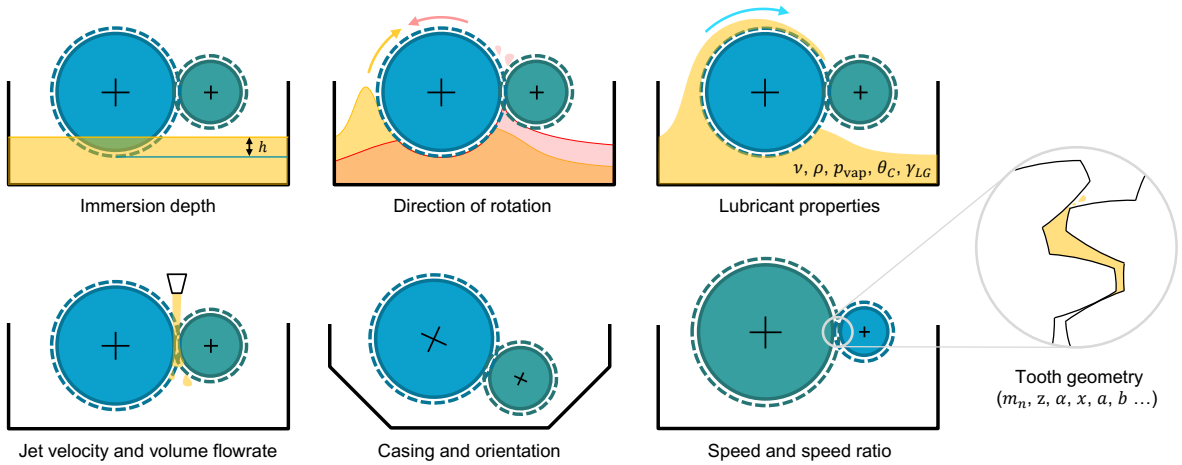


Figure 2.3: Factors affecting churning losses in geared transmissions

2.4.1 Lubricant Dynamic Viscosity

There has been some controversy over the impact of lubricant viscosity on churning loss. Luke and Olver [43] were unable to correlate churning torque on a partially immersed gear with lubricant kinematic viscosity, which they attributed to air entrainment in the flow resulting in dissipation being windage-governed and consequently depending only on the (constant) air viscosity. The model of Changenet and Velex [41] likewise at high speeds ($\mathrm{Re} \gtrsim 10^4$) is independent of fluid Reynolds number, and proposes that the flow forces are inertially dominated and therefore should not depend on viscosity in this regime. The model [53] and experimental results [54] of Seetharaman *et al.* contradict this conclusion however, finding significant dependence on oil viscosity even at higher speeds, and calling into question the rheology of the oil-air mixture. In particular, oil viscosity may affect oil aeration, and is acknowledged by LePrince *et al.* [46] as a key parameter for determining churning loss. Kakavas *et al.* [55] found spin loss increased significantly with viscosity in a hypoid axle for fluid viscosities between 22 cSt and 160 cSt, using an inertia rundown method. Shore *et al.* [56] found that the churning torque for a single gear does not necessarily increase monotonically with viscosity or gear speed, and that a local minimum churning torque exists at a certain viscosity, which varies with speed. Despite evidence to the contrary, the view that churning torque must increase as viscosity increases is still widely held among transmission designers.

2.4.2 Speeds

There is not a consensus on the reporting of transmission speeds in studies of churning losses. Changenet, Velex and Ville [40, 41, 44, 45], report pitch-line tangential velocity, and employ a pitch-line Reynolds number based on ΩR_p, where Ω is rotational speed and R_p is gear pitch radius, following the work of Terekhov [57] and Anderson and Loewenthal [58]. Ω in rpm however is widely reported [53, 59–61], providing only a frequency of rotation, which is not comparable between gears of different R_p. It would be prudent to quote both an angular and a linear velocity in order to determine the balance between linear and centripetal acceleration forces, which are likely to influence the flow, and hence churning torque. Neither parameter is able to capture the volume flowrate of fluid in the region between the tooth flanks, which additionally depends on tooth geometry. Qualitative observations by Chen and Matsumoto [62] suggest it is the fluid here which accounts for a significant proportion of both trapping (in-mesh) and drag (away from the mesh) churning losses. A new set of speed parameters based on entrained fluid volume flow rates above and beneath the addendum circle, and through the mesh, could go some way to unifying the results of existing work.

It has been suggested by Luke and Olver, and more recently by Shore *et al.* [43, 56, 63] that churning losses do not necessarily increase monotonically with speed. This may result from the competition between several forces acting on the fluid, including viscous shear, inertial, hydrostatic, centripetal and surface tension, which may each dominate the churning torque in different flow regimes existing at different speeds, complicating modelling of churning loss.

For meshed gears, the transmission ratio is also a significant factor. For a gear pair in mesh, the pitch line velocity of each gear is identical, but the differing angular velocity of each (except in the case of unity transmission ratio) may alter the balance between inertial, gravitational and centripetal forces on the fluid at any given speed, significantly altering oil flow and hence losses.

2.4.3 Lubrication Type: Grease, Dip, or Jet

Grease lubrication of gears is viable only at low speeds at which heat fluxes, shear rates and centripetal forces are sufficiently low so as not to overheat, degrade or expel the grease, which would ultimately lead to loss of lubrication and consequent early failure. The prediction

of grease churning losses in bearings has attracted considerable research attention [64, 65], but load-independent losses in grease-lubricated gears are rarely considered. Liu *et al.* [66] employed a finite volume model to predict grease flow in a meshing spur gear pair moving at peripheral speeds less than 1 m/s, but did not report drag or churning torques.

Dip, or splash lubrication, involving one or more gears partially immersed in a sump of liquid lubricant, is employed at intermediate tangential speeds, from around 3 m/s [41] up to around 20 m/s [67]. Spray, or jet lubrication involves a lubricant jet directed at the regions in which it is required, e.g. into the gear mesh, and may be used for very high-speed applications in which inertial fling-off or oil churning would render dip lubrication unsatisfactory. An additional lubricant pump is required, increasing transmission cost, weight, and power consumption, but in cases where this is nevertheless present for lubricant cooling/filtration systems, jet lubrication is popular.

Both dip and jet lubrication incur significant churning losses at high speeds, but not necessarily by the same mechanisms - in particular, jet-lubricated systems are often operated 'dry sump' with oil-scavenge, minimising drag loss. Neuroth *et al.* [61] claimed that tuning the axial clearance on a single gear could bring dip-lubricated losses in line with jet-lubrication losses at pitch-line velocities up to 60 m/s, but did not consider swell effects or trapping losses. Kakavas [51] found, using inertia rundown with a hypoid axle, that the volume flowrate of lubricant delivered significantly influenced spin losses, but that also the location of the jet (onto gears or bearings), and the viscosity of the lubricant modulated the strength of the volume flowrate effect.

2.4.4 Gear Geometry and Meshing

There is some controversy over the influence of gear geometry on churning loss. The most significant geometrical parameter is whether the gear stands alone, or meshes with another gear. For meshed gear pairs, directional and swell effects, trapping losses, and the inclination of the quiescent lubricant surface to the line of centres, become important additional parameters that cannot be examined with a single gear. Nevertheless, much work on oil churning considers only a single gear [43, 44, 49, 56]. Changenet and Velex [41] postulated that churning loss depends both on gear module and facewidth, but only found a dependence on facewidth at

high speeds, and no dependence on module at any speed, for a lone gear. This assumption was carried forward in their treatment of a meshing gear pair, and subsequently contradicted by the consideration of trapping losses by Chen and Matsumoto [62], who argued that the effect on the steady-state oil surface profile of the module and facewidth was non-negligible, and compounded by their effect on trapping loss. Liu *et al.* and Hildebrand *et al.* [67, 68] used a CFD model to find the relative contribution to total churning torque from tooth flank and gear side surfaces, and concluded that the majority of drag torque is imparted by pressure forces at the flank surfaces, that majority increasing with speed. For a jet lubricated gear pair in mesh, where trapping losses predominate, the module and facewidth influence the evolution throughout the mesh cycle of the volume enclosed beneath the addendum circle, so have been considered of primary significance by Ariura, Petry-Johnson and Seetharaman [54, 59, 69]. In addition, the profile shift and root clearance, which also influence this swept volume, are possible contributing factors. Nonzero helix angle was found to significantly increase windage and trapping torques for helical gears, the strength of the helix angle effect increasing with speed, by Diab *et al.* [70].

2.4.5 Immersion Depth

Immersion depth measures the depth to which the gears are immersed in lubricant when the fluid is quiescent, for example in the nondimensional form $\frac{h}{R_p}$ used by Changenet and Velex [41], symbols defined by Fig. 2.4a. For a meshing gear pair, this metric only accounts for the

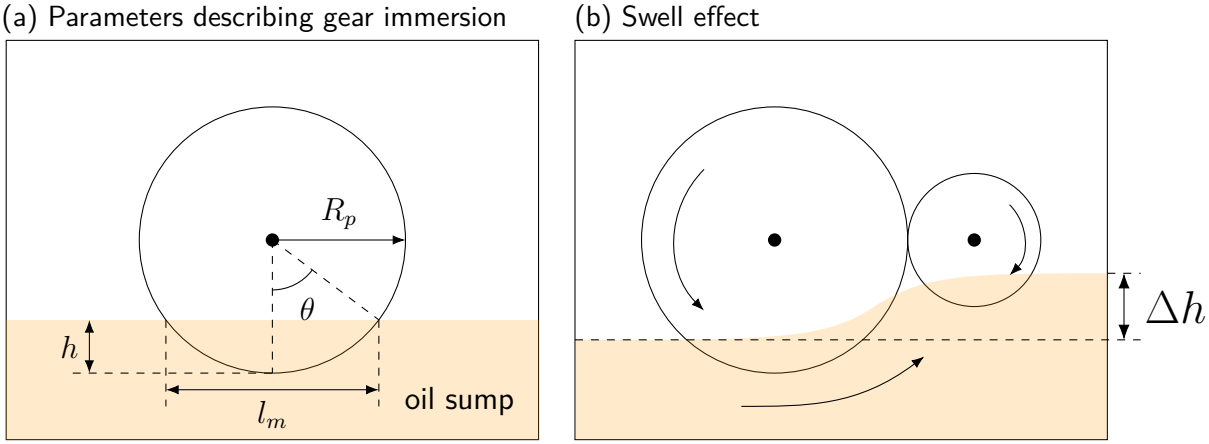


Figure 2.4: Quiescent and disturbed oil profiles assumed by Changenet and Velex, adapted from ref. [41]

immersion condition of one of the gears, except in the special case where the inclination of the line of centres creates equal immersion depth on pinion and wheel, and does not account for the change of gear immersion with speed, which depends on casing geometry as the lubricant is thrown away from the gear pitch circle. Chen and Matsumoto [62] observe that immersion depth affects both the drag loss due to shearing and impulse of the lubricant due to the gear teeth, and also the steady-state oil surface profile at a given speed, hence the trapping loss, because this is governed by the rate at which oil is induced into the mesh. It is universally observed that increasing immersion depth increases load-independent losses, however Höhn *et al.* [71] showed that increased immersion depth dramatically increased the scuffing load capacity in a series of four-square tests, highlighting the efficiency-reliability tradeoff to be made here.

2.4.6 Rotational Direction and Swell Effects

The direction of gear rotation may cause the teeth to splash the lubricant laterally away from the mesh, or up into it (Fig. 2.5). This greatly influences the volume of lubricant trapped in the dedendum through the mesh, and so the loss associated with the consequent pocketing [53], pumping [44], and trapping [60, 62] phenomena. Changenet and Velex [41] refer to 'swell effect' (Fig. 2.4b), meaning the difference in lubricant surface height between pinion and wheel as a result of a difference in drag-induced pressure between pinion and wheel, and propose a model to account for the effect of this on churning torque. The model is expressed in terms of speed ratio, but assumes that the line of centres is horizontal, which is frequently not the case in the reduction gearboxes typical of electric vehicle transmissions.

2.4.7 Casing, Clearances and Orientation

The geometry of the enclosure surrounding the gears has been shown to strongly influence both windage and churning effects, both for single gears and meshing gear pairs. Early work by Daily and Nece [42] showed that windage torque on an enclosed spinning disc was governed by the axial clearance from the circular faces of the disc, identifying four regimes created by the twofold combination of laminar or turbulent flow, and separate or merged boundary layers on the adjacent stationary and rotating faces. Diab *et al.* [70, 72] proposed that for a gear rotating in air, the axial pumping of fluid into the region between the teeth, before being

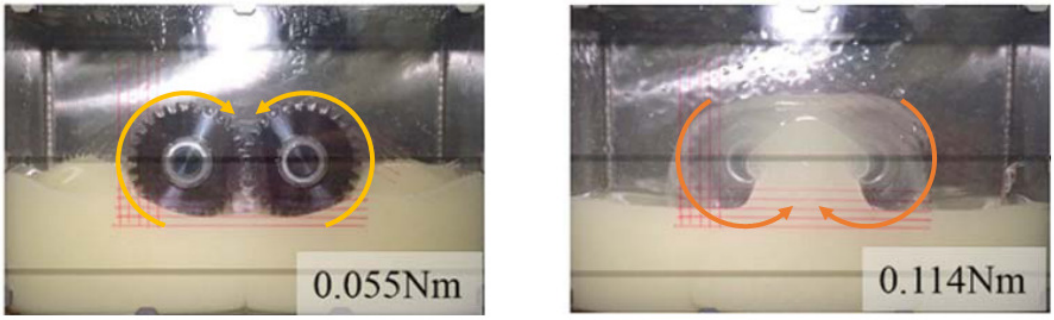


Figure 2.5: Effect of rotation direction on churning torque and steady-state oil surface profile, from a test with VG320 oil at 500 rpm by Chen and Matsumoto [62], reproduced with the permission of Taylor & Francis.

radially expelled, is responsible for a significant proportion of the windage torque. Changenet and Velex [44] likewise observed for a single partially immersed gear that churning torque shows very little sensitivity to radial clearance, but is a strong function of axial clearance, and propose an analogous dissipation mechanism for churning. Chen and Matsumoto [62] however found that placing boards beneath a rotating gear pair, reducing their minimum radial clearance, greatly reduced churning torque in certain cases, and found that the extent of this reduction was related the ratio of radial clearance to boundary layer thickness within the oil path. The opposite trend was observed where the boards caused the oil to wrap round into the mesh, explaining the results of Seetharaman and Kahraman [53] which demonstrated torque increase at high speeds for reduced clearance. Hildebrandt *et al.* [67] showed that the presence of a goggle-shaped oil guide plate considerably reduced the contribution of pressure forces at the tooth flanks to overall drag loss. Racetrack and goggle-shaped shrouds were also employed by Chen and Matsumoto [62], and it was found that there existed a radial clearance at which churning torque was minimum, corresponding approximately to the fluid boundary layer thickness. It was concluded that radial clearance alone is an insufficient metric to determine churning torque, and the influence of sidewall geometry on the oil surface profile must also be considered.

The same authors [62], using a gearbox with variable inclination of the line of centres, conclude that the orientation of the gearbox is highly significant for trapping losses because this determines how much oil reaches the mesh, although for small inclinations, once the oil does not reach the mesh, the dependence becomes negligible.

2.4.8 Cavitation and Aeration

Cavitation, the formation of vapour bubbles where the local static pressure falls below the fluid vapour pressure, was reported in meshing gears at relatively low speeds of 500 rpm by Hunt *et al.* [73]. Subsequent bubble collapse may dissipate energy by shock waves (responsible for cavitation damage commonly found on pumps and impellers), thermally due to the high temperatures achieved during vapour compression, and even as light via cavitation luminescence [74]. There exists a significant body of work on cavitation in gear pumps [75–77], and the canonical review by Dowson and Taylor [78] considers the phenomenon well-known to tribologists in fluid film bearings. The role of cavitation in power transmission gearbox churning losses is not well-studied however: the results of Hunt *et al.* in 1981 [73] are succeeded only by the experimental results used to validate the CFD solver of Concli and Gorla [79] in 2016, concluding that cavitation is a significant contributor to churning loss for fully immersed gears. Concli *et al.* [80] subsequently concluded however that for dip lubrication, cavitation is not significant because the presence of air precludes the necessary low static pressures, although a maximum speed of only 840 rpm was considered. Chen and Senlis [81] note that cavitation damage on gear teeth may be brought on by vibration, and Ouyang *et al.* [82] have suggested that vibration caused by existing fatigue damage on gear teeth induces further damage due to cavitation.

In the case of oil dip- or spray-lubricated gears, aeration effects may predominate vapour cavitation, due to the very low vapour pressure of oils (vapour pressures for several common oligomers are reported to fall below $1\ \mathrm{Pa}$ at $40^{\circ}\mathrm{C}$ by Karis and Nagaraj [83], a factor of around 10^4 lower than the vapour pressure of water). 'Aeration' may refer to either the presence of air bubbles due to foaming (churning of air bubbles into the oil), or to dissolved air which is brought out of solution at locally low pressures. Aeration and cavitation are distinguished by their differing bubble pressure - the bubbles in aerated oil will not collapse abruptly like cavitation bubbles, and conversely may serve to increase the compressibility of the bulk fluid so as to delay the onset of cavitation. Changenet *et al.* [45] note that lubricant aeration increases with bath temperature and at higher speeds, and postulate that bubble formation and subdivision leads to higher churning losses due to increased interfacial surface energy. It was found by LePrince *et al.* [46] that the correlation between churning loss and Reynolds

number may be undermined both by differing air solubility and surface tension of the fluid, and a new analytical model was proposed to account for these.

Dissolved air brought out of solution at low pressure may by contrast be subject to bubble collapse. Hunt *et al.* [73] found that reducing dissolved air content greatly suppressed the onset of 'cavitation' in a purpose-built off-line oscillating-plate cavitation test, but were unable to reproduce this effect in a (fully immersed) gearbox, possibly due to air contamination in the gearbox components undermining their control of the air content. Damage reminiscent of cavitation shock damage was observed on the plates of the off-line test. It was proposed that the 'cavitation' observed may therefore in fact be 'gaseous in nature', i.e. due to the dissolution of air.

2.4.9 Ambient Pressure Inside Gearbox

The static pressure of the gas surrounding a rotating gear pair has been found to influence churning loss under dip lubrication, while for jet lubrication the literature is less conclusive. For a single, shrouded gear, Kolekar *et al.* [49] found that increasing ambient pressure considerably reduced churning losses, and proposed that gravitational reflow was suppressed by windage effects that acted to decrease effective immersion depth and minimise drag losses. By contrast, Concli *et al.* [80] suggested, based on a series of CFD simulations, that *decreasing* ambient pressure should reduce churning loss by thickening the 'air pillow' (region of low lubricant volume fraction) surrounding the gear, reducing its contact with the lubricant. They also proposed tentatively that lower pressure could advance the onset of cavitation which serves to limit the negative gauge pressure on the trailing edge of the gear teeth thereby reducing churning torque. A possible explanation for the disagreement between the conclusions of Concli and Kolekar lies with the extent to which an oil-air foam is created - Kolekar reports observing no stable oil-air foam, and hence the lubricant was better dispersed when the chamber was held at higher pressure. Additionally, the gearbox geometries, the criticality of which for lubricant-recirculation-related losses is discussed above, differ: Kolekar uses a cylindrical chamber while Concli examines a meshing gear pair contained in a cuboidal sump. Massini *et al.* [84] investigated a single gear under an oil jet in a depressurised gearbox designed to simulate altitude for aeronautical applications, and found very little dependence on pressure of power loss. It was proposed on examination of high-speed photography of the impinging

jet that, were the jet further from the gear, ambient pressure might affect the onset of jet break-up which was shown to influence both lubrication condition and load-independent loss. Trapping losses were not investigated.

2.5 Load-dependent Losses: EHL Traction and Film Thickness at High Speeds

Elastohydrodynamic lubrication (EHL) is characterised by the coupling between two effects of the very high pressures in rolling-sliding contact between non-conforming surfaces: lubricant piezoviscosity (lubricating oils exhibit a dramatic increase in viscosity with pressure), and elastic deformation of the surfaces. When they are in motion, the rolling of the surfaces entrains lubricant into the contact, which is pressurised to approximately the Hertzian contact pressure (often of the order GPa) as the surfaces converge in the contact inlet. The resulting increase in oil viscosity generates a hydrodynamic film which may completely separate the surfaces, as shown in Fig. 2.6. The aspect ratio of the film is extremely high, often of the order 1000 times wider than it is thick, and consequently leakage of oil from the sides of the contact is minimal. As a result, the film thickness is not strongly affected by contact load, but depends principally on the rate at which oil is entrained, termed entrainment speed U_e, and oil viscosity in the inlet (governed both by the far-field oil viscosity, and the degree to which viscosity increases with pressure). Sliding speed U_s is defined as the difference between the surface speeds, and (at constant entrainment speed) the thickness of the film does not observably change with sliding speed unless enough heat is generated to bring about a change in fluid viscosity in the inlet. Sliding speed is often normalised by the entrainment speed to give the Slide-Roll Ratio (SRR).

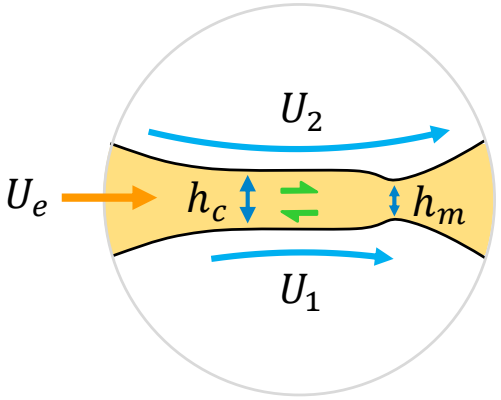
$$U_e = \frac{1}{2}(U_1 + U_2) \tag{2.3}$$

$$U_s = U_2 - U_1 \tag{2.4}$$

$$\mathrm{SRR} = \frac{U_s}{U_e} = 2\frac{U_2 - U_1}{U_1 + U_2} \tag{2.5}$$

Key features of an EHL contact are illustrated in Fig. 2.7. Rolling-sliding elastohydrodynamic (EHD) contacts are of particular significance because they transmit the loads in gears and

(a) Section view (schematic)



(b) Top view (white light interferogram)

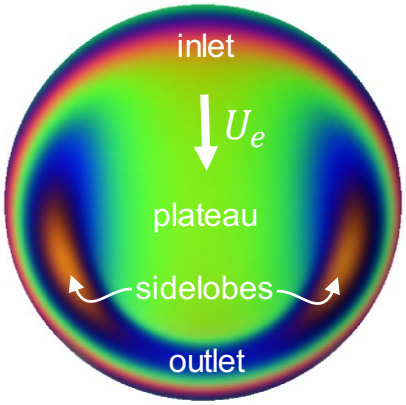


Figure 2.6: Schematic showing motion of surfaces and oil entrainment in an EHL contact (a), and white-light interference image of EHL contact (b) showing the shape of the contact: the colours are created by an optical path difference proportional to film thickness.

(a) Film thickness map of EHL point contact

(b) Film thickness profiles

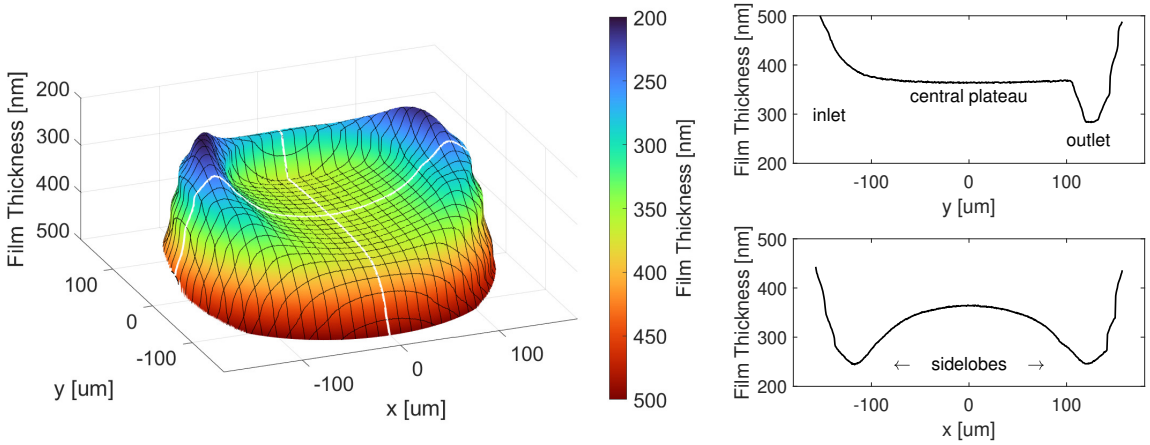


Figure 2.7: Film thickness measurement of an EHL point contact illustrating key topographical features (a), showing longitudinal and transverse sections (b) corresponding to white lines in (a). The measurement was made using colorimetric interferometry as described in Chapter 8, applied to the interferogram shown in Fig. 2.6b. Oil entrainment is in the positive y direction. The contact was between a 3/4" steel ball and a flat glass disc in pure rolling at 1.155 m/s entrainment speed under 20 N normal load with PAO6 at 20°C.

rolling element bearings, so both EHL friction and film thickness significantly affect gearbox efficiency and reliability. EHL has received much research attention during the last 80 years [85–87], leading to classical regression equations still widely used for predicting EHL film thickness [88] and their subsequent validation by experiments [89]. These predictions assume however that the temperature field is uniform throughout the contact, and so are not valid

at high entrainment speeds where there is significant inlet shear heating. Several thermal correction factors derived from numerical calculations have been proposed [90], but these do not generalise well to different lubricant chemistries. Unlike film thickness, prediction of EHL friction remains very challenging due to complex thermally-coupled rheological phenomena at high pressure and shear strain rate. Friction is less well-studied at high speeds, and there are no simple closed-form correction factors as there are for film thickness. The term 'traction' is used in this work to describe friction in the full-film EHL regime, to emphasise that the forces are transmitted via the fluid film, and not due to solid-solid interactions.

The need to simultaneously optimise both system energy efficiency and reliablity in electric vehicles has recently brought thermal EHL traction losses sharply into focus, and high-speed thermal EHL is also relevant to high-speed machine spindle bearings [91] and geared turbofan engines [92]. The problem of predicting and optimising losses is compounded by the thermal coupling to macroscopic thermal resistances in these systems, the complexity of their geometries, and therefore the wide range of lengthscales and timescales involved.

2.5.1 Traction Prediction

The pioneering EHL solution of Ertel [93, 94] assumed that film thickness and traction are largely decoupled. This is the case under conditions where the contact can be considered isothermal because the film thickness is governed by lubricant rheology in the inlet, in which the pressure and shear rate are low compared to the conditions in the contact itself. Film thickness is therefore well-predicted by low-shear lubricant properties measured at ambient pressure [95]. Traction however depends on the in-contact rheology, which is subject to sub-millisecond transit times, GPa pressures, and shear rates $\sim 10^7$ s^{-1}. The rheology of the fluid under these conditions is highly non-Newtonian and is still the subject of considerable debate [96, 97], in particular the treatment of the effect of high pressures and high shear rates. These effects are not well-resolved by EHL traction measurements due to the highly nonuniform temperature and pressure fields, a limitation of classical efforts to describe fluid behaviour in EHL contacts [98, 99]. High-pressure viscometers have so far been unable to simultaneously produce representative magnitudes of shear rate and transit time actually seen by EHL contacts, partly due to the very challenging problem of decoupling the influence of heat generation on the rheology from the rheology itself [100]. Nevertheless, the separate

treatment of pressure and shear rate by models fitted to various rheology studies has resulted in several numerical solvers whose outputs show very good agreement with experiments [101, 102].

2.5.2 Inlet Heating

Fluid which is not entrained into the contact must be diverted around it, creating an inlet flow field with significant shearing, which generates heat. The heating becomes more significant as the entrainment speed increases. The consequent reduction in fluid viscosity in the inlet reduces film thickness at high entrainment speeds. So-called 'inlet shear heating' has been studied numerically by Cheng [103, 104], by Wilson and Sheu [105], and by Pandey and Ghosh [106], who provided expressions for central film thickness h_c of the form $h_{c_{\text{thermal}}} = h_{c_{\text{isothermal}}} C_T$, where C_T is a correction factor expressible as a function of fluid properties and contact conditions. The more recent, and widely-used, correction by Gupta *et al.* [90] was appraised by the experimental study of Hili *et al.* [107] who used a high-speed ball-on-disc machine and ultra-thin-film interferometry [108]. Hili found qualitative agreement with Gupta's predictions, and provided alternative coefficients for four base oil types to better fit her measurements. Liang *et al.* [109] took a dual experimental and numerical approach, which they used to provide a unified set of modified coefficients for Gupta's correction and to investigate the influence of the temperature field on pressure profile and film shape.

There are three main sources of inlet heating:

1. *Inlet shear heating* which results from the coupling between the flow field and the viscosity field at the inlet, becoming particularly significant at high speeds [110].
2. *Conductive heating* as the upstream solid temperatures raise the temperature of the lubricant above that of the temperature-controlled sump before it is entrained into the contact. Olver [111] developed a method to calculate solid body temperatures based on a prediction of in-contact heat fluxes, and a thermal network model.
3. *Compression heating* resulting from lubricant pressurisation in the inlet. This phenomenon was investigated experimentally by Reddyhoff *et al.* [112], showing compression heating to increase with entrainment speed but to be quickly outstripped by shear heating when sliding was applied, a finding maintained by the numerical analysis of

Habchi and Vergne [113], who observed that even under nominally pure rolling conditions there is some shear which creates heating of the same order as the compression. Compression heating is therefore likely of little significance at high entrainment speeds for nonzero sliding.

These inlet heating mechanisms, as they happen upstream of the shear heating in the contact, considerably change the temperature and so the rheology of the fluid in contact. This creates a direct link between film thickness (governed by inlet rheology) and traction (governed by rheology in the contact), which stands in contrast to the classical assumption that these are decoupled (with the notable exception of minimum film thickness, as detailed in the recent, rhetorically-titled work of Habchi, Šperka and Bair [114]).

Analytical solutions for temperature rise of the solids based on thermal resistances for cylindrical specimens in line-contact geometries were proposed by Olver in 1991 [111] and are often used to correct inlet temperatures in the study of rolling contact fatigue where boundary friction and high sliding conditions generate considerable heat [115], but the same is not commonly done for ball-on-disc studies in the literature on account of the complexity of expressing the relevant thermal resistances.

2.5.3 Flash Heating

For contacting surfaces of the same material, the relationship in Eq. (2.6) has been used by Spikes and coworkers [96, 116, 117] to estimate mean flash temperature rise $\overline{\Delta T}$, which is taken to be the sum of the mean temperature rise developed by the surfaces $\overline{\Delta T_s}$ and that of the oil film $\overline{\Delta T_{\text{oil}}}$, as illustrated in Fig. 2.8.

$$\overline{\Delta T} = \overline{\Delta T_s} + \overline{\Delta T_{\text{oil}}} = \left(\left(\frac{a}{\pi \kappa_s \rho c_p U_e} \right)^{\frac{1}{2}} + \frac{h_c}{8\kappa_{\text{oil}}} \right) \mu \bar{p} U_s \tag{2.6}$$

The thermal conductivity, density and heat capacity of the surfaces are taken as κ_s, ρ and c_p respectively, while κ_{oil} is the thermal conductivity of the oil. U_e and U_s are respectively the entrainment and sliding speeds, μ is the traction coefficient and $\bar{p}$ is the mean pressure.

The $\overline{\Delta T_s}$ term follows the form of Jaeger [119], and was derived for a square contact assuming all of the heat is taken up by one surface. Archard [120] derived a very similar expression, based

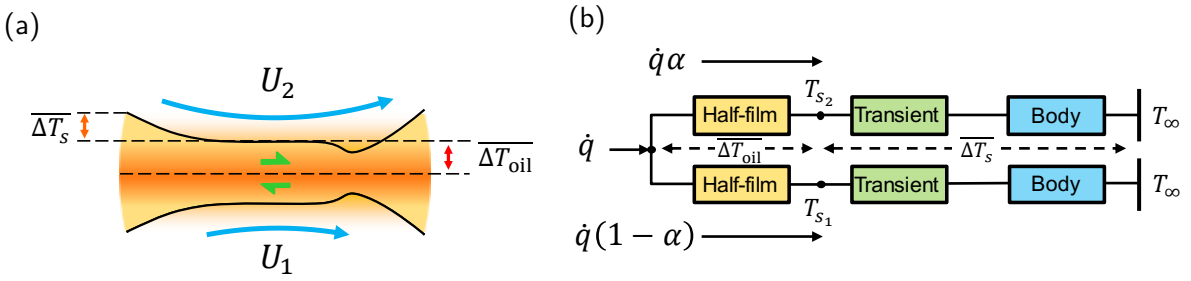


Figure 2.8: (a) Schematic showing mean 'flash' temperature due to heating of the surfaces $\overline{\Delta T_s}$, and temperature rise within the oil film $\overline{\Delta T_{\text{oil}}}$ in an EHL contact, and (b) thermal network illustrating the division of heat flow $\dot{q}$ according to thermal partition coefficient α by thermal resistances due to the film, transient conduction at the surface, and the steady-state thermal resistance of the body and its other thermal interfaces, adapted from [118].

on Jaeger's expression for maximum temperature, for a circular geometry giving $\overline{\Delta T_{\text{circ}}} \approx 0.92\overline{\Delta T_{\text{square}}}$. The work of Olver, following Jaeger's approach, employs a thermal partition coefficient which assumes the surfaces have equivalent mean temperature, so the partition coefficient is a function of the respective thermal resistances and velocities of the surfaces [111, 118]. The form of the $\overline{\Delta T_s}$ term in Eq. (2.6), although it appears exact and is often cited as being due to Archard, is in fact related to Jaeger's expression by a factor of $3/\sqrt{32} \approx 0.53$, and to Archard's by $1/(0.31\pi^{3/2}) \approx 0.58$, indicating a thermal partition coefficient slightly greater than 0.5 (for the faster surface) which is reasonable for a steel/steel ball-on-disc contact at modest SRRs. This 1D solution assumes that the contact is moving 'fast' relative to the time it would take the surfaces to reach a thermal equilibrium, or equivalently that the depth to which the heat penetrates is much smaller than the contact width, hence lateral heat flow can be neglected and heat flow is unidirectional, an assumption which under thermal EHL conditions remains quite robust. In the mixed regime, as in gears, the temperature is highly nonuniform throughout the contact, a situation addressed by the 2D numerical model of Kadiric *et al.* [121] which enabled the thermal partition coefficient to vary across the contact.

The $\overline{\Delta T_{\text{oil}}}$ term is given by Archard [120], and assumes the oil film is a 'parallel slab' with uniform volumetric heating, applying Dirichlet conditions at the inlet and on both surfaces. The value 8 in the denominator (Eq. (2.6)) arises from the assumption of uniform volumetric heating, and is the subject of some debate [117] but agrees approximately with infrared measurements [122] for SRRs less than 200%. The aspect ratio of the film and the fact that the surfaces have much greater thermal conductivity than the oil is taken to justify the

assumption that the heat flow is once again linear, which leads to the outlet being treated as adiabatic, i.e. advective heat transport is ignored. Heat storage by the thermal bulk of the oil is neglected, as the Fourier number $\mathrm{Fo} = 2\chi_{\mathrm{oil}}a/(U_e(h_c/2)^2)$ is said to be low ($\mathrm{Fo} < 2$) [118], although this assumption weakens for low viscosities, and for all conditions in Chapter 6 of this work, $2 < \mathrm{Fo} < 200$. The assumption of uniform volumetric heating, requiring uniform shear stress in the contact (highly unlikely if the temperature field is strongly nonuniform), and the treatment of advection at the inlet and outlet, are most problematic for thermal EHL, particularly when the surfaces rapidly recirculate back into the contact as in most tribometers. The summation of the two terms was proposed by Archard 'as a first approximation'.

Nevertheless, Eq. (2.6) was successfully used by Zhang and Spikes [116, 117] to 'isothermally correct' shear stresses for temperature rises below 10°C, preserving the agreement with the Johnson and Tevaarwerk model some way into the thermal regime. For larger temperature rises (particularly at high entrainment speeds) the assumptions made by the flash temperature calculation about flow profile and the distribution of heat generation begin to break down. It is possible that for these large temperature rises, the nonuniformity of the shear stress profile in the contact ceases to bear analogy to the isothermal case at the mean contact temperature.

2.5.4 Film Thickness Measurement

Measurement of sub-micron lubricant films in rolling-sliding elastohydrodynamic contacts has been approached using electrical resistance measurement [123], capacitance [124], ultrasound

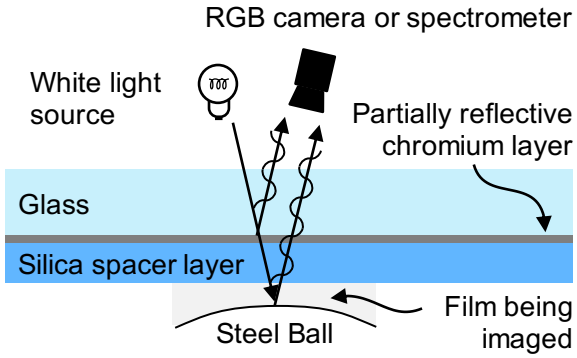


Figure 2.9: Schematic showing working principle of EHL film thickness measurement by optical interferometry including the use of the spacer layer to enable measurement of nanometre-thick films to nanometre resolution.

[125], and optical interferometry [126]. The optical family of techniques, by far the most accurate and widely-used today, originated from the work of Gohar and Cameron [127], who used a polished steel ball loaded against a transparent rotating disc through which light was directed. Interference images of the contact enabled detailed film thickness maps to be obtained, but the range and resolution of the technique were limited by the wavelength of visible light. This problem was overcome by Westlake and Cameron [128] by employing a silica spacer layer, and the technique was later extended and automated by Spikes and coworkers [108] to become ultra-thin-film interferometry. This technique has since been used to study numerous related tribological phenomena including grease lubrication [129], starvation [130], rough contact [131], soft EHL [132], boundary films [133], and polymer solutions [134]. The related family of colorimetric techniques including the Spacer Layer Imaging Method (SLIM) [135], and Differential Colorimetric Interferometry (DCI) [136] involve photographing the interferogram directly and using a colorimetric image analysis to produce a topographical film thickness map. Ultra-thin-film interferometry by contrast uses a spectrometer to determine the peak-intensity wavelengths, from which film thickness is calculable (to finer resolution and for thicker films than SLIM) along a 1D film thickness profile spanning the contact, although the leading implementation of the technique currently reports only a single mean value over a portion of this line. The Relative Optical Interference Intensity (ROII) technique, involving a formalised fringe-counting and sinusoidal interpolation procedure, has also been used to measure EHL film thickness [137, 138].

2.6 Bearing Losses

Frictional losses in rolling element bearings may be classified analogously to gear losses - load-independent losses due to macro-scale interactions with the fluid, and load-dependent losses due to EHD traction and micro-slip. The bearing frictional moment model by SKF [139] is the widest-reaching and most commonly used model in the public domain. The total frictional moment M is divided into losses from rolling M_{rr}, sliding M_{sl}, drag M_{drag} and seals M_{seal} according to

$$M = M_{\mathrm{rr}} + M_{\mathrm{sl}} + M_{\mathrm{drag}} + M_{\mathrm{seal}} \tag{2.7}$$

The rolling moment (load-dependent) may be determined from

$$M_{\mathrm{rr}} = \phi_{\mathrm{ish}}\phi_{\mathrm{rs}}G_{\mathrm{rr}}(\nu n)^{0.6} \tag{2.8}$$

where ϕ_{ish} is the reduction factor for inlet shear heating, ϕ_{rs} is the kinematic replenishment/starvation factor, G_{rr} is a factor depending on bearing type, size and loading, n is rotational speed, and ν is oil operating kinematic viscosity. The sliding moment (load-dependent) is given by

$$M_{\mathrm{sl}} = G_{\mathrm{sl}}\left[\phi_{\mathrm{bl}}\mu_{\mathrm{bl}} + (1-\phi_{\mathrm{bl}})\mu_{\mathrm{EHL}}\right] \tag{2.9}$$

where G_{sl} depends on the bearing type, size and loading, ϕ_{bl} is a weighting factor, and μ_{EHL} is an approximation of the sliding friction coefficient in full-film conditions based on bearing type and lubrication condition. The drag moment (load-independent) is obtained via one of

$$M_{\mathrm{drag}} = 0.4V_{\mathrm{M}}K_{\mathrm{ball}}d_{\mathrm{m}}^5n^2 + 1.093\times10^{-7}d_{\mathrm{m}}^3n^2\left(\frac{nd_{\mathrm{m}}^2f_{\mathrm{t}}}{\nu}\right)^{-1.379}R_{\mathrm{s}} \tag{2.10}$$

$$M_{\mathrm{drag}} = 4V_{\mathrm{M}}K_{\mathrm{roll}}C_{\mathrm{w}}Bd_{\mathrm{m}}^4n^2 + 1.093\times10^{-7}d_{\mathrm{m}}^3n^2\left(\frac{nd_{\mathrm{m}}^2f_{\mathrm{t}}}{\nu}\right)^{-1.379}R_{\mathrm{s}} \tag{2.11}$$

for ball and roller bearings respectively, where V_{M} is a drag loss factor depending on oil level and K_{ball}, K_{roll}, C_{w}, B, d_{m}, f_{t} and R_{s} are geometrical parameters.

Finally, the seal moment (load-independent) is calculated from

$$M_{\mathrm{seal}} = K_{\mathrm{S1}}d_{\mathrm{s}}^{\beta} + K_{\mathrm{S2}} \tag{2.12}$$

where d_{s} is the seal counterface diameter and K_{S1}, K_{S2} and β are constants depending on the seal type, bearing type and bearing size.

Several other bearing loss models exist [140–143], and all are limited to relatively low speeds (less than $5\times10^5\ ND_m$), around an order of magnitude lower than the speeds reached by EV motor bearings. Both measurement and prediction of bearing losses at these high speeds is challenging, and considerable research effort in this area is presently ongoing.

2.7 Scuffing

Scuffing describes surface damage caused by severe adhesive wear resulting from the sudden collapse of both fluid and boundary lubricating films, accompanied by locally elevated surface temperatures which lead to surface welding, plastic flow at the surface, and eventually catastrophic wear or seizure. Highly loaded non-conforming contacts at high sliding speeds are at particular risk of scuffing, and so scuffing is an important failure mode in gears (an example is given in Fig. 2.10), especially those operating simultaneously at high torques and speeds such as those in EVs. Although the later stages of scuffing are widely understood and the nature of scuffed surfaces is well-characterised, the mechanisms underlying scuffing initiation, and the conditions required to give rise to these, remain a subject of considerable debate. In 1937, Blok [144] introduced the flash temperature concept and proposed the critical temperature scuffing criterion, postulating that scuffing occurs when the total contact temperature (the sum of the bulk material temperature and the transient 'flash' temperature in the contact [145]) reaches a critical value. It was proposed that the critical temperature was characteristic of the combination of lubricant and sliding surfaces, and did not strongly depend on load, sliding speed or bulk temperature. The 1975 review of Dyson [146] notes that Blok's postulate was originally intended to be confined to unadditivised mineral oils, and that the body of empirical work examining the critical scuffing temperature criterion is far from conclusive on its validity. Although it is possible to specify limited ranges for load, sliding and rolling

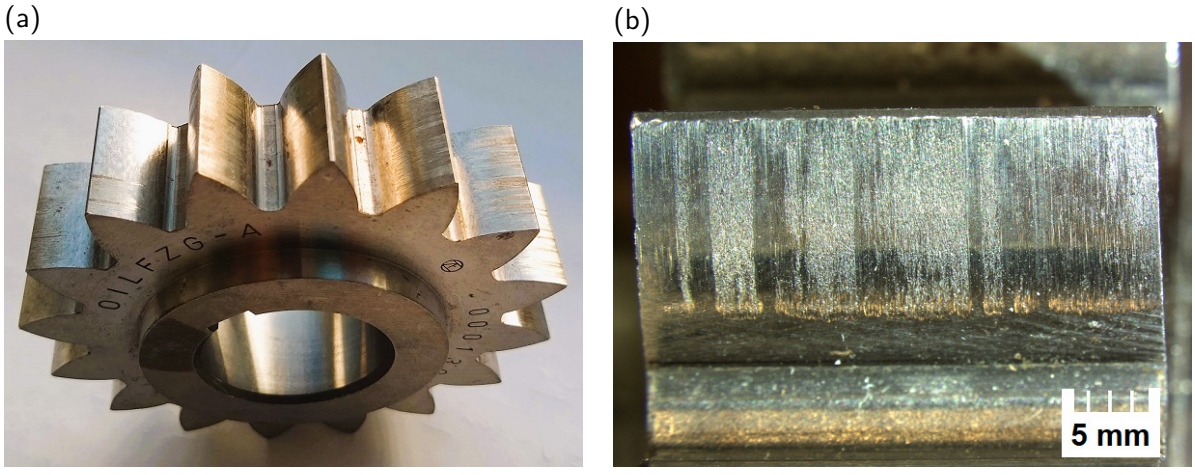


Figure 2.10: (a) Test gear showing severe scuffing on tooth faces and (b) microscope image of a tooth face of the same gear showing characteristic plastic flow on tooth surface.

speeds within which total contact temperature at scuffing is approximately constant, there is considerable variation outside these ranges. Dyson concluded that frictional power intensity [147, 148] is a more reliable, although also limited, predictor of scuffing based on studies then extant. Dyson later proposed a separate EHL-based model relating the onset of scuffing to the inability to generate sufficient pressure in the contact inlet to sustain an EHL film [149]. Barber [150] proposed that a thermoelastic instability due to local increases in frictional heating caused by thermal expansion at asperity peaks, could lead to scuffing. Several other physical phenomena contributing to the onset of scuffing are discussed in the 1996 review of Bowman and Stachowiak [151], including collapse of micro-EHL films [152], molecular desorption [153, 154], removal of oxides [155, 156] and additive films, asperity fatigue [157], and lubricant decomposition [158]. Enthoven *et al.* [159] examined the critical temperature and inlet pressure theories experimentally using infrared surface temperature measurements of a steel-on-sapphire contact, finding no agreement with these scuffing criteria. Enthoven and Spikes [160] also proposed that entrainment of debris is a possible cause for scuffing in a similar steel-on-sapphire contact, and that therefore the risk of scuffing may be increased by generation of wear debris. Hershberger *et al.* [161] provided evidence of scuffing initiation caused by adiabatic shear instability due to the thermal softening rate exceeding the rate of work hardening at the surface, causing gross plastic flow. The adiabatic shear instability criterion was later developed into an analytical predictive model by Ajayi *et al.* [162]. The computational approach of Li *et al.* [163] by contrast employed a mixed thermal-EHL point contact solver coupled with a heat transfer model, accounting also for asperity interactions and non-Newtonian rheology, whose predictions were in agreement with a series of ball-on-disc scuffing tests.

A variety of scuffing test methods have been used. Tests in pure sliding such as the four-ball test [164, 165], Timken test [164], and ball on cylinder test [166] have the limitation that the contact is stationary with respect to one of the surfaces and so the contact pressure is changed significantly by any wear which precedes scuffing, which hinders the application of models which estimate contact temperatures in the interpretation of results. Back-to-back (or four-square) gear scuffing tests including the Ryder test [167], used widely for the qualification of aviation lubricants, the IAE back-to-back test [168], and the FZG scuffing test [169] by contrast distribute the wear across a much wider surface area, but the kinematics

of the contacts are constantly varying. These tests hold speeds constant throughout, and introduce stepwise increases in load until scuffing occurs. At the higher load stages, heat generation in the contacts is sufficiently great to introduce considerable uncertainty as to contact temperatures, further limiting the usefulness of these methods in elucidating the mechanisms leading to scuffing. Several other test configurations including block-on-ring [161], reciprocating cylinder-on-disc [170] and twin-disc [171] have also been employed.

The approach taken by Ingram *et al.* [172], based on the contra-rotation proposed by Blok [173] in a ball-on-disc contact, distinguishes itself from other methods in two ways. Firstly, by using a ball-on-disc machine, entrainment and sliding speeds were decoupled so that the sliding speed could be varied while maintaining approximately constant EHD film thickness, which is not possible in the gear or pure-sliding methods without changing specimen geometry. Secondly, the effect of varying sliding speed at constant load was investigated, and compared to a similar method employing load increments at constant sliding speed. The sliding-speed-stepping method was considered to have the advantage that the contact size did not change between test stages, in contrast to the load-stepping methods which, for the point-contact case, take in fresh surfaces causing a characteristic friction spike at the beginning of each stage, which can itself initiate scuffing. The method was further developed in the thesis of Peng [174], who determined conditions for an initial running-in stage which maximised test repeatability, and this method has since been used to evaluate scuffing performance of oils by Peng *et al.* [175] and Ueda *et al.* [176], who also used the Spacer Layer Imaging Method (SLIM) to measure boundary films in-situ at intervals during the test. Bayat and Lehtovaara [177] employed a similar technique using a barrel-on-disc configuration, using SLIM to qualitatively observe the condition of the barrel surface.

In light of the multiplicity of scuffing initiation mechanisms proposed and tested, and the fact that several scuffing models have been found to give good predictions for part of the parameter space, but none has yet been shown to apply universally, it is plausible that scuffing initiation may occur by more than one route. The generally accepted requirements, for the breakdown of both hydrodynamic and boundary films, sustained by some thermal positive feedback, depend on high-dimensional factors such as surface topography, the rates of several simultaneous mechanochemical processes, and the highly nonlinear and base-stock-specific rheological response to severe transients in temperature, pressure and shear rate. It is therefore

unsurprising that such a wide range of explanations have been proposed (compare the very different approaches of the two contemporary papers proposing catalytic breakdown of the oil by nascent surfaces [158] and entrainment of debris [160] for example). It is likely, in machine elements which fail by scuffing, that various risk factors coexist and compete, or even co-operate, to cause scuffing under conditions which trigger one or more of the relevant processes. More possible mechanisms may also be added to the list in the future. A unified scuffing model, able to resolve the wide range of phenomena potentially involved, is therefore unlikely to take the shape of a closed-form expression in a few variables except under very limited conditions. Nevertheless, an attempt to create such a unified model, which would require considerable interdisciplinary research effort, would be a valuable contribution to future work on this widely relevant topic.

2.8 Micropitting

Micropitting is a fatigue damage mode in rolling-sliding contact characterised by a network of asperity-scale ($\mathcal{O}$ 10 μm) cracks which eventually coalesce and form 'micropits', leading to significant loss of material from the surface often termed micropitting wear, see Fig. 2.11. It is of particular relevance to gears [179], and also occurs in rolling element bearings. The

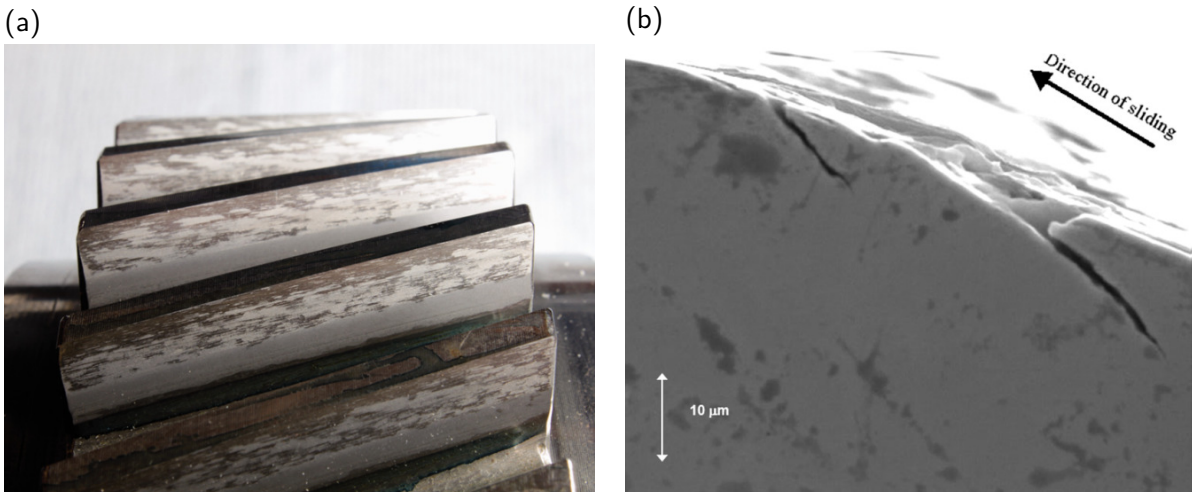


Figure 2.11: (a) Helical gear with distinctive frosted appearance on teeth as a result of micropitting and (b) SEM image of sectioned tooth surface from the same gear showing characteristic short cracks propagating at a shallow angle to the surface in the opposite direction to the friction force (scale arrow 10 μm). Images reproduced from ref. [178] with permission of SAGE publishing.

initiation and propagation of micropitting cracks have each been shown to be influenced by a large number of factors, and there is not a consensus in literature as to the relative importance of these. Berthe *et al.* [180] determined in 1980 that micropitting is caused by asperity-scale plasticity. Several experimental studies [181–184] have examined the influence of surface roughness, generally concluding that an increase in some surface roughness amplitude parameter increases the micropitting wear rate, and corroborating the conclusion of Berthe [180] that in cases where early running-in smoothens the asperities such that cyclic surface stresses become predominantly elastic, micropitting wear rates are greatly diminished. Lainé *et al.* [182] found that longitudinal roughness gave rise to more severe micropitting than transverse roughness. A detailed discussion of the effect of several roughness parameters including root-mean-square (RMS), asperity curvatures, mean absolute slope, autocorrelation function and structure function on EHL film thickness is given by De Silva [185] for both longitudinal and transverse roughnesses of various wavelengths. Roy *et al.* [186] found an inverse correlation between the evolution of autocorrelation length and surface damage, noting that skewness and kurtosis also reliably predict both micropitting initiation and propagation. Prajapati and Tiwari [187] however report a positive correlation between micropitting damage, autocorrelation length, and fractal dimension.

In 1986, Spikes *et al.* [188] observed strong hardness-dependence of micropitting wear rate, finding that when the central roller specimen in a triple-disc test machine was softer than the counterfaces, micropitting was promoted, and that likewise the wear rate fell drastically when the specimen was harder than the counterfaces, whose asperities *"showed considerable rounding of the crests"*. This rounding represents both a reduction in counterface roughness, and preferential plastic deformation on the counterfaces, which see far fewer contact cycles than the roller specimen. Ueda *et al.* [189] showed that a black oxide conversion coating on the harder surface accelerates this running-in procedure by decreasing asperity hardness, leading to rapid roughness reduction, and significantly reducing micropitting. Spikes *et al.* [188] also noted that plastic deformation introduces tensile residual stresses which promote fatigue cracking. The contact model of Zhou *et al.* [190] suggested that a decrease in the specific film thickness, (Λ ratio) at constant roughness leads to an increase in the magnitude of subsurface stresses and hence mode I (opening) and mode II (in-plane shear) stress intensity factors, accelerating crack propagation. The experimental study of Lainé [182], and the

model of Morales-Espejel *et al.* [191] found however that at low lambda ratios, micropitting was suppressed by wear, and so a worst-case micropitting lambda ratio (around 0.12 for the conditions used by Lainé) exists at which asperity plastic stresses are greatest in magnitude and asperities persist such that micropitting cracks rapidly propagate. Ueda *et al.* [192] found a strong inverse correlation between film thickness and micropitted area for a series of micropitting tests involving dumbbell base oil blends, arguing that these may be a solution for improving micropitting performance of low-viscosity fluids due to their greater pressure-viscosity coefficient compared to pure PAOs of equivalent viscosity, and hence their propensity to form thicker EHD films, if inlet shear-thinning can be avoided. A robust discussion of the influence of Λ is given by Wainwright *et al.* [193], who decoupled the effects of Λ and roughness on micropitting by controlling both the viscosity of the base fluid and the roughness of the surfaces. Wainwright found that micropitting wear increased monotonically as Λ decreased, and as RMS roughness increased. Over the ranges tested ($0.05 \leq \Lambda \leq 1.2$, $0.22\,\mu\mathrm{m} \leq R_q \leq 0.74\,\mu\mathrm{m}$) it was determined that in relative terms, roughness had the stronger effect on micropitting rate. The reported progression of material loss also agrees with the conclusion of Oila *et al.* [194] that Λ influences crack propagation rate more strongly than crack initiation.

Wainwright's tests used a high concentration of the antiwear additive zinc dialkyldithiophosphate (ZDDP), which was shown by Benyajati [195], Lainé [182] and Soltanahmadi [196] to considerably increase rates of micropitting wear by preventing the asperities from running in. The thick tribofilms deposited by ZDDPs may also modify effective surface roughness and increase friction [197], which is also a significant parameter. Lainé *et al.* [198] and Ueda *et al.* [199] both studied oil blends containing ZDDP, with and without the ZDDP-synergistic friction modifier additive molybdenum dithiocarbamate (MoDTC), showing that the addition of MoDTC and the resultant reduction in friction drastically reduced micropitting rate. Ueda *et al.* [199, 200] also showed that the presence of MoDTC resulted in longer cracks (despite the much lower micropitting wear rate), and proposed that this could be caused by a reduction in friction within the crack, reducing 'locking' and so increasing mode II stress intensity factors. The effect of lubricant entrainment into the crack has also been considered [201], and directly observed by Olver *et al.* [202]. This entrainment may contribute to mode I stresses by lubricant pressurisation at the crack tip during overrolling. In support of this theory, it has been widely observed that the rate

of micropitting crack propagation is greater for the slower surface, where the direction of overrolling acts to pressurise the crack [181]. Micropitting cracks have been shown [115, 181, 182] to characteristically propagate at a shallow angle ($< 30^{\circ}$) to the surface in the opposite direction to that of the friction force, regardless of rolling direction. Rycerz and Kadiric [115] demonstrated that micropitting rate is strongly influenced by sliding speed independently of film thickness, and found that the progression of micropitting correlated with sliding distance regardless of the sliding speed. They proposed that the effect of increasing sliding speed is to increase the rate of asperity stress cycles, and demonstrated using a contact model that the number of asperity stress cycles is proportional to sliding distance.

Water contamination has also been found by Cen and coworkers [203, 204] and by Soltanahmadi [196] to influence micropitting. Both micropitting nucleation and wear were increased by dissolved water, but in the presence of free water, micropitting was suppressed by accelerated mild wear. Several mechanisms by which water might directly infuence micropitting have been proposed including crevice corrosion, reduced EHL film thickness, degradation of oil by accelerated oxidation, hydrolysis of additives (particularly hindering ZDDP film formation), and hydrogen embrittlement. Tamayo *et al.* [205] found that the use of an aqueous glycerol base fluid promoted mild wear which outcompeted micropitting, but that the addition of a glycol was effective in reducing wear, promoting micropitting while exhibiting much lower friction compared to a commercial gear oil, at Hertz contact pressures betwen 1.5 and 2.5 GPa. Contact pressure was considered by Oila *et al.* [194] to be the most important factor influencing micropitting initiation, while Britton [206] found slide-roll ratio to be more significant at the initiation phase but concluded that contact pressure was the most significant factor considering both initiation and propagation phases. Kahraman [207] reported an increase in micropitting with contact pressure, except in the case where running-in conditions involving high contact pressure and low entrainment speed were used, in which case micropitting was reduced, perhaps due to reduction in asperity slopes, development of a protective boundary film, or an increase in surface hardness due to work hardening. No significant effect of steel substrate composition on micropitting was found by Ahlroos *et al.* [183], who demonstrated instead that micropitting was greatly reduced by a hydrogen-free tetrahedral amorphous carbon Diamond-Like Coating (ta-C DLC) which produced much lower friction, and by carbonitriding which produced similar friction, compared to carburised

specimens.

In summary, factors which have been found to strongly influence micropitting include:

- Surface roughness (particularly RMS roughness R_q or S_q) [180–187, 208]
- Hardness and hardness difference between surfaces [184, 188, 189]
- Λ ratio [178, 182, 190–193]
- Contact pressure [194, 206–208]
- Sliding speed [115, 187, 194, 208]
- Additives (particularly ZDDP) [195, 196, 198–200, 209]
- Water contamination [196, 203–205]
- Materials and coatings [183, 186, 189]

The mitigation of micropitting in the design of future geared transmissions in EVs therefore requires a multimodal approach, considering in parallel the influence of gear surface topography and manufacturing techniques, lubricant rheology and chemistry, gearbox design and loading patterns, and any changes to these factors over the life of the vehicle.

2.9 Fluid Formulation

The evolution of electric drive fluids (EDFs) is, at the time of writing, in its early stages. As manufacturers move away from ATF formulations, lubricant suppliers are formulating to a continuously evolving set of requirements. Considerable industrial research and development effort is currently focused on:

- Low viscosity - churning loss accounts for a considerable fraction of total gearbox power for current EV drive unit designs [210, 211], and it is widely believed that lower viscosity increases efficiency overall. Low viscosity also enhances heat transfer in turbulent flow and so has a strong influence on the ability of the lubricant to remove heat from the gearbox, and also from the motor in wet-motor designs. Fluids with KV100 values as low as 2.5 cSt have recently been proposed [211] - a lower limit around 2.0 cSt is

imposed by the volatility of the base fluid. Fluids of lower viscosity also typically have lower pressure-viscosity coefficients, both of which act to lower EHL film thickness.

- Extreme pressure (EP) performance - the high sliding speeds in EV gears and instantaneous torque capacity of the motor pose considerable scuffing risk, which must in part be mitigated by EP additives. This is particularly critical for low viscosity fluids which lead to low lambda ratios at higher entrainment (and hence sliding) speeds than previous formulations. EP additives containing active sulphur are copper-corrosive and consequently it is presently challenging to balance scuffing prevention with copper-compatibility. Additionally it is shown in Chapter 7 that scuffing and micropitting performance are inversely correlated, and fluid formulation and transmission design must mitigate both scuffing and micropitting together.
- Copper-compatibility - depending on drive unit design, EDFs may be exposed to motor-integral copper componentry such as wires, busbars, windings and rotors. In some designs, coatings are used to isolate the copper from the fluid, but corrosion may still occur via small cracks in the coatings at bends in copper wire, and the fluid may also corrode the coating [212]. In next-generation single-fluid designs, the EDF may also be required to cool the power electronics and even the battery, potentially involving direct exposure to PCBs. In some formulations, particularly those with high concentrations of sulphur-containing additives, both liquid and vapour-phase corrosion may act to degrade componentry, causing electrically catastrophic eventualities such as severe reduction in diameter of copper wires, wire breakage, or short-circuiting by conductive deposits. The ASTM D130 copper compatibility test, often reported alongside dissolved copper concentration measured by ICP with mass spectrometry, has so far been used to screen additives for EDFs, but the standardisation is in progress of new tests which better represent the requirements of EDFs, including energised wire corrosion and conductive deposit formation.
- Dielectric properties - electrical damage in tribological contacts is a concern in EV transmissions due to voltages induced by transient magnetic fields, particularly for motor bearings [213], but there is not currently a consensus among EV manufacturers on how to mitigate this. A recent review of a number of relevant underlying phenomena is given by Spikes [214], but the interaction between these and other prevalent damage modes is

presently unclear. The impact of lubricant chemistry, and drive unit architecture, both of which are still rapidly evolving, on electrified contact damage, is very strong. As a result, a diverse range of lubricant requirements have been specified by manufacturers according to their respective needs, including for example electrical conductivity ranging from highly insulating (< 1000 pS/m, reducing shock hazard) to conducting (> 1 mS/m, reducing the energy of damage-causing in-contact discharge events) [212], with other manufacturers specifying conductivity in the intermediate 'static dissipative' range. Conductivity has also been shown [212] to increase by up to an order of magnitude over the life of the fluid as a result of ageing due to oxidation products, and this must also be considered in specifying electrical conductivity. Mineral and synthetic base oils are generally insulating, but the addition of polar additives such as antioxidants, dispersants, detergents, friction modifiers and antiwear additives increases conductivity, and most EDFs have conductivities in the range $1 - 1000$ nS/m. Metallic debris, and dissolved metals below 1000 ppm however, were found to have no influence on conductivity. Dielectric breakdown voltage may also impact triboelectrical damage although test methods such as ASTM D1816 display poor repeatability ($\pm 40\%$ is quoted by D1816), and results do not generally correlate with conductivity or permittivity. The role of dielectric breakdown in surface damage in electrified contacts is still an active area of research [215, 216].

- Heat transfer performance, often quantified for turbulent flow by a figure of merit in the form of the Mouromtseff number $\mathrm{Mo} = \frac{\kappa^\alpha \rho^\beta c_p^\gamma}{\mu^\delta}$ [217], depends on thermal conductivity κ, density ρ, specific heat capacity c_p, and dynamic viscosity μ. The exponents α, β, γ and δ depend on flow velocity and geometry, and for EDFs the values of κ, ρ and c_p do not vary strongly between candidate hydrocarbon base oils within their usual operating temperature ranges. As a result, fluid viscosity and flow field, dictated by system design, are the strongest influences on fluid heat transfer.
- Aeration and foaming - high-speed dip- or spray-lubricated gearing creates conditions under which air is entrained into the oil. Fluids which readily retain entrained air under these circumstances experience temporary, but highly unfavourable changes to heat transfer and lubrication performance, potentially leading to loss of lubrication (for example starvation in circumstances where an oil pump fills with foam and

cannot distribute the intended volume flowrate of lubricant), overheating (the foam takes on the much inferior heat transfer properties of air), and other undesirable circumstances such as vent expulsions. Several factors increase foam stability by 'anchoring' bubbles, including solid debris, water contamination, biological entities, and oxidation. Antifoamants are additives with lower surface tension than the bulk fluid which enter and destabilise foam lamella, greatly reducing foam volume although generally also increasing air retention [218]. Several existing test methods, including ASTM D892, D3427, D6082 and the Flender method, are used to evaluate foaming performance, involving bubbling air through the oil at high temperature for a specified time and then monitoring the volume of the foam, aerated oil, and liquid phases. New test methods are presently required to create conditions more representative of EV gearboxes, including higher shear rates and lower temperatures.

For all of these parameters, widely-used standardised tests already exist, and where they fall short of the requirements of screening additives and lubricant formulations for EV applications, new and improved test methods are in development, standardisation of which will eventually follow (notably energised wire copper compatibility and conductive deposit formation). Efficiency however is not a material property, and to maximimise efficiency, OEMs and formulators must understand the fundamental loss mechanisms, and how they are influenced by key properties such as oil viscosity and high-pressure rheology, and also by application-dependent factors such as transmission architecture, geometry, environment, and use case. At the same time, the influence of oil and additive chemistry must be added to this list in analysing and maximising component durability and transmission reliability.

2.10 Conclusions from Literature Review

The design of electric drive units for EVs, and in particular the formulation of lubricants enabling them to be efficient and reliable, invites a multiparameter optimisation involving several hard-to-predict phenomena, including oil churning losses and EHL traction at high speeds, and the parallel mitigation of surface damage modes including wear, corrosion, scuffing, and rolling contact fatigue.

Existing analytical models for predicting oil churning losses do not presently resolve critical

phenomena such as casing geometry, gear orientation, and interaction between multiple stages. Furthermore, the range of validity of these models does not extend to the rotational speeds relevant to present and future EV motors. Computational models which could resolve the requisite thermally coupled multiphase flow on the wide range of lengthscales and timescales involved would incur considerable computational expense and still require experimental validation. At the time of writing there is no publicly available academic writing experimentally characterising churning losses or efficiency in an EV drive unit. Experimental data considering the influence of speed and oil viscosity on both churning losses, and power transmission efficiency, obtained from a representative EV drive unit, would be salient and of considerable benefit to further academic investigation of churning loss phenomena relevant to EV gearboxes, and drive unit efficiency optimisation.

The entrainment speeds in gear and bearing contacts in EVs exceed those achieved by the majority of work on EHL, particularly EHL traction, by an order of magnitude. The differing thermal conditions created by these high speeds, whose effects on traction are particularly relevant to gear and bearing losses, are not yet well-resolved, largely because the thermal consideration further complicates the already heated issue of how to treat lubricant rheology in an EHL contact. There is a small body of work considering thermal effects on EHL film thickness, but it does not generalise well to refined mineral and synthetic base stocks in common use in transmission fluids. This could be rectified by a systematic experimental study measuring EHL traction and film thickness over a wide range of speeds using transmission-relevant base fluids which are currently in production, but such a study would also require the development of new test equipment capable of making these measurements.

Optimising lubricant properties for efficiency is of no benefit if reliability requirements are not also met or exceeded. It is unclear to what extent existing fluid formulations protect against scuffing under conditions pertinent to EV gearing, including mature formulations of relevance to EV transmissions (ATFs and MTFs). Standardised scuffing test methods suffer poor repeatability and (in the case of 4-ball tests) employ contact conditions wholly irrelevant to well-designed machine elements found in EVs, or (in the case of gear-type tests) are highly laborious and expensive to conduct, and do not allow the influence of a single parameter to be isolated. Instead, the use of scuffing test methods such as the speed-stepping ball-on-disc contrarotation method, which employ inexpensive test specimens and enable relatively easy

testing, and recreate conditions of relevance to EV gearing, would be of considerable benefit to future additive development and fluid formulation for application-specific requirements such as scuffing performance with copper compatibility.

The design of high-speed transmissions whose components potentially experience billions of contact cycles over their lifetimes must mitigate rolling-contact fatigue, the principal manifestation of which, for the roughnesses and contact pressures typical of EV gear contacts, is micropitting. Micropitting is strongly influenced by surface roughness, hardness, EHL film thickness, contact pressure, friction, sliding, antiwear additives and friction modifiers. The author is not aware of a representative comparison of the micropitting performance of fully-formulated ATFs and next-generation EDFs under conditions relevant to EV gearing. A test method which can differentiate and quantify the performance of these fluids under EV-representative contact conditions, and the results of such a method applied to fluids currently in use in EVs, would be valuable in the design of both future EV drive units and lubricants.

2.11 Project Goals

In light of the above conclusions, the goals of this thesis span the dual concerns of efficiency (both load-independent and load-dependent losses), and reliability (EHL film thickness and surface damage), with a focus on the influence of lubricant viscosity. The goals are as follows:

1. Experimentally measure the dependence of oil churning losses on speed, immersion depth and oil viscosity, *in situ* for a representative EV drive unit.
2. Measure drive unit efficiency and determine the relative contribution of load-dependent and load-independent losses.
3. Characterise the range of contact conditions seen by the gears as the vehicle is driven, and apply these in a series of scuffing tests to quantify scuffing performance for candidate EV fluids.
4. Compare the nature and severity of micropitting for a series of candidate EV transmission lubricants under contact conditions relevant to EV gearing.
5. Establish the dependence on speed and oil viscosity of EHL traction and film thickness at speeds relevant to oil-lubricated high-speed gears and bearings in EVs, and compare

these to existing models for a range of EV-transmission-relevant base fluids.

These goals in combination aim to develop experimental techniques which can provide data suitable for reference or model validation in future efforts to computationally optimise electric vehicle transmission efficiency and reliability.

Chapter 3

Materials

This chapter presents measurements of the relevant physical properties of lubricants and contacting bodies referred to in subsequent chapters. These are gathered here for easy reference and to avoid duplication.

3.1 Fluids

The lubricants used and referred to throughout subsequent chapters comprise various transmission fluids, and base stocks relevant to transmission fluid development. Their relevant gravimetric, rheological and optical properties, and the methods by which these were measured, are detailed in this section.

3.1.1 Viscosity and Density Measurement

Fluid dynamic viscosity was measured using a Stabinger Viscometer (SVM 3000) employing a driven vaned rotor in a fluid-filled tube, the drive torque on which is correlated to viscosity for the operating speed. The rotor speed, and so the shear rate, varies with viscosity, but the shear rate was below $10^3\ \mathrm{s}^{-1}$ for all cases presented here. The viscometer also incorporates a density cell allowing measurement of density and hence kinematic viscosity, and is temperature controlled by a Peltier element. Dynamic viscosity and density were measured at atmospheric pressure, at $\{20, 40, 60, 80, 100\}^{\circ}$C. The Vogel-Fulcher-Tammann (VFT) viscosity model [219] (Eq. 3.1), was fitted to the viscosity-temperature data, incurring errors smaller than $\pm 0.5\%$ in all cases.

$$\eta = \eta_0 e^{\frac{B}{T - T_0}} \tag{3.1}$$

The parameters $\{\ln(\eta_0), T_0, B - T_0 \ln(\eta_0)\}$ were obtained by multivariate linear regression from Eq. 3.2, which follows from Eq. 3.1 and is of form $y = a_1 x_1 + a_2 x_2 + k$, to give η_0, T_0 and B.

$$T \ln \eta = T \ln \eta_0 + T_0 \ln \eta + B - T_0 \ln \eta_0 \tag{3.2}$$

Linear dependence of density ρ (Eq. 3.3) with temperature is assumed, incurring errors not exceeding $\pm 0.1\%$ compared to measurements.

$$\rho = \rho_1 T + \rho_0 \tag{3.3}$$

3.1.2 Refractive Index Measurement

Refractive index was measured at atmospheric pressure at the sodium D-lines at $\{40, 60, 80, 90\}^{\circ}$C using an Abbe refractometer. Linear dependence of refractive index n (Eq. 3.4) on temperature was assumed, incurring errors less than $\pm 0.1\%$ compared to measurements.

$$n = n_1 T + n_0 \tag{3.4}$$

3.1.3 Pressure-Viscosity Coefficient Measurement

Pressure-viscosity coefficients as used in the Materials parameter G of the EHL regression equations are required for predicting EHL film thickness. The values here have been derived from optical measurements of EHL film thickness described in Chapter 6, in a manner similar to that of LaFountain *et al.* [220] via the regression equation of Chittenden (Eq. (3.5)) [221].

$$\frac{h_c}{R} = 3.13 U^{0.68} G^{0.49} W^{-0.073} \tag{3.5}$$

$$U = \frac{\eta U_e}{E' R} \qquad W = \frac{w}{E' R^2} \qquad G = \alpha_p E' \qquad E' = 2\left(\frac{1-\nu_{ball}^2}{E_{ball}} + \frac{1-\nu_{disc}^2}{E_{disc}}\right)^{-1}$$

All parameters in Eq. (3.5) are known *a priori*, except h_c and α_p. Consequently, once h_c is known from measurements, α_p can in principle be calculated. Pressure-viscosity coefficient α_p is obtained in this way by regression for the best fit line with gradient 0.68 on the plot of $\log(h_c)$ vs $\log(U_e)$, for $U_e \leq 2.4$ m/s and SRR$\leq 4\%$. The values at (up to) 3 temperatures (depending on conditions tested) are given for reference in Table 3.1. The α_p parameter, which originates from the Barus equation [85] whose validity at high contact pressures is

limited, is not intended in this work to describe fluid rheology and is provided only for the purposes of film thickness prediction.

3.1.4 Physical Parameters of Fluids

A list of the fluids used in the following chapters is given in Table 3.1, along with measured kinematic viscosities of the fluids at 40°C and 100°C. For those fluids on which film thickness measurements were performed, pressure-viscosity coefficients derived as specified in Section 3.1.3 are also included.

The fluids used in Chapter 4 are ATF chemistries meeting or similar to the Dexron-VI standard, which at the time of writing are believed to be representative of those used in the majority of the existing fleet of EVs. In Chapter 5, the fluids used were those available in large quantities at the time, and containing appropriate additive packages to prevent an efficiency measurement becoming a wear test. These were an ATF on the US market very similar to that in Chapter 4, and a much more viscous SAE 75W-140 gear oil. Chapter 6 makes use of a series of neat base oils spanning API groups I-IV, a traction fluid on which traction data have been widely reported, Santotrac 50, and a low-viscosity electric vehicle transmission fluid - complete sets of traction and film thickness measurements for all of these are presented in Appendix I. By contrast the fluids used in Chapter 7 are specifically formulated to have similar viscosities and hence film-forming capabilities, but different additive chemistries chosen to represent gearbox fluids currently on the market, such that the tradeoff between propensity to scuff or to induce micropitting (or various forms of wear) can be examined. An unadditivised base fluid, and a PAO5 containing only a blend of the antiwear additive ZDDP (specifically a mixture of primary and secondary ZDDPs, to 0.1%wt Phosphorous, having no measurable effect on viscosity at this concentration), are also used as references. Results for a candidate water-based transmission fluid (for composition see Section 3.1.5) are also included for the interested reader, but this avenue of research is not the focus of this thesis.

Coefficients fitted to the models for viscosity, density and refractive index by the regressions described above are given in Table 3.2. The coefficients require temperature T in Kelvin, and yield dynamic viscosity η in $\mathrm{mPa \cdot s}$ and density in $\mathrm{kg/m^3}$.

Table 3.1: Lubricants used during this study, showing measured kinematic viscosities and pressure-viscosity coefficients fitted from film thickness measurements

Base Fluids	Base Oil Group	$\nu_{40°C}$ [cSt]	$\nu_{100°C}$ [cSt]	$\alpha_{20°C}$ [GPa^{-1}]	$\alpha_{60°C}$ [GPa^{-1}]	$\alpha_{100°C}$ [GPa^{-1}]
Heavy Mineral Oil	I	69.1	8.9	24.3	16.6	15.4
HVI 60	I	23.3	4.5	21.1	18.8	13.8
CHN 100R	II	21.2	4.4	21.1	16.5	13.6
Yubase 4	III	19.5	4.3	16.3	12.3	11.4
Spectrasyn 4 (PAO4)	IV	18.8	4.3	17.6	13.3	11.4
Durasyn 145 (PAO5)	IV	25.2	5.2	17.8	15.2	12.3
Santotrac 50	-	28.3	5.2	33.3	20.0	13.9
Transmission Fluids						
HV ATF	-	253.6	28.6	17.2	16.3	14.7
LV ATF	-	7.6	2.4	12.9	9.6	6.6
Model EDF	-	21.5	5.0	15.4	11.6	10.4
Dexron-VI ATF (UK)	-	29.3	6.1	-	-	-
Dexron-VI ATF (US)	-	27.6	5.6	-	-	-
SAE 75W-140 Gear Oil	-	187.9	27.8	-	-	-
Synthetic ATF	IV	26.9	5.7	-	13.1	12.6
Synthetic ATF Base	IV	27.2	5.5	-	14.8	14.7
Synthetic Gear Oil	IV	26.3	5.3	-	15.7	15.1
Water-Based Fluid	V	31.1	6.7	-	4.2	-
Water-Based Base	V	26.5	6.2	-	4.2	-
Tesla Drive Original Fill	-	25.2	5.6	-	-	-

Table 3.2: Regression parameters fitted from measurements of viscosity, density and refractive index for lubricants tested, as per Eqs. (3.1), (3.3) and (3.4).

	η_0	B	T_0	ρ_1	ρ_0	n_1	n_0
Base Fluids	[mPa.s]	[K]	[K]	[kg/m^{3}K]	[kg/m^3]	[K^{-1}]	[-]
Heavy Mineral Oil	0.0431	1057.1	166.8	-0.6055	1040.9	-0.000361	1.584
HVI 60	0.0695	797.4	172.2	-0.6315	1048.0	-0.000342	1.578
CHN 100R	0.0702	803.7	167.6	-0.6285	1024.0	-0.000315	1.557
Yubase 4	0.0697	807.7	164.6	-0.6310	1016.4	-0.000339	1.561
Spectrasyn 4 (PAO4)	0.0658	843.3	158.1	-0.6275	1000.7	-	-
Durasyn 145 (PAO5)	0.0536	951.7	153.0	-0.6235	1003.7	-0.000339	1.558
Santotrac 50	0.1330	630.2	193.0	-0.6450	1089.9	-0.000334	1.587
Transmission Fluids							
HV ATF	0.0531	1356.3	149.6	-0.5940	1022.4	-0.000327	1.567
LV ATF	0.0742	715.9	150.3	-0.6625	1002.5	-0.000358	1.554
Model EDF	0.0673	902.4	150.9	-0.6365	1009.8	-0.000331	1.555
Dexron-VI ATF (UK)	0.0922	817.0	166.7	-0.6285	1027.2	-	-
Dexron-VI ATF (US)	0.0740	862.9	162.8	-0.6325	1027.5	-0.000358	1.571
SAE 75W-140 Gear Oil	0.1362	1104.9	156.6	-0.6315	1039.6	-	-
Synthetic ATF	0.0611	956.0	151.0	-0.6360	1023.7	-0.000347	1.560
Synthetic ATF Base	0.0557	953.3	154.1	-0.6270	1013.1	-0.000344	1.561
Synthetic Gear Oil	0.0468	1011.1	148.7	-0.6360	1029.4	-0.000358	1.569
Water-Based Fluid	0.1112	891.1	156.6	-0.8135	1312.5	-0.000305	1.504
Water-Based Base	0.1429	795.1	162.5	-0.8110	1308.1	-0.000281	1.489
Tesla Drive Original Fill	0.0732	888.7	156.0	-0.6380	1027.6	-	-

3.1.5 Water-based fluid composition

An experimental water-based fluid was kindly formulated by collaborators at the Valvoline New Products Lab in Lexington, KY. The fluid was intended to contain at least 40% water, and to have similar film-forming properties to low-viscosity synthetic PAOs of KV100 $\sim$4 cSt. The composition of this fluid is given in Table 3.3. The base fluid, containing only the water, PG and PEG was also characterised, but was not used in the tests in Chapter 7 on account of its rapid corrosion of AISI 52100 steels.

Base Constituent	%wt	Additive	%wt
Deionised water	43.3	Glycol ether	5
Polyethylene glycol (PEG)	30	S-based EP/antiwear	4.7
Propylene glycol (PG)	15	Corrosion inhibitors	2
		Antifoamants	trace

Table 3.3: Composition of water-based fluid used in scuffing and micropitting tests in Chapter 7

3.2 Contacting Solids

The methods presented in chapters 6, 7 and 8 discuss EHL contacts bounded by steel, glass and sapphire surfaces. The relevant mechanical properties assumed of these substrate materials are included in Table 3.4. The bearing steel (AISI 52100, also known as 100Cr6) specimens used in these studies were through-hardened, while specimens made of the gear steel, 16MnCr5, were case carburised. Specimen dimensions, roughnesses and hardnesses are discussed for each method separately.

Table 3.4: Relevant mechanical and thermal properties assumed for steels, glass and sapphire surfaces used in the MTM, ETM, MPR, EHD and EHD-HS tribometers employed in the studies presented in chapters 6-8.

	Elastic Modulus E [GPa]	Poisson Ratio ν [-]	Density ρ [kg/m^3]	Heat Capacity c_p [J/kgK]	Thermal Conductivity κ [W/mK]
AISI 52100 Bearing Steel	210	0.293	7710	446	21
16MnCr5 Gear Steel (bulk)	210	0.3	7850	502	43
BK7 Borosilicate Glass	75	0.22	2510	858	1.114
Sapphire	345	0.27	3980	763	33

3.3 Coatings

The glass and sapphire discs used in Chapters 6 to 8 were coated on one of their flat faces with a partially reflective chromium layer of thickness approx. 20 nm by sputter deposition under vacuum. The intended reflectivity of the chromium layer was around 20%, so as to match the intensity of the reflected beam to that which has been twice-transmitted, accounting for the attenuation within the chromium layer and at the other intermediary interfaces. Further discussion of the effect of chromium layer thickness is provided by Guo and Wong [137] and by Ma and Zhang [138]. Covering the chromium layer was a thicker silica (SiO_2) 'spacer layer' sputter-deposited under Argon. The silica layer on the glass disc used for SLIM in Chapters 7 and 8 was approx. 130 nm in thickness (light blue colour), while the silica layers on the glass and sapphire discs used for ultra-thin-film interferometry in Chapter 6 were approx. 560 nm thick (green/pink colour). Glass and sapphire discs with only the chromium layer (no silica layer) were also used to white-balance the SLIM camera, and to measure the spectral response of the optical system for ultra-thin-film interferometry (EHD-HS).

The SLIM calibration in Chapter 8 was created using a disc with only the chromium coating for the measurement of the central-film interferogram colours, and using a disc with the 560 nm thick silica coating for the corresponding EHD film thickness measurements. The silica layer is assumed to have mechanical and thermal properties sufficiently similar to the glass that its thickness has no influence on the contact or film shape. The effect of the chromium layer is assumed to be negligible on account of it being very thin.

It has been shown that considerable compressive residual stress (~ 1 GPa) may be imparted to the silica layer by this method of deposition [222], which is compounded by the large local contact stresses in the EHL contact. Eventually, the coating is damaged by repeated passes of the contact and fails by brittle fatigue, flaking off to expose the chromium layer, which distorts the film thickness measurement (sometimes accompanied, under nonzero-sliding conditions at high speeds, by scuffing). This damage was greatly accelerated by the higher contact pressures achieved in the contact with the sapphire disc in Chapter 6 (and possibly also interfacial stresses arising from the unequal elastic properties of the silica and the sapphire). This considerably increased the difficulty of obtaining reliable results using the sapphire disc, and only one test using the sapphire disc is reported, all others used a glass disc.

Chapter 4

Influence of Oil Viscosity on Churning and Windage Losses at High Speeds

Churning and windage losses in EV gearboxes are thermally coupled multiphase turbulent flow phenomena whose prediction poses considerable challenge. Existing semi-analytical loss models necessarily ignore the effect of complex gearbox casing geometry which has a strong influence on losses, particularly in a multi-stage transmission. CFD approaches incur considerable computational expense owing to the high speeds at which the domain changes shape due to the gear mesh, and therefore the wide range of lengthscales and timescales that require consideration.

Measurements of gear churning and windage losses and bearing drag losses are also challenging owing to the several other parallel loss phenomena at play, including seal drag and bearing traction. One technique to do this is inertia rundown, which enables the total torque experienced by all rotating components, as a function of speed, to quickly be evaluated.

This chapter details the design, development and operation of a test rig to measure churning losses in-situ in an EV drive unit. The rig is used to quantify the relative contribution of each rotating shaft to the total loss, and to investigate the effect of gearbox speed, oil immersion depth, and oil viscosity on churning losses. Finally, an effort is made to compare results from inertia rundown to those obtained under steady-state conditions.

4.1 Development of Gearbox Churning Loss Rig

A test rig was developed for this study to enable the measurement of churning and windage losses in a gearbox representative of those currently used in many electric vehicles.

4.1.1 Gearbox

The gearbox selected was a second-hand front drive unit (Fig. 4.1) from a 2016 Tesla Model S (P90D, AWD), which had been written off due to water damage elsewhere on the vehicle with 31,589 miles on the clock. The front drive unit is the less powerful of the two drive units in the car, with a peak power of 193 kW, which alone exceeds the peak power of many other EVs currently on the market.

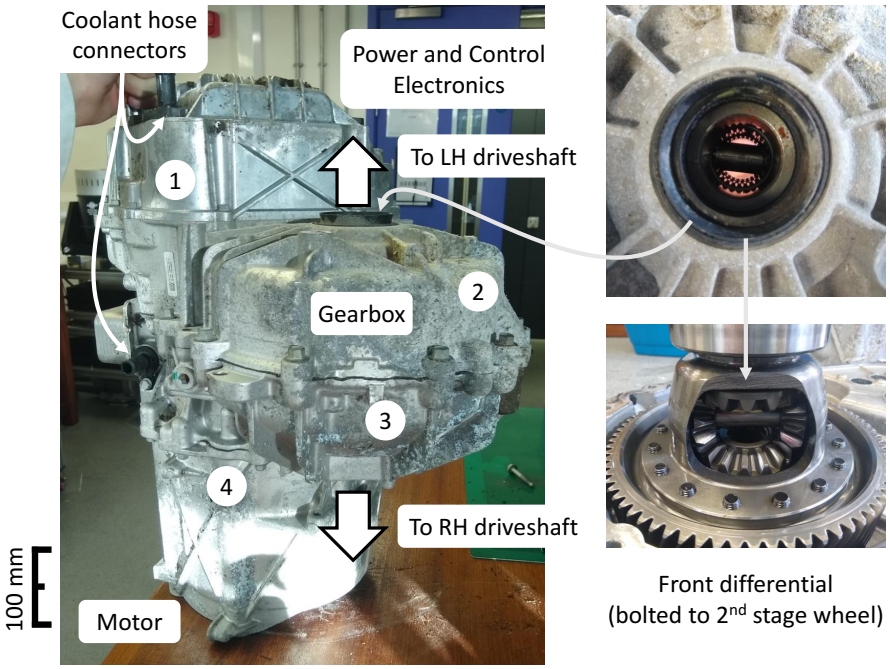


Figure 4.1: Drive unit showing (1) inverter casing, (2) LHS gearbox casing, (3) RHS gearbox casing and (4) motor casing

The gearbox is a two-stage helical reducer with total reduction $\approx 9.344 : 1$ as shown in Fig. 4.2.

The gearbox comprises three shafts, each supported by two rolling element bearings. The bearings (shown in Fig. 4.3) are listed in Table 4.1. All of these were manufactured by SKF and were from the Explorer range.

The four standard Deep Groove Ball Bearings (DGBBs) have the C3 designation indicating greater than normal internal clearance (but less than the C4 and C5 designations), perhaps to accommodate the high speeds and significant temperature gradients they must operate at. The Cylindrical Roller Bearing (CRB), bearing D, is an RNU type, meaning it has no separate

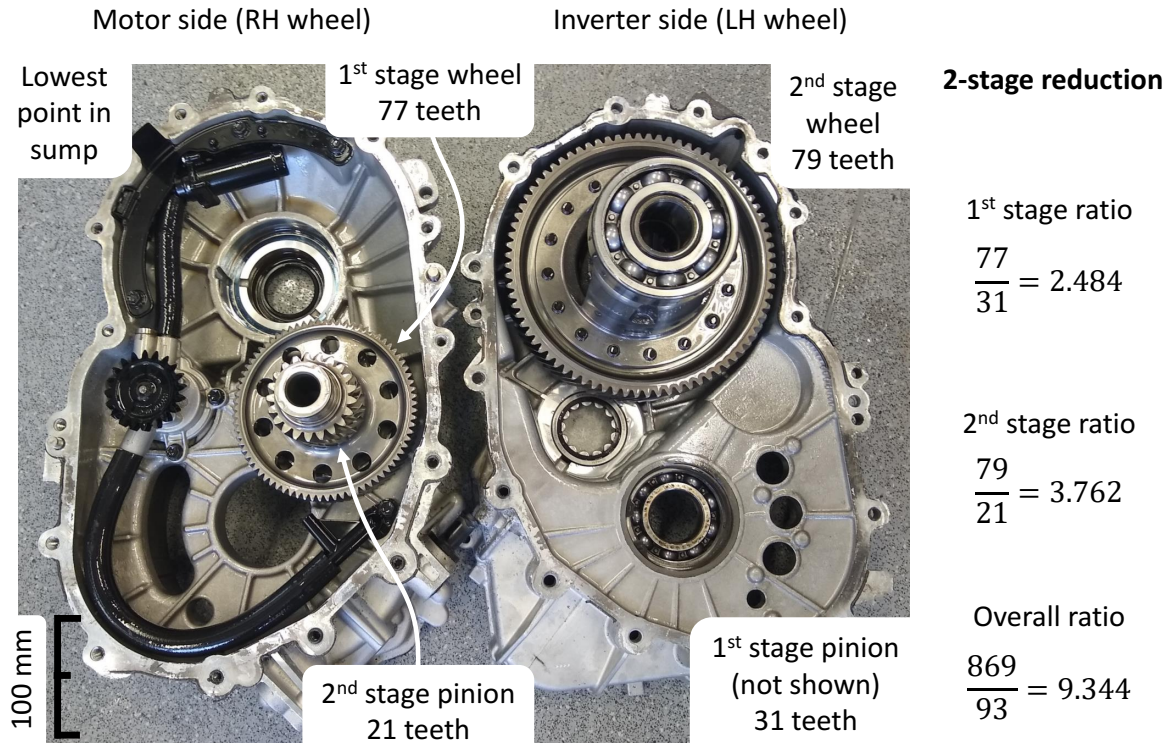


Figure 4.2: Gearbox from front drive unit of Tesla Model S P90D (rotor and drive pinion removed)

Table 4.1: Rolling bearings used in gearbox to support the three shafts shown in Fig. 4.8. The bearing inner and outer diameters are d and D respectively, and the axial width is B, all in mm.

Bearing	Shaft	End Nearest	Designation	Type	d	D	B
A	Low-speed	Differential	6309/C3	DGBB	45	100	25
B	Low-speed	LS Wheel Gear	6310/C3	DGBB	50	110	27
C	Intermediate	HS Wheel Gear	6307/C3	DGBB	35	80	21
D	Intermediate	LS Pinion	RNU 2206 ECP	CRB	42	62	25
E	High-speed	HS Pinion	6208/C3	DGBB	40	80	18
F	High-speed	Rotor	BB1-1107	Hybrid DGBB	35	62	15

inner race but rather rolls directly on the supported component - here the intermediate shaft. It is established in Sec. 4.1.3 that this is the bearing which carries the most radial load, explaining the choice of roller geometry. Bearing F carries comparatively little radial load as it is located much further from the mesh than bearing E. Bearing F however has ceramic rolling elements which act as electrical insulators, interrupting the path for loop currents via the shaft

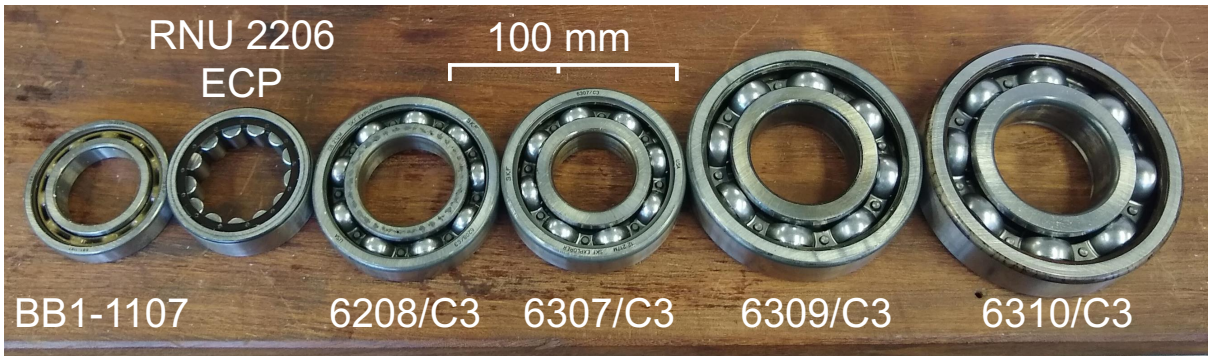


Figure 4.3: Bearings supporting 3 shafts in gearbox

and the casing, which might otherwise risk electrical damage to both bearings E and F.

When stationary, the low-speed wheel gear is immersed in oil (to more than 3/4 of its diameter), so the low-speed stage might be considered to be dip-lubricated. The gears of the high-speed stage sit almost completely above the fill level and an oil jet is angled at the high-speed mesh. The oil jet is supplied by an internal trochoid gear pump (Fig. 4.4) which is powered parasitically by a polymeric pinion meshing with the low-speed wheel gear (Fig. 4.5). The facewidth of the pump pinion is a small fraction of that of the low-speed wheel gear, and it has 20 teeth, giving a transmission ratio of 3.95 in overdrive.



Figure 4.4: Trochoid internal gear pump which moves oil from sump to high-speed spray jet, and via heat exchanger to motor shaft and windings

The oil flow path, from the lowest point in the sump beneath the oil filter, to the heat exchanger through which the oil rejects heat to the coolant, is shown in Fig. 4.6.



Figure 4.5: Polymeric 20-tooth helical pinion driving trochoid gear pump, driven by low-speed wheel gear

4.1.2 Speeds

The maximum speed of this model of car is 155 mph (250 kph). Assuming 19" wheels are fitted with the recommended tyre diameter, the rolling diameter is around 27.7" (rolling radius 352 mm), so the maximum rotational speed of the low-speed stage (which drives the wheels directly) is 1881 rpm. The intermediate stage therefore must reach 7076 rpm, and the high-speed stage 17575 rpm. This corresponds to tip circle speeds for the high-speed stage of 50 m/s (Mach 0.14 in air at 40°C), and 21 m/s for the low-speed stage. It should be noted that the car is unlikely to be designed to sustain speeds of more than 100 mph for any considerable time given the high torque requirement, and drivers wishing to travel at such speeds are hardly optimising for efficiency on account of the aerodynamic drag force, even if the drivetrain were optimally efficient at these speeds. Nevertheless, the increasing trend in drive motor speeds in electric vehicles extends the relevant speed range to the whole design range of this vehicle.

Taking the total driving torque from the wheels at constant speed as T, a preliminary analysis gives

$$T = r_w \left(F_{\text{drag}} + F_{\text{roll}} + F_{\text{incline}}\right) = r_w \left(\frac{1}{2}\rho_{\text{air}} C_D A v^2 + mg\mu_r \cos\alpha + mg \sin\alpha\right) \tag{4.1}$$

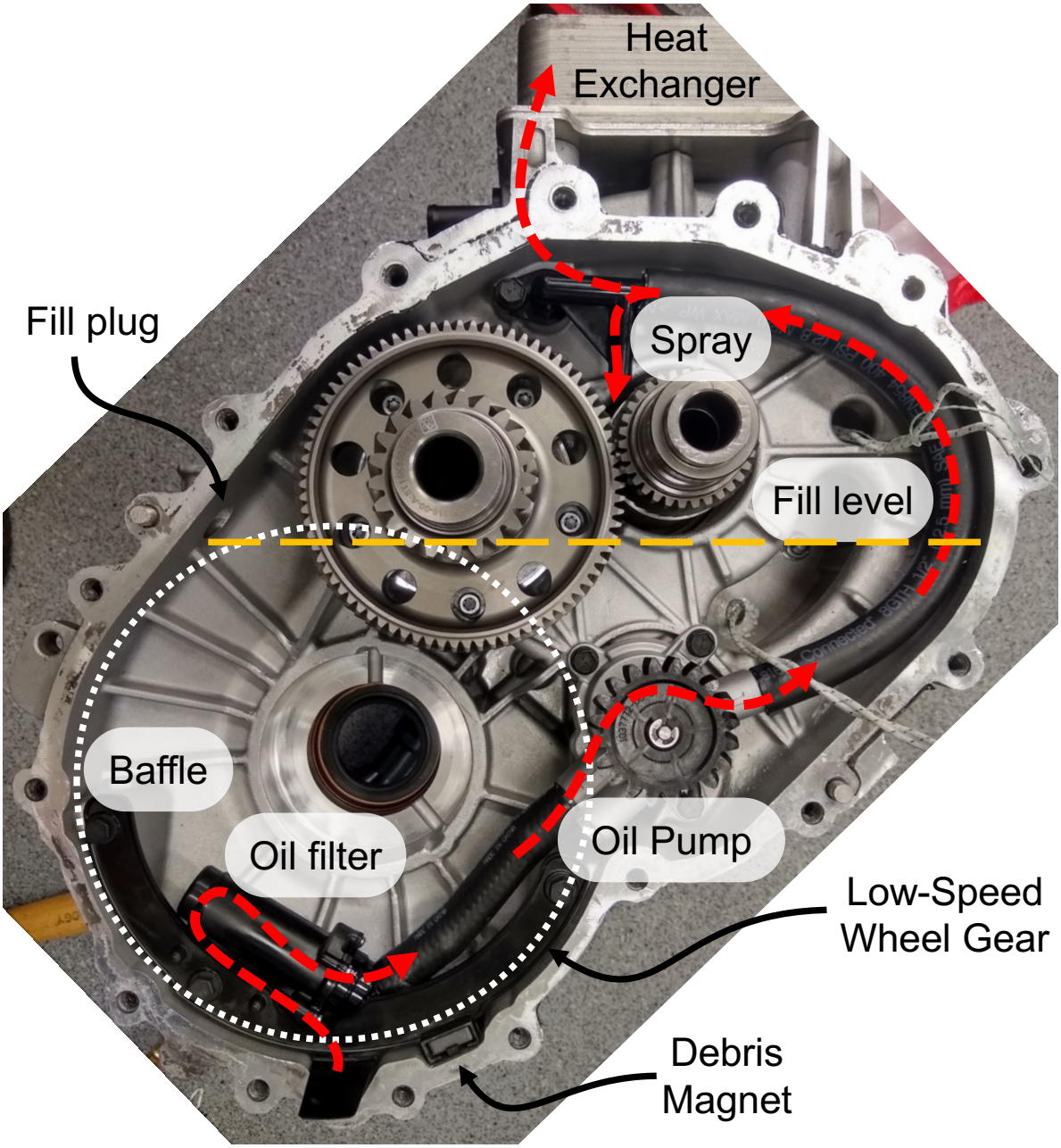


Figure 4.6: Oil flow path inside gearbox, oriented here with lowest point in sump at bottom of image (not shown, heat exchanger outlet leads to several spray nozzles directed at rotor and stator windings, after which oil flows back to sump)

where the wheel radius is r_w, the angle of incline is α and all other symbols take their usual meanings.

The value of T is shown for inclines between 0° and 20° in Fig. 4.7, clearly illustrating that the maximum acceleration of the car (0-60 mph in 2.8 s, using 'Ludicrous mode'), requires considerably more torque than the driver is likely to need for overcoming aerodynamic drag or

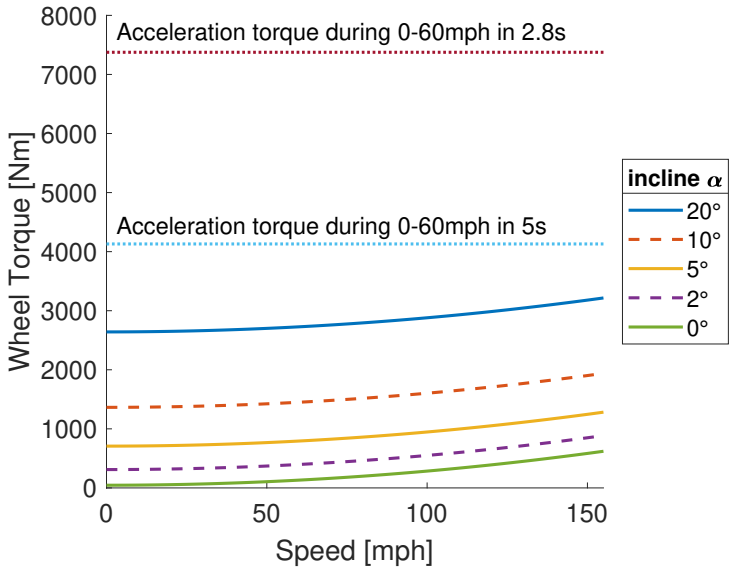


Figure 4.7: Estimate of wheel drive torque required to cruise at speeds between 0 and 155 mph for Tesla Model S P90D according to Eq. (4.1), assuming air density $\rho_{\text{air}} = 1.225$ kg/m^3, drag coefficient $C_D = 0.24$, $A = 2.34$ m^2, kerb mass $m = 2200$ kg, coefficient of rolling resistance $\mu_r = 0.006$ and gravitational acceleration $g = 9.81$ m/s^2.

climbing. (The 0-60 mph speed transient likely does not occur at constant torque so at some speeds a greater torque may be supplied. If the two drive units were to reach their nominal maximum torques simultaneously, which would require the front and rear axles to be turning at different speeds, the total wheel torque would be around 8.9 kNm without accounting for transmission losses [223]). Therefore, during everyday driving, the car is likely to be operating at a small fraction of its rated torque.

4.1.3 Mesh Forces

A schematic representation of the gearbox is given in Fig. 4.8.

The gears were measured manually using calipers and measuring tapes - these measurements are therefore only accurate to the order ± 1 mm and the dimensions given in this section should be interpreted with this in mind. The analysis presented here therefore does not claim to represent the forces or the geometry of the gearbox exactly. Nevertheless, an attempt was made to extract preliminary gear geometrical design parameters from these measurements (Table 4.2), assuming that the gears have involute profile and were generated from a standard

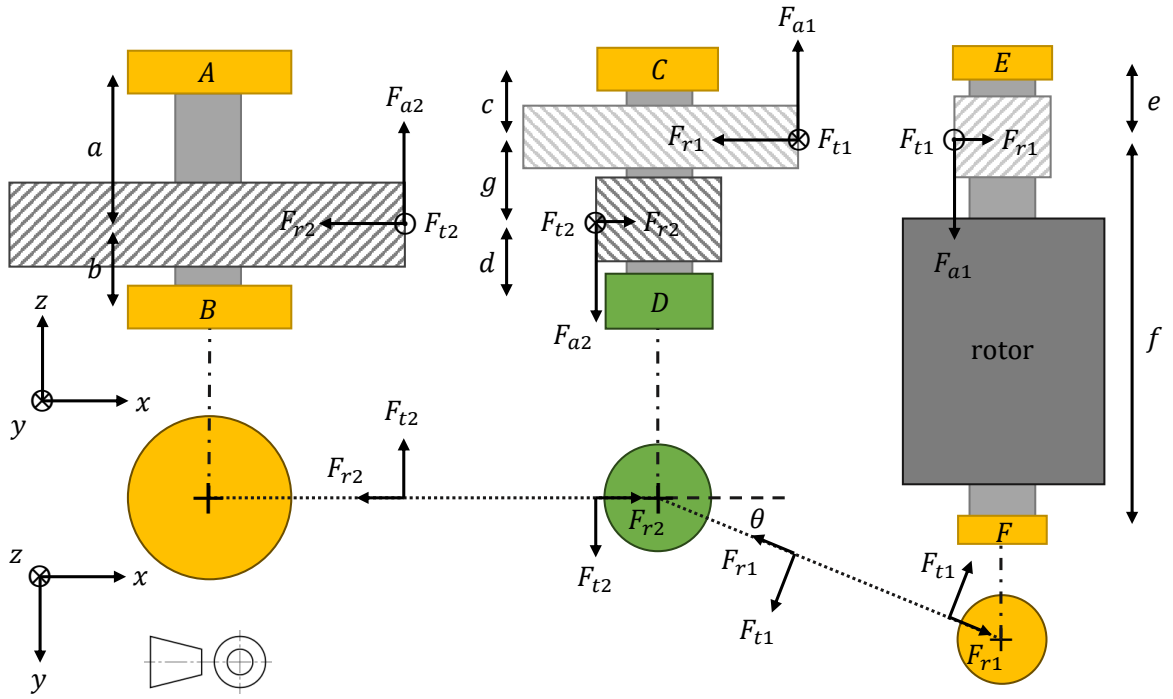


Figure 4.8: Schematic representation of helical gears showing bearing arrangement, handedness and gear mesh forces. For clarity, the upper part (xz plane) is drawn as if the axes of the three shafts lay in the same plane. The lower part (xy plane) illustrates that the radial and tangential mesh forces for stage 1 in fact act at an angle θ to those for stage 2.

rack according to BS436, namely that:

$$d_a = m_n \left(z \sec \beta + 2(x+1) \right) \tag{4.2}$$

$$d_f = m_n \left(z \sec \beta + 2(x-1.25) \right) \tag{4.3}$$

$$\alpha_n = 20^\circ \tag{4.4}$$

where z is the number of teeth on the gear, α_n is the reference pressure angle, β is the helix angle of generation, d_a and d_f are the tip and root diameters respectively, m_n is the normal module and x is the addendum modification coefficient.

A helix angle $\beta = 20^\circ$ was assumed for both gear pairs, which matched that calculated from measurements of the axial pitch p_x of both the wheel gears to within $\pm 1^\circ$, given by

$$\beta = \sin^{-1} \left(\frac{\pi m_n}{p_x} \right) \tag{4.5}$$

The module m_n was calculated independently for each of the 4 gears from Eq. (4.2) and

Table 4.2: Approximate geometrical parameters extracted from gear measurements.

Gear	z [-]	m_n [mm]	d_a [mm]	d_f [mm]	b [mm]	β [°]	x [-]
HS Pinion	31	1.5	54	47	41	20	0.25
HS Wheel	77	1.5	132	125	30	20	0.25
LS Pinion	21	2.5	59	47	44	20	0.5
LS Wheel	79	2.5	215	202	39	20	0

found, for the high-speed stage to be approx. 1.5 mm, and for the low-speed stage to be approx. 2.5 mm, which are both standard values for metric module. As the gearbox was designed to US specifications, the possibility of a standard inch diametral pitch (10, 16) was also considered, as these produce modules 2.54 and 1.588 respectively which are quite close to the metric values. The possibility of one stage being made to inch standards while the other stage is metric was eliminated.

On examining the tooth shape of the pinions, and considering the high design load of these gears, it is likely that addendum modification was used. Assuming that the sum of the addendum modification coefficients in each gear pair is within the range $0 \leq \Sigma x \leq 0.5$, and that the modules are *either* metric *or* inch for both gear pairs, no plausible combination of addendum modification coefficients and modules was found to fit the measurements to within the measurement uncertainty. These gears are evidently in high-volume production and so it is possible that bespoke tooling for a non-standard module was justified. Given the small discrepancy (< 0.05 mm) between the best-fitting and standard modules, it is considered more likely that this is attributable to measurement error. $\Sigma x = 0.5$ is assumed in both cases, a criterion which reduces sliding in the minimum film-thickness case (first contact between wheel tip and pinion dedendum) and increases tooth strength. The estimated metric modules, 1.5 mm and 2.5 mm, are therefore assumed to apply for the remainder of this section.

The centre distance a was assumed to be the null centre distance plus the total addendum modification

$$a = m_n \left(\frac{z_1 + z_2}{2} \sec \beta + (x_1 + x_2) \right) \tag{4.6}$$

These assumptions and the measurements underlying them are sufficiently accurate to

approximate mesh forces and entrainment and sliding speeds in the gear contacts, for which a tolerance up to $\pm$10% in each of these variables is acceptable given the sub-unity exponential dependence of contact pressure and film thickness on each. It should be noted that, in the maximum-sliding, minimum-film-thickness case, both curvature and sliding speed (hence contact pressure and SRR) are highly sensitive to the chosen addendum modification and to centre distance when these are near their lower limits. Realistic values which avoid these lower limits have therefore been selected.

The axial separations denoted $a-g$ are given in Table 4.3 along with the estimated geometrical parameters.

Table 4.3: Axial spacings in mm between centrepoints of bearings and gear meshes shown in Fig. 4.8.

a	b	c	d	e	f	g
126	72	25	34	31	270	40

Table 4.4: Pitch-point mesh forces from force equilibrium applied to Fig. 4.8, assuming a motor pinion torque of 330 Nm.

Stage	F_n [N]	F_t [N]	F_r [N]	F_a [N]
1	14810	12903	5065	5213
2	35255	30025	12058	14001

An analytical solution for reaction forces in x, y and z from each bearing, is presented in Appendix B. Numerical values for these forces are given in Table 4.5, assuming the maximum rated motor torque for the front drive unit is 330 Nm [223].

Table 4.5: Bearing reaction forces from force equilibrium applied to Fig. 4.8, assuming a motor pinion torque of 330 Nm. $F_r = \sqrt{F_x^2 + F_y^2}$ is the total radial bearing load.

	A	B	C	D	E	F
F_x [N]	11676	382	11673	-10201	-11886	-1644
F_y [N]	10946	19079	-9869	-23172	3073	-57
F_z [N]	14001	0	8788	0	5213	0
F_r [N]	16004	19083	15285	25318	12277	1645

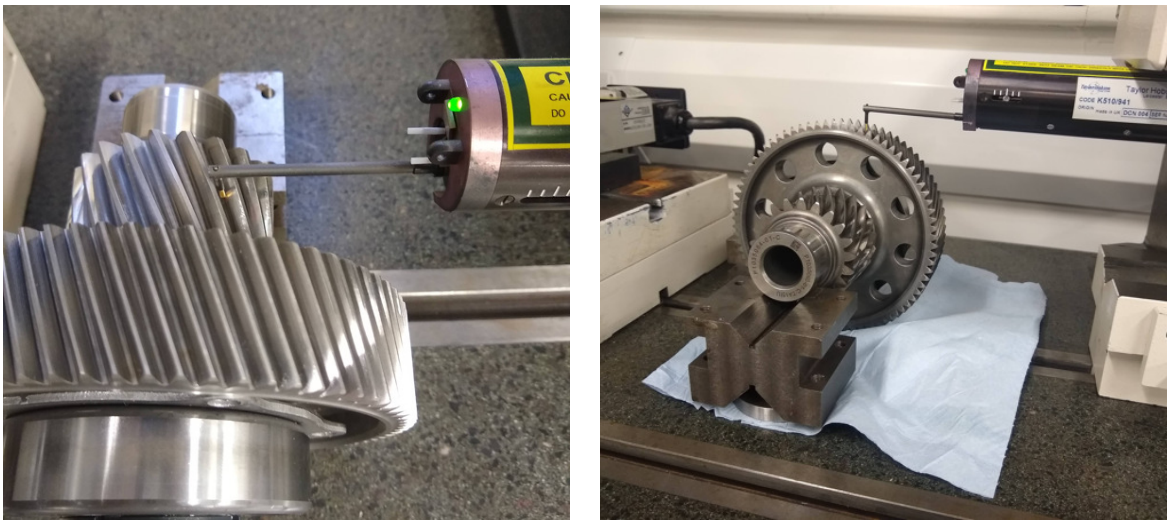


Figure 4.9: Stylus profilometer measurement of tooth flank surface roughness for gears on intermediary shaft.

4.1.4 Gear Tooth Surface Roughness

The roughnesses of the low-speed pinion and high-speed wheel (both located on the intermediate shaft), were measured using a Taylor-Hobson Form Talysurf as shown in Fig. 4.9, and are given in Table 4.6. On each gear, 4 teeth were selected, spaced equally around the gear, and on each tooth three traces were taken, in the radial direction. Arc form removal and Gaussian filtering were performed with cutoffs $L_c = 0.25$ mm and $L_s = 0.0025$ mm. Both the drive face, and the reverse face (loaded by regenerative braking when driving forward, or by acceleration in reverse) were measured. Within the path of contact along the tooth flank, both gears had a clear worn region (pinion dedendum, wheel addendum, concordant with the theoretical prediction of minimum film thickness here), and a rougher, less worn region (pinion addendum, wheel dedendum). Roughness parameters were calculated for each region based on a measurement length of around 1 mm for the high-speed wheel, and 1.5 mm for the low-speed pinion. The two gears measured belong to different stages, and are located on the same shaft, so do not mesh with each other.

4.1.5 Contact Conditions

It is of design interest to evaluate the minimum EHL film thickness seen by the gear teeth, which is assumed to occur at first contact between wheel tip and pinion dedendum where curvature is minimum and the sliding speed is at its negative extremum.

Table 4.6: Sample mean and standard deviation of roughness parameters measured on the driving (forward) and braking (reverse) faces of 4 teeth on each gear, with three measurements taken per tooth using a stylus profilometer. CLA (R_a), RMS (R_q), skewness (R_{sk}) and kurtosis (R_{ku}) are reported for both the addendum and the dedendum portion of each trace.

		Ra [um]		Rq [um]		Rsk [-]		Rku [-]	
Mean		Forward	Reverse	Forward	Reverse	Forward	Reverse	Forward	Reverse
HS wheel	Add.	0.147	0.183	0.184	0.235	-0.17	-0.37	2.8	4.0
	Ded.	0.172	0.158	0.220	0.211	-0.05	-0.12	3.3	4.9
LS pinion	Add.	0.259	0.295	0.332	0.381	-0.79	-0.74	4.1	4.4
	Ded.	0.105	0.213	0.139	0.270	-0.35	-0.19	4.3	3.2
Std. Dev.									
HS wheel	Add.	0.055	0.031	0.067	0.043	0.28	0.81	0.5	1.9
	Ded.	0.033	0.045	0.038	0.067	0.27	0.91	0.5	2.2
LS pinion	Add.	0.031	0.092	0.036	0.113	0.37	0.33	0.9	1.5
	Ded.	0.027	0.070	0.035	0.089	0.91	0.31	1.3	0.5

Representative material elastic properties for gear steels and lubricant rheological parameters for those typically used in recent electric vehicle transmissions are given in Table 4.7.

Table 4.7: Material and lubricant parameters for calculation of EHL film thickness in gears

Elastic modulus	Poisson ratio	Dynamic viscosity	Pressure-viscosity coefficient
E	ν	η	α_p
[GPa]	[-]	[mPa.s]	[GPa^{-1}]
207	0.293	20	15.7

The procedure for calculating the minimum EHL film thickness in the gear contacts from the relevant material and geometrical parameters is set out in Appendix C. The results of this procedure applied to the two gear pairs in question, assuming that the gearbox is operating at its maximum torque (330 Nm on motor pinion) and at 60 mph, are given in Table 4.8.

It is worthy of note that by this calculation, even at 60 mph, both gear pairs still operate in mixed lubrication ($\Lambda < 3$), and that as a result of the weak dependence of EHL film thickness on load, this is still the case at contact pressures more typical of everyday driving.

Table 4.8: Gear mesh parameters and contact conditions assuming $T_{\text{motor}} = 330$ Nm, $v_{\text{car}} = 60$ mph, where stage 1 is the high-speed stage and stage 2 is the low-speed stage.

			Stage 1	Stage 2
Transverse contact ratio	ε_α	[-]	1.51	1.42
Axial contact ratio	ε_β	[-]	2.18	1.70
Total contact ratio	ε_γ	[-]	3.7	3.1
Entrainment speed	U_e	[m/s]	6.1	2.7
Slide-roll ratio	SRR	[%]	51	55
Max. Hertz pressure	P_0	[GPa]	1.5	1.8
Minimum EHL film thickness	h_m	[nm]	340	190

4.1.6 Test Rig

The inertia rundown method requires a way of accelerating the gearbox to a high speed, and then leaving it to slow down with no external torque applied, while accurately measuring the speed during the transient. The rig built to do this is shown in Fig. 4.10. The rig employs a 3-phase AC induction motor which drives the low-speed stage of the gearbox via an electromagnetic clutch attached to a modified car driveshaft. The drive is disconnected by disengaging the clutch. Speed is measured by sampling the high-speed shaft encoder native to the gearbox, or by moving the encoder disc and Hall sensor to the driveshaft, when the high-speed shaft is absent.

The tripod joint and spline coupling from the driveshaft were isolated, and the shaft machined to fit a bellows coupling connected to the clutch. The motor was connected to the clutch via a jaw coupling, as shown in Fig. 4.11.

The low-speed stage is driven via only one side of an open differential, which therefore had to be locked (a similar approach was taken by Břoušek and Zvolský [224]). This was achieved by immobilising one of the spider gears using an M3 screw and nylock nut fixed in a hole drilled in the casing of the differential, as shown in Fig. 4.12. It should be noted that the rated torque of the external motor was 18 Nm, a very small fraction of the design torque of the differential (close to 10 kNm). The strength of this minimal locking device was therefore found to be adequate.

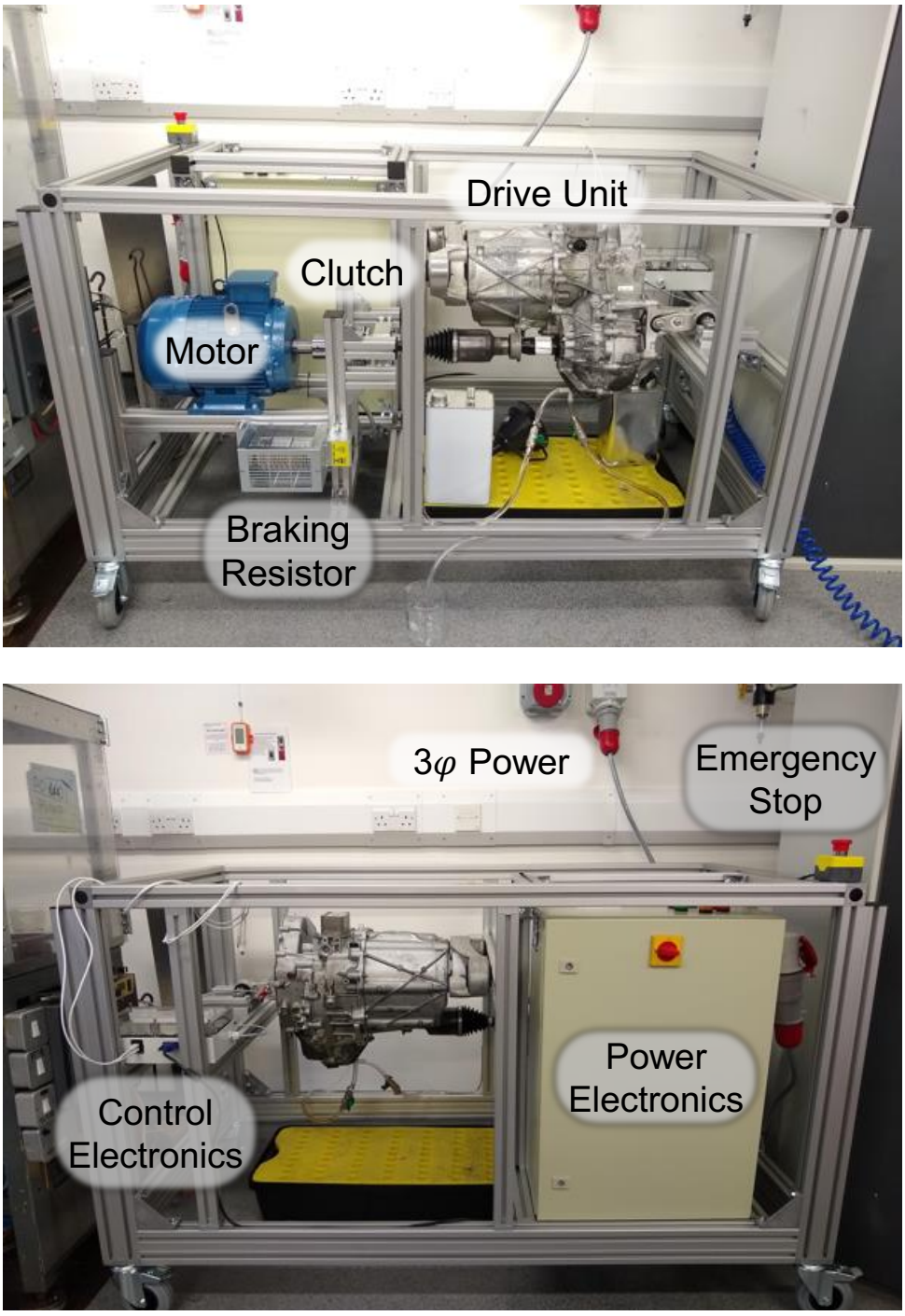


Figure 4.10: Churning loss measurement rig with Tesla drive unit mounted, seen from two sides showing main components. The bellows coupling and the reaction torque sensor were added subsequently.

4.1.7 Power Electronics

A high-power electrical system was designed to deliver the 5.5 kW required by the motor, and to supply various peripherals including the gearbox heaters, the 5V control electronics and

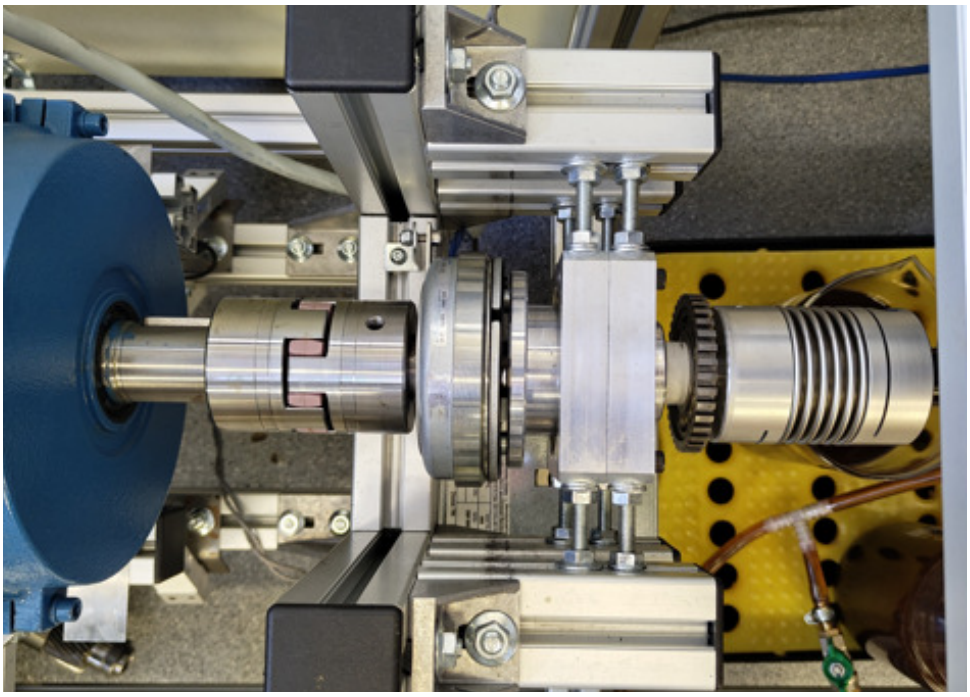


Figure 4.11: Transmission assembly connecting motor to gearbox via clutch. Left to right: motor, jaw coupling, electromagnetic clutch, support bearing housing, encoder disc, bellows coupling.

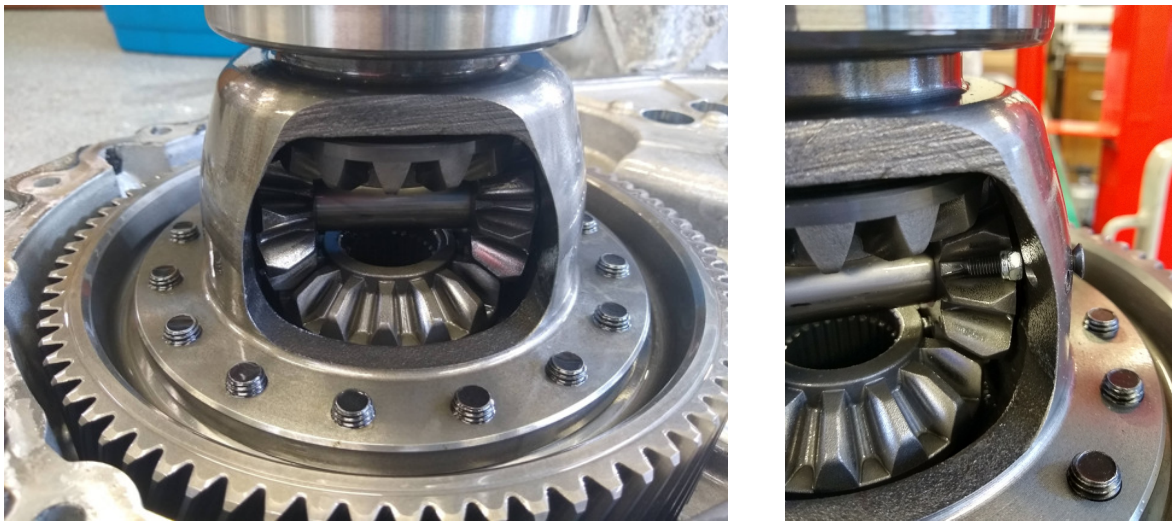


Figure 4.12: Open differential (left) and immobiliser nut (right) added to allow drive from a single sun gear.

the 24V safety circuit. A three-phase socket rated at 400V, 32A, bolted to the outside of the enclosure, was wired internally to an isolator. The three phases were then run through a 3-phase contactor with a 24V normally-open control relay, a motor protection circuit breaker (MPCB), and finally to the variable frequency drive (VFD), operating in delta-configuration. The VFD was connected to the motor via 4-core cable to provide dedicated earthing. An

external braking resistor and an RS232 link were also connected to the VFD. Between the isolator and the contactor, one of the phases was broken out to a 13A fuse and then to a residual current breaker with overcurrent protection (RCBO). The residual-current-protected single phase was used to power two switched-mode DC power supplies, one at 5V for the logic circuitry, and one at 24V to power the electromagnetic clutch and the safety circuit which energises the 3φ contactor. When the emergency stop is pressed, the 24V supply to the contactor is interrupted, and the VFD is isolated from 3φ power. The heaters were also powered via the single-phase circuit, and grouped into two separate arrays, each controlled via low-frequency pulse-width modulation. The relay bank houses opto-isolated electromagnetic relays rated to 230V, 10A, powered on the control side by the 5V supply. The logic inputs to the optocouplers, along with the RS232 link and a 5V bus, were connected to a 15-pin female D-subminiature port providing a link between the power electronics enclosure and the control electronics enclosure via a VGA monitor cable.

A schematic showing the original concept for the position of and connections between each of these components is given in Fig. 4.13. A photograph of the realisation of this concept is in Fig. 4.14.

4.1.8 Control Electronics and User Interface

The control electronics were designed to enable control of the clutch, motor and heaters, and to facilitate data acquisition, via a PC. Two microcontrollers were used, an nRF52840 from Nordic Semiconductor on a breakout board by Adafruit, and an RP2040 on the Raspberry Pi Pico board developed by the Raspberry Pi Foundation (not to be confused with the popular credit-card-sized Linux computer, Raspberry Pi). The nRF52840 was used to interface to the PC via a serial link over USB using an emulated COM port, and an ASCII-based serial protocol was developed for this purpose. The nRF52840 also handles relay control (clutch and heaters), services the thermocouple multiplexer (GPIO) and amplifier (I2C), and runs two concurrent discrete PI control loops to enable temperature control. Finally, the nRF52840 acts as the master device on the RS232 link to the VFD (via UART and a dedicated RS232 driver board), and as the master on the SPI link to the RP2040. The RP2040 is responsible for speed measurement using the incremental quadrature encoder native to the drive unit, and for torque measurement by sampling the load cell amplifiers.

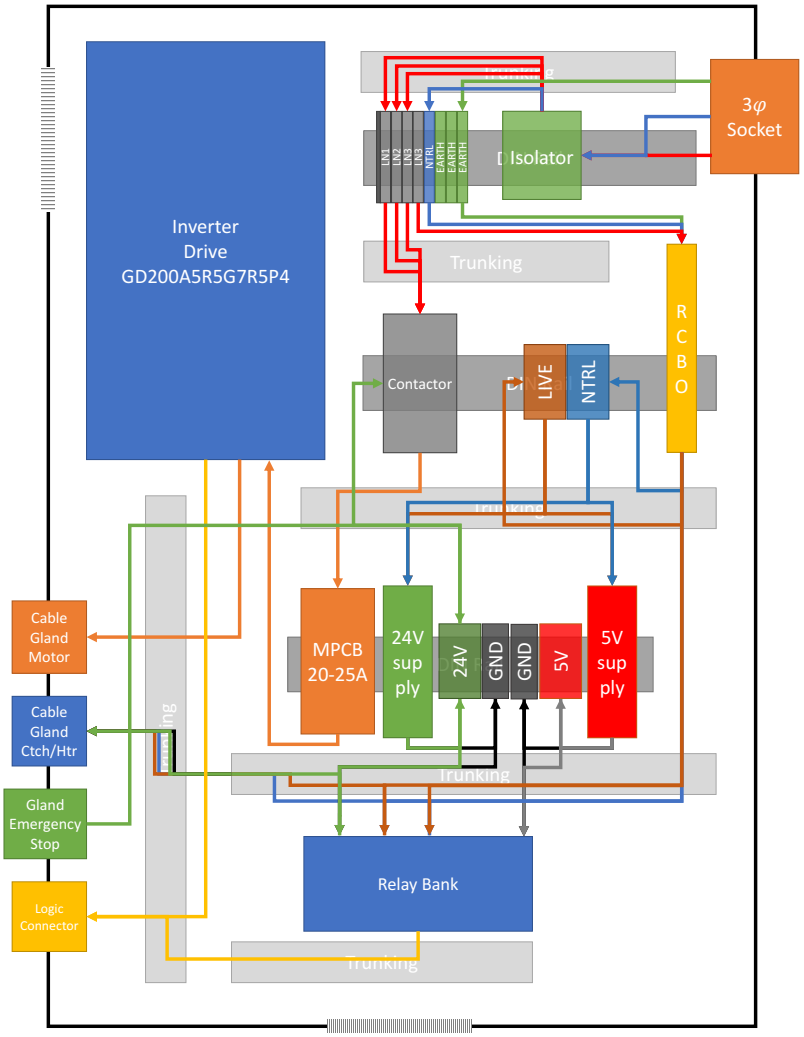


Figure 4.13: Schematic of initial concept for power electronics enclosure containing 3-phase variable frequency inverter drive (VFD), motor protection circuit breaker (MPCB), residual current breaker with overcurrent protection (RCBO), 5V and 24V power supplies, relay bank, and various terminal blocks.

The implementation takes advantage of the PIO programmable logic module on the RP2040 which can accurately sample the encoder at high rotational speeds (easily up to the maximum required speed of 42 kHz pulse-edge frequency), incurring no CPU overhead and enabling precise pulse counting and timing. As speed measurement resolution decreases with increasing samplerate, and the encoder only has 36 teeth (hence only 144 pulse edges per revolution), a samplerate of 5 Hz (user-configurable via the PC) was chosen in this study. A speed resolution of $5/144 \times 60 = 2.083$ rpm is achieved, while the latency in the measurement is



Figure 4.14: Power electronics enclosure for churning rig as-built including 3φ VFD, MPCB, RCBO, 3φ contactor, 3φ isolator, 5V and 24V power supplies, relay bank, and status indicators.

limited to 200 ms which is satisfactorily short compared to timescales over which significant speed changes are expected during gearbox operation. When the encoder is installed on the high-speed shaft, the speed resolution on the low-speed shaft improves by a factor of the gear ratio, becoming 0.223 rpm. A dedicated SPI communications protocol was developed, enabling the master (nRF52840) to request data from the slave (RP2040) including speed, load, and fault status information, such as encoder sequencing errors. The data is requested at the sampling frequency, here, 5 Hz. The nRF52840 also reads data from the VFD at the same rate, including motor voltage, current, field frequency, and estimated torque and speed. Only one thermocouple amplifier is used to sample 7 thermocouples, and so in order

to perform sufficient averaging to suppress electrical noise and to leave time for the ADC voltage to stabilise after the multiplexer switches, each individual thermocouple measurement has much greater latency than 200 ms. The amplifier acquisition time is also strongly affected by the desired ADC resolution. A resolution of approx. 0.25°C and a sampling rate for each individual thermocouple of approx. 0.5 Hz was chosen, with all thermocouples sampled in turn once in each 2 s period. The very large thermal bulk of the system means this samplerate is more than adequate for temperature measurement. Up to 16 thermocouples could be used simultaneously with this hardware, which would reduce the samplerate to approx. 0.2 Hz with no change to measurement resolution.

Bidirectional logic level shifters were used to enable communications between the 5V devices (encoder, relay bank, RS232 driver) and the 3V3 devices (nRF52840, RP2040).

These devices are all housed in a separate enclosure shown in Fig. 4.15. Wiring was undertaken using 0.1" pitch DuPont-style connectors to make the system easily modifiable during the development process.

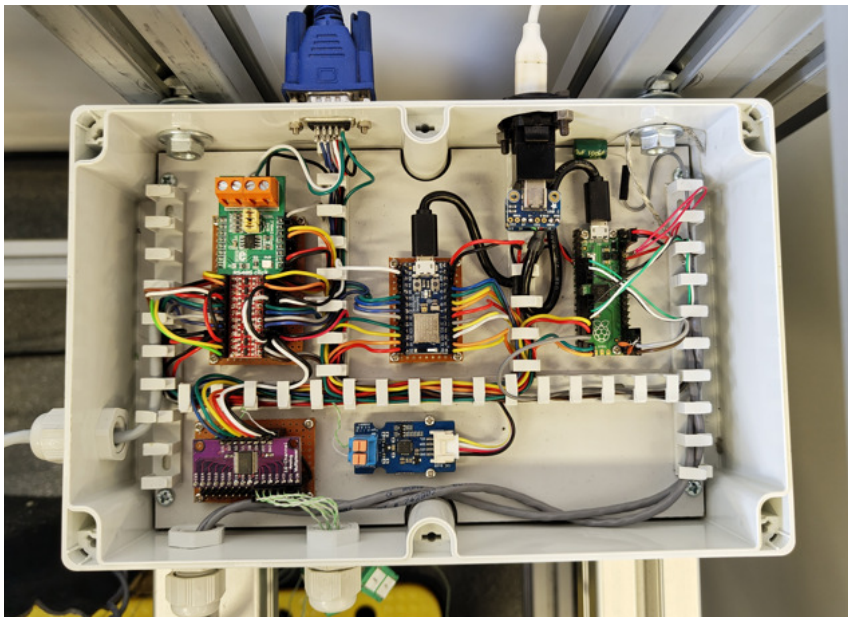


Figure 4.15: Control electronics including RS232 comms board (green, top-left), logic level shifters (red, centre-left), analog multiplexer (purple, bottom-left), nRF5280 board (blue, centre), thermocouple amplifier (blue, bottom-centre), and RP2040 board (green, top-right). The external connections are a 15-pin D-subminiature connector to power box (top-left), USB-C connectors (top-right) for programming and interfacing to PC, a 4-wire interface to the drive unit's high-speed shaft incremental encoder (left), two shielded I^2C links which service the torque sensor load cell amplifiers (bottom left), and seven thermocouple plugs (bottom left).

The load cell amplifiers were housed near to the load cells themselves to limit the electrical noise induced on the analog channels. A shielded box was designed and FDM 3D-printed, see Fig. 4.16, to house the amplifiers and to act as a junction box for the cables to the load cells and control electronics enclosure.

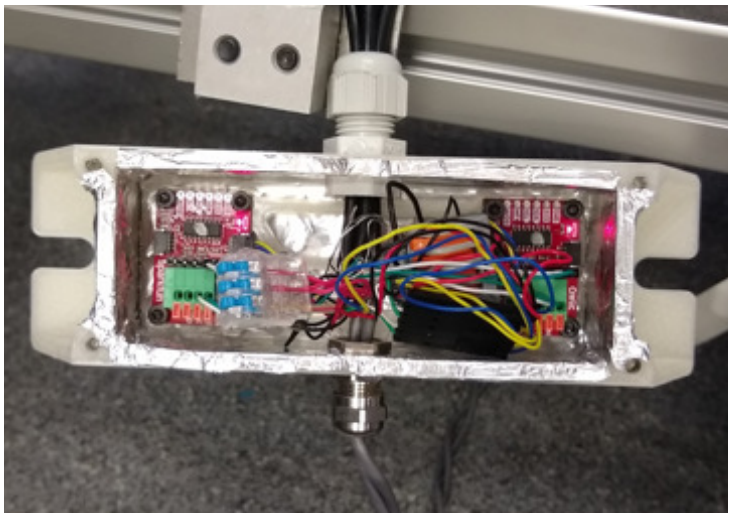
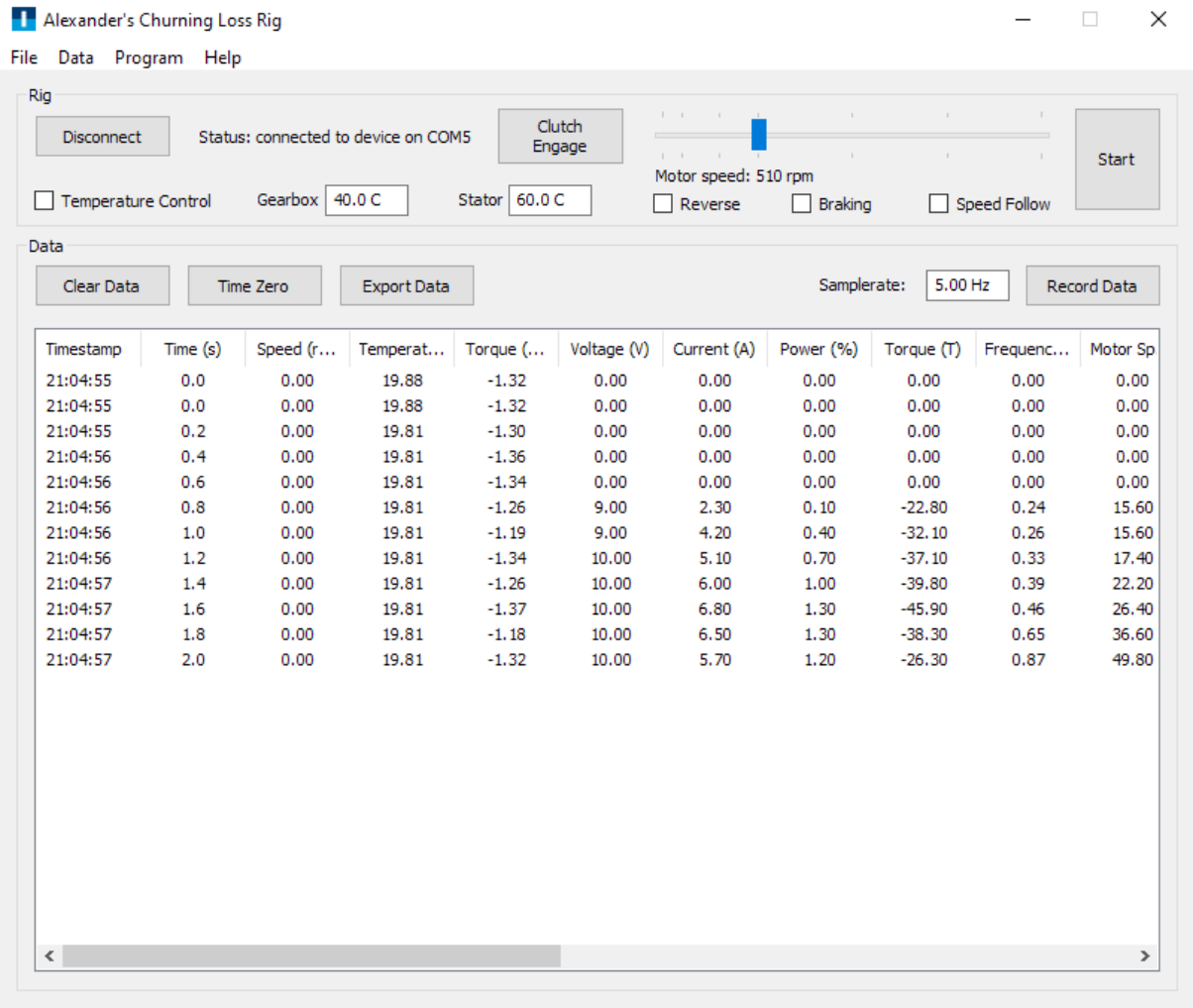


Figure 4.16: Shielded casing containing load cell amplifiers for reaction torque sensor

The program run by the nRF52840 was written in C++, and includes a driver developed for this project to interface with the VFD using a version of the MODBUS protocol. The RP2040 was programmed in the C language, and the PIO routine was written in the PIO assembly language defined in the device datasheet. The code for each can be found in the GitHub repository at https://github.com/AlexanderMacL/ChurningRig.

A GUI app, to be run on a Windows PC with a USB port, was written in C++ using the MFC framework by Microsoft, enabling rig control, status monitoring, and data acquisition. The app also supports user-defined subroutines, which can be loaded from an input file, enabling precise and repeatable timing and sequencing of GUI-supported tasks such as clutch disengagement, changes in motor setpoint speed, torque sensor zeroing, and data export. A function called speed-follow is included, which constantly updates the motor setpoint speed on the VFD to match the speed of the output stage of the gearbox as measured by the encoder, such that, even when the clutch is disengaged, there is minimal speed difference between the plates. This ensures that the double-row ACB which keeps the two sides of the clutch concentric, cannot contribute to the rundown torque measured. The speed-follow was seen during the rundowns to keep the two sides of the clutch completely in-phase at speeds



Timestamp	Time (s)	Speed (r...	Temperat...	Torque (...	Voltage (V)	Current (A)	Power (%)	Torque (T)	Frequenc...	Motor Sp
21:04:55	0.0	0.00	19.88	-1.32	0.00	0.00	0.00	0.00	0.00	0.00
21:04:55	0.0	0.00	19.88	-1.32	0.00	0.00	0.00	0.00	0.00	0.00
21:04:55	0.2	0.00	19.81	-1.30	0.00	0.00	0.00	0.00	0.00	0.00
21:04:56	0.4	0.00	19.81	-1.36	0.00	0.00	0.00	0.00	0.00	0.00
21:04:56	0.6	0.00	19.81	-1.34	0.00	0.00	0.00	0.00	0.00	0.00
21:04:56	0.8	0.00	19.81	-1.26	9.00	2.30	0.10	-22.80	0.24	15.60
21:04:56	1.0	0.00	19.81	-1.19	9.00	4.20	0.40	-32.10	0.26	15.60
21:04:56	1.2	0.00	19.81	-1.34	10.00	5.10	0.70	-37.10	0.33	17.40
21:04:57	1.4	0.00	19.81	-1.26	10.00	6.00	1.00	-39.80	0.39	22.20
21:04:57	1.6	0.00	19.81	-1.37	10.00	6.80	1.30	-45.90	0.46	26.40
21:04:57	1.8	0.00	19.81	-1.18	10.00	6.50	1.30	-38.30	0.65	36.60
21:04:57	2.0	0.00	19.81	-1.32	10.00	5.70	1.20	-26.30	0.87	49.80

Figure 4.17: Windows GUI application for churning rig control, developed in C++ with the MFC framework, including real-time data logging and acquisition, control of clutch, motor speed and direction, braking, simultaneous PID temperature control of sump and stator, and the execution of user-defined timed subroutines parsed from an input file, enabling unsupervised running and repeatable sequencing.

slow enough for their relative phase to be observed with the naked eye, until the motor's minimum speed (5 rpm) was reached. The source code for the GUI application is hosted at https://github.com/AlexanderMacL/ChurningRig.

4.1.9 Oil Fill Level

The gearbox was bought with its in-service transmission fluid still in it. The fluid was drained into a measuring cylinder and 1.9 l was extracted, suggesting the original fill volume was around 2.0 l, given the large wetted area and porosity of the bindings for the copper stator coils. After the transmission was cleaned and reassembled it was found that filling the transmission until

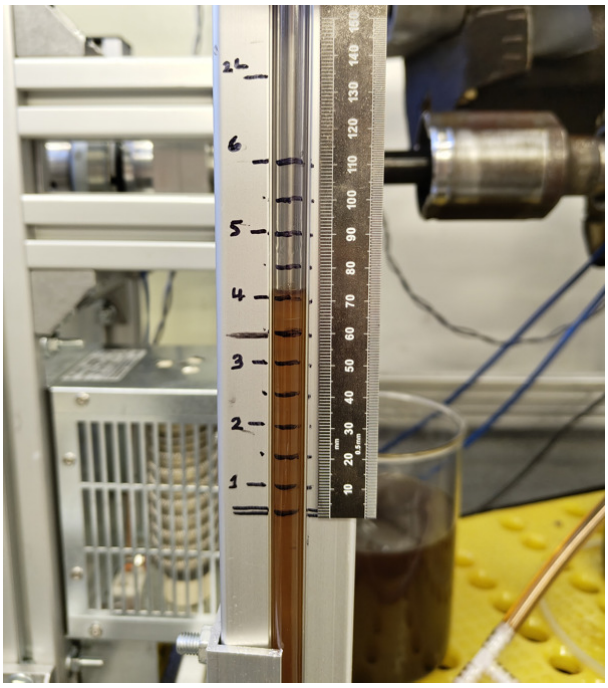


Figure 4.18: Oil level manometer comprising vertical length of transparent tubing open to the atmosphere at the upper end and connected to the gearbox oil drain.

the oil was level with the fill plug required 2.0 l of oil. It can be seen in Fig. 4.6 on page 82 however that this is an extremely large fill level, almost completely immersing the low-speed wheel gear! The service manual for the Tesla Model X 2015-2020 [225], one model of which shares the front drive unit discussed here (termed 'small drive unit') with the Model S, specifies 1.75 l of oil however. The same manual also specifies 1.45 l of oil for the rear ('large') drive unit which is the subject of Chapter 5. Note that the small drive unit is based on a wet-motor design and so the motor is cooled by the oil, whereas the large drive unit has a dry motor jacketed by dedicated coolant. The small drive unit therefore, somewhat counterintuitively, requires the larger oil volume.

A manometer, comprising a vertical length of pipe open to the air at the top, connected to the oil drain by a closeable valve, was used to measure the oil fill level of the gearbox (Fig. 4.18). The fill level at 2.0 l oil volume was found to be 123 mm.

When the vehicle, and hence the oil pump, are moving, the immersion depth is expected to decrease significantly as the oil is pumped through the heat exchanger and into the motor. The aluminium bucket in which the motor is housed contains significant free volume and the oil may take significant time to flow back to the sump. The motor bucket therefore effectively acts as a

second oil reservoir which the sump is pumped out into, and which slowly drains into the sump. This reduces the effective immersion depth of the low-speed stage (and probably leaves the high-speed stage entirely above the fluid level), but the extent to which this happens is likely to depend on vehicle (and so pump) speed, and also on oil viscosity (and so temperature). It was not possible to measure effective immersion depth using the manometer due to the contribution to static pressure in the oil drain of the flow field around the rotating low-speed wheel gear, which obscured that of the gravitational hydrostatic pressure. The manometer valve was therefore left closed during measurements to prevent flow into or out of the drain, simulating the oil drain plug. The notion of immersion depth is not well-defined when the gearbox is in motion, particularly when speeds exceed those that cause a laminar-turbulent transition, because the oil surface is constantly evolving with time over all lengthscales. As speeds increase, eventually there is no macroscopic subvolume in the gearbox which can be considered to comprise entirely oil or entirely air. The exposure of the gear surfaces to fluid impulse and viscous drag forces, and even the propensity of the heterogeneous fluid phase to supply them, is therefore unknown throughout this study.

4.1.10 Temperature Control

The gearbox was instrumented with 7 thermocouples whose locations are shown in Fig. 4.19. Cartridge heaters were also installed in dedicated holes drilled in the gearbox casing in the locations shown, with the heaters situated outside the gearbox so as not to come into direct contact with the lubricant. The cartridge heaters, operating at 220V AC, were wired in a parallel configuration on two separate circuits, one comprising 5 heaters positioned in the body of the gearbox, each with an output power of 100 W, and the other consisting of 2 heaters embedded in the aluminium stator as shown in Fig. F.3 each with a power of 250 W. The maximum heating power is therefore 1 kW. The circuits are switched by independent relays, and the total average power of each is varied independently by pulse width modulation (period of the order 5 seconds to prevent relay fatigue), with the duty cycle controlled by a dedicated discrete PI controller with feed-forward, implemented in C++. As a result, if desired, different setpoint temperatures can be achieved for the stator and the gearbox. The stator control loop measures temperature using the thermocouple embedded in the stator (labelled 7 in Fig. 4.19), and the gearbox control loop uses the thermocouple protruding into

the lowest point in the sump from the left-hand side of the gearbox casing (labelled 2).

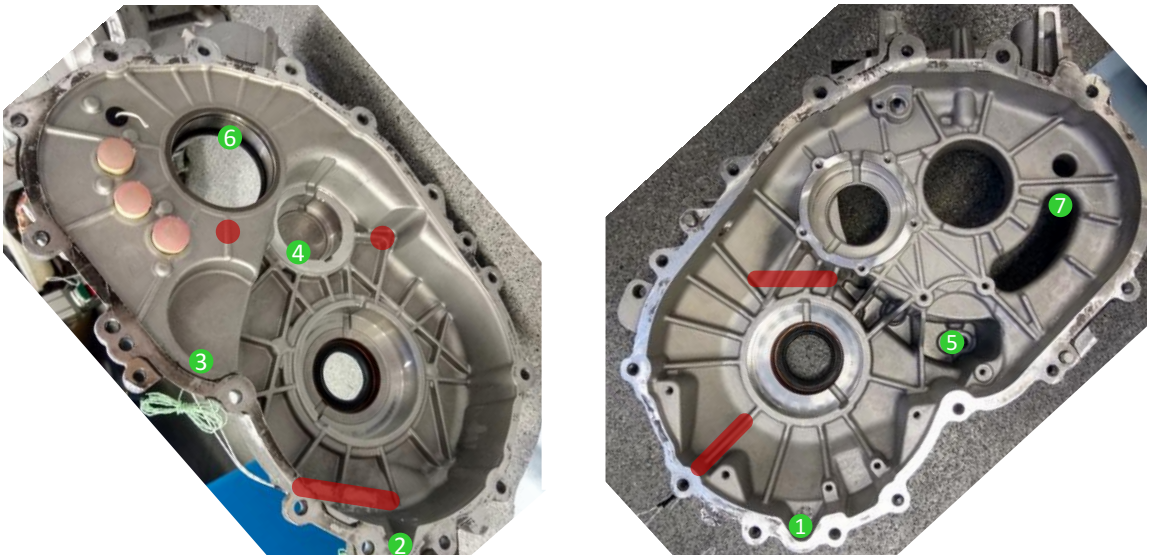


Figure 4.19: Two sides of the gearbox casing, showing the lowest point in sump at the bottom of the figure, detailing placement of thermocouples (green circles) and 100 W catridge heaters (red highlights). Thermocouples are placed to target (1) RH casing oil drain, (2) LH casing by oil filter inlet, (3) next to pump pinion exposed to LS wheel oil pickup, (4) behind CRB, (5) oil runoff from stator inside motor bucket, (6) encoder cover plate behind HS shaft DGBB and (7) embedded in aluminium stator (not shown).

4.1.11 Inertia Rundown

Load-independent loss torques may be measured in this setup using the rotational form of Newton's 2nd law:

$$T = I\dot{\omega} \tag{4.7}$$

where T is the total torque acting on the gearbox, I is the total inertia referred to a single rotational speed ω, and $\dot{\omega}$ is the angular acceleration. This technique, commonly termed 'inertia rundown' [49, 50, 56], involves accelerating a rotating system to a high speed, disconnecting the drive, and then recording the speed transient. From the time-derivative of the speed measurements, torque can be calculated at each speed if the total rotating inertia is known. If there are no external torques acting during the speed transient, it can be assumed that the deceleration of the system is due purely to torques acting from within it, such as those imparted by viscous drag, friction in contacts, fluid impulse etc. The inertia rundown method enables the measurement of the aggregate of all of these forces.

An advantage of this technique is that, assuming the transient is relatively short compared to the characteristic thermal timescales of the system, heat dissipated by the losses being measured does not drastically alter the temperature of the system, and so an approximately isothermal torque-speed response can be obtained. It is also assumed that the duration of the transient is much longer than the characteristic flow timescales such that the torques experienced at every speed arise from quasi-steady conditions. This assumption is particularly problematic for highly viscous lubricants at low speeds for which flow timescales are long, and transients are shortened by large decelerating torques.

Numerical calculation of the deceleration by, for example, a central difference time-derivative of the speed measurements, introduces considerable noise arising from the limited resolution of the encoder, which is not physical. The speed transients were therefore fitted with a polynomial in time t of the form

$$\omega(t) = P_N(t) \equiv \sum_{n=0}^{N} a_n t^n \tag{4.8}$$

where $a_0, a_1 \ldots$ are fitting coefficients and N is the polynomial order. Total decelerating torque is then found from

$$T(t) = -I\frac{\mathrm{d}\omega}{\mathrm{d}t} = -I\sum_{n=1}^{N} n a_n t^{n-1} \tag{4.9}$$

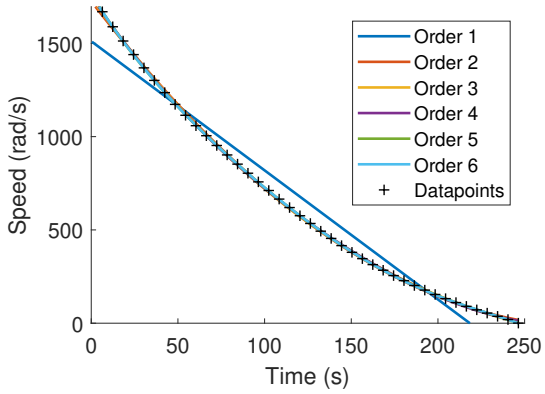
and torque can be found at an arbitrary speed using an interpolation to eliminate t provided the speed transient is monotonically decreasing, which is generally the case.

Polynomials with several values of N are fitted to a representative speed transient in Fig. 4.20a, and the resulting torques are plotted in Fig. 4.20b, and compared to a central difference derivative of the raw measurement. The choice of N makes a bias-variance tradeoff. The value $N = 5$ was deemed to realistically resolve the system behaviour without overfitting and so polynomials of 5th order are used subsequently in this study.

4.1.12 Inertia Measurement

The inertia rundown method relies on accurate knowledge of the total rotating inertia in the system. If both geometry and material properties are known, an analytical or numerical

(a) Speed Transient



(b) Torque Predictions

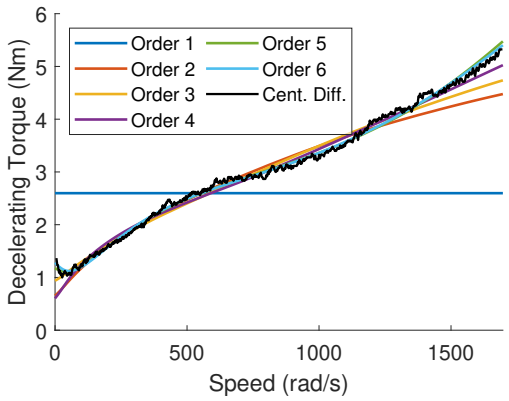


Figure 4.20: Best-fit polynomials of order 1-6 used to fit speed transient in (a) (only selected datapoints are shown), and whose derivatives are used to predict torque in (b) compared to the central difference derivative.

calculation (via CAD software) of the polar moment of inertia about the rotating axis is easily performed. In the case of the gearbox under study however, neither the material nor the internal geometry were known, and so direct measurement of the inertia was necessary.

A trifilar suspension method similar to that used by Kolekar [226] was employed to measure the rotating inertias of each component to within approx. $\pm 1\%$. A dedicated jig was made, suspended by three vertically-oriented fibres of known length, to hold the various parts of interest concentrically between the fibres, as shown in Fig. 4.21. The fibres were each made of 6 strands of braided ultra-high-molecular-weight-polyethylene intended for use as fishing line. The fibres were therefore strong and relatively inelastic in tension but had very low flexural stiffness.

The method involves the measurement of the period of torsional oscillation of the suspended system shown in Fig. 4.22.

For small amplitude of oscillation θ, we have

$$r\theta \approx L\phi \tag{4.10}$$

where r is the radius at which the fibres are connected, and L is the fibre length. The force acting to torsionally accelerate the system is the restoring force provided by the fibres,

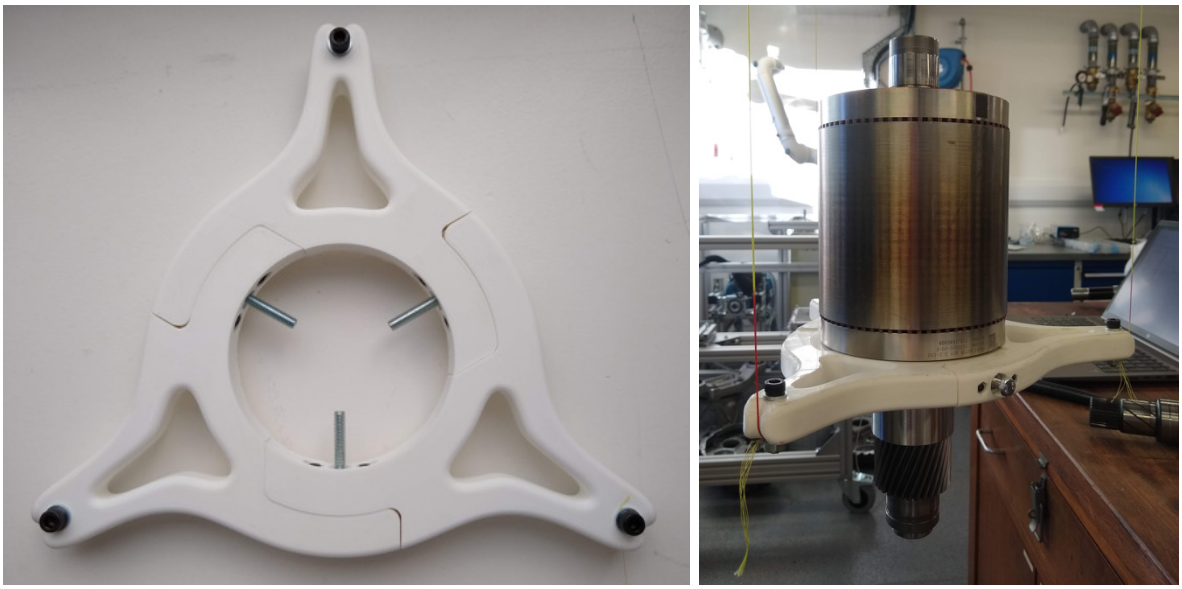


Figure 4.21: Trifilar suspension inertia measurement jig (left), being used to measure the rotor inertia (right)

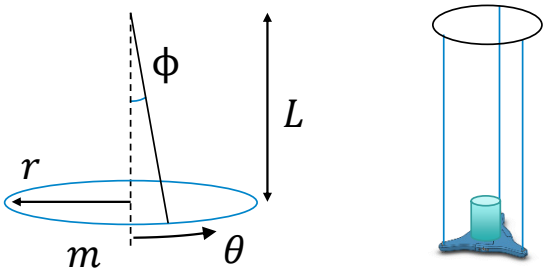


Figure 4.22: Oscillatory system used to model trifilar suspension inertia measurement

$mgr\tan\phi$, and so for small ϕ, the equation of motion is

$$I\ddot{\theta} + \frac{mgr^2}{L}\theta = 0 \tag{4.11}$$

where mg is the total weight of the system and I is its total rotating inertia. The solution has a natural frequency of oscillation ω_n given by

$$\omega_n = \sqrt{\frac{mgr^2}{IL}} = \frac{2\pi}{T_{\text{osc}}} \tag{4.12}$$

The period of oscillation T_{osc} is measurable using a stopwatch, or alternatively by frame-counting in a slow-motion video of the oscillation, and so rearranging, the inertia is given

by

$$I = \frac{mgr^2T_{\text{osc}}^2}{4\pi^2 L} \tag{4.13}$$

Values of the relevant physical parameters in Eq. (4.13) are given in Table 4.9.

Table 4.9: Physical properties of the trifilar suspension setup including inertia of measurement jig itself

Platform mass m [kg]	Grav. accel. g [m/s^2]	Radius r [m]	Platform time T_{osc} [s]	Fibre length L [m]	Platform inertia I_{platform} [kgm^2]
0.5584	9.81	0.162	1.153	0.993	0.00487

The inertia of the component under test is then found by subtracting the platform inertia from the inertia found from Eq. (4.13).

An aluminium cube of known density was used to verify the accuracy of the method, and its measured inertia was within 0.25% of the analytically predicted value. The primary contributor to the uncertainty in the measurement is the uncertainty in T_{osc}. A slow-motion video at 120 fps was taken using an Android smartphone, and a video angle chosen from which two of the fibres, coloured differently for this purpose, could be seen to pass each other twice per oscillation. The time between two consecutive crossings in the same direction was used to measure T_{osc}. The time-resolution is therefore of the order 10 ms but there is additional error incurred by the swinging of the platform, at a frequency different to that of the oscillation, which arises from a slight unbalanced force applied during the torsional excitation (depending on the skill of the operator). The swinging was seen to change the time between crossings of the fibres considerably (by several frames) even when minimised as much as manually possible. An alternative approach was taken, using a stopwatch (human reaction time ~ 250 ms), waiting for 20 oscillations to pass (reaction time divides across all oscillations so error is once more of the order 10 ms), and averaging the measurement across three repeats ($\sigma < 5$ ms) to reduce the effect of random errors. The shortest value of T_{osc} (produced by parts with large mass and small radius of gyration) was 0.52 s, so the worst-case error is slightly less than 2%. Considering the quadratic contribution of T_{osc} to I and accounting for the accumulation of errors in the effective lengths L and r, the total uncertainty in I is expected to be contained within $\pm 5\%$.

The measured inertias of the relevant rotating components are listed in Table 4.10.

Table 4.10: Inertia of gearbox components measured by trifilar suspension, and those referred about the low speed wheel shaft for comparison

	Mass [kg]	Inertia [kgm^2]	Referred to ω_{output} [kgm^2]
Differential	8.943	0.040919	0.040919
Intermediary	2.952	0.004673	0.066137
Rotor	18.775	0.038713	3.380089
Driveshaft	5.785	0.003108	0.003108
Encoder Teeth	0.093	0.000085	0.000798
Total Gearbox Bearings	2.999	0.000749	0.010322
Total Clutch Assembly	-	0.001143	0.001143

All inertias were referred to the output speed using the method of referred inertias, which is described in Appendix D. A method of referring the linear and angular inertias of the balls of a rotating rolling element bearing, given the angular velocities of each of its races, is also presented in Appendix D. For both of the deep groove ball bearings supporting the low-speed wheel and differential, the referred inertia of the balls represents an additional 28% of the inertia of the bearing inner race, and for the other three bearings with inner races, the contribution was between 15% and 25%. It was found that the total referred inertia of the rotating components of all bearings in the system was less than 0.3% of the total referred inertia of the gears and rotor.

The linear inertia of the kerb mass m_{kerb} of the car may also be referred to an equivalent rotating inertia via $I_{\text{ref}_{\text{lin.}}} = m_{\text{kerb}} r_w^2$. Assuming the wheel radius $r_w = 0.352$ m and $m_{\text{kerb}} = 2200$ kg, the total rotating inertia of the gearbox represents around 1.25% of the total referred inertia as the car accelerates. Note that this car contains two similar drive units, so the total rotating inertia is approximately equivalent in mass terms to adding an extra passenger of mass 70 kg to the car (considerably less than the combined weight of the drive units).

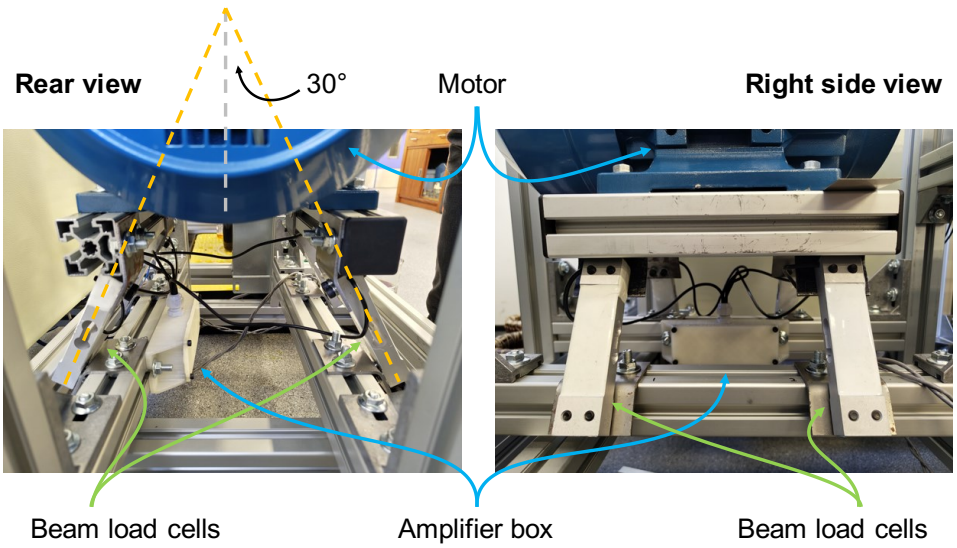


Figure 4.23: Angled beam load cells and extruded aluminium profile frame supporting motor, comprising the reaction torque sensor that enables torque measurement.

4.1.13 Torque Measurement

The motor was supported by a reaction torque sensor comprising 4 beam-type load cells each rated to 50 N load. The load cells were arranged so that the midline of each beam passed through the axis of the motor, see Fig. 4.23, maximising sensitivity to torque. The angle of the beams was chosen so that the bending component of the weight of the motor biased the load cells to the middle of their range, to improve the linearity of the reading, and dedicated mounting brackets were made from 3 mm sheet steel to achieve this angle.

Load cells 1 and 2 lie on one side of the motor, and are loaded positively by a positive torque force, while the load on cells 3 and 4 opposite is reduced. If the uncalibrated reading on the nth load cell is P_n, the torque T_r is calculated from Eq. 4.14, where K_s and K_o are calibration constants in Nm/LSB and Nm respectively.

$$T_r = K_s \left(P_1 + P_2 - P_3 - P_4\right) - K_o \tag{4.14}$$

It was found that value of $P_1 + P_2 - P_3 - P_4$ was insensitive to vertical and horizontal forces not acting to apply a net torque on the motor casing (e.g. balancing a weight centrally on the motor casing) even when the change in each of the terms P_1 *etc.* was a significant fraction

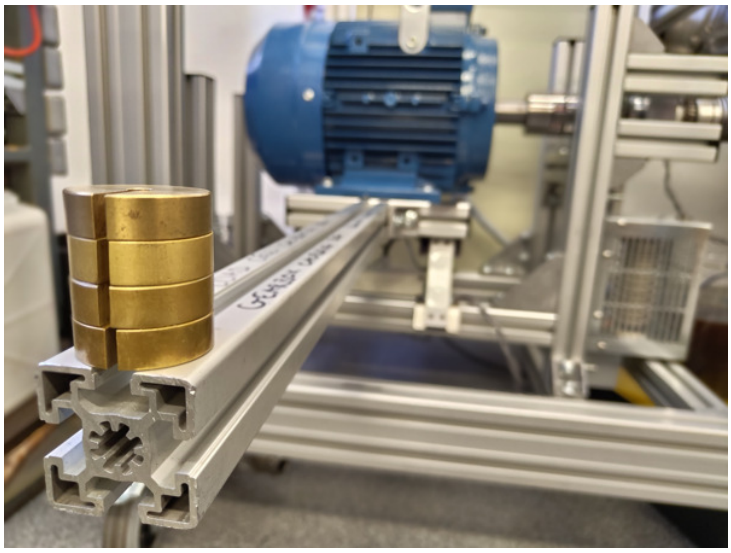


Figure 4.24: Torque calibration beam with 4×100 g weights

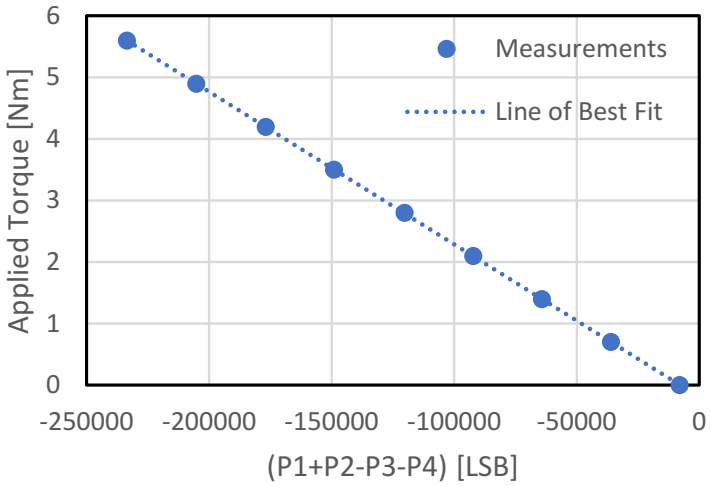


Figure 4.25: Torque applied to calibration beam by adding mass in 100 g increments, with a moment arm of 713 mm from the axis of the motor, vs value of $P_1 + P_2 - P_3 - P_4$, showing excellent linearity (the best fit line achieves $1 - R^2 < 10^{-4}$). The value of K_s, taken as 2.48×10^{-5}, is obtained from the slope of this line.

(10%) of the total range. The metric was also insensitive to pitch moments (e.g. by moving the weight towards the front or back of the motor), but highly sensitive to torque (e.g. by moving the weight slightly off-axis). This implies that the load cells are well-matched in their sensitivity and do not require individual balancing before their readings can be summed.

The value of the slope constant K_s was obtained by connecting a long beam to the structure supporting the motor, and applying successively larger known loads to a known position on the beam, thereby applying a known change in the moment applied to the structure by the

beam (Fig. 4.24). The results are shown in Fig. 4.25.

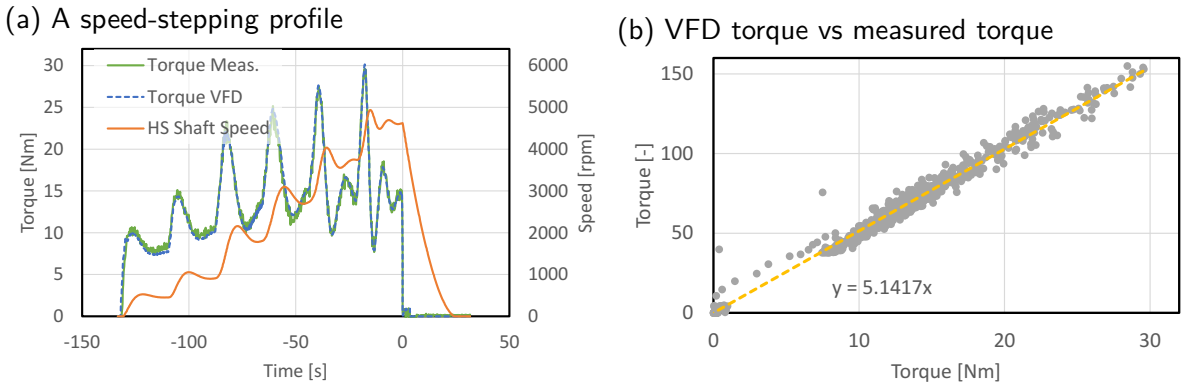


Figure 4.26: Correlation between torque value reported by VFD (scaled), and torque measured by reaction torque sensor, during a series of speed transients created by demanding speed steps at 20 s intervals with the speed control underdamped. Speed reported is that of the high-speed shaft of the gearbox measured by the native encoder. The clutch was disconnected at time 0 s, and the gearbox then slowed to a stop while the motor idled at constant speed, during which time a torque close to zero was reported.

The value of the offset K_o was found with the beam disconnected, where $K_o = K_s\,(P_1 + P_2 - P_3 - P_4)$ in the case where the torque is nominally zero, i.e. the motor is stationary and the clutch disengaged.

A good correlation between the reaction torque sensor reading (somewhat noisy) and the torque reported by the drive (less noisy but uncalibrated, i.e. in arbitrary units) is seen in Fig. 4.26. The use of both of these metrics in tandem, (using the reaction torque sensor to calibrate the VFD torque reading) provides the option of more precise torque measurement under conditions in which the fluctuation in the torque sensor reading is increased by electromagnetic noise and vibration, for example during fast transients at high motor speeds.

4.1.14 Overspeeding

During the development of the method, the gearbox was accelerated, accidentally, to an output stage speed of 3000 rpm (the maximum speed of the external drive motor). This resulted in, for a short time, the motor shaft reaching ~ 28000 rpm, which is considerably higher than the ~ 18000 rpm for which it was designed.

Shortly after a steady output speed of 3000 rpm was achieved, considerable noise and vibration was observed, and the rig was shut down. On disassembly, the copper endplates of the squirrel-

cage rotor were found to have reached centripetal plastic yield, the previously circular balancing holes having become elliptical, and the diameter of the ends having visibly increased. Although the deformation of the copper was limited by steel bands at each end, the yielding had caused the rotor to go out-of-balance, leading to the increase in vibration. The rotational inertia of the rotor was re-measured and found to have increased by 2%, due to the increase in radius of gyration.

The often-touted speed increases for EV motors must of course be accompanied by a decrease in motor diameter, and it would seem that the nominal maximum speed of this drive unit is relatively close to the limiting speed by yield of the motor (other models in the Model S line can reach 200 mph, which for this transmission would require a motor speed of 22,677 rpm). Obviously this wasn't the author's finest moment - this was an accident, but the results are noteworthy.

The rotor was subsequently unusable, so a new gearbox was sourced. The new gearbox was found to be identical to the previous model, except for an increase in spiral angle of the high-speed stage to 30°, perhaps to reduce gear whine (the mesh forces and bearing reactions are only slightly increased by this change, but the forces given in Tables 4.4 and 4.5 assume $\beta = 20°$). Steel panels were added to enclose the gearbox while in operation to reduce the risk posed by anything which might be centripetally expelled in operation. A maximum speed limit was hardcoded into the control software, in addition to constraint of user-selectable speeds, to prevent this accident from recurring.

4.2 Results and Discussion

Three studies were performed, which aimed to:

1. Investigate churning torque dependence on speed and immersion depth (Section 4.2.1)
2. Investigate churning torque dependence on oil viscosity (Section 4.2.2)
3. Compare churning torque in steady-state (direct torque measurement) and transient (inertia rundown) conditions at constant temperature (Section 4.2.3)

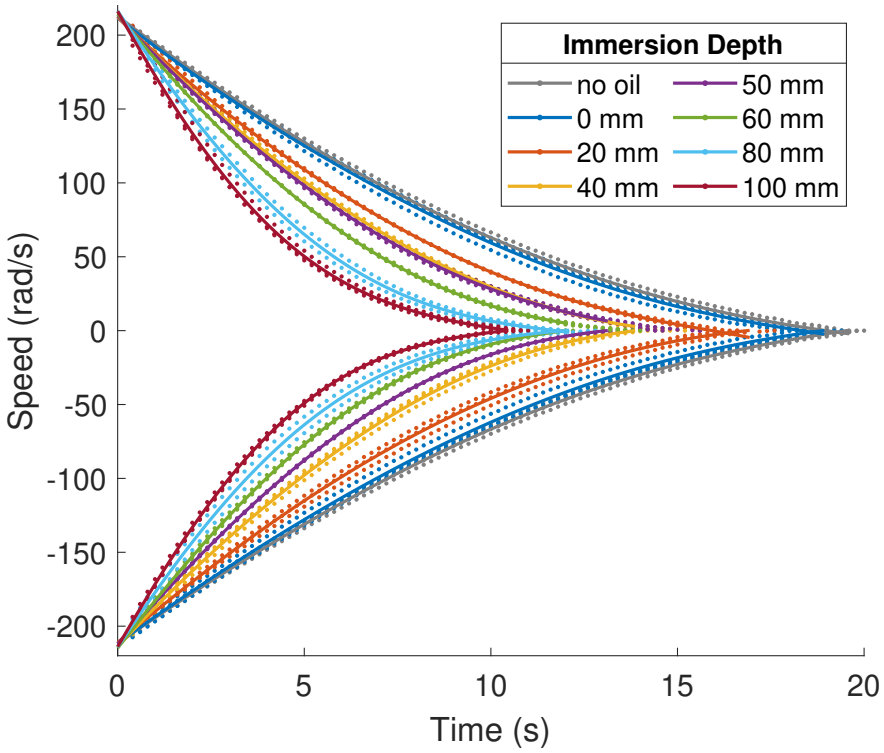
4.2.1 Speed and Immersion Depth

For this study, the bearings were replaced with new unsealed DGBBs from SKF to avoid any influence on the churning torque measurement, of damage the bearings might have experienced in transit after the removal of the drive unit from the vehicle. The custom-made hybrid bearing (BB1-1107) supporting the rotor end of the motor shaft was replaced by a 6007 DGBB which has the same external dimensions. The original CRB (bearing D in Fig. 4.8) was used because its inner raceway is the surface of the intermediate shaft which could not easily be replaced. The temperature was not controlled but the sump temperature (thermocouple 2 in Fig. 4.19 on page 100) was measured to be 30 ± 5°C during the transients. For more rigorous consideration of temperature and oil viscosity effects, see Section 4.2.2.

4.2.1.1 Direction of rotation

Speed transients in both the forward (positive speeds) and reverse direction (negative speeds) are shown for seven immersion depths in Fig. 4.27, where only the low-speed wheel gear is present, and the lubrication system (pump, pump pinion, piping, filter, inlet nozzle, baffles) has been removed. In this section, 'low-speed wheel gear' refers not only to the gear itself but also to the shaft, mounting flanges, and differential. The finely dotted lines in Fig. 4.27a represent speed measurements for three separate rundowns, and the continuous lines are the polynomial whose coefficients are the corresponding means of the best-fit polynomial coefficients of each of the three transients. The shaded regions in Fig. 4.27b and subsequent similar figures, are bounded by the extrema of the torques calculated by considering each of the three rundowns separately, while the lines show the average of these three torques, calculated by the method in Section 4.1.11. The torques and speeds reported refer to the low-speed shaft. The '0 mm'

(a) Speed transients $\omega(t)$



(b) Decelerating torque $T(\omega)$

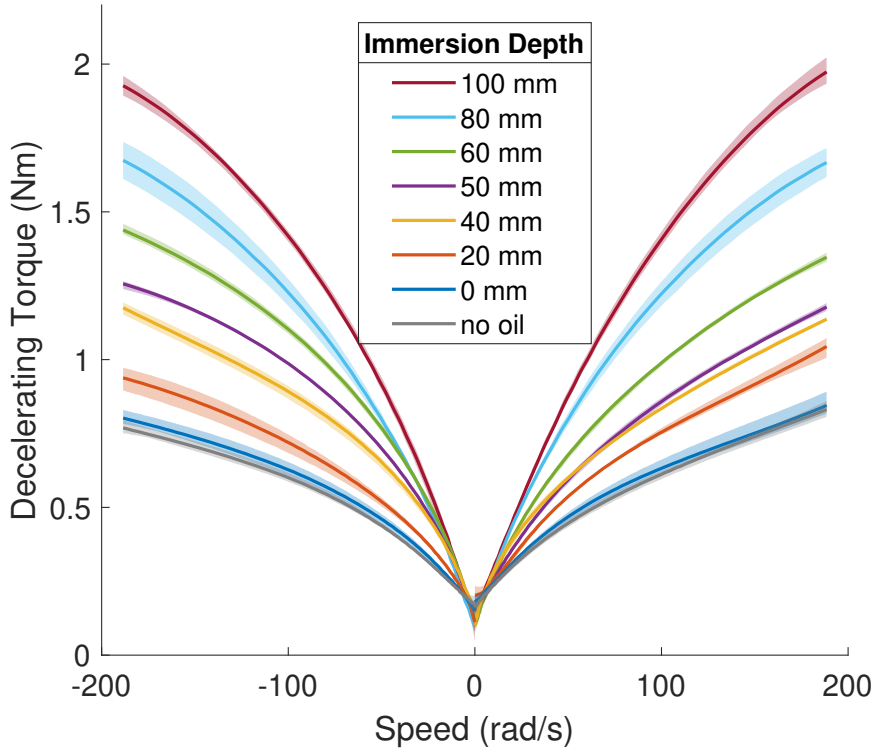
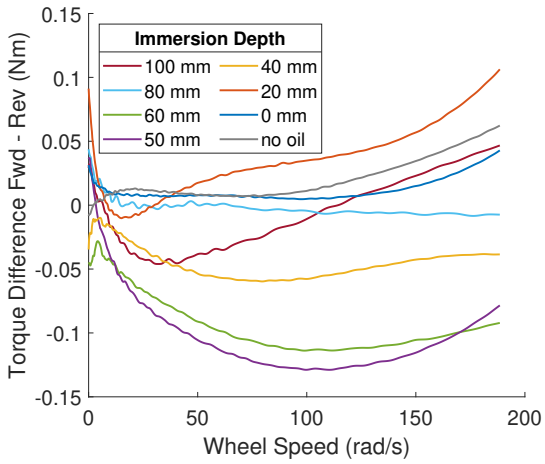


Figure 4.27: Speed transients (a) and corresponding torques (b) at several nominal immersion depths with DEX-VI ATF at ambient temperature for solely the differential and LS wheel gear, spray lubrication system removed

and 'no oil' cases are distinguished by approx. 5 mm oil depth on the manometer, the former implying that there is a small reservoir of oil present which does not impinge upon the wheel gear in the quiescent state, while the latter indicates the sump has been drained completely.

The difference between torque measured in the forward and reverse cases is given in Fig. 4.28, both with and without the lubrication system present. The pump is left unpowered in both cases by omitting the pinion which drives it, so the effect is purely one of the geometry of the piping and baffles, and the fill volume which they displace (note that comparable immersion depths therefore lead to different oil fill volumes with and without the lubrication system). Figure 4.28 suggests that in both cases the effect of the direction change on torque, with increasing oil fill, is quite complex. As there is no gear mesh with only the low-speed wheel gear present however, there are no trapping losses and so the influence of direction of rotation is relatively weak, less than 10% of the total torque, and arises from the reflective asymmetry of the casing about the plane containing the axis of gear rotation, and the gravity vector. It should also be noted for the larger immersion depths, that the variation in torque across the repeats is greater than the difference between the forward and reverse directions at some speeds, so the difference is close to the noise threshold of these data.

(a) No spray lubrication system



(b) Lubrication system present but unpowered

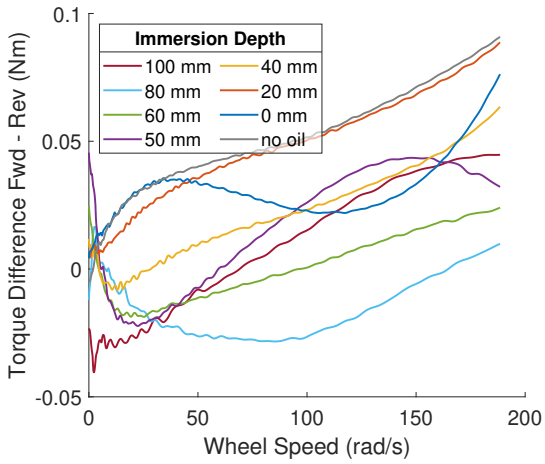


Figure 4.28: Difference between measured forward- and reverse-rotation decelerating torques with only the LS wheel gear present, for the case where the lubrication system (pump, filter, piping, nozzle, baffles) is (a) absent and (b) installed but unpowered by leaving out the pump pinion.

Figure 4.29 shows similar results with the intermediate shaft also present, so that trapping

losses in the low-speed stage (now with both gears in mesh) may contribute. The torque difference between forward and reverse direction becomes significant ($> 10\%$ of total torque) particularly at large immersion depths. In general the torque difference in Fig. 4.28 shows an increasing trend at maximum speed, whereas in Fig. 4.29b, the trend at maximum speed is decreasing and slope of the function increases in magnitude with immersion depth. In all cases, the 80 mm and 100 mm immersion depths produce torque differences which do not follow the trend set by the lower immersion depths, illustrating the nonlinear 3D effect of losses in a multiphase turbulent flow bounded by complex geometry.

(a) Torque $T(\omega)$ (b) Torque difference Fwd−Rev

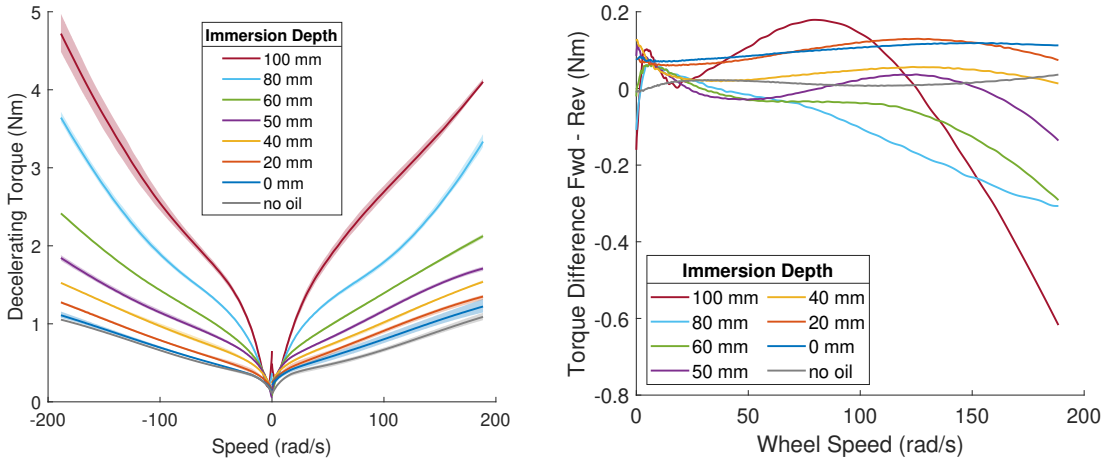


Figure 4.29: Decelerating torques measured with LS wheel gear, intermediate shaft, and lubrication system (unpowered) present in the gearbox (a). The difference between the forward and reverse cases is shown in (b).

4.2.1.2 Excess torque metric

There are several likely contributors to the net decelerating torque measured using the inertia rundown method:

- Viscous and inertial forces imparted by oil (churning)
- Viscous and inertial forces imparted by air (windage)
- EHD traction in gears
- EHD traction in bearings
- Seal friction
- Parasitic losses outside the gearbox (e.g. driveshaft bearing losses, coupling losses)

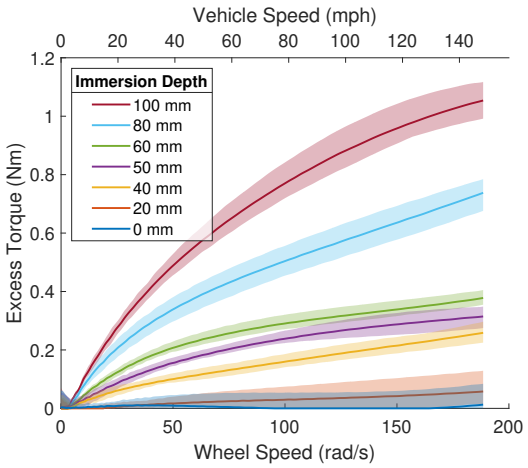
Changing the oil fill is not expected to significantly influence EHD traction, seal friction or parasitic losses (assuming that even at zero fill the surfaces are sufficiently wetted with oil for the contacts not to starve). However, churning losses are, by definition, considerably affected by the volume and depth of oil present. Churning and windage are inherently coupled - both are flow-field phenomena, and changing the oil fill level alters the total volume fraction of oil and air in the gearbox. In particular, at high speeds where oil and air become well-mixed with the oil forming a mist, the distinction between churning and windage dissolves. Considering these fluid losses together therefore, the net effect of oil immersion on fluid losses is found by subtracting the decelerating torque in the case where no oil is present, from each of the other cases in turn. This difference, whose magnitude is considered to isolate the effect of the fluid losses, is termed 'excess torque', given by

$$T_{\text{excess}}(\omega) = T(\omega) - T_{\text{no oil}}(\omega) \tag{4.15}$$

The excess torque is shown vs speed for several immersion depths in the case where the lubrication system is present but unpowered in Fig. 4.30, for the low-speed shaft in Fig. 4.30a and for the case where the intermediate shaft is also present in Fig. 4.30b.

In both cases in Fig. 4.30 there is a sudden increase in the sensitivity of excess torque to immersion depth between 60 mm and 80 mm. The case with the intermediary shaft shows

(a) LS wheel gear



(b) LS wheel gear with intermediary shaft

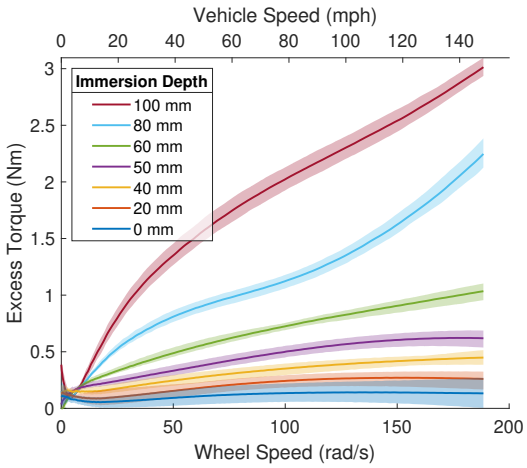


Figure 4.30: Excess torques measured with lubrication system (unpowered) present in the gearbox in the case where only the LS wheel gear is present (a), and adding the intermediary shaft (b).

a clear inflection point for the larger immersion depths, perhaps caused by a change in oil surface profile, e.g. a laminar-turbulent transition, or an oil wake starting to impinge on the high-speed wheel gear.

4.2.1.3 Effect of powering oil pump

The oil pump pinion was then added to the gearbox, and the tests were repeated with and without the intermediate stage. The tests with the pump driven were only conducted in the forward direction, as shown for the case where only the LS wheel gear is present in Fig. 4.31.

With both the LS wheel gear and the intermediary shaft, decelerating torques are shown with and without the pump pinion in Fig. 4.32. It can be seen that the no-oil torque increases significantly when the pump is powered, even when it is only pumping air, possibly due to viscous losses in oil films in the various internal journaled interfaces. At larger immersion depth when the intermediate shaft is present however, the pump decreases the excess torque by reducing the effective immersion depth of the gears, and so 'pays for itself' in terms of churning power loss.

Figure 4.33 shows the difference in excess torque between the pump powered and pump-unpowered cases. For the cases where the torque difference in Fig. 4.33b is negative, the addition of the pump causes a net decrease in excess torque in this configuration. Note that in this configuration, the high-speed stage jet, which points at the high-speed mesh, impinges

(a) Speed transients $\omega(t)$ (b) Excess torque $T_{\text{excess}}(\omega)$

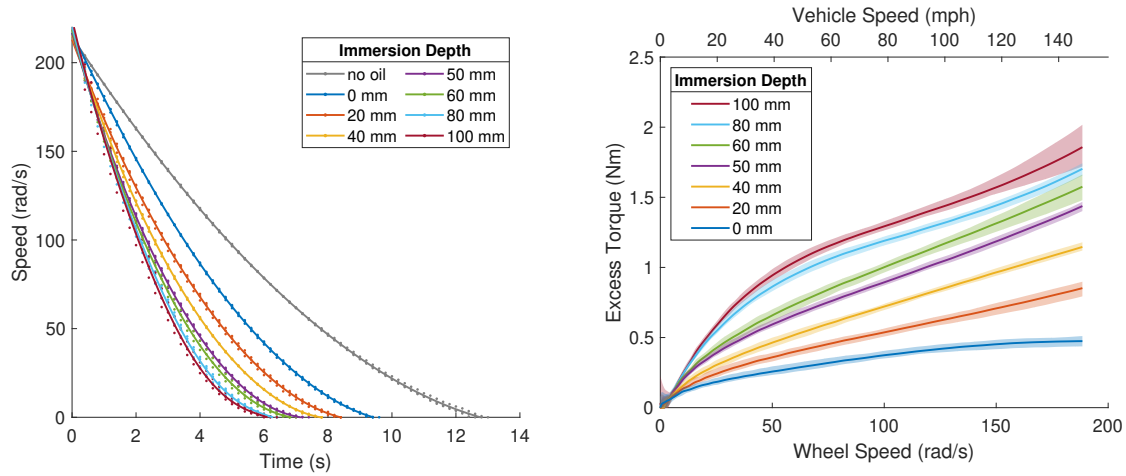


Figure 4.31: Speed transients (a) and excess torque (b) with the oil pump powered and the LS wheel gear present

(a) Pump unpowered (b) Pump powered

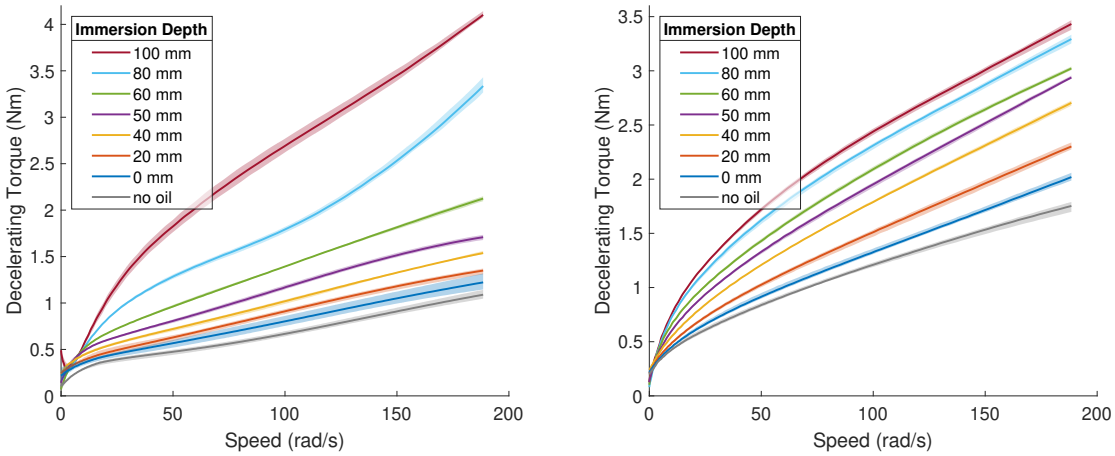


Figure 4.32: Decelerating torque for the LS wheel gear and intermediate shaft, without (a) and with (b) the oil pump pinion installed.

(a) LS shaft only (b) LS shaft with intermediary shaft

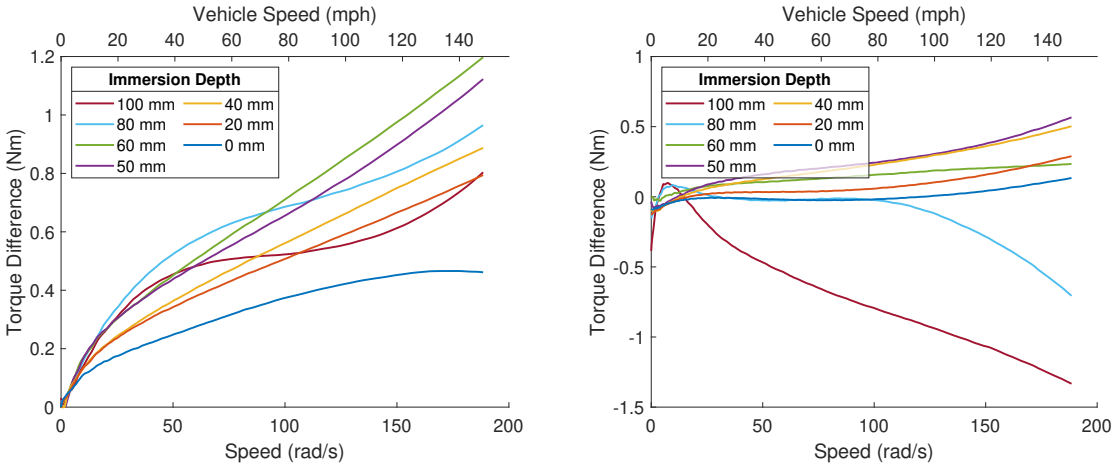


Figure 4.33: Difference in excess torque between pump powered and pump unpowered cases ($T_{\text{powered}} - T_{\text{unpowered}}$), for (a) the LS wheel gear only, and (b) the LS wheel gear and the intermediary shaft.

only on the high-speed wheel gear. The absence of the high-speed pinion gear means there are no trapping losses from the jet, and so the jet is deflected differently and the torque imparted by fluid impulse is likely to also be affected.

4.2.1.4 Churning torque and power of fully assembled transmission

The overspeeding happened during the first fully-assembled test on the original gearbox, rendering the rotor unusable. The 'fully assembled' results take advantage of the new gearbox

having not been disassembled, by performing the speed transient using the original fluid, and then draining the original fluid and conducting the necessary 'zero-fill transient'. The original fluid was then flushed out with a Dexron-VI ATF. After the Dexron-VI tests had been conducted, the fluid was drained and its viscosity was remeasured. There was no significant change in the viscosity measurements, indicating the effect on fluid viscosity of contamination with the original fluid was negligible. It should be noted that, although the effect on the results is not expected to be significant, the aforementioned difference in high-speed stage spiral angle applies in this section, and also that these results were obtained with the original stator still installed - the aluminium stator was fitted subsequently after disassembly.

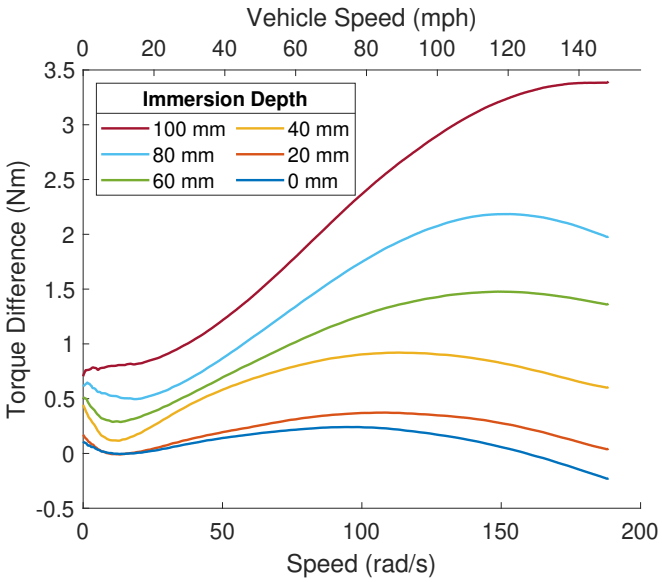
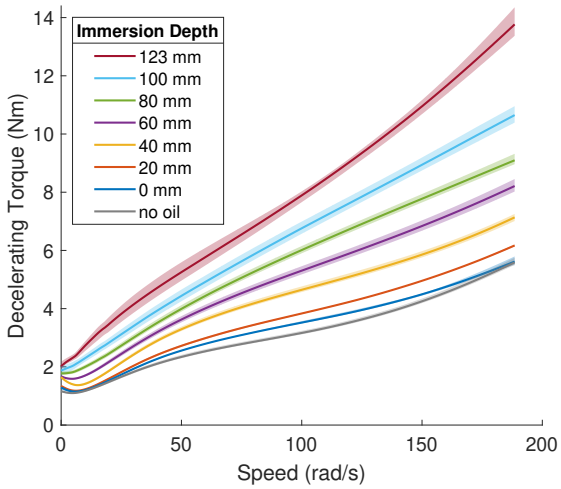


Figure 4.34: Difference between excess torques with and without HS shaft (pump powered).

Figure 4.34 compares the excess torques with and without the high-speed shaft (pinion and rotor). This is therefore a comparison of measurements from two different gearboxes and so should be treated with some caution. The excess torques at high speeds and low immersion depths should remain similar between the two cases, which is largely the case as the difference remains small across the whole speed range. The slight negative slope at the highest speeds, and the negative value of the comparison at 0 mm immersion is surprising, and perhaps arises from a geometrical difference between the gearboxes (e.g. the effect of high-speed wheel spiral angle on windage). This could equally however be a physical effect that would reproduce with the same gearbox, such as the interaction between the rotor and stator delaying the reflow of oil to the sump and so reducing effective immersion depth (while also incurring viscous losses

in the small flux gap). An increased no-oil torque as a result of fluid heating or starvation in the gear contacts at the highest speeds in the presence of the rotor is also a possible cause of this negative slope.

(a) Torque $T(\omega)$



(b) Excess torque

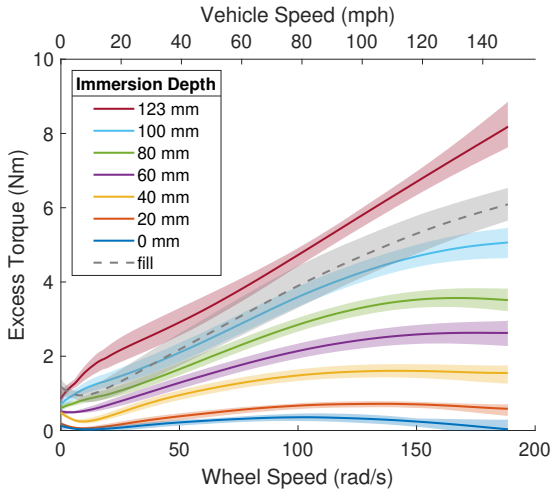
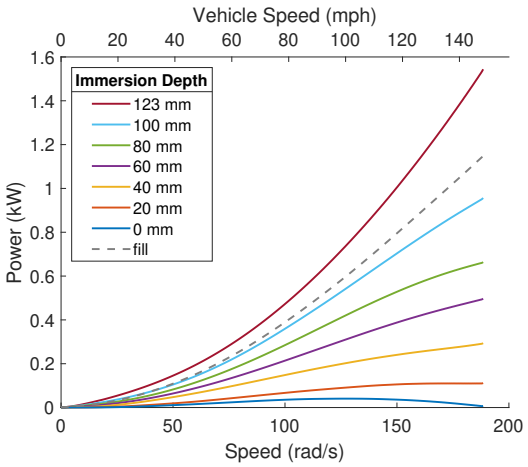


Figure 4.35: Decelerating torque (a) and excess torque (b) for fully assembled configuration.

The churning torques incurred by the fully assembled system both for the original fluid fill and for the slightly higher-viscosity Dexron-VI ATF, are plotted in Fig. 4.35. The power dissipated by the excess torque, i.e. purely due to oil churning in the gearbox (Fig. 4.36a), is of the order 350 W at motorway driving speeds (approximately tripling for the 155 mph maximum

(a) Power lost to oil churning



(b) Fraction of estimated driving power

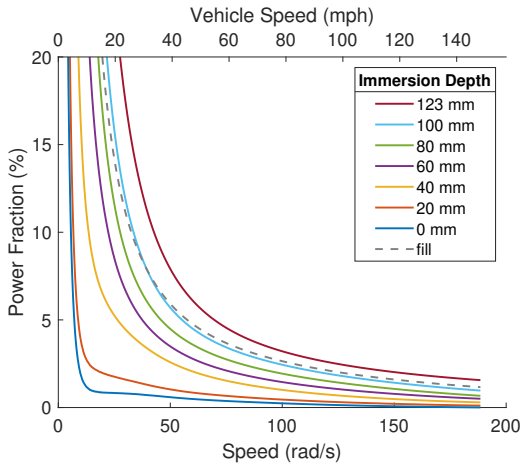


Figure 4.36: Churning power (a) and churning power as a fraction of estimated tractive power (b) vs speed showing output shaft rotational speed on lower abcissa and linear driving speed on upper abcissa, for the fully assembled gearbox

speed). The total power required to drive at 70 mph on flat ground, assuming a coefficient of rolling resistance of 0.006, is of the order 10 kW for a Tesla Model S (see Section 4.1.2 on page 81). Assuming the churning losses incurred by front and rear drive units to be similar (both are connected to the wheels whether or not they supply traction force, so total churning power 700 W), churning loss amounts to 7% of the output power of the car during motorway driving. (The rear drive unit has a larger gear ratio of 9.734, so its motor spins slightly faster, but it has a lower oil fill volume and different casing geometry, so expecting churning torques of the same order is rather approximate.) The fraction of total driving power estimated using Eq. (4.1) on page 81 incurred by excess torques measured for the front drive unit only is shown in Fig. 4.36b. A significant implication here is that churning torques become a less significant fraction as driving speed increases, with the relationship resembling a rectangular hyperbola for each immersion depth. This is because the churning torque measured appears to have linear or weaker-than-linear dependence on speed, whereas the aerodynamic drag term in the traction force estimate is quadratic with speed.

The wet-motor design of the EDU is worthy of note, particularly given that the stator clearance (and stator surface profile) of the aluminium stator were not perfect replicas of the original. Oil sprayed into the flux gap likely underwent couette-like cylindrical shearing which contributed significantly to churning losses (the addition of the high-speed shaft approximately doubled the churning torque, and a significant portion of this increase is likely attributable to fluid interaction with the rotor, whose outer diameter is more than double that of the high speed pinion to which it is attached). Assuming that the gap is completely filled with a Newtonian fluid whose radial velocity profile is well-approximated by a laminar Couette shear layer, and the rotor is a cylinder of length $L = 120$ mm and radius $R_1 = 65$ mm rotating concentrically with angular velocity ω inside the stator of radius $R_2 = 68$ mm, (considering the equivalent case of a concentric cylinder viscometer and applying the small gap approximation) we have

$$T = \frac{4\pi\mu L\omega R_1^2 R_2^2}{R_2^2 - R_1^2} \approx \frac{2\pi\mu L\omega R_1^2 R_2}{R_2 - R_1} \tag{4.16}$$

which assuming dynamic viscosity μ is of the order 20 mPa.s, produces a torque referred around the low speed stage in excess of 20 Nm at the highest speeds, considerably greater than any of the churning torques measured in Chapters 4 and 5. This discrepancy is perhaps

attributable to the gap not in fact being filled with oil as it is only supplied at a single point at either end, and oil is presumably rapidly expelled by centripetal pressure. Moreover, if the gap were filled with oil of density (830 kg/m^3) and heat capacity (2.0 kJ/kg K) typical of a Dex-VI ATF, and the oil were somehow retained in the gap, the viscous power dissipation would cause an adiabatic oil temperature rise approaching 10°C per second, indicating the local viscosity of the oil would be significantly lowered during any appreciable time spent in the gap. Nevertheless, the rotor likely contributes significantly to the churning torque increase seen by adding the high-speed shaft.

4.2.2 Oil Viscosity

The gearbox was dissassembled and instrumented with thermocouples and heaters as shown in Fig. 4.19 on page 100 and Fig. F.3 on page 302. The bearings were replaced with sealed bearings (internally grease-lubricated), which have the advantage that their losses are not influenced by the surrounding oil (except thermally). The transmission was then temperature-controlled to a series of temperatures between 40°C and 110 °C, producing oil viscosities in the range 4 mPa.s - 20 mPa.s for a model ATF with fully synthetic base oil (5.4 cSt at 100°C), and viscosities in the range 20 mPa.s - 180 mPa.s for the same ATF additives blended with a higher-viscosity base oil (23 cSt at 100°C).

Two immersion depths were tested for each temperature, the full-fill (2 l), and half-fill (1 l) as well as the necessary no-oil case to enable the calculation of excess torque. Churning torques sampled at 4 different speeds are plotted with respect to the corresponding oil viscosity at the sump temperature measured during the transient, at full fill, in Fig. 4.37.

The scatter in the data shown in Fig. 4.37 is considerable at the higher speeds. At each nominal temperature, 3 repeats were conducted, and are each shown separately - for the high-viscosity fluid there is a drift in the reported viscosity between the repeats as a result of viscous heating between transients as the gearbox was accelerated to a steady speed. There is also some overlap between the viscosity achieved by the low-viscosity fluid at the lowest temperature, and that of the high-viscosity fluid at the highest temperature - the excess torque measurements in these two cases (compare the filled to the unfilled markers) do not agree well at high speeds. At low viscosities (high temperature with low-viscosity fluid), the scatter

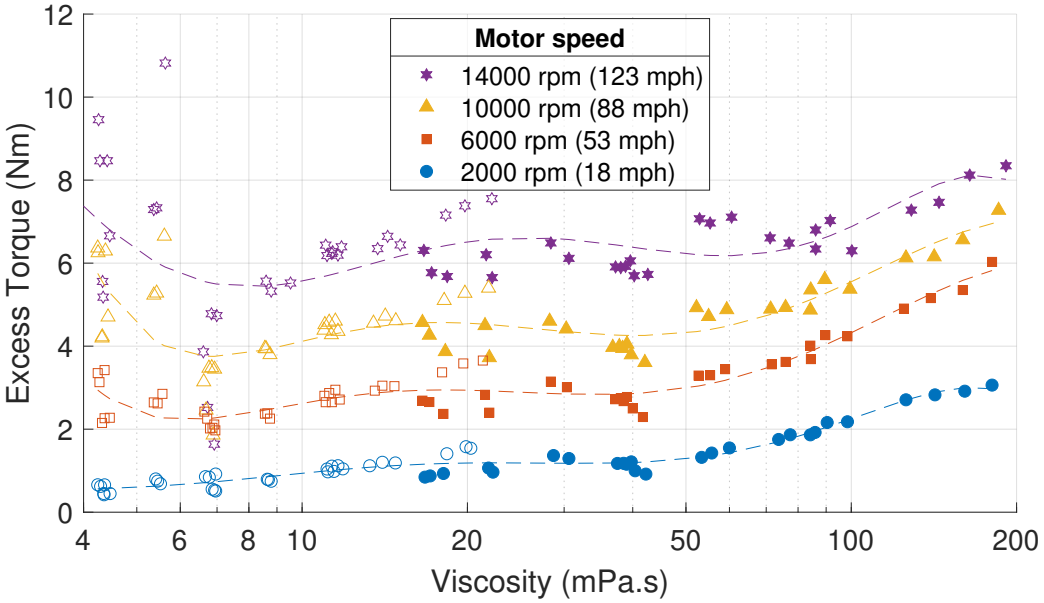


Figure 4.37: Viscosity effect on churning torque at 4 speeds, using 5.4 cSt ATF for viscosities at and below 20 mPa.s (empty markers), and 23 cSt ATF for viscosities at and above 20 mPa.s (filled markers), with 2 l fill volume.

in the data at high speeds completely obscures the measurement. It is possible that this is caused by thermal differences in lubrication condition of the bearings between the full-fill, half-fill and no-oil cases (the bearings are sealed and grease-lubricated and so are not well

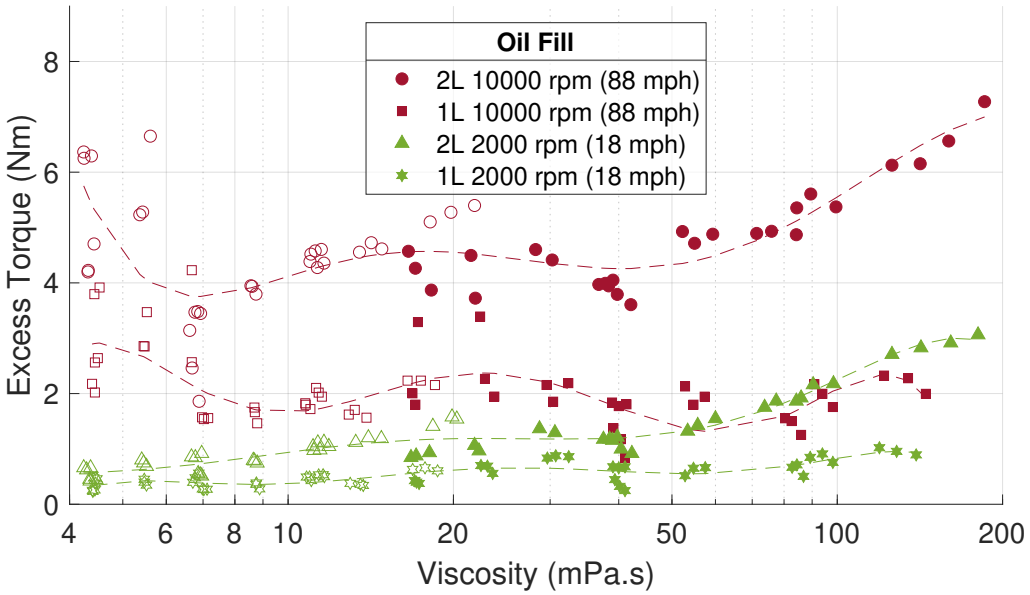


Figure 4.38: Viscosity effect on churning torque at 2 immersion depths and 2 speeds, using 5.4 cSt ATF for viscosities at and below 20 mPa.s (empty markers), and 23 cSt ATF for viscosities at and above 20 mPa.s (filled markers).

cooled during or between transients) at the extremes of temperature. Nevertheless, there are clear trends, particularly in the viscosity range in which many existing EV drive units usually operate (between 10 and 20 cSt, for a current Dexron-VI ATF in the range 40°C−60°C), for which churning loss does indeed appear to increase with increasing viscosity. The scatter at speeds more typical of driving below legal speed limits for this drive unit is less pronounced, and it appears that in the region between 20 and 50 cSt, churning loss hardly changes with oil viscosity.

The results in Fig. 4.38 show that the effect of immersion depth, and that of speed, are both far stronger than that of viscosity, over the whole viscosity range considered here.

4.2.2.1 Temperature Transience During Rundown

It should be noted that the seal torque from the sealed bearings leads to high no-oil torques, and hence large heat dissipation at high speeds. The no-oil torques in this case exceed the net excess torque (the no-oil torque at zero speed is above 1.5 Nm at all temperatures, and is always greater than 8 Nm at the highest speed). The considerable heat dissipated leads to significant temperature rise in the run-up to, and during the transients, particularly for the bearings supporting the high-speed shaft. Temperatures measured by the 7 thermocouples for three successive speed transients, at a nominal temperature of 60°C with both the 5.4 cSt fluid and the 23 cSt fluid are shown in Fig. 4.39. A key feature of these tests, illustrated in Fig. 4.39, is that temperature control of the gearbox was more challenging with the HV fluid than with the LV fluid due to the higher viscous heat generation and lower thermal diffusivity of the flow, causing temperatures to be less uniform throughout the gearbox. The oil in the sump may be considered to remain the same temperature during the rundown to within ± 2°C in all cases for the 60°C control temperature.

The temperature near the encoder on the HS shaft (i.e. next to the larger of the HS shaft bearings) increases considerably during the rundown (> 10°C) however, and the magnitude of the increase is augmented by the more viscous oil and by lower fill volume, both of which reduce heat removal from this bearing by the oil. This temperature rise is a significant limitation of these tests because it is likely to change the bearing torques on the HS shaft between the no oil and filled cases, distorting the excess torque obtained by inertia rundown. One solution to this would be to return to using unsealed bearings which are likely to cool faster, and to

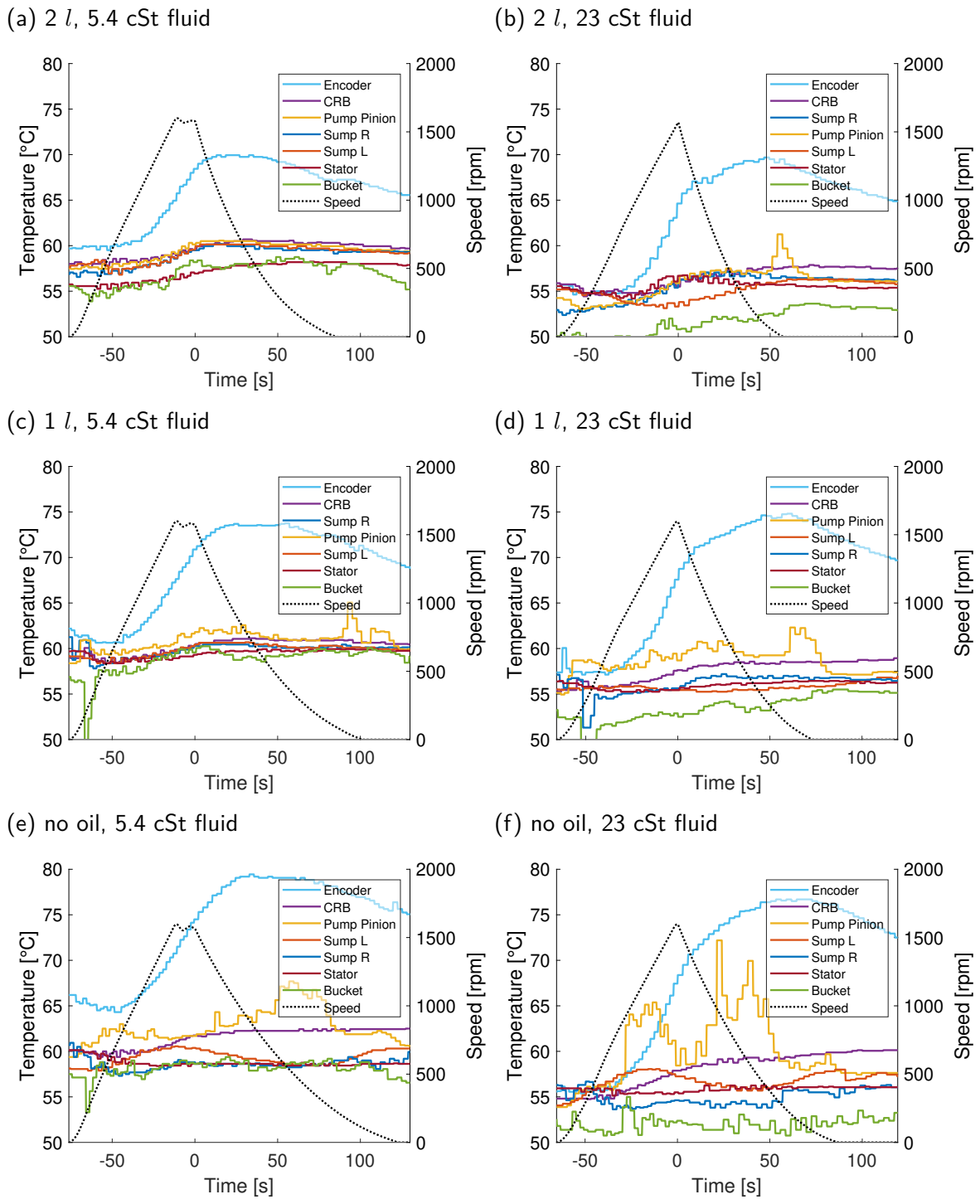


Figure 4.39: Temperatures measured at 7 points in the gearbox before, during and after speed transients conducted immediately after temperature stabilisation to a nominal control temperature of 60°C, for three oil volumes, and for two fluids, the 5.4 cSt ATF (left column, a, c, e) and the 23 cSt ATF (right column, b, d, f).

generate less heat due to the absence of seal friction and grease churning. The excess torque measurement would then also capture the contribution of bearing drag.

4.2.3 Steady-state vs Transient Conditions

It is likely that churning losses, which are often measured using inertia rundown, may be affected by speed transience as a result of flow inertia and time-dependent changes to effective immersion depth due to oil reflow to the sump. The inertia rundown measurement involves a speed transient whose deceleration is not controlled and therefore the effect of the transience is challenging to evaluate by this method. Shore [56] found for a single gear that several transients under equivalent conditions, but starting at different speeds, produced similar torque characteristics after the first few seconds of each had elapsed.

An effort was therefore made to instead measure churning torque under steady-state conditions and compare the results to those obtained by inertia rundown. This was done with the 23 cSt ATF, at 80°C, and with the sealed bearings, creating near-worst-case conditions in terms of drift in bearing friction between rundowns, and during the steady-state test, due to internal heat generation and slower cooling.

The LS shaft speed was increased in increments between 40 rpm and 2000 rpm, and held at each increment for 20 s, during which torque was recorded as the speed controller worked to achieve and then stabilise the speed, as shown in Fig. 4.40a. The tuning of the speed controller posed considerable challenge (compare the transients here to those in Fig. 4.26a on page 108) on account of the large driven inertia and considerable nonlinearity in the torque-speed characteristic of the load due to fluid flow effects. For this test a balance was found between rise time and overshoot to achieve sufficiently stable torques within 20 s. The speed was increased in large increments, and then gradually reduced in smaller increments. Measurements of torque and sump temperature were averaged over a time-window spanning 2 s, ending 1 s before the 20 s had elapsed. The results are shown vs speed in Fig. 4.40b, where the sparsely-spaced points are the speed-increasing portion, and the densely-spaced points the subsequent speed-decreasing portion. The apparent hysteresis in the torques measured may be attributed to the thermal response of the bearings during the test, whose temperature rise is not well-represented by the sump temperature measurement, particularly in the no-oil

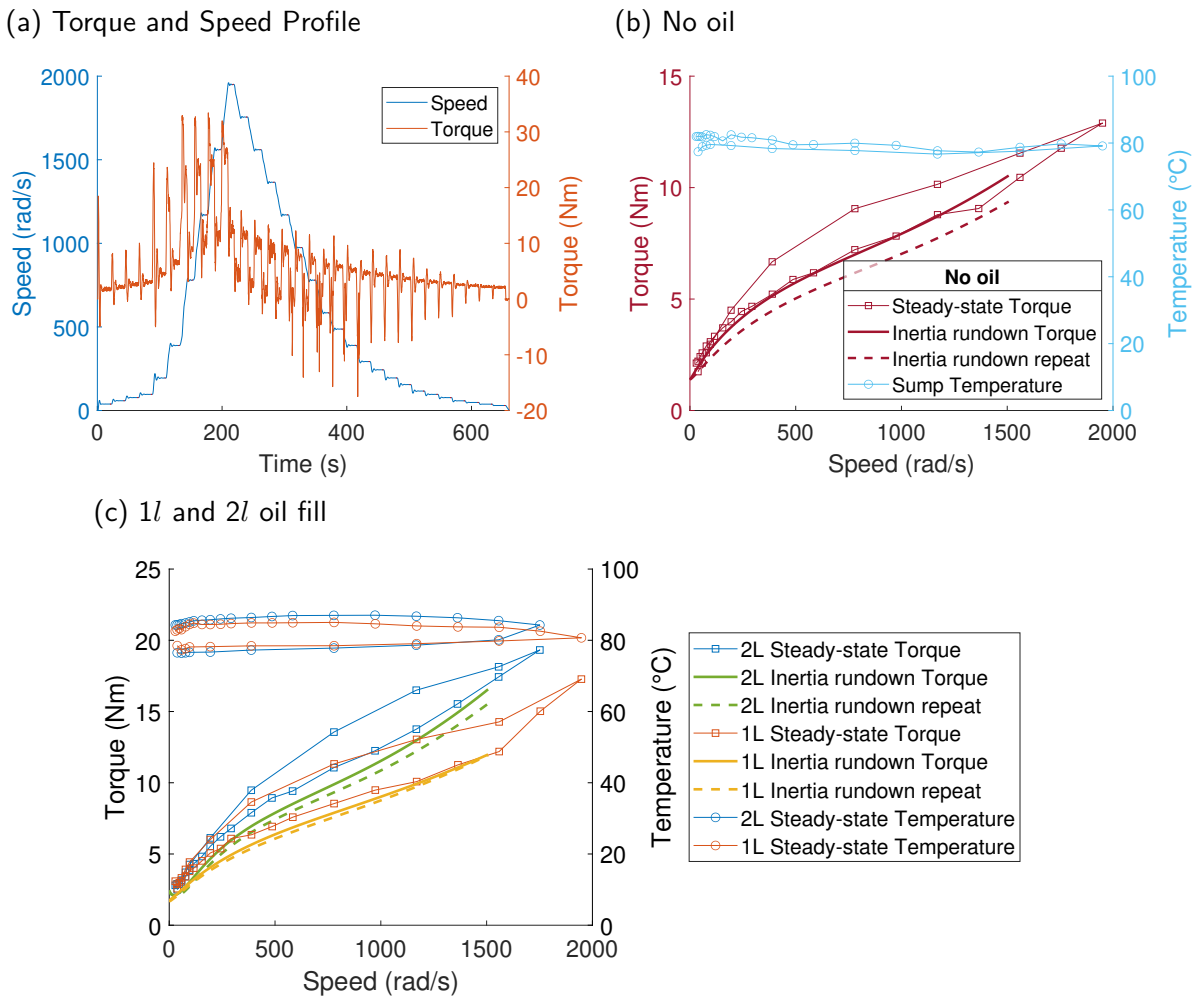


Figure 4.40: Torque and speed vs time during steady-state test with no oil in the gearbox (a), stable torques and temperatures taken from readings averaged over period of 2 s ending 1 s before the speed change during which torque is stable, with comparison of measurements from inertia rundown (b), and total torque measurements at two immersion depths from both steady-state and inertia rundown conditions (c), using the 23 cSt ATF at 80°C.

case here. Nevertheless, considering the speed-decreasing case, which matches the thermal conditions created by inertia rundown most closely, when there is no oil in the gearbox, the steady-state measurements match the results of inertia rundown quite closely.

Torque measurements in the case of a 1 l and 2 l fill are shown in Fig. 4.40c, along with total torques from inertia rundown with the same fluid at the same temperature (note that these are not excess torques, the no-oil torque has not been subtracted and this is therefore not in itself a churning loss measurement, rather it is being used for comparison of steady-state and inertia rundown measurements). The agreement is considerably less close than in the no-oil case. There are three possible explanations for this discrepancy:

1. Fluid flow transience causes significantly different churning torques to be imparted at any given speed when the gearbox is decelerating compared to when it is running at a constant speed.
2. A flaw exists in the calibration of one of the methods of torque measurement (e.g. the effective inertia of the system increases as a result of the inertia of the entrained oil vortices around the gears) such that they do not compare well.
3. Thermal transience, which affects the temperature profiles in the EHL contacts throughout the gearbox, invalidates the assumption that oil-fill-invariant losses (particularly bearing losses in sealed bearings) are unchanged between the filled and no-oil cases.

The considerable noise and hysteresis in the steady-state data, and poor repeatability of the inertia rundown data in Fig. 4.40c suggest that thermal transience is the principal contributing factor. Points 1. and 2. above are worthy of investigation but their contribution in the data presented here is likely obscured by that of point 3. for this oil and under these conditions, for which the thermal response, also influenced by oil volume, is quite strong.

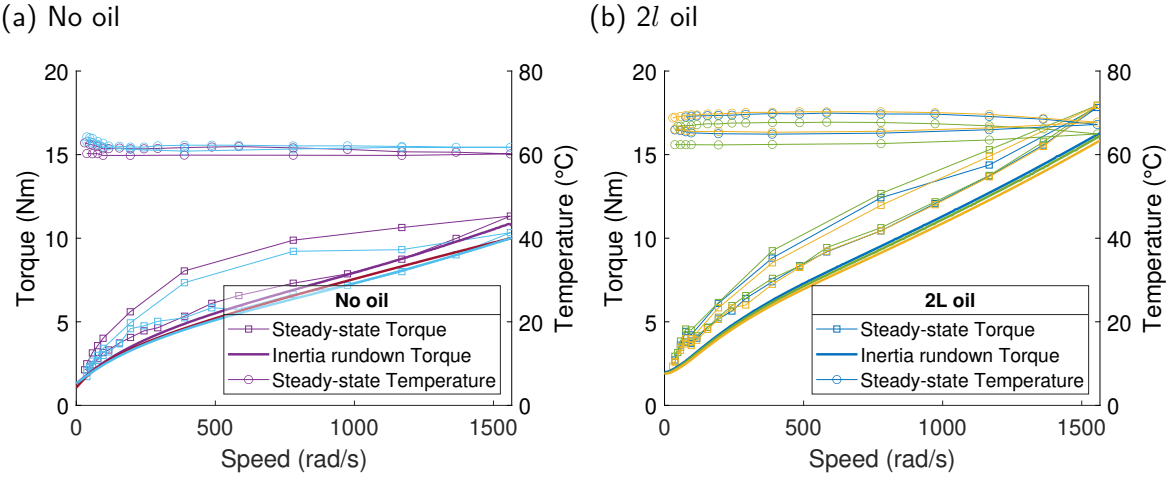


Figure 4.41: Comparison of steady-state motor torque measurement to inertia rundown measurements using the 5.4 cSt ATF at 65°C with (a) no oil in the gearbox and (b) 2l oil fill for three repeats (only 2 steady-state repeats are shown in (a)).

The comparison was repeated under more thermally favourable conditions by reducing the maximum speed to 1600 rpm and changing the oil to the 5.4 cSt ATF. Under these conditions, it can be seen in Fig. 4.41 that the inertia rundown measurements are more repeatable, and in the no-oil case (Fig. 4.41a) agree well with the steady-state measurements under similar

conditions (the portion of the steady-state test with the speed descending from the maximum, i.e. that with more densely spaced markers). When oil is present however (Fig. 4.41b), the inertia rundown measurements are once again lower than those in the steady-state. The systematic nature of this discrepancy, and its almost vanishing at low speeds, suggests an effect of flow transience. In this gearbox, where the flow path of the oil out of the sump and through the motor is long, a decelerating transient would cause a larger volume of oil to be absent from the sump at any given speed than under steady-state conditions, as a result of higher pump volume flowrates at the higher rotational speeds immediately preceding the speed in question (a similar argument also applies to reflow in a splash-lubricated system over shorter flow timescales). This would cause the inertia rundown torques to be lower than the steady-state torques as a result of a reduction in effective immersion depth by speed transience. The discrepancy might reasonably be expected to vanish when there is no oil in the gearbox - the results shown in Figs. 4.40b and 4.41 are consistent with this expectation.

Further work using unsealed bearings, enabling significantly shorter thermal response times and more closely isothermal conditions throughout the gearbox, is required to address the issue of speed transience however. A more detailed consideration of the influence in these tests of the mechanically-powered pump, and the wet-motor architecture, on both churning torques and the influence of speed transience on their measurement, would be relevant in informing design choices in future EV drive units.

4.3 Summary

A test rig has been designed, developed and built around an existing EV gearbox. The rig has been used to measure load-independent loss torques arising from oil churning. The relative effects of gearbox speed, immersion depth, and oil viscosity have been investigated and quantified under conditions representative of those for which this gearbox is designed, and also at considerably lower immersion depths and higher viscosities.

It is found that the effect of speed and immersion depth on churning losses are considerably stronger than the effect of oil viscosity within their realistic ranges in this EV gearbox. For the viscosities tested, churning losses are found to increase monotonically with speed and immersion depth, but to vary in a nonmonotonic fashion with viscosity at high speeds. The

use of sealed bearings, in an attempt to eliminate the effect of bearing drag losses on the churning torque measurement, resulted in thermal conditions within the bearings at high speed which adversely affected the precision of the measurement and led to discrepancies between the results obtained by inertia rundown, and those obtained in the steady state. Further work is required to decouple the effects of thermal transience and flow transience during inertia rundown, and to compare with steady-state results for which the bearings operate at constant temperature.

Chapter 5

Measurements of Total Drivetrain Efficiency in an EV Drive Unit

The T-Axle Electric Vehicle Dynamometer (EV Dyno) rig at the Valvoline Ashland Laboratory was used to measure the no-load losses, as well as the total losses and hence the mechanical efficiency, of a 2016 Tesla Model S EV rear drive unit (the *front* drive unit from the same car was used in Chapter 4). The test was conducted using two gear oils of differing viscosities, with the same drive unit, enabling the effect of the viscosity change on both no-load and load-dependent losses to be examined. The rig was also used to run the drive unit through the NEDC drive cycle and to measure drive unit efficiency and temperatures throughout. This work was completed during an eventful 8-week visit to the Valvoline Engine Lab in Ashland, KY, USA, during which the rig was commissioned, and adapted to perform the reported tests.

5.1 T-Axle EV Dyno Rig Overview

The T-axle rig comprises an EV drive unit connected to a pair of dynamometers - one on each driveshaft axle, as shown in Fig. 5.1. The drive unit is powered by 400 V DC via a battery simulator and controlled via CAN. The maximum continuous mechanical power the rig can circulate is ~ 500 kW. The dynamometers (dynos) are themselves 6-pole 3-phase AC asynchronous induction machines, each powered by a dedicated inverter drive, and rated to 250 kW, with a maximum speed of 2700 rpm. The rig receives power from the grid via a series of 3-phase transformers and filters, but is grounded separately by dedicated grounding rods.

The inverter drives, battery simulator and 3-phase power supply are manufactured by Unico Systems, and controlled via a common EtherCAT loop. The dynos are each connected to the driveshaft via a contactless torque transducer manufactured by Honeywell, rated to 10 kNm and nominally accurate to $\pm 0.05\%$ of full-scale, or ± 5 Nm. The torque signal is modulated over a 13 MHz RF carrier on a rotating aerial, and received by a stationary aerial in close

proximity. Each dyno also carries an optical incremental encoder which is connected directly to the inverter drive, enabling speed control. Torque was measured using the analog output of the Honeywell torque transducer signal conditioners, which were connected to two analog input channels on the relevant CompactRIO. These were very susceptible to noise, in the form of GHz second-order decay transients induced at twice the IGBT switching frequency (3.5 kHz) of the inverter drives when they were powered. Extensive efforts to isolate, ground and shield the appropriate components reduced the amplitude of these transients from $\approx \pm 30$ V to $\approx \pm 1$ V, but this is still a significant proportion of the ± 10 V range of the ADC. The ADC was sampled at 100 Hz, so the aliases of the noise presented as infrequent, instantaneous deviations in the measurement which were removed by a 5th order Butterworth filter and subsequent disturbance rejection algorithm in the post-processing phase, enabling a measurement precision an order of magnitude better than this nominal accuracy, as demonstrated in Section 5.2. Nominal specification data are tabulated in Table 5.1.

The central control system for the rig is located in a separate control room and comprises a series of data acquisition modules housed in several CompactRIO units from National Instruments. These communicate with an NI PXIe unit which in turn is controlled via ethernet by a PC running Veristand DyneEdge, which provides a UI for the relevant NI APIs, and enables

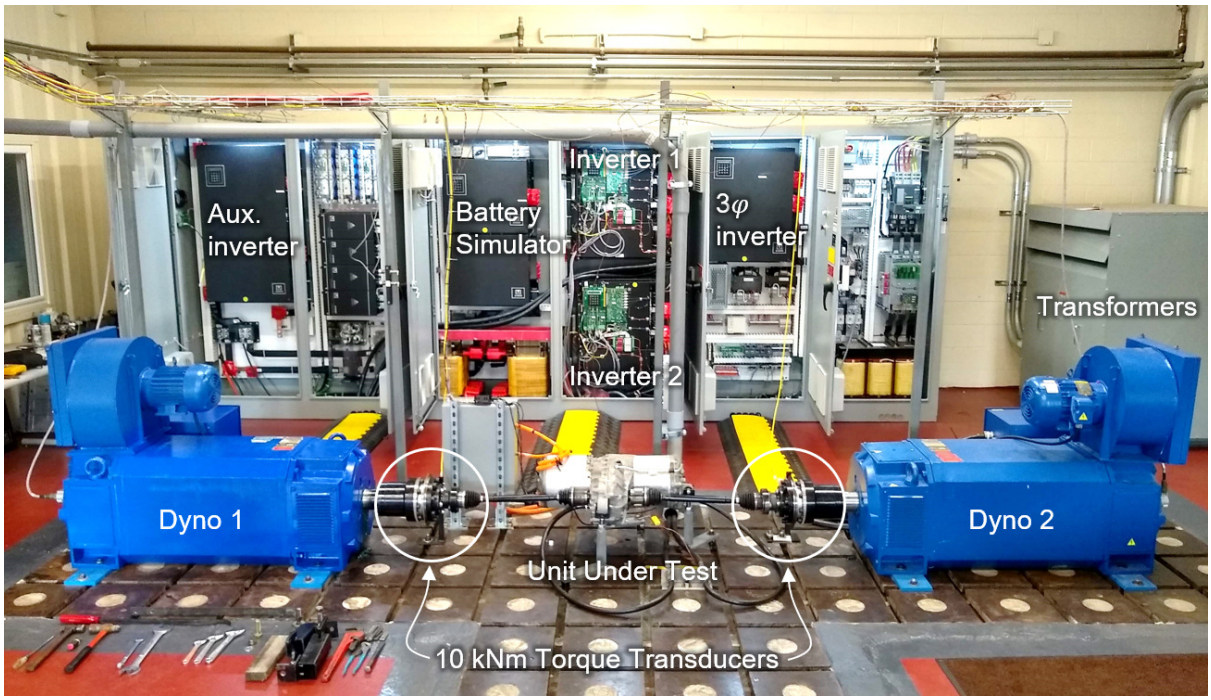


Figure 5.1: UUT, dynos and power electronics of EV T-axle rig

Table 5.1: Available instrumentation and motor specification data for T-Axle Dyno Rig

Dynos	Max. Speed	2700	rpm
	Max. Current	630	A
	Max. Voltage	322	V
	Poles	6	
	Rated Power	250	kW
Torque Transducers	Max. Torque	± 10	kNm
	Accuracy	± 5	Nm
	Manufacturer	Honeywell	
	Model	TMS 9250	
Unit Under Test	Manufacturer	Tesla	
	Max. Motor Power	375	kW [223]
	Max. Motor Torque	600	Nm [223]
	Gear Ratio	9.734	
	Part Number	1025598-00-H	Sport

system configuration and interface customisation. Data acquisition rates upwards of 100 Hz are possible across all channels, which include thermocouple amplifiers, digital and analog IO, CAN and EtherCAT comms.

The drive was cooled using building process water at a temperature ranging from $21 - 24\,^{\circ}\mathrm{C}$ (fluctuating throughout the working day). The flowrate of the water was likely higher than that of the coolant the drive receives from the car, and as a result, the cooling rates for these tests were likely higher than those that would be seen under normal driving conditions. No further attempt at temperature control was made, but sustained stator temperatures above 80°C were avoided in the interests of the health of the drive.

5.2 Drive Loss: No-Load

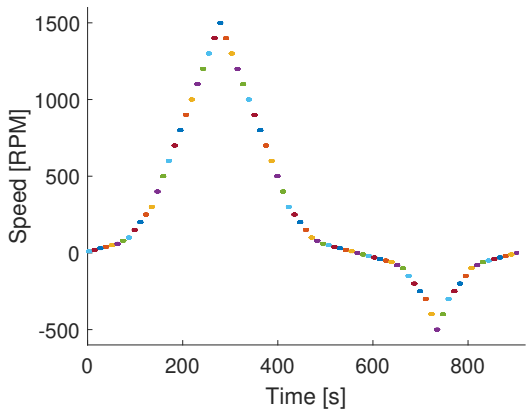
The unit under test was the rear drive unit from a Tesla Model S 2016 (whereas the front drive unit from the same model was used in Chapter 4). The drive was left unpowered, and was spun up using the dynos. Although the direction of the power flow through the gearbox in this case is opposite to that while the vehicle is accelerating, only the bearing and gear

traction losses are affected by this change. The effect of this on no-load-loss measurement may be assumed negligible if the small contribution from load-dependent losses is considered torque-symmetric for these very low loads. The test involved:

- Spinning both dynos in tandem to the desired speed
- Waiting for the speeds to stabilise
- Holding the speeds constant for a period of 5 seconds
- Measuring the average drive torque from each transducer during this time
- Advancing to the next speed

The speed history of the test during the periods where the torque is sampled are shown in Fig. 5.2a, and the torque history is given by Fig. 5.2b. The nature of the torque transducers and motor electrical characteristics resulted in very large torque fluctuations at low torques and speeds – the torque measurement was smoothed and averaged over a 5 second period to obtain realistic torque values. The speed-dependent fluctuation is thought to originate from a combination of dyno cogging torque and rotating-bending of the torque transducers.

(a) Speed History



(b) Torque History

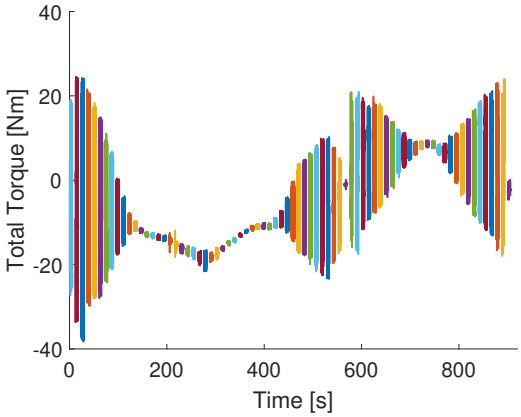
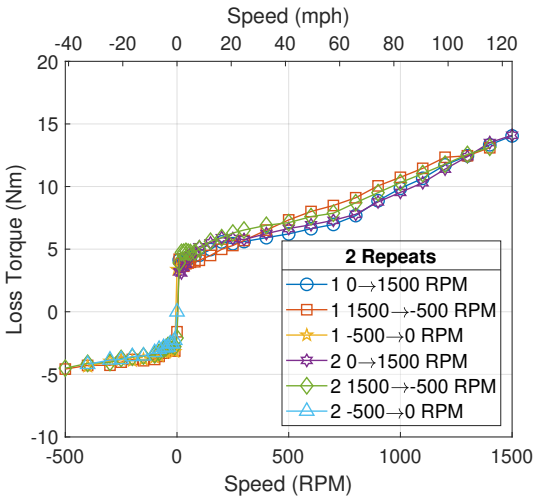


Figure 5.2: No-load loss test results - speed and torque vs. time during each sampling interval. Periodic fluctuations within this interval have been compressed in the time axis and so appear as a coloured band, the height of each representing the variation within a different sampling interval, corresponding to a single rotational speed.

The speed sequence used began from zero speed, and climbed gradually to 1500 rpm (dyno, i.e. output shaft speed), before falling to -500 rpm (negative $\Rightarrow$ reverse direction), and then climbing back to zero. This speed range was chosen to span the expected driving speed range (1500 rpm of the wheels in this vehicle corresponds to $\sim$ 120 mph, or $\sim$ 200 kph), and a

(a) Dexron-VI ATF (US)



(b) SAE 75W-140 Gear Oil

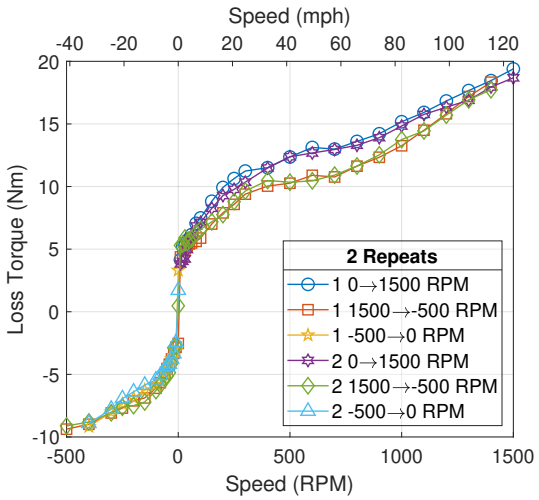


Figure 5.3: No-load loss test results - dyno torque vs speed

smaller reverse speed (up to ~ 40 mph) was chosen to enable a comparison with the forward case, highlighting the effect of the reversal of the oil pump. Two repeats were conducted, so that except at the extremes we have four measurements per speed, and the results are shown in Fig. 5.3. The results are consistent between repeats, implying the test is sufficiently short and/or mild to avoid the effects of thermal drift, but the jitter in the data close to zero speed is considerable, and can be attributed to limitations with the method for torque measurement, which, due to the transducer range, the dyno cogging torque, and the high-frequency switching noise, was difficult to interpret reliably at these torques.

The experiment was repeated with two fluids, Dexron-VI ATF (US) (Fig. 5.3a), and with the higher-viscosity SAE 75W-140 Gear Oil (Fig. 5.3b). There is clear thermal hysteresis with the higher-viscosity gear oil, but the results remain consistent between repeats. It can be seen that the no-load losses with the higher viscosity fluid (KV40 188 cSt) are considerably higher across the whole speed range than those with the lower viscosity fluid (KV40 28 cSt). The two fluids also have different additive chemistries (so are likely to produce differing boundary friction) and the difference in viscosity between them is very large, so direct comparisons should be approached cautiously. The gradient of the loss torque at low speeds is higher for the higher viscosity fluid, but levels off between 40 and 60 mph driving speed, before increasing at higher speeds. A feature of particular interest is the fact that, for the higher viscosity fluid, the loss torque is higher in the speed-increasing portion (blue squares and purple stars), and then is

reduced in the speed-decreasing portion (orange squares and green diamonds), presumably as a result of a thermal reduction in viscosity. The opposite is true of the low viscosity fluid, possibly implying a change in lubrication condition of load-bearing contacts (increasing mixed or boundary EHL friction) or perhaps a locally negative gradient in churning loss with viscosity, as observed at a similar viscosity with a similar fluid in Section 4.2.2.

5.3 Drive Efficiency

Mechanical efficiency η_m is defined in this section by

$$\eta_m = \frac{P_{\text{out}}}{P_{\text{in}}} = \frac{\omega_{\text{out}}}{\omega_{\text{in}}} \frac{T_{\text{out}}}{T_{\text{in}}} \approx \frac{1}{G} \frac{T_{\text{out}}}{T_{\text{in}}} \tag{5.1}$$

where P is a power, T is a torque, ω is an angular velocity and G is the reduction ratio defined such that $G > 1$ (for this drive, $G = 9.734$).

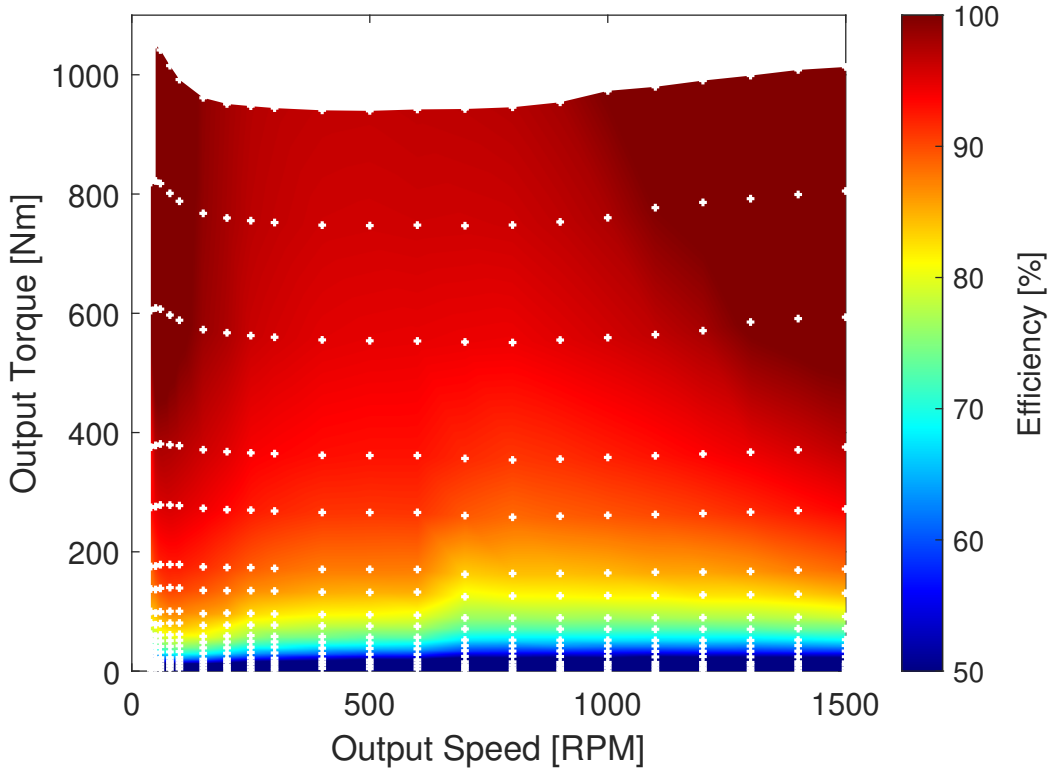
Measurement of T_{in} was achieved by polling the Tesla drive motor output torque estimate via the CAN bus, and T_{out} was found using the sum of the filtered, corrected torques from the torque transducers. We expect ω_{in} (also available from Tesla's on-board encoder via CAN) to exactly match $G\omega_{\text{out}}$ (available from the Unico inverter drives), but it is likely that the latency on the CAN bus reading exceeds that of the EtherCAT loop, so both readings for ω were multiplied by their corresponding torques at each sample time, and the results averaged over a 5-second period.

A matrix of torques and speeds was constructed, with much greater density in the low-torque and low-speed regions. The initialisation sequence of the test comprised:

1. Power up dynos and accelerate to 60 rpm (torque creep speed, ≈ 5 mph)
2. Initiate drive sequence, wait for precharge, enable torque creep mode
3. Wait for drive to report non-zero torque via CAN
4. Switch to drive torque control (closed-loop PID torque control using input torque reported via CAN to control throttle voltage) and ramp to 20 Nm
5. Ramp dynos to 1000 rpm
6. Wait for oil sump temperature to reach $25\,^{\circ}$C

The fluctuation in the reading from the torque transducers with angle of rotation presented a

(a) Driving Torque (Motoring)



(b) Regen Torque (Absorbing)

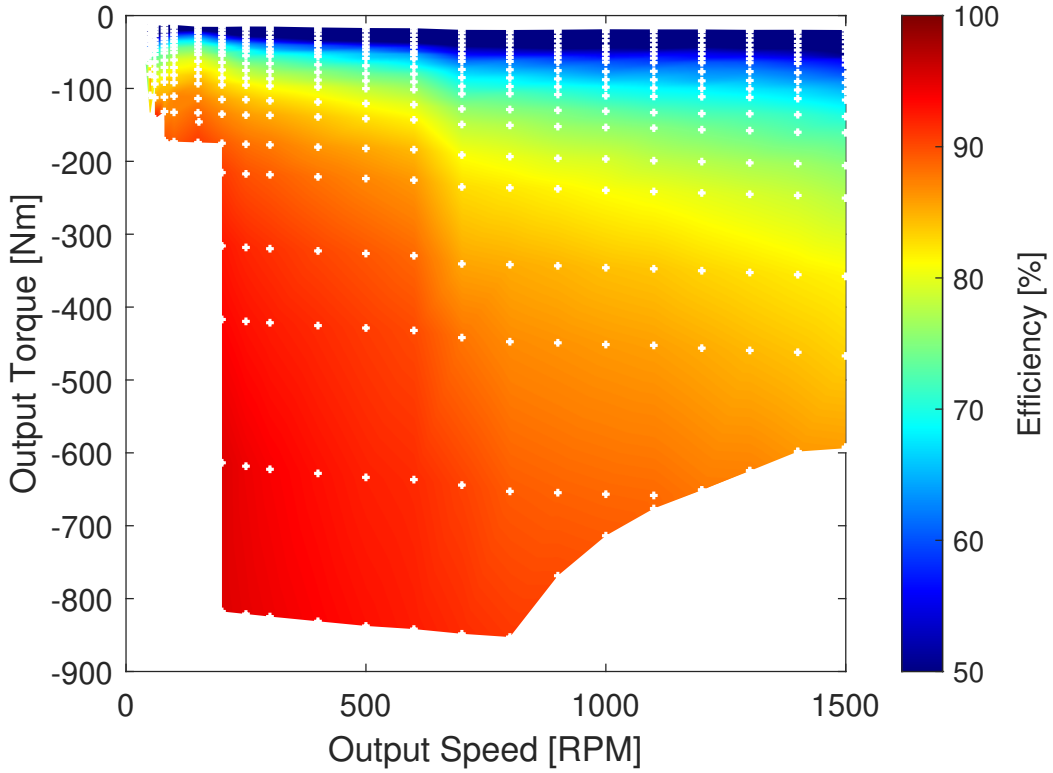


Figure 5.4: Drive unit efficiency maps for driving (a) and regenerative braking (b) with Dexron-VI ATF (US), showing measurement points as white crosses.

challenge in determining the offset value for each. This was done by sampling cogging torque for both dynos over several rotation cycles, while they were rotating, and averaging to find the 'zero-torque' reading. A condition was required where the dynos were rotating (and powered, to account for the electrical noise), but also neither sourcing nor sinking torque. This was achieved during step 2 above, using the 'torque creep' mode, which is a feature of the drive that appears to activate a speed control mode with setpoint around 5 mph, or 60 rpm of the output shaft. When the dynos were set to this speed and creep mode was enabled, the drive unit motor was seen to apply just enough torque to balance its own losses, and the dyno torque was very close to zero.

The remainder of the test sequence implemented the torque-speed matrix by speed control of the dynos and torque control of the Tesla drive (PID control with feedforward of the throttle voltage based on a comparison of the drive torque output reported via CAN and the setpoint from the matrix), as follows

- Ramp drive torque to desired torque while ramping dyno speeds to desired speed
- Wait for torque and speed to stabilise
- Measure for 5s
- Proceed to next speed
- Once finished speed sequence, proceed to next torque and repeat speed sequence

Data pertaining to the kinematic and dynamical condition of the rig was sampled at 100 Hz, and thermal and binary data such as thermocouple readings and drive controller flags were collected at 10 Hz.

The resulting effiencies were plotted in the torque-speed space using a colourmap, as shown in Fig. 5.4a. Note that not all efficiencies in this space lie below 100% (although they do not exceed 105%), and hence at very high torque we see evidence of a mismatch between the torques reported by the Tesla drive and those measured by the torque transducers. While 5% is a realistic error to expect of the torque estimated by an inverter drive, particularly that in a production vehicle, this reveals an inherent limitation with using this metric for input torque. It is emphasised here that no extrapolation from measurements has been made - the colour axis of the efficiency maps is strictly interpolated from measurements taken at the torques and speeds shown in Figs. 5.4a and 5.4b. The dependence of this error on torque or speed is

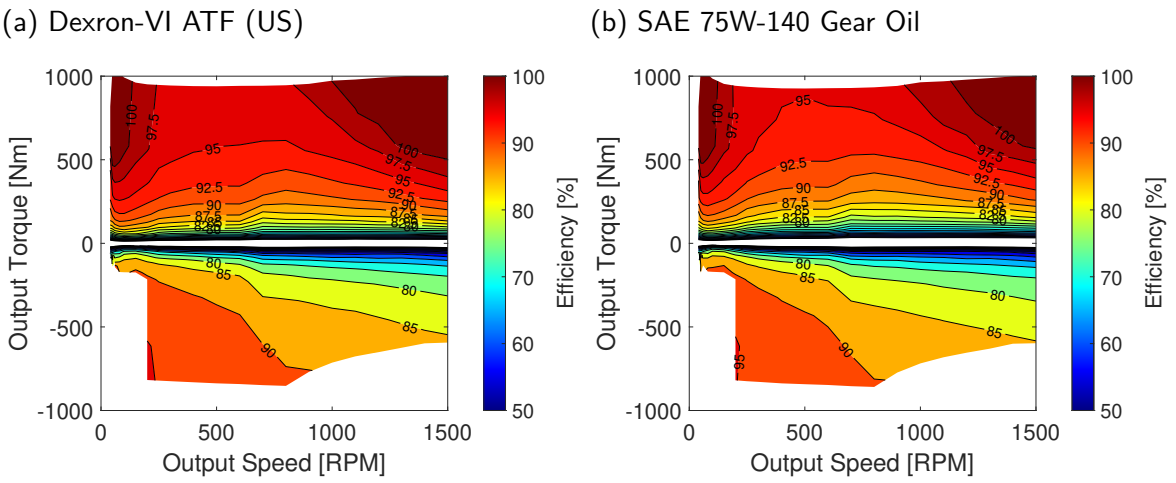


Figure 5.5: Efficiency maps - driving and regen combined, for two oils. The low-torque region is more finely resolved in Fig. 5.6.

not known, but it should be noted that this error does not undermine the comparison between otherwise equivalent tests for the two oils.

A similar procedure was used to obtain drive efficiencies over a range of torques and speeds with the direction of power flow reversed, but with the rotation direction still forwards, as shown in Fig. 5.4b, although note that for its own protection, the drive unit limits such 'regen' torques both at low speeds and at very high speeds, hence the shape of this region of the map.

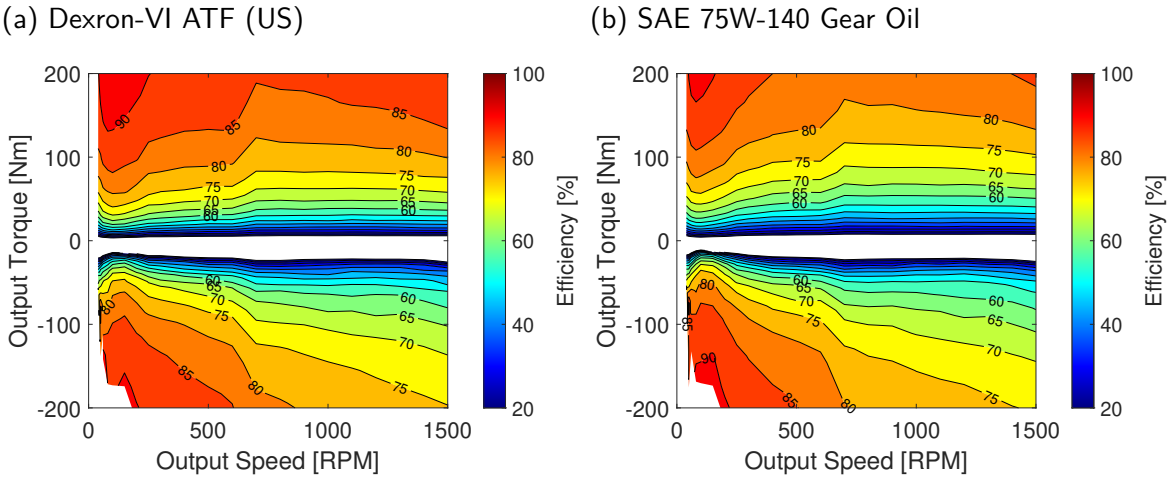


Figure 5.6: Efficiency maps for two oils showing $-200 \leq T_{out} \leq 200$ Nm portion of Fig. 5.5.

The efficiency maps shown in Fig. 5.5 show both the driving direction and reverse/braking torques, for the same two oils tested in Section 5.2. It is interesting to focus on the region

spanning -200 to 200 Nm output torque (Fig. 5.6), which represents normal driving conditions for the majority of the duty cycle of the vehicle. The comparison between the two oils is more apparent in this region, and the higher viscosity fluid clearly reduces efficiency by approximately 5% throughout this torque range.

(a) Dexron-VI ATF (US) (b) SAE 75W-140 Gear Oil

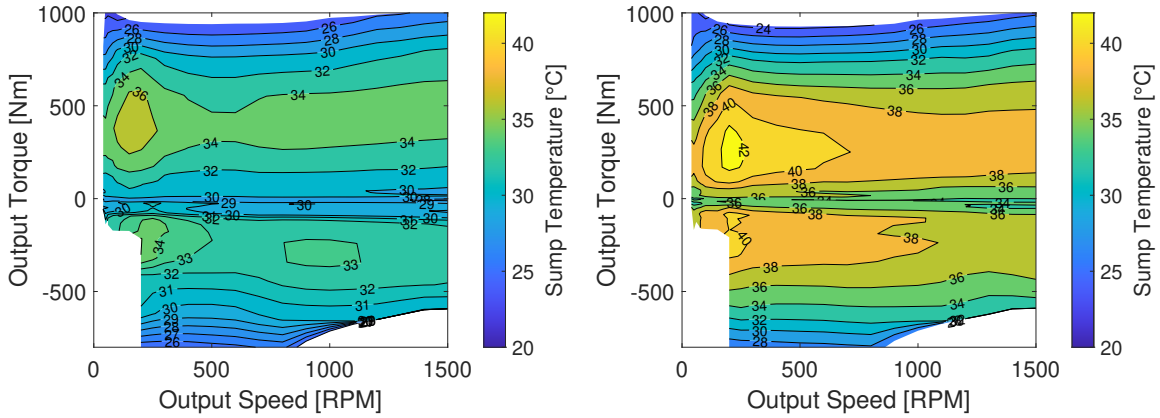


Figure 5.7: Oil sump temperature measured during efficiency tests

(a) Dexron-VI ATF (US) (b) SAE 75W-140 Gear Oil

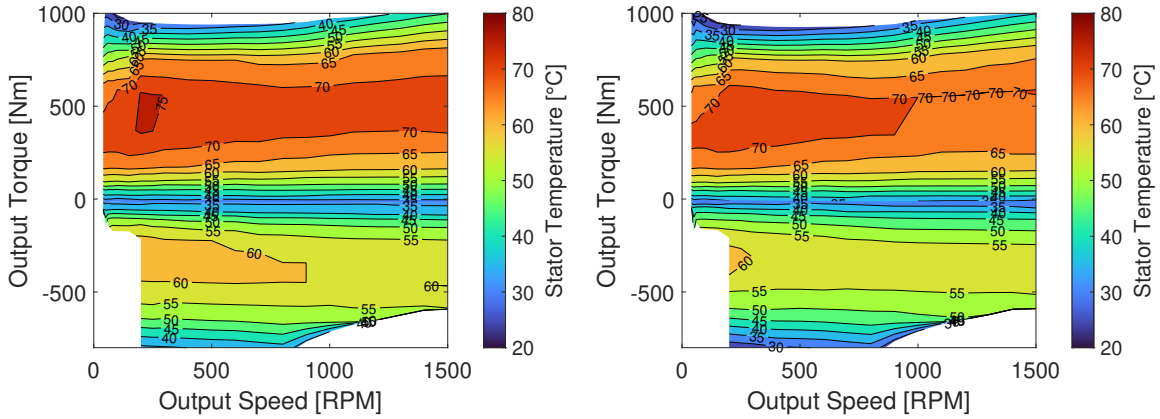


Figure 5.8: Motor stator temperature measured during efficiency tests

The oil temperature variation during the test was significant, and is shown in Fig. 5.7, reaching 40°C (initially 20°C) at the maximum-temperature point. It is interesting to note the location of the maximum oil sump temperature, which occurs (unsurprisingly) at high torque, but at relatively low speed, for which convective transport of heat by the oil is weak. Both the motor and the gearbox are jacketed by coolant channels, and the coolant flowrate was constant throughout these tests. The highest torques were measured first so as to take advantage

of the thermal inertia of the drive unit to minimise the total temperature rise. The sump temperature trends track the stator temperatures closely (Fig. 5.8), although the stator runs much hotter than the sump, and in this dry-motor design, the oil and the stator do not come into contact (not to be confused with the wet-motor design of the front drive unit presented in Chapter 4). This suggests that for these cooling rates, the sump heating was nevertheless primarily attributable to electromagnetic losses in the motor.

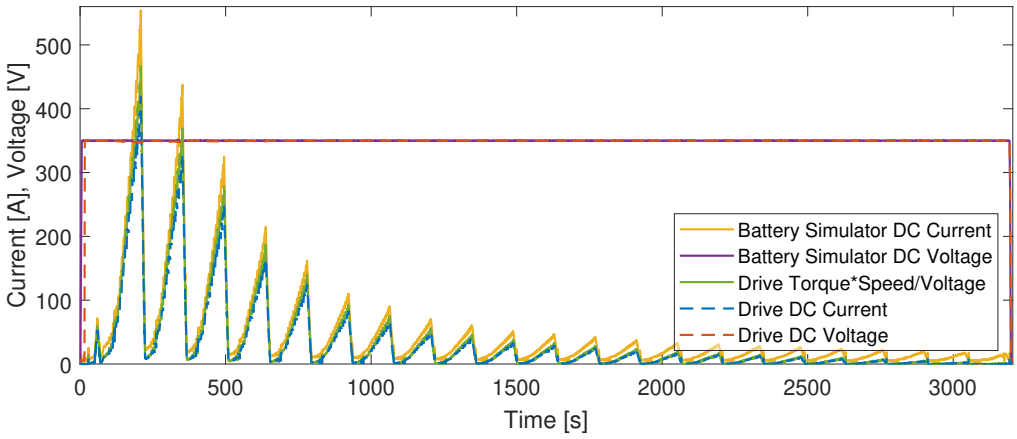


Figure 5.9: Voltage and Current measurements throughout test reported by battery simulator and Tesla drive unit

DC input voltage and current reported by the drive unit, and output voltage and current from the battery simulator, were also recorded. The two voltages matched well (nominal DC output voltage 350 V). It was found that the product of the voltages and currents from the drive was consistently less than the mechanical output power it reported, by a factor of ~ 10 %, implying a nonsensical electrical efficiency greater than unity - this is attributed to uncertainty in the current value from the drive. The current value from the battery simulator by contrast was higher than expected, resulting in a nominal power output of ~ 2 kW when the drive was idle (the discrepancy is illustrated in Fig. 5.9).

5.4 New European Drive Cycle Test

The New European Drive Cycle (NEDC) is one of the benchmarks for road vehicle powertrain efficiency under conditions which (somewhat reductively) simulate real-world driving. The NEDC was encoded for use with the T-Axle EV Dyno Rig to perform a mock-benchmark of the drive unit under test. Although the data from the single test that was performed do not

resolve the effect of operating temperature or oil viscosity, they illustrate for this vehicle the torques and speeds at which the car would operate under 'everyday driving', and the efficiencies measured may be compared to those predicted by models which have also simulated this drive cycle.

Thanks are due to Joseph Shore for the conception of this test, and for the calculation of the torque profile of the NEDC for the Tesla Model S (simulating inertia, rolling resistance and aerodynamic drag according to Eq. (4.1) on page 81). It is assumed that the car is operating in 2-wheel drive mode, so that this drive unit is solely responsible for providing the tractive power throughout.

The cycle was discretised into instantaneous torques and speeds at 1 second intervals. The dynos were speed controlled, while the drive unit was torque controlled. The throttle voltage fed to the drive unit was controlled by a PID controller with feed-forward, tuned to minimise the error between the total filtered sum dyno torque, and the torque demanded of the drive cycle. The drive was filled with the Dexron-VI ATF (US) fluid. Torques, speeds, and the drive unit mechanical efficiency calculated from Eq. (5.1) are reported in Fig. 5.10.

The mean value of the efficiency, in the regions of the drive cycle where it is well-defined (at nonzero speed and for positive torque), is 85.2%, which is relatively low for a two-stage, single-speed helical gearbox. This mean value excludes the small portion of the drive cycle (less than 5%) for which the efficiency is implausibly high ($\eta_m >= 100\%$) or low ($\eta_m <= 50\%$). This highlights the extent to which the maximum torque capacity of the gearbox exceeds the required torque for everyday driving, and the negative effect of this on transmission efficiency. The efficiencies measured here should also be treated with some caution due to the uncertainty in the torque measurement procedure. We expect 'efficiencies' greater than unity for the case where torque is negative (i.e. the direction of power flow is reversed; the dynos are driving the drive unit, which is absorbing power in regenerative braking mode), because the value of P_{out} in Eq. (5.1), which still pertains to the total mechanical power supplied by the dynos, must now be larger than P_{in}. The mean value of the 'efficiency' reported in this regen case (similarly rejecting the portion of the drive cycle where torque is positive, and where $\eta_m <= 50\%$ or $\eta_m >= 150\%$, such as during torque transients due to differences in measurement latency) is 107.8%. The reciprocal of this value, which reflects the usual definition of efficiency, is

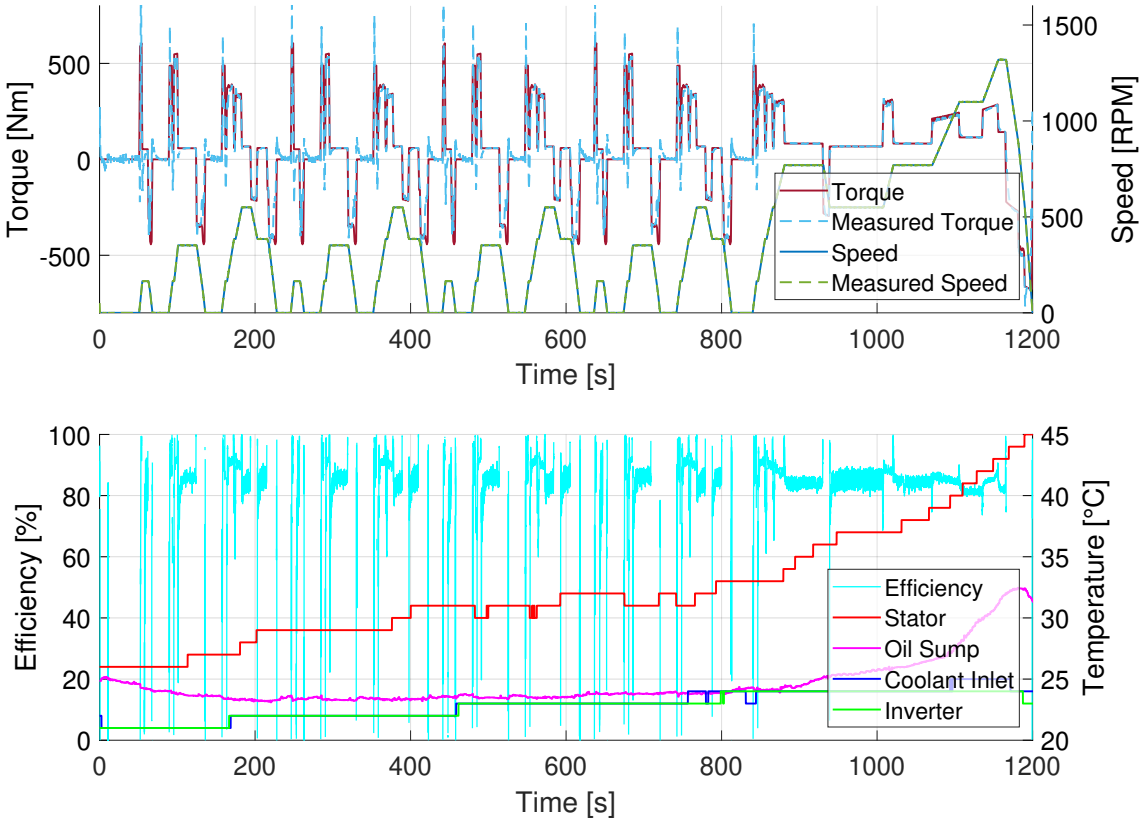


Figure 5.10: Torque, speed, efficiency, and temperatures measured during New European Drive Cycle, performed by Tesla Model S rear drive unit in T-axle EV dyno rig.

92.8%, considerably higher than the mean value in the forward direction.

The efficiency maps were created using a torque-zeroing procedure leveraging the creep mode of the drive unit, but this was not done for the NEDC measurements. The efficiency maps suggest that the efficency in regen is consistently lower than the driving efficiency for this fluid, whereas the measurements here suggest the opposite.

It was found that, when the speed is stable, the ratio of the speed measurements from the drive unit to that from the dynos takes a mean value of 9.733, incurring much less than 1% error compared to the nominal value of 9.7344, and suggests the speed measurements are not the source of the power discrepancy. It is therefore likely that this discrepancy arises from one of the torque measurements, either an overestimation of the motor torque reported by the internal VFD in the UUT, or an understimation of the total dyno torque. The latter could arise due to the torque zeroing procedure, which risks introducing a systematic error into the

torque measurement.

A single-parameter correction to the torque measurement is considered here, assuming that the mean efficiencies for positive and negative torques should be similar. This does not account for the difference in the magnitude of torque or speed between the drive and the regen parts of the drive cycle, or any other effects of reversing the power flow through the gearbox (but note that the direction of the speed is the same for both cases). The definition of η_m in Eq. (5.1) leads to an 'efficiency' η_{driven} when the UUT is driven by the dynos which, it is assumed, should match the reciprocal of the value η_{driving} when it is driving. We introduce the output torque correction δ so that the dyno torque T_{out} in the driving case is

$$T_{\text{out}} + \delta = \eta_m G T_{\text{in}} \tag{5.2}$$

Rearranging for η_m we have

$$\eta_m = \frac{T_{\text{out}}}{G T_{\text{in}}} + \frac{\delta}{G T_{\text{in}}} = \eta_m^{\text{meas}} + \Delta \tag{5.3}$$

where Δ is a normalisation of δ which can be thought of as an error in the efficiency measurement. Considering then the assumption that the mean efficiencies in the driving and driven cases are approximately reciprocal, and also assuming for simplicity that δ is approximately a constant fraction of the motor torque T_{in},

$$\eta_{\text{driving}}^{\text{meas}} + \Delta \approx \frac{1}{\eta_{\text{driven}}^{\text{meas}} + \Delta} \tag{5.4}$$

which is a quadratic expression in Δ and solves for the values of η_{driving} and η_{driven} above, to give $\Delta \approx 2.5\%$. This suggests the efficiency reported under steady-state driving conditions could be up to 87.7%. This figure remains lower than predictions from the model of Shore [11], perhaps due to the aggregate of smaller additional losses not considered by that model such as shaft seals, coupling losses and dynamical losses as a result of shaft vibrations. Further work is required to improve and to verify both the accuracy and precision of the torque measurement using this apparatus, a task requiring time and resources beyond the 8-week visit to the Ashland laboratory.

Chapter 6

High-speed Elastohydrodynamic Traction and Film Thickness

The study presented in this chapter has previously been published by the author in an open-access paper entitled 'Elastohydrodynamic Traction and Film Thickness at High Speeds' [227].

This chapter presents simultaneous measurements of traction and film thickness at entrainment speeds up to 20 m/s, using a new experimental setup which implements a novel traction measurement technique developed for this study. The magnitude of this entrainment speed is significant because it is pertinent to the entrainment speeds found in EV gear and bearing contacts (gear and bearing entrainment speeds respectively reach 18.5 m/s and 26.3 m/s in the transmission from Chapter 4). The extent to which the measurements deviate from the well-known EHL film thickness prediction of Chittenden, and the widely-used thermal correction of Gupta, is quantified over a wide speed range for several fluids chosen to represent base fluids commonly used in transmission lubricants. The traction measurements demonstrate the effect of fluid viscosity and chemical composition, showing the significant change in traction response with increasing entrainment speed. The implications of these measurements for understanding the thermal response of the contact, and the relevance of these findings to future efforts to measure traction at high speeds, particularly for dissimilar contacting materials, is discussed. The data are included for all fluids measured in full in Appendix I for reference.

6.1 Methods

6.1.1 Test Setup

A new test rig, the EHD-HS from PCS instruments, was used during this study. The machine comprises a rotating steel ball supported from below by three steel rollers, see Fig. 6.1, in contact with a transparent flat disc rotating directly above it, in the same manner as the EHD2 ultra-thin-film measurement system [108]. The ball and rollers are partially submerged in a temperature-controlled lubricant sump. The ball is loaded against the disc by the roller carriage, to which the load is transmitted via a load cell by a compliant lever connected to a lead-screw-type stepper motor, enabling load control. Ball and disc are mounted on separate perpendicular shafts driven independently by servomotors such that any surface speed between 0.05 m/s and 20 m/s can be achieved on either surface, enabling independent control of entrainment and sliding speeds.

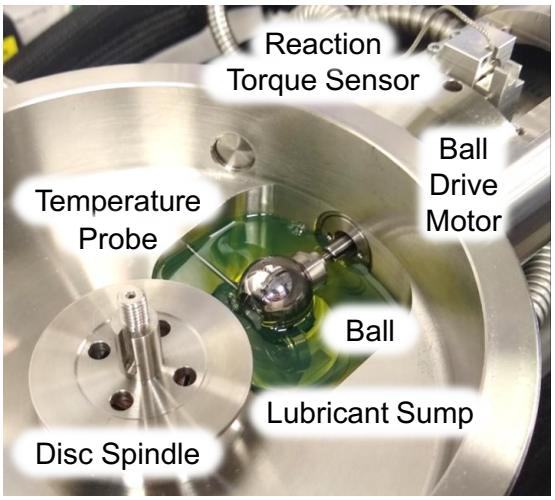


Figure 6.1: EHD-HS test setup showing driven steel ball resting on roller carriage, partially immersed in lubricant, with temperature probe positioned near to the contact outlet. The transparent disc (not shown) rests above the ball on the rotating disc spindle flange.

6.1.2 Contact Conditions

The ball specimens were made of standard AISI 52100 bearing steel, and discs made of both glass and sapphire were used. Specimen material properties are taken as those in Table 3.4 on page 75. The balls were polished to a roughness below $R_a \approx 10$ nm, and the ball radius

is 9.525 mm. The corresponding contact pressures are given in Table 6.1 for a ball load of 50 N.

Table 6.1: Contact conditions using Glass and Sapphire discs under 50 N load

	Reduced Modulus E' [GPa]	Max. Hertz Pressure P_0 [GPa]	Contact Half-Width a [μm]
BK7 Glass	117.5	0.72	182
Sapphire	284.9	1.3	137

6.1.3 Film Thickness Measurement

Film thickness measurements were made using ultra-thin-film interferometry [108], which is briefly described in this section. The transparent disc is coated on its contacting surface by a silica 'spacer layer', of thickness approximately 560 nm, beneath which is a very thin semireflective chromium layer, at the interface between the glass and the silica. White light is shone into the contact through the transparent disc, and is split by the chromium layer into a transmitted and a reflected beam, as shown in Fig. 6.2. When the surfaces are in motion, an elastohydrodynamic lubricant film is developed between the ball and disc. The transmitted beam travels through the spacer layer and lubricant film, reflects off the ball, and recombines with the reflected beam at the chromium interface. The optical path difference between the two beams causes them to interfere destructively or constructively depending on wavelength. The resultant interferogram is then analysed using a spectrometer, which detects the wavelengths of minimum and maximum intensity, from which the optical path difference, and hence the film thickness, are calculated. At the start of each test, the spectrometer is used to measure the thickness of the spacer layer when the ball and disc are motionless and the film thickness is therefore zero. The spectrometer triggers at the same pre-specified angular position on the disc each time to ensure the spacer layer thickness is consistent for each measurement.

To enable EHL film and traction measurements at high speeds, the EHD-HS rig used in this study includes several modifications compared to previous implementations of this technique on standard EHD rigs. The ball-carriage rollers (which in previous setups comprise the

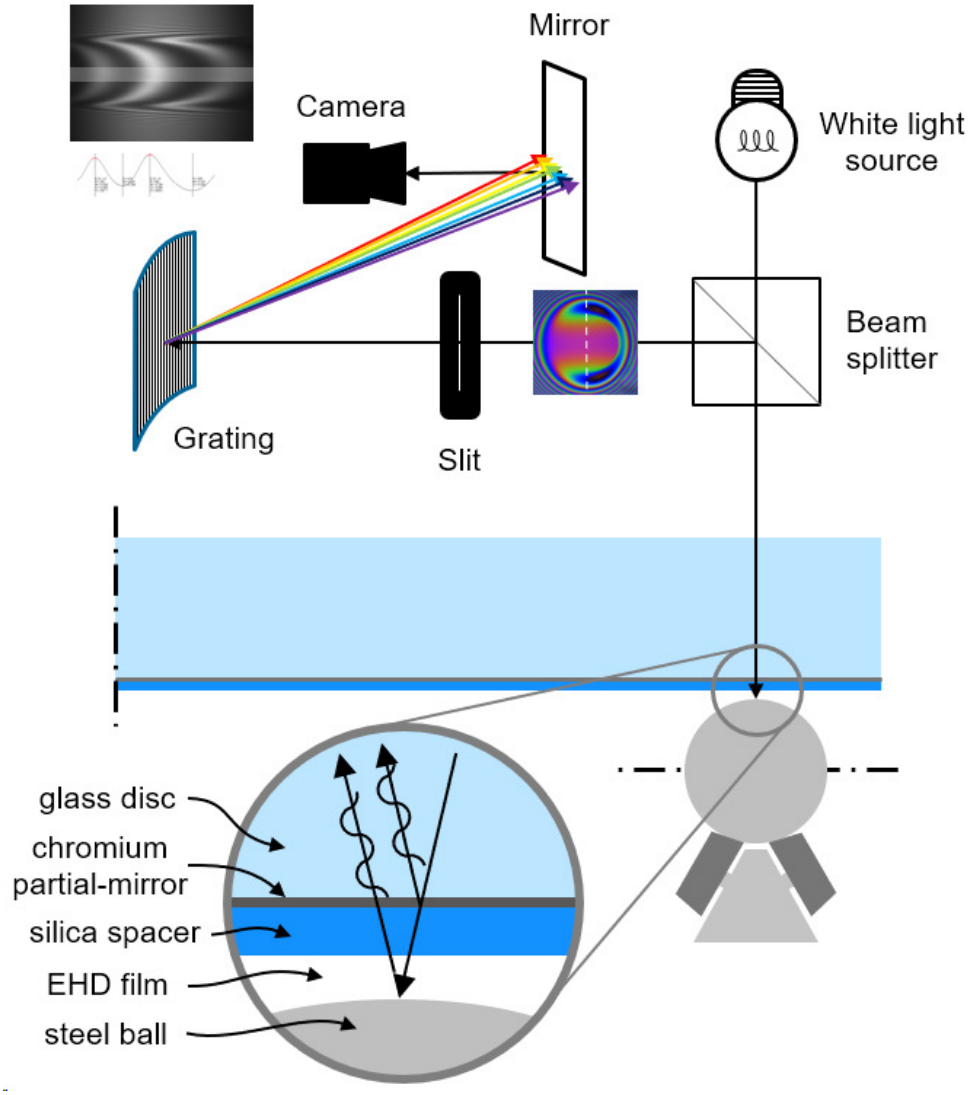


Figure 6.2: Schematic of film thickness measurement by ultra-thin-film interferometry

cylindrical outer race of a centrally-mounted bearing) are conical, their cone angle being chosen to amortise spin in the contacts with the ball, thereby reducing parasitic carriage traction. The drive motors used are capable of achieving surface speeds of 24.5 m/s, and a camera exposure time of 1 ms is used to limit motion blur. A telecentric objective of magnification 5X, achieving a working distance of over 60 mm, enables sufficient separation between lubricant and lens to avoid oil splashing onto the lens, a much greater issue at high speeds due to flow turbulence. Film measurements are performed from the analysis of five consecutive spectrometer measurements taken in quick succession (spaced by approx. 200 ms, or consecutive disc rotations, whichever is slower), so that the measurement is minimally affected by temperature transience. The temperature control of the lubricant is achieved

by circulating silicon oil via a cooler through separate cooling channels in the steel pot, which also houses electrical resistance heaters, with the controller tuned to respond to rapid changes in energy dissipated by viscous shear, as the motor speeds change during the test. The temperature is measured approx. 5mm from the outlet of the contact by a platinum resistance thermometer as in other setups. Temperature control to within $\pm 1^{\circ}$C is achieved below 10 m/s, and globally within $\pm 4^{\circ}$C of the nominal temperature.

6.1.4 Traction Measurement

The EHD ultra-thin-film measurement system, although an inline torque sensor is included between the ball drive shaft and ball motor, cannot measure traction in the same way as other ball-on-disc tribometers designed for this purpose, such as the MTM. This is because the ball torque due to the ball-on-disc contact traction is superposed with the parasitic torques from the three ball-carriage bearings, fluid drag, and the radial lip seal on the driveshaft where it enters the sump. These three additional torques are challenging to measure or estimate, and depend on the ball speed, temperature, load, and lubricant properties. In most cases they are of similar magnitude to the traction torque, thereby completely obscuring the measurement.

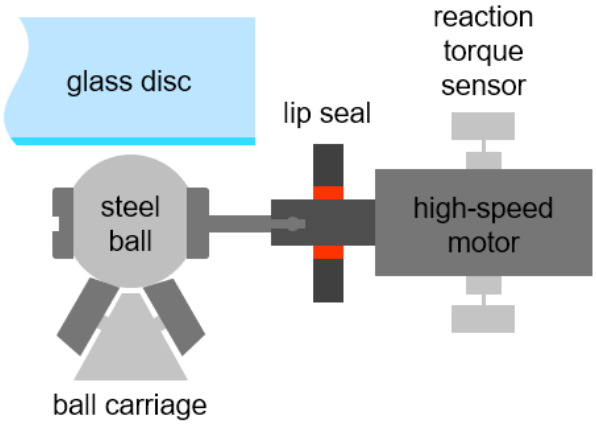


Figure 6.3: Schematic of ball drive mechanism

This study overcomes this problem by using a novel traction measurement procedure which enables these parasitic torques to be measured and eliminated. The technique relies on the assumption that the parasitic torques, although they depend on ball speed, are insensitive to disc speed. This assumption is weakest with reference to fluid drag, because the flow field depends on both surface speeds, but as the ball is only partially submerged in lubricant and the disc sits entirely above the fluid level, fluid drag is expected to be the smallest of the

parasitic torques, and the influence of disc speed due to oil and air interactions is expected to be relatively weak.

Consider the case where an entrainment speed U_e and slide-roll ratio SRR (Eq. (6.1)) are specified, and traction force under these conditions is to be measured. The meridional ball surface speed U_1 and disc tangential speed U_2 are given by Eq. (6.2), where a positive SRR implies the disc speed is greater.

$$\mathrm{SRR} = \frac{U_s}{U_e} = 2\frac{U_2 - U_1}{U_1 + U_2} \tag{6.1}$$

$$U_1 = U_e\left(1 - \frac{\mathrm{SRR}}{2}\right) \qquad U_2 \;= U_e\left(1 + \frac{\mathrm{SRR}}{2}\right) \tag{6.2}$$

If it is assumed that the traction forces due to positive and negative SRR are equal and opposite, then the sign of the nominal SRR is irrelevant for traction measurement; only the magnitude is significant (an assumption later discussed in the context of thermal EHL at high speeds). In this case, transducer offset can be removed by calculating the traction coefficient from Eq. (6.3) where traction force is denoted F, with a superscript indicating the sign of the sliding speed, such that F^+ and F^- have equal entrainment speed and opposite sliding direction, and w is contact load. This approach is relied upon in many widely-used tribometers, including the MTM for example. It assumes that the only force contributing to F that changes with ball and disc speeds, arises from contact traction.

$$\mu = \frac{F^+ - F^-}{2w} \tag{6.3}$$

The EHD by contrast sees several forces contributing to F which all depend on ball speed, and cannot therefore use the difference between F^+ and F^- to measure traction if the ball speed is different for the F^+ and F^- measurements. One approach to overcome this, used by the EHD2, is to set the ball speed equal to the nominal entrainment speed in both cases, and to enforce the sliding by changing only the disc speed. This is undesirable as the F^+ and F^- cases have different entrainment speeds and hence any nonlinearity in the traction response (such as that introduced by thermal effects) influences the measurement and is not itself quantifiable.

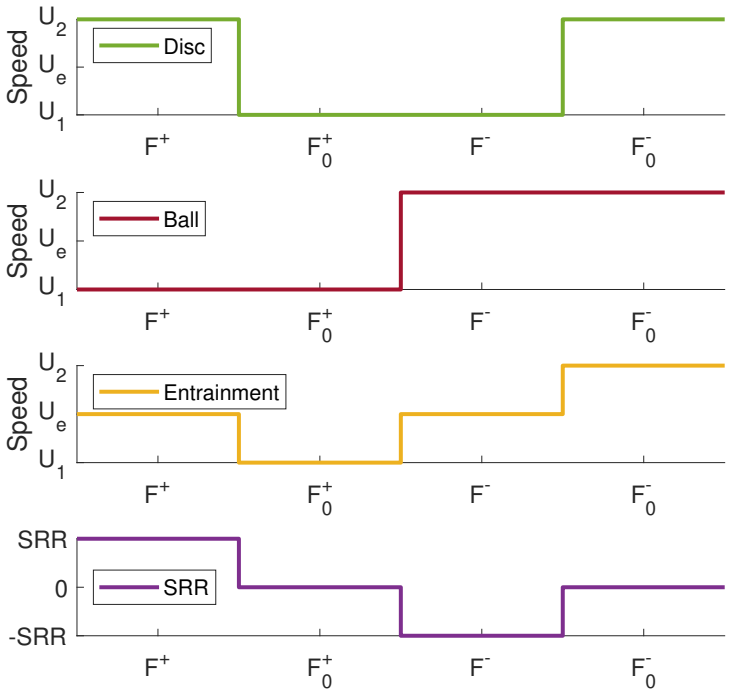


Figure 6.4: Summary of ball and disc speeds under four cases used for traction measurement

The novel method proposed here addresses this issue. An additional two new measurements of traction force are introduced, in which the SRR is zero, and so (close to) zero traction force is expected. In the F_0^+ case, the disc speed is brought to the same speed as the ball when F^+ was measured, and likewise F_0^- implies both surfaces match the ball speed used for F^- measurement. F_0^+ and F_0^- therefore measure the ball parasitic torques when the ball speed is equal to U_1 and U_2, respectively. The traction coefficient in each sliding direction can therefore be calculated from Eq. (6.4). The assumption that forward and reverse-sliding traction are equal and opposite leads to Eq. (6.5).

$$\mu_+ = \frac{F^+ - F_0^+}{w} \qquad \mu_- = -\frac{F^- - F_0^-}{w} \tag{6.4}$$

$$\mu_{\text{avg}} = \frac{\mu_+ + \mu_-}{2} = \frac{\left(F^+ - F_0^+\right) - \left(F^- - F_0^-\right)}{2w} \tag{6.5}$$

The $(F^+ - F_0^+)$ term represents forward traction force, and the $(F^- - F_0^-)$ term reverse traction force. The four traction measurements are taken in the sequence shown in Fig. 6.4 by a series of 10 ms bursts from the transducer, accumulated until a stable average is obtained over 10 consecutive bursts (total range within ± 0.032 N) or until 2 seconds have elapsed.

6.1.5 Test Procedure

Traction coefficient and film thickness were measured simultaneously for entrainment speeds in the set $\{0.05, 0.1, 0.2, 0.3, 0.6, 1.2, 2.4, 4, 7, 10, 13, 16, 18, 20\}$ m/s, and for slide-roll ratios in the set $\{0, 0.5, 1, 2, 4, 6, 8, 10, 15, 20, 30, 45, 60, 80, 100\}$ %, producing, for each test, a series of film thickness and traction measurements. These were performed at temperatures $\{20, 60, 100\}$ °C. In total, over 6500 film thickness and traction measurements were made. Measurements were taken only for conditions where:

- The minimum predicted film thickness h_m according to Chittenden [221] exceeded 40 nm, guaranteeing a Λ ratio greater than 3, and hence maintaining full-film conditions.
- The central film thickness measured was less than 2 μm, above which the resolution of the ultra-thin-film interferometry technique begins to degrade significantly.
- The specimen speeds were strictly slower than 24.5 m/s (hence the highest SRR tested at 20 m/s entrainment was 45 %).

6.2 Results

A selection of the results obtained are presented in this section. The full set of traction and film thickness measurements for 10 fluids are plotted in Appendix I on Page 314.

6.2.1 Measurements of Traction and Film Thickness

Example traction coefficients (μ^+, positive SRR, disc faster) for PAO4 (polyalphaolefin) are shown in Fig. 6.5 for a selection of entrainment speeds. The simultaneously-measured central film thicknesses are shown in Fig. 6.6.

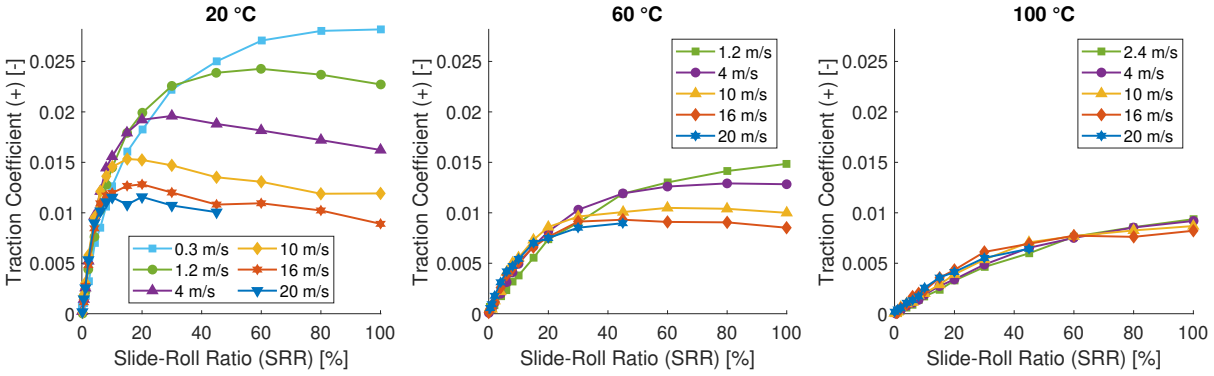


Figure 6.5: Traction curves measured for PAO4 at three temperatures for selected entrainment speeds in forward sliding, disc faster.

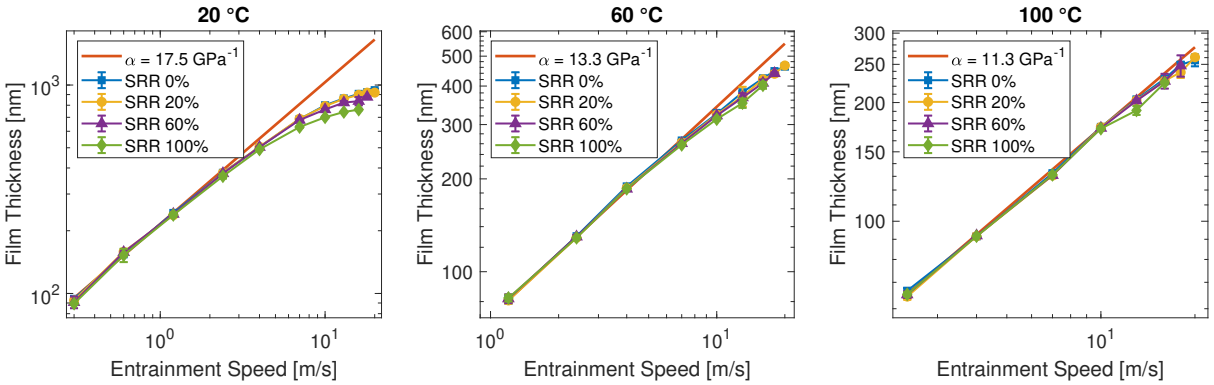


Figure 6.6: EHD central film thickness vs entrainment speed measured for PAO4 at three temperatures for selected SRRs in forward sliding. Each film thickness shown is the mean of 5 consecutive measurements with error bars located at $\pm 3\sigma$. The fit to film thickness for $U_e \leq 2.4$ m/s according to Chittenden obeying the relationship $h_c \propto U_e^{0.68}$ is also shown, where the only free parameter is the pressure-viscosity coefficient α given in the legend.

These data are summarised by the 3D plots in Fig. 6.7, which show the traction (Fig. 6.7a) and film thickness (Fig. 6.7b) measurements vs both U_e and SRR. Similar plots were obtained

for each fluid, over 400 simultaneous traction and film thickness measurements having been conducted for each, and these are included for reference in Appendix I.

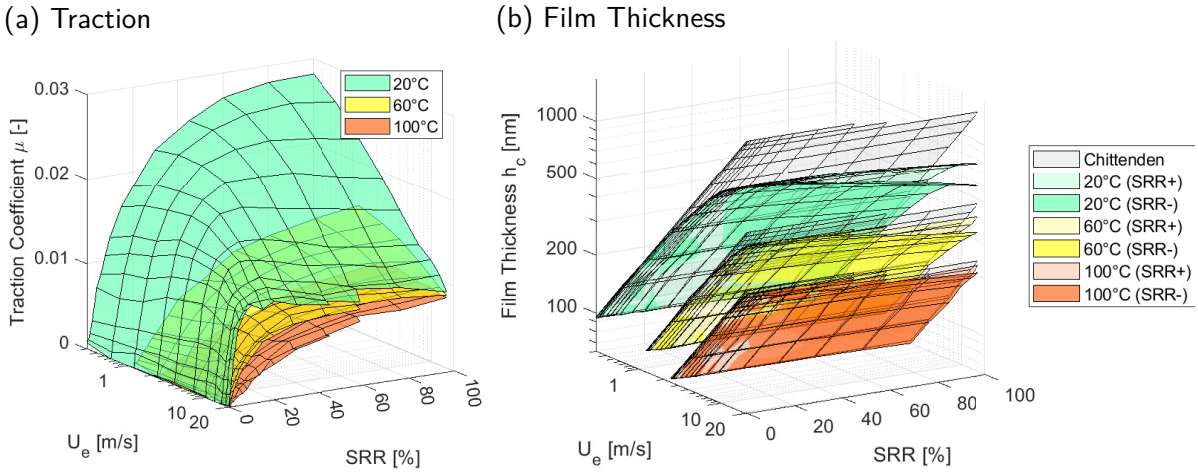


Figure 6.7: Traction and Film Thickness vs Entrainment Speed U_e and Slide-Roll Ratio SRR measured simultaneously for three temperatures with PAO4

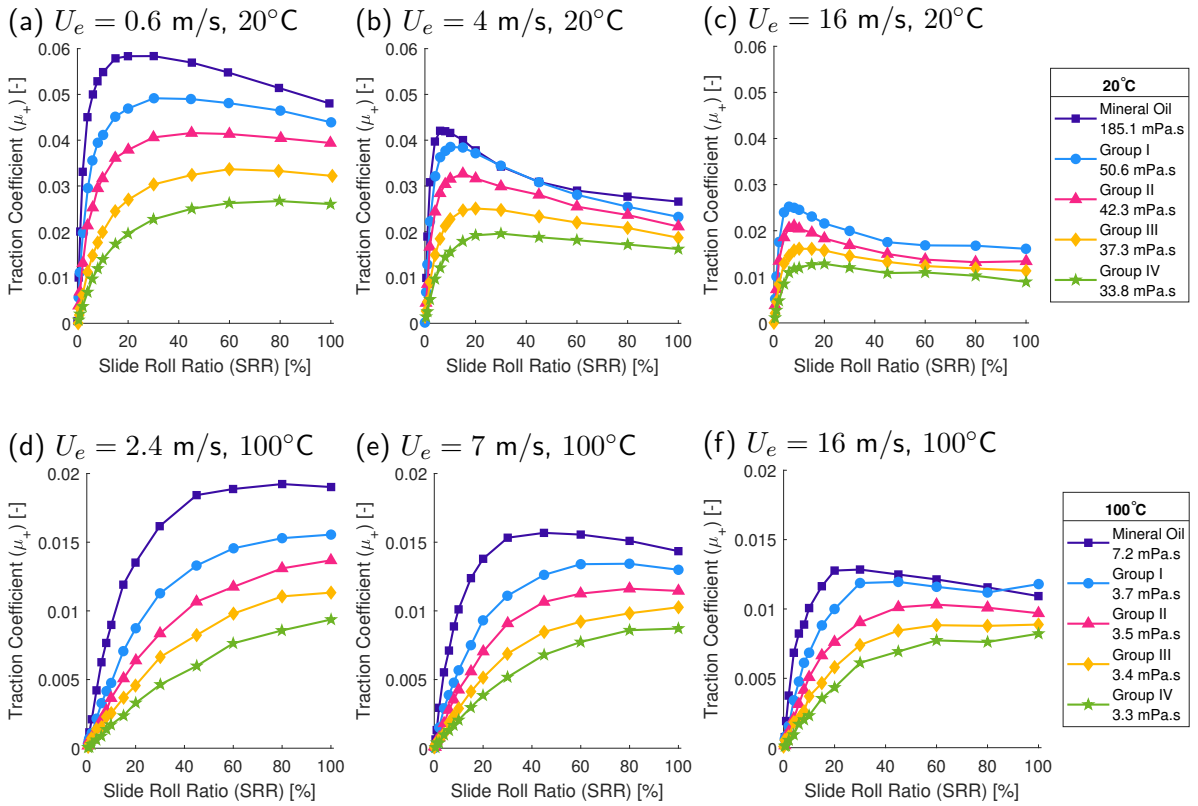


Figure 6.8: Traction curves for various speeds at 20°C (a, b, c) and 100°C (d, e, f), for five fluid types spanning Groups I - IV, with corresponding dynamic viscosities given in the legend for each. Steel ball on glass disc, 50 N load, 0.73 GPa max. Hertz pressure.

Traction curves for four base fluid types (Group I is represented twice at two different viscosities) are shown in Fig. 6.8, which demonstrates that the novel traction measurement method successfully replicates familiar trends and representative values of EHD friction for these base fluids at various speeds and temperatures. The four lowest-viscosity fluids are chosen to have comparable viscosity at 100°C, although their different viscosity indices lead to differing viscosity at lower temperatures.

It can clearly be seen in Figs. 6.6 and 6.7b that film thickness is lower than the corresponding Chittenden prediction [221] at high speeds. The reduction is the greatest at lower temperatures, high slide-roll ratios, and in the negative sliding direction. At higher speeds the traction curve has larger gradient at low slide-roll ratios, and flatter gradient above the maximum-traction point. Film thickness continues to depend comparatively weakly on SRR even beyond the maximum-traction point, until approx. 50% SRR when there is a slight reduction for forward sliding, and a more pronounced reduction for negative sliding. The contact remains fully flooded, and the reduction in film thickness at high speeds is not due to inlet starvation, as shown in Fig. 6.11 later.

6.2.2 Comparison to Film Thickness Predictions

The deviation from the film thickness predicted by Chittenden is quantified in Fig. 6.9. The film thickness deviation is given as a percentage of the measurement in forward sliding, according to Eq. (6.6). It is evident that the predicted film thickness can exceed the measured thickness by a factor of as much as 2 in pure rolling at 20 m/s. The overprediction is the largest at 20°C for the 4 cSt fluids. This effect depends on both base fluid type (Group I and II oils show greater deviation) and base fluid viscosity (compare PAO5 to PAO4, labelled 'Group IV', higher viscosity increases the deviation). At 100°C, and hence for low viscosities of the order 4 mPa.s however, the difference between measured and predicted film thicknesses is very small.

$$\delta h_c = \frac{h_{\text{Chittenden}} - h_c^+}{h_c^+} \times 100\% \tag{6.6}$$

Film thickness measurements are also compared in the same way to the model of Gupta, (Eqs. 6.7 and 6.8), where L_T is the thermal loading parameter, P_0 is the maximum Hertz pressure, and κ_{oil} is the thermal conductivity of the fluid, taken here as a first approximation

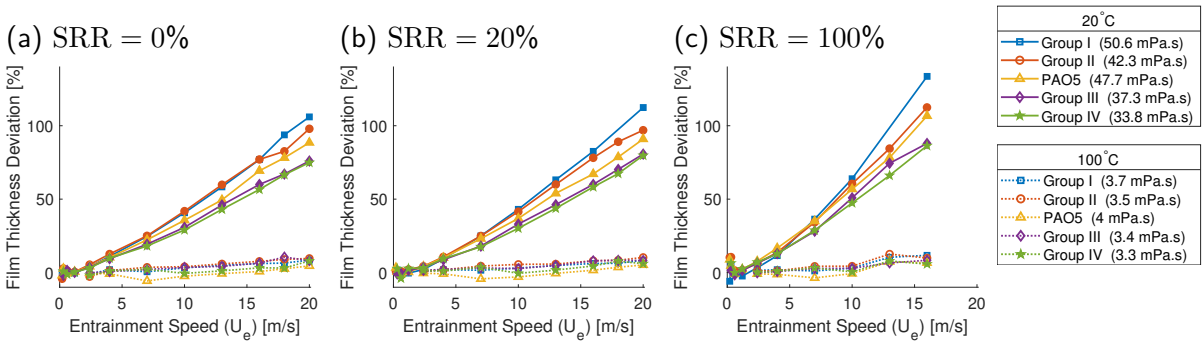


Figure 6.9: Percentage overestimation, compared to measurement in positive sliding direction, of central film thickness h_c from the Chittenden model at $20°$C and $100°$C for three SRRs, with corresponding dynamic viscosities shown in legend.

.

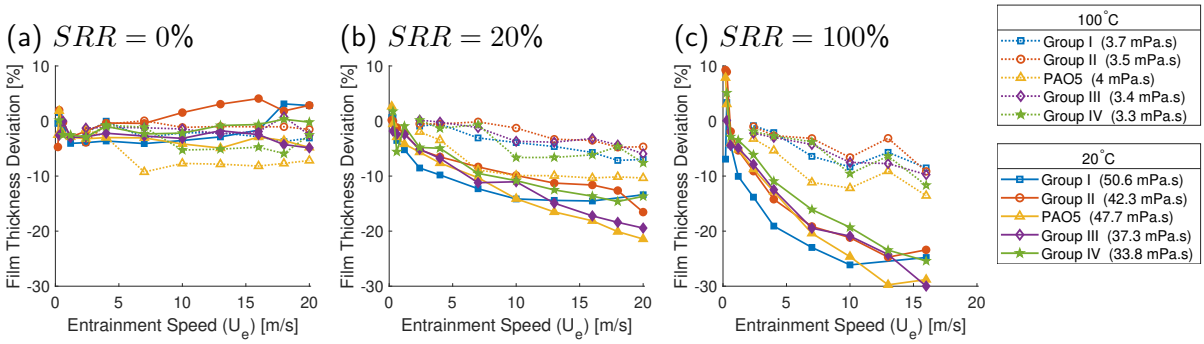


Figure 6.10: Percentage difference between central film thickness h_c predicted by Gupta model, and measurement in positive sliding direction, for $20°$C and $100°$C with corresponding dynamic viscosities shown in legend.

to be 0.15 W/mK.

$$h_{\text{Gupta}} = \frac{h_{\text{Chittenden}}\left(1 - 13.2\frac{P_0}{E'}L_T^{0.42}\right)}{1 + 0.213\left(1 + 2.23\text{SRR}^{0.83}\right)L_T^{0.64}} \tag{6.7}$$

$$L_T = -\left(\frac{\partial \eta}{\partial T}\right)\frac{U_e^2}{\kappa_{\text{oil}}} = \frac{\eta B}{(T - T_0)^2}\frac{U_e^2}{\kappa_{\text{oil}}} \tag{6.8}$$

The gradient of viscosity with temperature (Eq. (6.8)) is calculated analytically from Eq. (3.1) using the relevant parameters from Table. 3.2. The deviations of the current measurements for the Gupta predictions obtained in this way are plotted in Fig. 6.10, which shows that the Gupta model under-predicts the measurement by around 25% at 100% SRR in rolling-sliding conditions. However, the Gupta model is quite accurate in pure rolling, incurring errors not more than 10% for the fluids and conditions tested here. The Gupta model was originally based on a formulation intended for line-contact [228], and employed a rheological model

which Bair and coworkers [229] have since shown to have limited application in elucidating the rheological behaviour of lubricating oils as they are pressurised in the contact inlet. In addition, the propensity of the contacting bodies to advect heat away from the contact, which is not modelled by the thermal correction factor, may be significant in the situation where the contact repeatedly traverses a closed path on the surface, as is the case in most machine elements, and in this study. Consequently, the discrepancy between these results and the predictions of the Gupta model are not surprising, and are examined further in Section 6.3.

6.2.3 Interferometric Images of the Contact

An additional test was conducted with PAO5 at 20°C, using an LED white light source and an RGB camera to record the interferogram of the whole contact directly, instead of using the spectrometer. Interferometric images of the contact at selected speeds are shown in Fig. 6.11. These provide some insight in to EHL film shape at different entrainment and sliding speeds and confirm that:

- At all entrainment speeds up to 24 m/s, the characteristic features of an EHD contact are retained, namely a wide central plateau, a sharp constriction at the outlet, and regions of minimum film thickness on the sidelobes.
- The contact remains fully flooded, there is no starvation and no transition in behaviour of the cavitation region up to 24 m/s entrainment in this setup. This confirms that any reduction in film thickness observed at high speeds is not due to inlet starvation.
- The central plateau remains wide enough, and the image stable enough even at the highest speeds employed here (24 m/s), to reliably measure central film thickness.
- No central dimple was observed (this is true of all tests in this study).
- The shape of the outlet region changes under high-sliding conditions (SRR>10%) at high speeds, with the sidelobes coalescing as the outlet constriction expands in the entrainment direction, consistent with the findings of Hili [107] and Liang [109].

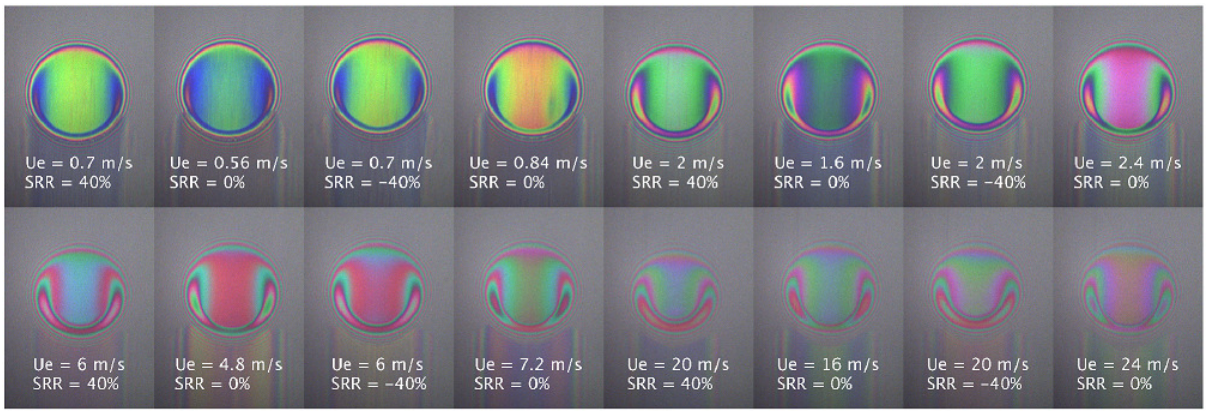


Figure 6.11: Interferometric images of ball-on-disc contact with steel-on-glass, PAO5 at 20°C, 50 N load (0.73 GPa), at four nominal entrainment speeds and 40% SRR, showing each of the four measurements from Fig. 6.4 in the sequence they were measured.

6.2.4 Mean Shear Stress and Shear Strain Rate

Simultaneous measurements of both traction and film thickness enable the calculation of both mean shear stress $\bar{\tau}$ (Eq. (6.9)) and shear strain rate $\dot{\gamma}$ (Eq. (6.10)).

$$\bar{\tau} = \frac{\mu w}{\pi a^2} = \mu \bar{p} \tag{6.9}$$

$$\dot{\gamma} = \frac{U_s}{h_c} \tag{6.10}$$

Mean shear stress vs strain rate is shown for a PAO5 in a steel-on-glass contact in Fig. 6.12a, and for steel-on-sapphire in Fig. 6.12b. Note that the strain rate ranges compare well between figures because the film thicknesses measured were similar, the dependence of reduced contact modulus in regression equations for film thickness being relatively weak ($h_c \propto E'^{-0.117}$).

These figures contain five features worthy of note:

1. At low shear strain rates a Newtonian/viscoelastic behaviour is seen as an increasing gradient on the linear/log graph.
2. At high strain rates, shear stress is considerably reduced as a result of the thermal response of the film to shear heating, which reduces mean viscosity in-contact. This reduction eventually becomes so severe that the gradient of shear stress with strain rate becomes negative.
3. At intermediate strain rates there is a region of shear-thinning behaviour which appears to obey the Eyring model, clearly seen here as a proportionality between $\bar{\tau}$ and $\log(\dot{\gamma})$.

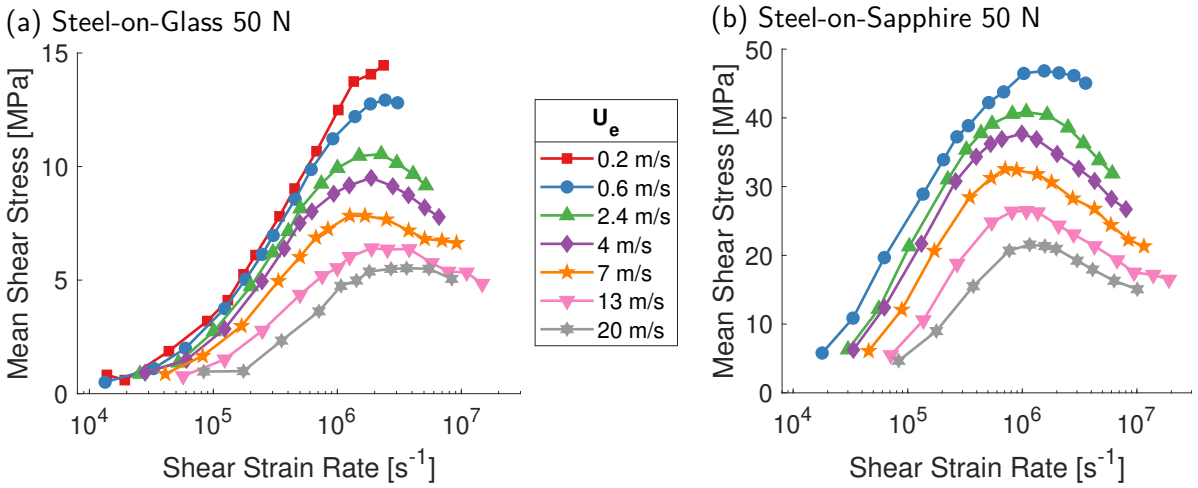


Figure 6.12: Mean shear stress $\bar{\tau}$ vs shear strain $\dot{\gamma}$ for PAO5 (Group IV) with a steel ball on glass disc (a) and sapphire disc (b) at 20°C and 50 N load for selected speeds (forward sliding, disc faster).

The origins, applications and limitations of the Eyring model are discussed in great detail by Spikes and Zhang [96].

4. At high entrainment speeds, the shear stress is lower than at low speeds, for equivalent shear rate. This effect is evident even at speeds below which there is significant reduction in film thickness, and at shear rates well below the bounds of the thermoviscous regime. Spikes and Zhang [96] note that the viscoelastic term is significant when contact transit times are short (less than $\sim 10^{-4}$ s) and shear rates are low (less than 10^5 s^{-1}). At $U_e = 20$ m/s, transit times are of the order 10^{-5} s, so we may consider the shortening of transit times at high entrainment speeds to extend the significance of the reduction in shear stress by viscoelasticity to higher shear rates.
5. The gradient of the linear regime (which corresponds to the Eyring stress τ_e) decreases at very high speeds, the onset of this decrease corresponding to the speeds at which the film thickness falls significantly below Chittenden's prediction.

6.2.5 Changes in Traction and Film Thickness with Sliding Direction

It was found during the development of the method that both traction and film thickness varied in a repeatable manner between forward (disc faster) and reverse (ball faster) sliding direction. The difference between the traction coefficients measured in forward and reverse sliding is shown in Fig. 6.13 for two fluids and three temperatures. The magnitude of the

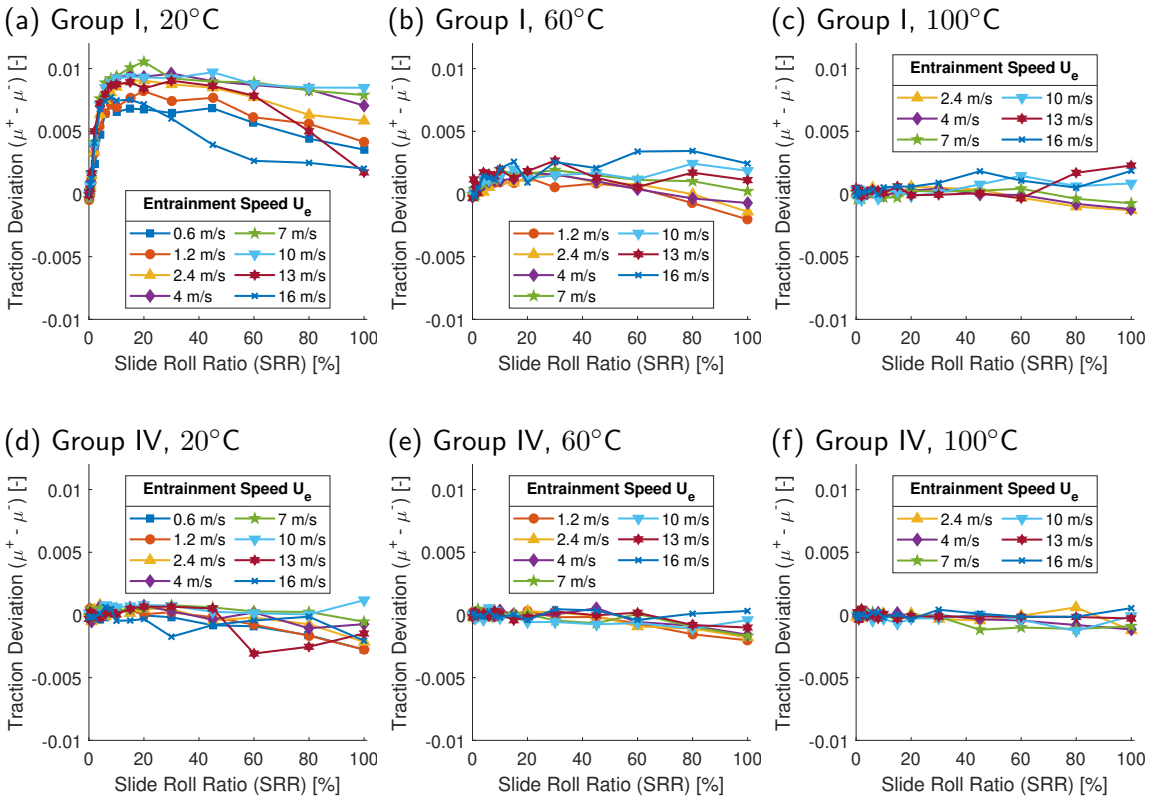


Figure 6.13: Difference between traction coefficient in forward and reverse sliding directions for Group I (a, b, c) and Group IV (d, e, f) fluids of similar ν_{100}, vs SRR for selected entrainment speeds. Traction difference is confined to within the noise threshold of ± 0.002 for PAO5 in the steel-on-glass contact at all three temperatures, but for the Group I fluid at the lowest temperature the average traction metric incurs errors $\sim \pm 0.005$.

traction difference varied with fluid viscosity, fluid type, and contact pressure, and was found only to be significant for fluids, viscosities and contact conditions leading to mean shear stresses greater than 4.0 MPa. Fig. 6.13 shows that the μ^+ and μ^- cases are significantly different at 20°C for the Group I fluid, but that this effect is not seen at the same temperature (and similar viscosity) for the Group IV fluid (at the lower contact pressure). This suggests that the effect originates from the rheology of the fluid in-contact, and not from the higher far-field fluid viscosity incurring a speed-dependent drag on the ball specimen and hence influencing the traction measurement. This demonstrates the validity of the assumption that the difference in drag due to oil flow around the ball between the forward and reverse sliding cases is negligible. In circumstances where the specimens in contact have different material properties, geometries and/or contact track lengths, it is therefore necessary to measure traction and film thickness in the forward and reverse cases separately, or at least to state the sliding direction. The definition in Eq. (6.5) should be avoided unless it can be shown not to

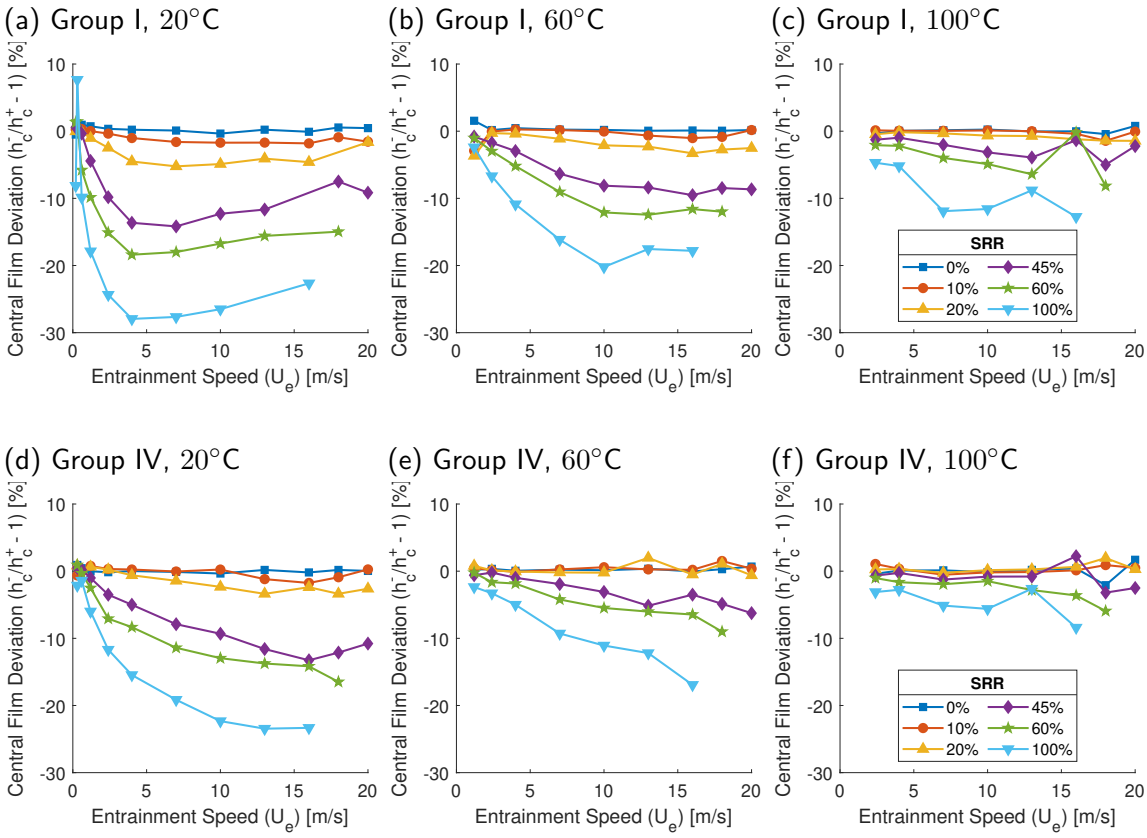


Figure 6.14: Percentage difference between central film thickness h_c in forward and reverse sliding directions for Group I (a, b, c) and Group IV (d, e, f) fluids of similar ν_{100}, vs entrainment speed for selected SRRs.

differ from the unidirectional case for all conditions tested.

The difference in central film thickness between forward and reverse sliding conditions is shown for a Group I and a Group IV fluid, each at three temperatures, in Fig. 6.14. This difference depends strongly on viscosity, and weakly on base fluid type at low speeds. It was only found to be significant at relatively high SRRs (>20%), and lower temperatures (higher viscosities, above ∼20 mPa.s) produce a more pronounced difference. At low speeds, the difference increases with entrainment speed. It appears from Fig. 6.14a that at 20°C there is an entrainment speed above which the effect diminishes in magnitude, approx. 4 m/s for the Group I fluid. From Fig. 6.14d this speed appears closer to 16 m/s for the Group IV fluid. Thus it seems that this speed depends on base fluid type (although the evident viscosity contribution may also be significant given these two fluids do not have the same viscosity at 20°C).

6.2.6 Shear Stress Response to Viscosity and Fluid Composition

Increasing the bulk fluid temperature, and hence reducing viscosity, has the effect of increasing shear strain rate due to the reduced film thickness, while also lowering friction in-contact, so reducing shear stress. The lower shear stress delays the onset of shear-thinning to higher strain rates. Mean shear stress vs strain rate is shown for three temperatures in Fig. 6.15, for two fluids. For the PAO, the forward and reverse sliding cases correspond very closely, whereas for the Group I oil they differ significantly across the whole speed range at low temperature, due to the traction coefficient difference shown in Fig. 6.13 for this fluid.

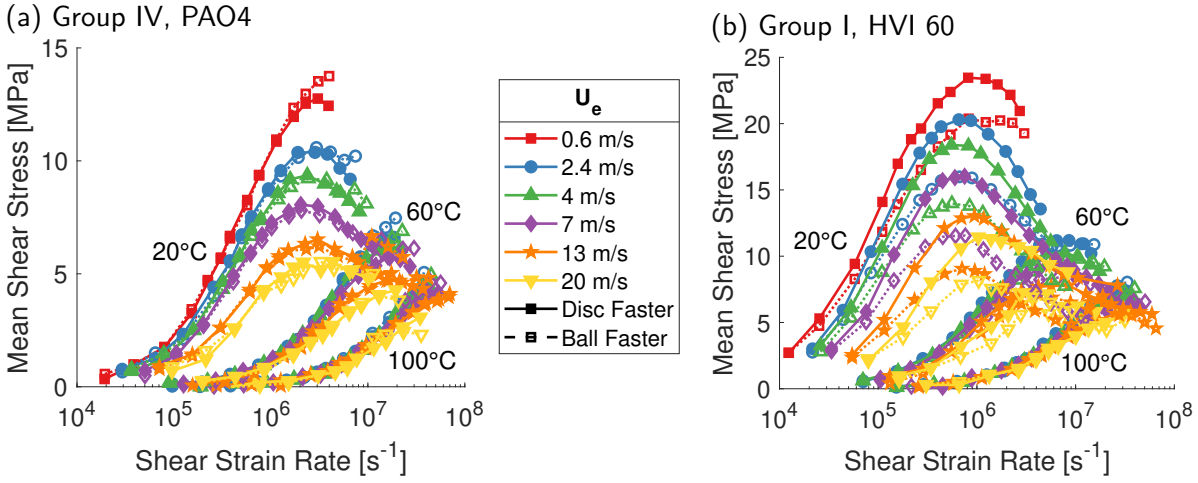


Figure 6.15: Mean shear stress $\bar{\tau}$ vs shear strain rate $\dot{\gamma}$ for base fluids in Group IV (a) and Group I (b) at three temperatures, steel ball on glass disc at 50 N load for selected speeds, showing the effect of base fluid type on shear stress under forward and reverse sliding.

Fig. 6.16 examines the mean shear stress vs shear strain for a higher-viscosity heavy mineral oil, for two temperatures. The shear stress in forward sliding is again higher than in the reverse direction and this discrepancy widens as entrainment speed increases. Note that the sequence of measurements was such that each slide-roll ratio was completed before moving on to the next, and that all slide-roll ratios were measured for a particular speed in order of increasing SRR, before moving on to the next entrainment speed. This means that the forward and reverse traction measurements (to give $\bar{\tau}$) for each SRR (hence for each $\dot{\gamma}$) were taken just seconds apart. The thermal inertia of the oil sump and steel casing are such that single-degree bulk temperature changes take minutes to come into effect, so the thermal contribution to the difference between forward and reverse traction seen here is certainly confined to contact length-scales (μm) and time-scales (μs).

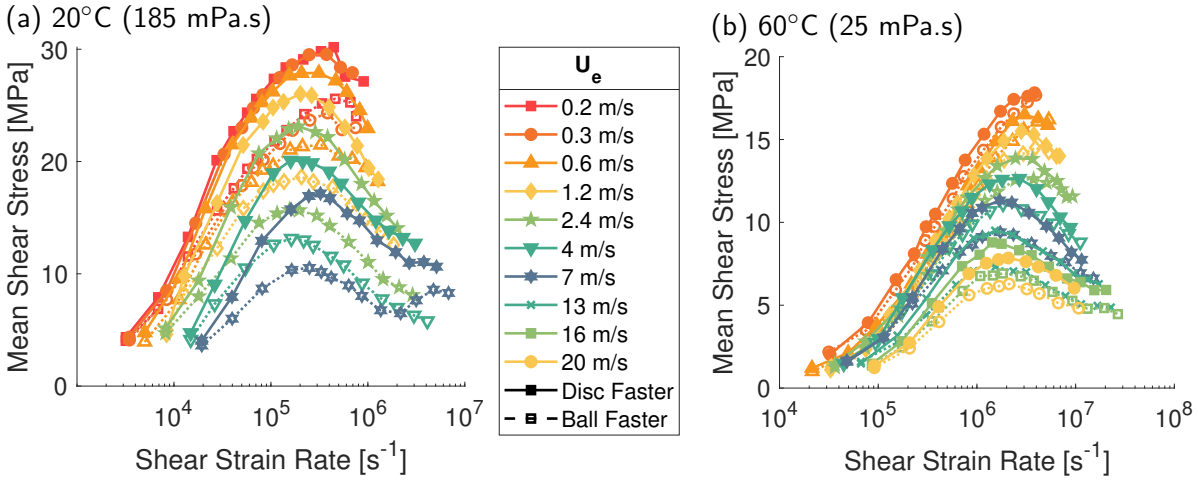


Figure 6.16: Mean shear stress $\bar{\tau}$ vs shear strain rate $\dot{\gamma}$ for higher-viscosity Mineral Oil at (a) 20°C and (b) 60°C, steel ball on glass disc at 50 N load for selected speeds, showing the effect of viscosity on shear stress under forward and reverse sliding.

Traction measurements and calculated mean shear stresses for the traction fluid Santotrac 50 are shown in Fig. 6.17. The rheology of this fluid differs significantly from the others studied here in that the fluid exhibits a far stronger pressure-viscosity response, and this leads to higher film thickness and to very high traction coefficients, which rise sharply in a Newtonian fashion with sliding speed and then (at low entrainment speeds) remain approximately constant, exhibiting a limiting shear stress [230]. For these high traction coefficients, sliding speeds were limited by the torque capacity of the ball drive motor, and so only slide-roll ratios below 20% were measured for this fluid.

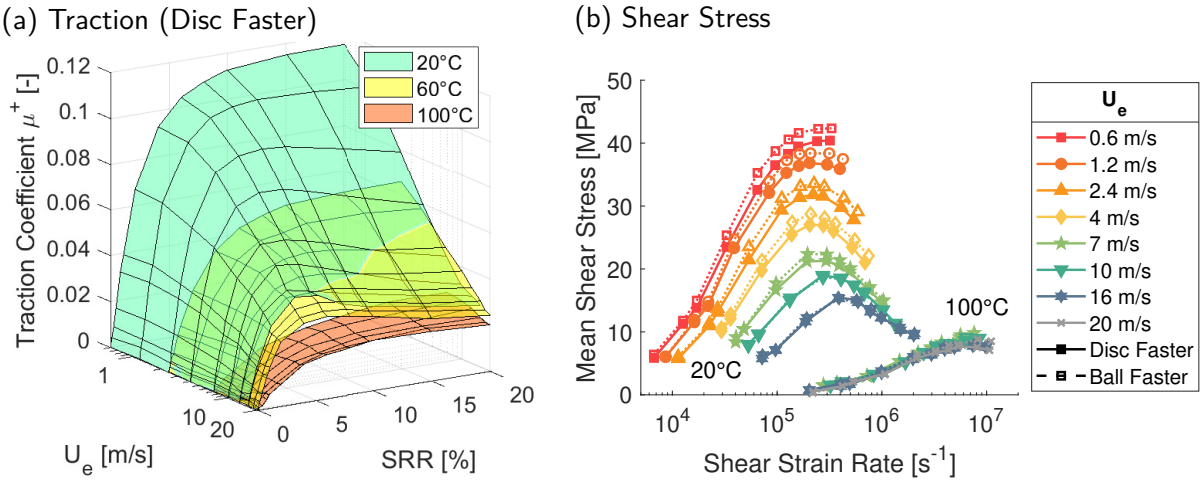


Figure 6.17: Traction vs U_e and SRR (a) and mean shear stress $\bar{\tau}$ vs shear strain rate $\dot{\gamma}$ (b) of the traction fluid Santotrac 50 for SRR$\leq$20%, steel-on-glass.

6.3 Discussion

As entrainment speed increases, it is seen that:

- Film thickness falls below the isothermal prediction of the form $h_c \propto U_e^{0.68}$. At lower viscosities, the effect is postponed to higher speeds.
- Film thickness and traction both depend increasingly on sliding direction. In a steel-on-sapphire contact, this dependence is stronger than in a steel-on-glass contact at the same load.
- Traction is increased in the Newtonian regime (at very low SRRs), and reduced elsewhere. The extent of this change strongly depends on viscosity - for viscosities around 4 cSt, traction almost does not depend on speed in the range 4 - 20 m/s.
- The 'plateau', shear-thinning, and Newtonian regimes are eventually absorbed by the thermoviscous regime, in which case traction is globally reduced, becoming a monotonically increasing function of sliding speed.

A prevailing question is, what is role of inlet heating in modifying traction and film thickness? Both inlet shear heating, and heating of the lubricant in the inlet by the solids must be considered (at high shear rates we may safely neglect the contribution of compression heating [112, 113]). Classical flash temperature analysis has followed Jaeger [119], who assumed the contact is bounded by two semi-infinite bodies whose inlet temperatures match the nominal bulk fluid temperature. At high speeds in a ball-on-disc tribometer with significant heat dissipation from the contact however, the surface temperatures at the inlet may become considerably higher than the bulk fluid temperature.

Consider the Biot number Bi (Eq. (6.11)), which examines the relative strength of convective and conductive modes at the ball surface, where κ is the thermal conductivity of steel.

$$\mathrm{Bi} = \frac{h_{\mathrm{conv}}}{\kappa} L_c \tag{6.11}$$

We shall assume a convective heat transfer coefficient $h_{\mathrm{conv}} \sim 500$ W/m^{2}K outside the contact, and conservatively take the characteristic length L_c as the ball radius (in reality the predominant thermal gradients are seen across much shorter lengthscales). This produces $\mathrm{Bi} \sim 0.2$, and so convection is slower than conduction, which means that heat diffusion within

the ball is the predominant path for heat energy from the contact track, before eventually being rejected elsewhere on the ball surface by convection. Conduction via the quill shaft which drives the ball can safely be neglected on account of its geometry.

Following Archard [120], we next consider a characteristic timescale for heat diffusion from the contact into the ball specimen t_d (Eq. (6.12)), where a is the contact half-width, and χ is the thermal diffusivity of steel. Consider also the time taken for the contact to traverse the circumference of the ball once, the recirculation time t_r.

$$t_d = \frac{a^2}{2\chi} \qquad t_r = \frac{2\pi R}{U_1} \qquad \frac{t_r}{t_d} = \frac{4\pi\chi R}{a^2 U_1} \tag{6.12}$$

We find that, for $U_{\text{ball}} \sim 20$ m/s, $t_r/t_d \sim 1$, and so for the EHD-HS which uses a 3/4" ball, and ignoring convection on account of the low Biot number, we conclude that the contact track is unable to reject heat to the rest of the ball fast enough for the surface temperature to have relaxed to the bulk temperature each time it re-enters the contact. The ball surface temperature will therefore rapidly rise during the test until a steady-state is reached, a circumstance which was observed during the tests by significant bulk fluid temperature rise in the vicinity of the ball at high speeds. Active cooling of the oil sump was employed to counteract this. It is worthy of note that high-speed EHD contacts in gears and bearings also recirculate, and the design of these machine elements will determine at what speed the thermal response of the solids becomes significant.

In Fig. 6.18, plots of two different calculations for mean temperature rise in the contact are overlaid on the shear stress plots from Fig. 6.12a on page 157. The first, shown by coloured lines, is given by Eq. (6.13) and follows the method of Olver (based on Jaeger's analysis) [118], with a modification for inlet shear heating given by $\overline{\Delta T_{\text{inlet}}}$ (Eq. (6.16)), which uses the measured film thickness h_c^{meas} to calculate a mean temperature rise in the inlet, found from the viscosity reduction required to bring the isothermal Chittenden prediction h_c^{iso} in line with the measurement, where T_{fluid} is the bulk fluid temperature in Kelvin. The expression for surface temperature rise in Eq. (6.14) assumes unity thermal partition coefficient, i.e. that all the heat is conducted into one surface only, which may be a good approximation in the case where the steel ball is the faster surface, given the thermal conductivity of glass is two orders

of magnitude smaller than that of steel.

$$\overline{\Delta T} = \overline{\Delta T_{\mathrm{s}}} + \overline{\Delta T_{\mathrm{oil}}} + \overline{\Delta T_{\mathrm{inlet}}} \tag{6.13}$$

$$\overline{\Delta T_s} = 1.064 \left(\frac{a}{k_s \rho c U_e} \right)^{\frac{1}{2}} h_c \bar{\tau} \dot{\gamma} \tag{6.14}$$

$$\overline{\Delta T_{\mathrm{oil}}} = \frac{\bar{\tau} \dot{\gamma} h_c^2}{8 k_{\mathrm{oil}}} \tag{6.15}$$

$$\overline{\Delta T_{\mathrm{inlet}}} = \frac{B}{\ln \left(\left(\frac{h_c^{\mathrm{meas}}}{h_c^{\mathrm{iso}}} \right)^{\frac{1}{0.68}} \frac{\eta(T_{\mathrm{fluid}})}{\eta_0} \right)} + T_0 - 273.15 - T_{\mathrm{fluid}} \tag{6.16}$$

The second prediction, shown by coloured markers in Fig. 6.18, invokes the rheology model of Johnson and Tevaarwerk [231], which employs the Eyring model with a viscoelastic term (Eq. (6.17)). A simplification for high-shear conditions is given in (Eq. (6.18)) which shows the linear relationship between $\bar{\tau}$ and $\log(\dot{\gamma})$ expected under isothermal conditions if the magnitude of the viscoelastic term can be ignored. The constant τ_e is the so-called 'Eyring stress', and η_p is the mean piezoviscous viscosity in the contact.

$$\tau = \sinh^{-1} \left(\frac{\eta_p}{\tau_e} \left(\dot{\gamma} - \frac{1}{G_p} \frac{\partial \tau}{\partial t} \right) \right) \tag{6.17}$$

$$\tau = \tau_e \ln(\dot{\gamma}) + \tau_e \ln \left(\frac{2\eta_p}{\tau_e} \right) \tag{6.18}$$

The prediction employs three (rather bold) assumptions:

1. At high shear rates the mean shear stress would continue to obey Eq. (6.18) if the contact were isothermal (i.e. Eyring shear thinning applies and a limiting shear stress is not reached).
2. The effect of heating in the contact is to modify the in-contact viscosity η_p, which at high pressures still obeys Eq. (3.1) on page 69, and the coefficients B and T_0 are independent of pressure.
3. The viscosity variation across the contact is linear such that the mean viscosity $\bar{\eta}_p$ can be found from the measurement of $\bar{\tau}$, and the viscosity variation is small enough that the mean contact temperature $\bar{T}_c$ is well-approximated by Eq. (3.1) given $\bar{\eta}_p$.

These assumptions are in strong contravention of the arguments of Bair [232] who has repeatedly pointed out that a traction curve is not a flow curve, and who argues that the Eyring

response is just a thermal artefact that masks true constitutive behaviour. They may therefore seem very limiting in the context of thermal EHL, but nevertheless they enable the calculation of a flash temperature rise using simple closed-form relationships which depend only on quantities measured in this study. The mean temperature rise in the contact $\overline{\Delta T}_E = \bar{T}_c - T_{\text{fluid}}$ is given by Eq. (6.20) where $\bar{\eta}_{p0}$ is the mean isothermal piezoviscous viscosity in-contact (that which would be achieved if all heating could be 'switched off'). Eq. (6.19) follows from assumption 2 above, and Eq. (3.1).

$$\frac{\bar{\eta}_{p0}}{\bar{\eta}_p} = \exp\left(\frac{B}{T_{\text{fluid}} - T_0} - \frac{B}{\bar{T}_c - T_0}\right) \tag{6.19}$$

Rearranging for $\bar{T}_c$ and letting $\overline{\Delta T}_E = \bar{T}_c - T_{\text{fluid}}$, we have

$$\overline{\Delta T}_E = \frac{B(T_{\text{fluid}} - T_0)}{B + (T_{\text{fluid}} - T_0)\left(\frac{\bar{\tau}}{\tau_e} - \ln\left(\frac{2\bar{\eta}_{p0}\dot{\gamma}}{\tau_e}\right)\right)} + T_0 - T_{\text{fluid}} \tag{6.20}$$

The value of $\bar{\eta}_{p0}$ is taken from the maximum-slope tangent fit to the shear stress data at the lowest speed. The Eyring stress τ_e, which varies with temperature [96] and hence, due to inlet shear heating, with entrainment speed, was found from the maximum-slope tangent at each speed. Consequently, τ_e was allowed to vary with speed while $\bar{\eta}_{p0}$ was not, the inlet-shear-heating temperature rise having been accounted for in Eq. (6.16).

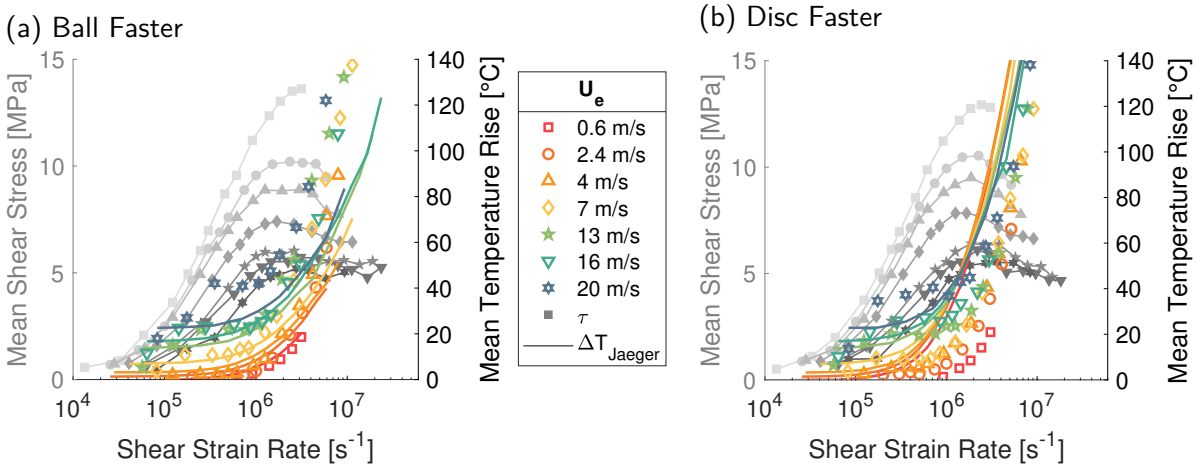


Figure 6.18: Two mean temperature predictions, one based on Eq. (6.13) (solid coloured lines) assuming all of the heat is taken by the faster surface, and one based on Eyring rheology (Eq. (6.20), coloured markers), overlaid on the measured mean shear stresses, in (a) the ball faster and (b) the disc faster case, for steel ball on glass disc

It is somewhat surprising considering the very unorthodox assumptions made in calculating the temperature rise $\overline{\Delta T}_E$ (coloured markers) that there is quite good agreement, for shear rates up to 2×10^6 s^{-1}, with the Jaeger-based prediction (coloured lines) in Fig. 6.18a. At higher speeds, where the recirculation effect is significant and the bulk solid temperatures rise, Eq. (6.13) must underpredict the true temperature rise in contact, and the markers illustrate this well, although the rheological and linearity assumptions in their evaluation also make their magnitude unreliable. This seems to suggest that at low speeds, the assumption that the ball takes almost all of the heat when it is the faster surface holds. At low shear rates but high entrainment speed, the effect of inlet shear on traction is considerable, and appears to be estimable from the film thickness measurement, which in itself is a significant finding. This does not hold in the case of the sapphire disc however, perhaps due to a much stronger recirculation effect from the higher heat flux arising from the high contact pressure even at low shear rates, which would cause the markers to considerably overpredict the temperature rise at low shear rates, as is seen in Fig. 6.19.

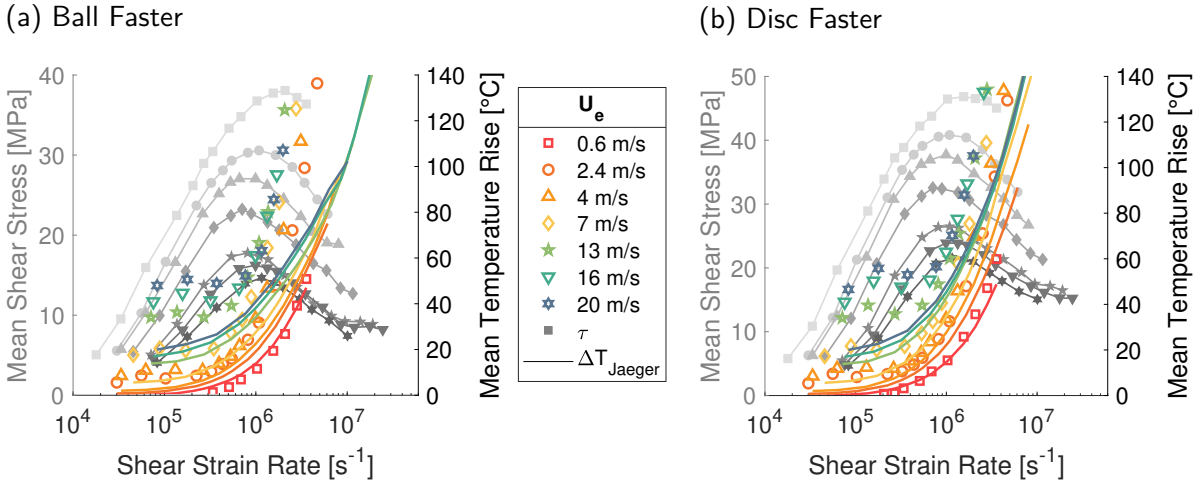


Figure 6.19: Two mean temperature predictions, one based on Eq. (6.13) (solid coloured lines) assuming all of the heat is taken by the faster surface, and one based on Eyring rheology (Eq. (6.20), coloured markers), overlaid on the measured mean shear stresses, in (a) the ball faster and (b) the disc faster case, for steel ball on sapphire disc

The Nahme-Griffith number Na describes the ratio of temperature rise caused by shearing to temperature rise required for significant ($\mathcal{O}(1)$) viscosity increase

$$\mathrm{Na} = \beta \frac{\tau \dot{\gamma} h_c^2}{\kappa_{\mathrm{oil}}} \tag{6.21}$$

where β is the temperature coefficient of viscosity taken here (at atmospheric pressure) as

$$\beta = -\frac{1}{\eta}\frac{\partial \eta}{\partial T} = \frac{B}{(T - T_0)^2} \tag{6.22}$$

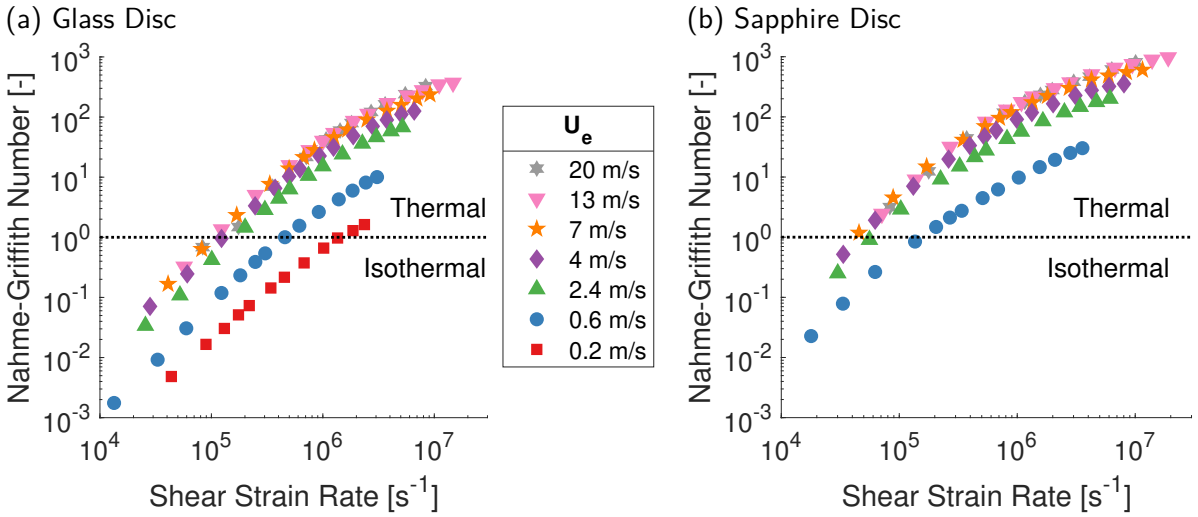


Figure 6.20: Nahme-Griffith number Na vs shear strain rate for the data from Fig. 6.12

When $\mathrm{Na} > 1$, the thermal viscosity reduction may be considered to make a significant change to contact traction. Na, is plotted in Fig. 6.20 for the results from Fig. 6.12, showing that for steel-on-glass, at the lowest speeds there is a clear isothermal region up to shear rates $\sim 10^6$, whereas for steel-on-sapphire, in almost all cases the fluid viscosity is strongly influenced by temperature change in contact (the Nahme-Griffith number does not, of course, account for the effect of inlet shear heating or solid recirculation). The results for steel-on-glass case at least, with a wide isothermal region, show that the Eyring stress is not just a thermal artefact. Fluid viscosity and entrainment speed therefore also fundamentally influence the contact temperature rise in this setup, as the ball and disc surface convective heat transfer coefficients outside the contact strongly depend on viscosity and speed (particularly as the flow transitions from laminar to turbulent).

The traction measurements clearly display the four distinct regimes detailed in the numerical study of Habchi, Bair and Vergne [233], namely linear, nonlinear-viscous, plateau and thermoviscous, as shown in Fig. 6.21. A key qualitative difference between their results and the experimental data obtained here however is the change in concavity of the traction curves in the thermoviscous region (see Fig. 6.8), indicating a second plateau at very high

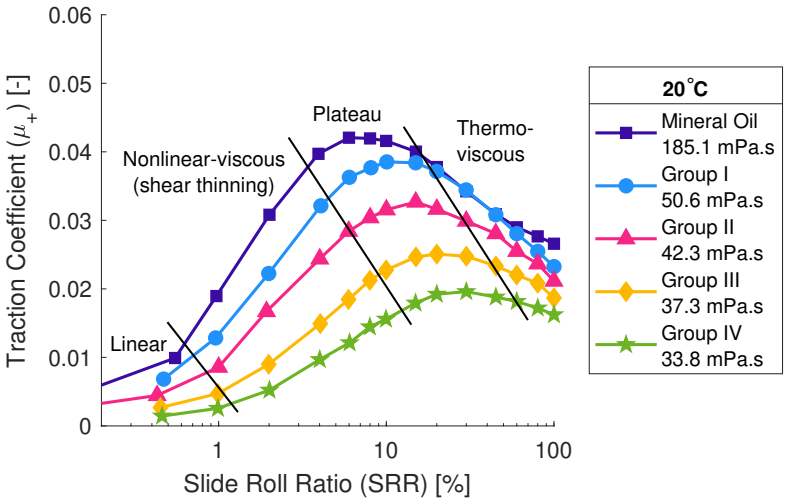


Figure 6.21: Traction curves from Fig. 6.8b, highlighting four distinct traction regimes as defined by Habchi *et al.* [233]

sliding speed. This difference is corroborated by the experimental results from Wedeven's WAM tribometer at lower speeds presented by those same authors in Björling *et al.* [101], which display the same change in concavity as the results presented here. The discrepancy is concluded by Björling to be attributable to the numerical treatment of fluid rheology. The higher-speed measurements here, combined with simultaneous film thickness measurement, enable the effect to be examined with respect to mean shear stress and shear strain rate.

Firstly, the thermal reduction in shear stress appears to act in all cases before a limiting shear stress is reached - the shear stress curves have quite sharp peaks even at low speeds in Fig. 6.16, and the deviation from the Eyring line in Fig. 6.12 coincides very closely with the point at which the Nahme-Griffith number rises above unity in Fig. 6.20.

Secondly, it appears that in the thermoviscous region, thermal recirculation by the specimens (even, in Fig. 6.16a, at quite low speeds) has a highly significant effect on traction, leading to quite different traction coefficients and shear stresses for equivalent shear strain in forward and reverse sliding for some fluids. Regrettably, it is rarely made clear in the literature whether measurements of forward, reverse, or an average traction value are being quoted - these three metrics may produce very different values. In some cases, choosing the average traction would widen the shear stress plateau, as the thermal reduction causes a local maximum at different shear rates for the two sliding directions, giving the illusion of limiting shear stress behaviour. In addition, the confounding effect of macroscopic viscous drag on the traction

measurement increases at high speeds under high sliding conditions in both the EHD-HS and WAM tribometers. The result may therefore be an artefact of the ball-on-disc experimental setup rather than the fluid rheology.

Thirdly, it appears, although the relevant shear rates were not reached in this study, that for very high shear rate ($\sim 10^8$ s^{-1}) there is some thermoviscous limit to which the mean shear stress converges at all speeds. For the fluids studied, regardless of viscosity, this appears to lie somewhere between 5 and 10 MPa. In this limit, it is tentatively proposed that the viscosity in-contact would become highly non-uniform in the entrainment direction and the central plateau would shrink. Toward the thermoviscous limit, the exponential decrease in viscosity with temperature would outstrip the lower-order dependence of temperature on shear strain rate, yielding approximately constant traction at very high sliding speeds as shear-heating competes with shear thinning. This is however only conjecture - the fluid rheological response under these extreme conditions is a subject of considerable debate, and experiments which could cool the fluid fast enough to obtain stable steady-state conditions and take relevant temperature measurements would be challenging. Only experimental work under EHD-representative pressures and shear stresses, for example in actual EHD contacts, is currently capable of definitively resolving this question. The use of the infrared mapping technique [234, 235] with the new EHD-HS for example, would enable contact-scale temperature variations to be measured in-situ in this setup, thereby allowing the rheological implications of both inlet shear heating and shear heating in-contact for traction and film thickness to be directly examined.

6.3.1 Difference in Traction with Sliding Direction

It can be seen from Fig. 6.12 that at high viscosities, even at modest sliding speeds within the Newtonian regime, shear stress is lower at high entrainment speeds, highlighting the thermal coupling between inlet shear and shear in-contact. (At low viscosities by contrast, the Newtonian regime proliferates to much higher strain rates ($\sim 10^7$ s^{-1}) on account of the shear stress remaining well below τ_e, which here is around 4.0 MPa, and the effect of entrainment speed is greatly reduced.)

The consistent discrepancy between film thickness in the positive and negative sliding cases is also relevant. By their nature, the specimens in the EHD-HS see the contact repeatedly

pass over any given point on the track, and the pass frequency increases with speed. A speed must exist where the specimen surface does not have time to cool to (nearly) the far-field temperature before it is recirculated into the contact, and in this case the temperature profile of the contact must change by comparison to the hypothetical case where the material ahead of the contact is always at the far-field temperature. This is different for each surface, and depends on the recirculation time, which is a function of the both the geometry and the speeds - here the disc track is between 3.6 and 4.6 times longer (depending on chosen disc track radius) than the ball track, and although the thermal bulk of the glass is larger in total, it has a much lower thermal conductivity than steel [236]. All of these conditions imply the ball would take on heat more rapidly (owing to its higher thermal diffusivity), and would lose it by convection less rapidly elsewhere (owing to its smaller surface area per unit volume) than the glass disc, if all else were equal.

Under sliding conditions however, a longer portion of the track on the faster surface is in contact per unit time than on the slower surface, affording the faster surface greater opportunity to take on heat. Consequently, if this surface becomes considerably hotter than the far-field temperature, there is less opportunity for the contact to cool via this surface, and near to the inlet, the entrained fluid may be heated. The ball, with its shorter recirculation time and higher diffusivity, is therefore likely to assume a higher upstream temperature, and therefore to give a higher temperature rise in-contact when it is the faster surface. The test constantly oscillates between forward and reverse sliding conditions, spending only a few seconds in each, too short a time for the bulk fluid temperature to change significantly, so this effect is certainly contact-local. The film thickness is lower in reverse sliding by up to 25% in some cases, the magnitude of the difference increasing with speed (shorter recirculation time) and SRR (higher heat flux).

It is therefore unsurprising that the effect of reversing sliding direction on traction and mean shear stress is considerable in cases of high shear stress, and in cases where a significant heat flux is likely to be very unequally partitioned between bodies. For all fluids except Santotrac 50, when the ball is faster, lower or equal traction is measured compared to the disc-faster case. Fig. 6.22 shows the disc-faster shear stresses from Fig. 6.12 overlaid with the ball-faster case. For steel-on-sapphire with PAO5 at 20°C, the traction difference is very significant. Fig. 6.16 shows the same is true of the high-viscosity mineral oil. The ball-faster case also

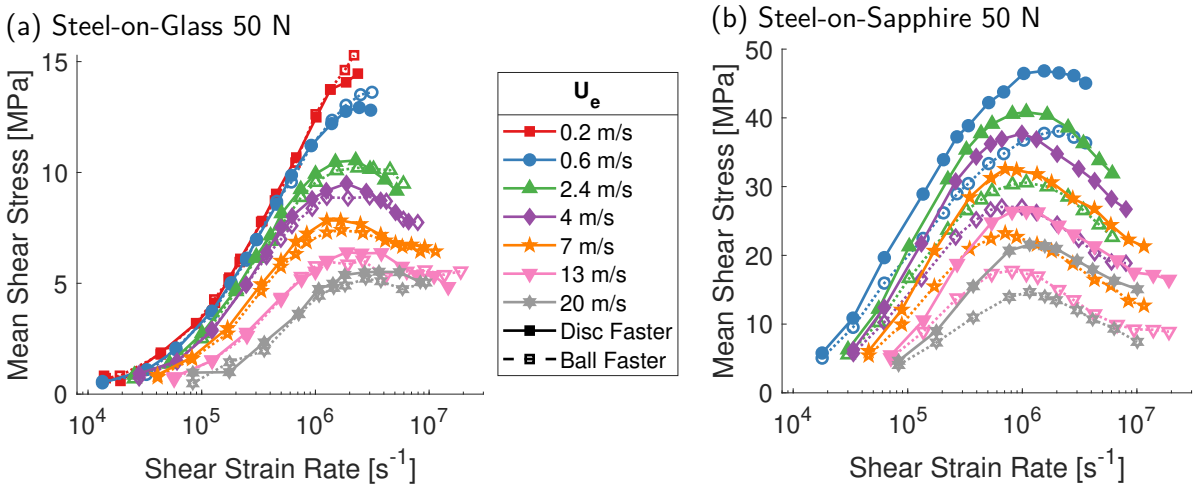


Figure 6.22: Mean shear stress $\bar{\tau}$ vs shear strain $\dot{\gamma}$ for PAO5 (Group IV) with a steel ball on glass disc (a) and sapphire disc (b) at 20°C and 50 N load for selected speeds showing both forward and reverse sliding directions.

produces lower film thickness, which implies higher inlet temperature, and hence lower viscosity in-contact, leading to lower traction. Both traction and film thickness differences are greater at higher entrainment speeds.

A notable exception is the traction fluid, for which the ball-faster case imparts slightly higher traction, and the effect is instead strongest at low speeds, although the film thickness trend remains the same as for the other fluids: ball-faster incurs (very slightly) lower film thickness. This suggests that in the case of the very high traction coefficients and therefore heat fluxes for Santotrac 50 at low speeds, the recirculated heat is small compared to the flash heating, and so the ball-faster condition enables the contact to run cooler on account of the greater thermal conductivity of steel. The thermal conductivity of Santotrac 50 was measured by Larsson [237] to be about half of that for other common lubricating base oils, and this effect proliferates at high pressures, which could further increase the influence of heat storage within the film, and diminish the effect of surface heat recirculation.

At high speeds, increasing the SRR (which strongly increases flash temperature) has a significant impact on film thickness, and this effect is stronger in reverse sliding, suggesting that the recirculation of shear heat from the contact into the inlet is responsible for this. It should be noted however that SRRs in the range between 60% and 200% are unusual in machine elements, so the influence of high-sliding conditions on EHL film thickness is not commonly seen in real applications. This effect is generally less significant than the influence

of entrainment speed on film thickness, compared to the isothermal case.

6.3.2 Viscoelasticity

The Johnson and Tevaarwerk model [238] expresses shear strain rate $\dot{\gamma}$ according to Eq. (6.23), as the sum of the viscous ($\sinh$ term) and elastic ($\frac{\mathrm{d}\tau}{\mathrm{d}t}$ term) response.

$$\dot{\gamma} = \frac{\tau_e}{\eta_p} \sinh\left(\frac{\tau}{\tau_e}\right) + \frac{1}{G_e}\frac{\mathrm{d}\tau}{\mathrm{d}t} \tag{6.23}$$

The relative strength of the elastic response is indicated by the Deborah number D (the ratio of fluid relaxation time to transit time), with elastic shear significantly lowering mean shear stress where $D > 1$.

$$D = \frac{\eta_p U_e}{2aG_e} \tag{6.24}$$

The equivalent shear modulus G_e, accounting approximately for the additional effect of elastic deformation in the solids, is found from the parallel combination of the fluid shear modulus G_p, and the reduced contact modulus multiplied by the aspect ratio of the contact [239].

$$\frac{1}{G_e} = \frac{1}{G_p} + \frac{2a}{E'h_c} \tag{6.25}$$

The conclusions drawn about the significance of viscoelasticity based on the value of D strongly depend on the assumptions made in evaluating G_p and η_p, both of which are strong functions of temperature, pressure, and molecular structure. In lieu of a model for G_p, the exponential in Eq. (6.26) is fitted to the values of $\bar{\tau}$ and $\dot{\gamma}$ calculated from the reported traction measurements where $\mathrm{SRR} < 5\%$ (Fig. 6.23a), and A and B are positive fitting coefficients. G_e is then obtained from Eq. (6.27), according to the method used by Loewenthal and Rohn [240].

$$\bar{\tau} \approx A\left(1 - e^{-B\dot{\gamma}}\right) \tag{6.26}$$

$$G_e \approx \frac{U_e}{a}\left.\frac{\partial\bar{\tau}}{\partial\dot{\gamma}}\right|_{\dot{\gamma}=0} \approx AB\frac{U_e}{a} \tag{6.27}$$

This method has the disadvantage that it requires the Deborah number to be high (Johnson and Tevaarwerk [238] suggest $D > 100$), which for most fluids requires pressures not achieved

in this study. However, if it is the case that D is low, then viscous shear superposes with elastic shear and the film appears more compliant, reducing G_e and increasing D. This means the values of D calculated here are in their upper limit.

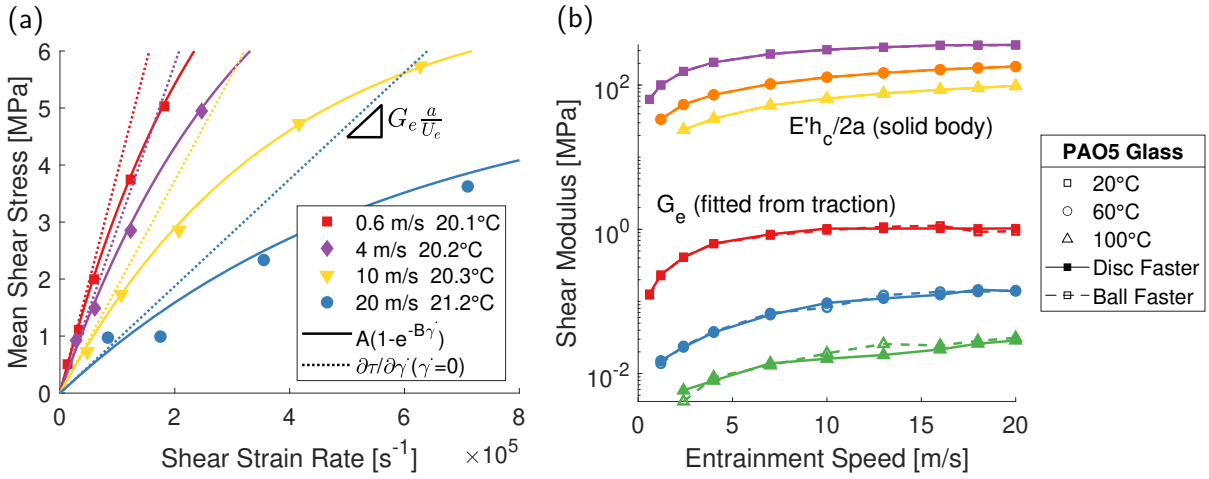


Figure 6.23: (a) Eq. (6.26) fitted to $\bar{\tau}$ vs $\dot{\gamma}$ for $\mathrm{SRR} < 5\%$ at four entrainment speeds, for PAO5 with glass disc, showing tangent to curve at $\dot{\gamma} = 0$ and gradient used to find shear modulus G_e. (b) shows the values of G_e calculated and compares them to the reciprocal of the solid elastic compliance term $E'h_c/2a$.

It can be seen in Fig. 6.23b that the reciprocal elastic compliance $E'h_c/2a$ is over 2 orders of magnitude higher than the value of G_e calculated from the fits to traction measurements, whereas we might expect them to be of comparable order, especially given the relatively low E' of the steel-glass contact. This supports the hypothesis that if D is low, and viscous shear predominates, the 'shear modulus' is underestimated. G_p is expected to increase approximately linearly with pressure (and the gradient is reduced by increasing temperature), so higher temperatures produce lower shear moduli. The fact that the 'shear modulus' appears to increase with speed here (instead of remaining constant, as would be expected isothermally, or decreasing due to inlet shear heating at high speeds) also supports this hypothesis.

The mean piezoviscous viscosity in the contact η_p is calculated using the improved Yasutomi correlation fitted to viscosity measurements of PAO4 at high pressure by Bair [241]. Firstly it is assumed that the PAO5 used in the present study bears sufficient rheological similarity to PAO4 that its viscosity can be estimated from fits for PAO4 by adjusting the temperature given to the Yasutomi correlation (downwards) to that at which PAO4 has the same atmospheric-pressure viscosity as PAO5 at the nominal temperature. Secondly, the pressure assumed is

the mean Hertz pressure. These two approximations allow η_p to be estimated to within an order of magnitude. Despite these assumptions, which are likely to significantly overestimate the value of D, the Deborah number is found to be less than unity in all cases except for the lowest temperature with the sapphire disc, where the value remains below 4. The shear modulus would therefore be underestimated by fitting to traction measurements, and as a result it is likely that $D < 1$ holds for PAO5 at both contact pressures tested. It is concluded that viscoelastic effects, which become more significant at high entrainment speeds when transit times are short, and at high shear stresses, are unlikely to dominate in this study, but may possibly be non-negligible for the higher-viscosity lubricants at the highest speeds. Definitively evaluating D for these cases would require values of η_p and G_p at high pressure which are challenging both to measure and to estimate, particularly at contact pressures for which viscous shear and elastic shear are of similar order and so difficult to decouple. At higher contact pressures, in the region of 2.0 GPa, the contribution of viscous shear is much reduced by the pressure-viscosity response of most oils, and this allows the shear modulus to be estimated from traction measurements with high-pressure rolling-sliding tribometers like the ETM [11, 117]. The relevance of shear modulus measurements at very high pressure to traction at lower contact pressures, such as those practicable in a steel-on-glass contact, is questionable.

6.3.3 Measurement Limitations

The assumption that, in the F_0^+ and analogous F_0^- cases, the zero-sliding traction force from the contact is negligible, may break down at high entrainment speed, where there is clearly a viscous (inlet shear) contribution to traction. The Poisseuille contribution (proportional to the streamwise pressure gradient) is also expected to change as the film thickness and pressure profiles change shape with speed. This may account for some of the reduction in traction at low-sliding but high-entrainment speed conditions. In addition, the spin in the contact, resulting from perpendicular axes of rotation of the ball and disc, may influence the traction behaviour, although the difference in entrainment speed from one side of the contact to the other is very slight, estimable by the ratio of the contact width to the disc track radius, which is less than 1%. The small contribution of both of these effects to traction force is not expected to significantly influence the trends presented except at very small slide-roll ratios

of less than 2% in magnitude, and no attempt is made here to quantify or compensate for these. The values for traction coefficient presented herein should therefore be considered in deference to these assumptions.

6.4 Conclusions

A new high-speed optical tribometer has been employed to simultaneously measure film thickness and traction in an elastohydrodynamic contact up to 20 m/s for the first time. Film thicknesses were measured using ultra-thin-film interferometry, and traction was measured using a novel traction measurement procedure developed in this study. The technique has been used to map traction and film thickness for entrainment speeds between 0.2 m/s and 20 m/s, and SRRs between 0% and 100%, for base fluids representing those in common use in transmissions, spanning API Groups I - IV and including a traction fluid. The main findings are:

- The results at low speeds show good agreement with existing traction and film thickness measurements for these fluids.
- The simultaneous measurement of film thickness and traction has enabled mean shear stress and mean shear strain rate to be calculated from measurements, enabling the thermal dependence of the mean shear stress in the plateau and thermoviscous traction regimes to be examined.
- At entrainment speeds above a certain threshold (the exact value of which depends on the fluid type and viscosity) the measured film thickness is lower than that predicted using classical isothermal EHL regression equations. A difference of up to 100% of the measurement was found at the highest speeds.
- The deviation from the isothermal film thickness prediction is found for all fluids to match the prediction of Gupta quite well in pure rolling, but for rolling-sliding contacts Gupta predicts considerably lower film thicknesses than those measured.
- The reduction in film thickness was observed under fully-flooded conditions, so was not caused by starvation in any of the tests here.
- The shear rate at which mean shear stress deviates from the Johnson and Tevaarwerk model is that at which the Nahme-Griffith number exceeds unity, up to a shear stress

of 35 MPa in a steel-on-sapphire contact with PAO5. Consequently no isothermal behaviour attributable to a limiting shear stress is seen under these conditions.

- Both traction and film thickness depend on sliding direction in a high-speed ball-on-disc setup where the bounding surfaces are made of dissimilar materials and the specimens rotate at different angular frequencies. The effects of sliding direction were found to increase with sliding speed, max. Hertz pressure, and fluid viscosity. The film thickness difference is significant in this study above 20% SRR. The traction difference is significant in cases where the mean shear stress exceeds 4.0 MPa. The magnitude of the difference is likely to depend on the relative thermal resistances of the two contacting bodies (which varies significantly among tribometers), and their relative recirculation rates, which varies with specimen geometry, entrainment and sliding speeds.
- The results show that at speeds which are commonly encountered in electric vehicle transmissions, aerospace engines, and other high-speed applications, the oil film thickness and traction behaviour differs significantly from the conventional theory derived from isothermal observations at low and moderate speeds. These results can therefore help to inform the design of such high-speed systems, not least in optimising lubricant formulation.

Chapter 7

Influence of Fluid Formulation on Surface Damage: Micropitting and Scuffing

Optimising fluid viscosity and formulation for maximum transmission efficiency is futile without also considering durability and surface damage. Efficiency and reliability must therefore be studied in parallel to arrive at a lubricant formulation of any practical use. It was seen in Chapter 6 that for thermal EHL contacts such as those in EV gears and bearings, particularly at high contact pressures, film thicknesses and hence lambda ratios are lower than those predicted isothermally, which extends the speed range in which gears potentially operate in mixed and even boundary lubrication. In this chapter, two studies are presented, each aiming to isolate the effect of fluid formulation on damage progression and severity in an accelerated test, for contact conditions otherwise representing those of EV drivetrain gears. Micropitting and scuffing are chosen as predominant gear failure modes which are difficult both to predict and to reproduce experimentally.

The fluids used are chosen as 'candidate transmission lubricants' to represent those which are in widespread use in geared transmissions: a gear oil, an ATF, the base fluid of the ATF (PAO6 blended with a small fraction of ester), PAO5, and (although not currently suitable for geared EV transmissions) an experimental water-based formulation. The fluids were each blended to have similar viscosity to PAO5 (around 5 cSt at 100°C, and 20 cSt at 40°C), by colleagues at the Valvoline New Product Development laboratory in Lexington, KY, USA, to whom many thanks are extended. The water-based fluid, on account of its much weaker pressure-viscosity response, was formulated to higher viscosity than the other fluids (∼30 cSt at 40°C) to enable similar elastohydrodynamic film thickness to be developed under equivalent conditions. Throughout these studies, controlled temperatures are chosen to match the minimum EHL film thickness generated by the fluids as predicted by isothermal regression equations. The

physical properties of these fluids are detailed in Chapter 3.

7.1 Micropitting

Low-viscosity lubricants, and therefore low lambda ratios in EV gear and bearing contacts which are also subject to high Hertz contact pressures ($\sim$1.5 GPa for gears, higher for bearings), are likely to increase the rate of micropitting [182, 194, 206, 242, 243]. The formulation of additive systems able to control micropitting therefore is a critical task in the development of low-viscosity EDFs. This is not an easy task however, given the many factors on which micropitting depends (an overview of previous work is given in Section 2.8), and the difficulty in quickly and repeatably comparing the micropitting performance of new formulations over many millions of contact cycles. One approach, used in this study, is to accelerate the test by imparting contact cycles in quick succession using high rotational speeds, adjusting temperature and contact geometry to match the lambda ratio to that experienced in application. It is assumed that the rate at which contact cycles are accumulated does not significantly influence the progression of micropitting, provided it is decoupled from all other parameters (e.g. film thickness, heat fluxes).

Each tooth on the high-speed drive pinion of the gearbox discussed in Chapter 4 sees 6803 cycles per mile, or 6.8×10^8 contact cycles per 100,000 miles, which means if the drive unit lifetime is expected to exceed 150,000 miles (240,000 km), the gear teeth must reach gigacycle fatigue life. Zhao *et al.* [244] found, by examining the odometer readings of used vehicle listings in the US, that many ICE-powered vehicles have driven considerably further than 150,000 miles in the first 9 years of their life, but that EVs have accrued mileage at a lower (although recently increasing) rate on average, and most have not exceeded 100,000 miles after 9 years. The load history during this lifetime depends strongly on vehicle use case. For an EV used primarily for long-distance driving at high speeds, assuming fluid viscosity similar to the ATFs of KV100 6 cSt presently in use, the gear contacts will likely spend most of their life operating at lambda ratios greater than 1, with minimal dynamic loading. Under full-film conditions, the thermal response of the contact at these high speeds reduces friction, and so local shear stresses, a finding discussed in Chapter 6. By contrast, an EV used for city driving at low speeds with a next-generation lubricant of KV100 4 cSt or lower, by a driver

prone to rapid acceleration and braking on routes involving steep gradients, creates a load history involving sustained high contact pressures at low lambda ratios for which the thermal feedback increases friction, thereby creating the conditions under which micropitting cracks form and grow.

Both entrainment and sliding speeds (hence film thickness and friction) vary across the path of contact on the gear tooth flank. The sliding speed is zero at pitch point, either side of which the sliding acts in opposite directions: the dedendum of a given tooth is the slower surface. For this case, in which the surface of interest moves more slowly than the counterface, the slide-roll ratio is commonly defined in the micropitting literature as negative. Rycerz et al [115] have recently shown the stress state in this case to be particularly deleterious to fatigue life. The addendum of the tooth is the faster surface and in this region SRR is positive. The tooth flank section at most risk of micropitting is therefore likely to lie just below the pitch point in the dedendum of the pinion, where film thickness is minimum and contact pressure is highest because of the smaller reduced radius of curvature, SRR is a small negative value, promoting micropitting, and the driving face of the pinion accrues the most contact cycles (although the location of the micropitted region has also been shown to depend strongly on wear [191]). The contact conditions used are chosen to match those in this region.

The micropitting tests presented here do not attempt to reach the gigacycle regime, nor do they aim to reconstruct the complex load history of an EV. A single contact pressure near the upper limit of that predicted for the gear contacts is chosen and sustained throughout the test, which is found to generate micropitting damage within millions of cycles. The specimen which sees most contact cycles has considerably lower hardness for these tests than the counterfaces, which acts to accelerate micropitting. These conditions do not represent the wide fluctuation in contact pressure seen by EV gears on the road, and a hardness difference of this size is not usually the case in a gearbox. However, these conditions reliably reproduce micropitting, enabling a robust and relatively quick comparison between fluids of propensity to cause micropitting - it is this comparison which is the focus of this section.

7.1.1 Micropitting Test Method

A micropitting test procedure developed incrementally by Olver and coworkers [198, 245] and more recently by Wainwright et al [193], employing a triple-disc test machine, is adopted to enable monitoring of micropitting damage progression, and a repeatable comparison to be drawn between fluids. The method uses the MPR from PCS Instruments, which comprises a roller test specimen rotating between three larger rings (see Fig. 7.1), such that any point on the roller contact track sees three contact cycles per roller revolution. The three rings co-rotate and are driven by a single servomotor via a gearbox. Another servomotor drives the roller via an inline torque sensor, allowing measurement of roller drive torque, which is proportional to the total friction force imparted by the three contacts. The centres of rotation of the three rings form an equilateral triangle, and the roller is positioned at the centre of this triangle. The shafts carrying the lower two rings are fixed, while the upper ring shaft is able to travel vertically and is supported via a distant pivot. The pivoting assembly is clamped to a compliant beam, shown in Fig. 7.2, which at its other end is connected via a hinge joint to a nut that translates on a rotating lead screw driven by a stepper motor via a reduction gearbox. The roller is loaded by turning the lead screw which advances the nut, thereby bending the beam and imparting a moment on the upper shaft mount block about its pivot. This moment transfers a load to the contact between the upper ring and the roller. The strain on the

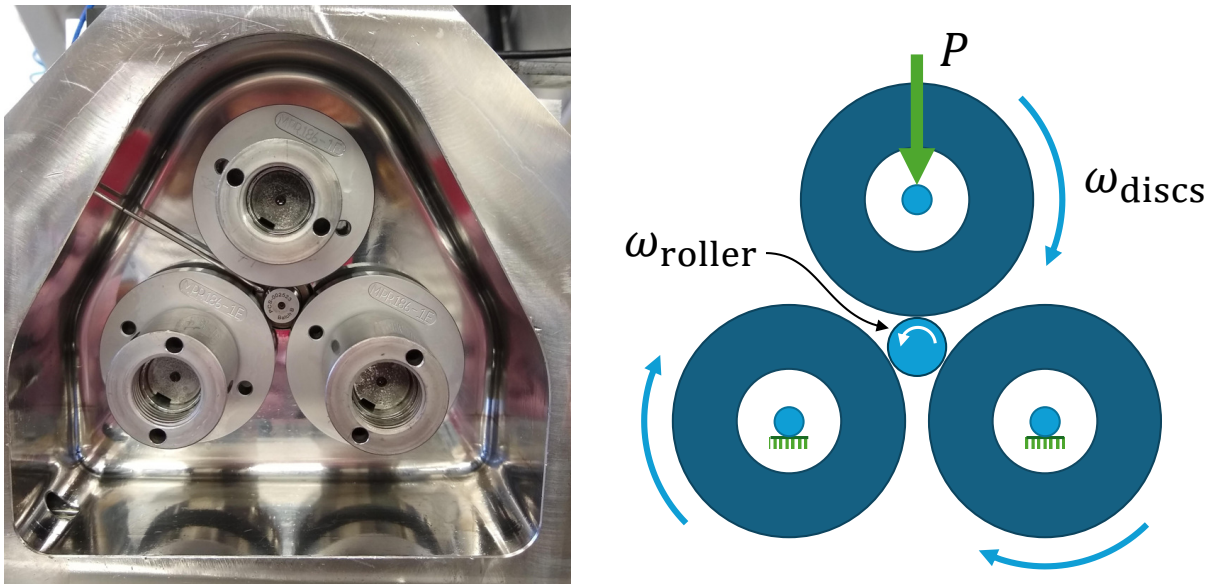


Figure 7.1: Configuration of 3 rings and roller in MPR rig, showing actual specimens and temperature probe placement (left), and direction of rotation and application of load (right).

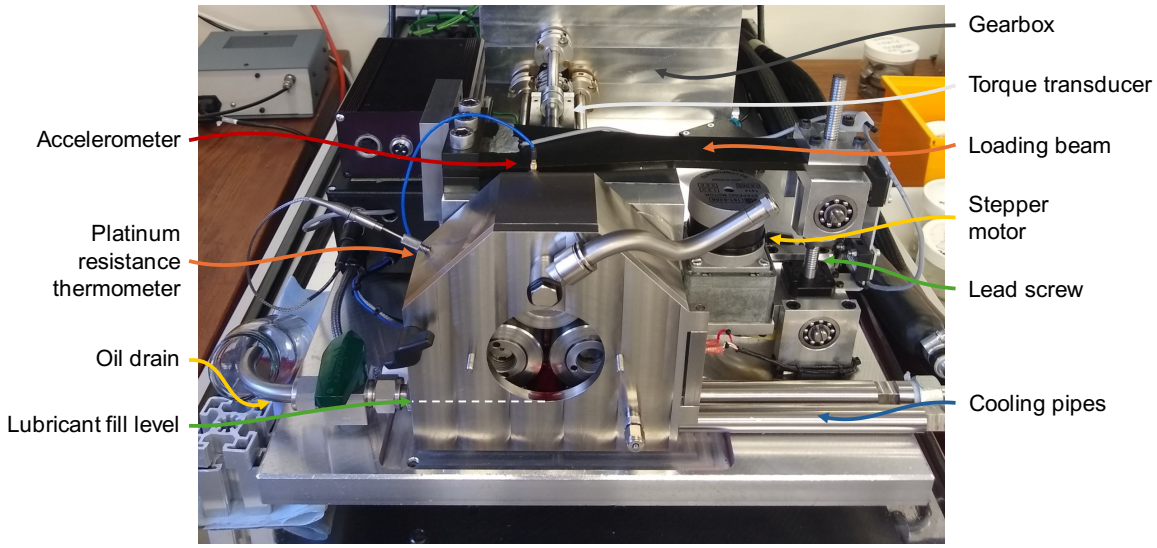


Figure 7.2: MPR rig showing configuration of driveshafts and loading system

surface of the beam near the clamping point is measured by a series of strain gauges, and the stiffness of the system is ascertained by calibration, enabling continuous measurement and control of contact loading via the stepper motor. The equilateral arrangement of the shafts causes each of the three contacts to supply the same load to the roller. The roller is therefore supported by three contacts whose loading, geometry and kinematics are identical.

Before beginning each test, the test chamber was cleaned with toluene, paper towel and compressed air until no oil residue remained, and then again with isopropanol to remove any traces of toluene. The test specimens and fixtures (rings, roller, collets, spacers, lock rings, damping rings and o-ring seals) were kept segregated in left, right and top shaft sets (as applicable). Each set was immersed in toluene in a glass jar placed in a water-bath sonicator for 5 minutes. The specimens and fixtures were then removed, dried with compressed air, immersed in isopropanol and returned to the sonicator for 5 minutes, after which they were dried again with compressed air. The specimens were mounted and the rig was filled with the oil to be used for that test. The rig was then heated up to 60°C and run at 3 m/s entrainment speed, 0 SRR, under no load, for 60 minutes, to flush the seals with the new fluid. The fluid was then drained, the specimens and fixtures removed from the rig and the cleaning process repeated as above. During the flushing procedure, dummy specimens were used and no roller was mounted.

Table 7.1: Micropitting test procedure of Wainwright [193], indicating number of roller cycles completed during each step, and which components are inspected once that step is complete. The roller is inspected using both optical microscopy and stylus profilometry, whereas the rings are inspected using a stylus profilometer only.

Step	Cycles $\times 10^6$	Cumulative	Roller inspected	Rings inspected
1	0.05	0.05	✓	✓
2	0.05	0.1	✓	✓
3	0.45	0.55	✓	✓
4	0.45	1	✓	✓
5	1	2	✓	×
6	1	3	✓	×
7	2	5	✓	×
8	2	7	✓	×
9	4	11	✓	✓

The ring specimens used were cylindrical in shape with radius 27.075 mm and 8 mm axial extent, chosen such that the RMS surface roughness of each set was $R_q = 500 \pm 20$ nm on the outer surface. It was shown by Wainwright [243] that R_q has a very strong effect on micropitting rate and so a tight tolerance for ring roughness is required to prevent this effect from undermining the comparison between fluids. The roller specimen comprises a convex biconic section of axial extent 8 mm, with a central 1 mm chamfer creating a cylindrical surface of radius 6 mm. At one end is a further 4 mm slotted boss used to drive the roller, with radius 6 mm.

The hardnesses of selected 16MnCr5 ring and roller specimens were measured by polishing the flat non-working face to a mirror finish, and conducting 4 hardness indents distributed across the polished face of each specimen using a Vickers hardness tester using a 30 kg load. Mean roller hardnesses were found to be 670 $\pm$ 15 HV30, and mean ring hardnesses were 770 $\pm$ 10 HV30, hence the hardness difference between rings and roller was ≈ 100 HV30.

The roller specimen and each of the rings were inspected using a Form Talysurf stylus profilometer by Taylor Hobson, as shown in Fig. 7.3. Four traces were taken on the cylindrical surface of each specimen, with the needle traversing axially, spaced equally around the circumference, A digital optical microscope by Hirox was used to inspect the roller in the same locations as shown in Fig. 7.4. These inspections were conducted before commencing

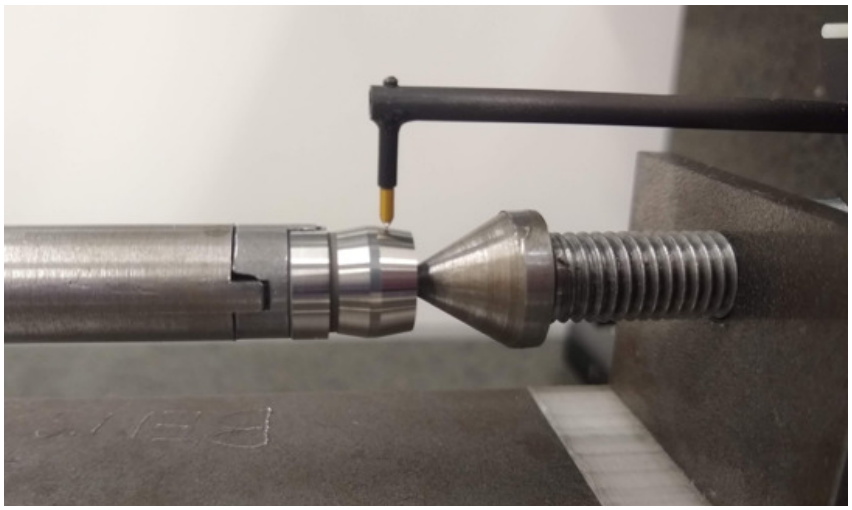


Figure 7.3: Roller configuration during stylus profilometry, enabling roughness measurement on cylindrical face of chamfered barrel. The stylus traverses axially and deflects radially with respect to the roller.



Figure 7.4: Roller configuration under optical microscope, enabling visual inspection of cylindrical face of chamfered barrel

the first test step, and between each test step, except in steps 5-8 where the rings were not inspected. The removal of the rings from the rig required the oil to be drained into a bottle so that the door could be opened. Before inspection the specimens were briefly immersed in toluene to remove the oil (but not sonicated) and dried with compressed air and paper towel. After inspection the specimens were replaced in the rig, and after steps 1-4, the same oil was transferred back to the test chamber (after steps 5-8 the oil was not drained as the roller could be accessed through the hole in the door).

At the beginning of each step, a load ramp was conducted, lasting 120 seconds, with the load controller setpoint ramping linearly from 0 N to the final value of 316 N. During the load ramp the entrainment speed matched that of the subsequent test step and the SRR was set to zero. Once the load had been reached, the desired SRR was imposed. The number of contact cycles quoted in this section excludes the load ramp due to the pure-rolling condition.

In this study, lambda ratio Λ is defined according to

$$\Lambda = \frac{h_{\min}}{R_{q_{\text{ring}}}} \tag{7.1}$$

where $h_{\min}$ is the minimum EHL film thickness in line contact according to Hamrock and Jacobson [246], and $R_{q_{\text{ring}}}$ is the mean RMS surface roughness measured on the rings at the start of the test. The roller roughness is ignored as the roller surface, being considerably softer than the rings, evolves rapidly with time on the asperity scale, while the ring surface asperities persist for a considerable portion of the test.

The minimum film thickness prediction of Hamrock and Jacobson is

$$h_{\min} = 3.07 \frac{\alpha_p^{0.57} R^{0.4} \left(U_e \eta_0\right)^{0.71}}{E'^{0.03} w_z^{0.11}} \tag{7.2}$$

where α_p is the pressure-viscosity coefficient, R the reduced radius of curvature, U_e the entrainment speed, η_0 is the inlet viscosity, E' is the reduced contact modulus and w_z is the load per unit transverse length. The thermal correction proposed by Olver [111] based on a thermal network model of the ring specimens was used to correct the inlet temperature used when calculating inlet viscosity η_0, assuming the fluid temperature in the inlet matches the surface temperature of the solids, in the same manner as Rycerz *et al.* [115]. The correction depends on the time-averaged friction coefficient, which was not known a priori, so a value representative of boundary friction for the fluid in question was estimated to enable the sump temperature control setpoint to be calculated, and the measured value of friction coefficient shown in Fig. 7.10 during the first 100,000 cycles was used after the test to establish the 'actual' lambda ratio. The predicted inlet temperature was between 4°C and 8°C greater than the nominal fluid temperature in all cases, so the thermal effects are quite mild under these conditions.

7.1.2 Effect of Fluid Formulation

The test conditions of Wainwright [243] were modified slightly as shown in Table 4.8, to mitigate wear for fluids not containing ZDDP. A lower SRR of 5% was therefore selected. The AISI 52100 specimens, whose rings had lower roughness of $R_q \approx 400$ nm than the 16MnCr5 specimens, resulted in a higher lambda ratio of $\Lambda = 0.4 \pm 0.02$, more closely representing the conditions seen during slow city driving in an EV gearbox. A lower nominal test temperature of 50°C was chosen (the work of Shore [11] suggests EV gearboxes are unlikely to exceed 60°C, at least for dry motor designs). Slight temperature setpoint variations (± 5°C) were employed to match the lambda ratio for each fluid, and for the water-based fluid, 35°C was used to limit evaporation and compensate for the lower pressure-viscosity coefficient. To achieve stable temperatures, the test chamber was both electrically heated, and cooled by a closed-loop water-cooling system. Rings were selected to achieve $R_q = 400 \pm 20$ nm.

Table 7.2: Test conditions used for comparison of fluid formulations in Fig. 7.6

Roller Speed [m/s]	Ring Speed [m/s]	SRR [%]	Track Width [mm]	Steel	Temp. [°C]	Load [N]	Max. Hertz Pressure [GPa]	Lambda Ratio [-]	R_q [nm]
3.805	4.000	-5.0	1.0	AISI 52100	50.0	316	1.5	0.4	410

A comparison of the radius loss incurred for five different fluids is shown in Fig. 7.5, showing that the least radius loss was incurred by the unadditivised base fluids. In the case of the ATF base fluid, the test labelled ATF base rep. was the first of these to be completed and the presence of the blue colour seen after 1 million cycles in Fig. 7.6f (sometimes generated by thin tribofilms slightly more than 100 nm in thickness as discussed in Chapter 8) was considered a sign of additive contamination. The test was therefore stopped, the rig cleaned again very thoroughly, and the flushing repeated. The test shown in Fig. 7.6e was then conducted through all steps to 11 million cycles, showing (for the first four steps) very similar radius loss to its predecessor, and forming the same characteristic blue film. The ATF base fluid is known to contain an ester additive designed to swell seals, which is perhaps responsible for this. A subsequent test using pure PAO5 exhibits even less radius loss, with colorful features forming on the surface towards the end of the test, presumably also due to additive contamination, or perhaps the catalysis by the metallic surfaces of a chemical reaction in which the oil breaks down under boundary-lubricated conditions to form new molecules which create these colours,

as proposed by Batchelor and Stachowiak [158]. For both base fluids, after 11 million cycles, some pitting is visible but the coverage of the surface is only partial, with mild wear apparently the dominant mechanism by which material is removed throughout the test.

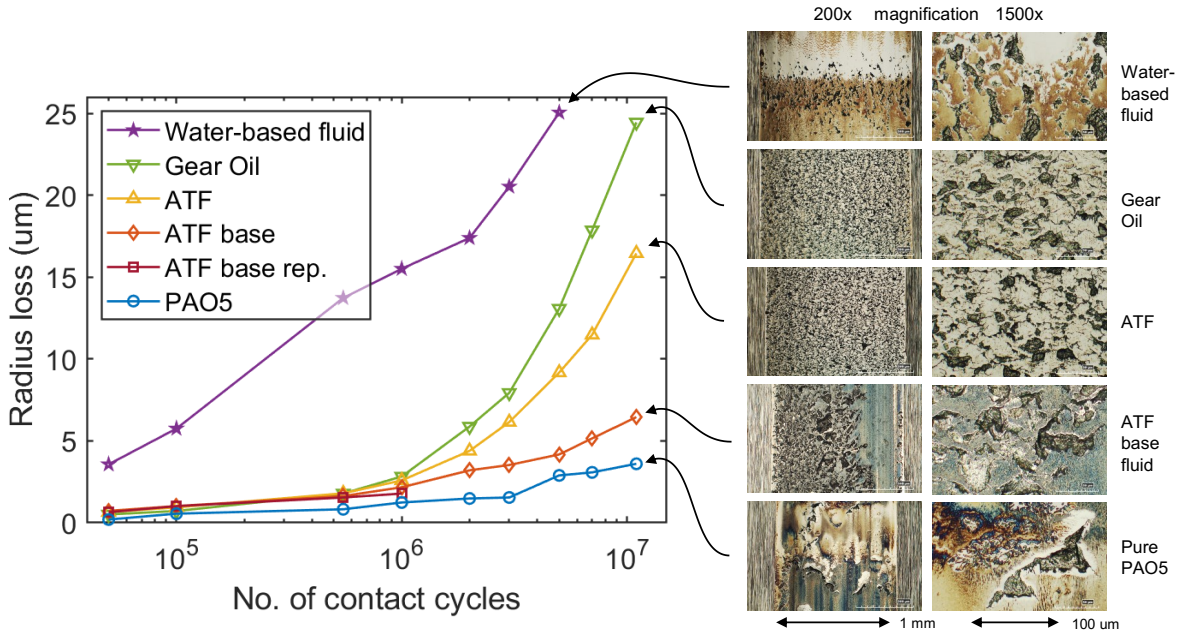


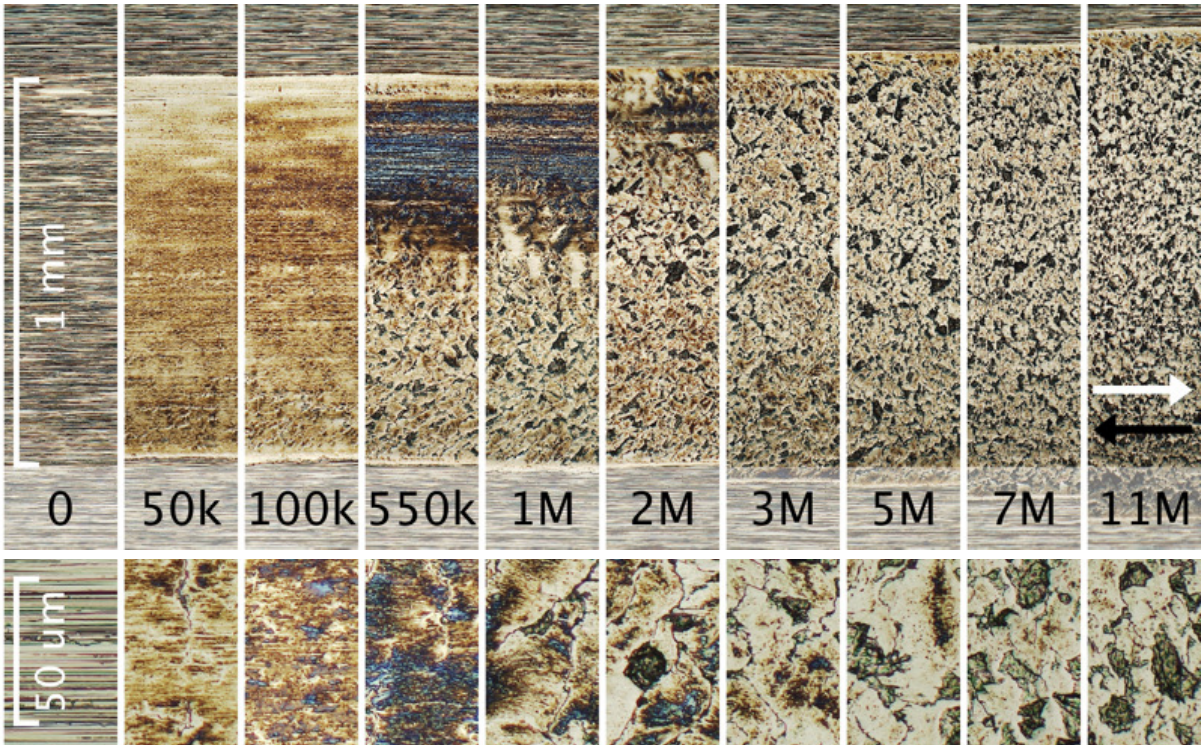
Figure 7.5: Comparison of radius loss in micropitting tests on 5 fluids showing optical microscope images of roller surfaces after final step (11 million contact cycles)

The ATF and the gear oil both produced advanced micropitting after 11 million cycles, with the crack network covering the full track width after 2 million cycles, leading to rapid material loss thereafter, as shown in Fig. 7.6a and 7.6b. The gear oil produced significantly more radius loss than the ATF.

No significant difference between the roughness evolution of the rings, shown for four roughness parameters in Fig. 7.7, can be seen for these tests. This is significant in the case of the water-based fluid for the first million cycles where the roller wears very fast but the rings do not, maintaining the asperity stresses that enable micropitting to continue to compete with roller wear in the later test stages. The relative similarity in counterface roughness evolution strengthens the comparison between fluids of roller radius losses and optical micrographs at each test step. The method used to determine the region over which these parameters were obtained is given in Section 7.1.4.

By far the most rapid radius loss is incurred by the water-based fluid. The shape of the radius

(a) Gear Oil



(b) ATF

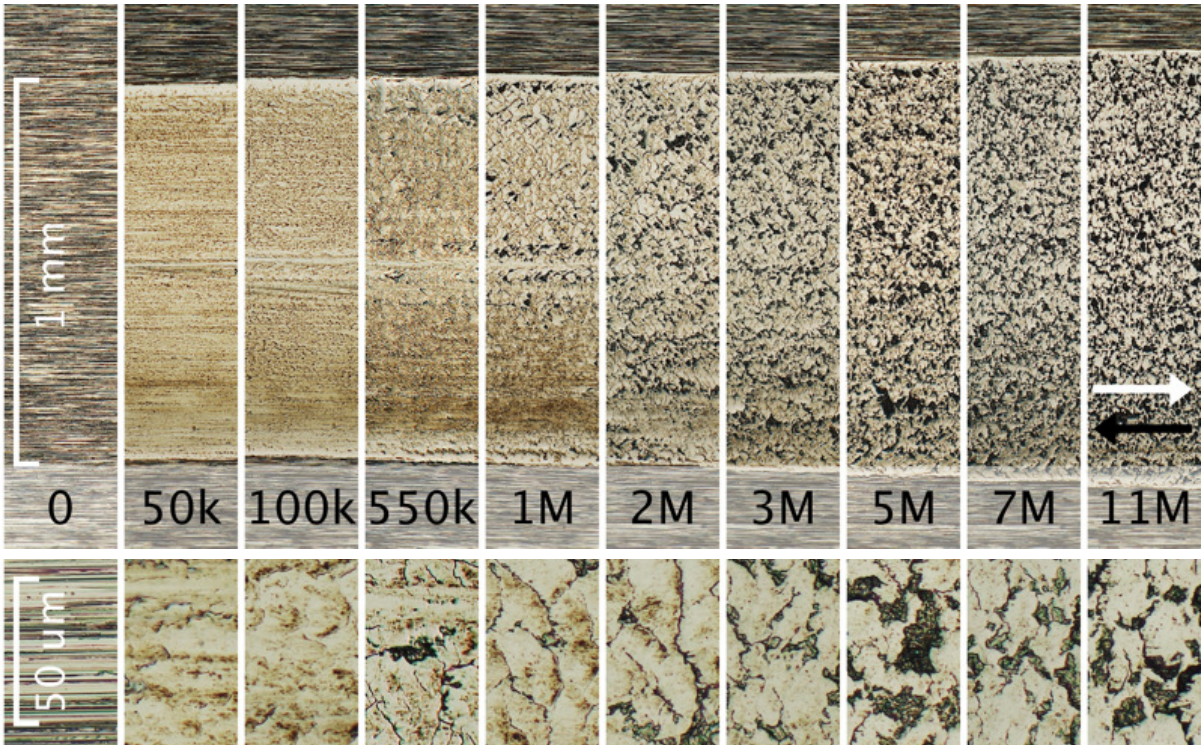
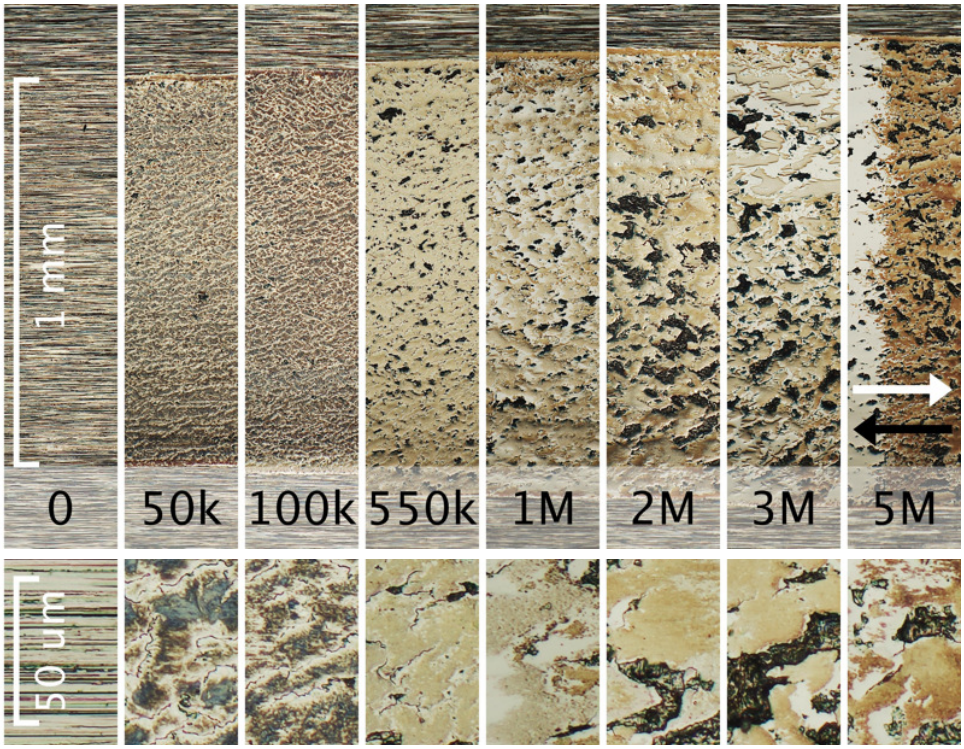


Figure 7.6: Optical microscope images showing evolution of roller surface with number of contact cycles throughout tests using 5 fluids (with AISI 52100 steel, batch B). The over-rolling direction is indicated by the white arrow, and the black arrow shows the friction force direction.

(c) Water-based Fluid



(d) PAO5

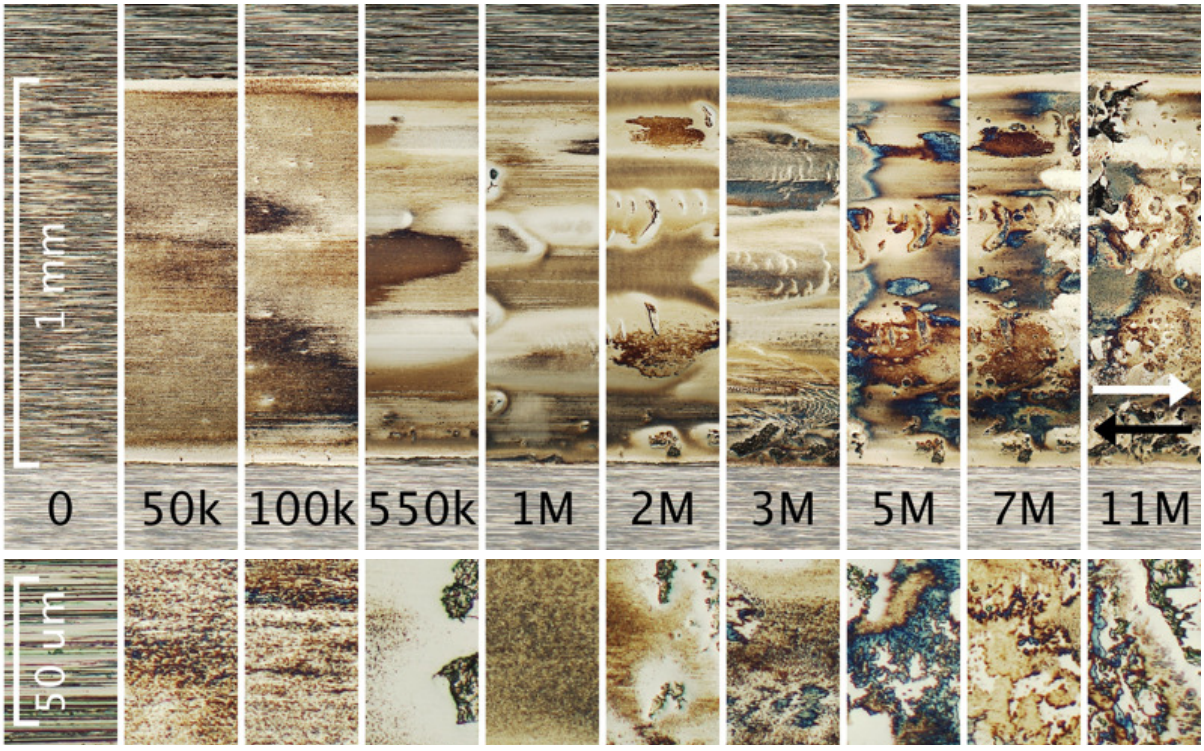
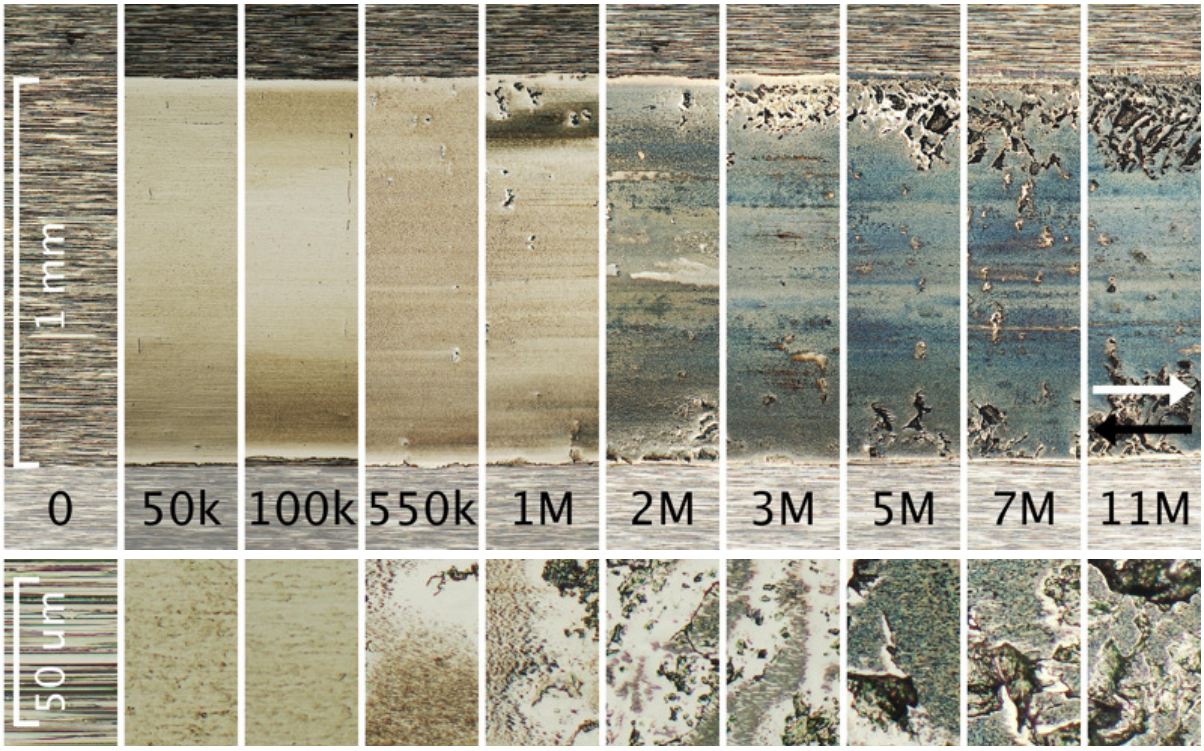


Figure 7.6: (continued) Optical microscope images showing evolution of roller surface with number of contact cycles throughout tests using 5 fluids (with AISI 52100 steel, batch B). The over-rolling direction is indicated by the white arrow, and the black arrow shows the friction force direction.

(e) ATF base fluid



(f) ATF base fluid partial repeat

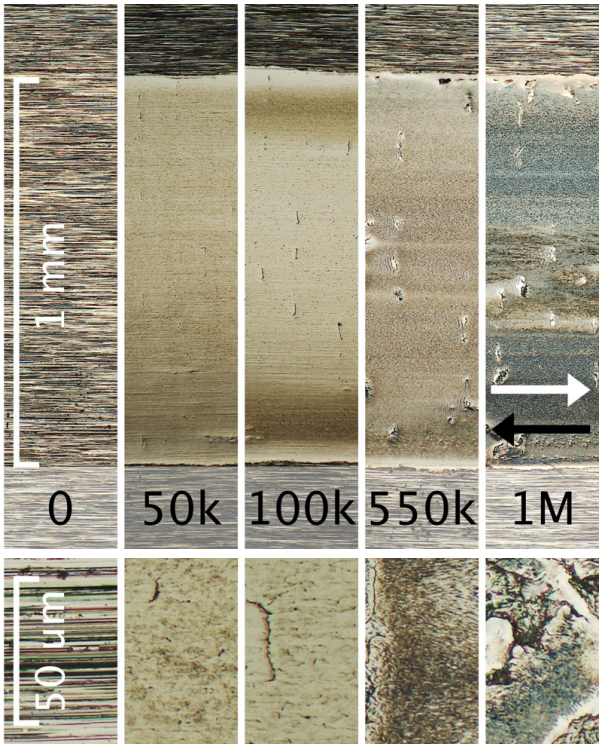


Figure 7.6: (continued) Optical microscope images showing evolution of roller surface with number of contact cycles throughout tests using 5 fluids (with AISI 52100 steel, batch B). The over-rolling direction is indicated by the white arrow, and the black arrow shows the friction force direction.

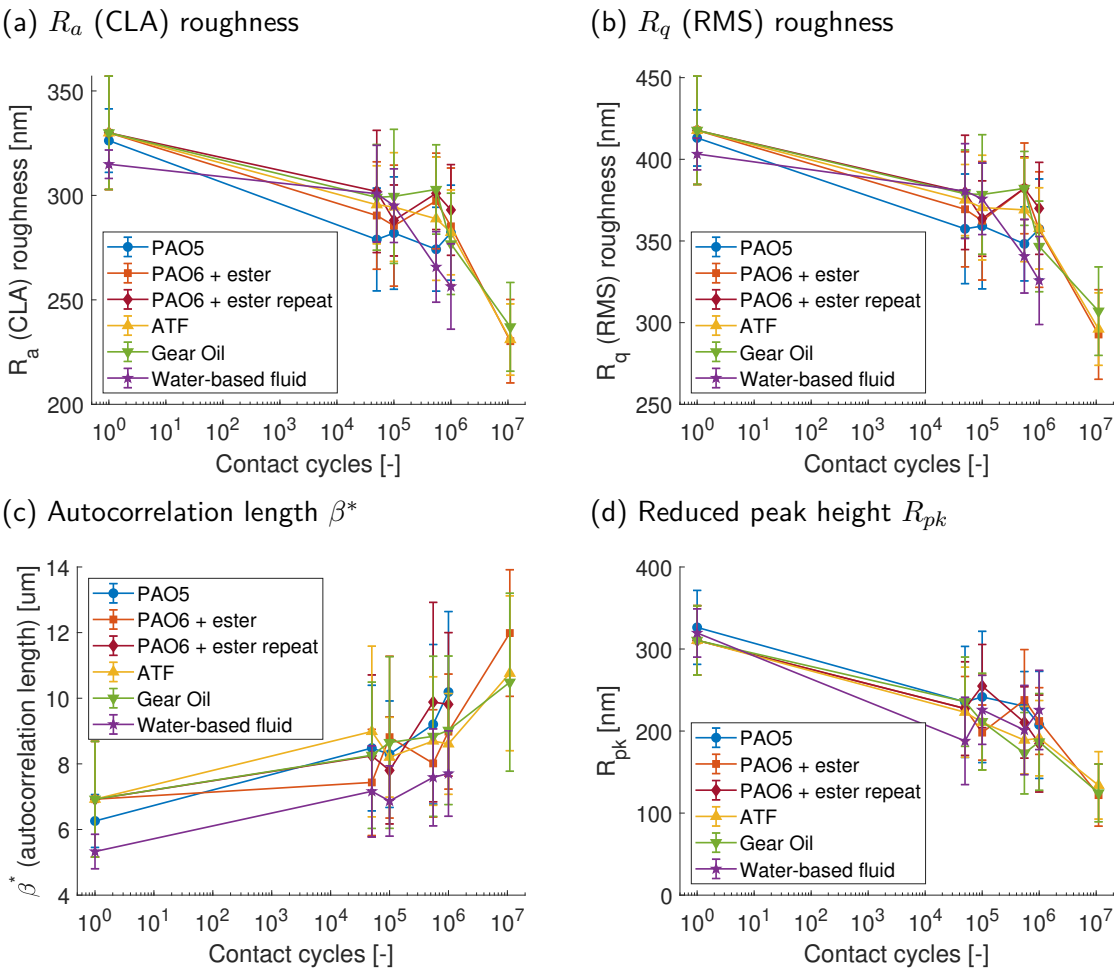


Figure 7.7: Selected roughness parameters calculated on 1 mm region of minimum accumulated slope averaged over 4 measurements on each of the three rings, plotted vs number of roller contact cycles accrued. The error bars are positioned at ± 1 standard deviation from the mean.

loss history in Fig. 7.5 indicates the material is lost early on in the test to wear at a rate similar to the growth of the crack network, which matures quickly in the first million cycles. The orange colour is possibly due to the presence of the ferric oxide due to the corrosive nature of water. A test was also attempted with the base fluid of the water-based fluid, which did not contain the anti-wear additives and corrosion inhibitors. After the 60-minute flushing step, the ring specimens were seen to have rusted all over, the fluid had turned a deep orange colour, and the test was not continued in the interests of the health of the rig. Corrosion rates as rapid as this may act to accelerate both wear and fatigue, by weakening the material at the surface while also intensifying sub-surface stress-concentrators.

It should be noted that this was an experimental fluid whose formulation could likely be

significantly improved upon in further iterations, considerably reducing the impact of foaming, corrosion and wear in particular. Solutions to these well-known problems with water-based lubrication of steels are considered beyond the remit of this study. Some phenomena specific to MPR testing with this water-based fluid were identified however. Figure 7.8 shows the MPR chamber immediately after the removal of the circular door, with highly aerated water-based fluid pouring out. The effect of the entrainment of air bubbles into elastohydrodynamic contacts on micropitting is not presently well studied, but it is possible that this causes temporary starvation, accelerating wear and increasing friction.



Figure 7.8: Significant foaming of water-based fluid after a test step

Several microscope images have been stitched together to create an image spanning 60°of the roller surface in Fig. 7.9, showing 5 periods of a repeating fluctuation in the wear pattern. These 'ridges' are of interest because the wear mode appears to vary throughout, the most worn regions having very little micropitting, while the least worn regions are pitted. The radius loss is qualitatively visible in this image by examining the track width, a wider track indicating greater material loss due to the chamfered roller geometry. An extremely loud high-pitched tone was heard from the rig during the latter stages of this test, with a frequency corresponding to that at which the ridges pass the contact. While this roller has 30 ridges on it, other tests on low-viscosity oils have anecdotally created 33 or 36 ridges, the divisibility by 3 suggesting



Figure 7.9: Microscope images stitched together while the roller was rotated about its axis, traversing 60°circumferentially, showing 5 complete 'ridges', indicating the total number of ridges on the roller is 30. The divisibility by 3 suggests a coupling to the dynamics of the MPR setup, the rate at which the ridges pass the contact being synchronous with a natural frequency of the loading system. The track is slightly narrower in the pitted regions, indicating less radius loss at these points.

a coupling to the vibration of the loading system. It is proposed that the ridges are the result of a positive feedback initiated by some excitation in the system (e.g. out-of-balance) and perpetuated by a wear mechanism sensitive to contact pressure, which creates a periodic wear pattern that acts to increase the excitation of the system. The three damping rings which sit on the ring shafts have internal clearances carefully chosen by the manufacturer such that an oil of considerably higher viscosity than those used in this study provides squeeze-film damping over the relevant frequency range. The damping is likely considerably reduced by the low viscosity (and perhaps by the larger bulk modulus) of the water-based fluid used here, whose wear characteristics conspire with this altered damping to create the ridge pattern. This image also illustrates the competition between wear and micropitting - the more worn regions have no micropitting because the wear outstrips the rate of crack growth, while micropits are able to form in the less worn regions.

The coefficients of friction measured by the MPR torque sensor during each test are shown in Fig. 7.10a. The variation of the friction coefficient between the oils and over the duration of the test is relatively slight, despite the very substantial difference in roller surface topography. The water-based fluid, as expected, produced much lower boundary friction, which decreased further around 3 million cycles, corresponding to a dramatic increase in acceleration in Fig. 7.10c likely due to ridge formation, see Fig. 7.9. The acceleration of the test with PAO5 increases sharply and then flattens off, the change apparently happening at the interruption of the test at the end of step 6 (3 million cycles). It is not known why this happened but this is possibly as a result of the roller being rotated 180° on being returned to the rig after

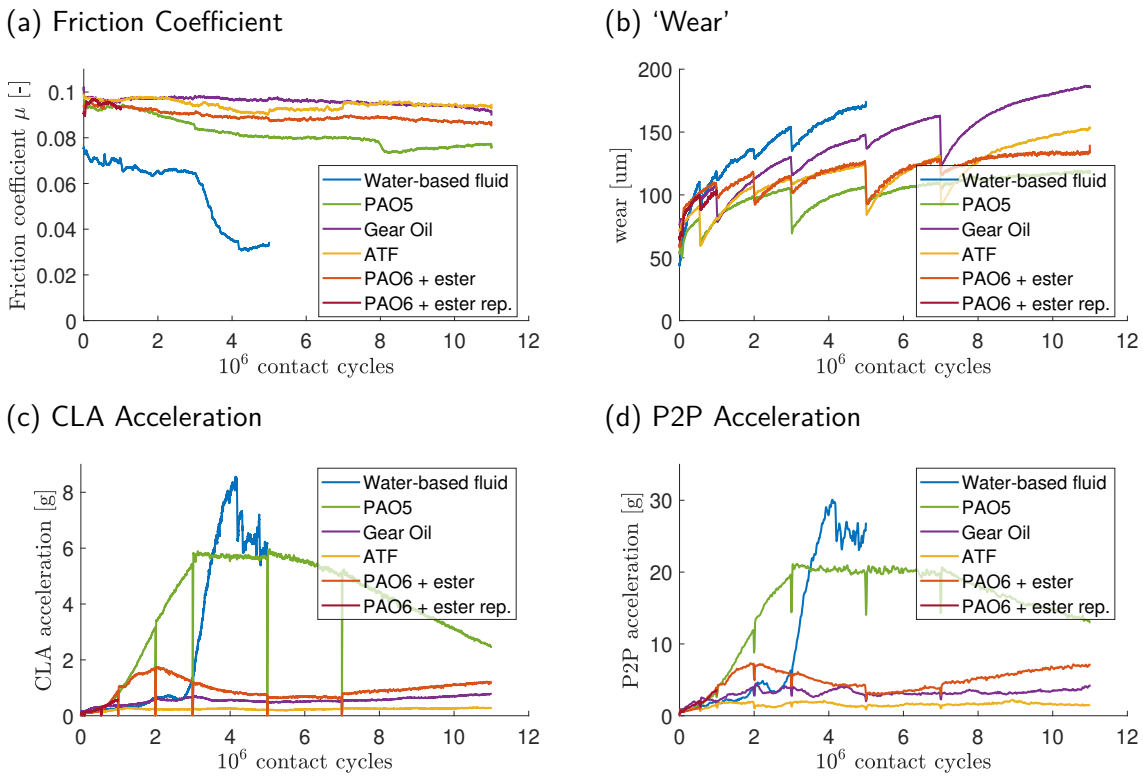


Figure 7.10: Friction (a), LVDT displacement (b), centreline average acceleration (c) and peak-to-peak acceleration (d) for six MPR micropitting tests shown in Fig. 7.6

inspection (the slot in the roller means there are two orientations in which it fits, and this orientation was not carefully controlled - usually this has no impact but if there were to be an odd number of ridges, 33 has been observed before, then this could change the phase angle between roller-synchronous out-of-balance excitation and wear pattern, altering the vibration characteristics). The wear values in Fig. 7.10b, measurements by an LVDT of the displacement of the translating shaft to which the upper ring is mounted, appear to be strongly affected by a first-order transient occupying a large fraction of each test-step duration. This is most likely thermal expansion, as the temperature of the peripheral components of the rig gradually stabilise long after the fluid temperature is controlled, and then cool again during the interruptions while the roller and rings are inspected.

7.1.3 Effect of Roller Batch

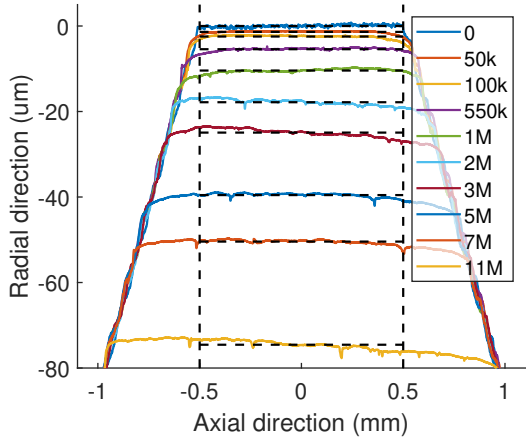
An attempt was made to reproduce the results of Wainwright [243] using the same case carburised gear steel, 16MnCr5. The work of Wainwright used rollers all from the same batch (marked J), which had been nearly exhausted, so new rollers from a different batch (marked

N) were obtained for this study. With these new rollers, it was found that under the same test conditions used by Wainwright, given in Table 7.3, on the same MPR machine, very different results were obtained. In both cases the fluid used was PAO5 blended with a mixture of primary and secondary ZDDPs to 0.1%wt Phosphorous. Stylus profilometer traces of the batch J roller are shown for each step according to the total contact cycles accumulated in Fig. 7.11a, and the averaged roller radius within the contact track for all 4 sets of profiles taken is shown in Fig. 7.11b. The same results are compared to the equivalent test on the batch N roller in Fig. 7.12, showing considerably less radius loss and slower propagation rate throughout the test.

Table 7.3: Test conditions used for batch J and N rollers

Roller Speed [m/s]	Ring Speed [m/s]	SRR [%]	Track Width [mm]	Steel	Temp. [°C]	Load [N]	Max. Hertz Pressure [GPa]	Lambda Ratio [-]	R_q [nm]
3.619	4.000	-10.0	1.0	16MnCr5	60.0	316	1.5	0.22	490

(a) Roller Profile



(b) Roller Radius Change

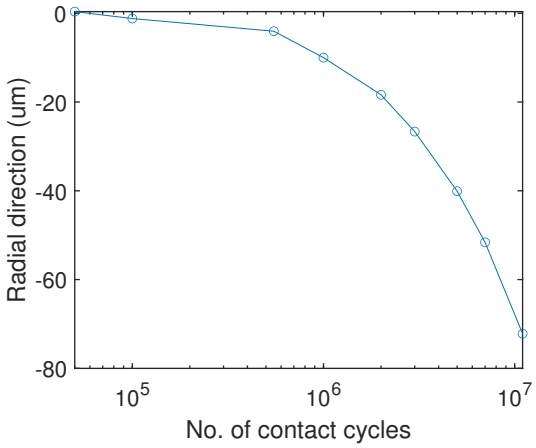


Figure 7.11: Change in roller profile (a) measured using stylus profilometry over 11 million contact cycles for batch J roller under conditions given in Table 7.3, showing roller radius averaged over contact track (black dashed lines), and mean change in roller radius (b) averaged over 4 positions on the roller taken in the same locations after every test step, spaced by 90°.

Optical microscope images of the roller surfaces at each stage of the two tests are shown in Fig. 7.13, demonstrating the differing tribofilm coverage, crack morphology and damage progression throughout the two tests. In the lower-magnification images, the contact track can be seen to widen significantly during the test, indicating radius loss on this chamfered geometry. The widening of the contact track has the effect of lowering nominal 'Hertz'

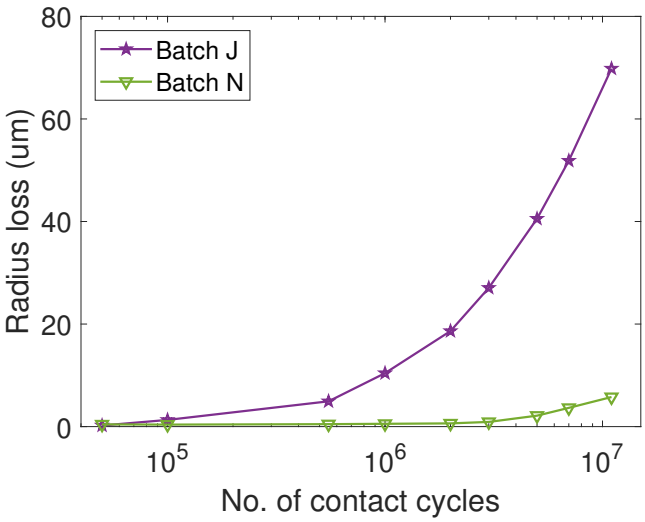


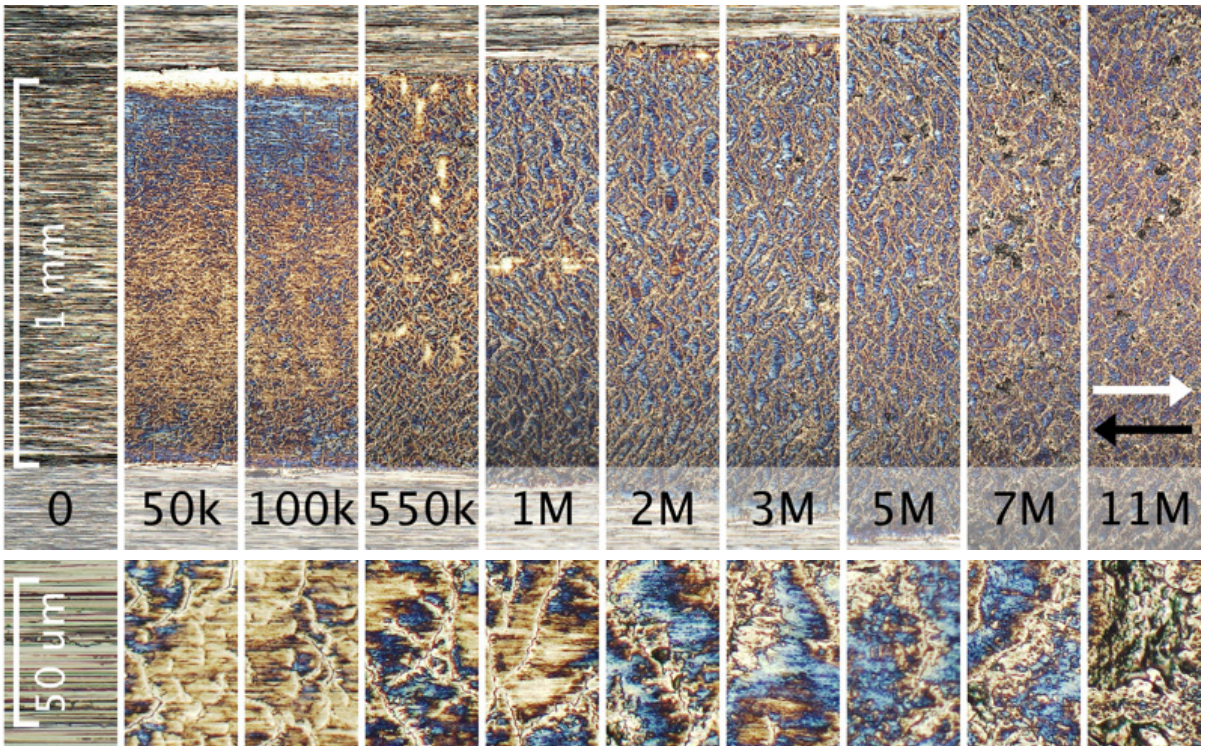
Figure 7.12: Radius loss comparison between batch J roller used by Wainwright, and batch N roller manufactured to the same specifications, run consecutively in the same MPR under the same test conditions.

contact pressure, but the pressure distribution inside the contact with these pitted, boundary-lubricated surfaces is far from Hertzian. The ring surface profile was changed comparatively little during the test, see Section 7.1.4, with only a slight roughness modification visible to the naked eye after $\sim 10^6$ cycles, on account of the higher hardness and far fewer contact cycles seen by each ring.

The tests on the batch J and N rollers used adjacent axial locations on the same rings, so the counterface roughness and material characteristics are as closely comparable as possible in these tests. Wainwright himself was surprised by these results and repeated the tests of his own accord using another batch J and batch N roller, on a set of rings from the set used in his own study, on a different MPR rig, using the same fluid as used for these tests. He obtained very similar results: the batch N roller did not develop a visible surface crack network until much later in the test, leading to much lower radius loss, and visual inspection showed that the film growth and crack morphology differed between the two, but compared well for each batch to the test presented here.

This implies that the surface properties of the batch J and N rollers differed, despite their very similar roughnesses and bulk hardnesses. The hardnesses near the surface of the case-carburised 16MnCr5 specimens, which were not measured, may have differed, perhaps as a result of differences in the carburising process, or due to differences in the amount of

(a) Batch J roller



(b) Batch N roller

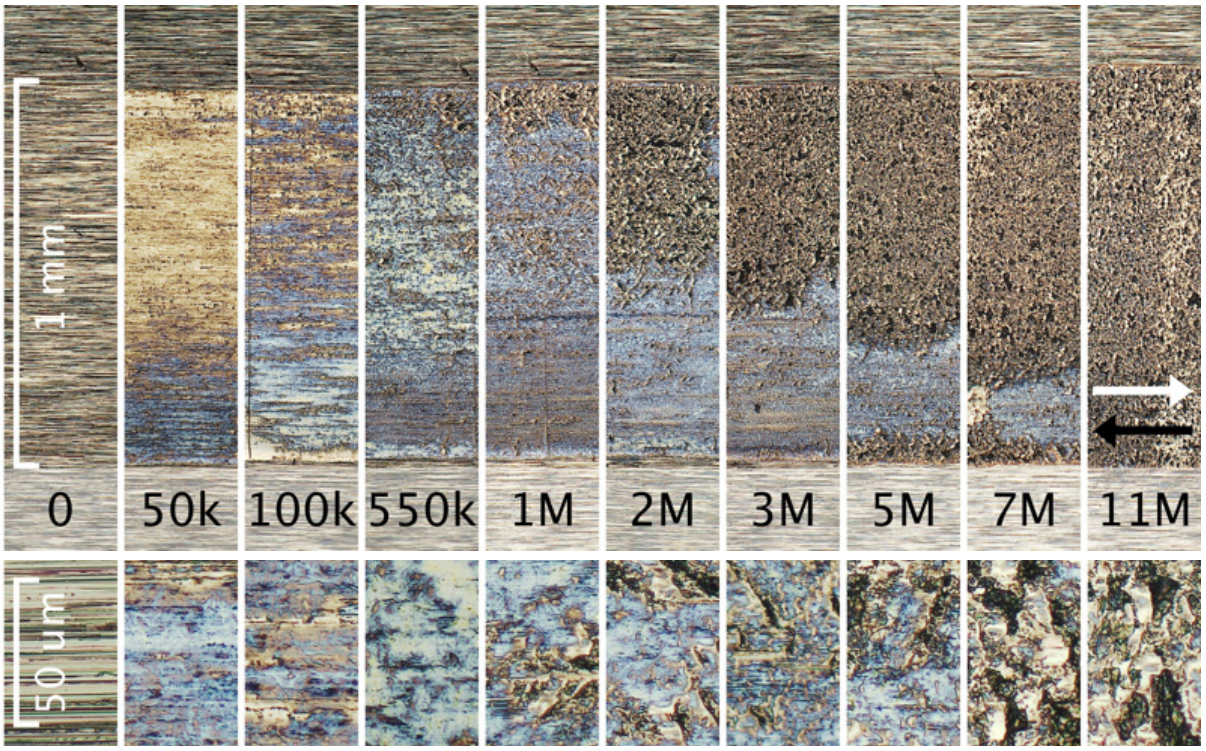


Figure 7.13: Comparison of optical microscope images showing evolution of roller surface with number of contact cycles accumulated during otherwise identical tests with (a) batch J roller used by Wainwright and (b) batch N roller manufactured to the same specifications. The over-rolling direction is indicated by the white arrow, and the black arrow shows the friction force direction.

material removed during the final grinding operation after the heat treatment, leaving a harder surface on one batch (N perhaps) than on the other (J). One way to verify this would be by microindentation and surface microscopy, but the problem of controlling the hardness of the available batch, which did not reproduce the damage mode under study, would remain. Instead, the uncontrolled case-hardness variable was eliminated for the other work in this study by using through-hardened 100Cr6 steel specimens.

7.1.4 Counterface Profile Evolution

The evolution of the ring surfaces provides important insight into changes in asperity stresses on the roller imparted during the test. For 11 million roller cycles, 9.0×10^5 cycles are accrued by each ring, and despite the hardness difference, some wear occurs, reducing surface roughness inside the contact track.

An example of one of the 12 traces taken on the rings after each test step is shown in Fig. 7.14, highlighting the track. The centre of the track is found from the centre $x_{\text{cent.}}$ of the 1 mm subsection of the trace, which minimises the total absolute slope over this subsection, according to

$$x_{\text{cent.}} = \operatorname{argmin} \left\{ \int_{x-0.5\,\text{mm}}^{x+0.5\,\text{mm}} \left| \frac{\mathrm{d}z}{\mathrm{d}\xi} \right| \mathrm{d}\xi \right\} \tag{7.3}$$

where the asperity profile is described by $z(\xi)$. This approach was found to consistently select the evident worn region, characterised by very flat peaks. Of several metrics trialled (accumulated curvature, skewness, kurtosis), total absolute slope was found to produce the smoothest minimum located consistently at the track centre.

The evolution of mean ring RMS roughness R_q and reduced peak height R_{pk} throughout the tests on batch J and batch N are shown in Fig. 7.15. These parameters are chosen because of their sensitivity to changes in asperity peaks, and hence their relevance to micropitting crack growth rates. The roughnesses here are calculated from a modified trace having undergone line form removal, and both short-pass and long-pass Gaussian filters, with cutoff wavelengths 0.0025 mm and 0.25 mm respectively. Warm thanks are extended to Ben Wainwright for his provision of the MATLAB code which performed this filtering, and enabled the calculation of R_{pk}. The error bars are located at $\pm$ one sample standard deviation of the mean of 12 measurements, highlighting the considerable variance in this dataset, a limitation inherent in

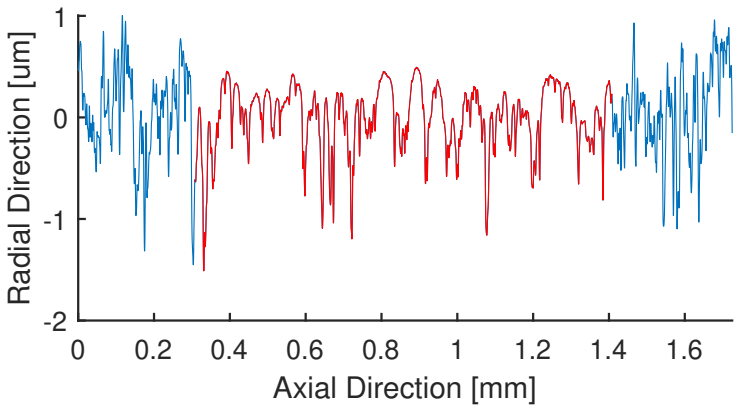


Figure 7.14: Axial profile of ring surface at end of test (11 million roller cycles, 9.0×10^5 ring cycles), highlighting in red the 1 mm span with minimum total absolute slope, corresponding to the worn region.

(a) RMS roughness R_q (b) Reduced peak height R_{pk}

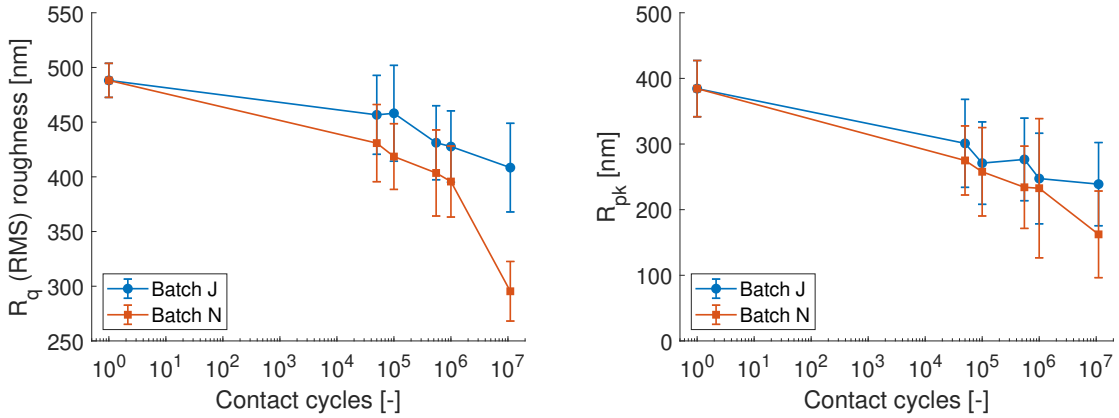


Figure 7.15: Two roughness parameters sensitive to peak heights, RMS roughness R_q (a) and reduced peak height R_{pk} (b), averaged over 4 measurements on each of the three rings, plotted vs number of roller contact cycles accrued for batch J and batch N roller tests at different axial locations on the same rings. The error bars are positioned at ± 1 standard deviation from the mean.

line roughness measurement of rough specimens such as these.

The same rings were used for both tests, so the initial roughness was nominally identical. The batch N roller then lowers the roughness of the rings more quickly than the batch J roller. Having eliminated the possibility of a bulk hardness difference between the two batches, it is possible the carburising process between the two differed sufficiently to create higher case hardness on the batch N roller, causing earlier counterface roughness reduction and hence different micropitting morphology. Alternatively a microstructural difference in the bulk

material may result in differing crack propagation rates. This issue was not investigated further - micropitting much more similar to that of the batch J roller was produced using AISI 52100 specimens (roller batch B), and these were used for the study in Section 7.1.2.

7.2 Scuffing

High sliding speeds in EV transmissions (of the order several m/s) and high loads during rapid acceleration, combine to increase the risk of scuffing, a mode of severe adhesive wear damage caused by rapid thermally-unstable lubricant- and boundary-film-collapse event typically followed by surface welding and catastrophic failure.

This section details the adaptation of an existing contrarotation scuffing test method, to compare the scuffing performance of a series of transmission fluids of differing additive chemistry, pertinent to the development of future EV-fluids, corresponding to the fluids used for the micropitting tests in Section 7.1.

7.2.1 Scuffing Test Method

A scuffing test method based on the contrarotation method of Peng et al [175] using a ball-on-disc tribometer, is employed to determine the onset of scuffing at two contact pressures. The two ball-on-disc tribometers used are detailed in this section, and the novel modifications to the test conditions are explained.

The fluids were deliberately formulated to be closely matched in viscosity, but the lower pressure-viscosity coefficient of the water-based fluid required lower temperature, and hence higher viscosity, to achieve equivalent film thickness. The temperatures were chosen to reasonably represent bulk fluid temperatures in an EV gearbox, 60°C for the oils, and 40°C for the water-based fluid, achieving a lambda ratio of $\Lambda \approx 0.8 \pm 0.1$ for all fluids, based on the isothermal Chittenden minimum EHL film thickness prediction, and assuming that the composite roughness of the surfaces is $R_{\mathrm{ac}} \approx 12$ nm (ascertained from white-light interferometry of ball and disc surfaces). This lambda ratio is representative of that experienced under sharp accelerations at slow speeds during city driving, as ascertained in Section 4.1.5. Similarly, maximum Hertz pressures of 1.3 GPa (perhaps experienced at near-maximum acceleration by gear contacts) were investigated initially. A higher pressure of 2.0 GPa (considerably higher than a realistic design pressure for EV gear systems at present, although achievable in rolling bearings and couplings [117]) was then used to differentiate the fluids which did not scuff at the lower pressure.

7.2.1.1 MTM and ETM Tribometers

The MTM (Mini-Traction Machine), and ETM (Extreme Traction Machine, in this case, extremes of pressure) are ball-on-disc tribometers by PCS Instruments. Both the ball and the disc rotate and are independently driven, enabling surface speeds between 1 mm/s and 4 m/s. Ball and disc are encased in a temperature controlled steel pot and immersed in lubricant, as shown in Fig. 7.16. The ball shaft and drive motor are mounted to a frame which pivots so

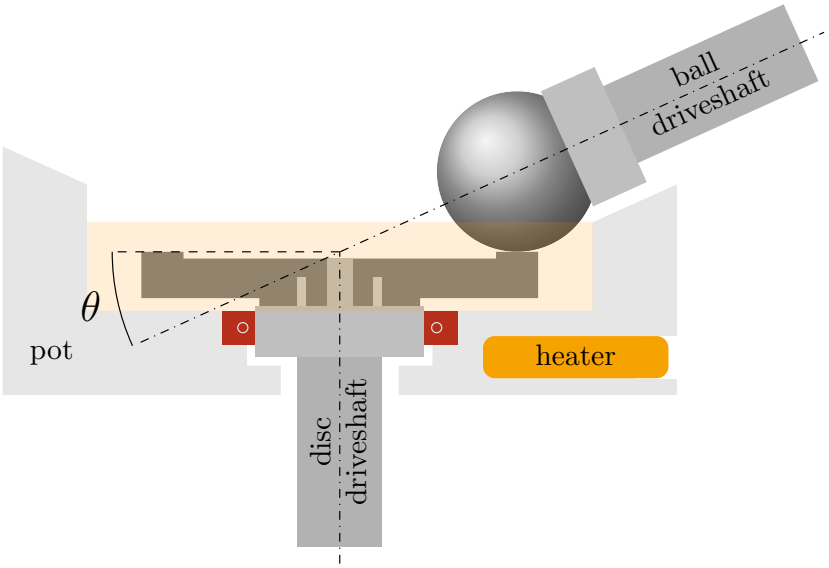
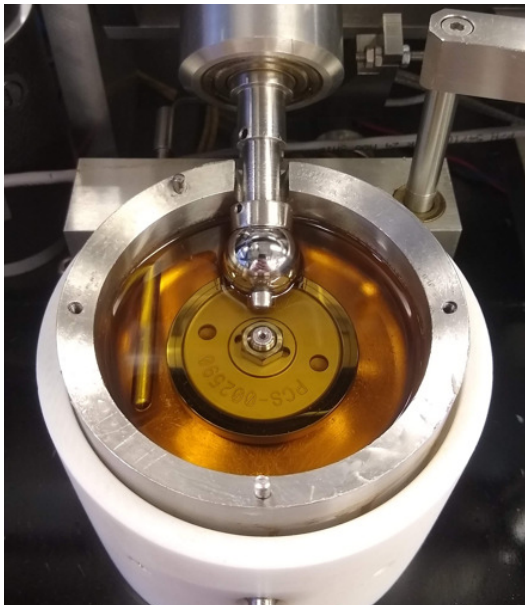


Figure 7.16: Schematic of ball and disc orientation in MTM and ETM pot

that the ball can pitch towards and away from the disc surface. The frame is supported by two coaxial bearings, and actuated by a compliant beam, connected at its far end to a lead screw which translates through a hollow stepper motor containing a rotating nut. The ball is brought into contact with the disc and then loaded against it, as the stepper motor bends the compliant beam, and the bending strain is measured by strain gauges attached to the beam. The stiffness of the beam is ascertained by calibration, enabling load control. The mounting of the ball shaft and drive motor constrains them rigidly to the pivoting frame in only 5 axes using flexure plates which are compliant in yaw (the yaw axis is mutually perpendicular to the axis of ball rotation, and the pivot axis). This rotational DoF is instead constrained by a piezoelectric load cell which measures the force applied on the ball by friction in the contact between ball and disc. The mounting position of the load cell is very finely adjustable so that the axes of the ball and disc can be precisely aligned, and skew (a difference in the direction of motion of the surfaces in contact) can be eliminated. The axis of rotation of the ball makes

an acute angle with the axis of rotation of the disc, chosen to equalise the gyration of the two surfaces under pure-rolling conditions (i.e. to amortise spin, discussed further in Appendix G).

(a) MTM pot



(b) ETM pot

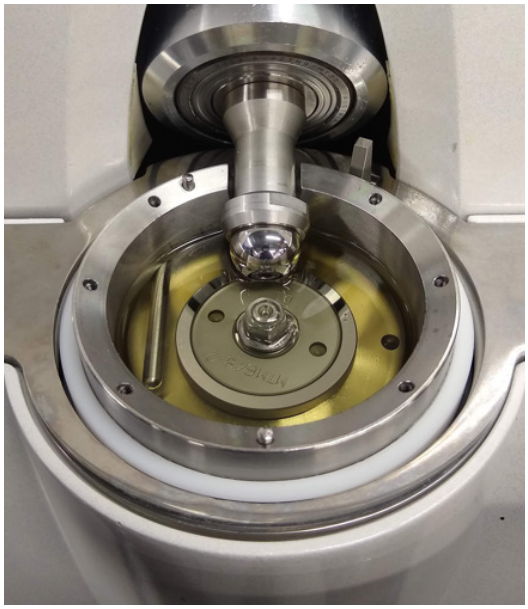


Figure 7.17: Comparison of MTM and ETM setups showing ball, disc and lubricant

The operating principle and contact geometry of the MTM and ETM rigs are identical, as shown in Fig. 7.17. The ETM is capable of applying much higher contact loads (between 50 N and 1650 N) than the MTM (between 10 N and 75 N). The ETM therefore has considerably higher motor torque capacity, a stiffer loading beam, and a traction transducer rated to higher loads. The range of achievable speeds and temperatures are also similar between the two rigs.

Various measurement routines ('steps') are pre-programmed, and the one of interest in this study is the 'timed' step, during which the rig

1. Waits for the temperature to stabilise while rotating the ball and disc out-of-contact to circulate the lubricant around the pot.
2. When the temperature is stable, rotates the ball and disc surfaces at the same user-specified speed, brings them into contact, and gradually applies the load.
3. When the load is stable, applies a user-specified slide-roll-ratio and entrainment speed, for a user-specified interval of time, during which data such as surface speeds, friction coefficient, temperature and μm-scale ball displacement (wear) are recorded.

4. When the time has elapsed, the ball is unloaded. The rig then saves the data and moves onto the next step in the profile.

7.2.1.2 Running-In

The first step in the test aims to lightly condition the surfaces, termed 'running-in', which was suggested by Ingram *et al.* [172] and by Peng [174] to improve repeatability. The surfaces are subjected to boundary-lubricated conditions for a certain time interval (e.g. 600 s) at the beginning of the test, with moderate sliding at a very low entrainment speed. This is intended to "*change the surface microtopography of the fresh specimens through a mild wear process in an attempt to ensure that variation in roughness across specimens is minimised prior to the start of the actual scuffing test*" [175].

The conditions used by Peng *et al.* [175] and Ueda *et al.* [176, 247] to do this involved a constant 20 N ball load (50 N for the ETM) regardless of the load chosen for the subsequent steps. The same authors also argue however that the load-stepping scuffing tests of Ingram *et al.* [172] are incomparable to other scuffing tests because the load variation causes fresh surface to come into contact when the load is increased. The low running-in load chosen by Peng *et al.* causes the same inclusion of fresh surface to happen when the load increases for the scuffing steps of the test. Peng [174] reports a number of candidate running-in conditions, but the ones which were found to give best reliability were used in ref. [175]. The entrainment speed is 3 mm/s, and the sliding speed is 10 mm/s, so the slide-roll ratio is 333%, greater than the 200% co-rotation threshold, meaning the surfaces contra-rotate. The ball and disc speeds respectively are -2 mm/s and 8 mm/s. The rotational speed of the ball motor is therefore 2.2 rpm (at the maximum speed of 4.5 m/s by contrast the motor spins at 4950 rpm), and the disc motor (which is connected to the disc shaft via a belt drive that reduces the speed by a factor of $\frac{9}{16}$) is spinning at 6.5 rpm - clearly the actual ball and disc speeds will vary considerably due to motor cogging and servomotor speed control fluctuation at these very low speeds. The ball surface also only sees 22 passes of the contact during the 10 minute running-in step. The tribological implications of the inevitable speed variation are likely to change from test to test, and from rig to rig as small variations in bearing preload and seal friction cause different speed responses at very low speeds. If the intended mild wear and microtopographical modification takes place during this step, these conditions are

therefore unlikely to lead to repeatable results. It was also observed during a separate study that friction measurements taken with the entrainment speed below 40 mm/s during Stribeck curves at 50% SRR (slower surface speed 30 mm/s) produced highly unrepeatable friction measurements which were typically much lower than the expected boundary friction, with large scatter.

The variation in surface topography between fresh specimens in Peng's study however is likely to have been greater at that time than the specimens used for the study presented here, which benefit from improvements to finishing methods, and this reduces the importance of the running-in procedure, and also potentially changes its effect if the discs were substantially rougher than those used here.

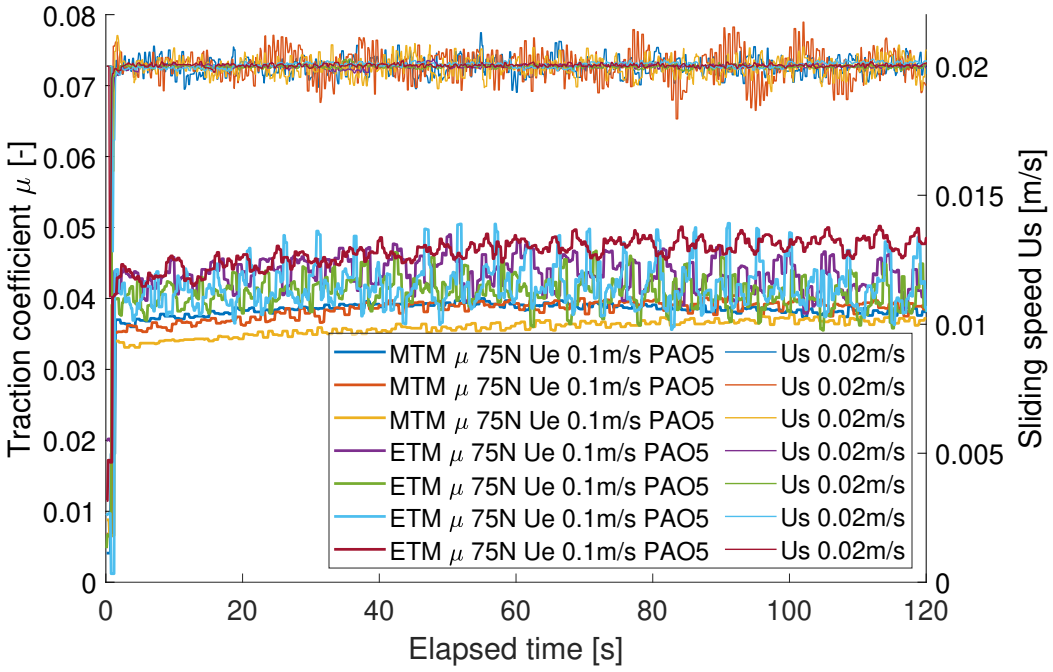


Figure 7.18: Friction coefficient μ and sliding speed U_s recorded during 7 repeats of the same running-in procedure, 3 with the MTM and 4 with the ETM, showing that the chosen running-in conditions achieve stable and similar friction coefficients by the end of the step. The fluid was PAO5, the ball load was 75 N, and the maximum Hertz pressure was 1.27 GPa.

The running-in procedure was modified to increase the surface speeds, by increasing the entrainment speed to 100 mm/s, and the lambda ratio to 0.8 (for PAO5 at 60°C in these tests). A sliding speed of 20 mm/s was chosen, hence the SRR is 20% and the surfaces co-rotate. A running-in time of 120 s was set, during which time the ball sees 200 contact cycles. The load was chosen to be the same as the load in the subsequent scuffing test, because a

change in load causes a change in contact area which is one of the arguments against load-stepping scuffing procedures. Seven repeats of these conditions are shown to achieve stable, and similar, traction coefficients within this time, in Fig. 7.18. It is apparent that even at this higher entrainment speed, the control of the 20 mm/s sliding speed on the MTM is vastly inferior to that on the ETM (thin lines pertaining to right-hand y-axis in Fig. 7.18), perhaps owing to the greater torque capacity of the motors on the ETM. The difference in the friction traces, although the motor speed control may be a factor, is also attributable to differences in traction transducer sampling protocol between the two rigs - here the ETM has been modified to report readings more frequently with less averaging. The ETM traction measurements are also systematically higher than those on the MTM, which is likely due to the 75 N load being at one extreme of the load range for both rigs, incurring linearisation errors in their respective calibrations. The reproducibility of friction measurements between MTM and ETM rigs is considered in more detail in Appendix H.

For the three tests on the MTM, the specimens were removed from the machine after the running-in step and examined using a scanning white-light interferometer. The recorded surface profiles are provided in Fig. 7.19 to enable qualitative comparisons of the effect of the running-in step. The fresh ball specimen, shown in Fig. 7.20, is both rougher and harder than the disc, so the greatest difference after running-in is seen on the disc surface.

Before each test, a new ball and disc test specimen were immersed in toluene in a glass jar, which was half-submerged in water and sonicated for at least two minutes. The specimens were removed and dried with compressed air before being placed in a similar jar containing 2-propanol and returned to the sonicator for at least two minutes. The specimens were then dried with paper towel, defluffed with clean compressed air, and mounted on the rig using steel tweezers.

Specimens made of AISI 52100 bearing steel, superfinished to surface roughness $R_a \lesssim 10$ nm were used for all scuffing tests, and a value of $R_{ac} = 12$ nm, based on the pythagorean combination of the averages of a series of areal roughness measurements using a scanning white light interferometer, was assumed in the calcuation of Lambda ratio Λ for this study. Pagkalis *et al.* [248] found that the formation of antiwear films is significantly influenced by steel composition due to the role of alloying elements in changing the availability of metal

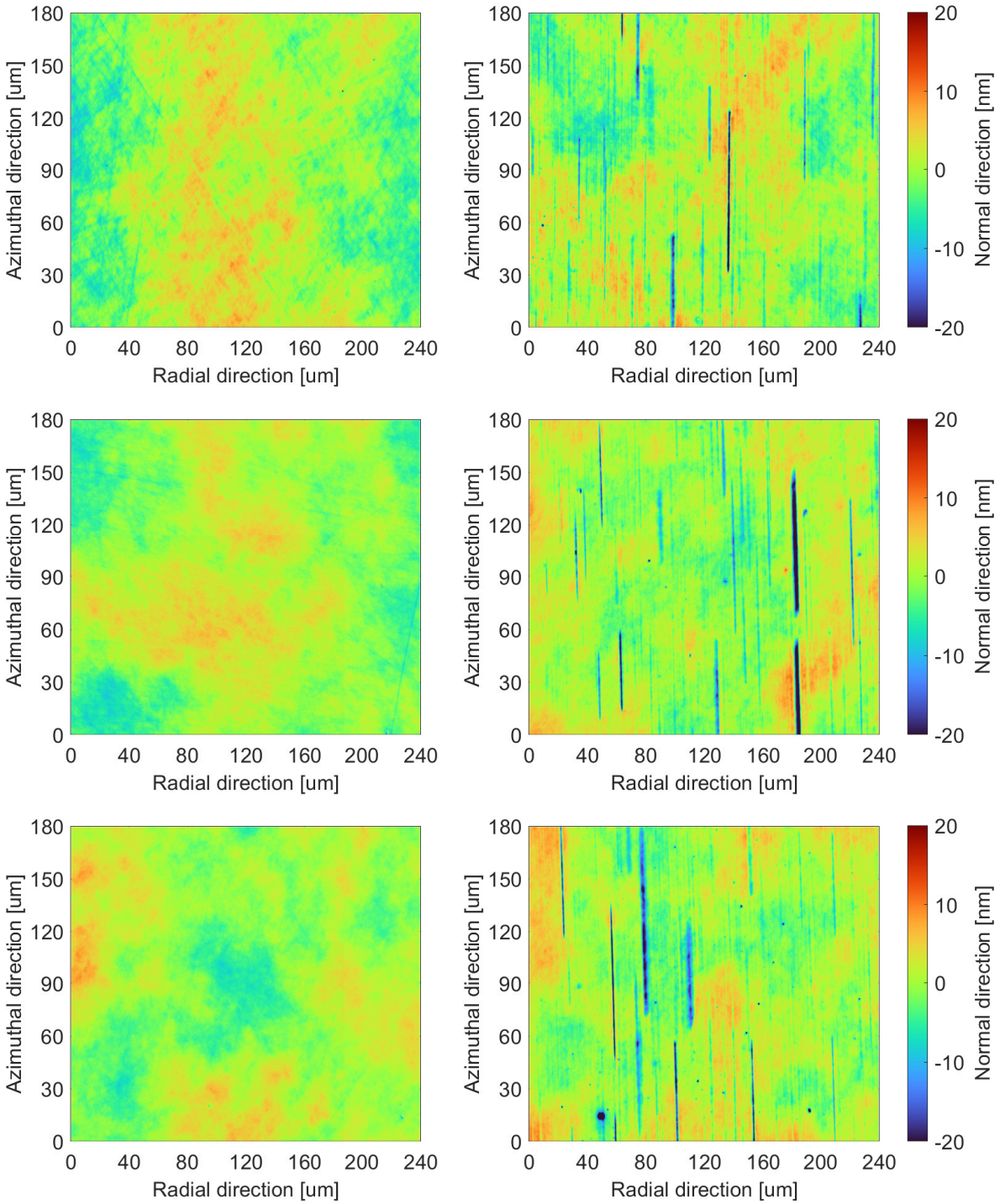


Figure 7.19: MTM disc profiles from white-light interferometer before (left column) and after running-in (right column) for three MTM tests (rows) shown in Fig. 7.18. The disc surface, which is initially less rough than the ball, is significantly modified by the running-in.

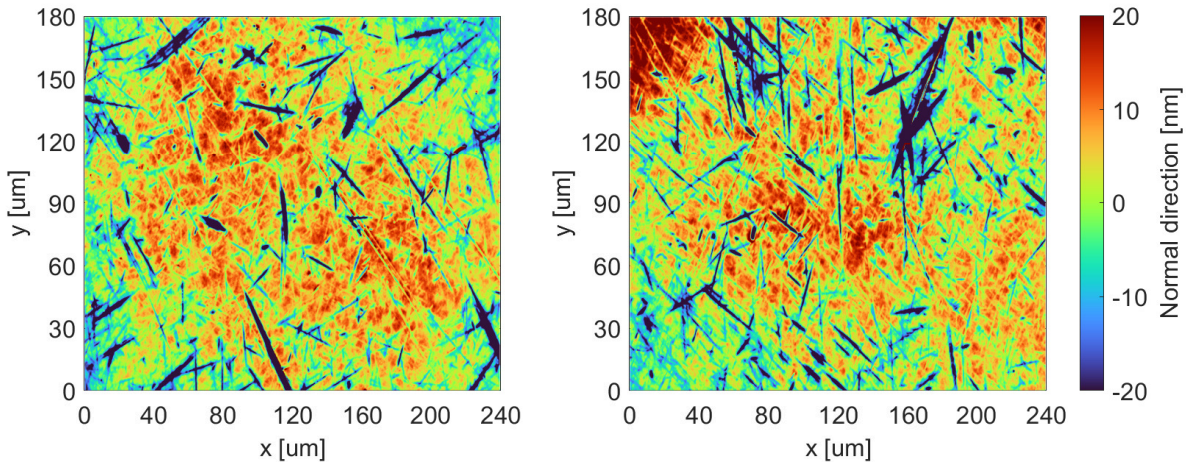


Figure 7.20: MTM ball profiles from white-light interferometer before (left) and after running-in (right) for one of the MTM tests shown in Fig. 7.18. The ball surface (initially rougher than the disc) is changed relatively little by the running-in.

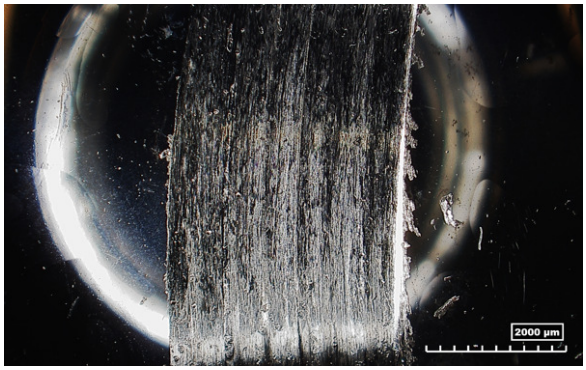
cations at the surface. AISI 52100 was chosen for this study to allow comparison with previous studies using similar specimens [172, 174, 176].

7.2.1.3 Speed-stepping in Contrarotation

The scuffing component of the test involves a series of 30-second timed steps, each with a sliding speed greater than the last. The entrainment speed, load, and lubricant temperature are kept constant throughout all of these steps, and match those during the running-in stage. An SRR of 300% was chosen for the first step to avoid the case at 200% where one of the specimens is stationary and any surface damage is therefore concentrated onto a small part of the wear track. The SRR was then increased in 100% increments, corresponding to 100 mm/s increments in sliding speed.

Friction coefficient was measured throughout these steps, and was seen at the onset of scuffing to increase suddenly from around 0.1 (representative lubricated steel-steel boundary friction coefficients) to greater than 0.2, accompanied by broadband audible noise and perceptible vibration. The scuffing criterion also stipulates that this increase is unrecoverable, and so the friction coefficient does not suddenly return to its initial lower value within 2 seconds. After this condition had occurred the surface roughness was found to have increased dramatically and the topography altered by local surface welding. After 2 seconds of high traction coefficient with noise and vibration, the test was stopped to avoid dynamically overloading the transducers or

(a) Ball Surface (scale bar 2 mm)



(b) Disc Surface (scale bar 2 mm)



(c) Ball Surface Magnified (scale bar 500 μm)



(d) Disc Surface Magnified (scale bar 200 μm)

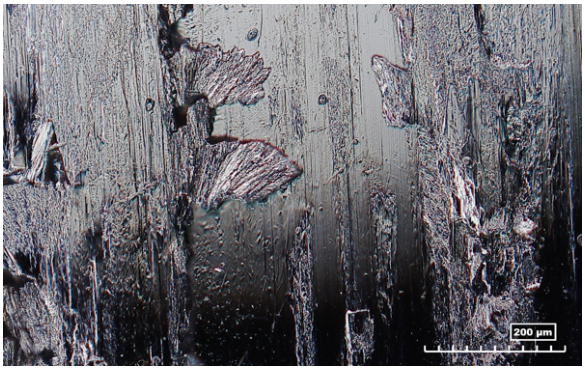
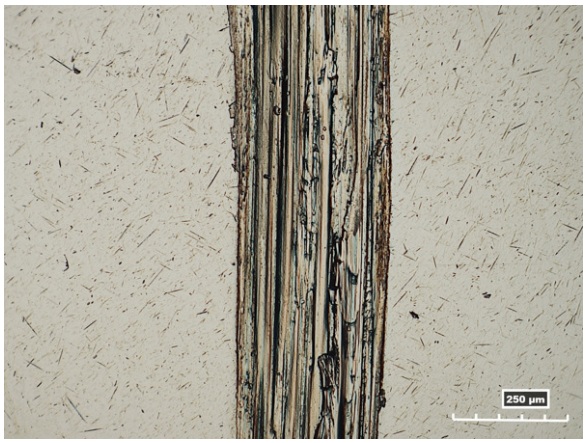


Figure 7.21: Ball and disc surfaces after advanced scuffing for PAO5, 45 N load, 200 mm/s entrainment speed, 3000 mm/s sliding speed, and 5 minute step time

motors. One test was conducted at lower load for several minutes after the onset of scuffing, and optical micrographs of the surface topography of this extreme example are shown in Fig. 7.21. In this case, the friction coefficient, which was initially around 0.08, increased to 0.34 after the onset of scuffing, and catastrophic wear followed, ultimately causing the

(a) Ball Surface (scale bar 250 μm)



(b) Disc Surface (scale bar 250 μm)

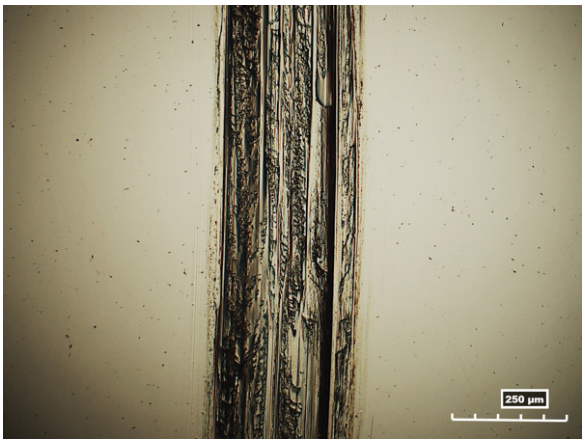


Figure 7.22: Ball (a) and disc (b) surfaces at end of ETM scuffing test with PAO5, 75 N load

ball surface to conform to the flat disc in the transversal direction. Even with the vastly reduced 'Hertz' contact pressure in this case (clearly the contact is far from Hertzian!), the increase in roughness has resulted in high-sliding boundary-lubricated conditions with highly localised shear stresses which give rise to a thermal feedback leading to self-sustaining adhesive wear, i.e. scuffing. The specimen surfaces after the speed-stepping scuffing tests reported here, although they were not allowed to accumulate such extensive wear, displayed similar characteristics as the surfaces in Fig. 7.21, an example is given in Fig. 7.22. These were dramatically increased surface roughness, a striated surface with evidence of adhesion and plastic flow of material, and a wear track wider than the Hertz contact width flanked by large flakes appearing to have been ploughed out of the contact track.

The creation of the test profiles for this task, requiring many very similar timed steps with distinct SRRs, was performed using a MATLAB script able to create MTM and ETM profile files. This was made possible by reverse-engineering the `.mtmp` and `.etmp` binary file formats using a hex editor. The script was then written to reconstruct the byte sequence of the file formats (which differs slightly between the MTM and ETM on account of the lack of the ECR option on the ETM, and the absence of the bidirectional traction and bidirectional Stribeck steps). The code is hosted at https://github.com/AlexanderMacL/mtmp2json. The scuffing test profile was constructed in this way by simply looping through the desired SRRs and creating the relevant timed and mapper steps for each (in addition to the initial running-in step). This approach had the advantage that, when it was necessary to change the test load or temperature, the profile could be regenerated after changing a single number, instead of manually clicking through many tens of steps in the MTM Profile Editor GUI application provided with the MTM, and so was much quicker and less error-prone.

7.2.1.4 Mapper Steps

Interspersed between the timed steps were a series of mapper steps, which wait for a pre-specified time before taking a photograph with the mapper camera. Mapper steps are designed to record the interferogram created by the SLIM technique, discussed at length in Chapter 8. In the case of these scuffing tests however, the accumulated wear changes the ball reflectivity and contact geometry such that the interferogram is of little use for tribofilm thickness measurement, but the image nevertheless provides an qualitative insight into the extent of

the wear, any changes in the surface topography, and the presence or absence of a boundary film.

More importantly however, the mapper step brings the ball and disc out of contact, and gives both surfaces, and the whole system, time to cool to the nominal test temperature before the next step starts. During the mapper step the disc spins to circulate the lubricant around the pot in the same way as during the temperature stabilisation before the timed step. The duration of the mapper steps in these tests was 30 s, to match those of Peng. If, at the end of the 30 s period, the lubricant temperature has not stabilised to within 1°C of the nominal temperature, the timed step once more waits for the temperature to stabilise before the load is applied.

The structure of the complete scuffing test is presented in schematic form in Fig. 7.23. An initial SLIM image was also taken before the running-in step.

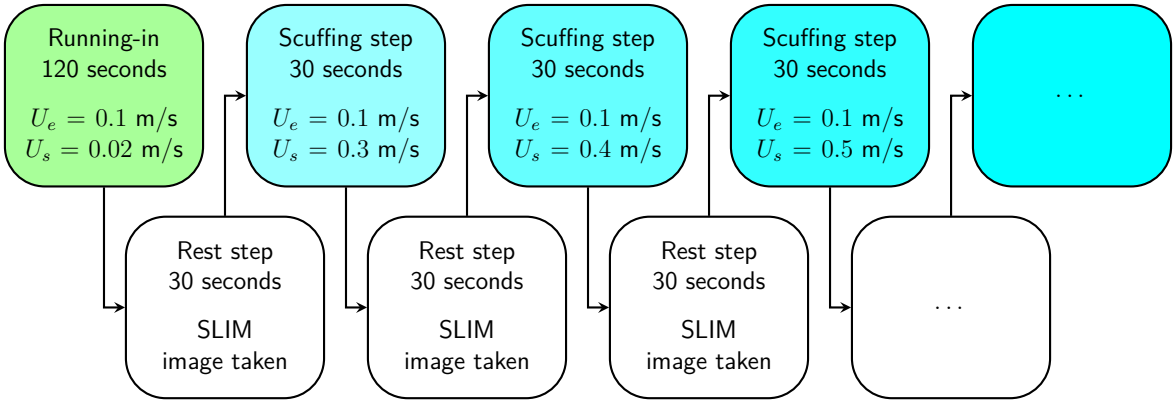


Figure 7.23: Schematic of modified contrarotation scuffing test following that of Peng [175]

7.2.2 Scuffing Performance of Transmission Fluids

Subsequent to each of the seven repeats of the running-in step with PAO5, the scuffing steps were performed in the sequence shown in Fig. 7.23. The friction coefficients, and hence the sliding speed at onset of scuffing, are presented for these tests in Fig. 7.24. The scuffing speed for this unformulated base oil is quite low and so some variation might be expected given the absence of stabilising additives, and the nature of scuffing as a sudden instability in the lubrication condition. On comparison with Fig. 7.18, it can be seen that the scuffing speed is not well-correlated to the variations in friction coefficient between repeats at the running-in stage. Variability of a greater order was seen by Peng across 15 repeats for a similar test on

the same rig, and the separation between repeats does not undermine the separation in the results to follow in this section (where load is also considered), so this variation is not a cause for concern, rather it is a feature of the resolution of this test, and the mechanisms underlying scuffing.

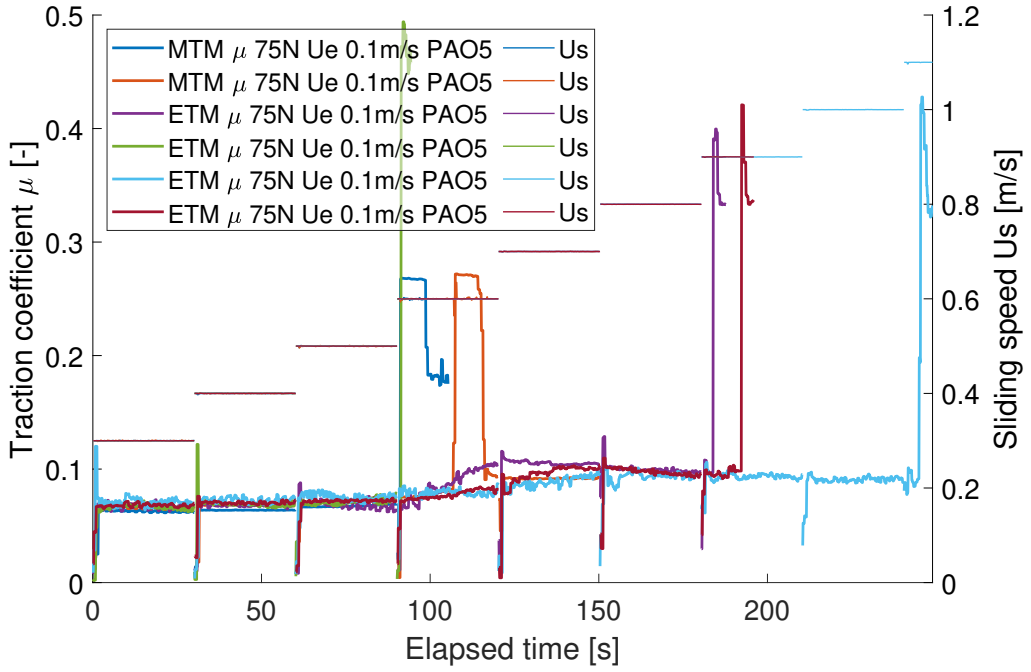
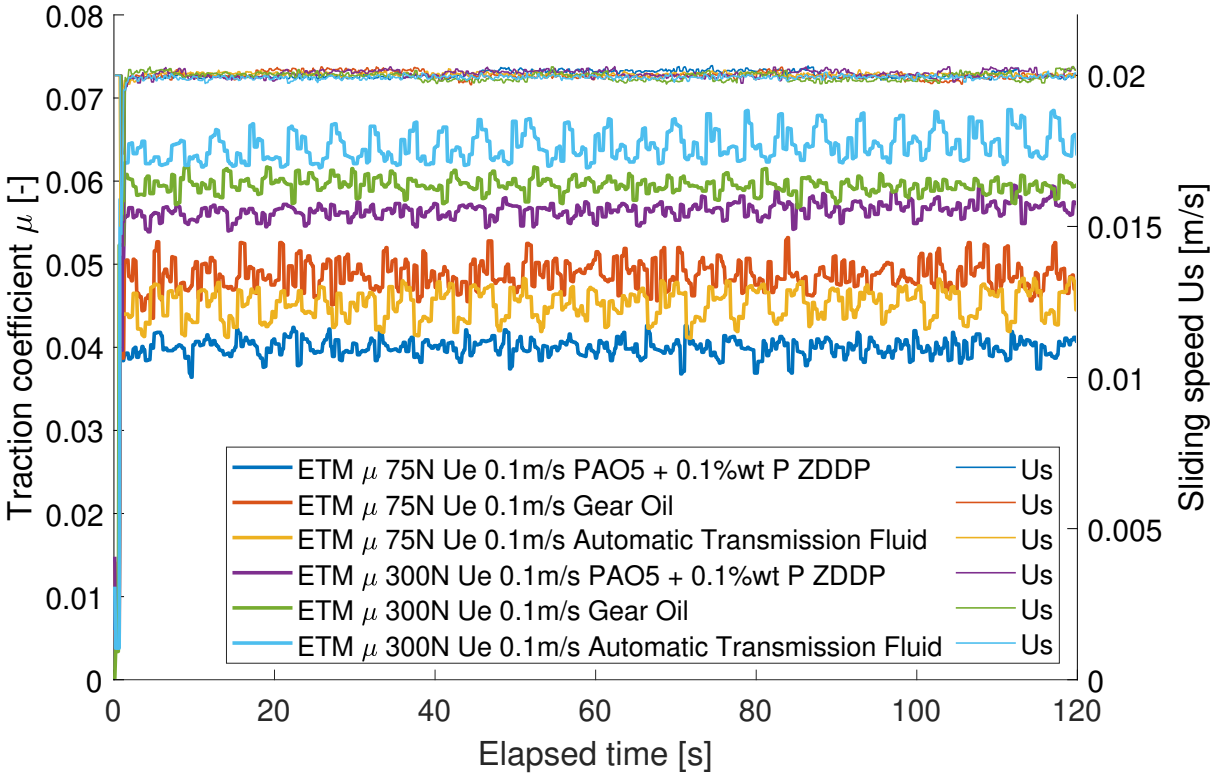


Figure 7.24: Friction coefficient μ and sliding speed U_s recorded during 6 repeats of the same scuffing procedure after running-in, two with the MTM and four with the ETM, for the same tests as shown in Fig. 7.18 (one of the MTM tests was not continued to the scuffing stage), showing that despite the similarity in behaviour during the running-in stage, there is considerable variation in the scuffing speed between repeats. The fluid was PAO5, the ball load was 75 N, and the maximum Hertz pressure was 1.27 GPa.

A comparison between three fluids of similar viscosity, at two different loads, is shown in Fig. 7.25. All three fluids contain EP (extreme pressure) additives which are successful in mitigating scuffing up to 6 m/s sliding speed at 75 N load (1.3 GPa max. Hertz pressure). ZDDP, known primarily for its antiwear function, also acts as a mild EP additive in this case when added to the PAO, greatly increasing its scuffing resistance. The ATF and the gear oil do not contain ZDDP.

On examining the results in Fig. 7.25b, it might be concluded that PAO5 + ZDDP outperforms the other formulations because it attains the highest sliding speed before scuffing, and produces lower friction coefficients in the running-in stage. The friction trace during the scuffing steps

(a) Running-in step



(b) Scuffing steps

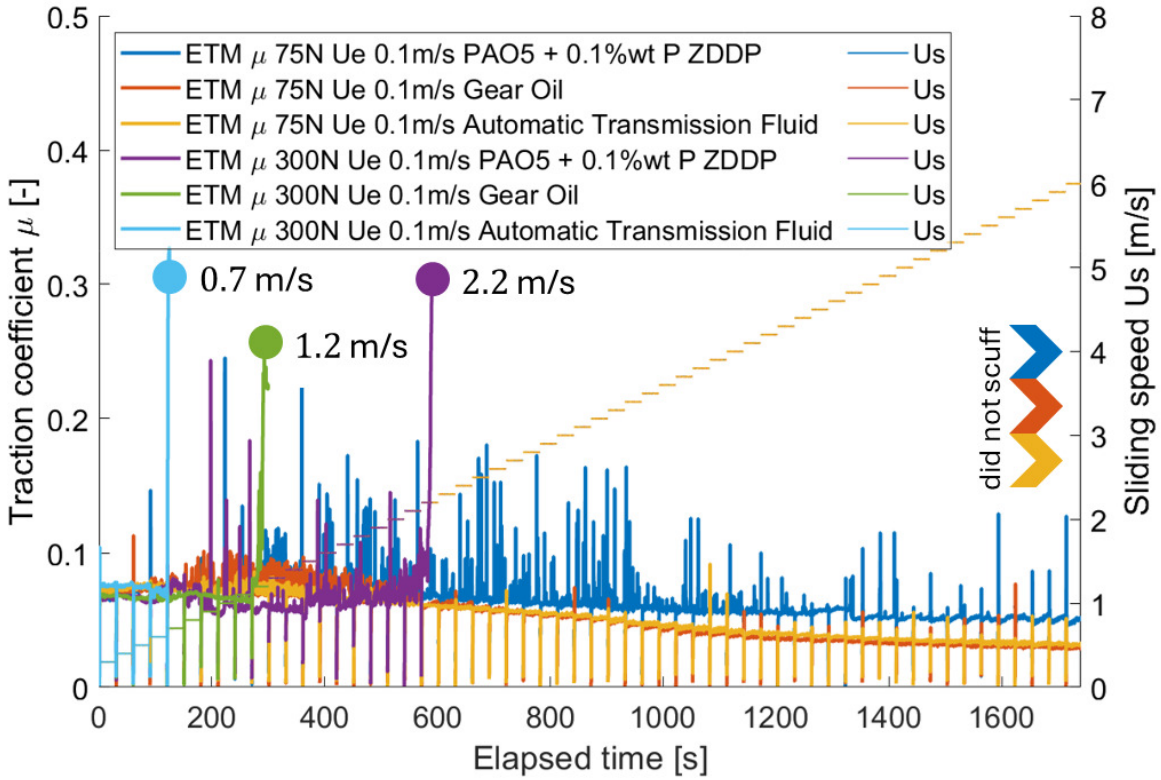


Figure 7.25: Scuffing tests conducted at 75 N and 300 N for two candidate transmission fluids and a blend of PAO5 and ZDDP, showing friction coefficient and sliding speed throughout.

however contains many brief excursions to much higher values, indicating some transient tribological process not present for the other fluids, and ZDDP is known also to act as a mild EP additive. On examination of the SLIM images shown in Fig. 7.27, evidence of wear can be seen (aberration from circular contact shape), and also of a thick tribofilm (visual inspection of the colours suggests $\sim$50 nm towards the centre of the contact track by the end of the test). The mechanochemical reaction leading to the formation of the glassy thiophosphate tribofilm is driven by the combination of high temperature and shear stress in sliding asperity-asperity contact, but the same shear stresses also act to remove layers of the tribofilm. At high pressures and sliding speeds such as these, the rate of removal may locally outstrip the rate of formation, resulting in considerable wear. The higher friction at high sliding speeds is also attributable to the roughness of the tribofilm formed, which (unlike in machine components where CLA roughnesses are typically hundreds of nm) is much greater than the initially very smooth surfaces used in these tests. This leads to greater shear transience than experienced by the ATF and gear oil tests where the surface is almost unchanged until scuffing occurs, and where no thick tribofilm develops. In a gearbox, the tribofilm formation (which may promote asperity persistence leading to fatigue damage), friction transience (with potential NVH implications) and greater wear rate (giving rise to a host of other damage modes such as 3rd-body wear, surface-initiated fatigue and debris-induced film collapse) incurred by the PAO5 + ZDDP are obviously not acceptable. The sliding speed and load at scuffing reported by such tests should therefore always be considered in the context of the evolution of the surfaces during the test, considering damage modes such as abrasive wear which occur instead of scuffing for certain formulations.

These results do not agree with one of the conclusions of Enthoven and Spikes [159, 160], who propose wear-debris-induced starvation as a possible cause of scuffing, and suggest that cases leading to higher wear rates should accelerate scuffing. There are several notable differences between the MTM/ETM and the setup used in that work, which uses a stationary sapphire disc in contact with a flat ball, and so is kinematically and thermally unlike the contrarotation test in which both surfaces move. The test equipment they used appears also to induce an oil flow field that promotes recirculation of debris into the contact, while the MTM pot is configured so that wear debris can be rejected into the space outside and below the disc surface, where the flow is stagnant and perpendicular to the path towards the surfaces. Finally,

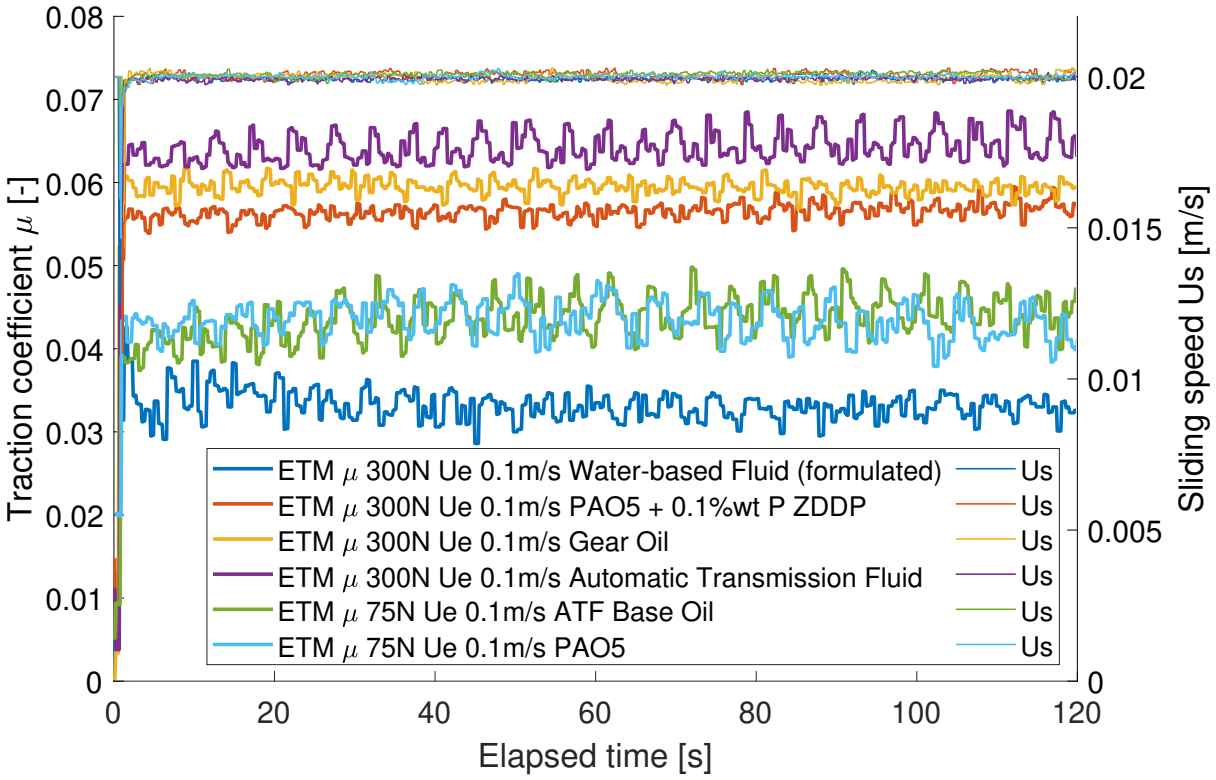
the system they examined did not include a thiophosphate tribofilm, which may change the nature of the debris itself, and influence its effect if it re-enters the contact. While debris entrainment is one possible cause of scuffing, this may be outcompeted by other causes and so it is clear that there are cases for which scuffing does not correlate with wear.

The scuffing tests during which each fluid scuffed under the most extreme conditions are shown in Fig. 7.26, including the water-based fluid. The sliding speeds at scuffing are indicated, and should be considered with reference to the corresponding loads, which are lower for the two base fluids. The separation between PAO5 and the ATF base fluid (primarily PAO6) is not statistically significant (bearing in mind the results of Fig. 7.24), as expected given their molecular similarity. The ATF and the gear oil, which did not scuff at 75 N (and whose SLIM images show almost no change to the surfaces up to a sliding speed of 7.2 m/s) scuff at relatively low sliding speeds with the 300 N load. The SLIM images of both directly preceding scuffing (Fig. 7.26c) show some preliminary damage, indicative of 'micro-scuffing' (a temporary, recoverable rise in friction coefficient caused by reversible film collapse).

The apparent competition between wear and scuffing is also illustrated by the water-based fluid, which, similarly to the PAO5 + ZDDP, shows extensive wear (at both 75 N, not shown, and 300 N, in Fig. 7.27a) and postpones scuffing to high sliding speed. Several key differences separate the water-based from the ZDDP-containing fluid however - water-based lubricants generally have much higher thermal conductivity, lower boundary friction, and are more corrosive than their oil-based counterparts. The water-based formulation also formed no thick boundary film and so appeared to incur a rapid corrosive-abrasive wear mode, reducing contact pressure early in the test. The lower friction (hence reduced heat generation) and greater thermal conductivity and heat capacity are also likely to reduce contact temperatures (both by reducing the thermal resistance of the EHL film and by faster cooling of the surfaces outside the contact). All of these factors act to retard the thermal feedback required for scuffing.

A series of mapper images is provided to illustrate the qualitative difference in surface evolution throughout the scuffing test for the water-based and ZDDP-containing fluids, compared to the ATF for which there is almost no wear at all. The slight lightening in colour of the images for the ATF (Fig. 7.27d) may indicate the presence of a very thin film, perhaps

(a) Running-in step



(b) Scuffing steps

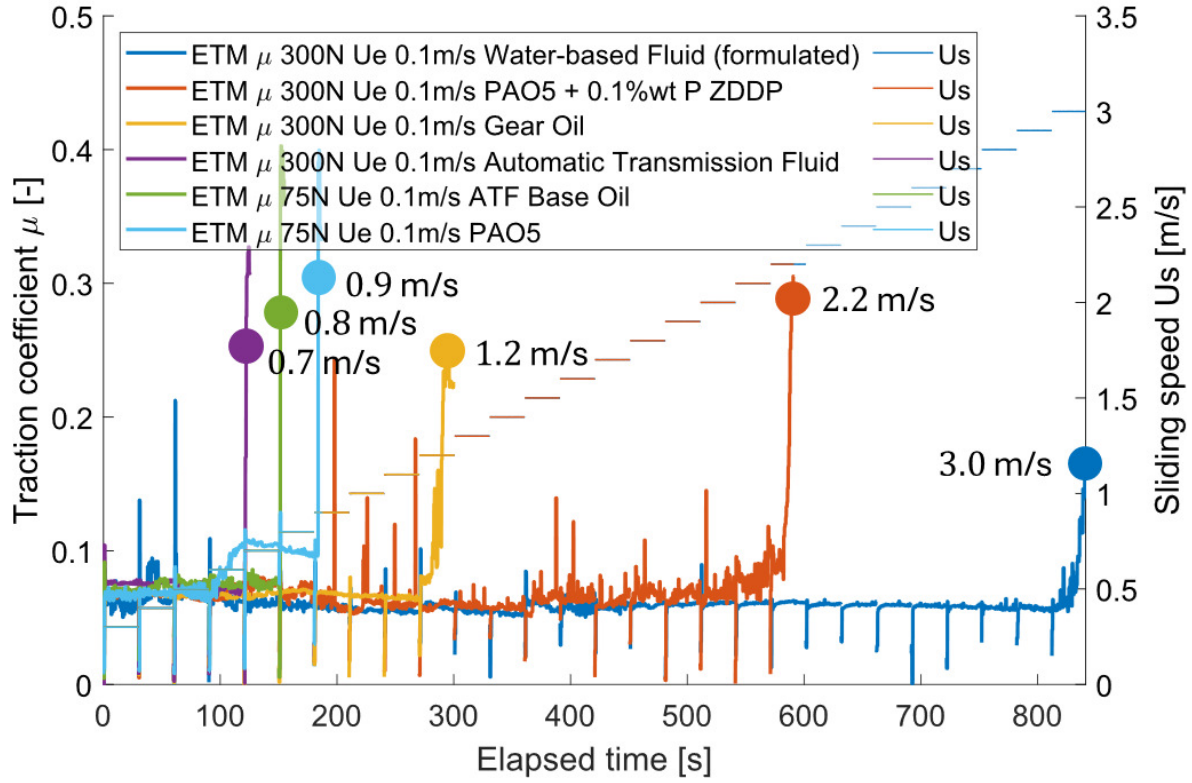


Figure 7.26: Scuffing performance of four candidate transmission fluids and two base stocks, indicating sliding speed at scuffing, with a 300 N (2.0 GPa) load used for those fluids which did not scuff for $U_s \leq 6$ m/s at 75 N (1.3 GPa).

(c) SLIM images for each fluid taken directly before earliest scuffing occurred

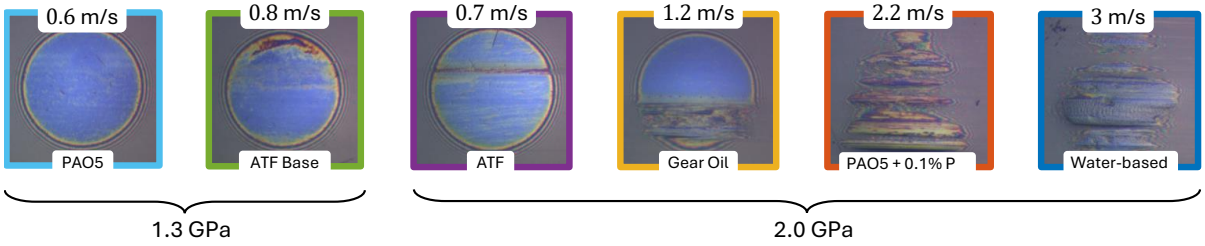


Figure 7.26: (continued) Scuffing performance of four candidate transmission fluids and two base stocks, indicating sliding speed at scuffing, with a 300 N (2.0 GPa) load used for those fluids which did not scuff for $U_s \leq 6$ m/s at 75 N (1.3 GPa).

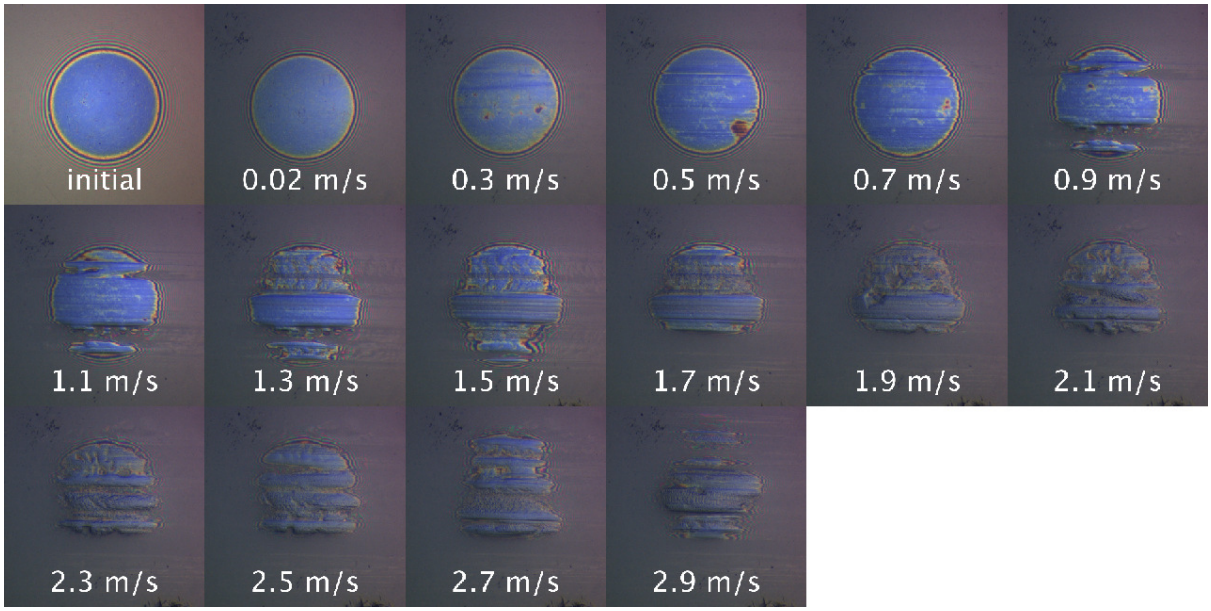
$\sim$ 10 nm (the ATF formulation is likely to contain several molecules which adsorb to the surface, including antioxidants, surfactants, friction modifiers, anti-wear and EP additives - the interaction between these is complex and is not examined in this study).

For the ZDDP-containing fluid at the lower load (Fig. 7.27c), a complex film geometry appears to develop outside the wear track in the upper part of the image. This region also experiences high temperature and shear stress, which promote film formation, but does not experience the harsh conditions leading to film removal within the contact. The blend used here contained a mixture of primary and secondary ZDDPs whose propensity to form durable crystalline, or less durable amorphous films, is not known. The brown colour in the lower half of the image implies a reasonably thick film ($\sim$ 50 nm) has formed within the contact track by the end of the test, and the aberration of the lower edges from their previously circular shape indicates some mild, localised wear has taken place.

These results, although preliminary, have important implications for future testing and development of EV transmission lubricants. In particular, the reporting of friction coefficient throughout the test, the quantitative and finely discretised nature of the sliding-speed-at-scuffing, the in-situ optical examination of the evolution of the ball surface, and the tight control of surface condition and contact dynamics, promise a considerably higher-dimensional dataset with greater repeatability at a fraction of the cost of gear-tester scuffing tests such as FZG A10/16.6R/90 and related methods. The choice of scuffing test methods used to screen new EV fluid lubricants in striking a balance between copper-compatibility and EP performance is critical - formulation of fluids to pass tests which are expensive and have poor repeatability, even if they claim application relevance in their use of gear test specimens,

will hinder the optimisation of efficiency and reliability in EV transmissions, so new test methods such as the one explored here are necessary. In the future, an investigation of the suitability of the contrarotation ball-on-disc scuffing test for rougher surfaces under contact conditions more kinematically similar to gear contacts in EV transmissions (for example, the use of rougher surfaces to attain reasonable mixed-lubrication lambda ratios at much higher entrainment speeds would allow more gear-realistic sliding speeds to be attained without the

(a) Water-based fluid at 300 N load



(b) PAO5 + 0.1%wt P ZDDP at 300 N load

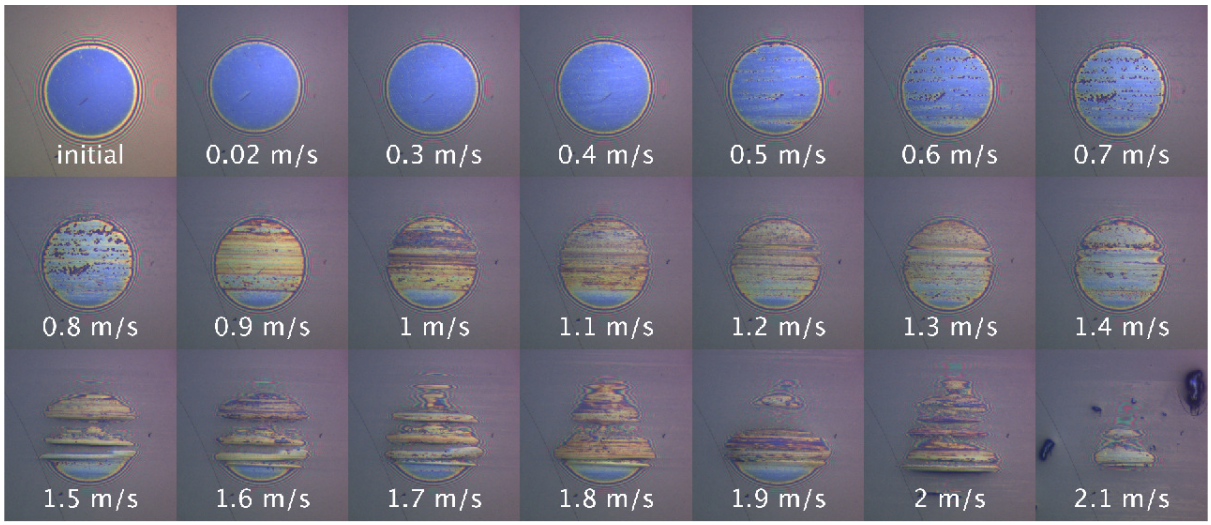
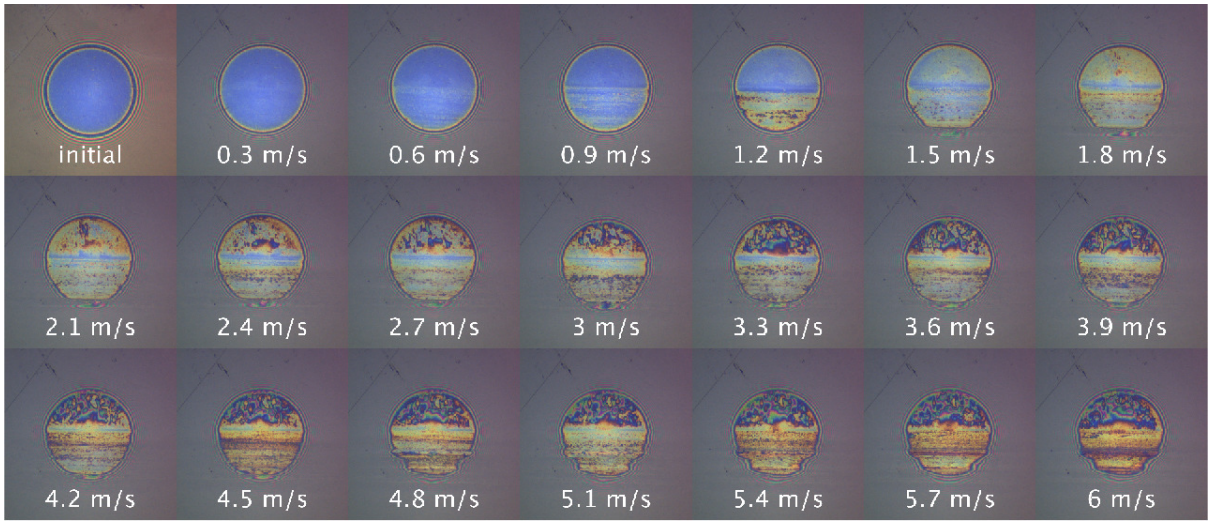
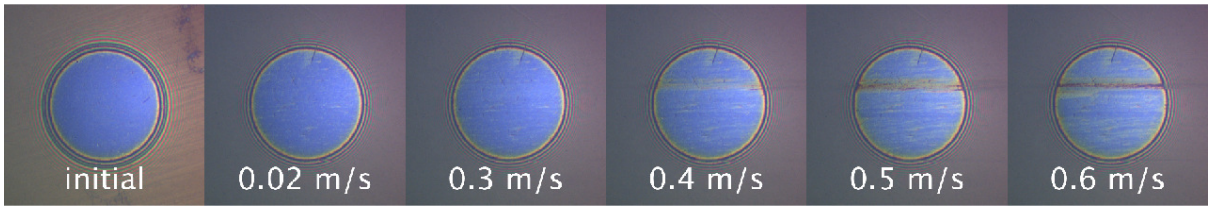


Figure 7.27: Selected mapper images taken during scuffing test, quoting sliding speed for step immediately preceding each image, and showing rapid wear for the water-based and ZDDP-containing fluids (a)-(c), but not for the formulated ATF (d), (e).

(c) PAO5 + 0.1%wt P ZDDP at 75 N load



(d) ATF at 300 N load



(e) ATF at 75 N load

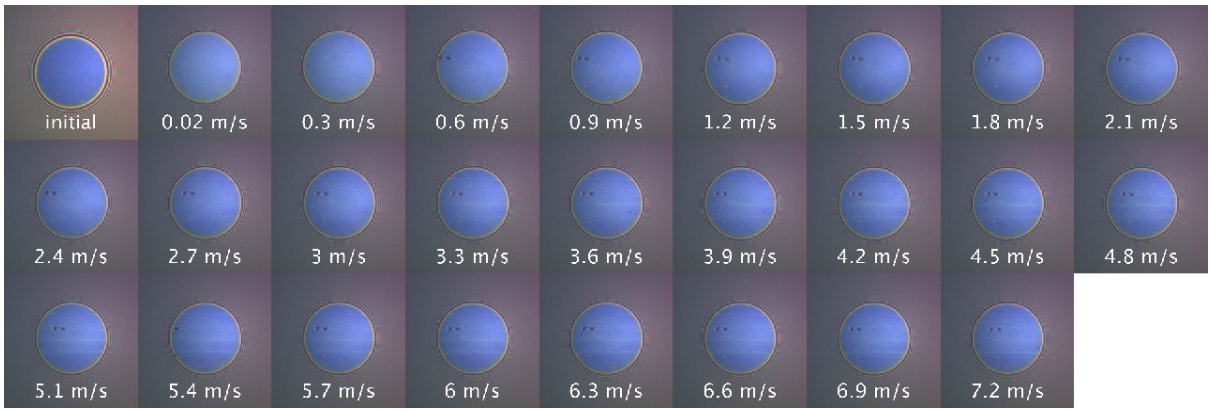


Figure 7.27: (continued) Selected mapper images taken during scuffing test, quoting sliding speed for step immediately preceding each image, and showing rapid wear for the water-based and ZDDP-containing fluids (a)-(c), but not for the formulated ATF (d), (e).

use of extremely high slide-roll ratios, so contact-scale advective heat transport by fluid and surfaces bears greater analogy to that in a gear), would be of interest. These implications are discussed further in Section 9.3 on page 250.

Chapter 8

Film Thickness Mapping using the Spacer Layer Imaging Method

The study presented in this chapter has previously been published by the author in an open-access paper entitled 'Enhancing the Range and Reliability of the Spacer Layer Imaging Method'*, in collaboration with Parker LaMascus and Robert Carpick of the University of Pennsylvania. Only the sections of that paper to which Alexander MacLaren was the principal contributor are included here.*

The Spacer Layer Imaging Method (SLIM) is widely used to measure the thickness of additive and lubricant films, in lubricant development and evaluation, and for fundamental research into elastohydrodynamic lubrication and tribofilm formation mechanisms. The film thickness measurement, as implemented on several popular tribometers, provides powerful, non-destructive *in situ* mapping of film topography with nanometre-scale film thickness resolution. However, the results can be highly sensitive to experimental procedure, machine condition, and image analysis, in some cases reporting unphysical film thickness trends. The prevailing image analysis techniques make it challenging to interrogate these errors, often hiding their multivariate nonlinear behaviour from the user by spatial averaging. Herein, several common 'silent errors' in the SLIM measurement, including colour matching to incorrect fringe orders, and colour drift due to the optical properties of the system or film itself, are discussed, with examples. A robust suite of novel and *a posteriori* methods to address these issues, and to improve the accuracy and reliability of the measurement, are also presented, including a novel, computationally inexpensive circle-finding algorithm for automated image processing. In combination, these methods allow reliable mapping of films up to at least 800 nm in thickness, representing a significant milestone for the utility of SLIM applied to elastohydrodynamic contact.

8.1 Introduction to SLIM

Film thickness measurement by optical interferometry has contributed to the study of elastohydrodynamic lubrication (EHL) since the 1960s [89, 127], but was later combined with the spacer layer technique by Spikes, Cann and Hutchinson [126, 135] to produce the Spacer Layer Imaging Method (SLIM). The use of white light and a colorimetric image analysis enables *in-situ* mapping of elastohydrodynamic (EHD) film thickness to nanometre resolution for films only a few nanometres thick.

The colorimetric image analysis used by Cann was subsequently extended by Hartl *et al.* [249], whose automated implementation later came to be known as differential colorimetric interferometry (DCI) [136]. This technique, following Gustafsson *et al.* [250], uses a calibration method based on colours measured in a stationary contact, whereas SLIM uses a calibration created using ultra-thin-film interferometry [108]. DCI has been used extensively to study film shape in EHL contacts with high sliding speeds [251], spin and skew [252], rheologically unusual lubricants [253], and under thermal-EHL conditions [251]. Studies using DCI have principally focused on full-film EHL and typically have not used the spacer layer, whose purpose is to increase the resolution of the technique for films thinner than $\sim$120 nm. Some DCI implementations have used the CIELAB [254] and hue-saturation-value (HSV) [255] colour spaces, while some, like SLIM, have used red-green-blue (RGB) [252, 256]. SLIM and DCI are otherwise essentially the same, but several aspects of their implementation remain unpublished. For the RGB colour space, the question of how to distinguish between similar colours belonging to different fringe orders created by very different film thicknesses in an optically noisy environment, without human input, for example, remains unaddressed. This fringe-order ambiguity problem may severely compromise film thickness measurements for certain colours produced by films thicker than 250 nm. Golafshan *et al.* [257] recently proposed a technique based on 2D phase unwrapping, which uses only the hue channel of the HSV colour space in their study of transient EHL, and a similar technique is applied by Tomota *et al.* [255] to rough contact. Several authors over the last 25 years [252–254] have nevertheless successfully overcome the fringe order ambiguity problem, but precisely how, and how easily, remains unclear.

The SLIM technique is an increasingly important part of industrial decision-making and

academic study. Its implementation on the MTM (Mini-Traction Machine) [258] and EHD2 tribometers [175] by PCS Instruments, has been used to help uncover several aspects of tribofilm formation kinetics [189, 200, 259–262], to study rough contact [131, 263, 264] and micro-EHL [265], and to assess lubricant additive performance for existing and next-generation technologies such as wind turbines and electric vehicles [266, 267]. In some cases, the scientific conclusions from such studies could be altered by a $10-20$ nm variation in the measurement, so the repeatability and accuracy of the SLIM technique within this range is paramount.

SLIM is one of several film thickness measurement techniques based on optical interferometry - it is not to be confused with ultra-thin-film interferometry [108], which uses a similar ball-on-disc contact with a thicker spacer layer, and employs a spectrometer to determine optical path difference to finer resolution. Ultra-thin-film interferometry obtains a 1D profile (and usually only a single-point measurement is recorded), rather than a 2D map of the film. The Relative Optical Interference Intensity (ROII) technique, involving a formalised fringe-counting and sinusoidal interpolation procedure, has also been used to measure EHL film thickness [137, 138, 268], but itself is not inherently colorimetric, although it has been used with trichromatic interferometry by Marx *et al.* [132].

This work discusses several 'silent errors' that can lead to inaccuracies in the measurements made using the SLIM technique. Multiple solutions are proposed and validated, including a suite of analysis tools to diagnose and remedy these errors, and experimental best practices to minimise the risk of error *a priori*. The film thickness range over which the colour-matching is reliable without manual intervention is extended from approximately 150 nm to 800 nm. These results and tools will help users to make the most of the SLIM technique, to be aware of and account for its limitations, and to examine the accuracy of their results.

8.2 The Spacer Layer Imaging Method

The SLIM technique is primarily used for the optical measurement of the spatially-resolved thickness of elastohydrodynamic fluid films [265] and of solid tribofilms, such as those formed by zinc dialkyl-dithiophosphates (ZDDPs) [262] or other additives [267]. This work will use the term 'film' to refer interchangeably to both EHD lubricant films and tribofilms, as the technique is analogous in its application to each. In the MTM, a rolling-sliding ball-on-disc

contact is often used to build up a solid tribofilm. Periodically, the ball is taken out of EHD contact with the disc and brought into stationary contact with a coated glass disc, which is used to measure the tribofilm thickness at multiple intervals throughout the experiment. The two contacts are distinct, although both involve the ball, and should not be confused: the elastohydrodynamic contact is not imaged by SLIM in the MTM, only the tribofilm on the ball. By contrast, optical tribometers such as the EHD2 [265], TriboGyr [252] and the WAM by Wedeven Associates [269] create a rolling-sliding ball-on-disc contact between a steel ball and coated transparent disc, enabling continuous, real-time imaging and measurement of the lubricant film formed under EHD conditions.

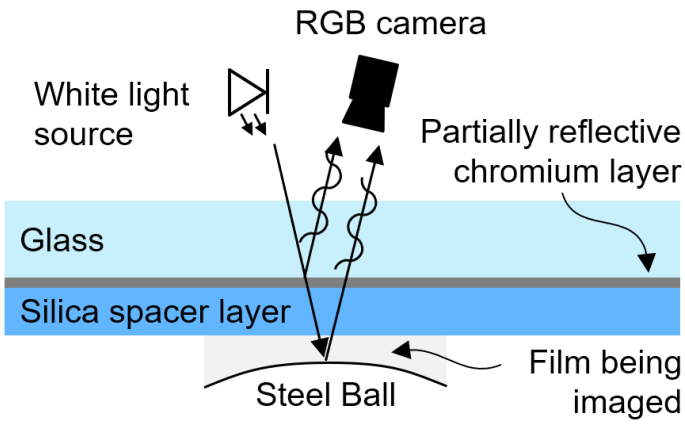


Figure 8.1: SLIM setup used to capture interferometric image of contact

The SLIM technique uses a partially-reflective chromium layer to split white light into two beams (Fig. 8.1). The reflected beam travels directly towards the camera. The transmitted beam travels through the chromium and the transparent film, and is reflected by the steel ball, back towards the chromium. On re-transmission through the chromium, it recombines with the reflected beam. The optical path difference between the two beams introduces a phase difference, causing the beams to interfere, producing a series of constructive and destructive fringes, distinguishing regions of different film thickness. The use of white light, comprising many different wavelengths, creates a coloured interferogram. The colours of the interferogram, recorded by an RGB camera, are correlated to their corresponding film thicknesses to yield a topographical film thickness map. The eponymous silica 'spacer layer' increases the zero-film-thickness path difference to avoid the lowest-order constructive and destructive fringes, allowing the measurement of very thin films (10 nm or less), with a

vertical resolution of the order 1 nm. Example images of an interferogram produced by a tribofilm and an EHD contact are given in Fig. 8.2.

The SLIM technique relies on accurate conversion of interferogram colour to film thickness for each pixel of the image. Analytical solutions to the inverse problem (colour given film thickness) are well-known [270], but require accurate knowledge of system spectral response, which for white light is challenging to measure and control in practice. Instead, an empirical calibration (Fig. 8.3a) is typically created. One widely-used approach is to measure EHD central film thickness using ultra-thin-film-interferometry, and then to capture images using optics analogous to the SLIM setup under the same conditions, and to sample the colour at the centre of the contact [135]. Alternatively, a single static image of a Hertzian contact may be taken, and the colour variation across the Newton's rings compared to an analytical expression for surface separation outside the contact area. The calibration colours are recorded at low pressure, so a correction must be applied to account for the change of refractive index with pressure when the calibration is used to calculate film thickness inside the contact [136].

Film thickness is found by matching the colour of each pixel, represented by the intensities of three colour channels, red (R), green (G), and blue (B), to the colours on the calibration curve. In practice, however, measured colours will not fall exactly on the calibration curve, so a 'nearest' calibration colour is assigned by minimising some distance metric. The distance is calculated in a 3D colour space, with each dimension representing the intensity of the R, G and B channels respectively (Fig. 8.3b). The shortest distance between two points in this space

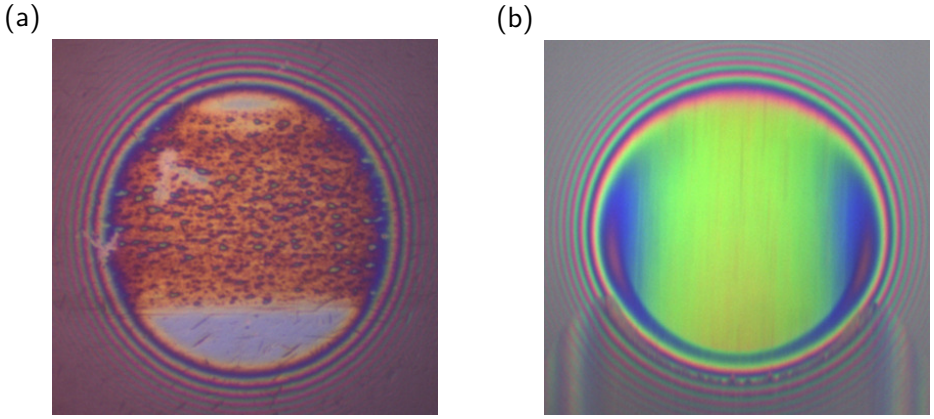


Figure 8.2: Example images of the interferogram produced by SLIM, showing (a) MTM-SLIM image of tribofilm (the entrainment direction is horizontal) and (b) EHD-SLIM image of EHD film (the entrainment direction is vertical)

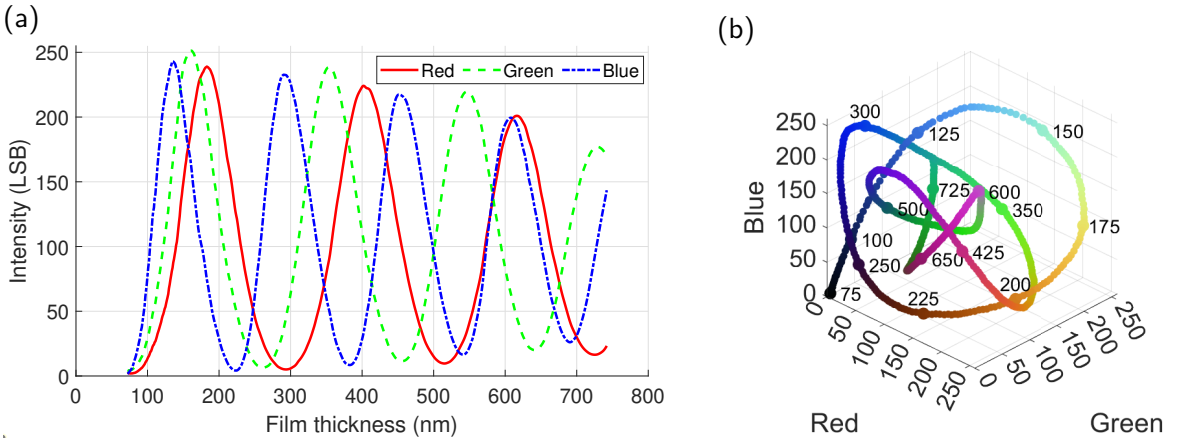


Figure 8.3: (a) Experimental data from an EHD2 showing colour channel intensities vs film thickness for films in the range 80-740 nm, and (b) the same data in RGB space showing the locations of selected film thicknesses, in nanometres.

is the L2 norm (Euclidean distance; the square root of the sum of the squared displacements in each co-ordinate dimension) of the vector joining them, although the L1 norm (Manhattan distance; the sum of the displacements in each co-ordinate dimension) is also widely used and several other metrics are possible. The accuracy of this nearest-colour algorithm varies considerably with parameter choice during analysis (sampling region, averaging block size, distance metric, distance cutoff), as well as the quality of the raw data. High-quality research findings depend on a robust understanding of and ability to monitor the system's limitations, but the tools to do this are not currently available to the majority of users of the technique. Section 8.3 details these limitations, and suggests ways to examine their severity. Section 8.4 presents modifications to analytical procedure which enable the limitations to be addressed.

8.3 Limitations of the SLIM Technique

The SLIM technique makes the following assumptions:

- The tribofilm and/or lubricant are optically transparent
- The absorption spectra of the film, the optical system spectral response, and any interfacial phase shifts, match those when the calibration curve was created
- The film's refractive index is constant spatially (both laterally and through its thickness) and does not change over time

- The thickness of the spacer layer remains constant throughout the test (no wear of the silica coating)
- The ball surface is optically reflective and its reflectivity does not change during the test

These idealized assumptions are frequently violated in reality. A particular problem is created when the interferogram colours no longer match the calibration, leading to two common discrepancies: *intensity shift* and *fringe order ambiguity*. If these are sufficiently severe, the pixel colour will be mapped to an unphysical film thickness, substantially distorting the final measurement.

Unfortunately, a spatial map of the calculated film thickness is often not provided in literature concerning tribofilms (even though the possibility of doing this is one of the benefits of the technique), making it impossible for the reader (or even the author) to judge to what extent these limitations affect the results.

8.3.1 Intensity shift

The most common discrepancy, but the least obvious to the user, arises due to a change in intensity envelope of one or more colour channels from the camera - usually a reduction in colour saturation as a result of optical absorptivity of the tribosystem, or camera ageing. Fig. 8.4 provides an example from the ETM (Extreme Traction Machine), from PCS instruments, analogous to the MTM but capable of applying much higher loads. The user has adjusted the brightness of the SLIM system's light to match the calibration curve in the 1st-order blue region at the beginning of the test, but the amplitude of colour variation is much smaller in this image than in the calibration, and the majority of the pixel colours fall very far from the correct portion of the calibration curve.

This intensity shift affects the measurement, causing portions of the calibration curve to be omitted from the mapping: as the pixel colours traverse the film thickness range, they 'jump' from one side of a calibration peak to the other, without matching the peak itself. In the extreme case in Fig. 8.4, this jump is ~ 150 nm wide, so unphysical film-thickness discontinuities are introduced into the measurement, the results being compressed on either side of the discontinuity as the colour difference increases. The 'missing' film thicknesses in-between will never appear in the result.

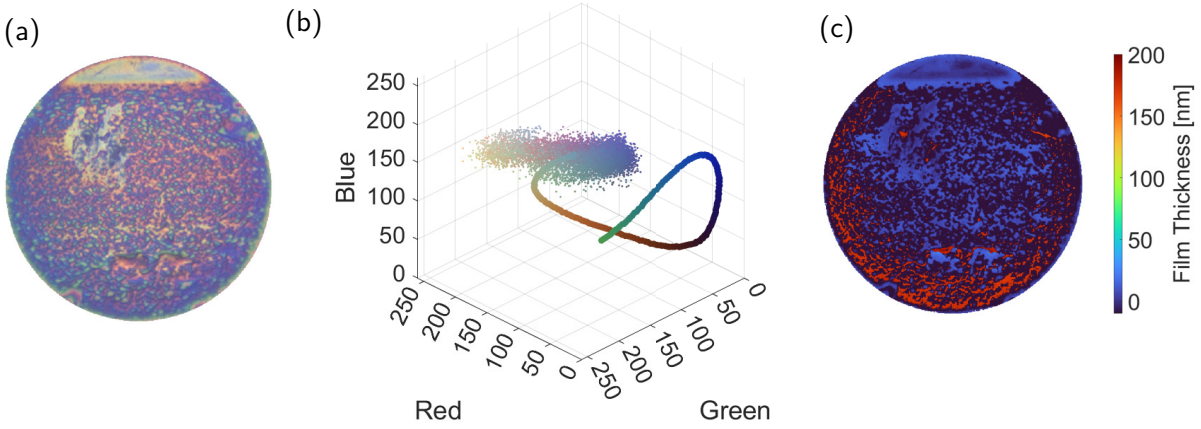


Figure 8.4: (a) ETM-SLIM image of a rough ZDDP tribofilm of thickness ranging from 50 to 200 nm, with selected pixels (b) plotted in RGB space alongside the calibration curve used for the colour matching, showing significant reduction in amplitude on the blue colour channel, causing unphysical film thicknesses (c) to be reported throughout the image.

Intensity shift is exacerbated by the common practice of averaging several pixels' colours before performing the colour matching, which tends to decrease colour saturation. A user may also subsequently average the resulting film thicknesses over an area of the map, obfuscating (but not compensating for, as the response is highly nonlinear) the adverse effect on the measurement - this is discussed further in Section 8.3.4.

Another limitation arises through the practice of measuring the spacer layer thickness at the beginning of the test using a 'zero' image, where the light source is adjusted by the user to create a zero-film colour which matches the calibration curve. The film thickness ascribed to that colour then becomes zero, all others are reduced by its former value, and the section of the calibration curve corresponding to film thicknesses thinner than this is removed. This means that the entire measurement can change ± 20 nm in addition to the stronger knock-on effect of the incorrect brightness setting on thicker films.

8.3.2 Fringe Order Ambiguity

The periodicity of the interference fringes causes the calibration curve to come close to intersecting itself several times during the first 800 nm (Fig. 8.3). The film thickness for a given colour near these intersections is therefore ambiguous, especially if the image colours do not lie exactly on the calibration curve, as is the case in practice (Fig. 8.5). The thickness of the spacer layer is usually $\sim$130 nm, so the 'zero' image colours should be close to the first

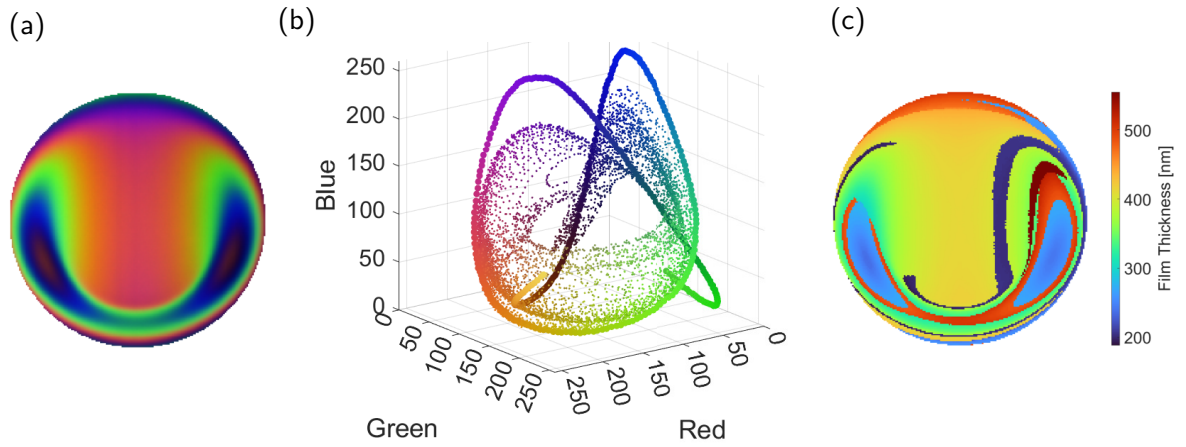


Figure 8.5: Fringe order ambiguity: selected pixels from an EHD-SLIM image (a) compared to calibration line showing reduction in peak saturation and three separate regions of fringe order ambiguity (b), resulting in an unphysical film thickness map (c).

blue peak. Therefore, for films whose thickness does not exceed 200 nm, only the similarity between colours of the 1st and 2nd blue peaks poses a problem. However, if thicker films are to be measured (e.g. EHD lubricant films using EHD-SLIM), the green and orange colours may also lead to order-ambiguity. The calibration used for MTM-SLIM is typically truncated at around 250 nm (excluding the spacer layer), meaning if thicker films are encountered (e.g. ZDDP films whose interferogram contains a pink colour), matching to an incorrect fringe order will certainly occur. The fringe order ambiguity problem worsens significantly when compounded by an intensity shift which moves the pixel colours further from the calibration curve, enlarging the regions where the incorrect order is chosen.

Several solutions to this problem have been proposed which combine colorimetric interferometry with aspects of the ROII technique [132, 256, 264], but these are not yet sufficiently robust or well-known to have found widespread application. Phase-unwrapping methods based on the HSV colour space have several disadvantages including a reduction in the dimensionality of the data (and hence the resolution of the mapping) if only the hue channel is used, and the introduction of cusps into the SLIM calibration curve by the hue-space representation, which causes this reduced resolution to oscillate several times per phase cycle. In addition, the change in permutation of the RGB fringes at the 3rd-order red peak makes the hue channel insensitive to film thickness and therefore unsuitable for phase-unwrapping thereafter. Smeeth and Hamer [271] proposed a camera with a 4th channel sensitive to wavelengths in the near infra-red, expanding the 3D RGB space to a 4D IrRGB hyperspace.

This enables greater separation between the blue, green and orange regions of the existing RGB calibration curve, but this hardware is not yet widely used, and so fringe order ambiguity remains a problem.

8.3.3 Test Procedure and Equipment Condition

The quality of SLIM results also depends on test procedure and equipment condition, which vary depending on the user. Features affecting SLIM data include:

- Intensity of the LED light source
- Selection of analysis area and averaging size
- Cleanliness of the specimens including the SLIM disc
- Specimen material (e.g. steel vs tungsten carbide) and surface roughness
- Whether or not the ball or disc are indexed to the same position each time before capturing an image
- Focus, cleanliness, and alignment of the optics, including lens, beam splitter, and CCD camera
- Spectral content of LED light source (which varies with age)
- Spectral response of CCD camera (which is influenced by age and camera settings)

8.3.4 Averaging Area

When taking average thickness values for areas within SLIM images, larger averaging areas may seem to return more sensible film thicknesses than smaller ones, but in fact this is often deleterious to the accuracy of the measurement. Two separate averaging procedures are discussed here:

1. A **colour average** over a square group (or 'averaging block') of pixels. Each colour channel is averaged separately and each pixel has equal weight (*i.e.*, an arithmetic mean). This procedure can occur *a priori* when taking the zero image, *a posteriori* during the film thickness calculation, or both.
2. A **film-thickness average** over a circular region (or 'sampling circle'), whose size and position are chosen to represent the region of the film to be measured, and each point in which corresponds to the result of the film thickness calculation performed on the

colour of one averaging block.

The former colour average suffers from the fact that the averaging process is a linear operation, while the variation in RGB intensities with film thickness is very nonlinear. Combining discernibly different colours in the same averaging block is therefore risky, as the arithmetically averaged RGB result is unlikely to fall near the calibration curve. However, when the image colour is mostly uniform, a large averaging block can compensate for local brightness variations. For the zero image, this might cover the majority of the Hertzian contact (leaving a small margin to avoid the Newton's rings).

The latter film thickness average yields a sensible result only if each film thickness in the sampling circle is physical in its own right. It is commonly the case that the spatial average acts to hide anomalies created by intensity shift or fringe order ambiguity, resulting in 'more-plausible' (but still grossly inaccurate) film thickness measurements. It should therefore be used with care, and only after a full-resolution film thickness map has been generated and checked for anomalies.

8.4 Analysis Techniques to Overcome Limitations

At present, it is challenging to use SLIM to reliably measure films thicker than 100 nm even under ideal conditions. As discussed above, this is because the coherence envelope and periodicity of the interference colours makes the SLIM measurement more sensitive to intensity shift and fringe order ambiguity for thicker films. This section presents novel techniques to make SLIM more robust, extending its reliable range to approximately 800 nm film thickness, and greatly improving reproducibility.

8.4.1 Context-Aware Colour Matching

One of the advantages of white light over monochromatic interferometry is that the colours inherently remove the need to fringe-count, because fringe order can usually be inferred from colour alone. The colour matching can inherently tolerate height discontinuities, and so a very smooth surface is not required. Nevertheless, it is uncommon in thin-film interferometry of tribosystems for a film to feature gradients greater than 80 nm per pixel (approximately the half-period of the blue channel intensity curve). For example, even if it is initially unclear

whether a single blue-coloured pixel corresponds to the 1st- or 2nd-order blue constructive fringes, a human can look at the surrounding pixels and judge to which order it belongs.

The colour matching used for SLIM analysis however, considers each pixel in isolation, and so is incapable of this context-based approach. Small colour perturbations can therefore lead to fringe order ambiguity for colours where the calibration curve comes close to self-intersection (notably the blue, orange, green, and pink regions in Fig. 8.6).

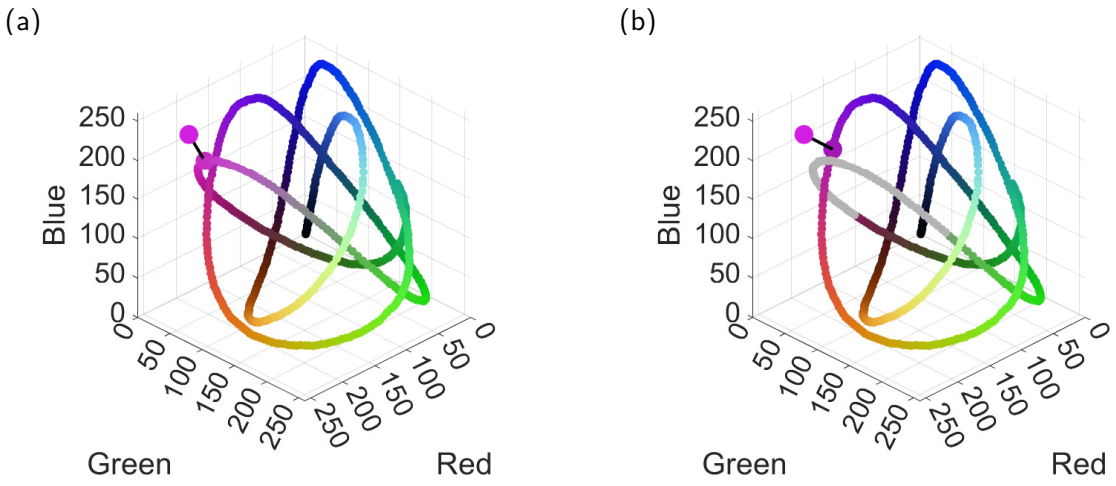


Figure 8.6: Example of colour matching to the calibration curve for nearest (a) and second-nearest (b) branch, used for proposed context-aware colour matching method. For a sample image pixel colour $[R, G, B] = [210, 30, 225]$ near the point where two pink fringes have similar colour, if the nearest colour (a) would lead to incorrect results, then (b) the analysis suppresses the overlapping region (shown in grey) and re-matches.

To bring human-like intuition to the SLIM colour-matching process, a context-aware algorithm is proposed. The algorithm matches each SLIM image pixel to the two nearest regions of the calibration curve (Fig. 8.6), and then selects the film thickness which fits most smoothly between the pixel's neighbouring values. As an example, Fig. 8.6b demonstrates that suppressing a quarter-period of the blue intensity (shortest-wavelength) curve from either side of the nearest colour ensures a match to the second-nearest branch of the calibration curve. This is a robust and powerful solution that can be implemented on existing hardware. The technique bears analogy to phase-unwrapping methods [257], but avoids the problematic transform to HSV.

To determine whether the nearest or second-nearest film thickness is correct, the proposed algorithm traverses the image pixel-wise, assigning to each pixel the value that minimises the

second derivative of the film thickness with respect to position. This is done sequentially by traversing the image only once. The pixel traverse pattern and the definition of the second derivative are both important for the algorithm's success. It is assumed that the local film curvature is small, which requires the variation in film thickness in the space of 1 pixel to be less than the film thickness difference between adjacent branches of the calibration curve. Assuming as a conservative estimate that the in-plane resolution is 1 μm/pixel, and considering the calibration curve to have periodicity equal to that of the blue channel, corresponding to ~ 150 nm film thickness, this means film slopes less than 0.15. This is clearly a safe assumption for most EHD films. For rough ZDDP tribofilms, in regions where the slopes locally exceed 0.15, the wavelengths are generally so short that the pixellation of the image would undermine the colour matching, [197, 272, 273], and so the assumption of low curvature holds whenever the horizontal resolution permits colorimetry.

A spiral traverse pattern is proposed in Fig. 8.7a. For each pixel n, curvatures are approximated by a backward-difference second derivative Δ, both parallel $\Delta_{\parallel}$ and perpendicular $\Delta_{\perp}$ to the traverse direction, given by

$$\Delta_{\parallel} = \left| \begin{bmatrix} -2, & 1, & 1 \end{bmatrix} \cdot \begin{bmatrix} h_n, & h_{n-1}, & h_{n-2} \end{bmatrix} \right| \tag{8.1}$$

$$\Delta_{\perp} = \left| \begin{bmatrix} -2, & 1, & 1 \end{bmatrix} \cdot \begin{bmatrix} h_n, & h_{n \dashv 1}, & h_{n \dashv 2} \end{bmatrix} \right| \tag{8.2}$$

where $|x|$ implies the absolute value of x. The $\dashv$ symbol represents a move perpendicular to the direction in which the numbering increments, or diagonally where the numbering turns a corner.

After the first 5 pixels have been processed, the $\Delta_{\parallel}$ and $\Delta_{\perp}$ derivatives are always calculable using film thicknesses which have already been determined. The film thickness which minimises $\Delta_{\parallel}$ is chosen for each pixel whose two predecessors are spatially adjacent, otherwise $\Delta_{\perp}$ is used instead. Fig. 8.7b illustrates the pixels used to calculate $\Delta_{\parallel}$ and $\Delta_{\perp}$ for several locations on the spiral.

To reduce sensitivity to noise, the algorithm swaps the location of the first two pixels in the sequence before calculating the second derivative, equivalent to a transformation in the second-derivative kernel from $\begin{bmatrix} 1, & -2, & 1 \end{bmatrix}$ to $\begin{bmatrix} -2, & 1, & 1 \end{bmatrix}$. This has the advantage of weighting

most heavily the film thickness h_n whose order is to be selected.

A demonstration of the context-aware matching algorithm for SLIM images produced by an EHD contact is given in Fig. 8.8, showing its success in selecting the correct fringe order throughout the film thickness maps of several EHD contacts. This process is manually laborious and is typically undocumented in literature except for 1D-profiles [132, 264]. This new approach therefore represents a milestone for the robustness of colorimetric interferometry applied to EHL contacts.

The procedure can also be generalised to the Nth-nearest film thickness which is useful for very thick films due to the similarity of the green colours over several successive fringe orders. The colour matching is performed for each pixel in the traverse pattern (Fig. 8.7a), and the nearest colour, second-nearest colour (and so on) film thicknesses are stored (it was found that $N \leq 4$ was sufficient for EHD films of $h_c \leq 800$ nm).

The vulnerability to the nearest colour creating the incorrect film thickness for the first 5 pixels is mitigated by performing the calculation in tandem for the nearest and second-nearest (etc.) colour film thicknesses as shown in Fig. 8.9, and then choosing the map with the smallest total distance once complete, assuming the majority of the image by area falls nearest to the correct branch of the calibration curve. This assumption is strengthened by the technique presented in Section 8.4.2.

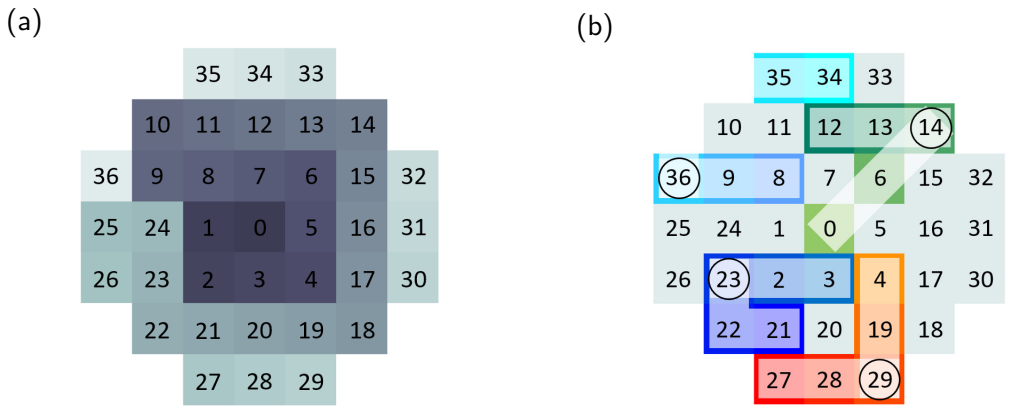


Figure 8.7: Sequence of pixels traversed during order correction, showing a) expanding spiral with alternating direction of rotation and truncated edges for circular sampling region, and b) pixels used (white rectangles) for traverse-tangential ($\Delta_{\parallel}$, sequential numbering) and normal ($\Delta_{\perp}$, non-sequential numbering) second derivatives at four points (circled) on the traverse pattern.

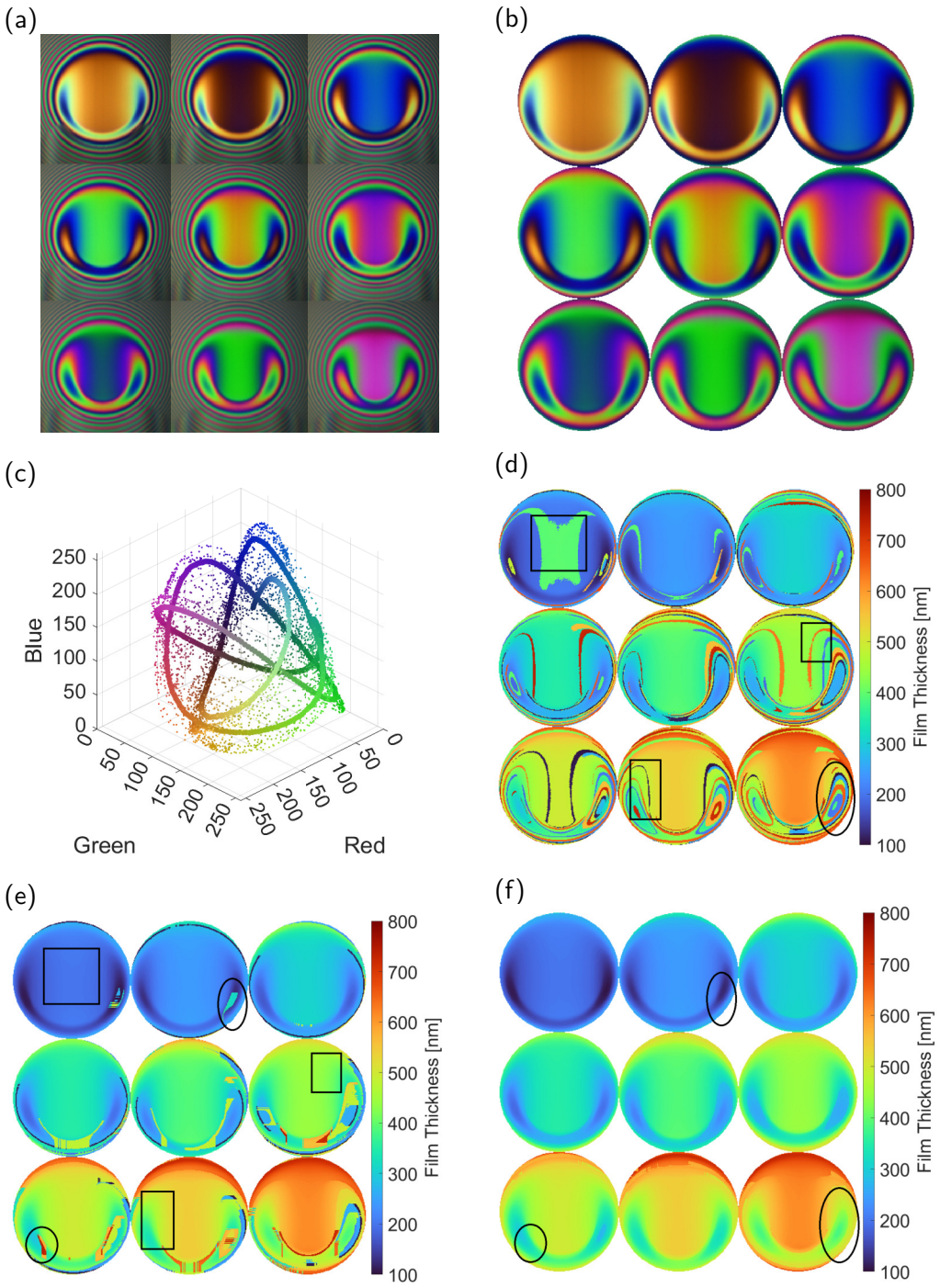


Figure 8.8: (a) Original SLIM images, (b) Cropped and averaged SLIM images (3 px block), (c) Calibration curve (solid) and selected pixels from images in RGB space, (d) Nearest-colour film thicknesses, (e) Context-aware film thicknesses, considering only nearest and 2nd-nearest colours, and (f) also considering 3rd and 4th-nearest colours. The black rectangles indicate some regions where the fringe order has been assigned incorrectly in (d), and where these aliases are removed by choosing the second-nearest film thickness if this minimises the local second derivative in (e), while the black ovals show regions where the second-nearest colour is still an alias. The film shapes in (f) are the most physically realistic. The images in (a) were taken in quick succession at 9 entrainment speeds under conditions given in Table 8.1.

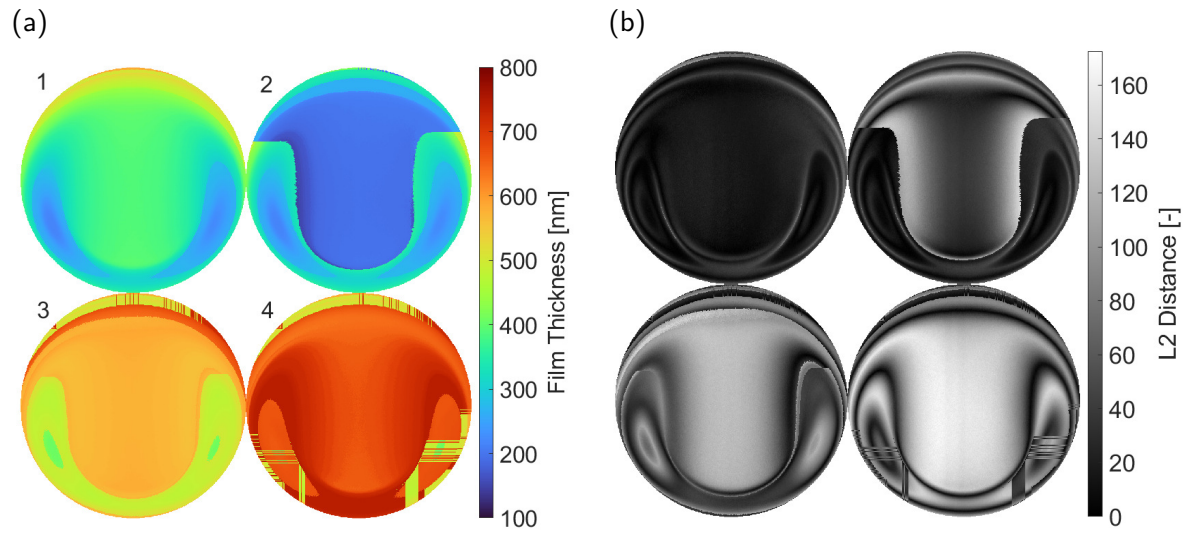


Figure 8.9: (a) Film thickness and (b) distance calculated by order correction assuming (1) nearest, (2) 2nd-nearest, (3) 3rd-nearest and (4) 4th-nearest colours for central region (first 5 pixels), showing the four possible maps created when calculating film thickness by context-aware colour matching for the 5th image (2nd row 2nd column) of those in Fig. 8.8a. The map chosen is that with the least total distance, which in this case is the one assuming the nearest colours are correct, labelled 1. The central region of the original image is a green colour, so the 4 'nearest' colours are at film thicknesses spaced by the period of the green channel of the calibration curve, ~ 190 nm.

Table 8.1: Contact conditions used to create images in Fig. 8.8

Base Fluid	Viscosity [mPa.s]	SRR [%]	Load [N]	Radius [mm]	Speeds [m/s]	Ball Material	Disc Material	Disc Coating
PAO6	57	0	20	9.525	0.5→2.2	52100 Steel	BK7 Glass	Chromium

In cases of poor fringe visibility, the minimisation of $\Delta_{\parallel}$ and $\Delta_{\perp}$ may artificially smoothen the image, and the operator should always inspect the film thickness map and consult their personal intuition for the most physically probable film shape as a check.

8.4.2 Calibration Curve Fitting

Intensity shift, which is not mitigated by order correction, can be resolved by manipulation of the colour intensities of the calibration curve to better fit the pixels in the interferogram. This, however, runs the risk of overfitting, thereby undermining the integrity of the film thickness calculation.

The risk of overfitting is reduced by using a parameterisation of the calibration curve with a small number of coefficients which have physical meaning. Such a fit might be analytically

determined by cross-correlation of a model light source power spectrum with a model spectral response of each channel of the camera, but the complexity of the resulting expressions would limit their utility, and the difficulty in measuring the relevant free parameters (phase shift, chromium reflectivity, absorption by oil contamination) as a function of wavelength would remain. Instead, a fit to existing calibration data is proposed, which is congruent with physical intuition while remaining simple enough to be of use. The fitting function should therefore have the following properties:

- The intensity is expected to vary as the cosine of the optical path difference within the coherence envelope [264]
- Given the short coherence length of white light, each successive fringe should decay in amplitude
- The contribution of higher-order reflections and/or nonlinear camera response to light intensity typically results in a positive skew (wider troughs and narrower peaks)

A function with these properties is given in Eq. (8.3), where the intensity of a colour channel I is related to film thickness h for each colour channel k via the rate of exponential decay p, the angular frequency ω, the constants A and B which together describe the zero-film amplitude and phase shift, and C, an offset. The exponential transform introduces a positive skew.

$$I_k(h) = \exp\left(e^{p_k h}\left[A_k \sin(\omega_k h) + B_k \cos(\omega_k h)\right] + C_k\right) \tag{8.3}$$

This expression has several advantages. Despite the nonlinear form, it is possible to fit the coefficients via two computationally inexpensive linear regressions via the method of Jacquelin [274], according to the integral expression given in Eq. (8.4), where the integrals are calculated trapezoidally.

$$\ln(I) = -\left(p^2 + \omega^2\right) \iint \ln(I)\,\mathrm{d}h + 2p \int \ln(I)\,\mathrm{d}h + Eh^2 + Fh + G \tag{8.4}$$

The first regression finds p, ω, E, F and G, and the second uses these to obtain A, B and C, in which the logarithm of Eq. (8.3) is then linear. Coefficients obtained by this method for the calibration curve in Figs. 8.10a and 8.12a are given in Table 8.2 (note that the film thickness has been reduced by the spacer layer thickness measurement, $\sim$120 nm).

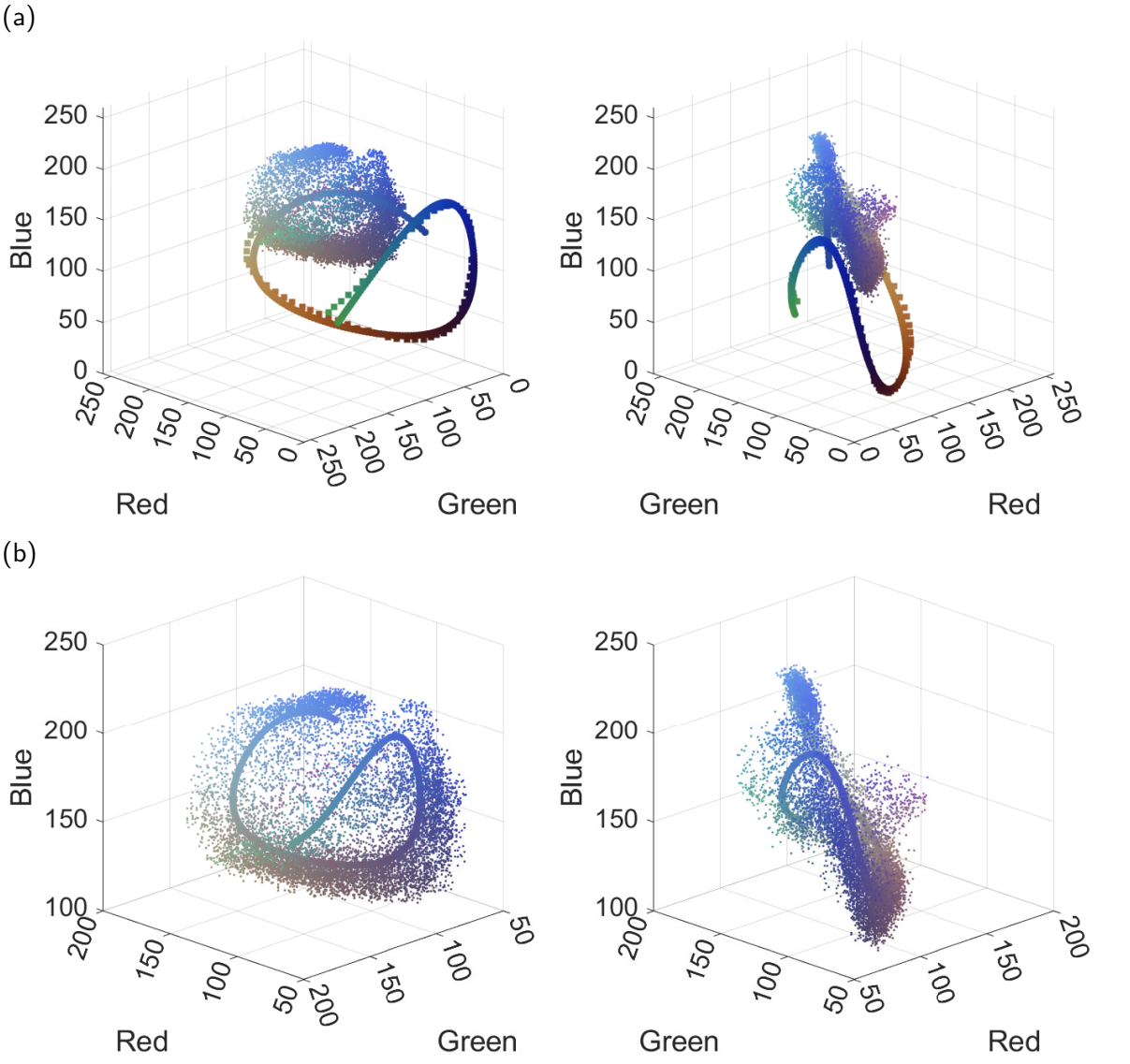


Figure 8.10: (a) Before calibration curve fit. (b) After calibration curve fit. Calibration curve (squares) in RGB space with pixels from MTM tribofilm interferogram (point cloud) showing the analytical fit (continuous) (a) before and (b) after the curve fitting.

Table 8.2: Regression parameters obtained by fit to MTM-SLIM calibration shown in Figs. 8.10a and 8.12a according to Eq. (8.3), assuming h in nm.

Channel	p	ω	A	B	C
R	-0.00020	0.0281	0.951	0.234	4.29
G	-0.00041	0.0317	0.755	0.636	4.20
B	-0.00008	0.0365	0.074	0.870	4.43

The choice of which parameters to change in fitting the calibration curve more closely to the pixel colours without compromising the film thickness is then clear: we do not expect ω to differ between the measurement and the calibration, nor do we expect a change in the phase, i.e. $\frac{A}{B}$. Therefore p, the decay coefficient, and C, which acts to scale the function, are used to fit the interferogram colours. We also introduce a constant offset term D on the RHS of Eq. (8.3) to decouple the mean value of the function from its skewness. These three coefficients can then be fitted for each of the three colour channels by a simultaneous optimisation of all 9 parameters via gradient descent. The total L2 distance between the pixel colours and their nearest point in the calibration curve is minimised.

An example of the refitting of the calibration curve by this method is shown in Fig. 8.10, and the effect on the film thickness calculation illustrated in Figs. 8.11a and 8.11b, with the redistribution of pixel film thickness allocation illustrated in Fig. 8.12. The image of the tribofilm shown was created by boundary friction in a steel-on-steel ball-on-disc contact under the conditions given in Table 8.3 using a PAO5 containing a blend of primary and secondary ZDDPs at a concentration of 0.1%wt Phosphorous, with a total rubbing time of 3 hours before this image was taken, in 9 intervals punctuated by brief unloading for a SLIM image to be taken - this is the 9th such image.

In Fig. 8.11b, the film thickness map created using the refitted calibration curve contains smooth transitions which match the colour transitions in the SLIM image, appealing to human intuition that these film thicknesses are physical. Additionally the reconstructed calibration colours are a good match to the original image, and the distance is uniform across different film thicknesses, indicating that the colour-matching has worked well. The same cannot be said for the original colour matching effort in Fig. 8.11a.

It is important to note that, because the angular frequency and phase of the calibration curve

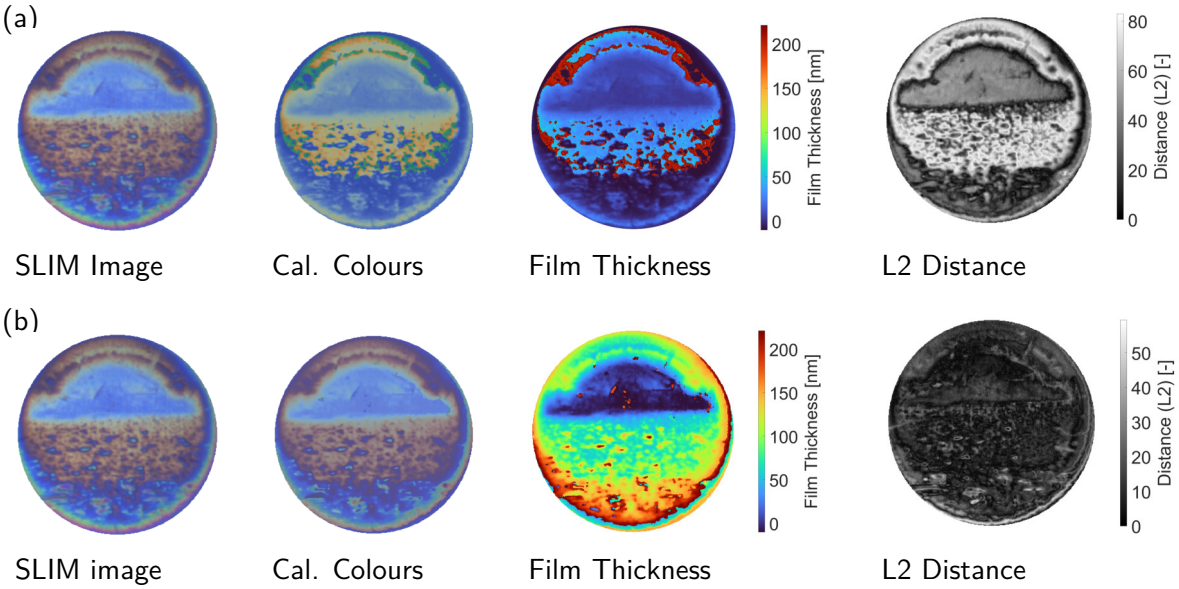


Figure 8.11: (a) Film thickness calculation for an MTM-SLIM image of a ZDDP tribofilm with severe intensity shift as shown in Fig. 8.10a, and (b) the same calculation using the refitted calibration curve from Fig. 8.10b. The lower part of the image shows a thick deposited tribofilm created under conditions shown in Table 8.3 (sliding direction horizontal). The horseshoe-shaped region at the top is a thin film developed outside the wear track due to the sliding contact between the ball and the SLIM disc during successive loading and unloading.

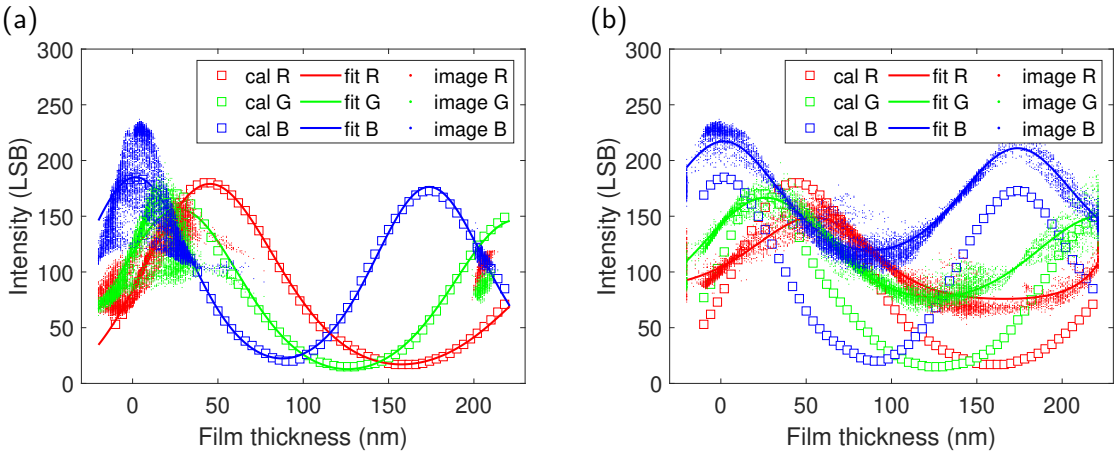


Figure 8.12: Original calibration curve colour channels (squares) compared to fit (lines) and pixels in SLIM image (Fig. 8.11) shown at assigned film thicknesses (points) before (a) and after (b) calibration curve refitting (Fig. 8.10). The redistribution of pixels in (b) matches the fit much more closely, implying that these film thicknesses are physical.

remain unchanged, the calibration curve retains its shape, while compensating for the changes in intensity on each channel, thereby greatly improving the reliability of the minimum-distance colour matching. The fit has the limitation that it requires a film-thickness range greater than 80 nm (approx. one half-period of the blue intensity curve) in the pixel colours used for it, to distinguish between similar colours with different order. This criterion is easily satisfied by incorporating pixels from the Newton's rings, provided they are well-resolved, and/or by using pixels from several successive SLIM images in a test where the film thickness changes (which is usually the case). Alternatively, the calibration curve can be truncated to incorporate only the correct order, for example if an additive film which remains thinner than 100 nm is to be measured, the curve could be truncated to remove the 2nd-order blue peak, thereby avoiding the common ambiguity between the 1st and 2nd-order blue fringes during the fitting process.

Another option is simply to scale the existing empirical calibration curve, but the fit to Eq. (8.3) has the following advantages:

- The fit reduces the sensitivity of the film thickness measurement to anomalies in the calibration data
- The fit can be used to extrapolate the calibration curve to higher or lower film thicknesses than were possible during the test(s) that created it
- The coefficients encode valuable information about the optical system such as interfacial phase shift and interference quality factor, which gives physical insight into spectral discrepancies between SLIM systems
- The fit is defined by less information than the calibration curve and is more portable

Small deviations in the position of the calibration line in any direction perpendicular to its tangent have very little effect on the film thickness measurement, because the nearest-colour film thickness matching does not depend on the colour distance itself (providing this does not exceed the distance threshold if one is used). Consequently, if the quality of the fit to the pixel

Table 8.3: Contact conditions used to create the film in Fig. 8.11

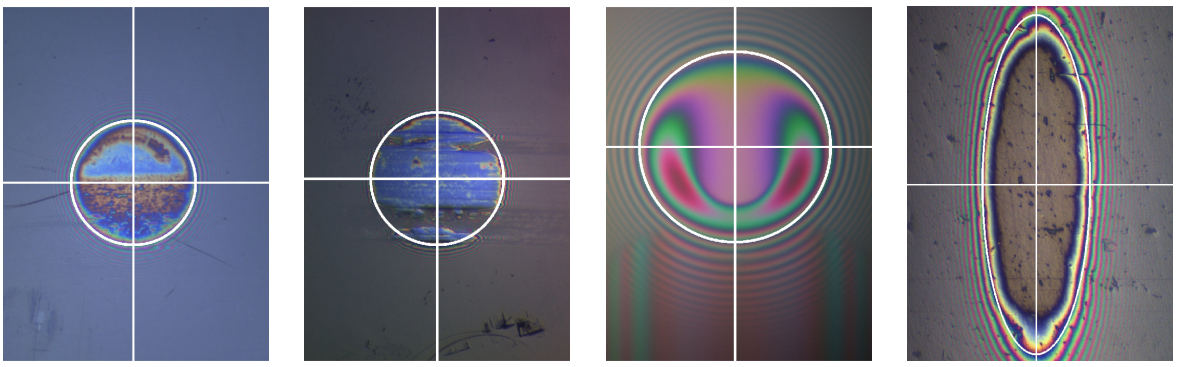
Base	Additive	Conc. [%wt P]	Entr. Speed [m/s]	SRR [%]	Load [N]	Radius [mm]	Temp. [°C]	Time [hr]
PAO5	ZDDP	0.1	0.115	50	36.6	9.525	70	3

colours achieved in the refitting process is reasonable, and the shape of the calibration curve is a good approximation of the shape occupied by the pixel colours in the colour space, the reproducibility of the film thickness measurement after the refitting is expected to be of the order of a few nanometres. The exponential decay parameter p for each channel significantly affects the shape of the calibration curve, and therefore the treatment of p by the refitting procedure has a strong influence on the measurement, particularly for higher-order fringes.

8.4.3 Circle Finding

It is of great practical advantage to locate the contact circle (or ellipse) in a SLIM image algorithmically, and thus users may seek to implement their own circle-fitting procedure in their offline image analysis. Circle-finding is often performed using the Hough transform method [275, 276], but this is notoriously computationally expensive and is adversely affected by interference fringes and colour gradients within the circle. A simpler, computationally inexpensive technique to find the location and radii of a single elliptical feature in the image, is proposed here.

The technique uses a cross-correlation of the image with a reflection of itself to find a line of symmetry, as illustrated in Fig. 8.14. This is done in both the horizontal and vertical axes, and the circle-centre co-ordinates are found from the two orthogonal lines of symmetry. The cross-correlation uses a square-difference integrand instead of a multiplier to reduce the sensitivity to local intensity. The process is simplified by first summing the gradient magnitude of the three colour channels which reduces the tensorial order of the image to two, and accelerates



(a) MTM tribofilm (b) ETM worn (c) EHD high-order (d) EHD barrel

Figure 8.13: SLIM images from MTM, ETM and EHD, showing crosshairs and successfully fitted circle or ellipse (white lines)

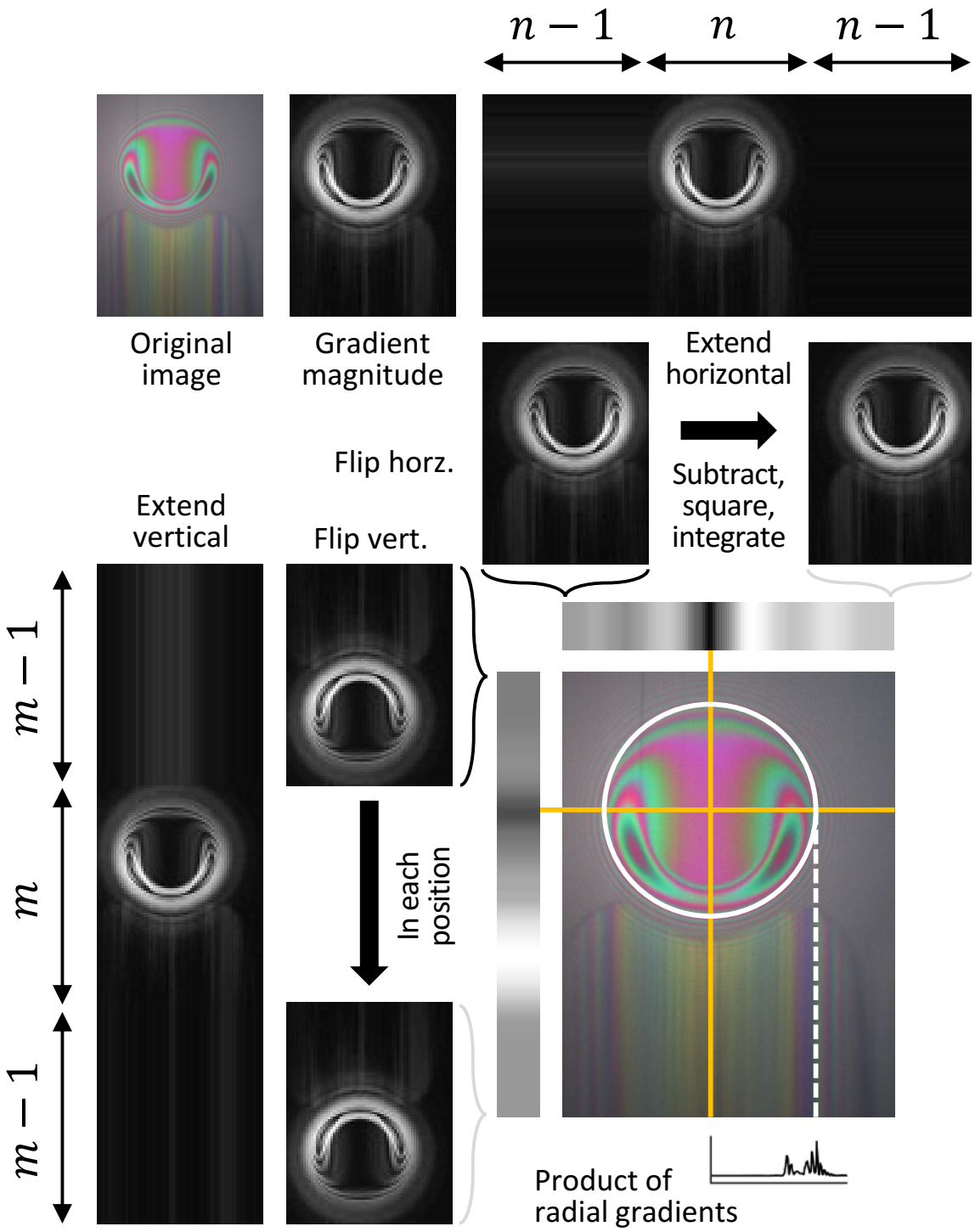


Figure 8.14: Graphical representation of the circle finding technique illustrating image gradient extension and inversion in each axis, the resultant minima in the cross-correlation function, the mapping to the image co-ordinates, and the radius found from the maximum of the product of 4 radial gradients

the calculation. The circle centre (ξ, γ) is found from Eq. (8.5) where $G_{\mathrm{ext}_{\mathrm{horz}}}$ and $G_{\mathrm{ext}_{\mathrm{vert}}}$ are respectively horizontal and vertical extensions of the gradient magnitude image G, achieved by copying the first/last row/column $m-1$ or $n-1$ times for an $(m \times n)$ image.

$$\begin{aligned} \xi &= \frac{N}{2N-1}\mathrm{argmin} \iint \left(G_{\mathrm{ext}_{\mathrm{horz}}}(x+\xi, y) - G_{\mathrm{flip}_{\mathrm{horz}}}(x, y)\right)^2 \mathrm{d}x\mathrm{d}y \\ \gamma &= \frac{M}{2M-1}\mathrm{argmin} \iint \left(G_{\mathrm{ext}_{\mathrm{vert}}}(x, y+\gamma) - G_{\mathrm{flip}_{\mathrm{vert}}}(x, y)\right)^2 \mathrm{d}x\mathrm{d}y \end{aligned} \tag{8.5}$$

The cross-correlations are performed between the extended image and its corresponding inversion of G, where $G_{\mathrm{flip}_{\mathrm{vert}}}$ inverts dimension 1, and $G_{\mathrm{flip}_{\mathrm{horz}}}$ inverts dimension 2. The radius of the circle is then found by evaluating the gradient function on four spokes extending radially from the circle centre (coinciding with the positive and negative directions of the two axes), and locating the maximum of their mutual elementwise product.

The technique also enables the location of an ellipse, and determination of its major and minor radii, by separately considering the gradient products of the orthogonal axes. This requires the ellipse axes to be aligned with those of the image.

The algorithm is shown to be highly robust in Fig. 8.13, even for relatively noisy images with false edges, asymmetry and ellipticity, which challenge the accuracy of the circle fitting.

The computational expense of the algorithm is polynomial up to the third order in the dimensions of the image, and so is greatly reduced by averaging. The concomitant uncertainty in the central position of $\pm$ one averaging block size can be amortised by performing a second cross-correlation of a less heavily averaged image gradient, whose domain is limited to $\pm$ one averaging block size. On an Intel i7-10810U processor clocked at 1.1 GHz running MATLAB 2021a, the wallclock runtime of MATLAB's imfindcircles function, which relies on the Hough transform, was 2.1 s per image, and the MATLAB implementation of the algorithm proposed here took 0.018 s per image.

8.4.4 Refractive Index Correction

The film thickness for a given fringe colour is inversely proportional to the refractive index of the film, which depends significantly on temperature, pressure, wavelength, and its chemical composition. The SLIM measurement, in matching colour to film thickness, must make

assumptions about these aspects of the film being imaged.

In the case of EHD-SLIM and MTM-SLIM with a calibration curve created using ultra-thin-film interferometry, it is assumed that the refractive index matches that of the lubricant film measured during the calibration for the relevant wavelengths. The calibration is typically created using a steel-on-glass contact at a maximum Hertz pressure of 0.5 GPa. Providing the influences of any differences in temperature and chemical composition between measurement and calibration are minimal, this assumption is typically acceptable for EHD-SLIM operating at similar pressures.

If the calibration is created at ambient pressure using Newton's rings outside the contact, as in the DCI method, and assuming a fluid film is being imaged, the difference in pressure between calibration and measurement incurs an error in the film measurement of the order 10%. Hartl *et al.* [254] used a correction for refractive index based on the Lorentz-Lorenz equation [277] (Eq. (8.6)) to compensate for this, where ρ is the fluid density, A is a constant dependent on fluid composition and wavelength, and n is the refractive index.

$$\rho A = \frac{n^2 - 1}{n^2 + 2} \tag{8.6}$$

A correlation for the dependence of density on fluid pressure and temperature is given by Dowson and Higginson [278] (Eq. (8.7)), where ρ_0 is the density under ambient conditions, p is the gauge pressure in GPa, β is the coefficient of thermal expansivity, T is temperature, and T_0 is ambient temperature. It is acknowledged that the validity of the pressure term in this correlation is limited for synthetic fluids, and several other correlations exist - nevertheless it serves here to illustrate the size of the effect of pressure on refractive index compared to that of temperature and wavelength.

$$\rho(p) = \rho_0 \left(1 + \frac{0.6p}{10^9 + 1.7p}\right) \left[1 - \beta \left(T - T_0\right)\right] \tag{8.7}$$

The dependence of refractive index on pressure and temperature is illustrated by Fig. 8.15 for a mineral oil with $T_0 = 20°$C, $\rho_0 = 860$ kg/m^3, n_0=1.475 and $\beta = 0.00071$, and for a PAO5 with $\rho_0 = 820$ kg/m^3, n_0=1.46 and $\beta = 0.00076$.

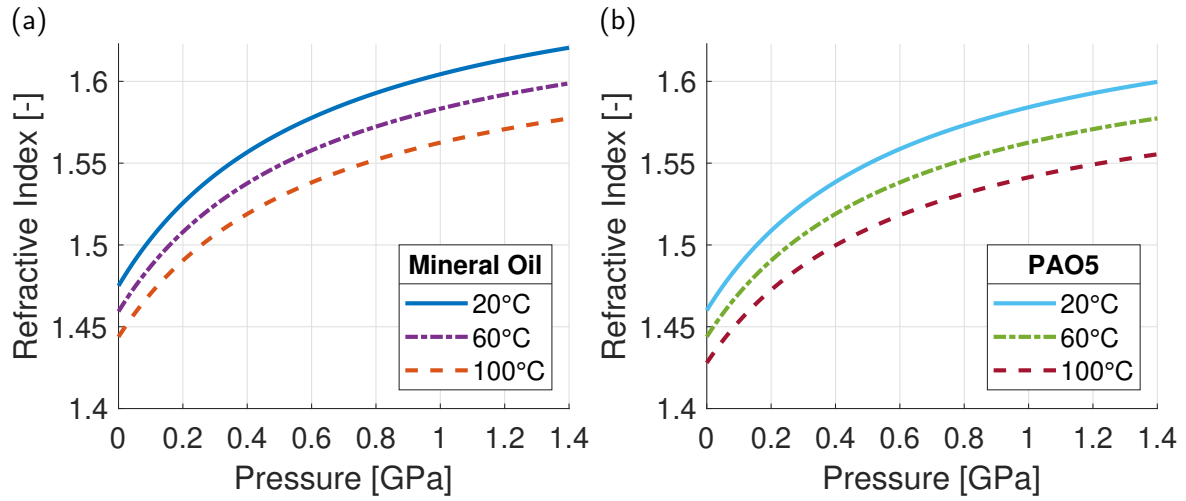


Figure 8.15: Refractive index vs pressure at three temperatures for (a) a mineral oil and (b) a PAO5

The refractive index was shown by Khodier [279] to depend more strongly on fluid type than on wavelength for 8 lubricating oils, for each varying by only $\sim 1\%$ in the range 400-700 nm.

For solid thin films the refractive index in general differs from that of the oil film. For example for ZDDP films, a refractive index of 1.6 was assumed by Fujita and Spikes [258] and in much subsequent related work. Recently, other tribofilm-forming materials have been studied with SLIM, notably ZrO_2, which may form tribofilms with refractive index close to 2.0 [280].

Measurements of tribofilm thickness h for solid films of known refractive index n have been corrected in several studies using Eq. (8.8) [258, 262, 267, 281], where nominal film thickness reported by the SLIM method is h_{nom} and $n_{\mathrm{nom}} \approx 1.4$, where n_{nom} approximates the refractive index of the oil used to make the calibration without accounting for the effects of pressure.

$$h = h_{\mathrm{nom}} \frac{n_{\mathrm{nom}}}{n} \tag{8.8}$$

This relationship can also be used to account for the pressure and temperature dependence of refractive index. The SLIM calibration takes the colour in the central region of the film and assigns it to the central film thickness reported by ultra-thin-film interferometry, so the pressure here is approximately the maximum Hertz pressure of this contact (often around 0.5 GPa). If the imaged contact is non-conformal, the pressure distribution is nonuniform, and this can be accounted for allowing the correction factor n_{nom}/n to vary with position in the

image.

This method assumes the refractive index is uniform throughout and does not depend on the thickness of the film. The refractive index of a solid film has also been shown to depend on film thickness (usually a monotonic increase with thickness) [282]. A further correction is necessary if a significant change from the nominal value is expected at the film thickness measured.

8.5 Summary

The Spacer Layer Imaging Method relies on matching the colours taken from the recorded interferogram to colours stored in a calibration created using an elastohydrodynamic contact whose film thickness is measured by ultra-thin-film interferometry. Steps in this process which are prone to error include:

1. The colour matching, typically performed in RGB space using a nearest-distance criterion which is sensitive to both the periodicity of the calibration curve in this space (creating ambiguity as to the correct fringe order and hence distorting the film thickness measurement by ≈ 200 nm), and to any mismatch in brightness or saturation.
2. The creation of the calibration, which assumes that the film thickness measurement is accurate (the pressure-dependence of the refractive index of the oil film is often ignored entirely, overpredicting film thickness by up to 10%).
3. The analogy between the optical characteristics of EHL films and tribofilms, when in reality the refractive index and spectral response of each may significantly affect the measurement.
4. The practice of averaging interferogram colours and/or reported film thicknesses, which in both cases linearises a highly nonlinear operation, making any anomalies in the reported data more difficult to detect.

To diagnose and correct for these issues, it is of primary importance to develop a robust understanding of the operations performed in the image analysis and film thickness calculation, and to avoid the pitfalls of using the technique as a black box.

The closeness of the match between the calibration and interferogram colours can quickly

be determined by inspecting a plot of selected pixels from the images for analysis, alongside a representation of the calibration curve in RGB space. If the colour envelopes differ, the calibration can be refitted to the data available using the proposed calibration curve fitting procedure.

The ambiguity in fringe order at certain points on the calibration curve is reduced by the proposed context-aware colour matching procedure which traverses the image and prefers film thicknesses which do not incur very steep spatial film thickness gradients, although care should be taken that this procedure does not artificially smoothen the film, particularly for high-order fringes.

Colour matching and reporting of film thickness should be performed at full resolution without averaging in the first instance, to ensure anomalies due to colour intensity mismatch or ambiguity in fringe order do not silently influence the average value.

A computationally efficient circle-finding algorithm based on image convolution can assist in SLIM data processing, and is found to be robust for several common scenarios in which other feature finding procedures may fail.

These recommendations and tools, along with fastidious attention to experimental best-practice, can extend the useful range of SLIM to film thicknesses of 800 nm, accelerate the film thickness calculation, enhance the resolution and quality of the data presented, and have widespread relevance both academically and industrially for this widely-used technique.

Chapter 9

Discussion

This work provides several new insights and datasets of relevance to both academic analysis and industrial development of current and future EDUs and EDFs, including the direct measurement of load-independent and load-dependent power losses in two existing drive units. Thermal EHL film thickness and traction are measured at entrainment speeds up to 20 m/s under conditions relevant to gear contacts in these drive units, and the influence of oil viscosity and composition is examined directly for a series of relevant base fluids and candidate transmission lubricants. Two existing test methods have been employed to study the effect of oil formulation for a series of fluids on scuffing and micropitting, enabling field-relevant comparisons and emphasising the tradeoff to be made by antiwear and EP additives in new low-viscosity EDF formulations. Equally importantly, this work details the development and use of a series of new experimental methods by which these data were obtained, and which are relevant to tribology research and its industrial application, including a comparison of inertia rundown and steady-state spin loss measurements for an EDU, and a procedure for the simultaneous measurement of traction and film thickness in a novel high-speed optical tribometer.

9.1 Load-independent losses

Load-independent losses were found in Section 4.2.2 on page 120 to increase with viscosity in the range currently achievable by EV transmissions operating between 40°C and 60°C using 5 cSt fluids. This increase was however relatively weak compared with the influence of speed and fill volume. As viscosity was increased beyond this, churning losses were seen to decrease slightly, and then increase once more at the highest viscosities. The lowest churning losses were observed at a viscosity around 40 cSt, considerably higher than that for a 5 cSt fluid between 40°C and 60°C. These findings should be considered in the context of several limitations of the method, and details of the design of the drive unit used.

- The churning losses measured may have been affected by changes in load-dependent

losses (incurred by bearings supporting the weight of the components, and more significantly by power transmission of the churning losses themselves, as discussed in Section 2.3) with oil fill level, both as a result of thermal inequivalence between the no-oil and filled cases, and as a result of the change in magnitude of any mechanically transmitted fractions of the churning power during the rundown.

- A significant fraction of the losses measured with the high-speed shaft installed may result from oil shearing in the motor flux gap which is a feature of wet-motor designs. It is instructive to compare however the 'no-load' torques measured in the steady-state with a dry-motor drive unit (Fig. 5.3 on page 133), to those with the wet-motor design (Fig. 4.35a on page 118), which are similar, although the measurements in Chapter 5 also include several parasitic torques in the driveline, e.g. those from linkshaft and driveshaft supporting bearings. This can be seen in the no-load torque at close to zero speed, which is around 3 Nm higher for the dyno tests (wet motor) than for the rundown tests (dry motor). At 1500 rpm output speed however (ignoring the slight difference between the gear ratios in the two drive units), the measured churning torques at full-fill still differ by approx. 3 Nm. The total torque in the dry-motor case is therefore quite similar to the wet-motor case, perhaps due to the additional seals (both for oil and coolant) and motor shaft bearings (grease-lubricated, also sealed), which appear in this design to balance any torque imparted by viscous shear of oil in the wet-motor flux gap.
- The results in Section 4.2.3 are inconclusive as to the equivalence between churning torques derived by inertia rundown vs those obtained in the steady-state. Both techniques are limited by their resolution - the inertia rundown method due to bearing-local thermal effects (see Fig. 4.39 on page 123), and the steady-state method additionally due to torque measurement resolution. It would be of interest in future work to repeat both experiments with unsealed bearings, which, although their drag loss is dependent on fill level, would reach less extreme temperatures during run-up and therefore enable better comparison between rundown and steady-state conditions.

9.2 EHL Traction and Film Thickness at High Speeds

It is illustrated in Figs. 6.18 and 6.19 that the influence of the material and geometry of each of the contacting surfaces, and of the contact kinematics, on the thermal state of the contact has strong implications for both film thickness and traction, particularly at high entrainment speeds. This highlights the importance of the macroscopic thermal coupling affecting and affected by load-dependent losses, which has significant implications for both efficiency and reliability. A recent and extensive treatment of this issue is presented in the thesis of Shore [210].

It is found in Chapter 6 that the influence of entrainment speed on traction (Stribeck-like) and on the reduction in film thickness compared to isothermal predictions, depends strongly on viscosity. At high viscosities (hence at low temperatures) these effects are significant - even for fluids with KV100 of 4 cSt (comparable to or lower than current EDF formulations). With these fluids at 20°C, point-contact EHL central film thickness is around half the predicted value at 20 m/s, and traction coefficient was seen to reduce by a factor of nearly 3 compared to the value at 0.2 m/s in some cases. The surfaces in these tests were extremely smooth, so these effects were not modulated by mixed lubrication conditions, but with rough EV gear tooth surfaces, given the film thickness reduction, the reduction of traction with increasing entrainment speed could be further amplified in the mixed lubrication regime. Gupta predicts sliding conditions under which the central film thickness begins to decrease as speed increases, although this situation was not observed experimentally under the conditions used. Both traction and film thickness were found to be modified by sliding direction, with lower film thickness (by up to 25%) observed in the ball-faster case for all fluids, and lower traction (up to 40%) in the ball-faster case for all fluids except the traction fluid, particularly at high speeds and high viscosities. This highlights the increasingly significant influence of the thermal response of the contacting bodies at high speeds, and also the need to supply information about the direction of sliding used in tribometers for which dissimilar specimen geometries (and/or materials) are in contact.

9.3 Surface Damage

Scuffing and micropitting are both damage modes of increasing relevance to EVs given the prevailing trends in decreasing viscosity and increasing power density. They are also challenging to reproduce in a field-representative manner, and standardised tests which aim to do so are presently laborious, notoriously unrepeatable, and expensive. Nevertheless they are widely used. The methods presented here, employing a ball-on-disc scuffing setup and a triple-disc fatigue rig, are more versatile, and promise to be relatively cheap and easy to use.

It is shown in Section 7.2 that, for the fluids tested, lower friction and more wear at the early stages of the test leads to greater scuffing resistance. Considerable wear may reasonably be expected to suppress scuffing, particularly with point contacts for which wear very considerably reduces contact pressure. The fluids which showed the most wear early in the test were the water-based and ZDDP-containing fluids, for which (although likely by different mechanisms) the anti-wear additive was able to arrest the onset of scuffing under these harsh conditions (transience implied by short spikes in the friction trace throughout the tests), but not to mitigate wear. The base oils by contrast contained no agents capable of forming boundary films, or of reversing or arresting the collapse of micro-EHL films, so scuffed before significant wear could accumulate. The more complex additive systems of the ATF and the gear oil, both of which are likely to contain dedicated anti-wear additives, EP additives and friction modifiers, were able to mitigate both scuffing and significant wear up to and beyond 6 m/s sliding speed at 1.3 GPa maximum Hertz pressure, but at 2.0 GPa (a much higher pressure than would likely be experienced alongside these sliding speeds, e.g. in gears) also scuffed relatively quickly. Gear oils typically have stronger EP additives and fewer friction modifiers than ATFs, which are designed to tune friction in wet clutch packs - this is reflected in the slightly higher scuffing speed of the gear oil.

Next-generation low-viscosity EDFs are likely to have lower pressure-viscosity coefficients and so less stable micro-EHL films, but as a result may also exhibit lower full-film EHL friction and improved cooling performance, potentially lowering contact temperatures. Nevertheless, the lower viscosity extends the boundary lubrication regime to higher gear speeds and so there is an increased risk of scuffing in next-generation EDUs with low-viscosity lubricants. New EDFs may require more sophisticated EP additives to mitigate scuffing, particularly in light

of the copper-compatibility issues with existing S-based EP chemistries.

The speed-stepping ball-on-disc contrarotation method employed has several advantages over standardised scuffing test methods, including a relatively short and repeatable test with the flexibility to tailor the test conditions to the needs of simulating a particular application, and to decouple the influence of entrainment and sliding speeds. Several useful datasets are obtained in a single test in addition to the scuffing speed/load, including the friction trace and SLIM images of the ball surface taken between steps. It has the disadvantage however, for most oils, of requiring very high slide-roll ratios to induce scuffing, which themselves could introduce thermally and rheologically anomalous phenomena such as a central dimple (although Peng *et al.* [175] showed this did not occur in a similar steel-on-glass contact at 0.5 GPa maximum Hertz pressure below 4 m/s sliding speed for base oils in groups III and IV), or severe inlet temperature rise due to the rapid recirculation of the specimens, limiting the comparability to contacts in machine elements even if all other conditions are similar. The test method is nevertheless promising for comparing the scuffing performance of similar fluids, in screening additives for example, and of evaluating scuffing risk under given contact conditions for a particular fluid.

It has been widely shown [182, 195, 209] that the antiwear additive ZDDP promotes micropitting by preventing running-in so that asperities persist and accumulate many more, more severe, plastic stress cycles, which lead to residual stresses that cause micropitting cracks to form and grow. A similar mechanism appears to apply to the antiwear and EP additives in the (non-ZDDP-containing) formulated gear oil and ATF (the gear oil moreso, perhaps related to its greater EP activity). The least micropitting was observed with pure PAO5 for which the rate of wear appears to match or exceed that of micropitting crack growth, leaving only a small number of larger cracks which eventually form pits later in the test. The progression of these cracks may also be related to ridging of the roller, shown for the water-based fluid in Fig. 7.9 on page 192. A similar cyclic wear pattern was observed for the PAO5, to a lesser extent, and may have caused wide fluctuations in contact pressure, promoting the formation of larger, discrete pitting cracks. The ATF base fluid contained a single unknown ester 'seal swell' additive which appears to modify the surface chemistry, creating a blue colour around 1M cycles in both repeats conducted, but which produces largely similar results to the PAO otherwise, with smaller and more numerous edge cracks forming after 11 million cycles.

Next-generation EDFs clearly must contain anti-wear and EP additives (see the scuffing test results), so the question of how to mitigate micropitting for formulated fluids remains. The large number of factors at play in the micropitting performance of a given gearbox and formulation bring with them a large number of possible mitigations, including reducing gear surface roughness, changing gear geometry to reduce contact pressure, increasing viscosity to increase lambda ratios, and tuning the hardness of the surfaces using heat-treatment, PVD or conversion coatings. Surface modifications including finishing and coatings are likely to incur considerable cost, and the necessary increase in gear size or oil viscosity to significantly increase lambda or reduce contact pressures are contrary to prevailing trends. It is important to note however that the relatively high maximum Hertz pressure used in these tests (1.5 GPa) considerably exceeds the contact pressure likely to be seen by gears in EDUs for the majority of their lifetimes, and so only lifetime tests imposing representative torque histories in actual EDUs can determine the extent to which micropitting is an issue for a given fluid and architecture. Other possible mitigations relate to optimising the use case, which in EVs is under computer control at all times: limiting motor torque at speeds for which lambda is low (inexpensive but may be perceived as a performance reduction), or as has been suggested by Olver and coworkers, 'running-in' the gearbox under controlled conditions with weak EP and antiwear additives, and then introducing strong ones when in service (logistically more complex).

The triple-disc micropitting test used has the considerable advantage that contact cycles can be accumulated very quickly, and that the test is highly repeatable if specimen roughness, hardness and microstructure are adequately controlled. The separate control of ring and roller speeds enables the decoupling of entrainment and sliding speeds which are both of considerable importance. The rate at which cycles are accumulated may itself however modify crack initiation and propagation, particularly if stresses and crack-local material properties are affected by thermal transience or diffusion of species through the lattice, both of which are time-dependent. Additionally, the extent to which the dynamics of the rig contribute to rapid fluctuations in contact pressure (evidenced by ridges on roller with certain fluids at some speeds), and the effect of these fluctuations on rolling contact fatigue cracks, is unknown, and potentially poses an issue with test reproducibility if different MPR rigs have differing dynamical characteristics (e.g. arising from small changes in bearing preloads, load beam

stiffness, gearbox vibration).

The metric for scuffing in Section 7.2 notably does not consider material loss due to wear, and is based only on a sudden increase of noise and vibration and a sustained increase in friction. The radius loss metric for micropitting progression in Section 7.1 however, does not distinguish between material loss due to wear and due to micropitting, and firmly depends on both of these. In addition to the widely-accepted conclusion discussed in Section 2.8 that micropitting and wear are in competition, these two have many causal factors in common: low lambda, high contact pressure creating plastic asperity stresses, high sliding distance, many overrolling cycles, and large hardness difference. The competition is therefore mediated by additives which act to suppress wear while allowing the accumulation of stress cycles, and by the hardness of the softer surface.

Even though no scuffing was seen during the micropitting tests, and vice versa, an inverse correlation in the respective scuffing and micropitting resistance of the fluids tested is apparent. In order of increasing wear and micropitting wear rate (increasingly poor performance) and increasing sliding speed at scuffing (increasingly good performance), the fluids are ranked:

1. PAO5 only
2. PAO5 + ester additive (ATF base)
3. ATF
4. MTF
5. PAO5 + ZDDP
6. Water-based fluid

It should be noted that the comparable micropitting test with PAO5 + ZDDP on 52100 steeel was not conducted, but similar test conditions using 16MnCr5 specimens reported elsewhere in Section 7.1 are consistent with this position in the ranking.

In the case of the water-based fluid, the wear mechanism is also likely to be influenced by corrosion, and the mechanisms underlying scuffing and micropitting characteristics by the differing additive system used, given the high polarity of water (and monoglycol solubilisers). The small molecule size of water reduces the free volume of the blend, which has been correlated for water-glycol fluids by Wan and Spikes [283] to lower pressure-viscosity coefficient

and hence lower EHD film thickness. Even though the weaker piezoviscous response was compensated by higher viscosity and lower temperature, the high-pressure, high-shear transient rheology of water-glycol fluids may also otherwise differ fundamentally to the other hydrocarbon base fluids, which may influence micro-EHL film formation and asperity deformation, and hence accelerate wear. Given the extremes of temperature at the asperity scale in sliding contact, it is unlikely that the 20°C-lower bulk fluid temperature had a significant impact on Arrhenius processes at the surface but this remains a possibility. As seen in Fig. 7.25b on page 212, the weak piezoviscosity of water also considerably reduces friction [284], and in aqueous solutions friction may also be lowered by hydrated adsorbed layers at the surfaces [285], or by the electrical double-layer [214]. Lower friction acts to mitigate both scuffing (by lowering the frictional power intensity/contact temperature) and micropitting, (by reducing stress intensity factors). The durations of both scuffing and micropitting tests are in the range where hydrogen diffusion and consequent embrittlement (particularly that accelerated by contact stresses) may be significant [286, 287]. Finally, the thermal feedback required for scuffing may be affected by the differing heat transfer properties both of water (higher thermal conductivity and heat capacity than PAOs [237]) and polyglycols (higher thermal conductivity and lower heat capacity than PAOs) [288].

Scuffing and micropitting manifest predominantly in contacts operating in mixed or boundary lubrication. The mitigation of these damage modes in EVs in the design of both system and lubricant therefore requires an understanding of the likely film thickness history of each contact, and hence the time-distribution of the lubrication regime in which these operate. In Chapter 6 however, it it shown that classical isothermal film thickness predictions, and existing thermal corrections for inlet shear heating, are to differing degrees inaccurate in predicting film thickness at high speeds for modern base fluids. This is all the more pertinent because at higher speeds, sliding distance and number of contact cycles are accumulated more quickly. If the speed threshold between mixed and full-film lubrication were overestimated, for example by an isothermal film thickness prediction where a thermal one is necessary, design decisions made on this basis could be severely life-limiting due to the overestimation of lambda ratios and underestimation of micropitting- or wear-inducing contact cycles. Scuffing may also occur in otherwise full-film EHD contact at very high loads or sliding speeds if the EHD film becomes unstable, for example thermally, or as a result of oil starvation or debris entrainment.

(An excellent demonstration of this was possible using an early version of the EHD-HS by conducting a film thickness test at high speed and then pressing the emergency stop button - the deceleration of ball and disc at different rates, thereby suddenly increasing the sliding speed, rapidly led to scuffing despite indubitable full-film conditions immediately beforehand at the intermediate entrainment speeds when the sliding speeds were lower. The solution was to ensure at all times that ball and disc surfaces accelerated and decelerated at the same linear rate.)

9.4 Influence of viscosity on load-dependent and load-independent losses

A critical link between efficiency and reliability therefore lies in the response of film thickness and friction to thermal effects which strongly depend on viscosity. Treating these one at a time:

- Reduction in central film thickness (and changes to outlet geometry at high sliding speeds) reduces lambda ratio which has a strong influence on micropitting [193] at lambda ratios of the order 1, and also influences scuffing [175]. The shear rate in the contact is increased by this reduction. The reduction in film thickness is caused by inlet shear heating which then results in reduced viscosity in the contact - the stress fields in both the surfaces and the fluid are therefore altered. Inlet shear heating is stronger, and the rate of change of viscosity with temperature is greater, at higher bulk viscosity. The film thickness reduction is therefore more significant at higher viscosities.
- Reduced traction is a natural consequence of viscosity reduction by inlet shear heating. The viscosity (and response of viscosity to pressure) are further reduced by shear heating under the much more extreme conditions within the contact. The greater $\frac{\partial \eta}{\partial T}$ at higher viscosity therefore contributes even more strongly to traction reduction than to film thickness reduction at high speeds. Consequently however this also depends strongly on the temperature distribution in the contact, which in turn depends on the thermal resistances of the bounding surfaces. The size of the steel ball in these experiments, and hence the circulation rate of the contact, may overstate the effect by comparison to gear teeth and understate it for bearing balls and rollers, whose surface temperatures depend

on the differing materials, geometry, and contact kinematics in these applications. Nevertheless, the data in Appendix I allow a representative comparison of the traction behaviour of 10 fluids, and from these data it is clear that the influence of speed on traction in the full-film EHL regime is once again more significant at higher viscosities. This suggests that load-dependent losses would be considerably reduced at higher speeds with higher viscosity fluids. For the 4 cSt fluids, the reduction in traction as speed increases at 20°C brings it close to, but never lower than, the traction at the same speed and at 100°C. For the conditions tested therefore, lower viscosity was seen to incur lower traction in the full-film regime except in some cases very marginally at SRRs above 100% where lower viscosity resulted in higher traction, see Appendix I. Consequently, lower-viscosity fluids can be expected globally to incur lower load-dependent losses in gears and bearings *if full-film conditions are maintained*, and traction coefficients can be expected to depend much less strongly on entrainment speeds for low-viscosity fluids.

Gear roughnesses of the order several hundreds of nanometers however imply that full-film conditions are *not* necessarily maintained, as estimated for the Tesla Model S drive unit in Section 4.1.5 on page 87. Further work establishing the effect of viscosity on mixed and EHL friction at high speeds for material roughnesses and hardnesses relevant to EV gearing (accounting for the fact that these do not necessarily remain constant over gearbox lifetime), lubricated by EDFs, would be of benefit in the holistic consideration of the effect of viscosity on load-dependent losses.

Although a clear influence of oil viscosity on full-scale transmission losses is found from dyno testing of a drive unit under load (Fig. 5.6 on page 137), it can be seen (Fig. 5.3) that even at high speeds, differences in no-load losses do not nearly account for the efficiency change. Full-film traction losses were found in Section 6.2 to change relatively little with viscosity at high entrainment speeds, but the effect of viscosity in the mixed lubrication regime was not considered, and in Section 4.1.5 it was shown that gears in a very similar gearbox operate in mixed lubrication over the majority of their speed range. It would be expected however that in the mixed regime, if all else were equal, higher viscosity would reduce friction as a result of increased lambda ratio, but the efficiency measurements imply that this is not the case even at high speeds. This can be attributed to the high-pressure rheology of the more viscous fluid, particularly in micro-EHL films at very high contact pressures, for which in-contact viscosity

is perhaps not diminished by inlet shear heating to the same extent as in full-film EHL. The consideration of mixed-EHL friction also calls into question the differing chemistries of the two oils (particularly with regard to friction modifiers and antiwear/EP additive activity), on which it is difficult to comment generally for a whole gearbox. It is worthy of note that at 40°C, the viscosity of the 75W-140 oil is around 8 times that of the ATF, and considering this, the reduction in efficiency by only 5% (although an improvement of this size would be a cause for much celebration!) is somewhat surprising, and further evidence of the relatively small effect of viscosity on load-independent losses, compared to other factors (torques, speeds, fill volume). Only two viscosities were tested however, and churning losses vary nonmonotonically with viscosity (it is possible mixed-EHL friction losses at high speeds do too) so not enough viscosities were tested in the drive unit to draw definitive trends for total efficiency with viscosity. The time-dependent nature of surface modification by mild wear and the resultant change in mixed and boundary friction also render the results of the low-speed portion of the efficiency measurement likely to change over time, particularly as roughnesses, and therefore lambda ratios, change during the initial running-in process.

Chapter 10

Conclusions

EV fluid formulation and transmission design must be approached in tandem in order to balance the conflicting requirements of efficiency and reliability. This thesis examines the influence of transmission fluid viscosity on efficiency and reliability. This is done by measuring oil churning losses an existing electric drive unit (EDU) using a churning rig developed during this study, and by measuring load-dependent power losses in an EDU using an existing dyno setup. Elastohydrodynamic friction and film thickness are measured at high speeds using a high-speed optical tribomoter in combination with a novel traction measurement procedure. Scuffing, wear and micropitting performance of a series of candidate EV lubricants are evaluated using a triple-disc fatigue rig and a speed-stepping ball-on-disc scuffing test. The following tasks were completed:

- A novel test rig incorporating a front drive unit from a Tesla Model S 2016 is developed and used to measure load-independent losses.
- The rig is employed to study the relative effects of speed, oil fill volume and oil viscosity on oil churning losses. An effort is also made to compare the results of inertia-rundown to steady-state torque measurements.
- A T-Axle dyno rig is used to measure load-independent losses, and gearbox efficiency under load, of the rear drive unit from a Tesla Model S 2016.
- The rig is used to compare the effects of two oils of differing viscosities, an ATF and a 75W-140 gear oil, on both load-independent and load-dependent losses.
- Torque control of the drive unit and speed control of the dynos was implemented to enable efficiency measurement during the NEDC drive cycle.
- EHL friction and central film thickness are measured simultaneously at speeds up to 20 m/s for the first time in a new test rig, the EHD-HS from PCS Instruments, to the development of which this study contributed. A novel traction measurement method was developed and implemented simultaneously with the ultra-thin-film interferometry

technique for this purpose. Measurements spanning entrainment speeds from 0.2 to 20 m/s, and slide-roll ratios between 0 and 100%, are provided for 10 fluids relevant to automotive transmissions, including low-viscosity base fluids spanning API groups I-IV, a traction fluid, two ATF formulations of differing viscosities, and a model EDF.

- A contra-rotating ball-on-disc scuffing test method was further developed and applied to compare the scuffing performance of five transmission fluids including an experimental water-based formulation, in an accelerated test at high sliding speeds under contact conditions otherwise representative of those experienced in gear contacts in EVs.
- A series of triple-disc micropitting tests were conducted for the same fluids used for the scuffing tests, enabling the relative effect of fluid formulation on the progression of micropitting, and the evolution of various surface roughness parameters throughout the test, to be determined.
- A new set of tools to improve the reliability and extend the range of techniques to measure EHL film and tribofilm thickness by colorimetric interferometry, such as the widely-used Spacer Layer Imaging Method (SLIM), are developed and presented, including robust solutions to correct for drift in colour channel intensities, a context-aware colour matching solution to the fringe order ambiguity problem, and a computationally efficient feature-finding algorithm.

The main findings from the results obtained are:

- Load-independent losses are shown in a typical EV drive unit to vary nonmonotonically with viscosity, exhibiting a local minimum in churning loss around 40 cSt. However, churning losses are found to increase monotonically with viscosity within the 5-20 cSt viscosity range in which this and other EV transmissions are expected to operate.
- In relative terms, speed, oil fill volume, and effective immersion depth have a much stronger influence on churning losses than oil viscosity.
- EHL central film thickness at entrainment speeds up to 20 m/s in a steel-ball-on-glass-disc contact was found to be significantly under-predicted (by up to 30%) at 100% SRR by the thermal correction factor of Gupta, however under pure-rolling conditions

the discrepancy remains within 10% of the measurement for a range of base fluids and viscosities.

- For 4 cSt fluids at 100°C, the effect of entrainment speed on full-film EHL traction between 0.2 and 20 m/s was found to be negligible. EHL traction was found to have very little dependence on viscosity in the range 4-20 cSt at high entrainment and sliding speeds (SRR 100% at 20 m/s entrainment) under full-film conditions, thought to be due to a thermally shear-stress-limited condition. Fluids with higher film-thickness-derived pressure-viscosity coefficients exhibited more strongly speed-dependent traction and film thickness behaviour, illustrating the role of shear heating modulated by piezoviscosity.
- Load-dependent losses in full-film EHL at high entrainment speeds become insensitive to viscosity (and to speed) due to thermal effects, and these depend also on the thermal characteristics of the system. This is in contrast with the isothermal case at lower speeds for which EHL friction depends very strongly on viscosity.
- For load-dependent losses, the stronger piezoviscosity of more viscous fluids amplifies the thermal effects on both traction and film thickness in the full-film regime, and it would appear from the drive unit dyno tests that, for the high viscosity gear oil tested, both load-dependent and load-independent losses were increased compared to the ATF for which the drive unit was designed.
- The mean efficiency of the rear drive unit during the NEDC drive cycle for a Dexron-VI ATF was measured as $87\pm5\%$.
- Oil churning torques are estimated to be contained within 10 Nm resolved to the output stage for typical motorway driving speeds for both front and rear drive units. Measurements of the torque required to spin the unpowered drive unit externally were around 3 Nm higher for the rear drive unit under steady-state conditions than those obtained by inertia rundown for the front drive unit. Steady-state churning torque measurements of the front drive unit, with sealed and grease-lubricated bearings, were also slightly higher than transient inertia rundown measurements under equivalent conditions.
- Scuffing and micropitting performance were inversely correlated for the fluids tested, and it was found that both modes are also in competition with wear. To within the

measurement uncertainty, the evolution of counterface roughnesses was well-matched between fluids throughout the micropitting tests despite the very different evolution of the (lower-hardness) roller surface. All formulated fluids tested gave rise to micropitting on the roller after 1 million cycles at 3.9 m/s entrainment speed, Λ ratio 0.4 $\pm$ 0.02, 5% SRR, 1.5 GPa maximum Hertz pressure for AISI 52100 bearing steels with a hardness difference of 100 HV30 (roller softer) and R_q RMS ring roughness of 400 $\pm$ 20 nm. The widely-recognised negative influence of the antiwear additive ZDDP on micropitting performance also appears to apply for antiwear+EP additives in fully-formulated transmission fluids which do not form thick boundary films.

The effect of viscosity on transmission losses is shown to be multifaceted. This work provides several arguments, substantiated by experimental data, both for (reducing churning losses, weakening thermal response, improving heat transfer) and against (increasing lambda ratios, extending rolling contact fatigue life, churning losses may in fact be lowered by increasing viscosity for some gearbox designs, EHL friction is insensitive to viscosity at high speeds) the further reduction of lubricant viscosity in EV drive unit gearboxes. The transmission architecture, casing geometry, thermal characteristics, and which functions the fluid is required to perform, have a strong effect on the optimal viscosity and fluid formulation, and these parameters differ starkly among the current fleet of EVs, so no one fluid fits all. Now more than ever, the dual optimisation of efficiency and durability therefore requires a synergistic, multi-disciplinary, collaborative approach to both transmission design and lubricant formulation. The work presented here provides new insights and testing methods to help in ongoing efforts to optimise EV lubricants for improved vehicle efficiency and reliability.

10.1 Future Work

The work in this thesis might be fruitfully continued in the following areas:

- Controlled studies of mixed and boundary friction in concentrated contacts at EV-representative speeds, particularly for next-generation low-viscosity synthetic fluids with gear-characteristic surface topographies and steel compositions, would be of considerable interest in determining the effect of low-lambda conditions on both efficiency and reliability. Time-series data, which are difficult to include on simple

traction or Stribeck curves, are vital in understanding the inherently time-dependent phenomena at play, particularly where the macroscopic thermal response of the system affects microscale phenomena such as asperity plasticity, mechanochemical reactions at the surfaces, and the rheology of the fluid within EHL and micro-EHL lubricant films.

- Several aspects of gearbox design merit further investigation of their influence on churning losses, including:

    1. casing geometry (particularly the effect of ribs, baffles, shrouds and clearances in a 2-stage helical gearbox) - these have been shown in single-stage gearboxes to strongly influence churning losses and the relevant design changes in next-generation EV drive units could be inexpensive to implement and effective in increasing efficiency
    2. spray lubrication system (volume flowrate vs speed, jet dimensions)
    3. gear geometry (tooth geometry is strongly dictated by permissible stresses, but the non-working surfaces of the gears may contribute significantly to churning losses and could be optimised by modification of their geometry and/or wetting properties)
    4. gearbox architecture, particularly concentric architectures for which churning losses are less well-studied including epicyclic and pericyclic reducers
    5. the impact of grease rheology on external components such as linkshaft bearing and coupling losses

    A well-integrated research collaboration between gearbox designer, EV manufacturer, lubricant supplier and churning loss researcher would be critical to this approach, which if successful could have substantial impact.

- The comparison of the results obtained here to the relevant parts of existing and future gearbox models which predict churning losses, EHL traction losses, and gearbox efficiency, may be of use in validating or updating these models.

- The further development and standardisation of a ball-on-disc speed-stepping scuffing test is long overdue and has the potential to provide considerably more useful, repeatable, field-relevant (and considerably less laborious and expensive) comparisons between fluids compared to existing standards. The provision of more than one metric

at the end of the test (friction, for instance, may also be of relevance!) would enable the creation of higher-dimensional datasets which could be interrogated by machine-learning techniques, providing further insight into the action of new additives and additive synergies, and potentially helping to examine the mechanisms by which scuffing takes place. The challenges include sensitivity to specimen surface finish and mechanical properties which are difficult to tightly control for large numbers of test specimens, and the optimisation of the running-in stage, if used, in which not only the surfaces but also the lubricant play an important role.

- The even greater effect of surface roughness and hardness on micropitting, and the further difficulty of controlling these for very rough and hard surfaces used, for example, in triple-disc micropitting tests, is a barrier to robust, field-relevant comparisons of micropitting performance between fluids. If these barriers in reliably controlling specimen roughness and hardness could be overcome, this could enable relatively quick (single-day) and repeatable tests with smaller and cheaper test specimens than existing gear-machine tests. Unlike pitting initiation which, due to its highly localised nature is inherently stochastic, micropitting involves a distributed network of many cracks, and characterising their behaviour therefore statistically requires far fewer repeats, making it somewhat easier to study. The dynamics of the triple-disc rig require more robust treatment than they have so far received for the study of low-viscosity fluids which provide weaker fluid damping of vibrations.
- Direct temperature measurements, for example using infra-red detectors [122], of EHL contacts at the speeds employed in this study, particularly in the thermoviscous regime where the relative effects of shear-thinning and shear-heating are unclear from traction measurements alone, would be highly illuminating. These could be made simultaneously with traction measurements using the technique developed in Chapter 6. The phenomenological understanding of the communication between fluid rheology, traction and thermal response would be further deepened by applying fluorescence techniques which measure flow profile [289] or viscosity [290, 291]. This would enable a more definitive treatment of the effect of base oil chemistry and sliding direction on apparently thermal differences between traction and film thickness behaviour at low and high speeds.

- The techniques developed in Chapter 8 have the potential to make the SLIM film thickness measurement considerably more accurate, repeatable and robust, which could have considerable impact on the quality and utility of film thickness measurements in the development of additives which form boundary films, particularly given the large number of MTM-SLIM systems in research labs worldwide. However, to be of widespread use these techniques require packaging in a user-friendly GUI application which exposes the relevant free parameters to the user and enables them to quickly examine the effect of each on the calibration curve fit, colour matching procedure and film thickness calculation. The techniques could also be further developed (and their range extended further) using a 4th infra-red channel, and the use of 4D colour-space visualisation methods would be required to appraise the quality of the fit.
- An implementation of ultra-thin-film interferometry which scans the contact at high speed could be used to quickly construct film thickness maps of steady-state contacts retaining the advantages of spectrometric interferometry while also enabling 3D topographical mapping of the film.

References

[1] IEA. *Net Zero Roadmap: A Global Pathway to Keep the 1.5 °C Goal in Reach*. Tech. rep. Paris: IEA, 2023.

[2] IPCC. *Climate Change 2023: Synthesis Report. Contribution of Working Groups I, II and III to the Sixth Assessment Report of the Intergovernmental Panel on Climate Change*. Tech. rep. Intergovernmental Panel on Climate Change, 2023. DOI: 10.59327/IPCC/AR6-9789291691647.

[3] IEA. *Global EV Outlook 2023*. Tech. rep. Paris, 2023.

[4] D. L. Bleviss. "Transportation is critical to reducing greenhouse gas emissions in the United States". *Wiley Interdisciplinary Reviews: Energy and Environment* 10.2 (2021), e390. DOI: 10.1002/WENE.390.

[5] IEA. *Global EV Outlook 2024*. Tech. rep. Paris, 2024.

[6] A. Ajanovic. "The future of electric vehicles: Prospects and impediments". *Wiley Interdisciplinary Reviews: Energy and Environment* 4.6 (2015), pp. 521–536. DOI: 10.1002/wene.160.

[7] M. Muratori et al. "The rise of electric vehicles—2020 status and future expectations". *Progress in Energy* 3.2 (2021), p. 022002. DOI: 10.1088/2516-1083/ABE0AD.

[8] M. S. Koroma, D. Costa, M. Philippot, G. Cardellini, M. S. Hosen, T. Coosemans, and M. Messagie. "Life cycle assessment of battery electric vehicles: Implications of future electricity mix and different battery end-of-life management". *The Science of the Total Environment* 831 (2022). DOI: 10.1016/J.SCITOTENV.2022.154859.

[9] I. Husain, B. Ozpineci, M. S. Islam, E. Gurpinar, G. J. Su, W. Yu, S. Chowdhury, L. Xue, D. Rahman, and R. Sahu. "Electric Drive Technology Trends, Challenges, and Opportunities for Future Electric Vehicles". *Proceedings of the IEEE* 109.6 (2021), pp. 1039–1059. DOI: 10.1109/JPROC.2020.3046112.

[10] K. Holmberg and A. Erdemir. "The impact of tribology on energy use and CO2 emission globally and in combustion engine and electric cars". *Tribology International* 135 (2019), pp. 389–396. DOI: 10.1016/j.triboint.2019.03.024.

[11] J. F. Shore, A. I. Christodoulias, A. S. Kolekar, F. E. Lockwood, and A. Kadiric. "Prediction of Electric Vehicle Transmission Efficiency Using a New Thermally Coupled Lubrication Model". *SAE Technical Papers* (2022). DOI: 10.4271/2022-01-5026.

[12] K. Aiso and K. Akatsu. "Performance Comparison of High-Speed Motors for Electric Vehicle". *World Electric Vehicle Journal 2022, Vol. 13, Page 57* 13.4 (2022), p. 57. DOI: 10.3390/WEVJ13040057.

[13] Z. Wang, L. Zhao, Z. Kong, J. Yu, and C. Yan. "Development of accelerated reliability test cycle for electric drive system based on vehicle operating data". *Engineering Failure Analysis* 141 (2022), p. 106696. DOI: 10.1016/J.ENGFAILANAL.2022.106696.

[14] Y. Kwak, C. Cleveland, A. Adhvaryu, X. Fang, S. Hurley, and T. Adachi. "Understanding Base Oils and Lubricants for Electric Drivetrain Applications". *SAE Technical Papers* December (2019). DOI: 10.4271/2019-01-2337.

[15] W. Feng, Z. Feng, and L. Mao. "Failure analysis of a secondary driving helical gear in transmission of electric vehicle". *Engineering Failure Analysis* 117 (2020), p. 104934. DOI: 10.1016/J.ENGFAILANAL.2020.104934.

[16] Y. Zhang, J. Du, J. Mao, and M. Xu. "Dynamic Analysis of High-Speed Helical Gear Transmission in Pure Electric Vehicle Gearbox". *Shock and Vibration* 2020 (2020). DOI: 10.1155/2020/6639372.

[17] F. Jia, Y. Lei, X. Liu, Y. Fu, and J. Hu. "Simulation and experimental study on lubrication of high-speed reducer of electric vehicle". *Industrial Lubrication and Tribology* 73.3 (2021), pp. 500–507. DOI: 10.1108/ILT-08-2020-0309.

[18] C. D. P. Rodrigues. *Design of a high-speed transmission for an electric vehicle*. Masters Thesis. 2018. URL: https://core.ac.uk/download/pdf/160238923.pdf.

[19] G. Belingardi, V. Cuffaro, and F. Curà. "Dynamic additional loads influencing the fatigue life of gears in an electric vehicle transmission". *Frattura ed Integrita Strutturale* 30 (2014), pp. 469–477. DOI: 10.3221/IGF-ESIS.30.57.

[20] H. Laitinen, A. Lajunen, and K. Tammi. "Improving electric vehicle energy efficiency with two-speed gearbox". *2017 IEEE Vehicle Power and Propulsion Conference, VPPC 2017 - Proceedings* 2018-Janua (2018), pp. 1–5. DOI: 10.1109/VPPC.2017.8330889.

[21] B. Gao, Q. Liang, Y. Xiang, L. Guo, and H. Chen. "Gear ratio optimization and shift control of 2-speed I-AMT in electric vehicle". *Mechanical Systems and Signal Processing* 50-51 (2015), pp. 615–631. DOI: 10.1016/J.YMSSP.2014.05.045.

[22] J. O. Han, J. W. Shin, J. C. Kim, and S. H. Oh. "Design 2-Speed Transmission for Compact Electric Vehicle Using Dual Brake System". *Applied Sciences 2019, Vol. 9, Page 1793* 9.9 (2019), p. 1793. DOI: 10.3390/APP9091793.

[23] W. Huang, J. Huang, and C. Yin. "Optimal Design and Control of a Two-Speed Planetary Gear Automatic Transmission for Electric Vehicle". *Applied Sciences 2020, Vol. 10, Page 6612* 10.18 (2020), p. 6612. DOI: 10.3390/APP10186612.

[24] T. Hofman and C. H. Dai. "Energy efficiency analysis and comparison of transmission technologies for an electric vehicle". *2010 IEEE Vehicle Power and Propulsion Conference, VPPC 2010* (2010). DOI: 10.1109/VPPC.2010.5729082.

[25] A. Sorniotti, S. Subramanyan, A. Turner, C. Cavallino, F. Viotto, and S. Bertolotto. "Selection of the Optimal Gearbox Layout for an Electric Vehicle". *Source: SAE International Journal of Engines* 4.1 (2011), pp. 1267–1280. DOI: 10.2307/26278222.

[26] M. R. Ahssan, M. M. Ektesabi, S. A. Gorji, M. R. Ahssan, M. M. Ektesabi, and S. A. Gorji. "Electric Vehicle with Multi-Speed Transmission: A Review on Performances and Complexities". *SAE International Journal of Alternative Powertrains* 7.2 (2018), pp. 169–181. DOI: 10.4271/08-07-02-0011.

[27] E. Gözen, M. S. Çevirgen, and E. Özgül. "Transmission speed and ratio optimization for heavy-duty electric truck". *Heliyon* 8.8 (2022). DOI: 10.1016/j.heliyon.2022.e10028.

[28] H. J. Stadtfeld. "Introduction to Pericyclic Transmissions". *Gear Technology* March/April (2021), pp. 40–46.

[29] Lucid. *Lucid Motors Tech Talk On Drive Unit & Motor*. 2022. URL: https://www.lucidinsider.com/2022/09/13/lucid-motors-tech-talk-on-drive-unit-motor/ (visited on 04/30/2024).

[30] D. Tokozakura, T. Sano, T. Nakamura, A. Tada, Y. Susukida, H. Moritani, and T. Shinyoshi. "Development of Transaxle Fluid for Electrified Vehicles: Validating Optimized Viscosity through Targeted Hardware Testing". *SAE Technical Papers* (2022), pp. 1–9. DOI: 10.4271/2022-01-1103.

[31] N. Schenk. *RAV4 EV drive unit "Milling" noise repair*. 2019. URL: https://docs.google.com/document/d/1A6n0bkLowViFNtoD2bjzkL_IHk5RLS-mvYRUpe2qzGA/edit (visited on 04/30/2024).

[32] M. Waddle. *RAV4 EV Motor Repair*. 2024. URL: https://mandmwaddle.ca/projects/rav4-ev-motor-repair/ (visited on 04/30/2024).

[33] R. Errichello. "How to analyze gear failures". *Journal of Failure Analysis and Prevention* 2.6 (2002), pp. 8–16. DOI: 10.1007/bf02715492.

[34] B. Zhmud, M. Najjari, and B. Brodmann. "The Effects of the Lubricant Properties and Surface Finish Characteristics on the Tribology of High-Speed Gears for EV Transmissions". *Lubricants* 12.4 (2024), p. 112. DOI: 10.3390/lubricants12040112.

[35] H. Xu, G. T. Götz, S. Zhang, and R. W. De Doncker. "Experimental Study of a Directly Oil-Cooled Electrical Machine for a Full-Electric Vehicle by Using Low Viscosity Oil". *24th European Conference on Power Electronics and Applications*. Hannover: EPE'22 ECCE Europe, 2022.

[36] M. Beyer et al. "Lubricant concepts for electrified vehicle transmissions and axles". *Tribology Online* 14.5 (2019), pp. 428–437. DOI: 10.2474/trol.14.428.

[37] K. Matsubara, H. Tatsumi, Y. Nakahara, D. Takekawa, and K. Narita. "Effect of Viscosity Characteristics of Lubricants for Electric Vehicles on Thermal Conductivity and Gear Protection". *SAE Technical Papers* (2023). DOI: 10.4271/2023-32-0144.

[38] D. Vanhooydonck, W. Symens, W. Deprez, J. Lemmens, K. Stockman, and S. Dereyne. "Calculating energy consumption of motor systems with varying load using iso efficiency contours". *19th International Conference on Electrical Machines, ICEM 2010* (2010). DOI: 10.1109/ICELMACH.2010.5607992.

[39] S. Dereyne, P. Defreyne, E. Algoet, S. Derammelaere, and K. Stockman. "Efficiency measurement campaign on gearboxes". *Energy efficiency in motor driven systems*. Helsinki: EEMODS, 2015.

[40] C. Changenet, X. Oviedo-Marlot, and P. Velex. "Power loss predictions in geared transmissions using thermal networks-applications to a six-speed manual gearbox". *Journal of Mechanical Design, Transactions of the ASME* 128.3 (2006), pp. 618–625. DOI: 10.1115/1.2181601.

[41] C. Changenet and P. Velex. "A model for the prediction of churning losses in geared transmissions - Preliminary results". *Journal of Mechanical Design, Transactions of the ASME* 129.1 (2007), pp. 128–133. DOI: 10.1115/1.2403727.

[42] J. W. Daily and R. E. Nece. "Chamber dimension effects on induced flow and frictional resistance of enclosed rotating disks". *Journal of Fluids Engineering, Transactions of the ASME* 82.1 (1960), pp. 217–230. DOI: 10.1115/1.3662532.

[43] P. Luke and A. V. Olver. "A study of churning losses in dip-lubricated spur gears". *Proceedings of the Institution of Mechanical Engineers, Part G: Journal of Aerospace Engineering* 213.5 (1999), pp. 337–346. DOI: 10.1243/0954410991533061.

[44] C. Changenet and P. Velex. "Housing influence on churning losses in geared transmissions". *Journal of Mechanical Design, Transactions of the ASME* 130.6 (2008), pp. 0626031–0626036. DOI: 10.1115/1.2900714.

[45] C. Changenet, G. Leprince, F. Ville, and P. Velex. "A note on flow regimes and churning loss modeling". *Journal of Mechanical Design, Transactions of the ASME* 133.12 (2011), pp. 1–5. DOI: 10.1115/1.4005330.

[46] G. LePrince, C. Changenet, F. Ville, P. Velex, C. Dufau, and F. Jarnias. "Influence of Aerated Lubricants on Gear Churning Losses–An Engineering Model". *Tribology Transactions* 54.6 (2011), pp. 929–938. DOI: 10.1080/10402004.2011.597542.

[47] Q. Peng, L. Gui, and Z. Fan. "Numerical and experimental investigation of splashing oil flow in a hypoid gearbox". *Engineering Applications of Computational Fluid Mechanics* 12.1 (2018), pp. 324–333. DOI: 10.1080/19942060.2018.1432506.

[48] S. Laruelle, C. Fossier, C. Changenet, F. Ville, and S. Koechlin. "Experimental investigations and analysis on churning losses of splash lubricated spiral bevel gears". *Mechanics and Industry* 18.4 (2017). DOI: 10.1051/meca/2017007.

[49] A. S. Kolekar, A. V. Olver, A. E. Sworski, and F. E. Lockwood. "Windage and churning effects in dipped lubrication". *Journal of Tribology* 136.2 (2014). DOI: 10.1115/1.4025992.

[50] S. I. Jeon. "Improving Efficiency in Drive Lines: an Experimental Study on Churning Losses in Hypoid Axle". PhD thesis. Imperial College London, 2010.

[51] I. Kakavas. "Development of high efficiency passenger vehicle axle". PhD thesis. Imperial College London, 2015.

[52] H. G. Chothani and K. D. Maniya. "Experimental investigation of churning power loss of single start worm gear drive through optimization technique". *Materials Today: Proceedings* 28 (2020), pp. 2031–2038. DOI: 10.1016/J.MATPR.2019.12.365.

[53] S. Seetharaman and A. Kahraman. "Load-independent spin power losses of a spur gear pair: Model formulation". *Journal of Tribology* 131.2 (2009), pp. 1–11. DOI: 10.1115/1.3085943.

[54] S. Seetharaman, A. Kahraman, M. D. Moorhead, and T. T. Petry-Johnson. "Oil Churning Power Losses of a Gear Pair: Experiments and Model Validation". *Journal of Tribology* (2009). DOI: 10.1115/1.3085942.

[55] I. Kakavas, A. V. Olver, and D. Dini. "Hypoid gear vehicle axle efficiency". *Tribology International* 101 (2016), pp. 314–323. DOI: 10.1016/j.triboint.2016.04.030.

[56] J. F. Shore, A. S. Kolekar, N. Ren, and A. Kadiric. "An Investigation Into the Influence of Viscosity on Gear Churning Losses by Considering the Effective Immersion Depth". *Tribology Transactions* 0.0 (2023), pp. 1–14. DOI: 10.1080/10402004.2023.2247041.

[57] A. S. Terekhov. "Basic problems of heat calculation of gear reducers". *JSME International Conference on Motion and Power Transmissions*. Hiroshima, Japan. 1991, pp. 490–495.

[58] N. E. Anderson and S. H. Loewenthal. "Effect of geometry and operating conditions on spur gear system power loss". *Journal of Mechanical Design, Transactions of the ASME* 103.1 (1981), pp. 151–159. DOI: 10.1115/1.3254854.

[59] T. T. Petry-Johnson, A. Kahraman, N. E. Anderson, and D. R. Chase. "An experimental investigation of spur gear efficiency". *Journal of Mechanical Design, Transactions of the ASME* 130.6 (2008), pp. 0626011–06260110. DOI: 10.1115/1.2898876.

[60] A. Lasri, F. Ville, L. Belfals, and B. Najji. "Mechanics & Industry Preliminary modeling of the oil trapping between teeth for spur gears". *Mechanics & Industry* 15 (2014), pp. 393–402. DOI: 10.1051/meca/2014046.

[61] A. Neurouth, C. Changenet, F. Ville, M. Octrue, and E. Tinguy. "Experimental Investigations to Use Splash Lubrication for High-Speed Gears". *Journal of Tribology* 139.6 (2017). DOI: 10.1115/1.4036447.

[62] S. W. Chen and S. Matsumoto. "Influence of Relative Position of Gears and Casing Wall Shape of Gear Box on Churning Loss under Splash Lubrication Condition—Some New Ideas". *Tribology Transactions* 59.6 (2016), pp. 993–1004. DOI: 10.1080/10402004.2015.1129568.

[63] A. V. Olver. "Gear lubrication—a review". *Proceedings of the Institution of Mechanical Engineers, Part J: Journal of Engineering Tribology* 216.5 (2002), pp. 255–267. DOI: 10.1243/135065002760364804.

[64] P. M. Lugt. "A review on grease lubrication in rolling bearings". *Tribology Transactions* 52.4 (2009), pp. 470–480. DOI: 10.1080/10402000802687940.

[65] G. Ianus, D. Cojocaru, M. C. Oprisan, V. Paleu, and D. N. Olaru. "Power loss in grease lubricated ball bearings". *IOP Conference Series: Materials Science and Engineering* 724.1 (2020), p. 012009. DOI: 10.1088/1757-899X/724/1/012009.

[66] H. Liu, F. Dangl, T. Lohner, and K. Stahl. "Numerical Visualization of Grease Flow in a Gearbox". *Chinese Journal of Mechanical Engineering (English Edition)* 36.1 (2023), pp. 1–14. DOI: 10.1186/S10033-023-00831-7/TABLES/5.

[67] L. Hildebrand, F. Dangl, M. Sedlmair, T. Lohner, and K. Stahl. "CFD analysis on the oil flow of a gear stage with guide plate". *Forschung im Ingenieurwesen/Engineering Research* 86.3 (2022), pp. 395–408. DOI: 10.1007/S10010-021-00523-5/TABLES/7.

[68] H. Liu, T. Jurkschat, T. Lohner, and K. Stahl. "Detailed Investigations on the Oil Flow in Dip-Lubricated Gearboxes by the Finite Volume CFD Method". *Lubricants 2018, Vol. 6, Page 47* 6.2 (2018), p. 47. DOI: 10.3390/LUBRICANTS6020047.

[69] Y. Ariura, T. Ueno, T. Sunaga, and S. Sunamoto. "The Lubricant Churning Loss in Spur Gear Systems". *Bulletin of JSME* 16.95 (1973), pp. 881–892. DOI: 10.1299/jsme1958.16.881.

[70] Y. Diab, F. Ville, H. Houjoh, P. Sainsot, and P. Velex. "Experimental and numerical investigations on the air-pumping phenomenon in high-speed spur and helical gears". *Proceedings of the Institution of Mechanical Engineers, Part C: Journal of Mechanical Engineering Science* 219.8 (2005), pp. 785–800. DOI: 10.1243/095440605X31652.

[71] B. R. Höhn, K. Michaelis, and H. P. Otto. "Influence of immersion depth of dip lubricated gears on power loss, bulk temperature and scuffing load carrying capacity". *International Journal of Mechanics and Materials in Design* 4.2 (2008), pp. 145–156. DOI: 10.1007/s10999-007-9045-z.

[72] Y. Diab, F. Ville, P. Velex, and C. Changenet. "Windage losses in high speed gears-preliminary experimental and theoretical results". *Journal of Mechanical Design, Transactions of the ASME* 126.5 (2004), pp. 903–908. DOI: 10.1115/1.1767815.

[73] J. B. Hunt, A. J. Ryde-Weller, and F. A. Ashmead. "Cavitation between meshing gear teeth". *Wear* 71.1 (1981), pp. 65–78. DOI: 10.1016/0043-1648(81)90140-X.

[74] C. E. Brennen. *Cavitation and bubble dynamics*. Pasadena: Oxford University Press, 2013, pp. 1–249. DOI: 10.1017/CBO9781107338760.

[75] D. del Campo, R. Castilla, G. Raush, P. Gamez-Montero, and E. Codina. "Pressure effects on the performance of external gear pumps under cavitation". *Proceedings of the Institution of Mechanical Engineers, Part C: Journal of Mechanical Engineering Science* 228.16 (2014), pp. 2925–2937. DOI: 10.1177/0954406214522990.

[76] E. Frosina, A. Senatore, and M. Rigosi. "Study of a high-pressure external gear pump with a computational fluid dynamic modeling approach". *Energies* 10.8 (2017). DOI: 10.3390/en10081113.

[77] M. G. Mithun, P. Koukouvinis, I. K. Karathanassis, and M. Gavaises. "Numerical simulation of three-phase flow in an external gear pump using immersed boundary approach". *Applied Mathematical Modelling* 72 (2019), pp. 682–699. DOI: 10.1016/j.apm.2019.03.022.

[78] D. Dowson and C. M. Taylor. "Cavitation in bearings". *Annual Review of Fluid Mechanics* 11.1 (1979), pp. 35–65.

[79] F. Concli and C. Gorla. "Numerical modeling of the power losses in geared transmissions: Windage, churning and cavitation simulations with a new integrated approach that drastically reduces the computational effort". *Tribology International* 103 (2016), pp. 58–68. DOI: 10.1016/j.triboint.2016.06.046.

[80] F. Concli, C. Gorla, F. Rosa, and E. Conrado. "Effect of the static pressure on the power dissipation of gearboxes". *Lubrication Science* 31.8 (2019), pp. 347–355. DOI: 10.1002/ls.1476.

[81] Y.-M. Chen and C. Senlis. "Cavitation Erosion". *Failure Analysis and Prevention* (2002), pp. 1002–1012. DOI: 10.31399/ASM.HB.V11.A0003569.

[82] T. Ouyang, Y. Li, H. Tian, J. Wang, and N. Zhang. "Cavitation mechanism of high-speed helical gears induced by vibration". *Tribology International* 193 (2024), p. 109440. DOI: 10.1016/J.TRIBOINT.2024.109440.

[83] T. E. Karis and H. S. Nagaraj. "Evaporation and flow properties of several hydrocarbon oils". *Tribology Transactions* 43.4 (2000), pp. 758–766. DOI: 10.1080/10402000008982405.

[84] D. Massini, T. Fondelli, B. Facchini, L. Tarchi, and F. Leonardi. "Experimental investigation on power losses due to oil jet lubrication in high speed gearing systems". *Proceedings of the ASME Turbo Expo*. Vol. 5B-2017. American Society of Mechanical Engineers (ASME), 2017. DOI: 10.1115/GT2017-64703.

[85] H. A. Spikes. "Sixty years of EHL". *Lubrication Science* 18.4 (2006), pp. 265–291. DOI: 10.1002/LS.23.

[86] P. M. Lugt and G. E. Morales-Espejel. "A Review of Elasto-Hydrodynamic Lubrication Theory". *Tribology Transactions* 54.3 (2011), pp. 470–496. DOI: 10.1080/10402004.2010.551804.

[87] R. Gohar. *Elastohydrodynamics*. 2nd ed. London: Imperial College Press, 2001.

[88] A. A. Lubrecht, C. H. Venner, and F. Colin. "Film thickness calculation in elasto-hydrodynamic lubricated line and elliptical contacts: The Dowson, Higginson, Hamrock contribution". *Proceedings of the Institution of Mechanical Engineers, Part J: Journal of Engineering Tribology* 223.3 (2009), pp. 511–515. DOI: 10.1243/13506501JET508.

[89] C. A. Foord, W. C. Hammann, and A. Cameron. "Evaluation of lubricants using optical elastohydrodynamics". *ASLE Transactions* 11.1 (1968), pp. 31–43. DOI: 10.1080/05698196808972206.

[90] P. K. Gupta, H. S. Cheng, D. Zhu, N. H. Forster, and J. B. Schrand. "Viscoelastic effects in MIL-L-7808-type lubricant, part I: Analytical formulation". *Tribology Transactions* 35.2 (1992), pp. 269–274. DOI: 10.1080/10402009208982117.

[91] J. Takabi and M. M. Khonsari. "On the thermally-induced failure of rolling element bearings". *Tribology International* 94 (2016), pp. 661–674. DOI: 10.1016/J.TRIBOINT.2015.10.004.

[92] S. Jafari, T. Nikolaidis, A. S. van Heerden, C. P. Lawson, and D. Bosak. "Physics-based thermal model for power gearboxes in geared turbofan engines". *Proceedings of the ASME Turbo Expo* 1 (2020), pp. 1–7. DOI: 10.1115/GT2020-14637.

[93] J. A. Greenwood. "An extension of the Grubin theory of elastohydrodynamic lubrication". *Journal of Physics D: Applied Physics* 5.12 (1972), pp. 2195–2211. DOI: 10.1088/0022-3727/5/12/309.

[94] A. Cameron. "Righting a 40-year-old wrong". *Tribology International* 18.2 (1985), p. 92. DOI: 10.1016/0301-679x(85)90038-6.

[95] J.-D. Wheeler, P. Vergne, N. Fillot, and D. Philippon. "On the relevance of analytical film thickness EHD equations for isothermal point contacts: Qualitative or quantitative predictions?" *Friction* 4.4 (2016), pp. 369–379. DOI: 10.1007/s40544-016-0133-7.

[96] H. Spikes and Z. Jie. "History, origins and prediction of elastohydrodynamic friction". *Tribology Letters* 56.1 (2014), pp. 1–25. DOI: 10.1007/S11249-014-0396-Y/FIGURES/20.

[97] S. Bair, P. Vergne, P. Kumar, G. Poll, I. Krupka, M. Hartl, W. Habchi, and R. Larsson. "Comment on "History, Origins and Prediction of Elastohydrodynamic Friction" by Spikes and Jie". *Tribology Letters* 58.1 (2015), pp. 1–8. DOI: 10.1007/S11249-015-0481-X/FIGURES/7.

[98] S. Bair. "Is it possible to extract the pressure dependence of low-shear viscosity from EHL friction? Revised May, 2020". *Tribology International* 151.April (2020), p. 106454. DOI: 10.1016/j.triboint.2020.106454.

[99] S. Bair. "A Traction (Friction) Curve Is Not a Flow Curve". *Lubricants 2022, Vol. 10, Page 221* 10.9 (2022), p. 221. DOI: 10.3390/LUBRICANTS10090221.

[100] H. Spikes and J. Zhang. "Reply to the Comment by Scott Bair, Philippe Vergne, Punit Kumar, Gerhard Poll, Ivan Krupka, Martin Hartl, Wassim Habchi, Roland Larson on "History, Origins and Prediction of Elastohydrodynamic Friction" by Spikes and Jie in Tribology Letters". *Tribology Letters* 58.1 (2015), pp. 1–6. DOI: 10.1007/S11249-015-0483-8/FIGURES/2.

[101] M. Björling, W. Habchi, S. Bair, R. Larsson, and P. Marklund. "Towards the true prediction of EHL friction". *Tribology International* 66 (2013), pp. 19–26. DOI: 10.1016/j.triboint.2013.04.008.

[102] S. Ardah, F. J. Profito, T. Reddyhoff, and D. Dini. "Advanced modelling of lubricated interfaces in general curvilinear grids". *Tribology International* 188 (2023), p. 108727. DOI: 10.1016/J.TRIBOINT.2023.108727.

[103] H. S. Cheng. "A refined solution to the thermal-elastohydrodynamic lubrication of rolling and sliding cylinders". *ASLE Transactions* 8.4 (1965), pp. 397–410. DOI: 10.1080/05698196508972110.

[104] H. S. Cheng and B. Sternlicht. "A Numerical Solution for the Pressure, Temperature, and Film Thickness Between Two Infinitely Long, Lubricated Rolling and Sliding Cylinders, Under Heavy Loads". *Journal of Basic Engineering* 87.3 (1965), pp. 695–704. DOI: 10.1115/1.3650647.

[105] W. R. D. Wilson and S. Sheu. "Effect of Inlet Shear Heating Due to Sliding on Elastohydrodynamic Film Thickness". *Journal of Lubrication Technology* 105.2 (1983), pp. 187–188. DOI: 10.1115/1.3254563.

[106] R. K. Pandey and M. K. Ghosh. "Thermal effects on film thickness and traction in rolling/sliding EHL line contacts - An accurate inlet zone analysis". *Wear* 192.1-2 (1996), pp. 118–127. DOI: 10.1016/0043-1648(95)06778-7.

[107] J. Hili, A. V. Olver, S. Edwards, and L. Jacobs. "Experimental investigation of elastohydrodynamic (EHD) film thickness behavior at high speeds". *Tribology Transactions* 53.5 (2010), pp. 658–666. DOI: 10.1080/10402001003658326.

[108] G. J. Johnston, R. Wayte, and H. A. Spikes. "The measurement and study of very thin lubricant films in concentrated contacts". *Tribology Transactions* 34.2 (1991), pp. 187–194. DOI: 10.1080/10402009108982026.

[109] H. Liang, D. Guo, T. Reddyhoff, H. Spikes, and J. B. Luo. "Influence of thermal effects on elastohydrodynamic (EHD) lubrication behavior at high speeds". *Science China Technological Sciences* 58.3 (2015), pp. 551–558. DOI: 10.1007/s11431-014-5564-7.

[110] H. S. Cheng. "Calculation of elastohydrodynamic film thickness in high speed rolling and sliding contacts". *MTI Report 67TR24* (1967).

[111] A. V. Olver. "Testing Transmission Lubricants: The Importance of Thermal Response". *Proceedings of the Institution of Mechanical Engineers, Part G: Journal of Aerospace Engineering* 205.1 (1991), pp. 35–44. DOI: 10.1243/PIME_PROC_1991_205_235_02.

[112] T. Reddyhoff, H. A. Spikes, and A. V. Olver. "Compression heating and cooling in elastohydrodynamic contacts". *Tribology Letters* 36.1 (2009), pp. 69–80. DOI: 10.1007/S11249-009-9461-3/FIGURES/15.

[113] W. Habchi and P. Vergne. "On the compressive heating/cooling mechanism in thermal elastohydrodynamic lubricated contacts". *Tribology International* 88 (2015), pp. 143–152. DOI: 10.1016/J.TRIBOINT.2015.03.025.

[114] W. Habchi, P. Sperka, and S. Bair. "Is Elastohydrodynamic Minimum Film Thickness Truly Governed by Inlet Rheology?" *Tribology Letters* 71.3 (2023), pp. 1–9. DOI: 10.1007/S11249-023-01771-Y/FIGURES/9.

[115] P. Rycerz and A. Kadiric. "The Influence of Slide-Roll Ratio on the Extent of Micropitting Damage in Rolling-Sliding Contacts Pertinent to Gear Applications". *Tribology Letters* 67 (2019), p. 63. DOI: 10.1007/s11249-019-1174-7.

[116] J. Zhang, A. Tan, and H. Spikes. "Effect of Base Oil Structure on Elastohydrodynamic Friction". *Tribology Letters* 65.1 (2016). DOI: 10.1007/S11249-016-0791-7.

[117] J. Zhang and H. Spikes. "Measurement of EHD Friction at Very High Contact Pressures". *Tribology Letters* 68.1 (2020), p. 42. DOI: 10.1007/s11249-020-1281-5.

[118] A. V. Olver and H. A. Spikes. *Prediction of traction in elastohydrodynamic lubrication*. Tech. rep. 1998, pp. 321–332.

[119] J. C. Jaeger. "Moving sources of heat and the temperature at sliding contacts". *Journal and proceedings of the Royal Society of New South Wales* 76.3 (1942), pp. 203–224. DOI: 10.5962/p.360338.

[120] J. F. Archard. "The temperature of rubbing surfaces". *Wear* 2.6 (1959), pp. 438–455. DOI: 10.1016/0043-1648(59)90159-0.

[121] A. Kadiric, R. S. Sayles, and E. Ioannides. "Thermo-mechanical model for moving layered rough surface contacts". *Journal of Tribology* 130.1 (2008). DOI: 10.1115/1.2805440.

[122] J. Lu, T. Reddyhoff, and D. Dini. "3D Measurements of Lubricant and Surface Temperatures Within an Elastohydrodynamic Contact". *Tribology Letters* 66.1 (2018), pp. 1–16. DOI: 10.1007/s11249-017-0953-2.

[123] T. B. Lane and J. R. Hughes. "A study of the oil-film formation in gears by electrical resistance measurements". *British Journal of Applied Physics* 3.10 (1952), pp. 315–318. DOI: 10.1088/0508-3443/3/10/305.

[124] A. Crook. "The lubrication of rollers II. Film thickness with relation to viscosity and speed". *Philosophical Transactions of the Royal Society of London. Series A, Mathematical and Physical Sciences* 254.1040 (1961), pp. 223–236. DOI: 10.1098/rsta.1961.0015.

[125] R. S. Dwyer-Joyce, B. W. Drinkwater, and C. J. Donohoe. "The measurement of lubricant-film thickness using ultrasound". *Proceedings of the Royal Society A: Mathematical, Physical and Engineering Sciences* 459.2032 (2003), pp. 957–976. DOI: 10.1098/rspa.2002.1018.

[126] H. A. Spikes and P. M. Cann. "The development and application of the spacer layer imaging method for measuring lubricant film thickness". *Proceedings of the Institution of Mechanical Engineers, Part J: Journal of Engineering Tribology* 215.3 (2001), pp. 261–277. DOI: 10.1243/1350650011543529.

[127] R. Gohar and A. Cameron. "Theoretical and experimental studies of the oil film in lubricated point contact". *Proceedings of the Royal Society of London. Series A. Mathematical and Physical Sciences* 291.1427 (1966), pp. 520–536. DOI: 10.1098/rspa.1966.0112.

[128] F. J. Westlake and A. Cameron. "Fluid Film Interferometry in Lubrication Studies". *Nature 1967 214:5088* 214.5088 (1967), pp. 633–634. DOI: 10.1038/214633a0.

[129] P. Cann and A. A. Lubrecht. "An analysis of the mechanisms of grease lubrication in rolling element bearings". *Lubrication Science* 11.3 (1999), pp. 227–245. DOI: 10.1002/LS.3010110303.

[130] P. M. Cann. "Starvation and reflow in a grease-lubricated elastohydrodynamic contact". *Tribology Transactions* 39.3 (1996), pp. 698–704. DOI: 10 . 1080 / 10402009608983585.

[131] G. Guangteng, P. M. Cann, A. V. Olver, and H. A. Spikes. "An experimental study of film thickness between rough surfaces in EHD contacts". *Tribology International* 33.3-4 (2000), pp. 183–189. DOI: 10.1016/S0301-679X(00)00025-6.

[132] N. Marx, J. Guegan, and H. A. Spikes. "Elastohydrodynamic film thickness of soft EHL contacts using optical interferometry". *Tribology International* 99 (2016), pp. 267–277. DOI: 10.1016/J.TRIBOINT.2016.03.020.

[133] M. Smeeth, H. Spikes, and S. Gunsel. "Boundary film formation by viscosity index improvers". *Tribology Transactions* 39.3 (1996), pp. 726–734. DOI: 10 . 1080 / 10402009608983590.

[134] E. Gendreau. "Effect of polymers on lubricant rheology in an elastohydrodynamic contact". PhD thesis. Imperial College London, 2022.

[135] P. M. Cann, H. A. Spikes, and J. Hutchinson. "The development of a spacer layer imaging method (SLIM) for mapping elastohydrodynamic contacts". *Tribology Transactions* 39.4 (1996), pp. 915–921. DOI: 10.1080/10402009608983612.

[136] M. Hartl, I. Krupka, R. Poliscuk, M. Liska, J. Molimard, M. Querry, and P. Vergne. "Thin film colorimetric interferometry". *Tribology Transactions* 44.2 (2001), pp. 270–276. DOI: 10.1080/10402000108982458.

[137] F. Guo and P. L. Wong. "A multi-beam intensity-based approach for lubricant film measurements in non-conformal contacts". *Proceedings of the Institution of Mechanical Engineers, Part J: Journal of Engineering Tribology* 216.5 (2002), pp. 281–291. DOI: 10.1243/135065002760364822.

[138] L. Ma and C. Zhang. "Discussion on the technique of relative optical interference intensity for the measurement of lubricant film thickness". *Tribology Letters* 36.3 (2009), pp. 239–245. DOI: 10.1007/S11249-009-9479-6/FIGURES/9.

[139] SKF. *The SKF model for calculating the frictional moment*. Tech. rep. SKF, 2017, pp. 1–15.

[140] A. Feldermann, D. Fischer, S. Neumann, and G. Jacobs. "Determination of hydraulic losses in radial cylindrical roller bearings using CFD simulations". *Tribology International* 113 (2017), pp. 245–251. DOI: 10.1016/j.triboint.2017.03.020.

[141] Y. Marchesse, C. Changenet, and F. Ville. "Drag Power Loss Investigation in Cylindrical Roller Bearings Using CFD Approach". *Tribology Transactions* 62.3 (2019), pp. 403–411. DOI: 10.1080/10402004.2018.1565009.

[142] Timken. *Syber Advanced Bearing System Analysis by Timken*. 2021. URL: https://www.timken.com/timken-world/syber-bearing-analysis/ (visited on 05/05/2024).

[143] A. Wemecamp, A. Dover, and G. Morales-Espejel. "Friction theory, thermal modelling and validation for industrial gearbox". *VDI Gear Conference Munich*. Munich, 2013.

[144] H. Blok. "Theoretical Study of Temperature Rise at Surfaces of Actual Contact under Oiliness Lubricating Conditions". *Proc. Instn. Mech. Engrs. (General discussion on lubrication and lubricants)* 2 (1937), p. 222.

[145] H. Blok. "The flash temperature concept". *Wear* 6.6 (1963), pp. 483–494. DOI: 10.1016/0043-1648(63)90283-7.

[146] A. Dyson. "Scuffing - a review". *Tribology International* 8.2 (1975), pp. 77–87. DOI: 10.1016/0301-679X(75)90056-0.

[147] R. M. Matveevsky. "The critical temperature of oil with point and line contact machines". *Journal of Fluids Engineering, Transactions of the ASME* 87.3 (1965), pp. 754–759. DOI: 10.1115/1.3650672.

[148] J. C. Bell, A. Dyson, and J. W. Hadley. "The effects of rolling and sliding speeds on the scuffing of lubricated steel discs". *ASLE Transactions* 18.1 (1975), pp. 62–73. DOI: 10.1080/05698197508982748.

[149] A. Dyson. "The Failure of Elastohydrodynamic Lubrication of Circumferentially Ground Discs". *Inst Mech Eng*. Vol. 190. 52. London: SAGE PublicationsSage UK: London, England, 1976, pp. 699–711. DOI: 10.1243/pime_proc_1976_190_074_02.

[150] J. R. Barber. "Thermoelastic instabilities in the sliding of conforming solids". *Proceedings of the Royal Society of London. A. Mathematical and Physical Sciences* 312.1510 (1969), pp. 381–394. DOI: 10.1098/RSPA.1969.0165.

[151] W. F. Bowman and G. W. Stachowiak. "A review of scuffing models". *Tribology Letters* 2.2 (1996), pp. 113–131. DOI: 10.1007/BF00160970.

[152] S. C. Lee and H. S. Cheng. "Scuffing Theory Modeling and Experimental Correlations". *Journal of Tribology* 113.2 (1991), pp. 327–334. DOI: 10.1115/1.2920624.

[153] M. W. Bailey and A. Cameron. "The effects of temperature and metal pairs on scuffing". *ASLE Transactions* 16.2 (1973), pp. 121–131. DOI: 10.1080/05698197308982713.

[154] H. A. Spikes and A. Cameron. "Scuffing as a desorption process—An explanation of the Borsoff effect". *ASLE Transactions* 17.2 (1974), pp. 92–96. DOI: 10.1080/05698197408981442.

[155] R. Bjerk. "Oxygen—an "extreme-pressure agent"". *ASLE Transactions* 16.2 (1973), pp. 97–106. DOI: 10.1080/05698197308982710.

[156] E. C. Cutiongco and Y. W. Chung. "Prediction of scuffing failure based on competitive kinetics of oxide formation and removal: Application to lubricated sliding of AISI 52100 steel on steel". *Tribology Transactions* 37.3 (1994), pp. 622–628. DOI: 10.1080/10402009408983338.

[157] K. C. Ludema. "A review of scuffing and running-in of lubricated surfaces, with asperities and oxides in perspective". *Wear* 100.1-3 (1984), pp. 315–331. DOI: 10.1016/0043-1648(84)90019-X.

[158] A. W. Batchelor and G. W. Stachowiak. "Model of scuffing based on the vulnerability of an elastohydrodynamic oil film to chemical degradation catalyzed by the contacting surfaces". *Tribology Letters* 1.4 (1995), pp. 349–365. DOI: 10.1007/BF00174259.

[159] J. C. Enthoven, P. M. Cann, and H. A. Spikes. "Temperature and scuffing". *Tribology Transactions* 36.2 (1993), pp. 258–266. DOI: 10.1080/10402009308983157.

[160] J. Enthoven and H. A. Spikes. "Infrared and visual study of the mechanisms of scuffing". *Tribology Transactions* 39.2 (1996), pp. 441–447. DOI: 10.1080/10402009608983550.

[161] J. Hershberger, O. O. Ajayi, J. Zhang, H. Yoon, and G. R. Fenske. "Evidence of scuffing initiation by adiabatic shear instability". *Wear* 258.10 (2005), pp. 1471–1478. DOI: 10.1016/J.WEAR.2004.10.010.

[162] O. O. Ajayi, C. Lorenzo-Martin, R. A. Erck, and G. R. Fenske. "Analytical predictive modeling of scuffing initiation in metallic materials in sliding contact". *Wear* 301.1-2 (2013), pp. 57–61. DOI: 10.1016/J.WEAR.2012.12.054.

[163] S. Li, A. Kahraman, N. Anderson, and L. D. Wedeven. "A model to predict scuffing failures of a ball-on-disk contact". *Tribology International* 60 (2013), pp. 233–245. DOI: 10.1016/J.TRIBOINT.2012.11.007.

[164] ASTM. *D2782 Standard Test Method for Measurement of Extreme-Pressure Properties of Lubricating Fluids (Timken Method)*. 2020. URL: https://www.astm.org/d2782-20.html.

[165] ASTM. *D2596 Standard Test Method for Measurement of Extreme-Pressure Properties of Lubricating Grease (Four-Ball Method)*. 2010. URL: https://www.astm.org/d2596-20.html.

[166] P. I. Lacey. "Development of a gear oil scuff test (gost) procedure to predict adhesive wear resistance of turbine engine lubricants". *Tribology Transactions* 41.3 (1998), pp. 307–316. DOI: 10.1080/10402009808983753.

[167] ASTM. *D1947 Standard Test Method for Load Carrying Capacity of Petroleum Oil and Synthetic Fluid Gear Lubricants*. 1983.

[168] Energy Institute (Formerly Institute of Petroleum). *Determination of Load-Carrying Capacity of Lubricants—IAE Gear Machine Method*. Tech. rep. 1992.

[169] ISO. *14635-1. Gears–FZG Test Procedure - Part 1: FZG Test Method A/8, 3/90 for Relative Load Carrying Capacity of Oils*. Tech. rep. DIN, 2000.

[170] D. Massocchi, M. Lattuada, S. Chatterton, and P. Pennacchi. "SRV Method: Lubricating Oil Screening Test for FZG". *Machines 2022, Vol. 10, Page 621* 10.8 (2022), p. 621. DOI: 10.3390/MACHINES10080621.

[171] M. Savolainen and A. Lehtovaara. "An experimental approach for investigating scuffing initiation due to overload cycles with a twin-disc test device". *Tribology International* 109 (2017), pp. 311–318. DOI: 10.1016/J.TRIBOINT.2017.01.005.

[172] M. Ingram, C. Hamer, and H. Spikes. "A new scuffing test using contra-rotation". *Wear* 328-329 (2015), pp. 229–240. DOI: 10.1016/J.WEAR.2015.01.080.

[173] H. Blok. "Gear wear as related to viscosity of gear oils". *Proc. Summer Conf.—MIT, Mech. Wear*. Vol. 61. 25. 1948, pp. 199–227.

[174] B. Peng. "An Experimental Study of the Onset of Scuffing Using a New Contra-rotation Test Method". PhD thesis. Imperial College London, 2018.

[175] B. Peng, H. Spikes, and A. Kadiric. "The Development and Application of a Scuffing Test Based on Contra-rotation". *Tribology Letters* 67.2 (2019), p. 37. DOI: 10.1007/s11249-019-1149-8.

[176] M. Ueda, H. Spikes, and A. Kadiric. "In-Situ Observation of the Effect of the Tribofilm Growth on Scuffing in Rolling-Sliding Contact". *Tribology Letters* 70.3 (2022), pp. 1–21. DOI: 10.1007/S11249-022-01621-3/.

[177] R. Bayat and A. Lehtovaara. "Scuffing evaluation of fully formulated environmentally acceptable lubricant using barrel-on-disc technique". *Tribology International* 160 (2021), p. 107002. DOI: 10.1016/J.TRIBOINT.2021.107002.

[178] A. Clarke, H. P. Evans, and R. W. Snidle. "Understanding micropitting in gears". *Proceedings of the Institution of Mechanical Engineers, Part C: Journal of Mechanical Engineering Science* 230.7-8 (2016), pp. 1276–1289. DOI: 10.1177/0954406215606934.

[179] R. L. Errichello. "Morphology of micropitting". *American Gear Manufacturers Association Fall Technical Meeting 2011* December (2012), pp. 255–273.

[180] D. Berthe, L. Flamand, D. Foucher, and M. Godet. "Micropitting in Hertzian contacts." *Journal of Tribology* 102.October (1980). DOI: doi.org/10.1115/1.3251583.

[181] M. N. Webster and C. J. Norbart. "An experimental investigation of micropitting using a roller disk machine". *Tribology Transactions* 38.4 (1995), pp. 883–893. DOI: 10.1080/10402009508983485.

[182] E. Lainé, A. V. Olver, and T. A. Beveridge. "Effect of lubricants on micropitting and wear". *Tribology International* 41.11 (2008), pp. 1049–1055. DOI: 10.1016/J.TRIBOINT.2008.03.016.

[183] T. Ahlroos, H. Ronkainen, A. Helle, R. Parikka, J. Virta, and S. Varjus. "Twin disc micropitting tests". *Tribology International* 42.10 (2009), pp. 1460–1466. DOI: 10.1016/J.TRIBOINT.2009.05.023.

[184] A. Vrček, T. Hultqvist, Y. Baubet, P. Marklund, and R. Larsson. "Micro-pitting Damage of Bearing Steel Surfaces under Mixed Lubrication Conditions: Effects of Roughness, Hardness and ZDDP Additive". *Tribology International* 138 (2019), pp. 239–249. DOI: 10.1016/J.TRIBOINT.2019.05.038.

[185] G. de Silva. "Model Rough Surfaces in Elastohydrodynamic Lubrication". PhD thesis. University of London, 1981.

[186] S. Roy, D. White, and S. Sundararajan. "Correlation between evolution of surface roughness parameters and micropitting of carburized steel under boundary lubrication condition". *Surface and Coatings Technology* 350 (2018), pp. 445–452. DOI: 10.1016/J.SURFCOAT.2018.05.083.

[187] D. K. Prajapati and M. Tiwari. "Experimental analysis of contact fatigue damage using fractal methodologies". *Wear* 450-451 (2020), p. 203262. DOI: 10.1016/J.WEAR.2020.203262.

[188] H. A. Spikes, A. V. Olver, and P. B. Macpherson. "Wear in rolling contacts". *Wear* 112.2 (1986), pp. 121–144. DOI: 10.1016/0043-1648(86)90236-X.

[189] M. Ueda, H. Spikes, and A. Kadiric. "Influence of Black Oxide Coating on Micropitting and ZDDP Tribofilm Formation". *Tribology Transactions* (2021), pp. 1–21. DOI: 10.1080/10402004.2021.1940407.

[190] R. S. Zhou, H. S. Cheng, and T. Mura. "Micropitting in Rolling and Sliding Contact Under Mixed Lubrication". *Journal of Tribology* 111.4 (1989), pp. 605–613. DOI: 10.1115/1.3261984.

[191] G. E. Morales-Espejel, P. Rycerz, and A. Kadiric. "Prediction of micropitting damage in gear teeth contacts considering the concurrent effects of surface fatigue and mild wear". *Wear* 398-399 (2018), pp. 99–115. DOI: 10.1016/J.WEAR.2017.11.016.

[192] M. Ueda, J. S. Wong, and H. Spikes. "Influence of dumbbell base oil blends on micropitting". *Tribology International* 185 (2023), p. 108578. DOI: 10.1016/J.TRIBOINT.2023.108578.

[193] B. Wainwright, H. Takeuchi, T. Makino, and A. Kadiric. "The influence of Λ ratio and surface roughness on the initiation and progression of micropitting damage". *Wear* 508-509 (2022), p. 204473. DOI: 10.1016/j.wear.2022.204473.

[194] A. Oila and S. J. Bull. "Assessment of the factors influencing micropitting in rolling/sliding contacts". *Wear* 258.10 (2005), pp. 1510–1524. DOI: 10.1016/J.WEAR.2004.10.012.

[195] C. Benyajati and A. V. Olver. "The effect of a ZnDTP anti-wear additive on micropitting resistance of carburised steel rollers". *AGMA* (2004), pp. 1–10.

[196] S. Soltanahmadi. "Tribochemical investigation of micropitting in rolling-element bearing applications: the influence of lubricant additives and water contamination". PhD thesis. University of Leeds, 2017.

[197] J. Zhang, M. Ueda, S. Campen, and H. Spikes. "Boundary Friction of ZDDP Tribofilms". *Tribology Letters* 69.1 (2021), pp. 1–17. DOI: 10.1007/s11249-020-01389-4.

[198] E. Lainé, A. V. Olver, M. F. Lekstrom, B. A. Shollock, T. A. Beveridge, and D. Y. Hua. "The effect of a friction modifier additive on micropitting". *Tribology Transactions* 52.4 (2009), pp. 526–533. DOI: 10.1080/10402000902745507.

[199] M. Ueda, B. Wainwright, H. Spikes, and A. Kadiric. "The effect of friction on micropitting". *Wear* 488-489 (2022), p. 204130. DOI: 10.1016/J.WEAR.2021.204130.

[200] M. Ueda, H. Spikes, and A. Kadiric. "In-situ observations of the effect of the ZDDP tribofilm growth on micropitting". *Tribology International* 138 (2019), pp. 342–352. DOI: 10.1016/j.triboint.2019.06.007.

[201] R. Balcombe, M. T. Fowell, A. V. Olver, S. Ioannides, and D. Dini. "A coupled approach for rolling contact fatigue cracks in the hydrodynamic lubrication regime : The importance of fluid / solid interactions". *Wear* 271.5-6 (2011), pp. 720–733. DOI: 10.1016/j.wear.2011.02.005.

[202] A. V. Olver, L. K. Tiew, S. Medina, and J. W. Choo. "Direct observations of a micropit in an elastohydrodynamic contact". *Wear* 256.1-2 (2004), pp. 168–175. DOI: 10.1016/S0043-1648(03)00374-0.

[203] H. Cen, A. Morina, A. Neville, R. Pasaribu, and I. Nedelcu. "Effect of water on ZDDP anti-wear performance and related tribochemistry in lubricated steel/steel pure sliding contacts". *Tribology International* 56 (2012), pp. 47–57. DOI: 10.1016/j.triboint.2012.06.011.

[204] H. Cen, D. Bai, Y. Chao, Y. Li, and R. Li. "Effect of Relative Humidity on Micropitting Behavior in Rolling–Sliding Contacts with Zinc Dialkyldithiophosphate-Containing Lubricants". *Journal of Materials Engineering and Performance* 30.4 (2021), pp. 2781–2797. DOI: 10.1007/s11665-021-05561-2.

[205] J. G. Z. Tamayo, M. Björling, Y. Shi, B. Prakash, and R. Larsson. "Micropitting performance of glycerol-based lubricants under rolling-sliding contact conditions". *Tribology International* 167 (2022), p. 107348. DOI: 10.1016/J.TRIBOINT.2021.107348.

[206] W. Britton. "The running-in and incipient micropitting of ground gear surfaces under mixed lubrication condition". PhD thesis. University of Cardiff, 2021.

[207] A. Kahraman. *An Experimental and Theoretical Investigation of Micropiiting in Wind Turbine Gears and Bearings*. Tech. rep. Golden, CO (United States): Golden Field Office, 2012. DOI: 10.2172/1037344.

[208] S. Li and A. Kahraman. "Micro-pitting fatigue lives of lubricated point contacts: Experiments and model validation". *International Journal of Fatigue* 48 (2013), pp. 9–18. DOI: 10.1016/J.IJFATIGUE.2012.12.003.

[209] S. Soltanahmadi, A. Morina, M. C. Van Eijk, I. Nedelcu, and A. Neville. "Investigation of the effect of a diamine-based friction modifier on micropitting and the properties of tribofilms in rolling-sliding contacts". *Journal of Physics D: Applied Physics* 49.50 (2016). DOI: 10.1088/0022-3727/49/50/505302.

[210] J. Shore. "A New Thermally Coupled Lubrication Model for the Prediction of Transmission Efficiency in Electric Vehicles". PhD thesis. Imperial College London, 2024.

[211] T. Wellmann. "Simulation and Test-Based Methodologies for EDU Fluids Development". *STLE Annual Meeting 2024*. Minneapolis, 2024.

[212] M. Shamszad. "Lubricant Requirements for Electric Vehicles". *STLE Annual Meeting 2024*. Minneapolis, 2024.

[213] L. Guo, H. Mol, T. Nijdam, L. de Vries, and J. Bongaerts. "Study on the electric discharge behaviour of a single contact in EV motor bearings". *Tribology International* 187 (2023), p. 108743. DOI: 10.1016/J.TRIBOINT.2023.108743.

[214] H. A. Spikes. "Triboelectrochemistry: Influence of Applied Electrical Potentials on Friction and Wear of Lubricated Contacts". *Tribology Letters* 68.3 (2020), pp. 1–27. DOI: 10.1007/s11249-020-01328-3.

[215] F. He, G. Xie, and J. Luo. "Electrical bearing failures in electric vehicles". *Friction* 8.1 (2020), pp. 4–28. DOI: 10.1007/s40544-019-0356-5.

[216] L. I. Farfan-Cabrera, A. Erdemir, J. A. Cao-Romero-Gallegos, I. Alam, and S. Lee. "Electrification effects on dry and lubricated sliding wear of bearing steel interfaces". *Wear* 516-517 (2023), p. 204592. DOI: 10.1016/J.WEAR.2022.204592.

[217] L. Yu and D. Liu. "Study of the thermal effectiveness of laminar forced convection of nanofluids for liquid cooling applications". *IEEE Transactions on Components, Packaging and Manufacturing Technology* 3.10 (2013), pp. 1693–1704. DOI: 10.1109/TCPMT.2013.2265261.

[218] S. Peerzada. "Effects of Foam and Aeration on Electric Vehicle Fluids". *STLE Annual Meeting 2024*. Minneapolis, 2024.

[219] H. Vogel. "The law of the relation between the viscosity of liquids and the temperature". *Phys. Z* 22.1 (1921), pp. 645–646.

[220] A. LaFountain, G. J. Johnston, and H. A. Spikes. *Elastohydrodynamic friction behavior of polyalphaolefin blends*. Vol. 34. Elsevier Masson SAS, 1998, pp. 465–475. DOI: 10.1016/s0167-8922(98)80102-8.

[221] R. J. Chittenden, D. Dowson, J. F. Dunn, and C. M. Taylor. "A theoretical analysis of the isothermal elastohydrodynamic lubrication of concentrated contacts. I. Direction of lubricant entrainment coincident with the major axis of the Hertzian contact ellipse". *Proceedings of the Royal Society of London. A. Mathematical and Physical Sciences* 397.1813 (1985), pp. 245–269. DOI: 10.1098/RSPA.1985.0014.

[222] A. F. Jankowski, J. P. Hayes, T. E. Felter, C. Evans, and A. J. Nelson. "Sputter deposition of silicon–oxide coatings". *Thin Solid Films* 420-421 (2002), pp. 43–46. DOI: 10.1016/S0040-6090(02)00741-1.

[223] EVSpecifications. *2016 Tesla Model S P90D - Specifications*. 2024. URL: https://www.evspecifications.com/en/model/14ef45 (visited on 05/07/2024).

[224] J. Břoušek and T. Zvolský. "Experimental study of electric vehicle gearbox efficiency". *MATEC Web of Conferences*. Vol. 234. EDP Sciences, 2018, p. 02004. DOI: 10.1051/matecconf/201823402004.

[225] Tesla. *Tesla Model X Service Manual - Fluid Capacities*. 2020. URL: https://service.tesla.com/docs/ModelX/ServiceManual/en-us/GUID-37B6AA65-332C-4A5D-89EE-036C72DC9320.html (visited on 02/25/2024).

[226] A. S. Kolekar. "Lubrication & Efficiency of Rear Wheel Drive Axles in Road Vehicles". PhD thesis. Imperial College London, 2013.

[227] A. MacLaren and A. Kadiric. "Elastohydrodynamic Traction and Film Thickness at High Speeds". *Tribology Letters* 72.3 (2024). DOI: 10.1007/s11249-024-01894-w.

[228] P. K. Gupta. "On Thermal Reduction Factor for Elastohydrodynamic Film Thickness in Rolling/Sliding Contacts". *Tribology Transactions* 67.6 (2024), pp. 1303–1304. DOI: 10.1080/10402004.2024.2428697.

[229] S. S. Bair. *High pressure rheology for quantitative elastohydrodynamics*. Elsevier, 2019.

[230] N. Fang, L. Chang, M. N. Webster, and A. Jackson. "A non-averaging method of determining the rheological properties of traction fluids". *Tribology International* 33.11 (2000), pp. 751–760. DOI: 10.1016/S0301-679X(00)00116-X.

[231] J. Tevaarwerk and K. L. Johnson. "A simple non-linear constitutive equation for elastohydrodynamic oil films". *Wear* 35.2 (1975), pp. 345–356. DOI: 10.1016/0043-1648(75)90081-2.

[232] S. Bair. "Viscous Heating in Compressed Liquid Films". *Tribology Letters* 68.1 (2020), pp. 1–12. DOI: 10.1007/S11249-019-1252-X/FIGURES/12.

[233] W. Habchi, S. Bair, and P. Vergne. "On friction regimes in quantitative elastohydrodynamics". *Tribology International* 58 (2013), pp. 107–117. DOI: 10.1016/J.TRIBOINT.2012.10.005.

[234] H. A. Spikes, V. Anghel, and R. Glovnea. "Measurement of the rheology of lubricant films within elastohydrodynamic contacts". *Tribology Letters* 17.3 (2004), pp. 593–605. DOI: 10.1023/B:TRIL.0000044509.82345.16/METRICS.

[235] J. Lu. "Experimental and Numerical Analysis of Thermal Elastohydrodynamic Contacts". PhD thesis. Imperial College London, 2019.

[236] T. Reddyhoff, A. Schmidt, and H. Spikes. "Thermal Conductivity and Flash Temperature". *Tribology Letters* 67.1 (2019), pp. 1–9. DOI: 10.1007/s11249-018-1133-8.

[237] R. Larsson and O. Andersson. "Lubricant thermal conductivity and heat capacity under high pressure". *http://dx.doi.org/10.1243/1350650001543223* 214.4 (2000), pp. 337–342. DOI: 10.1243/1350650001543223.

[238] K. L. Johnson and J. L. Tevaarwerk. "Shear Behaviour of Elastohydrodynamic Oil Films." *Proc R Soc London Ser A* 356.1685 (1977), pp. 215–236. DOI: 10.1098/rspa.1977.0129.

[239] C. R. Evans and K. L. Johnson. "Regimes of Traction in Elastohydrodynamic Lubrication". *Journal of Mechanical Engineering Science* 200.5 (1986), pp. 313–324. DOI: https://doi.org/10.1243/PIME_PROC_1986_200_135_02.

[240] S. H. Loewenthal and D. A. Rohn. "Elastic Model of the Traction Behavior of Two Traction Lubricants". *ASLE Transactions* 27.2 (1984), pp. 129–137. DOI: 10.1080/05698198408981553.

[241] S. Bair and S. Flores-Torres. "The viscosity of polyalphaolefins mixtures at high pressure and stress". *Journal of Tribology* 141.2 (2019), pp. 1–7. DOI: 10.1115/1.4041124.

[242] G. E. Morales-Espejel and V. Brizmer. "Micropitting modelling in rolling–sliding contacts: Application to rolling bearings". *Tribology Transactions* 54.4 (2011), pp. 625–643. DOI: 10.1080/10402004.2011.587633.

[243] B. Wainwright and A. Kadiric. "The Effect of Surface Roughness and the Λ Ratio on the Initiation and Progression of Micropitting Damage". *STLE Virtual Annual Meeting & Exhibition*. 2021.

[244] L. Zhao, E. R. Ottinger, A. H. C. Yip, and J. P. Helveston. "Quantifying electric vehicle mileage in the United States". *Joule* 7.11 (2023), pp. 2537–2551. DOI: 10.1016/j.joule.2023.09.015.

[245] C. Benyajati, A. V. Olver, and C. J. Hamer. "An experimental study of micropitting, using a new miniature test-rig". *Tribology Series* 43 (2003), pp. 601–610. DOI: 10.1016/s0167-8922(03)80088-3.

[246] B. J. Hamrock and B. O. Jacobson. *Elastohydrodynamic lubrication of rectangular contacts*. Tech. rep. NASA, 1983.

[247] M. Ueda, A. Kadiric, and H. Spikes. "Influence of PMA on the anti-scuffing properties of AW/EP additives". *Tribology International* 174 (2022), p. 107756. DOI: 10.1016/J.TRIBOINT.2022.107756.

[248] K. Pagkalis, H. Spikes, J. Jelita Rydel, M. Ingram, and A. Kadiric. "The Influence of Steel Composition on the Formation and Effectiveness of Anti-wear Films in Tribological Contacts". *Tribology Letters* 69.2 (2021), p. 75. DOI: 10.1007/s11249-021-01438-6.

[249] M. Hartl, I. Křupka, R. Poliščuk, and M. Liška. "An automatic system for real-time evaluation of EHD film thickness and shape based on the colorimetric interferometry". *Tribology Transactions* 42.2 (1999), pp. 303–309. DOI: 10.1080/10402009908982221.

[250] L. Gustafsson, E. Höglund, and O. Marklund. "Measuring Lubricant Film Thickness with Image Analysis". *Proceedings of the Institution of Mechanical Engineers, Part J: Journal of Engineering Tribology* 208.3 (1994), pp. 199–205. DOI: 10.1243/PIME_PROC_1994_208_371_02.

[251] K. Yagi, K. Nishida, and J. Sugimura. "Traction behaviour of elastohydrodynamic lubrication films with anomalous shapes". *Proceedings of the Institution of Mechanical Engineers, Part J: Journal of Engineering Tribology* 235.11 (2021), pp. 2247–2256. DOI: 10.1177/1350650121997240.

[252] T. Doki-Thonon, N. Fillot, G. E. Morales Espejel, M. Querry, D. Philippon, N. Devaux, and P. Vergne. "A dual experimental/numerical approach for film thickness analysis in TEHL spinning skewing circular contacts". *Tribology Letters* 50.1 (2013), pp. 115–126. DOI: 10.1007/S11249-013-0122-1/FIGURES/12.

[253] K. Yagi and P. Vergne. "Abnormal film shapes in sliding elastohydrodynamic contacts lubricated by fatty alcohols". *Proceedings of the Institution of Mechanical Engineers, Part J: Journal of Engineering Tribology* 221.3 (2007), pp. 287–300. DOI: 10.1243/13506501JET253.

[254] M. Hartl, I. Křupka, and M. Liška. "Differential colorimetry: tool for evaluation of chromatic interference pattern". *https://doi.org/10.1117/1.601415* 36.9 (1997), pp. 2384–2391. DOI: 10.1117/1.601415.

[255] T. Tomota, M. Tohyama, and K. Yagi. "Elucidation of contact state on various rough surfaces via highly robust colorimetric optical interferometry". *Scientific Reports* 12.1 (2022), pp. 1–14. DOI: 10.1038/s41598-021-04104-y.

[256] J. D. Wheeler, J. Molimard, N. Devaux, D. Philippon, N. Fillot, P. Vergne, and G. E. Morales-Espejel. "A Generalized Differential Colorimetric Interferometry Method: Extension to the Film Thickness Measurement of Any Point Contact Geometry". *Tribology Transactions* 61.4 (2018), pp. 648–660. DOI: 10.1080/10402004.2017.1386809.

[257] R. Golafshan, B. Su, G. Jacobs, and J. Berroth. "Characterization of elastohydrodynamic contact film thickness under high frequency force excitation using a 2D unwrapping-based image processing technique". *Tribology International* 175 (2022), p. 107841. DOI: 10.1016/J.TRIBOINT.2022.107841.

[258] H. Fujita and H. A. Spikes. "The formation of zinc dithiophosphate antiwear films". *Proceedings of the Institution of Mechanical Engineers, Part J: Journal of Engineering Tribology* 218.4 (2004), pp. 265–277. DOI: 10.1243/1350650041762677.

[259] J. Zhang and H. Spikes. "On the Mechanism of ZDDP Antiwear Film Formation". *Tribology Letters* 63.2 (2016), pp. 1–15. DOI: 10.1007/S11249-016-0706-7/.

[260] M. Ueda, A. Kadiric, and H. Spikes. "On the Crystallinity and Durability of ZDDP Tribofilm". *Tribology Letters* 67.4 (2019), p. 123. DOI: 10.1007/s11249-019-1236-x.

[261] J. Zhang, J. P. Ewen, M. Ueda, J. S. Wong, and H. A. Spikes. "Mechanochemistry of Zinc Dialkyldithiophosphate on Steel Surfaces under Elastohydrodynamic Lubrication Conditions". *ACS Applied Materials and Interfaces* 12.5 (2020), pp. 6662–6676. DOI: 10.1021/ACSAMI.9B20059.

[262] L. Fang, S. Korres, W. A. Lamberti, M. N. Webster, and R. W. Carpick. "What stress components drive mechanochemistry? A study of ZDDP tribofilm formation". *Faraday Discussions* 241.0 (2023), pp. 394–412. DOI: 10.1039/D2FD00123C.

[263] R. P. Glovnea, A. V. Olver, and H. A. Spikes. "Lubrication of rough surfaces by a boundary film-forming viscosity modifier additive". *Journal of Tribology* 127.1 (2005), pp. 223–229. DOI: 10.1115/1.1828069.

[264] J. Guegan. "Experimental Investigation into the Influence of Roughness on Friction and Film Thickness in EHD Contacts By". PhD thesis. Imperial College London, 2015.

[265] J. W. Choo, R. P. Glovnea, A. V. Olver, and H. A. Spikes. "The effects of three-dimensional model surfaces roughness features on lubricant film thickness in EHL contacts". *Journal of Tribology* 125.3 (2003), pp. 533–542. DOI: 10.1115/1.1538617.

[266] T. Haque, S. Korres, J. T. Carey, P. W. Jacobs, J. Loos, and J. Franke. "Lubricant Effects on White Etching Cracking Failures in Thrust Bearing Rig Tests". *Tribology Transactions* 61.6 (2018), pp. 979–990. DOI: 10.1080/10402004.2018.1453571.

[267] M. B. Elinski, P. LaMascus, L. Zheng, A. Jackson, R. J. Wiacek, and R. W. Carpick. "Cooperativity Between Zirconium Dioxide Nanoparticles and Extreme Pressure Additives in Forming Protective Tribofilms: Toward Enabling Low Viscosity Lubricants". *Tribology Letters* 68.4 (2020), pp. 1–17. DOI: 10.1007/S11249-020-01346-1/.

[268] J. Luo, S. Wen, and P. Huang. "Thin film lubrication part I: Study on the transition between EHL and thin film lubrication using a relative optical interference intensity technique". *Wear* 194.1-2 (1996), pp. 107–115. DOI: 10.1016/0043-1648(95)06799-X.

[269] G. E. Morales-Espejel, R. Meeuwenoord, A. F. Quiñonez, and R. Hauleitner. "Film thickness and traction measurements of refrigerant R1233zd used as lubricant in elastohydrodynamic conditions". *Proceedings of the Institution of Mechanical Engineers, Part C: Journal of Mechanical Engineering Science* 229.2 (2015), pp. 244–253. DOI: 10.1177/0954406214533530.

[270] P. de Groot. "Principles of interference microscopy for the measurement of surface topography". *Advances in Optics and Photonics* 7.1 (2015), p. 1. DOI: 10.1364/aop.7.000001.

[271] M. Smeeth and C. Hamer. "The Measurement of Tribo-film Formation Using a Combination of Visible and Infrared Light". *STLE Annual Meeting 2022*. Orlando, 2022.

[272] J. Dawczyk, J. Russo, and H. Spikes. "Ethoxylated Amine Friction Modifiers and ZDDP". *Tribology Letters* 67.4 (2019), pp. 1–15. DOI: 10.1007/S11249-019-1221-4/.

[273] J. Dawczyk, N. Morgan, J. Russo, and H. Spikes. "Film Thickness and Friction of ZDDP Tribofilms". *Tribology Letters* 67.2 (2019), pp. 1–15. DOI: 10.1007/S11249-019-1148-9/.

[274] J. Jacquelin. *Regressions et Equations Integrales*. 2014. URL: https://fr.scribd.com/doc/14674814/Regressions-et-equations-integrales (visited on 07/11/2023).

[275] C. Hollitt. "A convolution approach to the circle Hough transform for arbitrary radius". *Machine Vision and Applications* 24.4 (2013), pp. 683–694. DOI: 10.1007/s00138-012-0420-x.

[276] A. O. Djekoune, K. Messaoudi, and K. Amara. "Incremental circle hough transform: An improved method for circle detection". *Optik* 133 (2017), pp. 17–31. DOI: 10.1016/j.ijleo.2016.12.064.

[277] M. Born and E. Wolf. *Principles of optics : electromagnetic theory of propagation, interference and diffraction of light*. 7th. Cambridge: Cambridge University Press, 1999.

[278] D. Dowson and G. R. Higginson. *Elasto-hydrodynamic lubrication*. London: Pergamon Press, 1977, p. 235.

[279] S. A. Khodier. "Refractive index of standard oils as a function of wavelength and temperature". *Optics and Laser Technology* 34.2 (2002), pp. 125–128. DOI: 10.1016/S0030-3992(01)00101-3.

[280] S. J. Thrush et al. "Growth and morphology of thermally assisted sinterable zirconia nanoparticle tribofilm". *Tribology International* 175 (2022), p. 107820. DOI: 10.1016/J.TRIBOINT.2022.107820.

[281] K. Topolovec-Miklozic, T. R. Forbus, and H. A. Spikes. "Film thickness and roughness of ZDDP antiwear films". *Tribology Letters* 26.2 (2007), pp. 161–171. DOI: 10.1007/S11249-006-9189-2.

[282] M. Jerman, Z. Qiao, and D. Mergel. "Refractive index of thin films of SiO2, ZrO2, and HfO2 as a function of the films' mass density". *Applied Optics, Vol. 44, Issue 15, pp. 3006-3012* 44.15 (2005), pp. 3006–3012. DOI: 10.1364/AO.44.003006.

[283] G. T. Wan, P. Kenny, and H. A. Spikes. "Elastohydrodynamic properties of water-based fire-resistant hydraulic fluids". *Tribology International* 17.6 (1984), pp. 309–315. DOI: 10.1016/0301-679X(84)90093-8.

[284] M. Yilmaz, M. Mirza, T. Lohner, and K. Stahl. "Superlubricity in EHL Contacts with Water-Containing Gear Fluids". *Lubricants* 7.5 (2019), p. 46. DOI: 10.3390/lubricants7050046.

[285] Z. Chen, Y. Liu, S. Zhang, and J. Luo. "Controllable superlubricity of glycerol solution via environment humidity". *Langmuir* 29.38 (2013), pp. 11924–11930. DOI: 10.1021/LA402422H.

[286] S. J. Kim and K. Y. Kim. "An Overview on Hydrogen Uptake, Diffusion and Transport Behavior of Ferritic Steel, and Its Susceptibility to Hydrogen Degradation". *Corrosion Science and Technology* 16.4 (2017), pp. 209–225.

[287] N. Oberle, T. Amann, D. Kürten, R. Raga, and A. Kailer. "In-situ-determination of tribologically induced hydrogen permeation using electrochemical methods". *Proceedings of the Institution of Mechanical Engineers, Part J: Journal of Engineering Tribology* 234.7 (2020), pp. 1027–1034. DOI: 10.1177/1350650119889196.

[288] Y. Kou, S. Wang, J. Luo, K. Sun, J. Zhang, Z. Tan, and Q. Shi. "Thermal analysis and heat capacity study of polyethylene glycol (PEG) phase change materials for thermal energy storage applications". *The Journal of Chemical Thermodynamics* 128 (2019), pp. 259–274. DOI: 10.1016/j.jct.2018.08.031.

[289] A. Ponjavic. "Local rheology of lubricants in the elastohydrodynamic regime". PhD thesis. Imperial College London, 2014.

[290] J. Dench, N. Morgan, and J. S. Wong. "Quantitative Viscosity Mapping Using Fluorescence Lifetime Measurements". *Tribology Letters* 65.1 (2017), pp. 1–13. DOI: 10.1007/s11249-016-0807-3.

[291] T. Otsu and K. Imado. "Study on Changes in the Rheologic Properties of EHL Film Using Fluorescence Measurements". *Tribology Letters* 66.1 (2018), pp. 1–10. DOI: 10.1007/s11249-018-0983-4.

[292] A. Porras-Vazquez, N. Fillot, P. Vergne, D. Philippon, and G. E. Morales-Espejel. "Influence of spin on film thickness in elastohydrodynamic starved point contacts". *Tribology International* 156.December 2020 (2021), p. 106825. DOI: 10.1016/j.triboint.2020.106825.

[293] S. H. Loewenthal. "Spin Analysis of Concentrated Traction Contacts." *NASA Technical Memorandum* 108.March (1984), pp. 77–84.

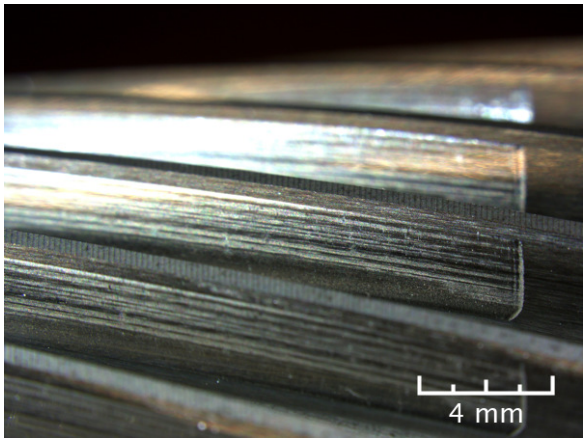
[294] H. Dormois, N. Fillot, W. Habchi, G. Dalmaz, P. Vergne, G. E. Morales-Espejel, and E. Ioannides. "A numerical study of friction in isothermal ehd rolling-sliding sphere-plane contacts with spinning". *Journal of Tribology* 132.2 (2010), pp. 1–10. DOI: 10.1115/1.4001104.

Appendix A: Gearbox Tooth Flank Surfaces

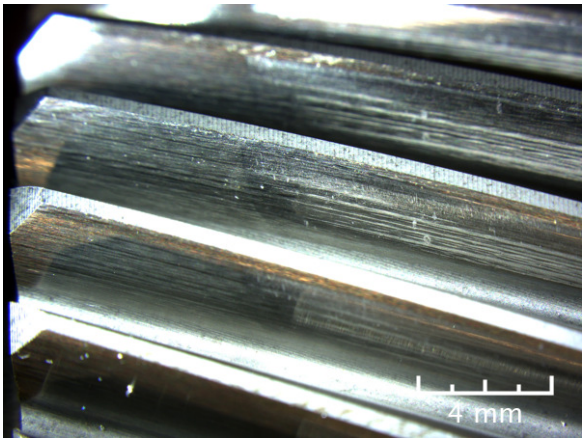
This section contains a factual description of the visible appearance of the gear teeth surfaces of the EV gearbox used in Chapter 4, which was obtained 2nd hand from a vehicle salvage yard. This should not be read as an assessment of the reliability of this drive unit, or any other performance characteristic.

After dismantling the gearbox in Chapter 4, the gears were removed, cleaned with paper towel, toluene, compressed air and isopropanol, and the working surfaces of the gears inspected with a long-working-length optical microscope. Images of the pinion teeth on both the driving and braking surfaces (or equivalently, forward and reverse driving faces) are shown in Fig. A.1.

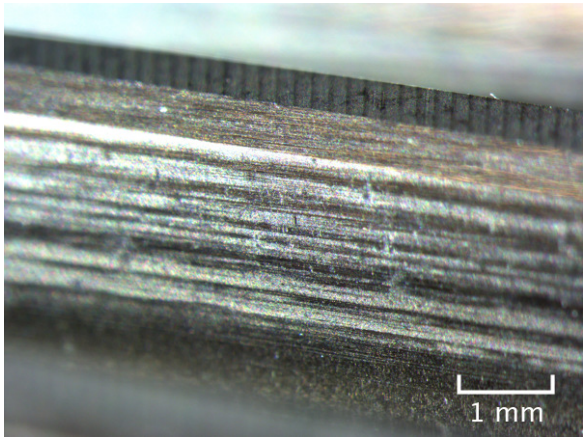
(a) Driving surfaces



(b) Braking surfaces



(c) Driving surface



(d) Braking surface

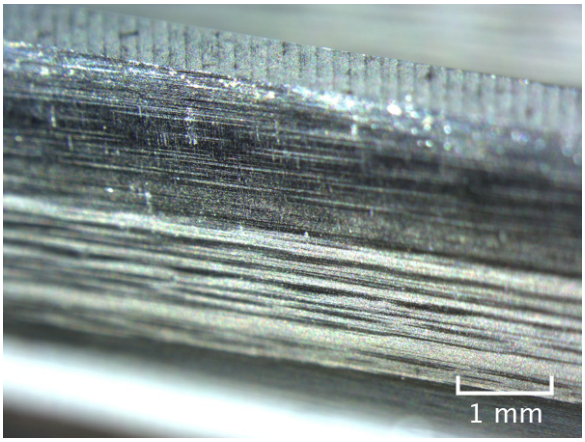
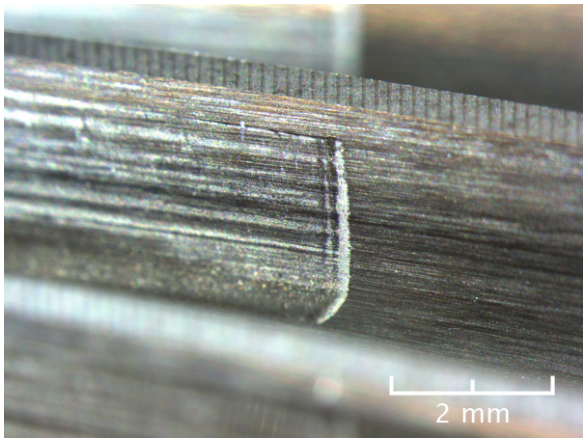


Figure A.1: Microscope images of both driving and braking surfaces of the high-speed motor shaft pinion gear, after 21,589 miles, or 1.47×10^8 contact cycles.

Some wear of the driving pinion teeth is apparent in Fig. A.1a from the wear step at the end of the region which contacts the wheel (the pinion facewidth considerably exceeds that of the wheel so both working and non-working flank are visible, see Fig. A.2a). On the reverse faces, responsible for

(a) Wear Step



(b) Tooth Flank

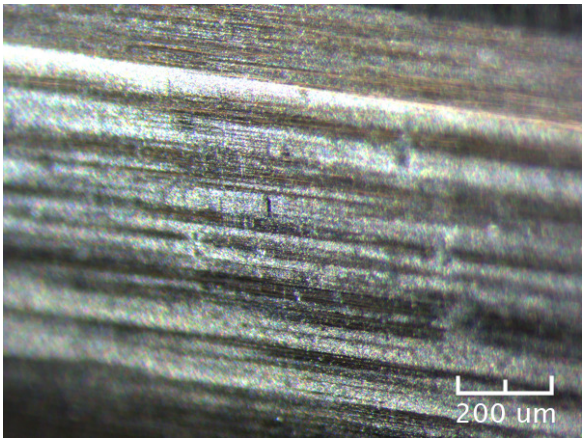


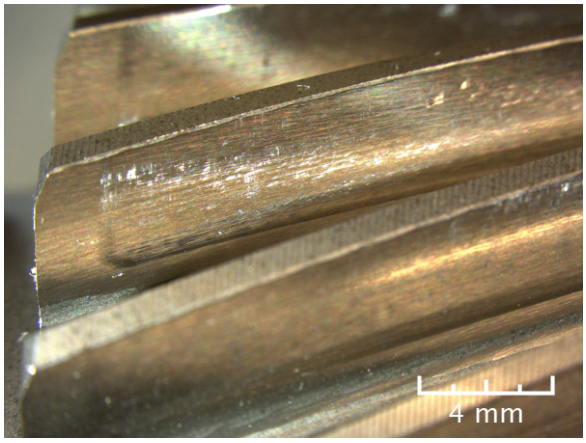
Figure A.2: Microscope images of driving surface of the tooth shown in Fig. A.1c of the motor shaft pinion gear, after 21,589 miles, or 1.47×10^8 contact cycles.

acceleration in reverse and regenerative braking, the wear is less apparent (Fig. A.1b) and on closer inspection is confined to the dedendum of the gear tooth (Fig. A.1d), in which the over-rolling and friction force are in opposite directions. The visible damage, which appears to follow the grinding marks, appears to span both the addendum and dedendum for the driving face however (Fig. A.2b). The magnification here is not sufficient for a definitive classification of the damage, and the use of a microscope with such magnification would have necessitated the destruction of the gear, which was needed, intact, for the churning loss study. Note that while the horizontal scaling is comparable between images, the vertical direction is compressed by the angle from which the tooth is viewed, which varies picture-to-picture.

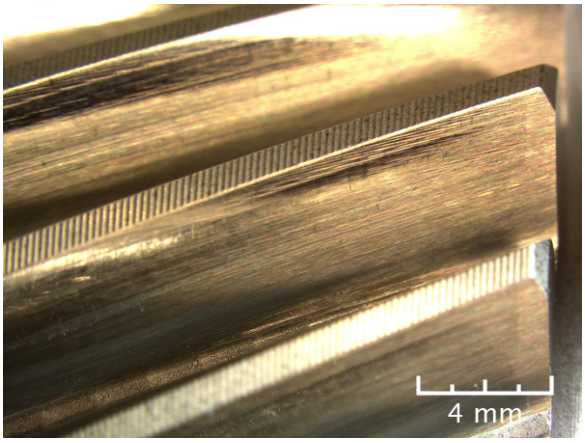
The low-speed pinion, which has seen 2.48 times fewer contact cycles than the high-speed pinion, but considerably higher normal loads, shows some small signs of wear on the driving face (Fig. A.3a) and almost no wear visible to the naked eye on the braking face (Fig. A.3b). Some smearing of the grinding marks in the overrolling direction is visible under a microscope on the driving face, perhaps as a result of very mild micro-scuffing under transient high-torque conditions (Fig. A.3c). Mild polishing with directional features caused by overrolling is the only visible damage in Fig. A.3d.

The high-speed wheel gear, which meshes with the high-speed pinion gear but sees fewer contact cycles per tooth, shows similar evidence of moderate wear (frosted appearance highlighting the grinding marks), but also shows dark pits on the driving face. On closer inspection (Fig. A.5) these were seen to reflect light under oblique illumination, possibly indicating debris damage. The frosted appearance is also much more pronounced in the dedendum.

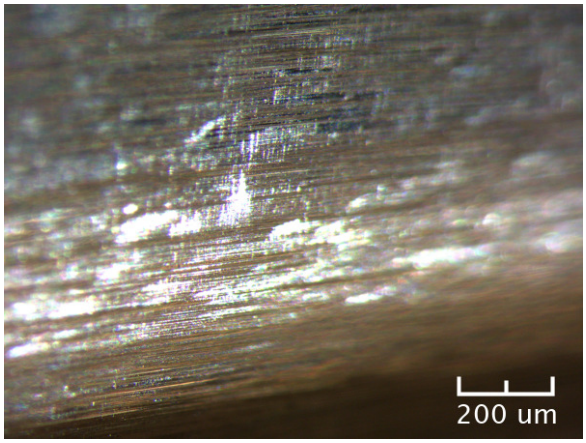
(a) Driving surfaces



(b) Braking surfaces



(c) Driving surface



(d) Braking surface

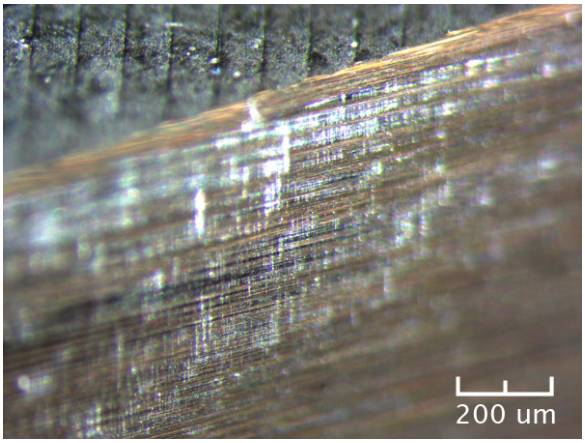
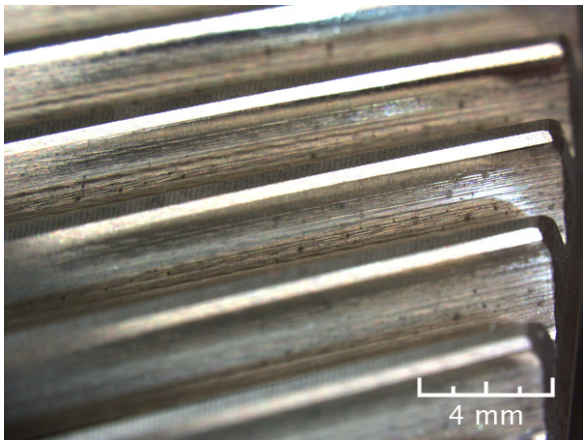


Figure A.3: Microscope images of driving and braking surfaces of the low-speed stage pinion gear on the intermediate shaft, after 21,589 miles, or 5.91×10^7 contact cycles.

(a) Driving Surfaces



(b) Braking surfaces

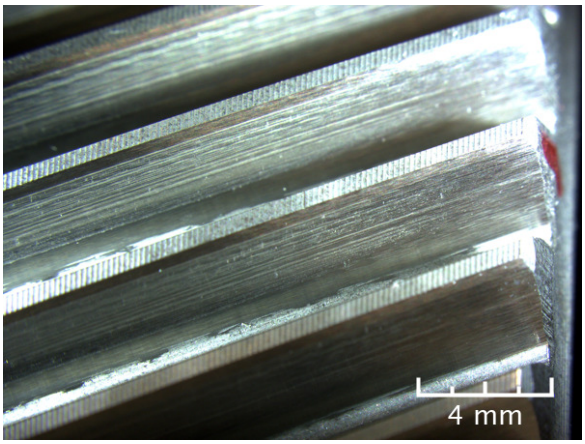


Figure A.4: Microscope images of driving and braking surfaces of the high-speed stage wheel gear which meshes with the motor pinion shown in Fig. A.1, after 21,589 miles, or 5.91×10^7 contact cycles.

(a) (b)

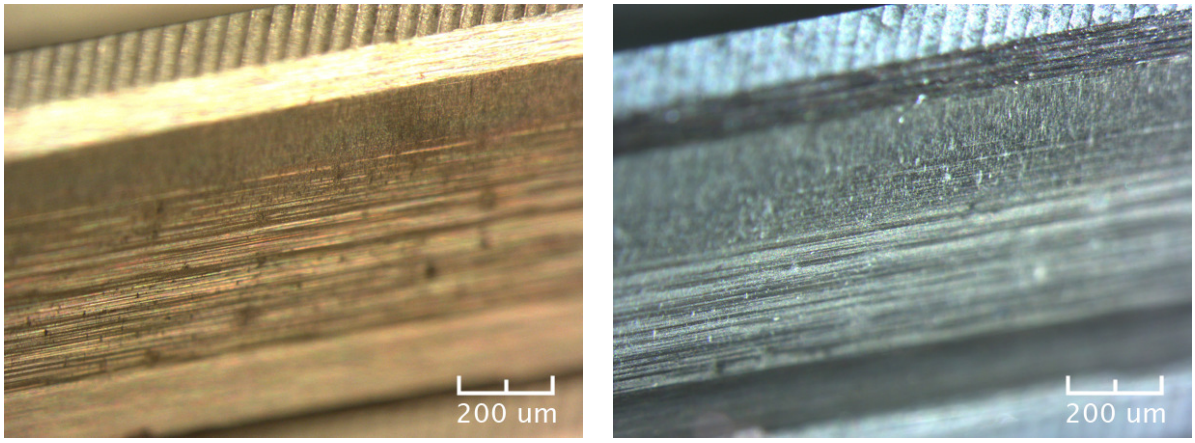


Figure A.5: Identically-positioned microscope images of the same location on the driving surface of a tooth on the high-speed stage wheel gear, using two illumination angles, showing dark pits in Fig. A.4a to also be reflective.

The primary conclusion from these images is that the damage to the gear surfaces is relatively mild - in terms of contact cycles this gearbox has served approximately 15% of its likely life (assuming a lifetime of 150,000 miles, a reasonable lifetime for a Tesla EV sold in 2016 [244]). The load history however is unknown.

It is worthy of note that the results of the accelerated tests for scuffing and micropitting in Chapter 7 do not correspond to the condition of the gears as seen here. In both cases one of the accelerating factors is the high contact pressure, and although far more contact cycles have been seen by these surfaces than the ones in the ex-situ tests, only a small (and in this case, unknown) fraction of these will have been at comparable contact pressures. It should also be noted that the hardness difference likely does not favour micropitting on the surface seeing the highest number of contact cycles on the gear surfaces, by contrast to the micropitting test for which the rings are much harder than the roller - this is also an accelerating factor. Nevertheless, several features of the surfaces shown here have analogies in the early stages of the accelerated tests (frosted appearance during crack initiation phase of micropitting tests, light scratching and subsequent micro-scuffing during running-in and lower-sliding-speed stages of scuffing tests).

Appendix B: Gear Mesh and Bearing Reaction Force Calculation

Mesh forces are calculated at pitch point for each gear, given the torque T, the reference pressure angle α_n, the spiral angle β, the centre distance a, the normal module m_n and the number of teeth z. The value of α at pitch point is the working pressure angle α_{tw}

$$\alpha_{tw} = \cos^{-1}\left(\frac{m_n \cos\alpha_t \sec\beta}{2a}\right) \tag{B.1}$$

$$\alpha_t = \tan^{-1}\left(\tan\alpha_n \sec\beta\right) \tag{B.2}$$

For nonzero addendum modification, the pitch circle does not necessarily coincide with the reference circle. The pitch circle radius can be found given that the pitch point divides the line of centres in the gear ratio $G = \frac{z_2}{z_1}$. The spiral angle at pitch point β_P is therefore

$$\beta_P = \tan^{-1}\left(\frac{a\sin\beta}{(z_1+z_2)m_n}\right) \tag{B.3}$$

The tangential, radial and axial components of the mesh force F_t, F_r and F_a respectively are then

$$F_t = \frac{2T}{zm_n \sec\beta_P} \tag{B.4}$$

$$F_r = F_t \tan\alpha_{tw} \sec\beta_P \tag{B.5}$$

$$F_a = F_t \tan\beta_P \tag{B.6}$$

Applying this analysis to each gear, where the subscript 1 indicates the high-speed stage, 2 the low-speed stage, p the pinion (smaller gear) of that stage and w the wheel (larger gear), we note that reaction forces on meshing gears are equal and opposite so $F_{t2p} = F_{t2w} = F_{t2}$ etc. The radius of the high-speed pinion gear, adopting the same convention, is r_{1p}, and the axial lengths a, b etc are shown in Fig. 4.8 on page 84.

Considering (statical) force equilibrium, and letting each bearing take reactions in x, y and z, we have:

Low-speed shaft

$$\Sigma F_x \qquad F_{r2} = F_{xA} + F_{xB} \tag{B.7}$$

$$\Sigma F_y \qquad F_{t2} = F_{yA} + F_{yB} \tag{B.8}$$

$$\Sigma F_z \qquad 0 = F_{a2} + F_{zA} + F_{zB} \tag{B.9}$$

$$\Sigma M_x \qquad bF_{yB} = aF_{yA} \tag{B.10}$$

$$\Sigma M_y \qquad r_{2w}F_{a2} + bF_{r2} = (a+b)F_{xA} \tag{B.11}$$

$$\Sigma M_z \qquad r_{2w}F_{t2} = T_2 \tag{B.12}$$

Intermediate shaft

$$\Sigma F_x \qquad F_{xC} + F_{xD} + F_{r2} = F_{r1}\cos\theta + F_{t1}\sin\theta \tag{B.13}$$

$$\Sigma F_y \qquad F_{r1}\sin\theta = F_{yC} + F_{yD} + F_{t1}\cos\theta + F_{t2} \tag{B.14}$$

$$\Sigma F_z \qquad F_{a2} = F_{zC} + F_{zD} + F_{a1} \tag{B.15}$$

$$\Sigma M_x \qquad F_{r1}\sin\theta = F_{yC} + F_{yD} + F_{t1}\cos\theta + F_{t2} \tag{B.16}$$

$$\Sigma M_y \qquad cF_{xC} - (g+d)F_{xD} = gF_{r2} + r_{1w}\cos\theta F_{a1} + r_{2p}F_{a2} \tag{B.17}$$

$$\Sigma M_z \qquad r_{2p}F_{t2} = r_{1w}F_{t1} \tag{B.18}$$

High-speed shaft

$$\Sigma F_x \qquad 0 = F_{xE} + F_{xF} + F_{r1}\cos\theta + F_{t1}\sin\theta \tag{B.19}$$

$$\Sigma F_y \qquad F_{t1}\cos\theta = F_{yE} + F_{yF} + F_{r1}\sin\theta \tag{B.20}$$

$$\Sigma F_z \qquad F_{a1} = F_{zE} + F_{zF} \tag{B.21}$$

$$\Sigma M_x \qquad eF_{yE} = fF_{yF} + r_{p1}\sin\theta F_{a1} \tag{B.22}$$

$$\Sigma M_y \qquad eF_{xE} = fF_{xF} + r_{p1}\cos\theta F_{a1} \tag{B.23}$$

$$\Sigma M_z \qquad r_{1p}F_{t1} = T_1 \tag{B.24}$$

Bearing D in 4.8 is a cylindrical roller bearing, so takes no axial load. Assuming that the outer races of bearings B and F are left floating such that they also do not take axial load, the system solves to

give

$$\begin{aligned} F_{xA} &= \frac{r_{2w}F_{a2} + bF_{r2}}{a+b} \\ F_{yA} &= \frac{bF_{t2}}{a+b} \\ F_{zA} &= F_{a2} \end{aligned} \tag{B.25}$$

$$\begin{aligned} F_{xB} &= F_{r2} - F_{xA} \\ F_{yB} &= F_{t2} - F_{yA} \\ F_{zB} &= 0 \end{aligned} \tag{B.26}$$

$$\begin{aligned} F_{xC} &= F_{r1}\cos\theta + F_{t1}\sin\theta - F_{xD} - F_{r2} \\ F_{yC} &= F_{r1}\sin\theta - F_{yD} - F_{t1}\cos\theta - F_{t2} \\ F_{zC} &= F_{a2} - F_{a1} \end{aligned} \tag{B.27}$$

$$\begin{aligned} F_{xD} &= \frac{1}{c+d+g}\left[c\left(F_{r1}\cos\theta + F_{t1}\sin\theta\right) - (c+g)F_{r2} - r_{1w}\cos\theta F_{a1} - r_{2p}F_{a2}\right] \\ F_{yD} &= \frac{1}{c+d+g}\left[c\left(F_{r1}\sin\theta - F_{t1}\cos\theta\right) - (c+g)F_{t2} - r_{1w}\sin\theta F_{a1}\right] \\ F_{zD} &= 0 \end{aligned} \tag{B.28}$$

$$\begin{aligned} F_{xE} &= \frac{1}{e}\left(fF_{xF} + r_{p1}\cos\theta F_{a1}\right) \\ F_{yE} &= \frac{1}{e}\left(fF_{yF} + r_{p1}\sin\theta F_{a1}\right) \\ F_{zE} &= F_{a1} \end{aligned} \tag{B.29}$$

$$\begin{aligned} F_{xF} &= \frac{-1}{e+f}\left[e\left(F_{r1}\cos\theta + F_{t1}\sin\theta\right) r_{p1}\cos\theta F_{a1}\right] \\ F_{yF} &= \frac{1}{e+f}\left[e\left(F_{t1}\cos\theta - F_{r1}\sin\theta\right) - r_{p1}\sin\theta F_{a1}\right] \\ F_{zF} &= 0 \end{aligned} \tag{B.30}$$

Appendix C: Minimum EHL Film Thickness in Helical Gear Pairs

EHL film thickness in the line contact made between helical gear teeth is given approximately by the regression equation of Dowson and Higginson [278], which requires knowledge of surface speeds, elastic properties, curvature, lubricant viscosity, and contact loading.

$$h_m = 1.6\alpha_p^{0.6}(\eta_0 U_e)^{0.7} E'^{0.03} R^{0.43} w^{-0.13} \tag{C.1}$$

The reduced contact modulus E' is

$$E' = 2\left(\frac{1-\nu_1^2}{E_1} + \frac{1-\nu_2^2}{E_2}\right)^{-1} \tag{C.2}$$

The radii of curvature of the pinion and wheel teeth, R_1 and R_2 respectively, are the radii resolved normal to the line of contact between two identical cones with semi-angle β_b, the spiral angle at the base circle.

$$\beta_b = \sin^{-1}\left(\sin\beta\cos\alpha_n\right) \tag{C.3}$$

The cones point in opposite directions so that their axes are parallel, and they align such that their radii in normal section are

$$R_2' = \frac{m_n}{2}\left(\left(z_2\sec\beta + 2(x_2+1)\right)^2 - \left(z_2\sec\beta\cos\alpha_t\right)^2\right)^{\frac{1}{2}} \tag{C.4}$$

$$R_1' = a\sin\alpha_{tw} - R_2' \tag{C.5}$$

and so resolving perpendicular to the contact line we obtain the reduced radius of curvature R from

$$R_1 = R_1'\sec\beta_b \tag{C.6}$$

$$R_2 = R_2'\sec\beta_b \tag{C.7}$$

$$R = \left(\frac{1}{R_1} + \frac{1}{R_2}\right)^{-1} \tag{C.8}$$

In a reference frame fixed on the contact, the surface speeds of the two tooth flanks are

$$U_1 = R_1'\omega_1 \tag{C.9}$$

$$U_2 = R_2'\omega_2 \tag{C.10}$$

and the entrainment and sliding speeds are then

$$U_e = \frac{1}{2}(U_1 + U_2) \tag{C.11}$$

$$U_s = U_2 - U_1 \tag{C.12}$$

$$\mathrm{SRR} = \frac{U_s}{U_e} = 2\frac{U_2 - U_1}{U_1 + U_2} \tag{C.13}$$

The tangential contact ratio ε_α, the ratio of the length of the path of contact to the tangential base pitch, describes the 'average' number of tooth pairs in contact for any given tangential section. The axial contact ratio ε_β is the number of axial pitches $p_x = \frac{\pi m_n}{\sin\beta}$ in the facewidth b. The total contact ratio ε_γ is the sum of the tangential and axial contact ratios.

$$\begin{aligned}\varepsilon_\alpha = \frac{1}{2\pi}\Big(&\sqrt{(z_1 + (x_1+1)\cos\beta)^2 \sec^2\alpha_t - z_1^2} \\ &+ \sqrt{(z_2 + (x_2+1)\cos\beta)^2 \sec^2\alpha_t - z_2^2} \\ &-(z_1+z_2)\tan\alpha_{tw}\Big)\end{aligned} \tag{C.14}$$

$$\varepsilon_\beta = \frac{\pi b m_n}{\sin\beta} \tag{C.15}$$

$$\varepsilon_\gamma = \varepsilon_\alpha + \varepsilon_\beta \tag{C.16}$$

The total contact ratio ε_γ for both gear pairs of interest was found to exceed 3, so at the point of wheel tip contact there are 3 other tooth pairs in contact, but the load is not shared equally between tooth pairs. Except in the case where ε_β is an integer, the total contact length is also constantly changing, but takes a mean value of $b\varepsilon_\alpha \sec\beta_b$. Owing to the low exponent of the load per unit length w in Eq. (C.1), the film thickness estimate does not incur a large error by making the assumption that

$$w = \frac{F_n \cos\beta_b}{b\varepsilon_\alpha} \tag{C.17}$$

where F_n is the normal load at pitch point assuming single-tooth-pair contact.

Appendix D: Referred Inertia of Bearing Rolling Elements

The balls or cylinders in a rolling element bearing both rotate and translate as they roll. For bearings whose loading is entirely radial (DGBBs, CRBs, and NRBs), this analysis assumes that the axes of rotation of the rolling elements are all parallel to the axis of revolution of the races. Assuming also that there is no (macro-) slip in the contacts, the rotational speed of a rolling element ω_b about its axis is found using the same analysis applicable to a planet gear in an epicyclic gear system, and is given by

$$\omega_b = \frac{r_o\omega_o - r_i\omega_i}{r_o - r_i} \tag{D.1}$$

where r_o and r_i are the radii, and ω_o and ω_i the angular velocities of the outer and inner races of the bearing respectively (equivalent to the ring and sun gears in planetary gearing, relaxing the integer tooth number constraint). Similarly the angular velocity of the cage which spaces the rolling elements, hence that of their centres of rotation about the central axis, ω_c (equivalent to the planet carrier), is given by

$$\omega_c = \frac{r_o\omega_o + r_i\omega_i}{r_o + r_i} \tag{D.2}$$

The method of referred inertias finds the inertia I_{ref} required to maintain the same rotational kinetic energy when rotating at a fictitious speed ω_{ref}, as is attained in the case where a real inertia I_1 is rotating at its actual speed ω_1. The rotational kinetic energy $E_{k_{\mathrm{rot}}}$, a conserved quantity, is found in each case from

$$E_{k_{\mathrm{rot}}} = \frac{1}{2}I_{\mathrm{ref}}\omega_{\mathrm{ref}}^2 = \frac{1}{2}I_1\omega_1^2 \tag{D.3}$$

And so rearranging, the inertia I_{ref} 'referred' to speed ω_{ref} is

$$I_{\mathrm{ref}} = \left(\frac{\omega_1}{\omega_{\mathrm{ref}}}\right)^2 I_1 \tag{D.4}$$

Similar reasoning is applied to a single bearing rolling element of mass m_b, whose total kinetic energy (accounting now for rotation and translation) is

$$E_{k_{\mathrm{tot}}} = \frac{1}{2}I_b\omega_b^2 + \frac{1}{2}m_b(r_c\omega_c)^2 \tag{D.5}$$

The inertia I_b of the rolling elements of radius r_b rotating about their central axes is

$$I_{\text{ball}} = \frac{2}{5} m r_b^2 \qquad \text{for balls} \tag{D.6}$$

$$I_{\text{roller}} = \frac{1}{2} m r_b^2 \qquad \text{for cylindrical rollers} \tag{D.7}$$

where the orbital radius of the rolling elements r_c and their rolling radius r_b are

$$r_c = \frac{1}{2}(r_o + r_i) \tag{D.8}$$

$$r_b = \frac{1}{2}(r_o - r_i) \tag{D.9}$$

Substituting and simplifying, for a system where there are n rolling elements each with mass m, we obtain

$$E_{k_{\text{balls}}} = \frac{nm}{40}\left(7 r_o^2 \omega_o^2 + 6 r_o \omega_o r_i \omega_i + 7 r_i^2 \omega_i^2\right) \tag{D.10}$$

$$E_{k_{\text{rollers}}} = \frac{nm}{16}\left(3 r_o^2 \omega_o^2 + 2 r_o \omega_o r_i \omega_i + 3 r_i^2 \omega_i^2\right) \tag{D.11}$$

Many rolling element bearings are configured such that the outer race is fixed, giving $\omega_o = 0$. The inner race is free to rotate, so it is ω_i to which we wish to refer the inertia of the rolling elements. The rotational kinetic energy of the referred inertia is $\frac{1}{2} I_{\text{ref}} \omega_i^2$, hence

$$I_{\text{ref}_{\text{balls}}} = \frac{7}{20} n m r_i^2 \tag{D.12}$$

$$I_{\text{ref}_{\text{rollers}}} = \frac{3}{8} n m r_i^2 \tag{D.13}$$

Appendix E: Contact Cycles in Ball and Roller Bearings

Continuing the analogy between a rolling element bearing and a system of planetary gears, we seek to calculate the contact pass rate at a given point on a given bearing raceway, or on one of the rollers. It is assumed that, for ball bearings, the balls only ever rotate about an axis parallel to the axis of revolution of the raceways, which is the worst-case scenario - in reality, cage interactions and axial loading may cause the ball contact track to drift over time.

The rate at which cycles are accrued on the raceways is the number of rolling elements n times the difference between the speed of that raceway and the cage speed ω_c.

$$f_i = \frac{n}{2\pi}|\omega_i - \omega_c| = \frac{n}{2\pi}\left|\omega_i - \frac{r_o\omega_o + r_i\omega_i}{r_o + r_i}\right| \tag{E.1}$$

$$f_o = \frac{n}{2\pi}|\omega_o - \omega_c| = \frac{n}{2\pi}\left|\omega_o - \frac{r_o\omega_o + r_i\omega_i}{r_o + r_i}\right| \tag{E.2}$$

On each rolling element, the contact cycle rate due to each raceway is similarly the difference between the ball and cage rotational speeds, so in total

$$f_b = \frac{|\omega_b - \omega_c|}{\pi} = \frac{2}{\pi}\left|\frac{r_o^2\omega_o - r_i^2\omega_i}{r_o^2 - r_i^2}\right| \tag{E.3}$$

For a stationary outer race, $\omega_o = 0$ and so

$$f_i = \frac{n\omega_i r_o}{2\pi(r_o + r_i)} \tag{E.4}$$

$$f_o = \frac{n\omega_i r_i}{2\pi(r_o + r_i)} \tag{E.5}$$

$$f_b = \frac{2\omega_i r_i^2}{\pi(r_o^2 - r_i^2)} \tag{E.6}$$

It is also worthy of note, for bearings whose *inner* raceway is stationary and the outer race rotates, such as for a wheel mounted on a stationary axle, that if all else is equal and the required rotational speed is the same, the contact cycle rate on both of the raceways is unchanged, but the rolling elements see more contact cycles in the same time period by a factor r_o^2/r_i^2.

Appendix F: Aluminium Stator Core

The aluminium stator core was designed as a non-ferromagnetic replacement to the iron/copper stator, closely matching its external dimensions and internal radial clearance. This large hollow part was created by stacking 10 mm thick aluminium 6082-T6 plate cut to shape by CNC water-jet cutting. To enable the parts to tessellate so as to incur minimum wastage, each annular plate was split into two parts, spanning 120° and 240° respectively. Holes were cut into the plates at 60° intervals and the plates were stacked the arrangement shown in Fig. F.1 chosen so that the joins between plates were distributed evenly throughout its angular and axial extent. Only 4 distinct plate geometries were required, as shown in Fig. F.2. A 3D model of the assembled plate pattern is shown next to the fully assembled stator, held together by 6 lengths of M8 studding each with a nut and washer at either end, including cartridge heaters and thermocouple for temperature control, in Fig. F.3.

0°	60°	120°	180°	240°	300°	Type
p	|	|	p	|	|	2
p	|	|	p	|	|	1
p	|	|	p	|	|	2
p	|	|	p	|	|	2
p	|	|	p	|	|	1
p	|	|	p	|	|	2
p	|	|	p	|	|	2
p	|	|	p	|	|	1
p	|	|	p	|	|	2
p	|	|	p	|	|	2
p	|	|	p	|	|	1
p	|	|	p	|	|	2

Figure F.1: Pattern used to assemble 24 plates, using only 4 distinct parts, where type A (120°) plates are shown in red, and type B (240°) plates are in green. The 1A and 1B plates are distinguished from 2A and 2B plates by the position of the boss that accommodates the dowel pin pilot hole (marked p).

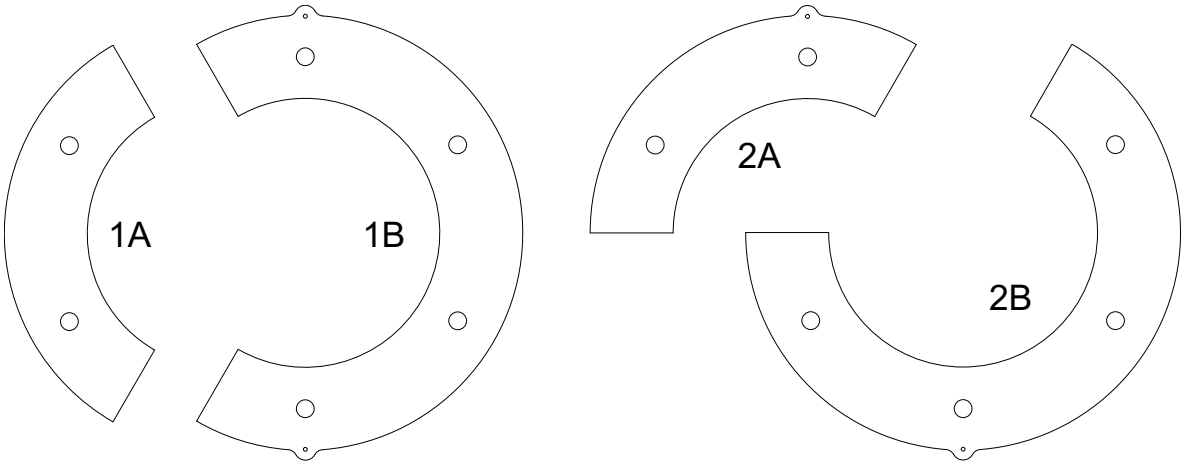


Figure F.2: Four plate designs used to build aluminium replacement stator core

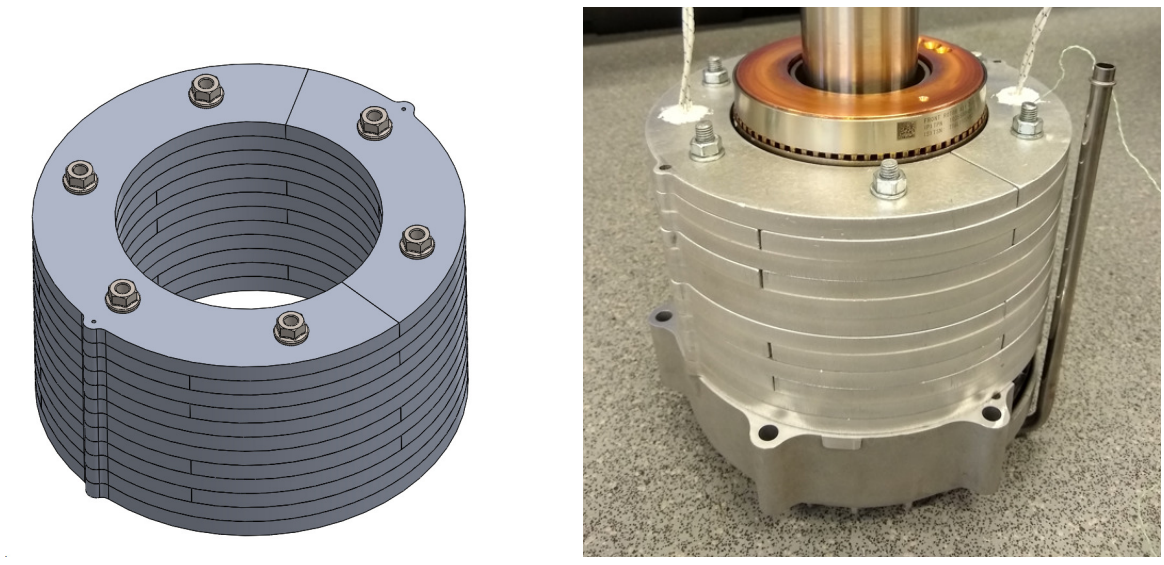


Figure F.3: Aluminium stator as designed (left) and as built (right)

Appendix G: Spin in Ball-on-Disc Contact

The angle of inclination of the MTM and ETM ball shafts, θ in Fig. 7.16 on page 201, is found from the ball radius r_b and disc track radius r_d by

$$\theta = \tan^{-1}\frac{r_b}{r_d} = \tan^{-1}\left(\frac{9.525}{21.0}\right) \approx 24.4^\circ \tag{G.1}$$

The spin in the contact is only zero when the sliding speed is zero, and in general is given by

$$\xi = \Omega_2 - \Omega_1 = U_e\left[\frac{1}{r_d}\left(1+\frac{\mathrm{SRR}}{2}\right) - \frac{1}{r_b}\left(1-\frac{\mathrm{SRR}}{2}\right)\tan\theta\right] \tag{G.2}$$

It is also instructive to consider the Spin-to-Roll ratio B_ζ given by

$$B_\zeta = \frac{2\xi a}{U_e} \tag{G.3}$$

as proposed by Porras-Vazquez *et al.* [292], which is the difference in entrainment speed from one side of the contact to the other, per unit entrainment speed. The value of B_ζ as a function of the slide-roll ratio SRR is shown for the MTM and ETM setups in Fig. G.1 ($\theta = 24.4^\circ$), and for several other possible angles of ball axis inclination, assuming that the specimens are both AISI 52100 steel, and that the contact load is 36.6 N which produces a maximum Hertz pressure of $P_0 = 1.0$ GPa and a contact half-width $a = 132$ μm. The findings of Porras-Vazquez *et al.* [292] suggest that minimum film thickness is only very slightly affected by spin for the small values of B_ζ in Fig. G.1a ($\delta h_m < 5\%$). Based on these results, the minimum film thickness is also not reduced by more than 10% up to 6000% SRR by spin in the MTM/ETM at 1.0 GPa max. Hertz pressure, and the reduction is less than 20% for the ETM at 2.0 GPa (Fig. G.1b). At these contact pressures, it is therefore likely that thermal effects play a much greater role than spin in reducing minimum film thickness (see Chapter 6), which may increase the risk of scuffing as sliding increases. The early work of Loewenthal [293] and more recently Dormois *et al.* [294] shows that the influence of spin on traction (in the entrainment direction) is also very slight for these small spins.

The ball shaft inclination axis in the EHD and EHD-HS (Chapter 6) by this definition is 0°, and also the value of r_d ranges between 34 mm and 44 mm as the ball carriage is moved. The resultant spin-to-roll ratios are shown in Fig. G.2 to be very small, and hence almost completely insignificant in terms of traction and film thickness in the SRR range employed in Chapter 6 ($-100\% \leq SRR \leq 100\%$).

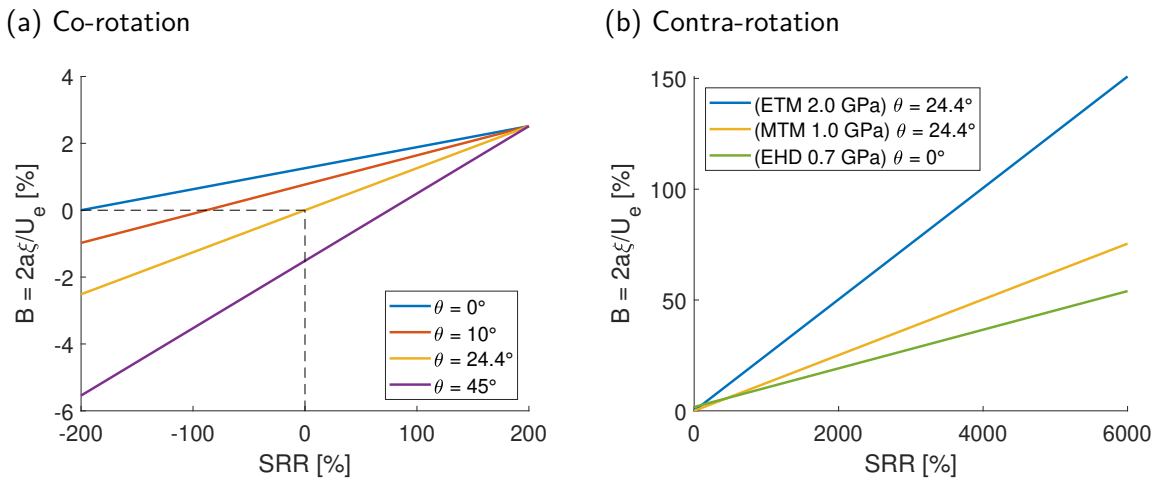


Figure G.1: Spin-to-Roll ratio B_ζ as a function of Slide-to-Roll Ratio SRR (a) in co-rotation for a selection of ball inclination angles, assuming max. Hertz pressure 1.0 GPa in a steel-on-steel point contact, showing how the MTM ball inclination angle of 24.4° amortises spin in the contact in the pure-rolling case, and (b) in contra-rotation spanning the SRR range of the scuffing tests in Section 7.2 considering the ball inclination angles of ETM, MTM and EHD, and accounting for the contact radius (264, 132 and 186 μm respectively) produced by a representative contact pressure and material combination for each.

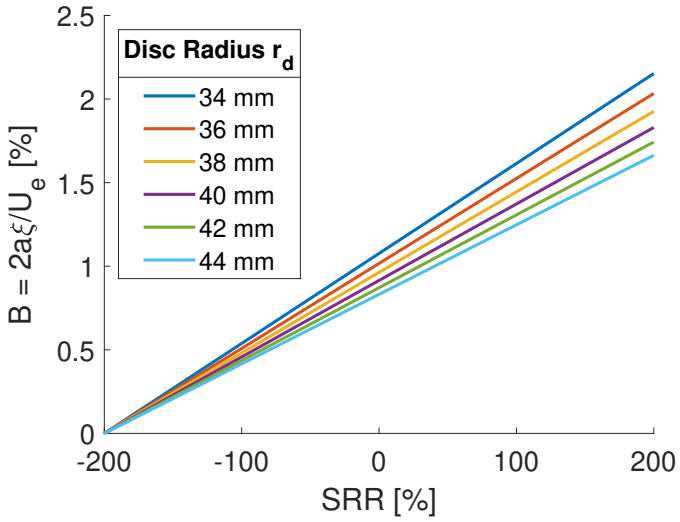


Figure G.2: Spin-to-Roll ratio B_ζ as a function of Slide-to-Roll Ratio SRR with 0° inclination angle, for a selection of disc track radii representative of the EHD and EHD-HS.

Appendix H: Traction Measurements over a Wide Range of Entrainment and Sliding Speeds

In rolling-sliding nonconformal contact, both rolling (or entrainment) and sliding speeds have a significant, but distinct, influence on friction. The dependence of friction on entrainment speed (typically at constant SRR) is one way of constructing the well-known Stribeck curve (whose abcissa is variously the Sommerfeld number, the Hersey number, and the Lambda ratio, all of which are proportional to a positive power of entrainment speed). The dependence of friction on sliding is called the traction curve, and in studies on EHL this is usually conducted keeping the entrainment speed constant, so sliding speed is varied by changing the speed of both the contacting surfaces by an equal amount. When the sliding speed is equal to twice the entrainment speed ($\mathrm{SRR} = 200\%$), one surface becomes stationary, and for $\mathrm{SRR} > 200\%$ the surfaces move in different directions with respect to the contact, termed contra-rotation.

Simultaneous reporting of the effect of both entrainment and sliding speeds on traction, spanning a wide measurement range, is regrettably uncommon in literature (with the notable exceptions of LaFountain *et al.* [220] and Björling *et al.* [101]). A series of MTM and ETM tests are presented here which measure friction for a matrix of points, allowing a series of Stribeck curves and an orthogonal series of traction curves to be extracted from the same surface plot. A set of measurements like this is informative for several reasons:

- The friction response of the fluid over a wide range of conditions is established, which provides *indirect* evidence of both its rheological properties and the action of additives such as friction modifiers.
- This friction response is a useful direct measurement for validation of or input to models estimating EHL friction for that fluid under similar conditions.
- The sensitivity of friction to speed and SRR is important in the optimisation of frictional power losses but is difficult to predict.
- The measurement allows the reproducibility of the friction measurement between tribometers to be examined over a wide range of conditions.

An MTM test profile comprising multiple successive traction curves each at a different entrainment speed, but with multiple points per SRR, the number of points depending on the entrainment speed, was constructed using the same MATLAB script developed to generate the scuffing profiles in Section 7.2. Between 3 and 9 measurements (each involving a traction force measurement in

both the positive and negative sliding directions, as discussed further in Chapter 6) were conducted for each combination of speed and SRR - at speeds greater than 100 mm/s, only 3 points were taken, and below this entrainment speed 7 or 9 points were measured successively for the same combination of speed and SRR before moving on to the next. The measurements for each result were then averaged, and the procedure repeated for multiple normal loads, to produce a smooth surface as shown in Fig. H.1. Mapper images were also taken periodically between traction steps to ensure no significant change to the ball surface was occurring during the test - except where specified otherwise, none was seen during the tests reported in this section. The fluid used was the Synthetic ATF, at 60°C. The specimens used throughout this section were the same polished AISI 52100 specimens used in Section 7.2.

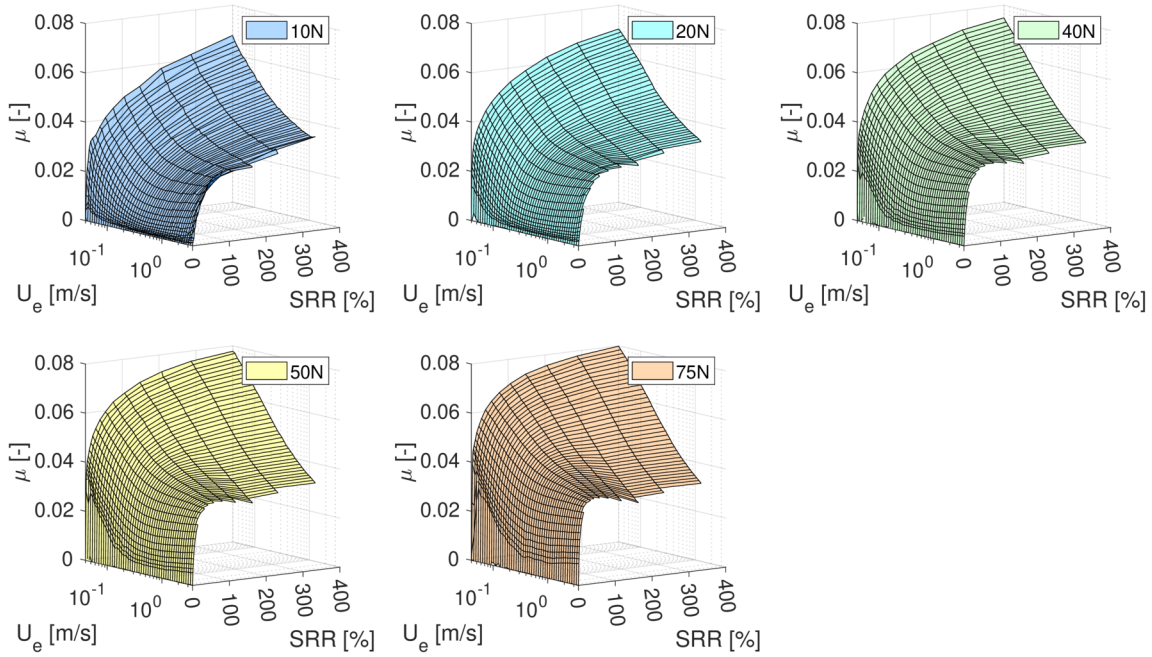


Figure H.1: A series of traction measurements spanning entrainment speeds between 40 mm/s and 4 m/s and SRRs between 0 and 400%, at selected loads between 10 and 75 N using the Synthetic ATF at 60°C, obtained using the MTM of serial number MTM305.

The superposition of the surfaces from Fig. H.1 in Fig. H.2 shows that at high speeds and high SRRs, friction coefficient almost does not depend on load, while at high speeds and low SRRs, the dependence on load is quite strong. Each traction curve divides into four regimes as discussed by Habchi *et al.* [233], clearly represented in these maps. At the lowest SRR is the Newtonian regime where the relationship between traction coefficient and SRR (which are proportional respectively to shear stress and shear strain rate, given the assumptions discussed in Chapter 6) is almost linear. The nonlinear-viscous (shear-thinning) regime follows, in which the nature of the shear-thinning

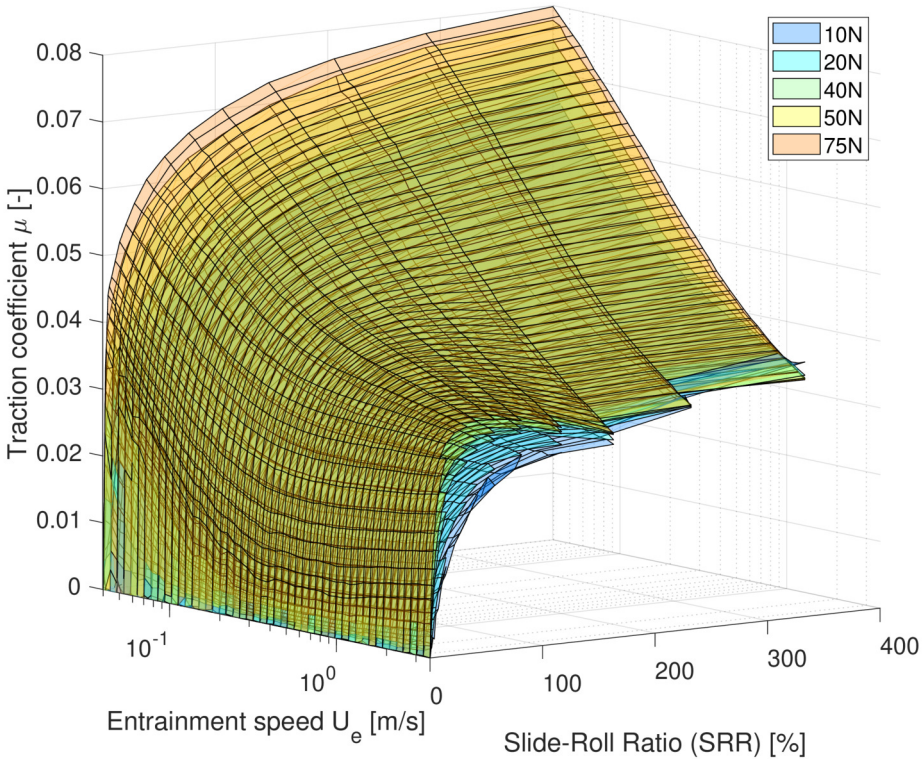


Figure H.2: Traction surfaces from Fig. H.1 superimposed

is the subject of considerable debate, arising from the dual complexities of high-pressure-high-shear rheology and the transient nonuniform pressure and flow fields within in EHD contact. In broad terms, the dependence of friction on SRR becomes weaker-than-linear, but still increasing, in this regime. At higher sliding speeds the energy dissipated within the contact begins to create significant heat, which modifies the rheology, further weakening the relationship between friction and sliding as shear-heating (and the consequent reduction in effective viscosity with increasing temperature) competes with the additional shear stress incurred by sliding. The so-called 'plateau' regime is therefore characterised by a relatively flat portion of the traction curve, often marking a transition from isothermal to thermal EHL. In some cases a limiting shear stress may be reached under isothermal conditions which has a similar effect on traction. At very high sliding speeds, the traction response is said to be thermoviscous, implying the (higher-order) dependence of friction on temperature takes over from the (lower-order) dependence on shear rate. These regimes clearly appear on the surface plots shown. An interesting feature is the disappearance of the plateau regime at high entrainment speeds and high contact loads, which increase the thermal power of the contact and hence advance the transition to thermal behaviour to lower SRRs.

A similar set of measurements was conducted on a different MTM, and the results are shown in

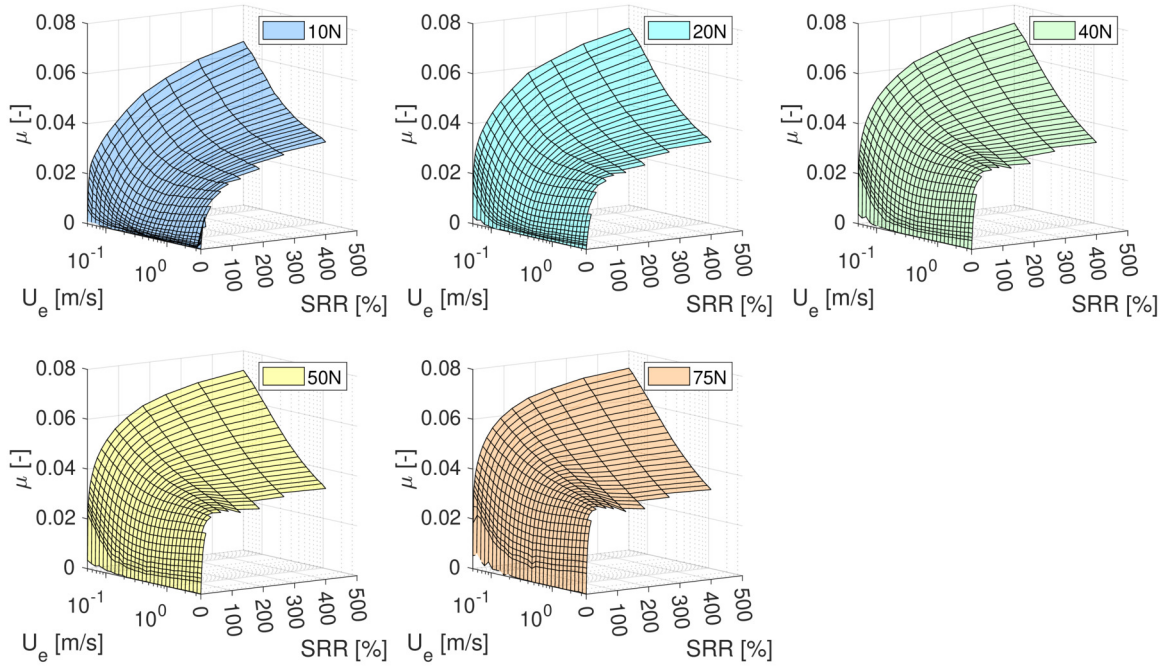


Figure H.3: A series of traction measurements spanning entrainment speeds between 50 mm/s and 3.6 m/s and SRRs between 0 and 500%, at selected loads between 10 and 75 N using the Synthetic ATF at 60°C, obtained using the MTM of serial number MTM202.

Fig. H.3. A comparison in terms of the fractional error between the two sets of results (linearly interpolating in 2 dimensions) is given in Fig. H.4 for SRRs greater than 5%.

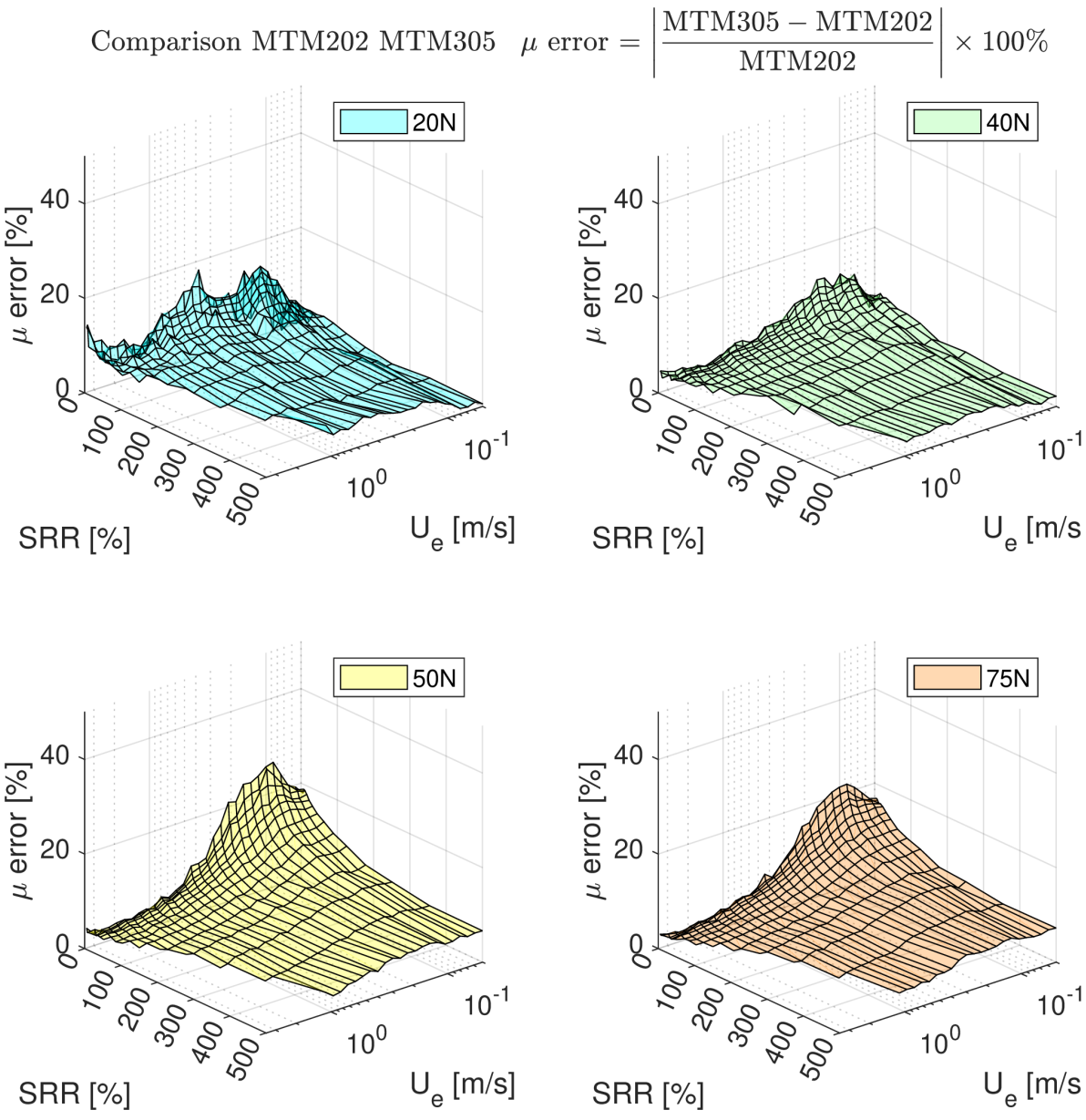


Figure H.4: Comparison between MTM202 and MTM305 as a fraction of the traction measurement by MTM202, showing the normalised discrepancy is greater at low SRRs (for which friction is lower) and at low speeds.

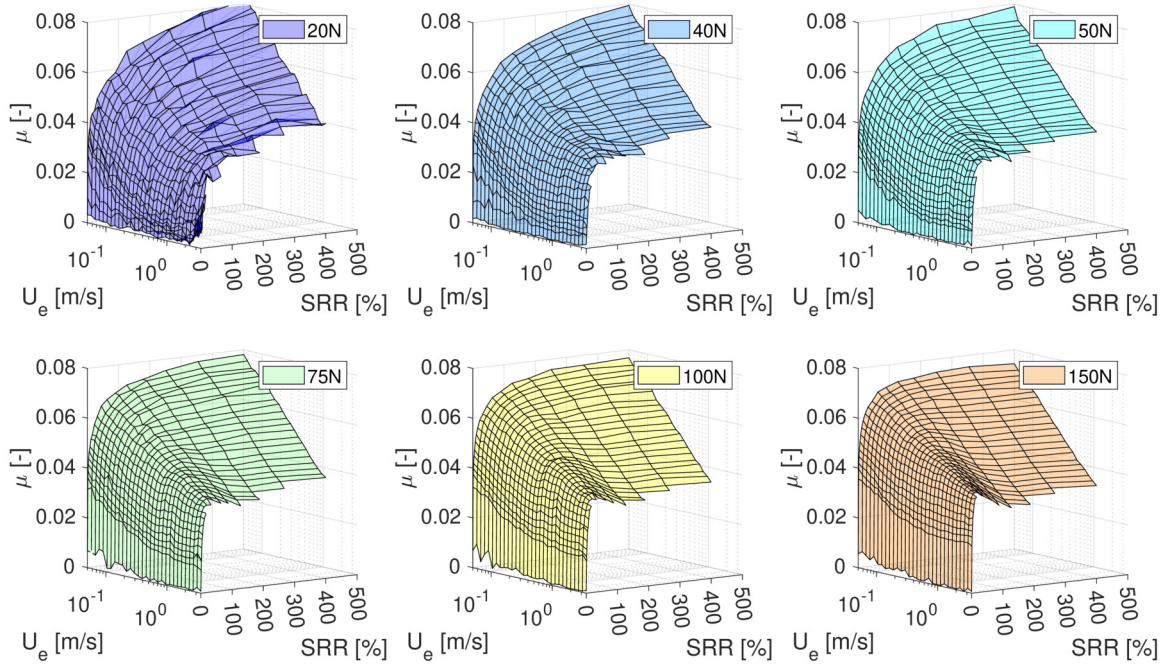


Figure H.5: A series of traction measurements spanning entrainment speeds between 50 mm/s and 3.6 m/s and SRRs between 0 and 500%, at selected loads between 20 and 150 N using the Synthetic ATF at 60°C, obtained using the ETM of serial number ETM102.

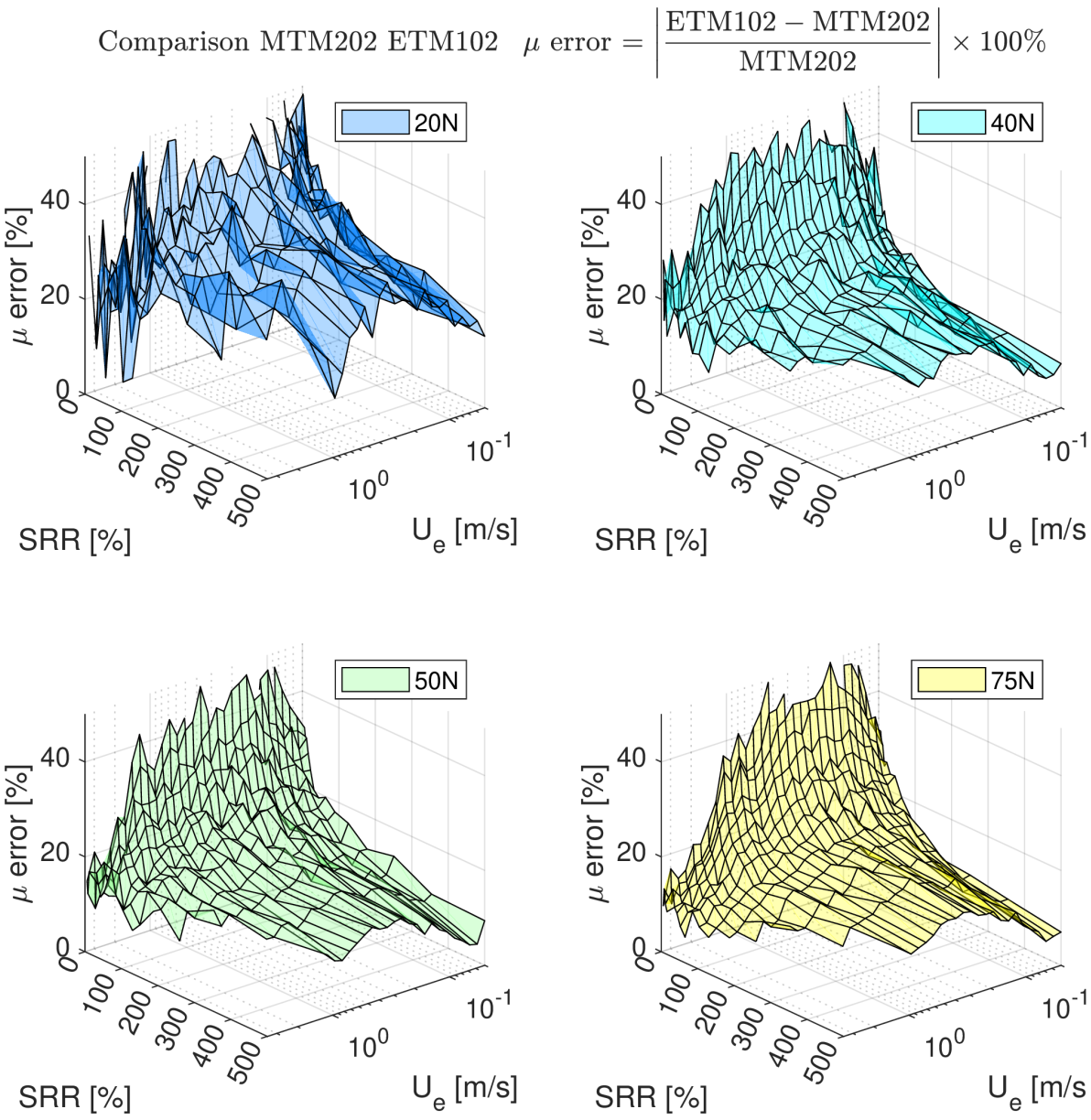
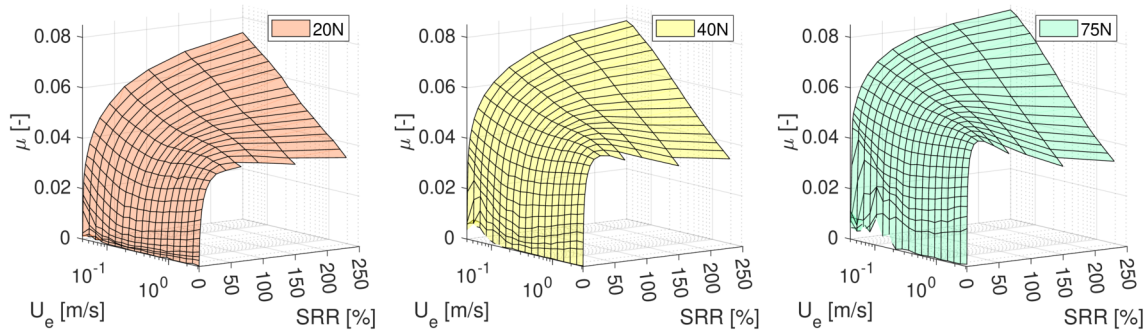


Figure H.6: Comparison between traction measurements by ETM102 (on which scuffing tests were conducted in Section 7.2) and MTM202 as a fraction of the MTM202 measurement, showing the normalised discrepancy is greater at low SRRs (for which friction is lower) and at low speeds, but nevertheless comparable to the difference between MTM rigs, even at loads much lower than the reported ETM minimum load of 100 N.

(a) Dexron-VI ATF (US)



(b) Santotrac 50

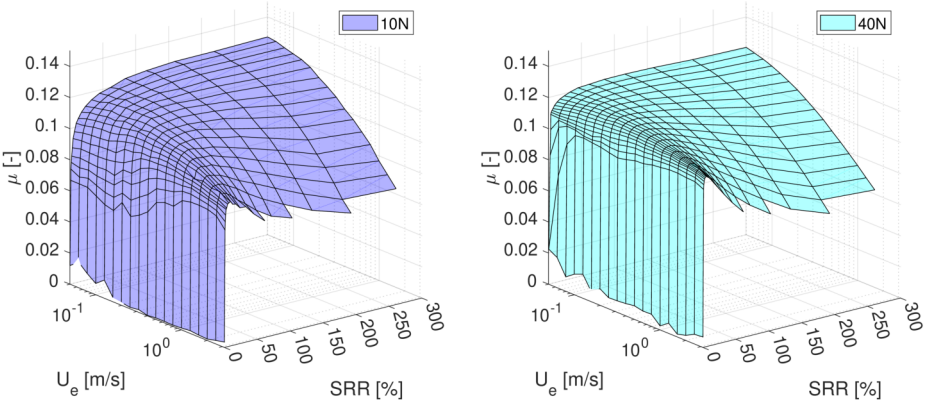


Figure H.7: A series of traction measurements spanning entrainment speeds between 40 mm/s and 4 m/s and SRRs between 0 and 300% for an ATF and a traction fluid at 40°C, obtained using the MTM of serial number MTM356.

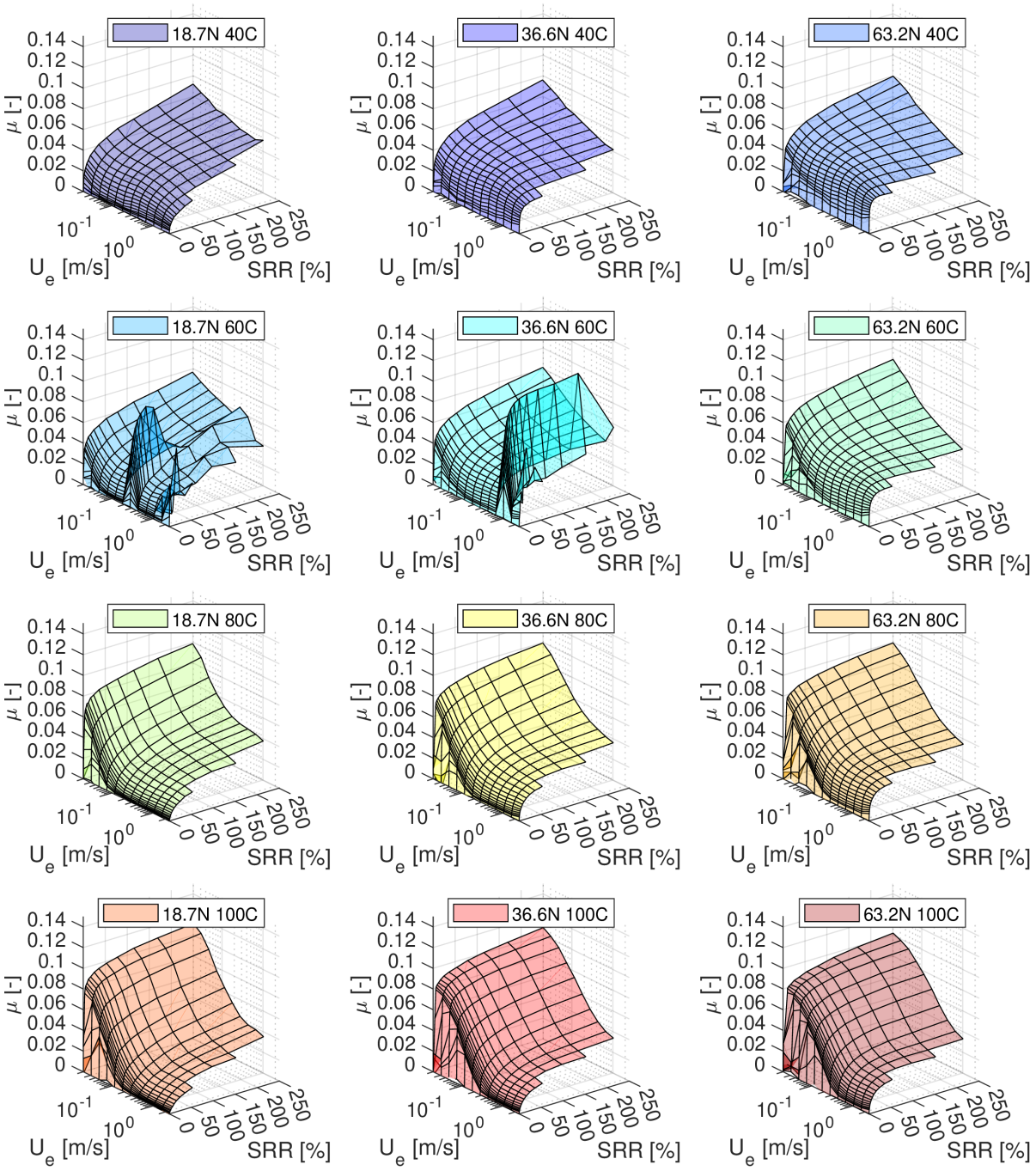


Figure H.8: MTM traction matrices for an experimental EV bearing grease using the traction test method developed here to establish the effects of contact load and grease temperature on traction. Two of the subplots show evidence of temporary starvation causing a recoverable increase in friction coefficient.

Appendix I: Measurements of EHL Traction and Film Thickness at High Speeds

Measurements of traction and film thickness according to the method presented in Chapter 6 for all fluids tested are included here for reference. In all following figures, filled markers and solid lines indicate the 'forward sliding' (disc faster) condition, and empty markers with dashed lines indicate 'reverse sliding' (ball faster).

I.1 Traction Measurements

Traction measurements at selected speeds but for all SRRs measured are included in the following figures.

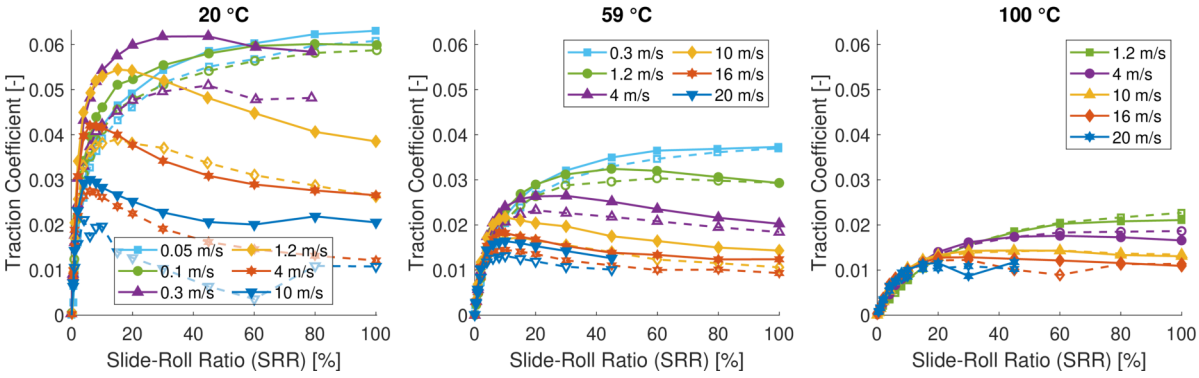


Figure I.1: Heavy Mineral Oil (Sigma Aldrich 330760)

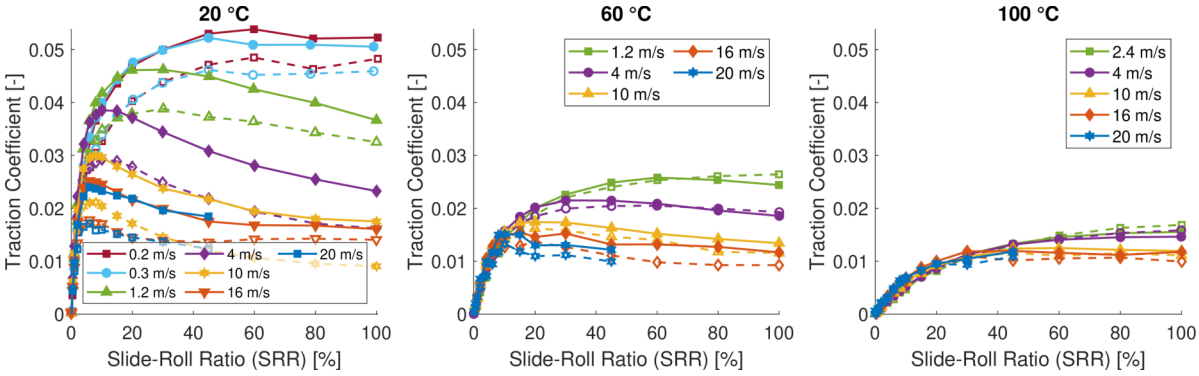


Figure I.2: HVI 60 Group I

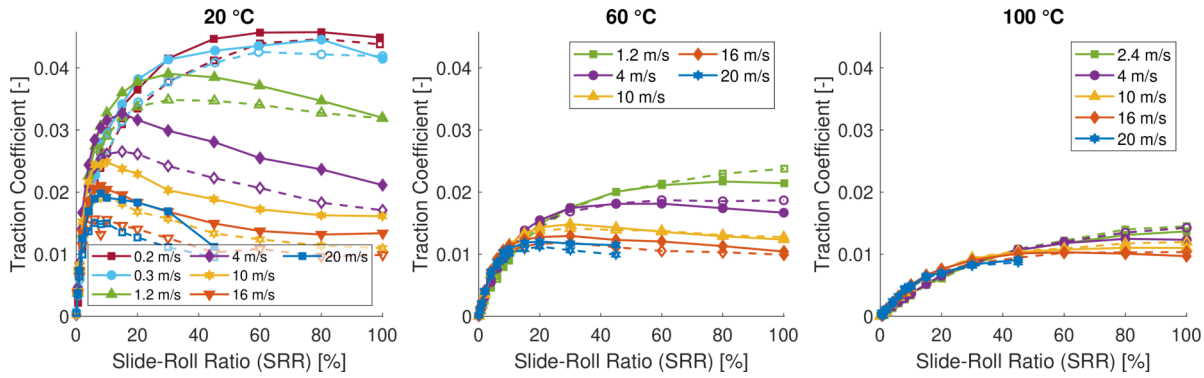


Figure I.3: CHN 100R Group II

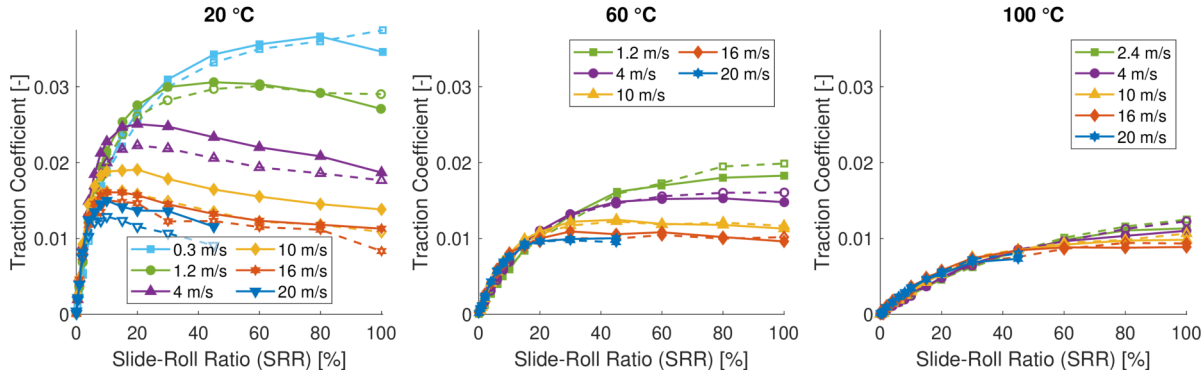


Figure I.4: Yubase 4 Group III

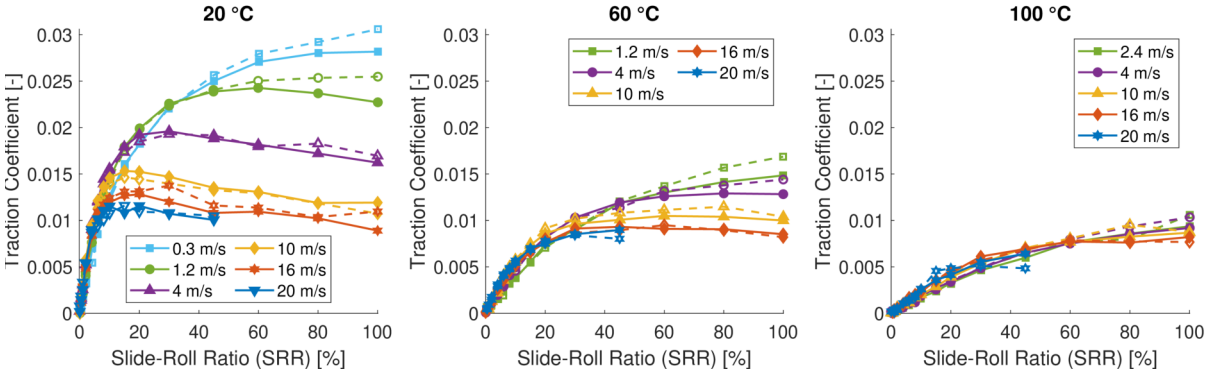


Figure I.5: PAO4 Group IV

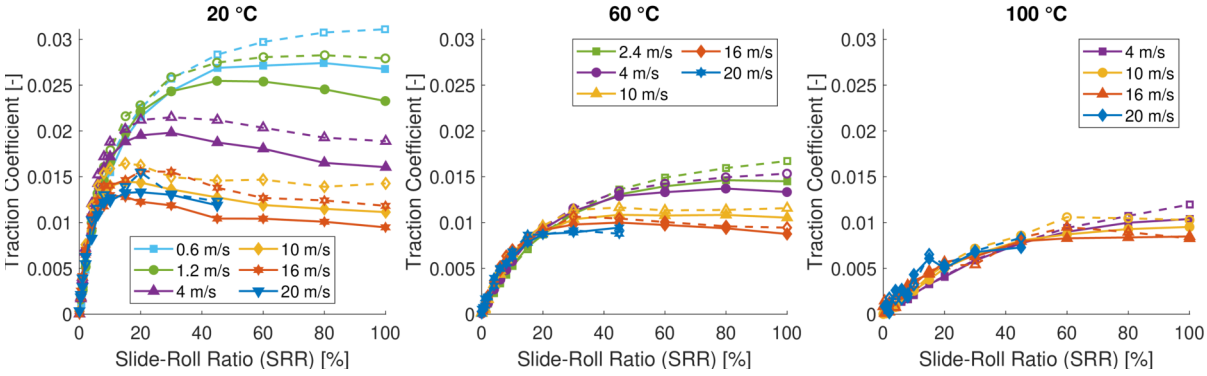


Figure I.6: PAO5 Group IV

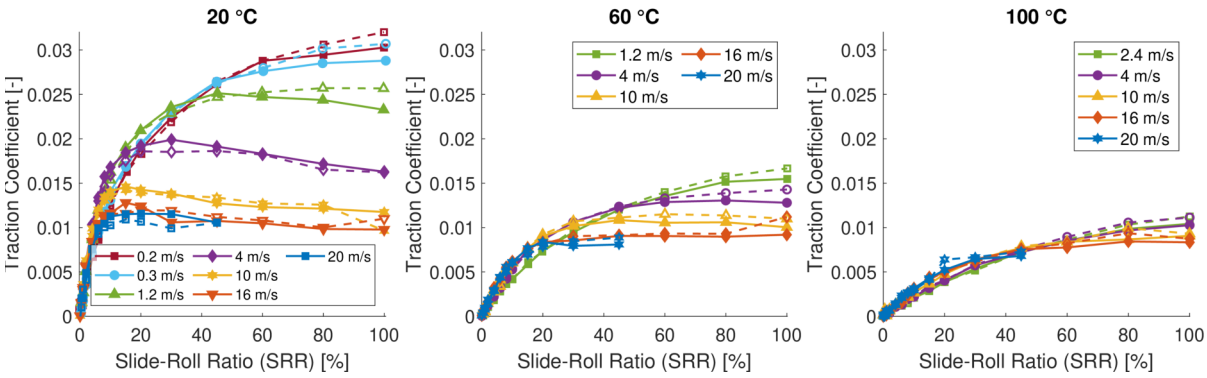


Figure I.7: PAO5 Group IV, a repeat measurement with more speeds

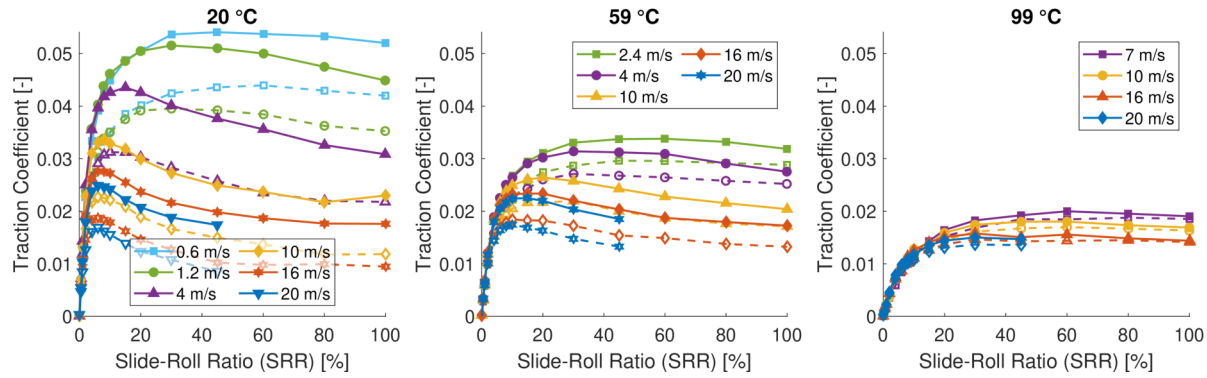


Figure I.8: PAO5 Group IV on Sapphire Disc

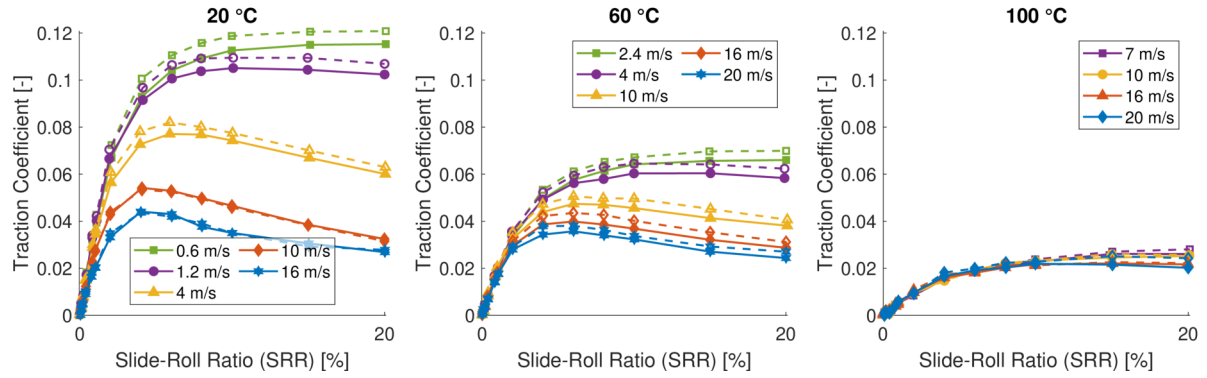


Figure I.9: Santotrac 50 at 20 N

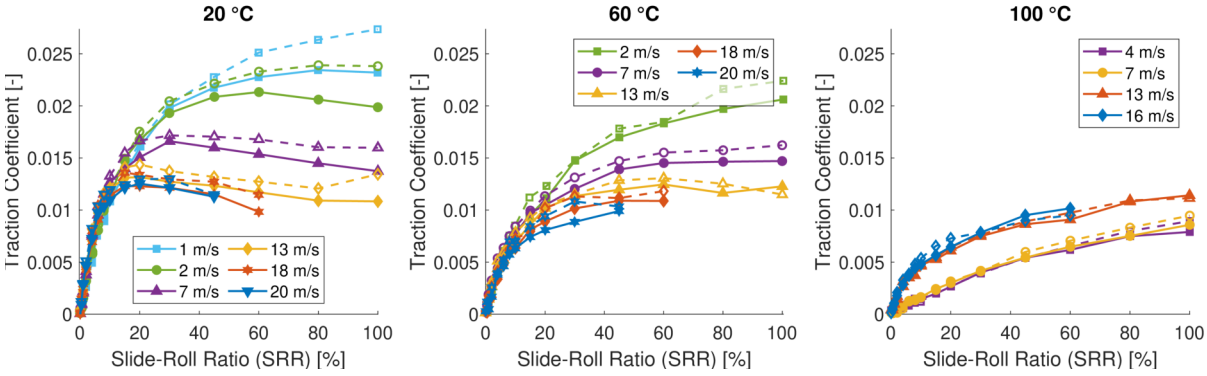


Figure I.10: Low-viscosity (2.4 cSt) ATF

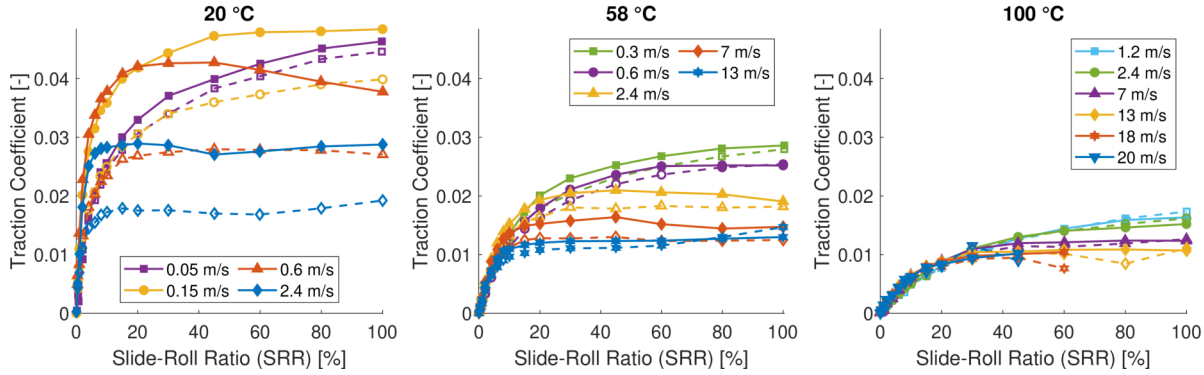


Figure I.11: High-viscosity (23 cSt) ATF

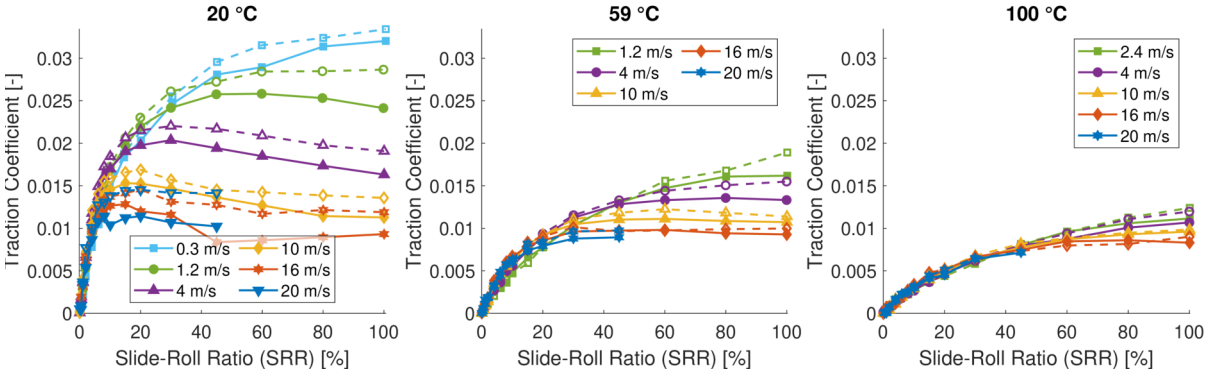


Figure I.12: Model EV fluid

I.2 Film Thickness Measurements

Film thickness measurements at selected SRRs, for all speeds measured are included in the following figures.

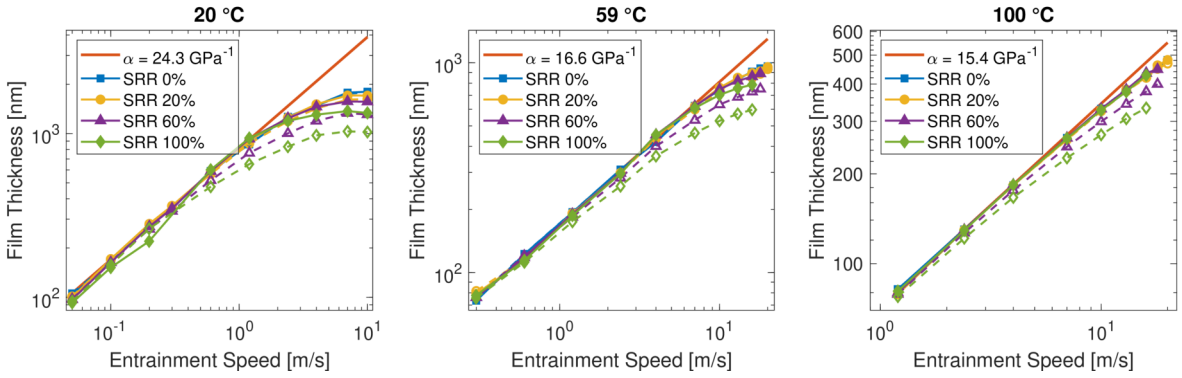


Figure I.13: Heavy Mineral Oil (Sigma Aldrich 330760)

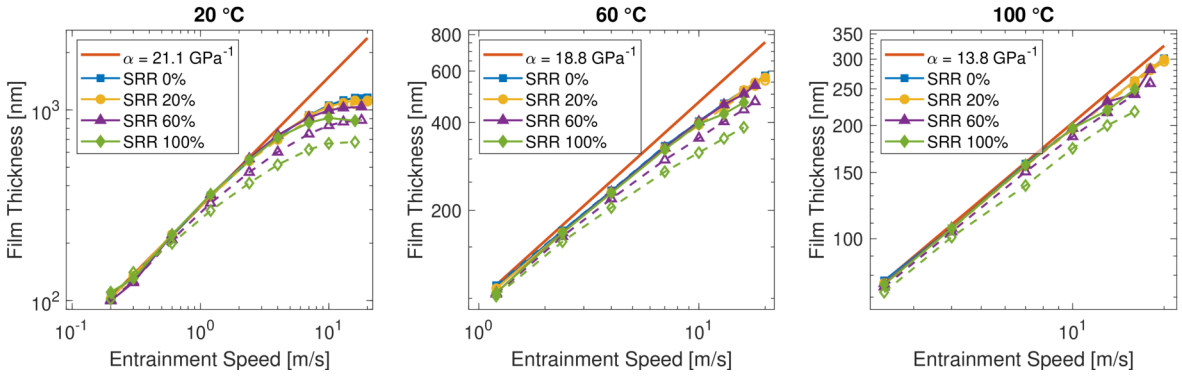


Figure I.14: HVI 60 Group I

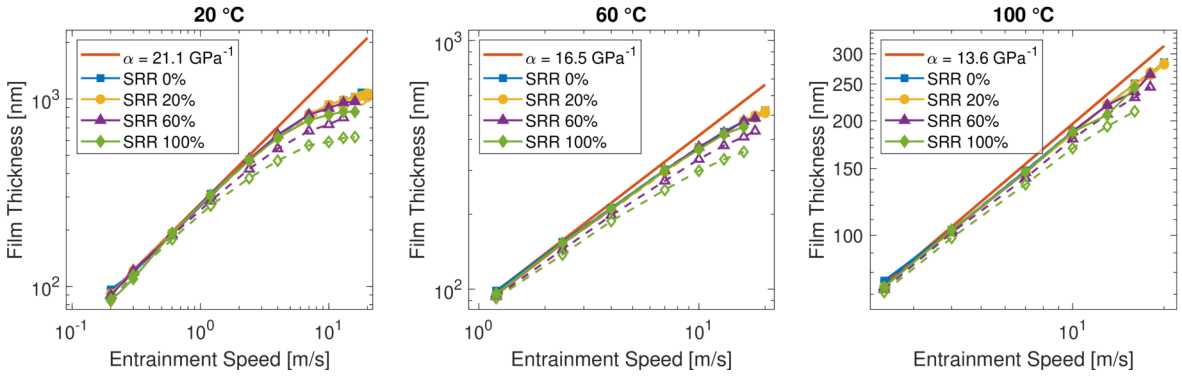


Figure I.15: CHN 100R Group II

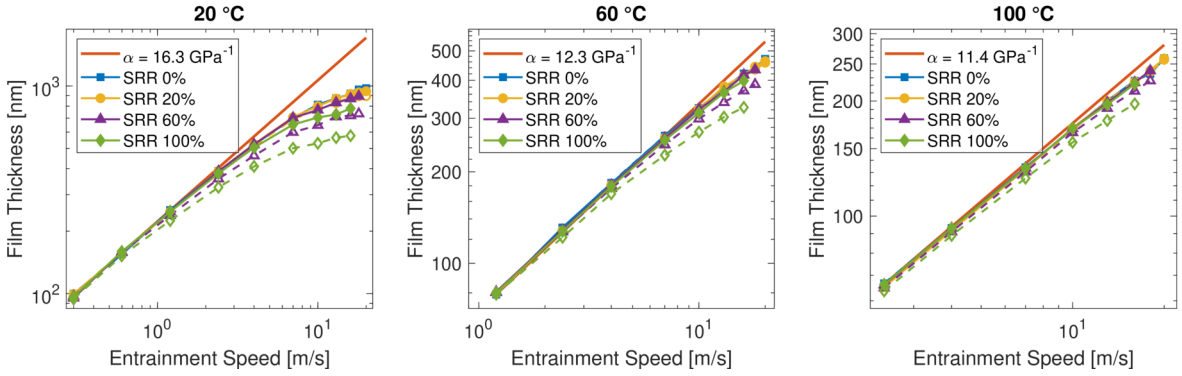


Figure I.16: Yubase 4 Group III

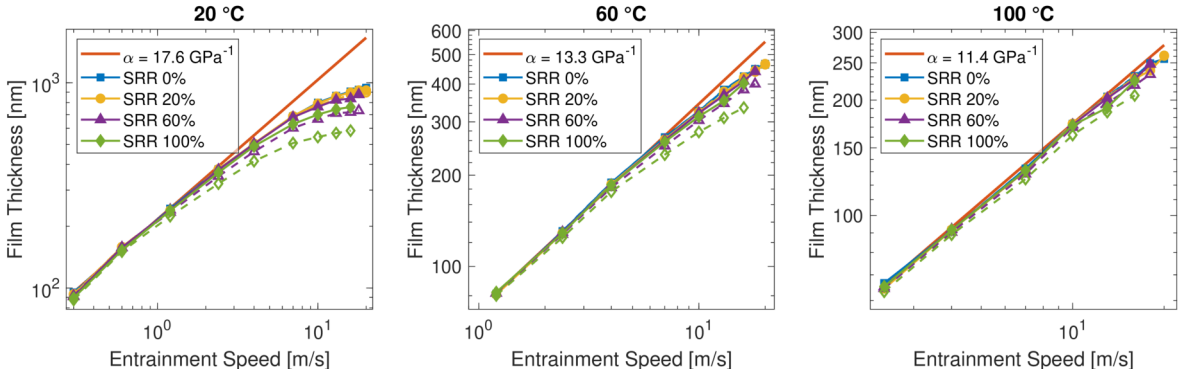


Figure I.17: PAO4 Group IV

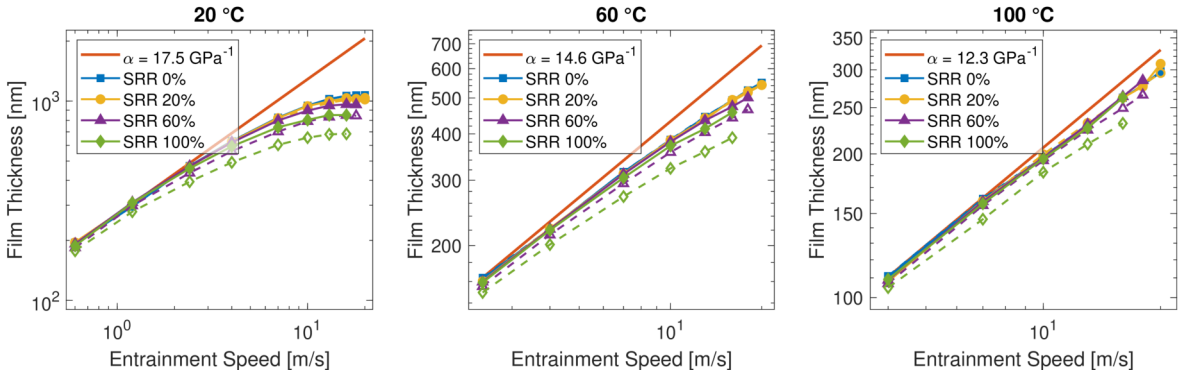


Figure I.18: PAO5 Group IV

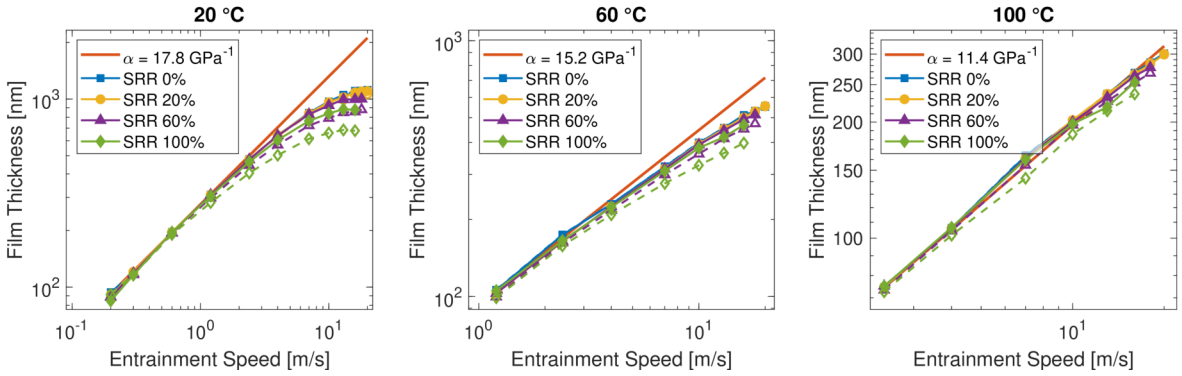


Figure I.19: PAO5 Group IV, a repeat measurement with more speeds

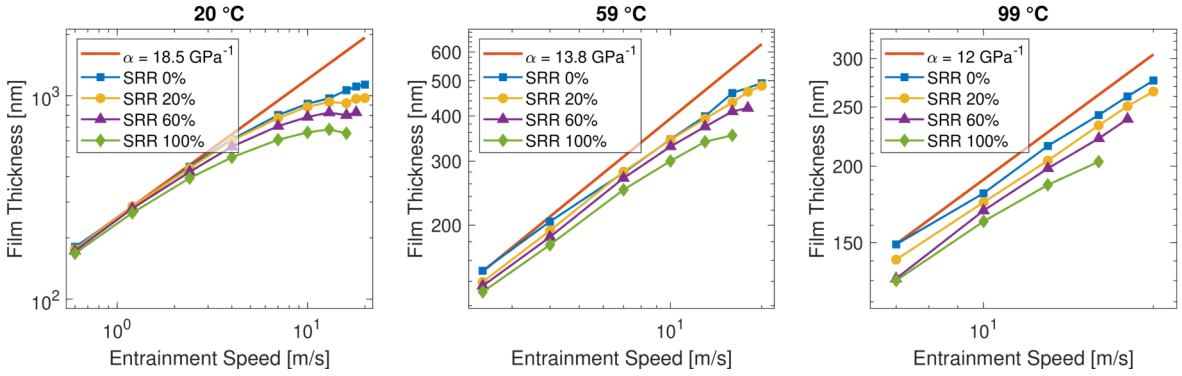


Figure I.20: PAO5 Group IV on Sapphire Disc

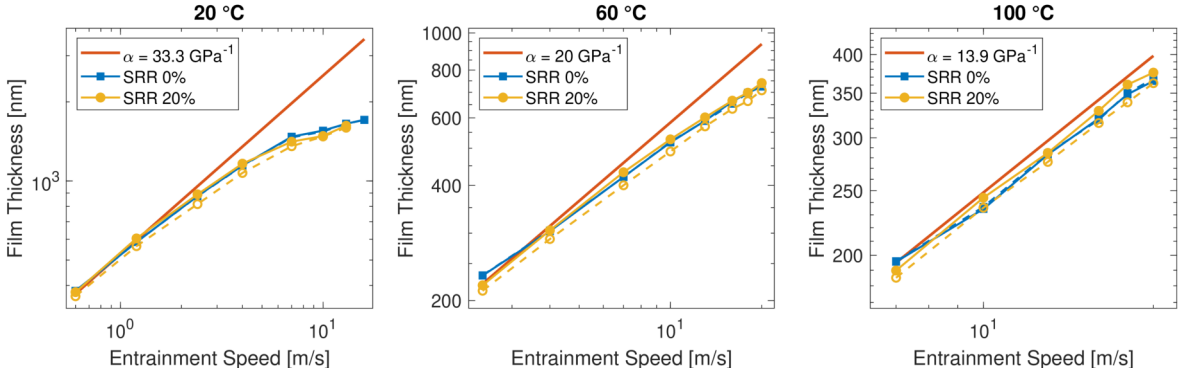


Figure I.21: Santotrac 50 at 20 N

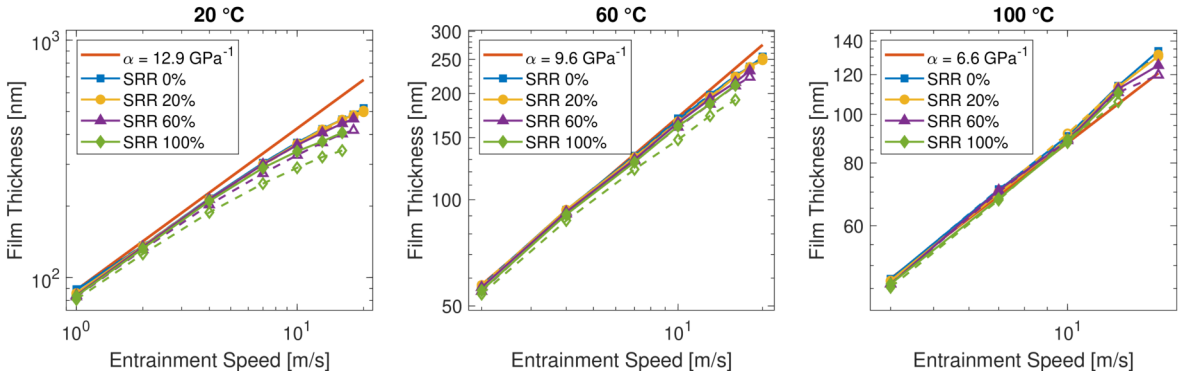


Figure I.22: Low-viscosity (2.4 cSt) ATF

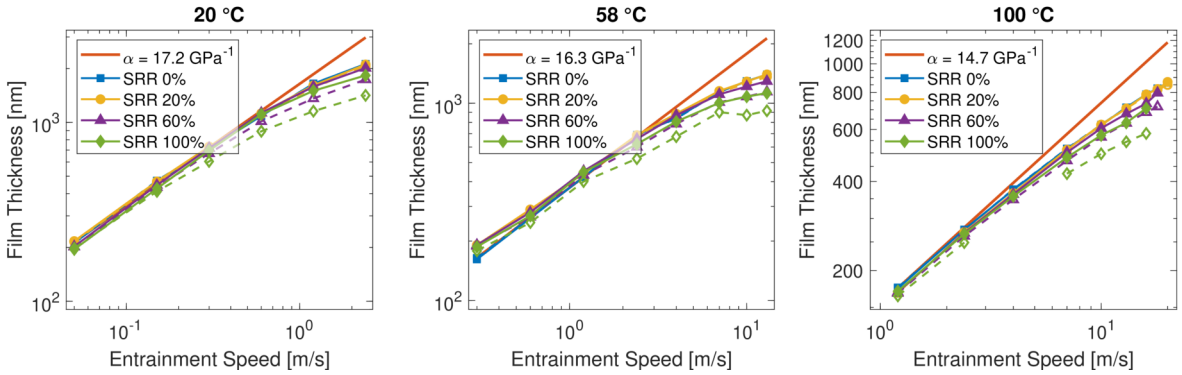


Figure I.23: High-viscosity (23 cSt) ATF

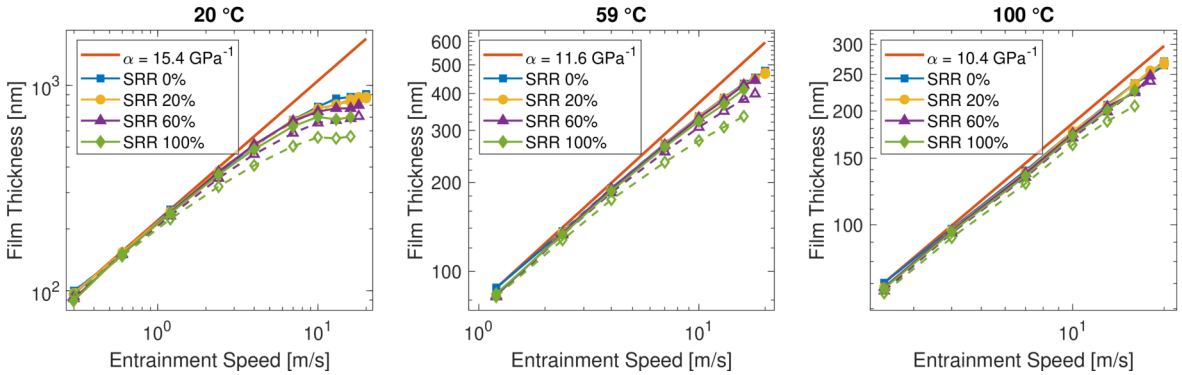


Figure I.24: Model EV fluid

I.3 Traction and Film Thickness 3D Plots

Surface plots illustrating the values of traction and film thickness for all speeds and SRRs measured are presented in this section.

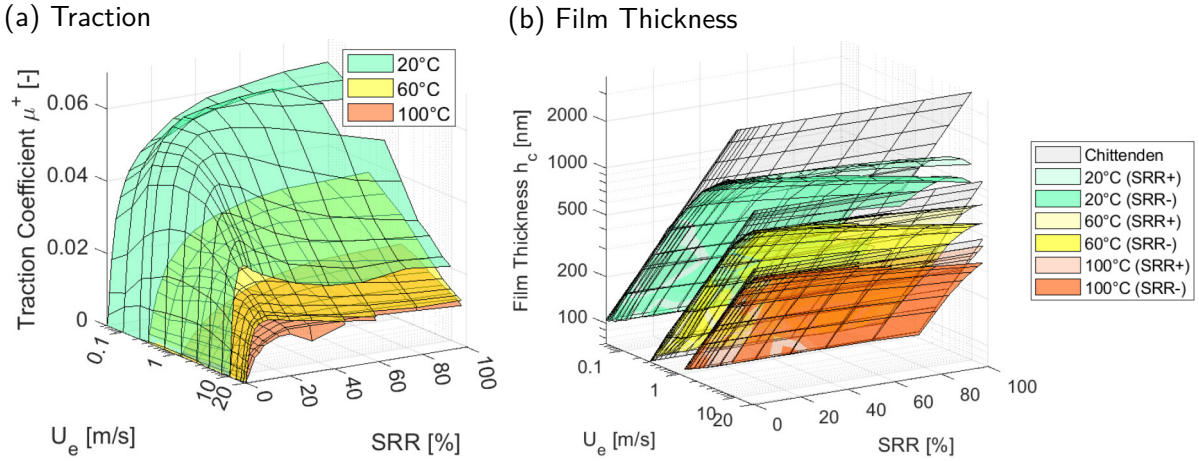


Figure I.25: Heavy Mineral Oil (Sigma Aldrich 330760)

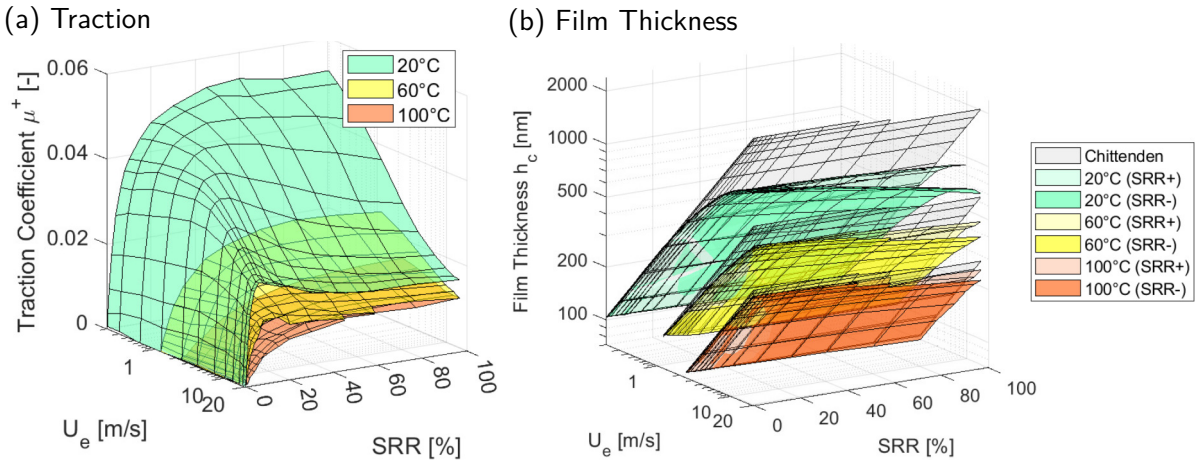


Figure I.26: HVI 60 Group I

(a) Traction (b) Film Thickness

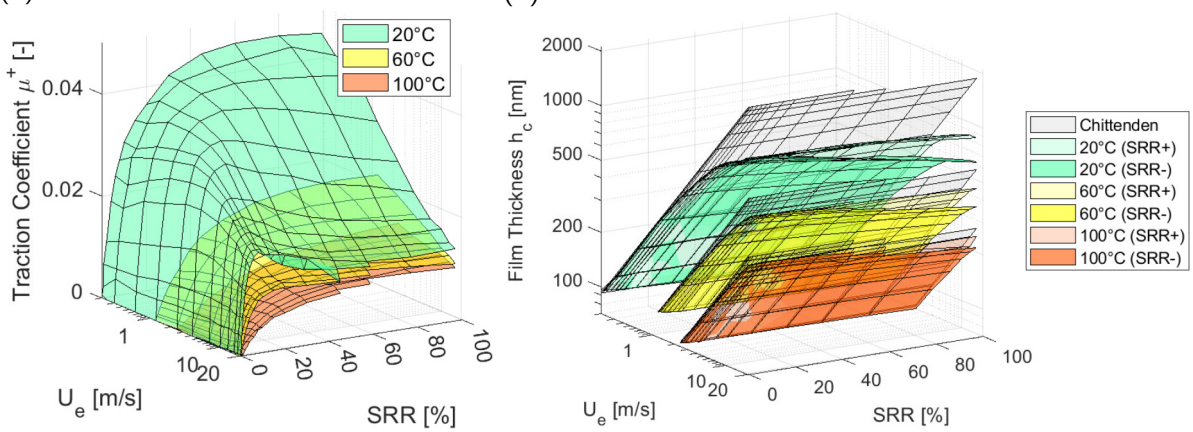


Figure I.27: CHN 100R Group II

(a) Traction (b) Film Thickness

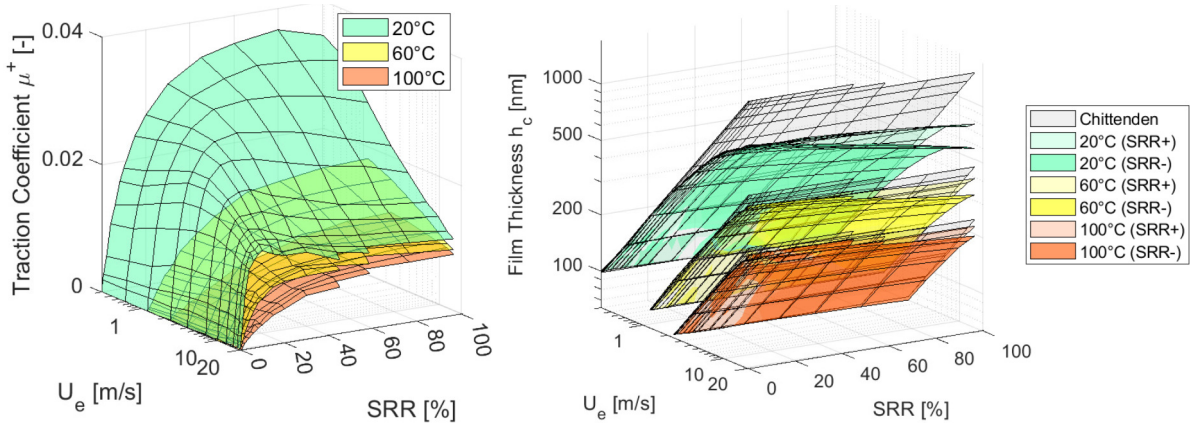


Figure I.28: Yubase 4 Group III

(a) Traction (b) Film Thickness

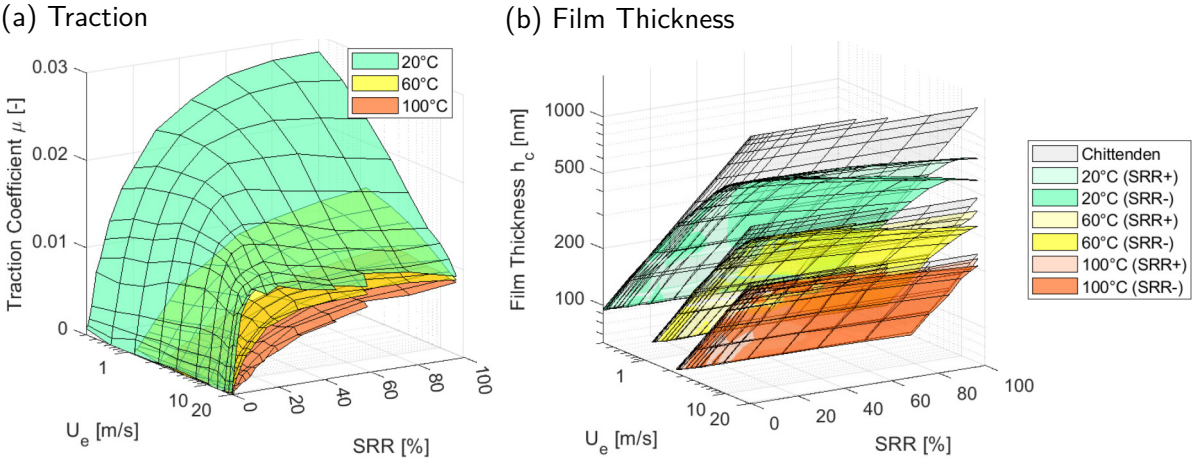


Figure I.29: PAO4

(a) Traction (b) Film Thickness

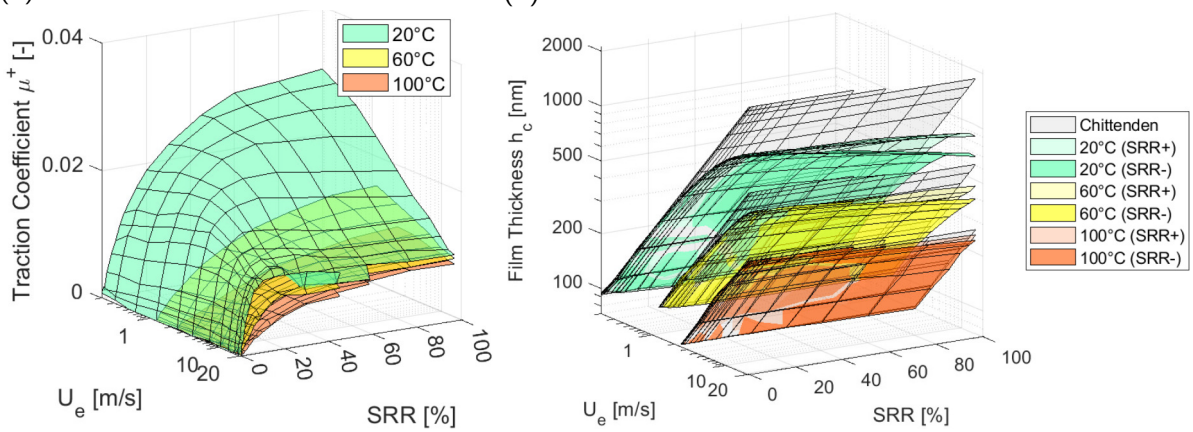


Figure I.30: PAO5

(a) Traction (b) Film Thickness

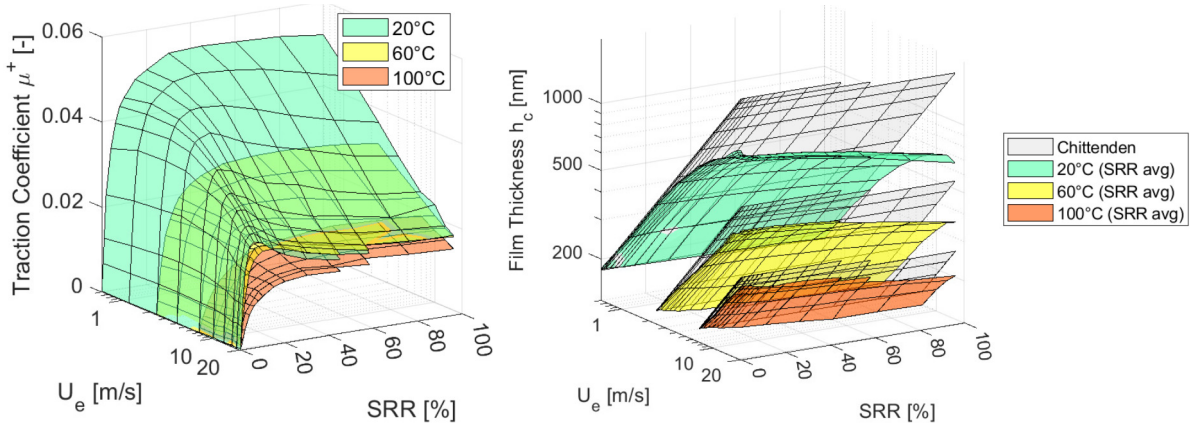


Figure I.31: PAO5 Group IV on Sapphire Disc

(a) Traction (b) Film Thickness

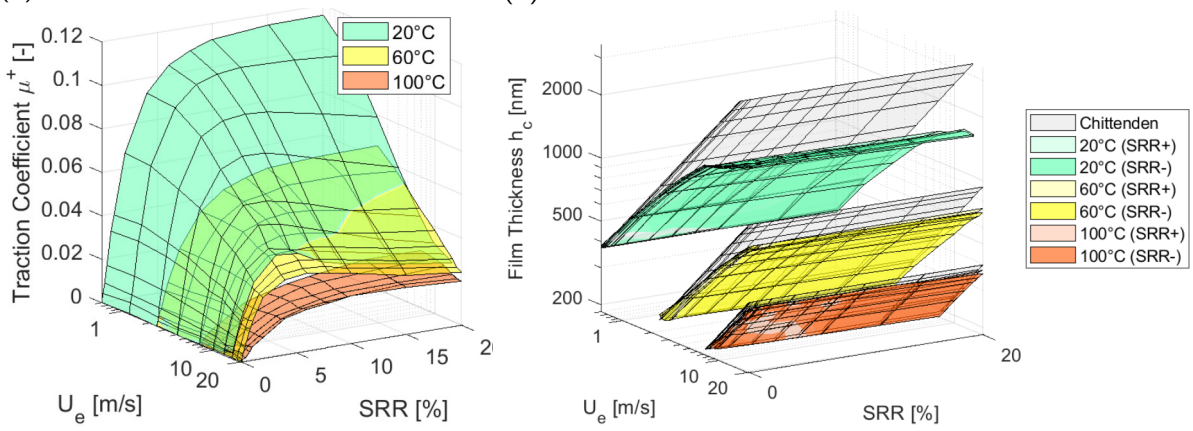


Figure I.32: Santotrac 50

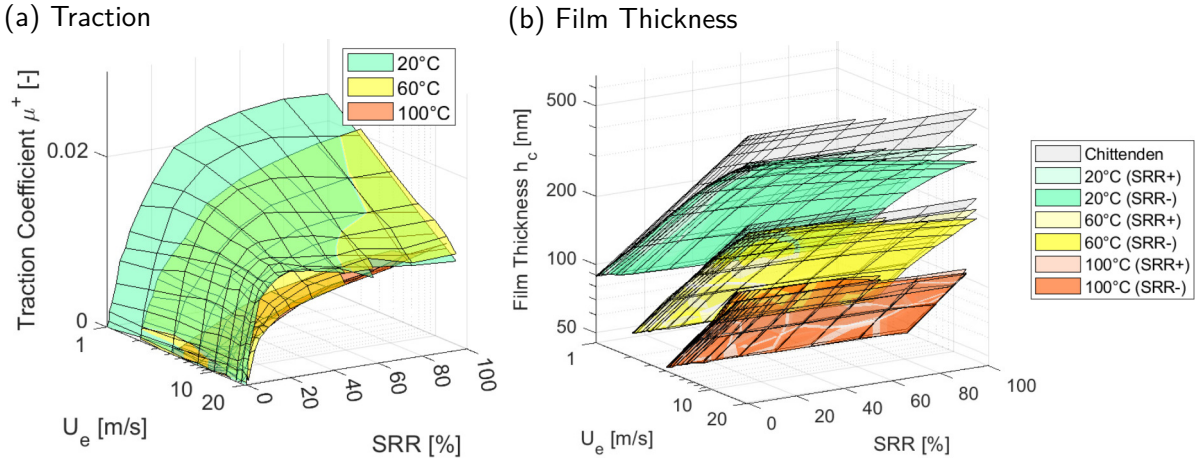


Figure I.33: Low-viscosity ATF

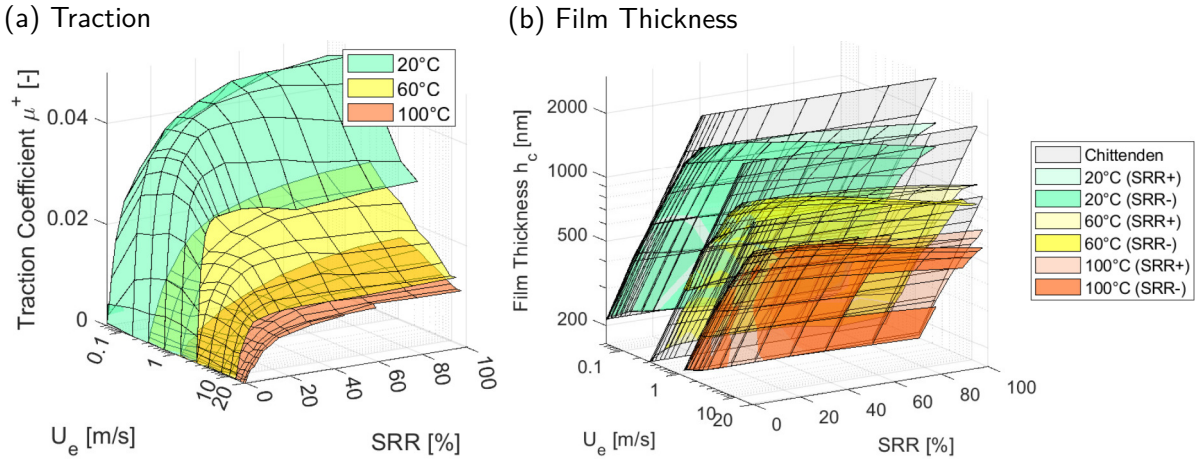


Figure I.34: High-viscosity ATF

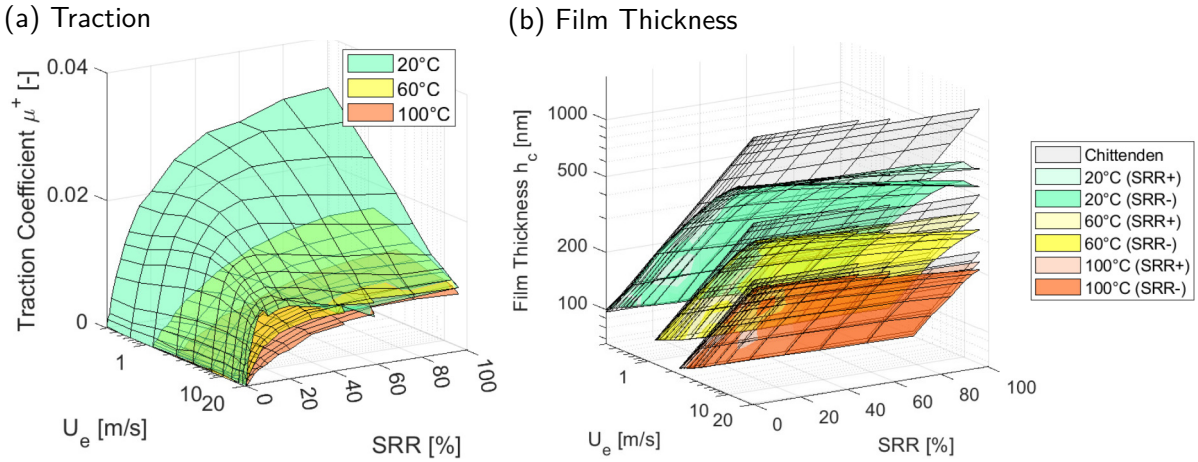


Figure I.35: Model EV fluid

Appendix J: Words

A granular wordcount is provided here for the sheer thrill.

```
Sum count: 71149
Words in text: 63729
Words in headers: 482
Words outside text (captions, etc.): 5926
Number of headers: 137
Number of floats/tables/figures: 174
Number of math inlines: 934
Number of math displayed: 78
Subcounts:
  text+headers+captions (#headers/#floats/#inlines/#displayed)
  42+0+0 (0/1/0/0) _top_
  301+1+0 (1/0/1/0) Chapter: Abstract
  327+1+0 (1/0/0/0) Chapter: Acknowledgements
  31+3+0 (1/0/0/0) Chapter: Statement of Originality
  148+2+0 (1/0/0/0) Chapter: Copyright Statement
  388+1+0 (1/0/114/0) Chapter: Nomenclature
  305+1+0 (1/0/2/0) Chapter: Abbreviations
  1158+1+132 (1/2/1/0) Chapter: Introduction
  94+2+0 (1/0/0/0) Chapter: Literature Review
  712+3+45 (1/1/0/0) Section: Electric Vehicle Transmissions
  148+3+23 (1/1/0/0) Section: Efficiency - Gearbox Losses
  623+3+0 (1/0/13/0) Section: Gearbox Efficiency Measurement
  194+5+7 (1/1/0/0) Section: Load-independent Losses: Churning and Windage
  226+3+0 (1/0/1/0) Subsection: Lubricant Dynamic Viscosity
  324+1+0 (1/0/5/0) Subsection: Speeds
  321+6+0 (1/0/0/0) Subsection: Lubrication Type: Grease, Dip, or Jet
  296+4+19 (1/1/0/0) Subsection: Gear Geometry and Meshing
  194+2+0 (1/0/1/0) Subsection: Immersion Depth
  131+5+0 (1/0/0/0) Subsection: Rotational Direction and Swell Effects
  377+4+32 (1/1/0/0) Subsection: Casing, Clearances and Orientation
  518+3+0 (1/0/3/0) Subsection: Cavitation and Aeration
  291+4+0 (1/0/0/0) Subsection: Ambient Pressure Inside Gearbox
  539+10+143 (1/2/3/0) Section: Load-dependent Losses: EHL Traction and Film
     Thickness at High Speeds
  227+2+0 (1/0/2/0) Subsection: Traction Prediction
  496+2+0 (1/0/3/0) Subsection: Inlet Heating
  645+2+65 (1/1/25/1) Subsection: Flash Heating
  259+3+28 (1/1/0/0) Subsection: Film Thickness Measurement
  305+2+0 (1/0/26/4) Section: Bearing Losses
  1178+1+28 (1/1/0/0) Section: Scuffing
  1287+1+59 (1/1/13/0) Section: Micropitting
  1127+2+0 (1/0/16/0) Section: Fluid Formulation
  643+4+0 (1/0/0/0) Section: Conclusions from Literature Review
```

```
204+2+0 (1/0/0/0) Section: Project Goals
30+1+0 (1/0/0/0) Chapter: Materials
41+1+0 (1/0/0/0) Section: Fluids
145+4+0 (1/0/10/3) Subsection: Viscosity and Density Measurement
34+3+0 (1/0/3/1) Subsection: Refractive Index Measurement
193+3+0 (1/0/11/0) Subsection: Pressure-Viscosity Coefficient Measurement
353+4+39 (1/2/4/0) Subsection: Physical Parameters of Fluids
85+3+13 (1/1/1/0) Subsection: Water-based fluid composition
68+2+29 (1/1/0/0) Section: Contacting Solids
423+1+0 (1/0/2/0) Section: Coatings
208+12+0 (1/0/0/0) Chapter: Influence of Oil Viscosity on Churning and
   Windage Losses at High Speeds
29+6+0 (1/0/0/0) Section: Development of Gearbox Churning Loss Rig
416+1+144 (1/7/4/0) Subsection: Gearbox
340+1+44 (1/1/13/1) Subsection: Speeds
600+2+126 (1/5/23/3) Subsection: Mesh Forces
181+4+64 (1/2/6/0) Subsection: Gear Tooth Surface Roughness
180+2+35 (1/2/3/0) Subsection: Contact Conditions
255+2+66 (1/3/0/0) Subsection: Test Rig
318+2+64 (1/2/5/0) Subsection: Power Electronics
911+5+148 (1/3/4/0) Subsection: Control Electronics and User Interface
529+3+24 (1/1/0/0) Subsection: Oil Fill Level
225+2+86 (1/1/0/0) Subsection: Temperature Control
401+2+37 (1/1/11/3) Subsection: Inertia Rundown
812+2+55 (1/4/26/4) Subsection: Inertia Measurement
435+2+169 (1/4/15/1) Subsection: Torque Measurement
355+1+0 (1/0/3/0) Subsection: Overspeeding
45+3+0 (1/0/0/0) Section: Results and Discussion
2170+23+310 (5/10/16/2) Subsection: Speed and Immersion Depth
795+6+156 (2/3/3/0) Subsection: Oil Viscosity
992+4+128 (1/2/0/0) Subsection: Steady-state vs Transient Conditions
212+1+0 (1/0/0/0) Section: Summary
141+10+0 (1/0/0/0) Chapter: Measurements of Total Drivetrain Efficiency in
   an EV Drive Unit
525+5+19 (1/2/12/0) Section: T-Axle EV Dyno Rig Overview
644+3+66 (1/2/4/0) Section: Drive Loss: No-Load
1087+2+98 (1/6/22/1) Section: Drive Efficiency
930+5+24 (1/1/21/3) Section: New European Drive Cycle Test
218+6+0 (1/0/0/0) Chapter: High-speed Elastohydrodynamic\\ Traction and Film
    Thickness
0+1+0 (1/0/0/0) Section: Methods
138+2+39 (1/1/0/0) Subsection: Test Setup
63+2+11 (1/1/1/0) Subsection: Contact Conditions
495+3+8 (1/1/2/0) Subsection: Film Thickness Measurement
688+2+18 (1/2/26/3) Subsection: Traction Measurement
```

```
123+2+0 (1/0/8/0) Subsection: Test Procedure
30+1+0 (1/0/0/0) Section: Results
277+6+168 (1/4/24/0) Subsection: Measurements of Traction and Film Thickness
413+5+58 (1/2/17/1) Subsection: Comparison to Film Thickness Predictions
225+5+39 (1/1/3/0) Subsection: Interferometric Images of the Contact
354+7+177 (1/3/31/0) Subsection: Mean Shear Stress and Shear Strain Rate
419+9+0 (1/0/7/0) Subsection: Changes in Traction and Film Thickness with
   Sliding Direction
365+8+135 (1/3/17/0) Subsection: Shear Stress Response to Viscosity and
   Fluid Composition
2115+1+152 (1/4/50/6) Section: Discussion
840+6+45 (1/1/8/0) Subsection: Difference in Traction with Sliding Direction
710+1+46 (1/1/41/3) Subsection: Viscoelasticity
194+2+0 (1/0/3/0) Subsection: Measurement Limitations
497+1+0 (1/0/0/0) Section: Conclusions
311+10+0 (1/0/1/0) Chapter: \RaggedRight Influence of Fluid Formulation on
   Surface Damage: Micropitting and Scuffing
781+1+0 (1/0/2/0) Section: Micropitting
1237+3+120 (1/5/15/2) Subsection: Micropitting Test Method
1443+4+219 (1/9/9/0) Subsection: Effect of Fluid Formulation
577+4+166 (1/4/1/0) Subsection: Effect of Roller Batch
411+3+98 (1/2/13/1) Subsection: Counterface Profile Evolution
94+1+0 (1/0/0/0) Section: Scuffing
2653+13+254 (5/8/13/0) Subsection: Scuffing Test Method
1594+5+134 (1/6/5/0) Subsection: Scuffing Performance of Transmission Fluids
265+9+0 (1/0/0/0) Chapter: Film Thickness Mapping using the Spacer Layer
   Imaging Method
648+3+0 (1/0/2/0) Section: Introduction to SLIM
768+5+77 (1/3/0/0) Section: The Spacer Layer Imaging Method
196+5+0 (1/0/0/0) Section: Limitations of the SLIM Technique
386+2+54 (1/1/2/0) Subsection: Intensity shift
384+3+36 (1/1/1/0) Subsection: Fringe Order Ambiguity
111+5+0 (1/0/0/0) Subsection: Test Procedure and Equipment Condition
311+2+0 (1/0/0/0) Subsection: Averaging Area
75+5+0 (1/0/0/0) Section: Analysis Techniques to Overcome Limitations
913+3+357 (1/5/26/0) Subsection: Context-Aware Colour Matching
1137+3+223 (1/5/25/2) Subsection: Calibration Curve Fitting
450+2+68 (1/2/12/1) Subsection: Circle Finding
629+3+16 (1/1/24/3) Subsection: Refractive Index Correction
467+1+0 (1/0/1/0) Section: Summary
195+1+0 (1/0/0/0) Chapter: Discussion
487+2+0 (1/0/0/0) Section: Load-independent losses
359+8+0 (1/0/0/0) Section: EHL Traction and Film Thickness at High Speeds
2052+2+0 (1/0/0/0) Section: Surface Damage
```

912+8+0 (1/0/1/0) Section: Influence of viscosity on load-dependent and load-independent losses
1276+1+0 (1/0/5/0) Chapter: Conclusions
894+2+0 (1/0/0/0) Section: Future Work
682+4+163 (1/5/4/0) Chapter: Gearbox Tooth Flank Surfaces
415+7+0 (1/0/20/9) Chapter: Gear Mesh and Bearing Reaction Force Calculation
304+8+0 (1/0/15/9) Chapter: Minimum EHL Film Thickness in Helical Gear Pairs
345+6+0 (1/0/23/8) Chapter: Referred Inertia of Bearing Rolling Elements
306+7+0 (1/0/4/0) Chapter: Contact Cycles in Ball and Roller Bearings
162+3+74 (1/3/0/0) Chapter: Aluminium Stator Core
345+4+122 (1/2/19/3) Chapter: Spin in Ball-on-Disc Contact
891+11+324 (1/8/2/0) Chapter: Traction Measurements over a Wide Range of Entrainment and Sliding Speeds
50+10+0 (1/0/0/0) Chapter: Measurements of EHL Traction and Film Thickness at High Speeds
304+2+0 (1/0/0/0) Section: Traction Measurements
303+3+0 (1/0/0/0) Section: Film Thickness Measurements
275+6+0 (1/0/0/0) Section: Traction and Film Thickness 3D Plots